Technical Report
RAL-TR-1998-085

Third International Workshop on the Fast Ignition of Fusion Targets

P A Norreys

8th January 1999

COUNCIL FOR THE CENTRAL LABORATORY OF THE RESEARCH COUNCILS

Enquiries about copyright, reproduction and requests for additional copies of this report should be addressed to:

The Central Laboratory of the Research Councils
Library and Information Services
Rutherford Appleton Laboratory
Chilton
Didcot
Oxfordshire
OX11 0QX
Tel: 01235 445384 Fax: 01235 446403
E-mail library@rl.ac.uk

ISSN 1358-6254

Introduction.

The 3rd International Workshop on Fast Ignition of Fusion Targets was held at the Rutherford Appleton Laboratory in the UK between 21-23rd September 1998. The workshop brought together a small number of physicists from the world's leading laboratories to discuss new results and progress in this rapidly evolving field. This 3rd workshop followed the highly successful meetings in February 1997 at Berkeley, California and at the Max Planck Institute for Quantum Optics, Germany in September 1997.

The proceeding here demonstrate that tremendous progress is being made both in both theory and experiment. In addition to new physical insights provided by two and three dimensional particle in cell simulations to describe relativistic laser plasma interactions, new hybrid codes have been developed to provide integrated descriptions of electron transport in solid density plasmas. A striking feature of the presentations was the necessity to integrate electron acceleration mechanisms arising in the coronal plasma, mechanisms which had previously been thought to be useful only to new accelerator concepts. Another new feature of this workshop was the inclusion of a session devoted to nuclear physics techniques to diagnose the plasma conditions, techniques which will undoubtedly grow in importance in future experimental work in the field.

It is hoped that this collation of viewgraphs from the workshop will assist the community in assimilating the latest results from those laboratories represented from around the world. We look forward with great anticipation to the next workshop to be held in 1999.

Peter Norreys.

Final Programme for the Third International Workshop on the Fast Ignition of Fusion Targets

Monday 21 September.

8.30 a.m. - 9.30 a.m. Registration.

9.30 a.m. - 10.30 a.m. Introduction.

9.30 - 9.50 M.H.R.Hutchinson (Director, Central Laser Facility, Rutherford Appleton Laboratory, UK).

"Welcome to the Rutherford Appleton Laboratory".

9.50 - 10.15 R.Bingham (Rutherford Appleton Laboratory, UK).

"A review of electron acceleration mechanisms with short pulse, ultra-intense laser pulses".

10.15-10.40 P.Mulser (TQE, Darmstadt, Germany)

"Fast Ignitor-relevant results from the Euronetwork SILASI (superintense laser-solid interaction)".

10.40 a.m. - 11.00 a.m. tea / coffee

11.00 a.m. - 12.30 a.m. Channelling and anomalous transmission.

11.00- 11.25 A Pukhov (Max Planck Institute for Quantum Optics, Garching, Germany).

"Physics of Short Pulse Laser Interaction with Near-Critical Plasmas via 3D PIC Simulations".

11.25 - 11.50 S Bulanov (General Physics Institute of Russian Academy of Sciences, Moscow, Russia).

"Formation of a hot plasma filament during the focusing of imploding cylindrical corona"

11.50- 12.10 M.Borghesi, A.MacKinnon, O.Willi (Imperial College, London, UK).

"Channelling in pre-formed plasmas and propagation in capillaries"

12.10- 12.30 A.Giulietti, L.Gizzi (Institute of Atomic and Molecular Physics, Pisa, Italy).

"Experiments on propagation of intense ultra-short laser pulses through thin foil plasmas"

12.30 - 1.30 p.m. Lunch

Monday 21st 1.30 p.m. - 3.00 p.m.

Electron transport theory.

1.30-1.55 J.C.Gauthier (LULI, Ecole Polytechnique, France).

"Combined PIC and MC simulations of supra-thermal electron energy deposition"

1.55-2.20 S Wilks (Lawrence Livermore National Laboratory, USA).

""PIC Simulations and Plasma Physics of Ultra-Intense Laser-Plasma Interactions"

2.20-2.45 C.Deutsch and P.Fromy, (LPGP,U-Paris XI, 91405-Orsay, France)

"Correlated Stopping of Relativistic Electrons in Super-compressed DT fuel"

2.45-3.10 M.Honda and J. Meyer-ter-Vehn (Max Planck Institute for Quantum Optics, Garching, Germany).

"PIC simulation of relativistic electron transport including collisions"

3.10p.m. - 3.30p.m. tea / coffee

3.30 p.m. - 5.00 p.m. Electron transport theory continued.

3.30 - 3.55 J.C.Adam (CPT, Ecole Polytechnique, France)

"Interaction of ultra intense pulses with strongly overdense plasma via 2D PIC simulations"

3.55 - 4.20 M.G.Haines (Imperial College, London, UK).

"Estimate of magnetic fields including the effects of microturbulence"

4.20 - 4.40 J.Davies and A.R.Bell (Imperial College, London, UK).

"The effects of magnetic fields in collimating electron flows in ultra-intense interactions"

4.40 - 5.00 Y. Sentoku (Institute of Laser Engineering, Osaka University, Japan).

"Particle simulations and experimental results on plasma jets formation and magnetic field generation".

5.00 - 5.25 R.Piriz (E.T.S.I.Industriales, Universidad de Castilla-La Mancha, Spain).

"Fast ignition dynamics"

5.45 Return to Cosener's House.

Tuesday 22nd 8.45 a.m. - 10.30 a.m Electron transport experiments.

8.45 - 9.15 M.H.Key (Lawrence Livermore National Laboratory, USA).

"Petawatt laser target physics studies relevant to fast ignition and intense MeV x-ray sources."

9.15 - 9.45 R.Kodama (Institute of Laser Engineering, Osaka University, Japan).

"The recent results on fast ignition and related plasma physics".

9.45 - 10.05 E.Clark (Imperial College, London, UK).

"A comparison of temperatures derived from measurements of the x-ray bremsstrahlung emission with those from escaping electrons generated during ultra-intense interactions with solids"

10.05 - 10.30 K. Eidmann (MPQ, Garching, Germany).

"Electron transport experiments with high contrast 150fs pulses"

10.30a.m. - 10.50 a.m. tea / coffee

10.50 a.m. - 12.30 p.m. Electron transport experiments continued.

10.50 - 11.15 F.Pisani & L.Gremillet (LULI, Ecole Polytechnique, France).

"Fast electron deposition experiment at the new TW laser in LULI: part I (Pisani) and part II (Gremillet)".

11.15 - 11.40 M.Tatarakis (Imperial College, London, UK).

"Observations of collimated electron flows in ultra intense laser interactions with thick foils"

11.40 - 12.05 D.Batani (University of Milan, Italy).

" Explanations for the increased range of fast electrons in shock compressed plasmas".

12.05 - 12.30 T.A.Hall (University of Essex, UK).

"X-ray and fast particle preheat in femtosecond laser driven transport experiments"

12.30 p.m. - 1.30 p.m. Lunch

Tuesday 22nd 1.30 - 3.00 p.m. Nuclear reactions.

1.30 - 1.55 D.Pennington (Lawrence Livermore National Laboratory, USA)

"Nuclear activation observations at the LLNL petawatt laser ."

1.55 - 2.20 L.Disdier (CEA, Bruyeres-le-Chatel, France)

"Neutron emission produced by high intensity subpicosecond laser pulse"

2.20 - 2.45 C.Toupin (CEA, Bruyeres-le-Chatel, France).

"Fast Ion generation and correlated neutron production in the interaction of an ultra-intense laser pulse with an overdense plasma"

2.45 - 3.10 R.P Singhal **(University of Glasgow, UK)**

"Observation of a highly directional gamma-ray beam from ultra-short, ultra-intense laser pulse interactions with solids"

3.10p.m. - 3.30p.m. tea / coffee

3.30 p.m. - 5.00 p.m.

PIC code validation experiments & electron parametric instabilities:

3.30 - 3.55 M.Zepf (Imperial College, London, UK).

"Validation of PIC simulations for fast ignition: the role of density scale-lengths in the generation of harmonics from overdense plasmas".

3.55 - 4.20 P.Mora (CPT, Ecole Polytechnique, France).

"Propagation of ultra-intense laser pulses in underdense plasmas"

4.20 - 4.45 A.Machacek (University of Oxford, UK).

"Observation and discussion of stimulated optical scattering in ultra-intense laser interactions with solids."

4.45 - 5.10 H.C. Barr, P. Mason and D.M. Parr (University of Essex, UK)

"Electron parametric instabilities driven by ultraintense linearly polarised laser pulses in under and overdense plasma"

6.30 p.m. Dinner at the Coseners' House.

7.30 p.m. - 9.30 p.m. Round table discussion on the outstanding issues to be tackled for the Fast Ignitor.

Session to be led by Professor J.Meyer-ter-Vehn "A critical review of the fast ignitor concept"

FUTURE ACCELERATORS USING LASERS

R BINGHAM (RAL)

Workshop: Particle Accelerators for Particle Physics - 23 October 1998

High Energy Particles.

Relativistic Plasma Wave Acceleration

The problem is to generate large amplitude plasma wave travelling with a velocity close to the speed of light c

4 Approaches

1. Plama Beat Wave
2. Laser Plasma Wakefield
3. Electron Beam Plasma Wakefield
4. Self-Modulated Laser Wakefield (RFS).

- Conventional accelerators limited by electrical breakdown of accelerating structures ($E_{\text{acc}} \sim 20MV/m$)

- Plasmas are already broken down.
  The accelerating fields limited only by plasma density.

- Plasmas can support longitudinal accelerating electric fields moving close to the speed of light; Relativistic electron plasma waves.

- Lasers easily couple to plasmas and can generate relativistic electron plasma waves.

Drivers for Plasma Based Accelerators

1. Lasers — Terawatt, Petawatt Compact Lasers $10^{12}--10^{15}Watts$ already exist.
   Some with high rep. rates ie **10Hz**.
   Capable of $10^{19}--10^{21}Watts/cm^2$ on target.
   Future $\sim 10^{23}W/cm^2$ using OPCPA.

2. Electrons Beams — Shaped electron beams such as the proposed Stanford/USC/UCLA experiment to generate $1GV/m$ accelerating gradient using the $30-50GeV$ beam in a 1 meter long Lithium Plasma.

LASER PLASMA ACCELERATORS

- Large Accelerating Fields

$$\sim 1 GeV/cm$$

- No Electrial Breakdown Limit
- Low repetion rates.
- can be expensive.

TABLE 1. Generation of high-intensity optical fields by femtosecond laser systems

Systems	Limiting parameters		Experimental achievements*			Expected values		
	τ (fs)	w_s (J/cm^2)	τ (fs)	W (J)	I (W/cm^2)	τ (fs)	W (J)	I (W/cm^2)
XeCl eximer ($\lambda = 0.308$ μm)	160	0.002	160	0.4	10^{17}	160	10	10^{21}
KrF eximer ($\lambda = 0.24$ μm)	70	0.002	80	1.5	10^{18}	70	10	10^{22}
Dye (visible)	10	0.001	20	5×10^{-4}	10^{14}	10	0.01	10^{17}
Broad band solid state (visible, IR)	10	1.0	100	0.05	10^{18}	10	10	10^{24}
Nd-glass	600	1.0	700	8	10^{19-20}	600	100	10^{23}
CO_2 ($\lambda = 10.6$ μm)	60	0.4	2500	0.2	10^{16}	100	1	10^{19}

CLRC

LASER PLASMA ACCELERATORS

- The electric field of a laser in vacuum is given by

$$E_\perp = 30\sqrt{I}\ GV/cm \qquad (1)$$

for short pulse intense laser,

$$P = 10TW, \lambda_o = 1\mu m,\ I = 1.6 \times 10^{18} W/cm^2$$

$$E_\perp = 40\ GV/cm$$

- Unfortunately this field is perpendicular to the direction of propagation and no significant acceleration takes place

- The longitudinal electric fields $E_\parallel$ associated with relativistic electron plasma waves can be extremely large and can accelerate charged particle.

CLRC

- The Lorentz force due to the interaction of the lasers produces a longitudional force or "ponderomotive" force of the beat pattern proportional to the gradient of $< E_\perp^2 >$.

- Each beat (pulse) adds to the plasma waves amplitude.
  The growth in time

$$eE_\parallel = \frac{m_e c\omega_p}{4} \int_o^{t_o} \alpha_1 \alpha_2 dt \qquad (2)$$

$\alpha_{1,2} = \frac{eE_{\perp 1,2}}{m_e c\omega_{1,2}}$ is the quiver velocity of an electron in the laser field, normalized to the speed of light c

- From Gauss' Law the accelerating field $E_\parallel$ can be estimated

$$E_\parallel = \epsilon \frac{m_e c\omega_p}{e} \qquad (3)$$

or

$$E_\parallel = \epsilon\sqrt{n_o} V/cm$$

ϵ is plasma wave amplitude (fractional electron density bunching n_1/n_o, n_o is ambient density.

- For $n_0 = 10^{18} cm^{-3}$, $\quad \varepsilon = n_1/n_0 = 10\%$

$$E_{\parallel} = 10^8 V/cm \tag{4}$$

- Gain in energy of electron ΔW

$$\Delta W = 2\varepsilon\gamma^2 m_e c^2 \tag{5}$$

$\gamma = \frac{\omega_1}{\omega_p}$ the Lorentz factor

For a neodymium laser $\frac{\omega_1}{\omega_p} \sim 30$ for
$n_0 \sim 10^{18} cm^{-3}$

$$\underline{\Delta W \simeq 100 MeV}$$

- **Maximum energy gain** $\Delta W \simeq eE_p/\ell$

$E_p = \frac{e}{k_p}\delta n = \frac{ec}{\omega_p}\delta n$

$\ell = \frac{\lambda_p}{2}\chi \; ; \; \chi = \frac{c}{c - v_{ph}} \; ; \; v_{ph} \simeq c\left(1 - \frac{\omega_p^2}{\omega^2}\right)^{\frac{1}{2}}$

$\ell = \frac{\lambda_p}{2}\frac{\omega^2}{\omega_p^2} = \frac{\lambda_p}{2}\gamma^2$

$eE\ell = 2\varepsilon\gamma^2 mc^2$

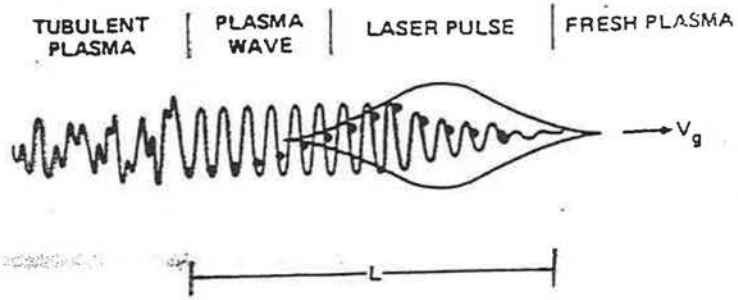

PULSE MUST BE SHORT $\tau_{PULSE} < \omega_{Pi}^{-1}$

FOR LONG PULSES - MODULATIONAL INSTABILITY INVOLVING IONS BECOMES IMPORTANT

(F. AMIRANOFF et al PRL 68 1992)

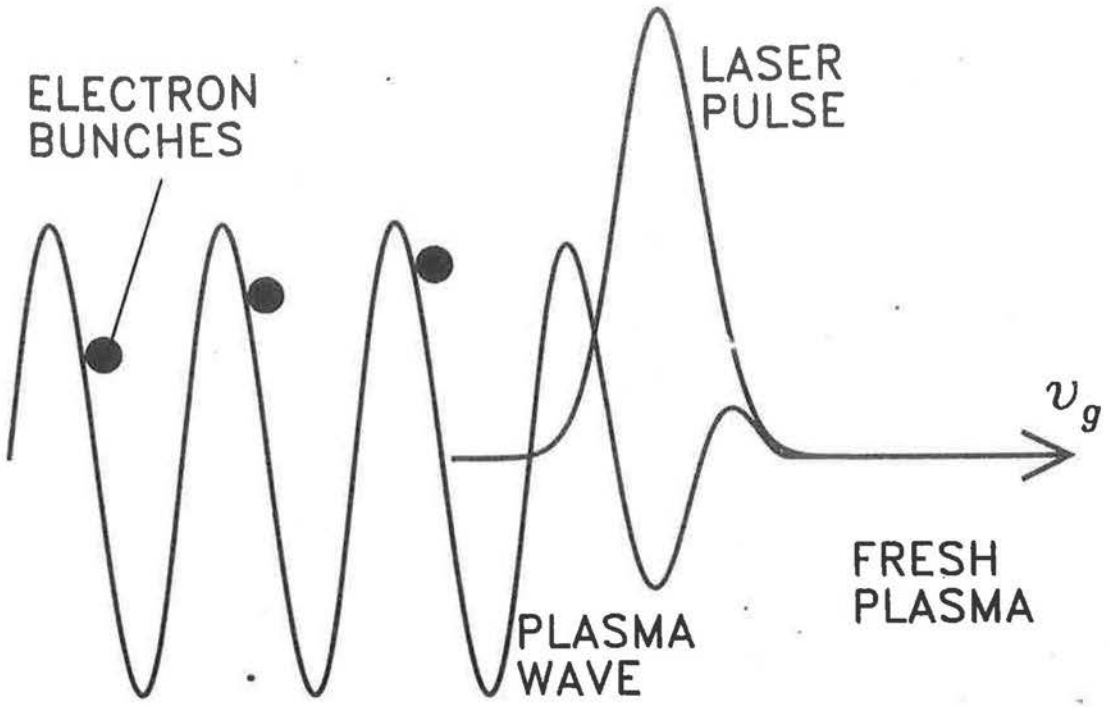
ELECTRON
BUNCHES
LASER
PULSE
v_g
FRESH
PLASMA
PLASMA
WAVE

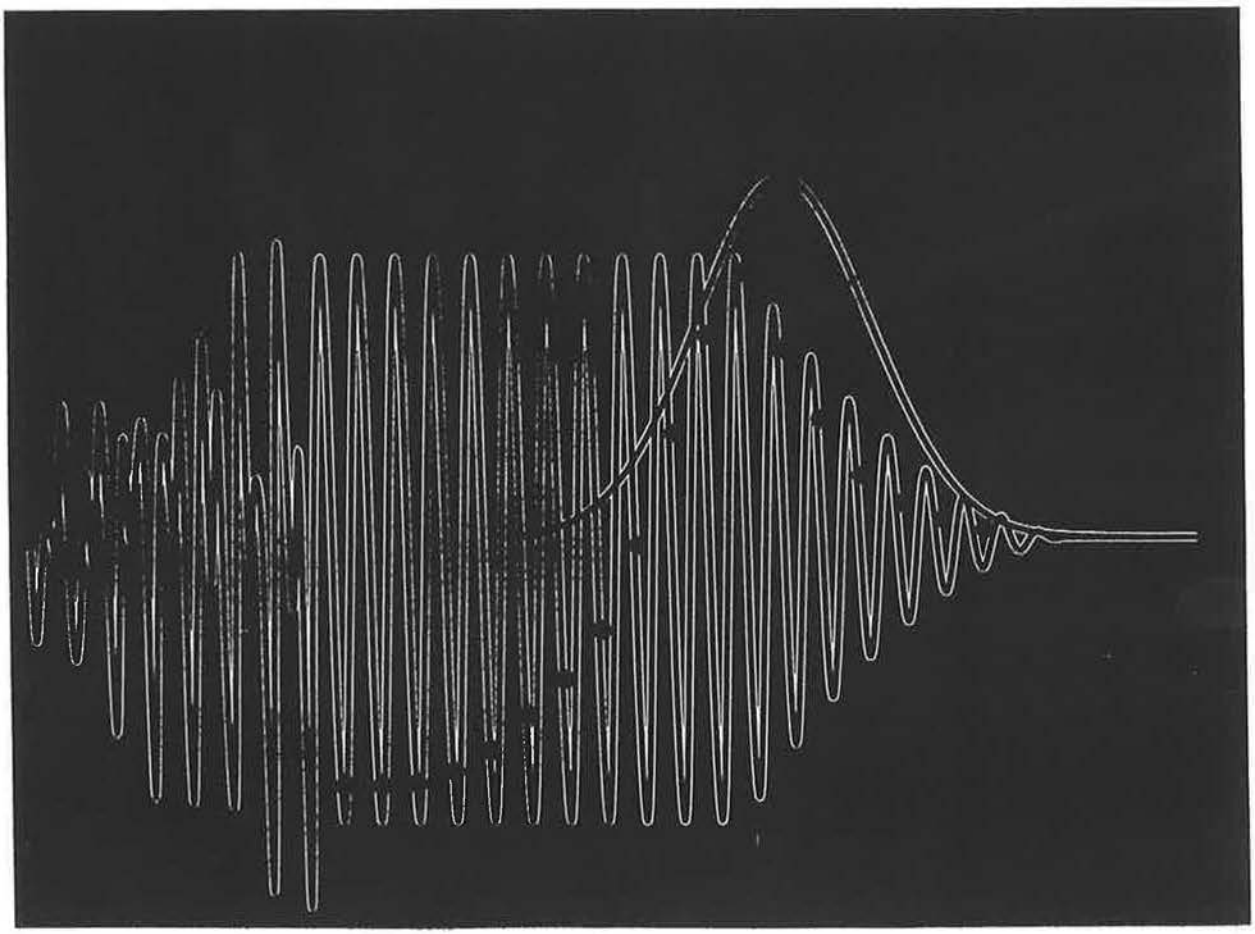

CLRC

WAKEFIELD EXPERIMENTS (LWFA)

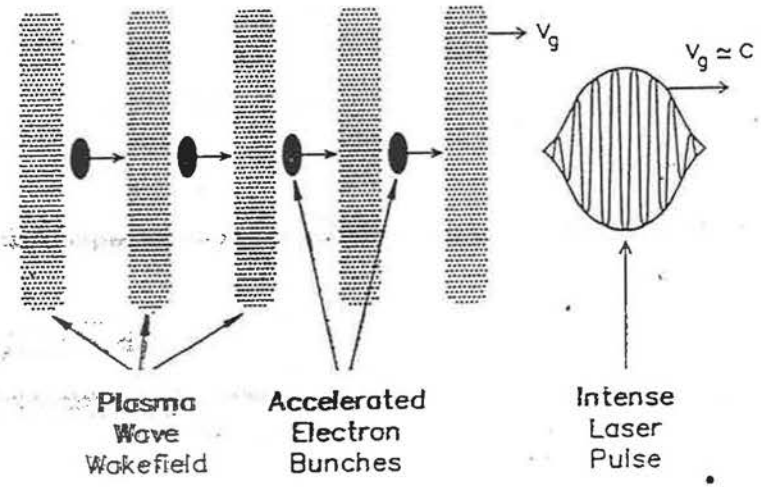

RECENT CONFIRMATION OF WAKEFIELD GENERATION – J.R. MARQUES et al PRL 76 2506(19
C.W. SIDERS et al PRL 76 3570 (1996).

ACCELERATION – F. AMIRANOFF et. al. PRL 81, 995 (1998)

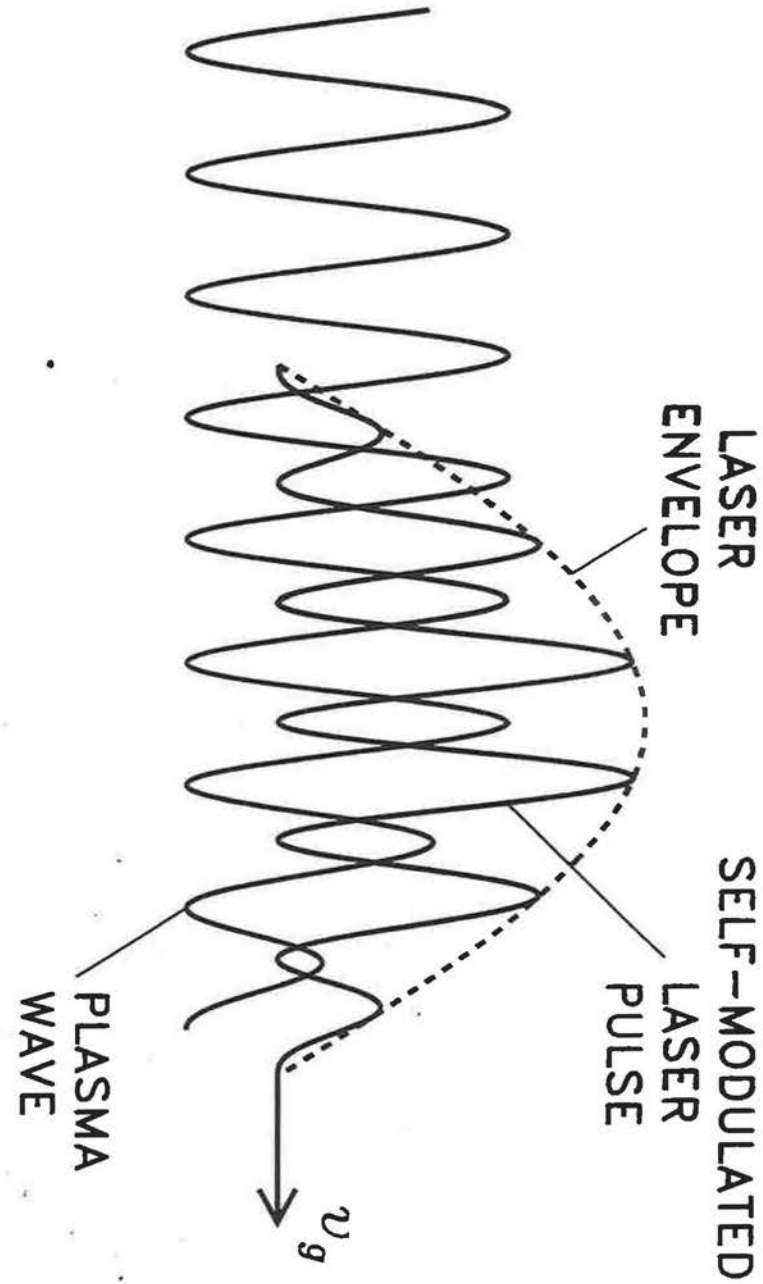

CLRC

- In the Plasma Beat Wave Accelerator (PBWA) a relativistic plasma wave is resonantly excited by the "ponderomotive" force of two lasers seperated by the plasma frequency ω_p.

- The two laser beams beat together forming a modulated beat pattern in the plasma.

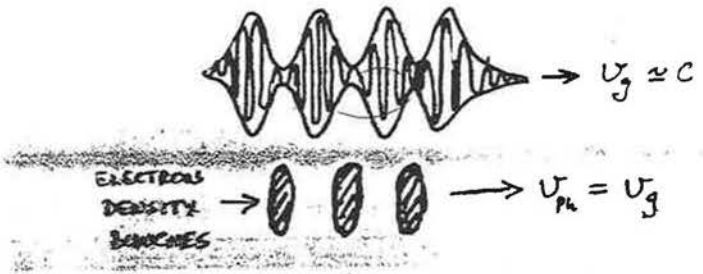

- For relativistic plasma waves the accelerating field $E_\parallel$ is given by

$$E_\parallel = \epsilon\sqrt{n_o}\ V/cm$$

ϵ is the fractional electron density bunching, n_o is the plasma density. For $n_o = 10^{18} cm^{-3}$, $\epsilon = 10\%$

$$E_\parallel = 10^8\ V/cm$$

Plasma Beat Wave

Relativistic plasma wave driven by beating 2 lasers in a plasma

$$\omega_1 - \omega_2 \simeq \omega_p \qquad \text{energy}$$

$$\underline{k}_1 - \underline{k}_2 \simeq k_p \qquad \text{momentum}$$

For $\omega_1, \omega_2 \gg \omega_p$ ie $\omega_1 = 10\omega_p$, $\omega_2 = 9\omega_p$

Then $\left.\begin{matrix} k_1 - k_2 \sim \Delta k \\ \omega_1 - \omega_2 \sim \Delta\omega \end{matrix}\right\}$ $\frac{\Delta\omega}{\Delta k} = v_g$

v_g is group velocity of laser bet pattern.

But $k_1 - k_2 \sim k_p$; $\omega_1 - \omega_2 \sim \omega_p$

$$\Longrightarrow \frac{\omega_p}{k_p} = v_{ph} \equiv v_g \qquad v_g = c\left(1 - \frac{\omega_p^2}{\omega_{1,2}}\right)^{\frac{1}{2}}$$

For $\omega_1, \omega_2 \gg \omega_p \Longrightarrow v_g \approx c$ "Hence relativistic"

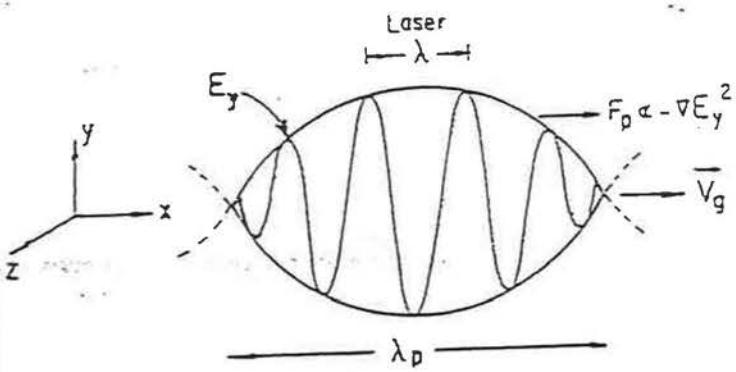

Envelope of high frequency field moving at group speed v_g;

$$v_g = c\left(1 - \frac{\omega_{pe}^2}{\omega^2}\right)^{\frac{1}{2}}$$

$$\left\{ \begin{array}{l} \omega^2 = \omega_{pe}^2 + c^2k^2 \\ v_g = \frac{d\omega}{dk} = \frac{c^2k}{\omega} = c\left(1 - \frac{\omega_{pe}^2}{\omega^2}\right)^{\frac{1}{2}} \end{array} \right\}$$

Ponderomotive force $F_p = -\nabla E_y^2$

Laser field E_y

- From Poisson's equation we can estimate how large these longitudinal electron plasma waves can be

$$\nabla \cdot E = 4\pi e \delta n_e$$

δn_e is perturbed electron density of the plasma ions immobile on short time scales.

Largest fields exist for $\delta n_e = n_o$ ie background density.

- Electron plasma waves oscillate with frequency $\omega_p = (4\pi n_o e^2/m_e)^{\frac{1}{2}}$ cgs, or $(n_o e^2/m_e \varepsilon_o)^{\frac{1}{2}}$ MKS.

Relativistic plasma waves have phase velocities close to c ie $\frac{\omega_p}{k_p} \simeq c$.

- With Poisson's equation we get

$$eE_{\mathrm{MAX}} \approx \frac{4\pi n_o e^2}{(\omega_p/c)} + mc\omega_p \simeq 0.97\sqrt{n}eV/cm$$

ie $eE_{\mathrm{MAX}} \approx \sqrt{n}eV/cm$

LASER AND ELECTRON BEAM GENERATED PLASMA WAVES.

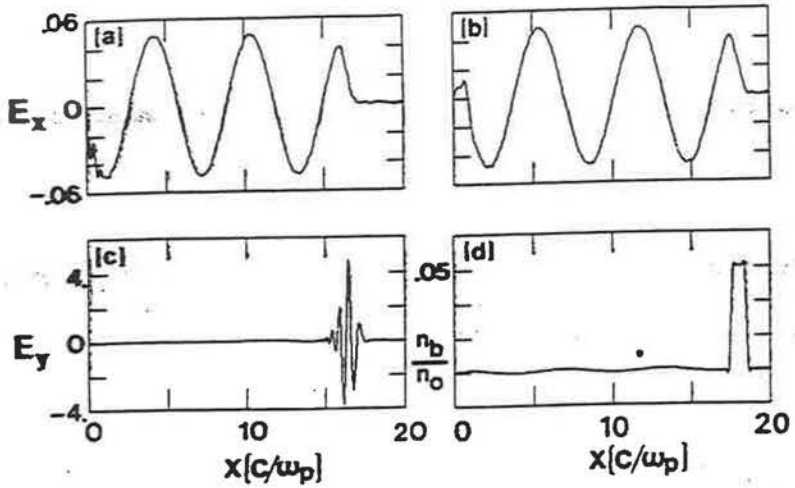

SHORT LASER PULSE.

NARROW SHORT e- beam.

BEAT WAVE GENERATED PLASMA WAVE

PBWA - PLASMA BEAT WAVE ACCELERATOR

[S. WILKS PPS. 1262]

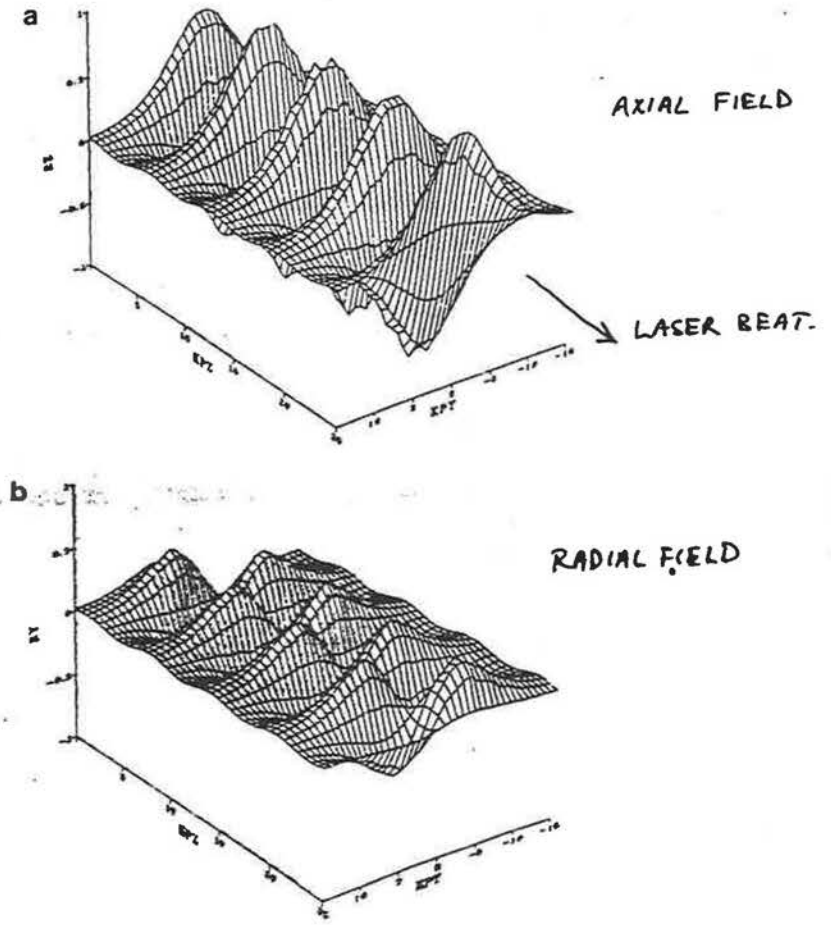

ELECTRON BEAM GENERATED PLASMA WAVE

(PWFA – PLASMA WAKEFIELD ACCELERATOR)

[S. WILKS et al PPS-1262]

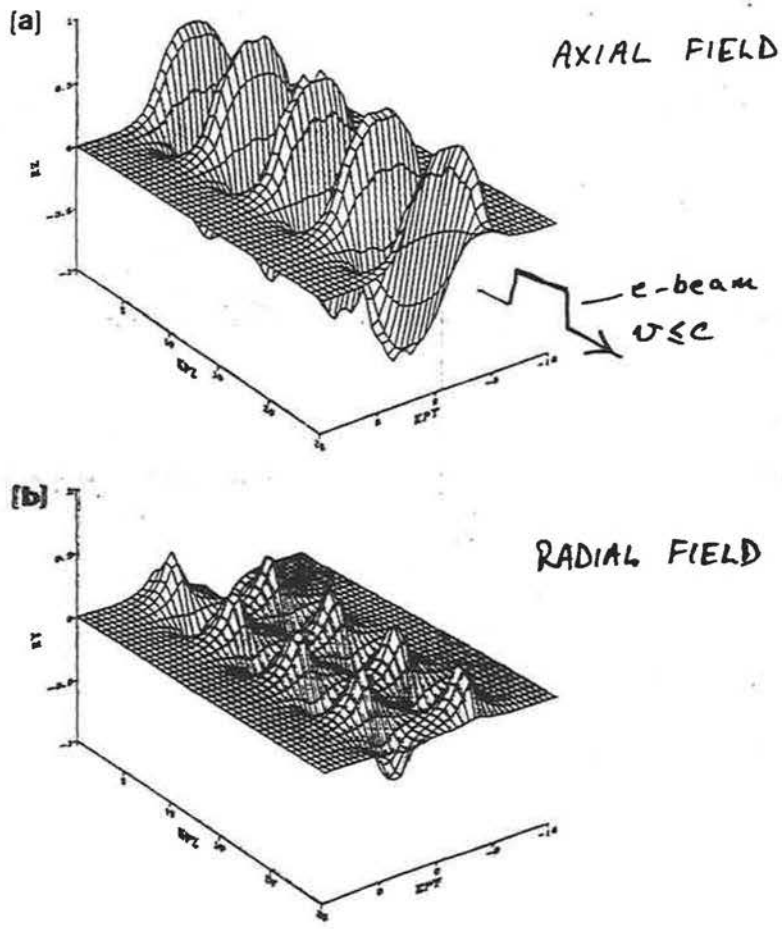

BEAM LOADING.

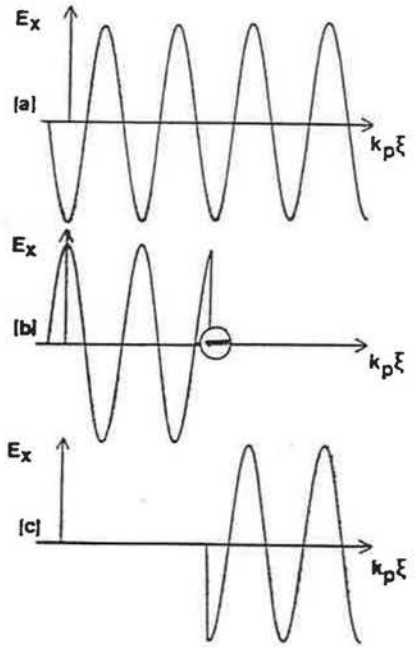

- Fields in a plasma of finite extent.

  Plasma Beat Wave Accelerator.

$$\frac{\partial n_1}{\partial t} + n_o (\underline{\nabla} \cdot \underline{v}_1) = 0 \qquad (1a)$$

$$\frac{\partial \underline{v}_1}{\partial t} = \frac{eE_1}{m_e} + \frac{F_{\text{ext}}}{m_e} \qquad (1b)$$

solve for n_1. E_1 is electric field due to n_1 and F_{ext} is external force due to driver for the laser this is the ponderomotive force.

The averaged Hamiltonian for the laser case is

$$H = \frac{p^2}{2m} + e\phi_1 + \frac{e^2}{4m\omega^2} E_o^2(r) \cos(k_p z - \omega_p t) \qquad (2)$$

(averaged over fast space and time scales of the laser ω_o laser $> \omega_p$ of plasma following P Chen and R Ruth (AIP conf. No.130, 1985) the radial dependence of Ponderomotive potential given by

$$E_o^2(r) = 2E_o^2 \begin{cases} K_2(k_p a) I_o(k_p r) + \frac{1}{2} - \frac{2}{(k_p a)^2} - \frac{r^2}{2a^2} & ; r < a \\ I_2(k_p a) K_o(k_p r) & ; r > a \end{cases} \qquad (3)$$

K_n and I_n are the modified Bessel functions.

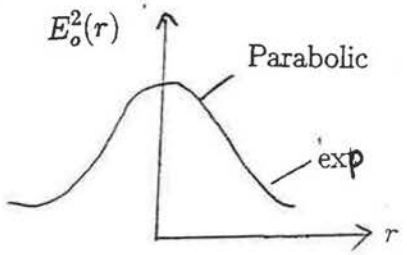

$$\nabla \cdot F = 4\pi n_1 e^2 + \frac{e^2 E_o^2 k_p^2}{4m\omega^2} \left(1 - \frac{r^2}{a^2}\right) \cos(k_p z - \omega_p t) \qquad (4)$$

Substituting 4 into equations 1 yields

$$\frac{\partial^2 n_1}{\partial t^2} + \omega_p^2 n_1 = \left\{ -\left(\frac{\omega_p}{\omega}\right)^2 \frac{E_o^2 k_p^2}{16\pi m} \left(1 - \frac{r^2}{a^2}\right) \cos(k_p z - \omega_p t) \right.;$$

For the case of the Plasma Wakefield Accelerator the situation is very similar.

Driving beam of electrons, density n_b

$$\underline{\nabla} \cdot \underline{F} = 4\pi e^2 (n_1 + n_b)$$

$$n_{vb} = \sigma(r)\delta(z - u_b t)$$

Then $N_1(r) = k_p \sigma(r) \sin(k_p z - \omega_p t)$

Using a parabolic distribution for the beam

$$\begin{aligned} \sigma(r) &= \tfrac{2N}{\pi a^2}(1 - r^2/a^2) && r < a \\ &= 0 && r > a \end{aligned}$$

This gives

$$E_z = -\frac{16eN}{a^2}\left\{K_2(k_p a) I_o(k_p r) + \frac{1}{2} - \frac{2}{(k_p a)^2} - \frac{r^2}{2a^2}\right\} \cos(k_p z - \omega_p t$$

$$E_r = -\frac{16eN}{a^2}\left\{K_2(k_p a) I_1(k_p r) - \frac{r}{k_p a^2}\right\} \sin(k_p z - \omega_p t)$$

solution of (5)

$$n_1(r, z, t) = f(r, z, t) \sin(k_p z - \omega_p t)$$

$$f(r, z, t) = -\frac{E_o^2 k_p^2}{32\pi m \omega^2}\left(1 - \frac{r^2}{a^2}\right)$$

From Poissons equation

$$\frac{1}{r}\frac{\partial}{\partial r}\left(r\frac{\partial}{\partial r}\phi_1\right) = \frac{\partial^2 \phi_1}{\partial z^2} = -4\pi e n_1$$

Solving for ϕ_1 we can get E_z and E_r ie longitudinal and radial electric field gradients.

$$E_z = -\frac{\omega_p \tau k_p e E_o^2}{4\omega^2 m}\left\{K_2(k_p a) I_o(k_p r) + \frac{1}{2}\left(1 - \frac{r^2}{a^2}\right) - \frac{2}{(k_p a)^2}\right\} \times \cos(k_p z - \omega_p t)$$

$$E_r = -\frac{\omega_p \tau k_p e E_o^2}{4\omega^2 m}\left\{K_2(k_p a) I_1(k_p r) - \frac{r}{k_p a^2}\right\} \sin(k_p z - \omega_p t)$$

τ is pulse length.

The fields are remarkably similar in both cases.

if $k_p a \gg 1$

$$E_z \approx -A\left(1 - \frac{r^2}{a^2}\right)\cos\left(k_p z - \omega_p t\right)$$

$$E_r \approx 2A\frac{r}{k_p a^2}\sin\left(k_p z - \omega_p t\right)$$

$A = \frac{\omega_p \tau k_p e E_o^2}{8\omega^2 m}$ for Lasers

$A = \frac{8eN}{a^2}$ for e-beam

eE_z force accelerates or decelerates electrons.

eE_r will focus or defocus electrons.

- Acceleration and focussing over $\frac{1}{4}$ of the plasma wavelength.

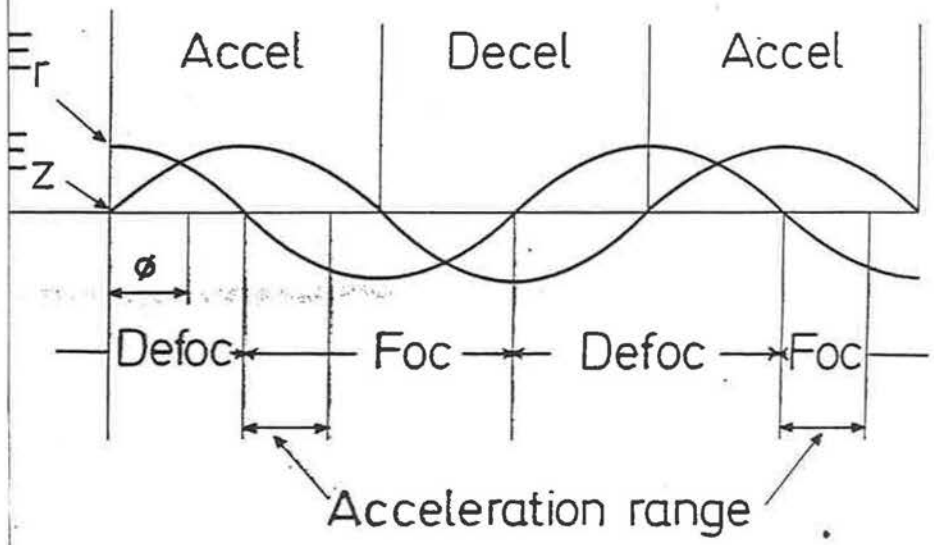

Fig 1 Accelerating and focusing fields, illustrating the phase range available for acceleration.

Laser Plasma Experiments

Experiments are being conducted world wide using the Plasma Beat Wave Scheme UK (RAL), USA (UCLA), France (CNRS) and Japan (KEK).

RAL Experiments

- 2 variations a) Plasma Beat Wave Accelerator and b) Self-Modulated Laser Wavefield Accelerator.

b) The Self-Modulated Laser Wavefield Accelerator uses a short pulse intense laser (Vulcan)

$P = 25TW(25 \times 10^{12} Watts)$

$\tau = 500 - 800 fsec$

Max Intensity $I = 6 \times 10^{18} W/cm^2$

Plasma density $n_{PLASMA} = 1.5 \times 10^{19} cm^{-3}$

Particles accelerated from background to $44MeV$ in a distance of $.035cm$

This corresponds to an accelerating field of

$$E_{\parallel} \simeq 1\ GV/cm$$

⇒ PARTICLE ENERGY ~ 100 MeV

L ~ 1-2 mm ; n ~ 10^{8}

Current Experiments

Experiment	Mech.	P(TW)	Target/ Gas	E_{inj}	F(HZ)	Guide?	n_0	a_0	dn/n (%)	E_{acc} (GeV/m)	Dg_{max} (MeV)
JAPAN	LWFA	0.5	-	33	10	Self-Channeling	10^{18}	0.5	5	~5	100
FRANCE Wakefield	LWFA	0.2	Back filled He	1.5	10	No	$5x10^{15}$ - $1.5x10^{17}$	0.3	~100	1	1.6
UT	LWF	0.2	He	-	10	No, but possible modification	$3x10^{17}$	0.3	~100	-	-
RAL	self-mod (FRS)	20	4mm jet He	self-trapped (1)	10^{-3}	Not necessary but often observed	$1.5x10^{19}$	2.0	50-100	>100	100
UM/UT	self-mod	1-6	He 0.75 mm	-	1/200	Yes	$3x10^{19}$	1-2	10-30	5-100	>20MeV
NRL	self-mod	3	H_2/He Gas jet	-	1/180	Yes	$1.4x10^{19}$	2.2	10	~60	30MeV
LLNL	self-mod (FRS)	3	0.8mm jet He	self-trapped (1)	$3x10^{-3}$	Not diagnosed	$2x10^{19}$	1.0	>1	>2.5	>2MeV
UCLA	PBWA	0.2	Static fill H_2	2MeV	$3x10^{-3}$	No	$5.8x10^{16}$	0.2	35	3	30
FRANCE	PBWA	0.022 0.13	Static D_2 2.27mb	5.9	1/1000	No	$1.1x10^{17}$	0.01 .025	2.4	0.7	1.3
AWA/ UCLA	PBWA	20nc 1kA peak e beam	Ar	26	1-30	self-formed ion channel	10^{13}	-	~100		0.5 measured 5 projected

UCLA Experiments

- UCLA Plasma Beat Wave Accelerator

CO_2 Laser, 2 wavelengths $\lambda_1 = 10.29\mu m, \lambda_2 = 10.59\mu m, \lambda_p = 360\mu m, n_{PLASMA} = 10^{16} cm^{-3} \alpha_1 = 0.17, \alpha_2 = 0.07, \tau = 150 psec$

Electrons injected at $2.1 MeV$ are accelerated to $30 MeV$ in a plasma length $1 cm$ corresponding to an accelerating field

$$E_{\parallel} = 30 MeV/cm$$

AMPLITUDE OF REL. PLASMA WAVE $\epsilon = .30\%$

1st SUCCESSFUL DEMONSTRATION.

C. CLAYTON et al PHYS. REV. LETT. 70, 37 (1994)

M. EVERETT et al NATURE 368, 527 (1994).

0.3 GHz rf LINAC ⇒ TRAIN OF PULSES, 10 μs DURATION.

EMITTANCE 6π mm-mrad.

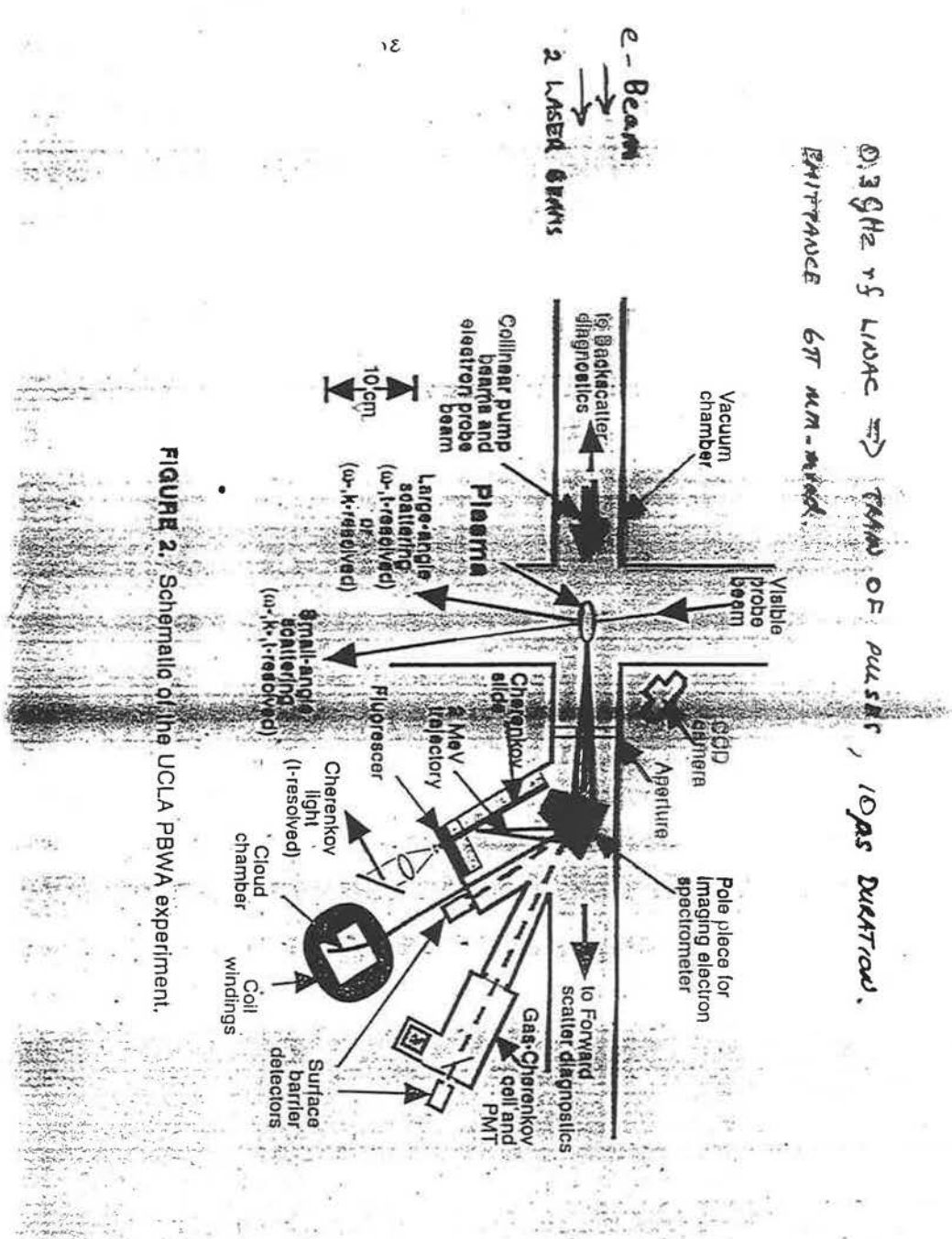

FIGURE 2. Schematic of the UCLA PBWA experiment.

UCLA EXP. RESULTS.

ELECTRONS INJECTED FROM 0.3GHz rf LINAC.

⇒ TRAIN OF MICRO PULSES <10ps.

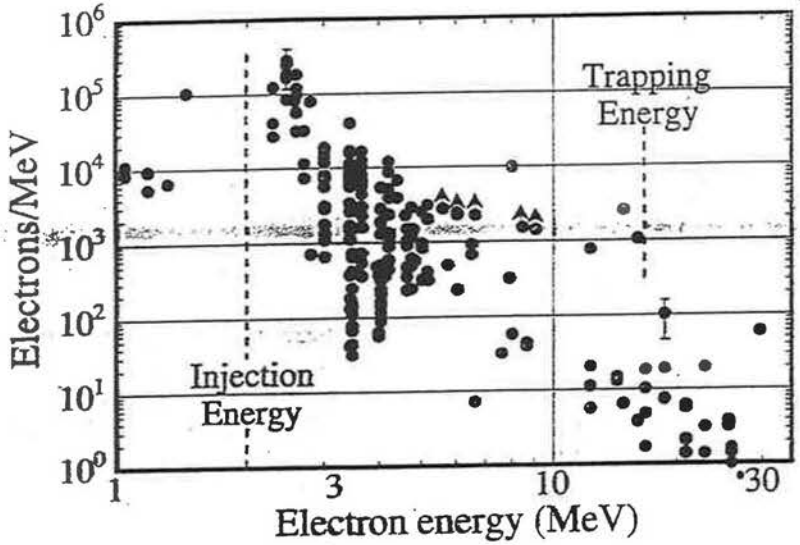

1% or 10^5 ELECTRONS ARE ACCELERATED. IN THE DIFFRACTION LENGTH OF ~1cm.

2 → 30 MeV

GRADIENT OF 3GeV/m

RAL, UCLA, IC, E.P. EXPERIMENT

(GORDON et al PRL 80, 2133 (1998)

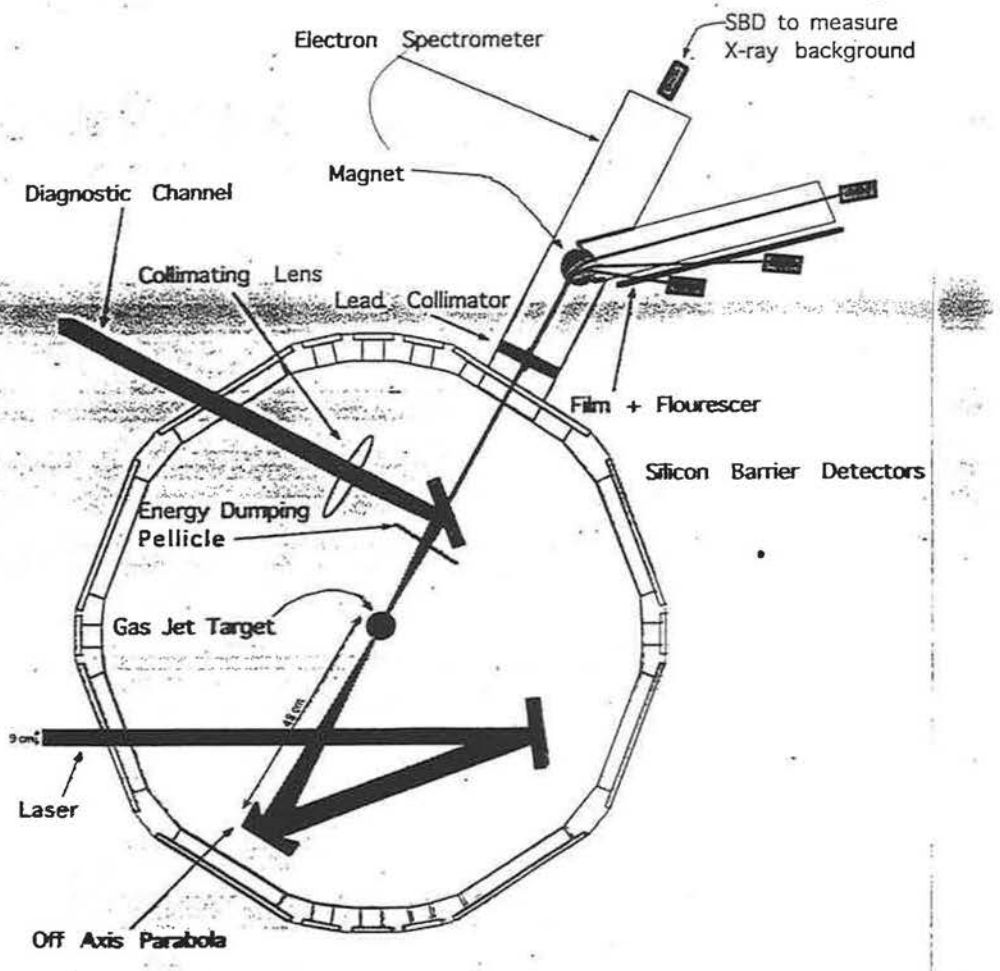

CORRECTED LASER SPECTRA.

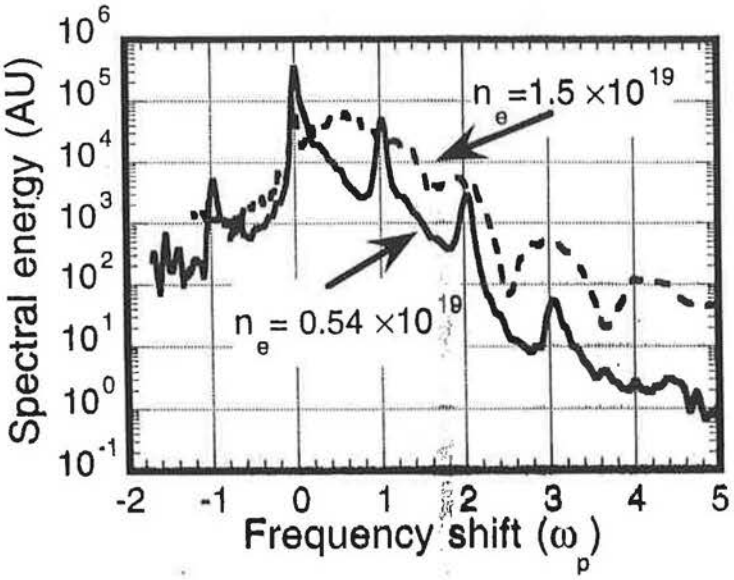

FIG 4

(A. MODENA IEEE 1996)

ELECTRON FLUX VS LASER POWER

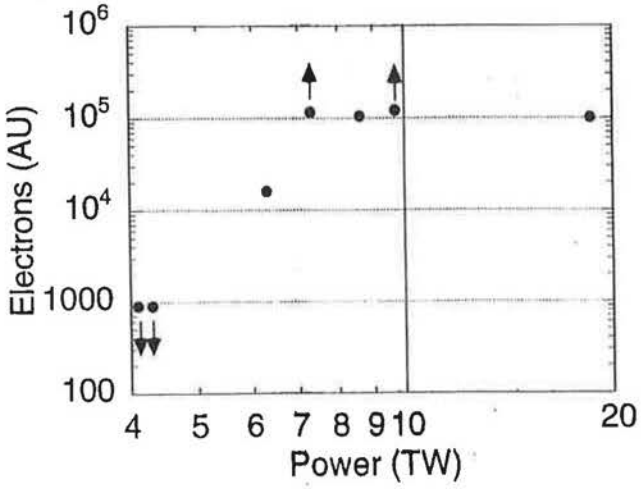

FIG 5

(MODENA et al IEEE 1996

GORDON et al PRL 80, 2133 (1998

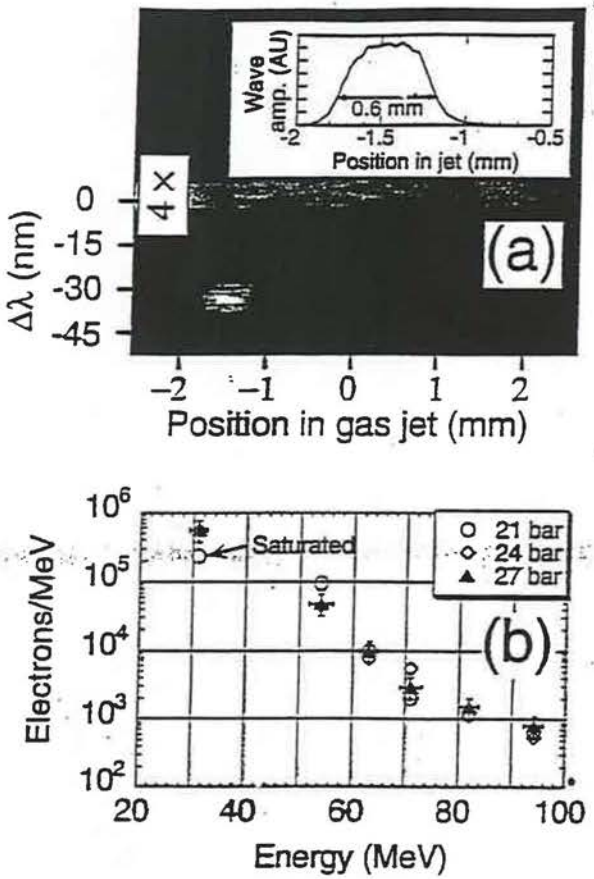

FIG. 1. (a) Thomson scattered spectrum vs distance along the gas jet indicating the spatial extent of the relativistic plasma wave. Position zero is the center of the 4 mm diameter gas jet. The laser propagates from left to right and is focused at −2.0 mm. The stray light at $\Delta\lambda = 0$ has been attenuated by 4. The gas jet backing pressure was 21 bars. Wave amplitude vs position is shown in inset. (b) The electron spectra measured in the forward $f/100$ cone angle at three backing pressures. The horizontal error bars indicate the range of energies incident on each detector as well as taking into account possible positioning errors. The vertical error bars reflect the uncertainty in detector sensitivity. The signal to noise ratio is independent of this error

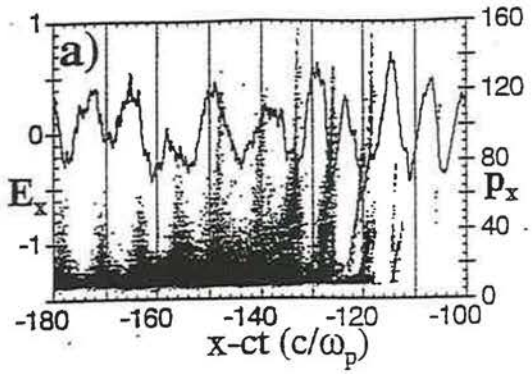

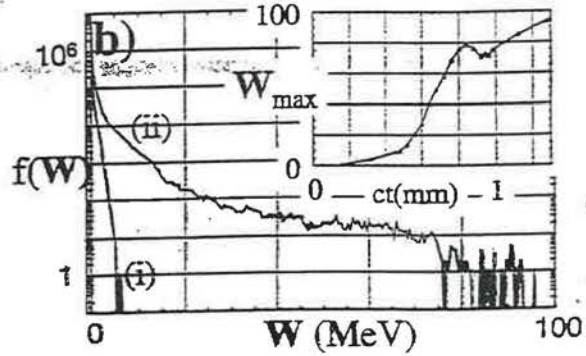

FIG. 2. (a) The normalized electric field E_x (lines) in units of $mc\omega_p/e$ and the normalized electron longitudinal momentum P_x (dots) in units of mc vs distance from the leading edge of the laser pulse $(x - ct)$ in units of c/ω_p fixing x at 1 mm into the plasma. (b) Maximum electron energy W_{max} in MeV vs ct (inset) and the electron distribution functions at $ct = 0.4$ mm (i) and 1.3 mm (ii).

GORDON et al. PRL 80, 2133 (1998)

IC, ECOLE POLYTECHNIQUE, UCLA, RAL EXP.

Distribution Function vs. k-spectrum for Run L1.4 2

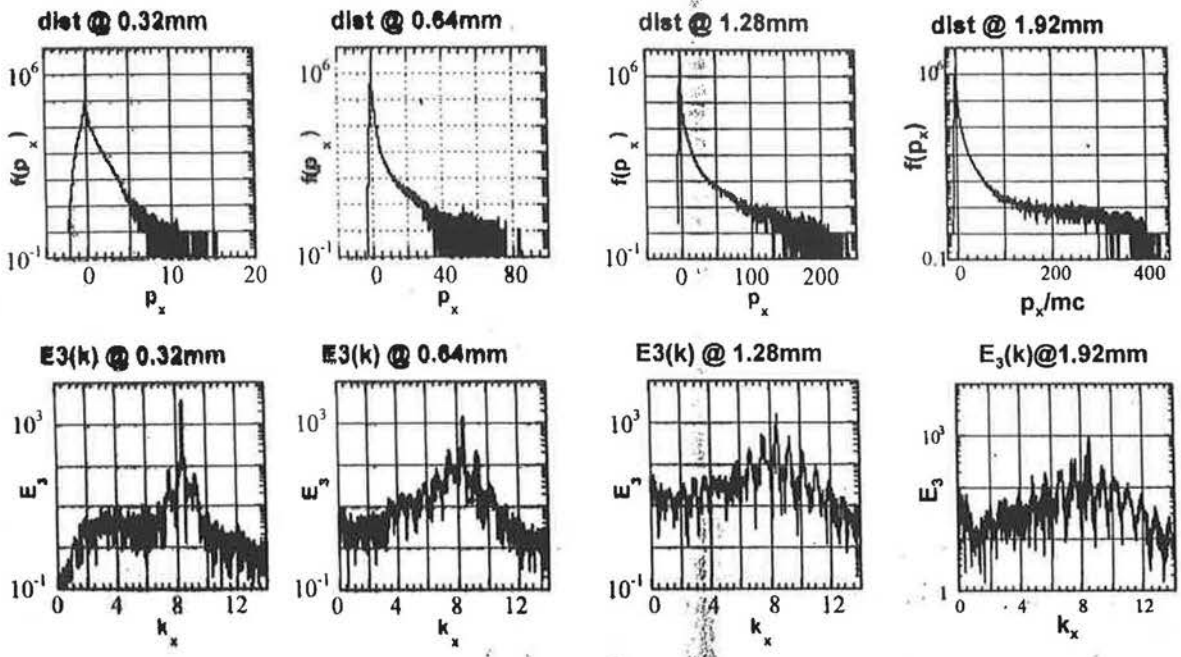

DOE Review 1996 by K-C Tzeng

K-C TZENG & W.B. MORI (1996

Evoluation of Laser Intensity and Accelerating Electric Field -- a Simulation for RAL experiment

Laser Intensity

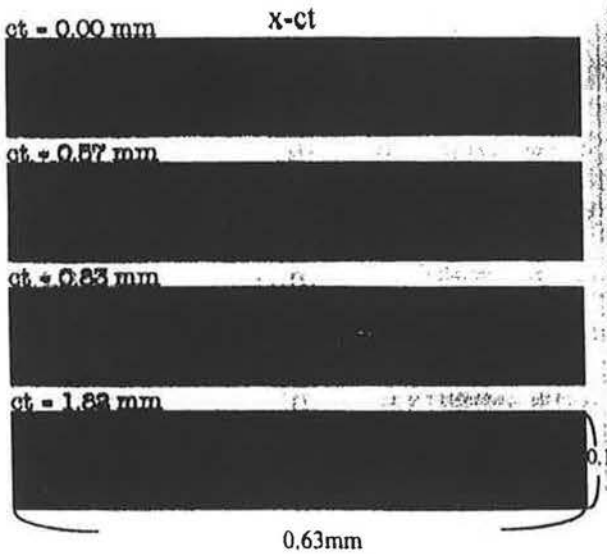

Accelerating Electric Field

Max=3 GeV/cm

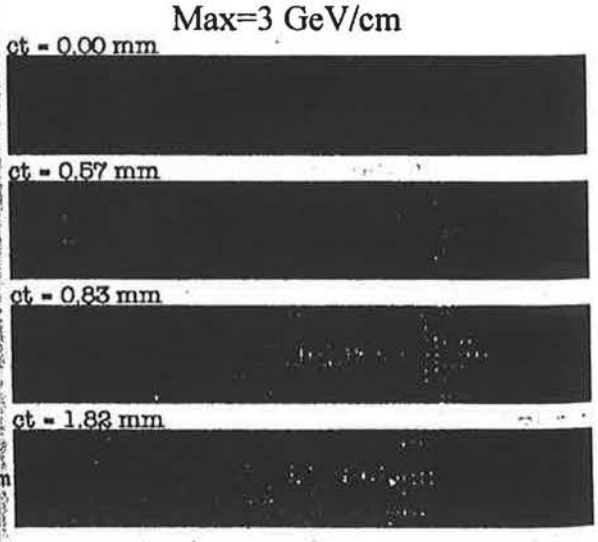

K-C TZENG & W MORI 1996

by K.-C. Tzeng

Laser Accelerators

Limits to Energy Gain

Diffraction

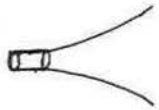

$$eE_{max} = 1GeV \left(\frac{n_0}{10^{18}}\right)^{1/2} \left(\frac{\sigma}{33\mu}\right)^2 \frac{1\mu}{\lambda}\varepsilon \qquad \text{linear theory } (\varepsilon < 1)$$

Dephasing

$$eE_{max} = 1GeV \frac{10^{18}}{n_0} \frac{1\mu}{\lambda^2} \cdot \varepsilon$$

Pump Depletion/Instabilities

$$eE_{max} = 1GeV \frac{10^{18}}{n_0} \frac{1\mu}{\lambda^2} \qquad \textbf{pump depletion}$$

PLASMA FOCUSSING LENS

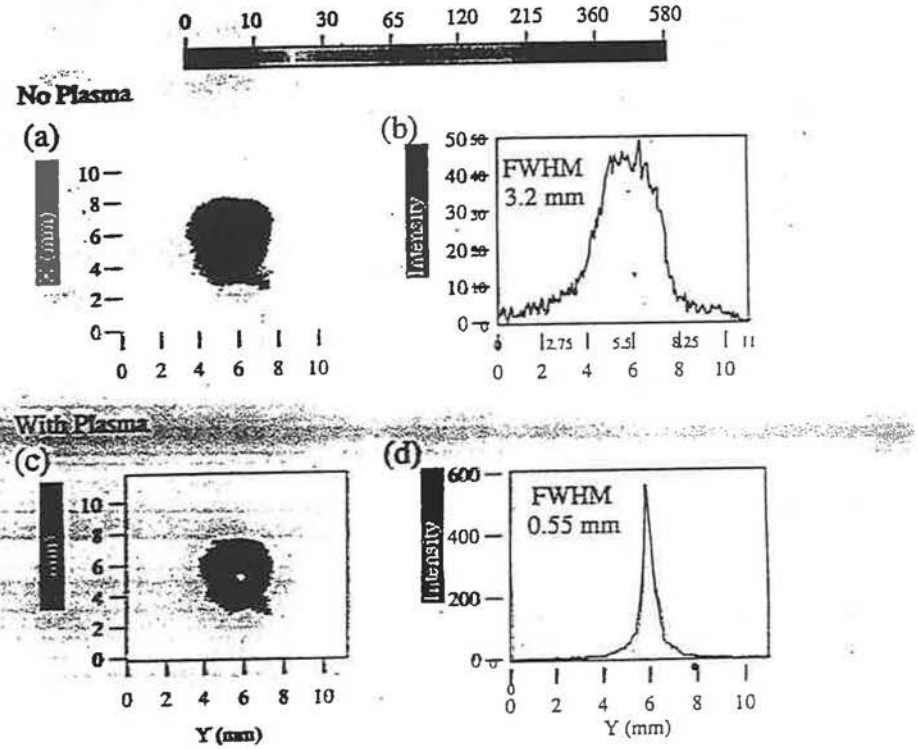

Figure 3. (a) Time-integrated bunch image with no plasma taken 21 cm downstream of the plasma. (b) A vertical lineout of the image in (a). (c) Time-integrated bunch image in the presence of the plasma. (d) A vertical line-out of the image in (c).

[S. HIRAPETAIN et al PRL 72, 2403 (1994)]

Key Issue	Experiment	Theory/Simulation
Acceler. Length	Channel Formation	1-to-1 models
mm $\longrightarrow$ cm +		parallel
	Plasma Sources	3-D hybrid
Beam Quality	Injectors	Beam Dynamics
$\Delta\gamma$	50 fs bunch	matching β
ε	50 μ spot	injection phase
N	Blowout regime	
Efficiency		Drive beam evolution
(new)		Shaped driver and load
		Transformer Ratio
		Energy Spread

Future Experiments

UCLA proposal for a $1GeV$ beam of 10^8 electrons

Injection electron energy $10MeV$ at $100A$

Laser Power $14TW$ $\left(14 \times 10^{12} Watts\right)$

Pulse duration $\tau = 4psec.$,

Energy $= 56J$ Joules

$\lambda_1 = 1.05\mu m,\ \lambda_2 = 1.06\mu m$

Plasma density $n_{PLASMA} = 10^{17} cm^{-3}$

Interaction length $L \simeq 3cm$

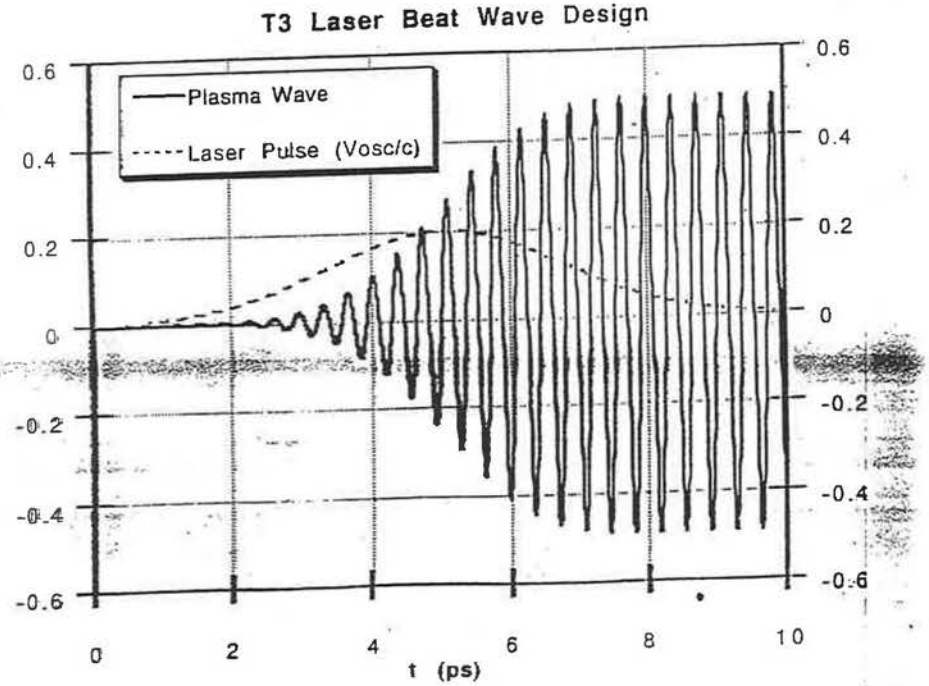

(T. KATSOULEAS e W. MORI 1993).

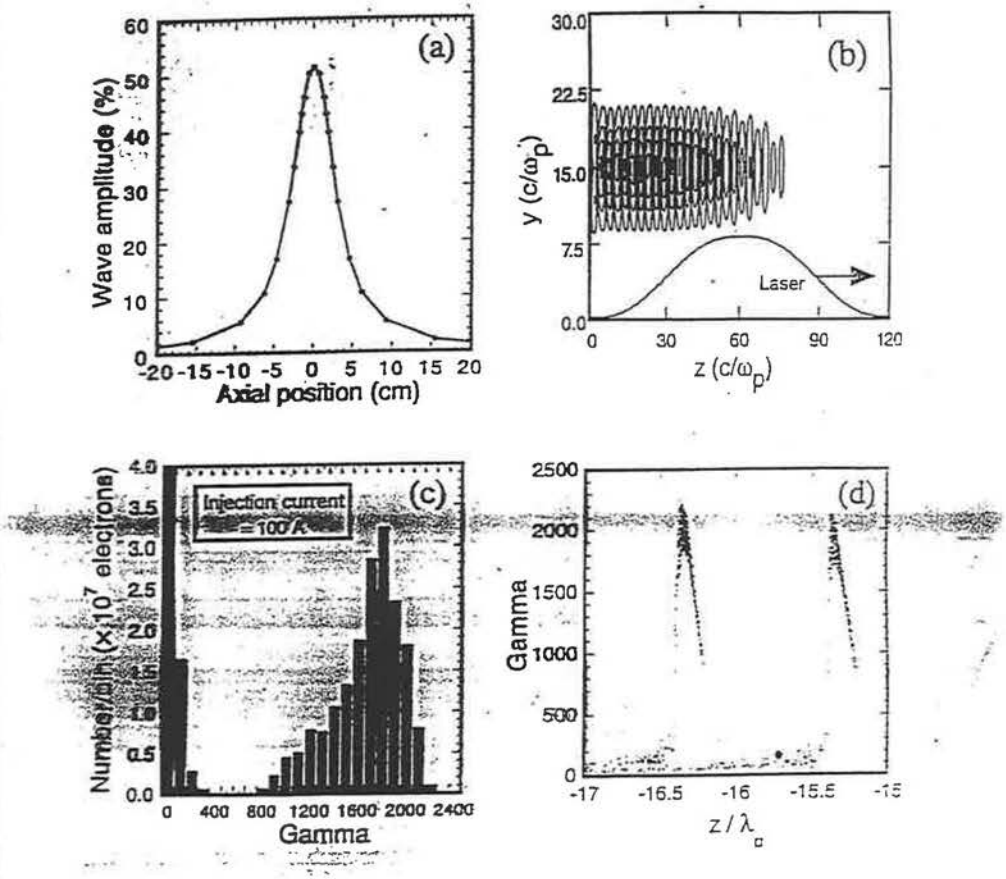

FIGURE 4. Simulation results from a possible 1 GeV PBWA experiment. Details can be found in Reference 32.

C. JOSHI et. al Comm : PLASMA PHYS AND CONTR. FUSION 16, 65 (1974)

TABLE I

Laser Wavelengths	1.05 μm and 1.06 μm
Plasma Density	10^{17} cm^{-3}
Plasma Source	Multiphoton Ionization
Laser Pulselength	4 ps
• Laser Power	14 TW
Laser Spot Size (2σ)	200 μm
Rayleigh Length (Z_0)	3.1 cm
Plasma Homogeneity	±7%
Peak Plasma Wave Amplitude	0.5
• Peak Gradient	160 MeV/cm
• Final Energy	1 GeV

FUTURE SLAC e-BEAM-PLASMA TEST EXPERIMENT.

LONG 1m PLASMA COLUMN.

SLAC e-BEAM 30-50 GeV

- FRONT OF BEAM GENERATES PLASMA WAKEFIELD
- TAIL OF BEAM PARTICLES INTERACTS WITH WAKEFIELD
  ⇒ ACCELERATED AND DECELERATED BEAM.

CHANNELLED BEAM

TWO LASER TECHNIQUE.

$L \simeq 70 L_R$

MILCHBERG HAS PRODUCED 2.2 cm CHANNELS WITH 75% ENERGY COUPLED INTO THE WAVEGUIDE.

DURFEE et al P.R.E 51 2368 (1995)

INVERSE CERENKOV - VAVILOVA ACCELERATION. (ICVA)

FIGURE 1. Schematic for the interaction region from the axicon focal geometry. This geometry can be used for vacuum acceleration or the ICA. In the ICA the interaction region is filled with a gas of index of refraction $n = c/(v \cos\theta)$.

KIMURA (1996) 10^6 ELECTRONS GAINED 2 MeV. => 31 MeV/m.

APPLICATIONS

- **High rep.** rate lasers in the $10^{12} - 10^{15} Watt$ range will produce $> 10^8$ particle/shot in the $100MeV - 1GeV$ range.
  - * Present RAL exp $\sim 100MeV$ in $1mm$
  - * Future $1GeV$ in $1 - 2cm$ plasma.

- **Isotope** production

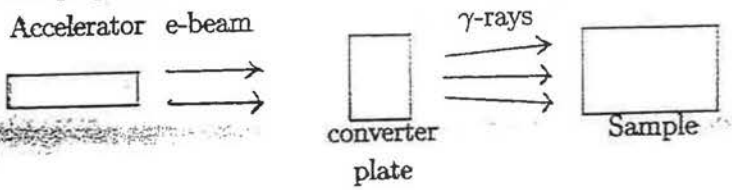

- Compact **Neutron** Source,
  - * Photo-**neutron** production.

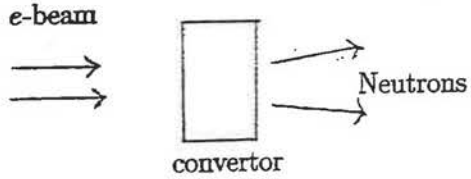

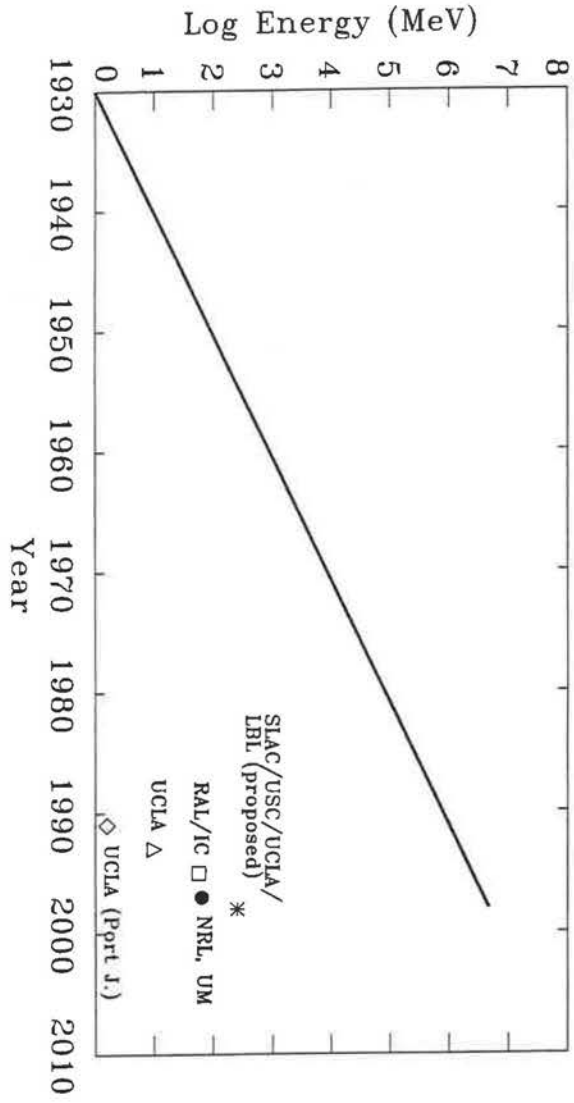

- Electron-Positron relativistic Plasmas

  Study of Astrophysical objects eg. Pulsar magnetospheres, γ-ray bursters. etc.

- Hard X-ray source $\sim 100MeV$

- Particle Physics

  Pion Production energies $> 350MeV$

  Test Detectors

  Calibrate Detectors

  Possible size of unit $\sim$ Portal cabin size.

- Radiation sources

  ie FEL etc.

Requirements for High Energy Experiments)

Use Collider Parameters

Luminosity $= 10^{31} cm^{-2} sec^{-1}$

Beam Energy $\sim 1TeV$

No of particles per pulse $\sim 10^{11}$

Total Laser Energy (assuming 5% transfer efficiency) $= 320kJ/pulse$

Multiple staging required

For a 100 stage accelerator requires $100\times$ ***3kJ* lasers**

Power requirements :

$$P_{TOTAL} = 320kJ \times f(\text{pulse rate } sec^{-1})$$

$$P_{TOTAL} = 1\ GW \text{Power}$$

Key Issue	Experiment	Theory/Simulation
Acceler. Length	Channel Formation	1-to-1 models
mm $\longrightarrow$ cm +		parallel
	Plasma Sources	3-D hybrid
Beam Quality	Injectors	Beam Dynamics
$\Delta\gamma$	50 fs bunch	matching β
ε	50 μ spot	injection phase
N	Blowout regime	
Efficiency		Drive beam evolution
(new)		Shaped driver and load
		Transformer Ratio
		Energy Spread

Conclusions

- Laser Plasma Accelerators > 100 MeV
- 1 GeV Beam is possible with present technology
- Beam quality requires attention.
- Require staging to reach TeV
- Numerous application for 10 MeV - 1 GeV beams.

Fast Ignitor relevant SILASI physics

P. Mulser, TQE, Darmstadt Univ. of Tech.

Introduction

α) Standard scenario

∃ critical density n_c : laser beam is blocke

Bow shock

$P_a = \rho_0 v_s^2 (1 - \frac{1}{\kappa})$ κ = compression rat

$v_s = v_{\text{hole boring}} \simeq \frac{c}{30}$

Essential: good absorption

⇒ energy coupling to dense co

β) Self-induced transparency (SIT):

$\nexists\, n_c$ ⇒ non-standard scenario

Contents

$v_{ei} = 0$

Experiment

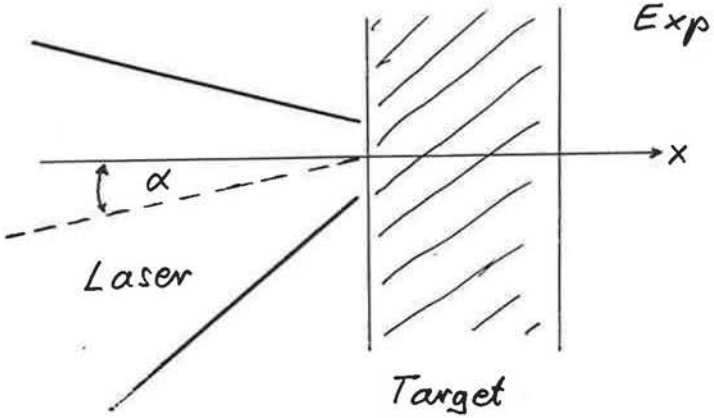

Simulation

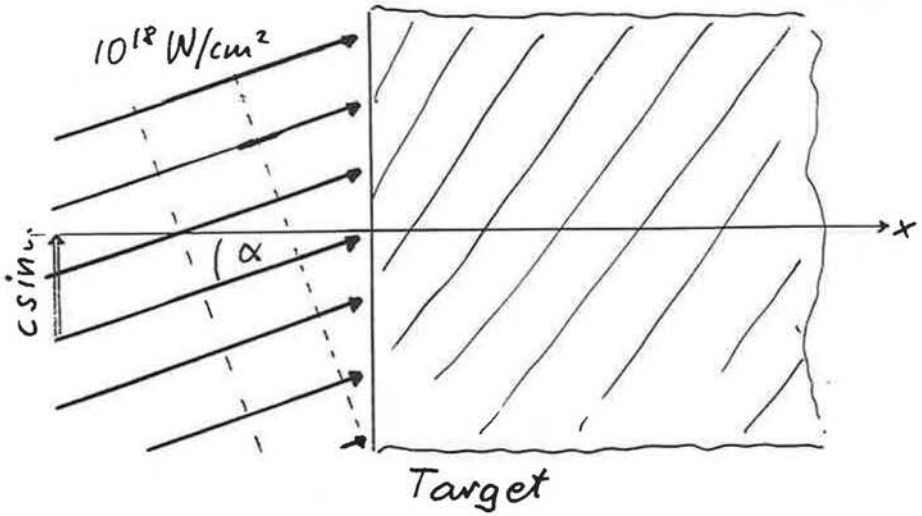

Relativistische Vlasovgleichung (1+2)D:

$$\frac{\partial f}{\partial t} + \frac{\vec{p}}{\gamma m_e}\frac{\partial f}{\partial \vec{x}} - \frac{e}{\gamma m_e}(\vec{E} + \vec{v}\times\vec{B})\frac{\partial f}{\partial \vec{p}} = 0; \quad \nabla\vec{F} = -J; \quad \nabla\cdot$$

Maxwell Eq.

Contour line plot of

Electron distribution function $I\lambda^2 = 10$

Numerical calculation

Step-like density profile

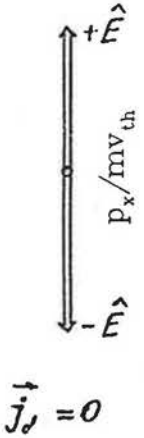

$\vec{j}_d = 0$

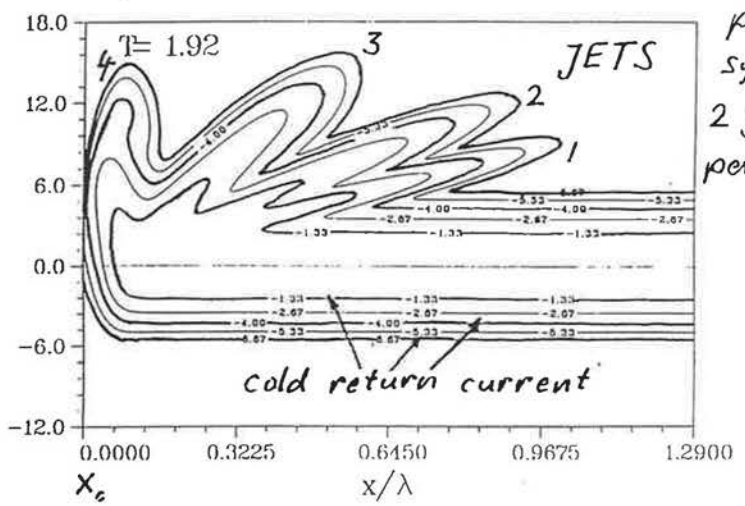

perfect symmet
2 jets per cycl

$\theta = 0°$

perpendicular inciden

$I\lambda^2 = 10^{18}\,W\,cm^{-2}\,\mu m^2$

$n/n_c = 25$

$I = 10^{18}\ W\,cm^{-2}\,\mu m^2$

$\omega t = 79.33$

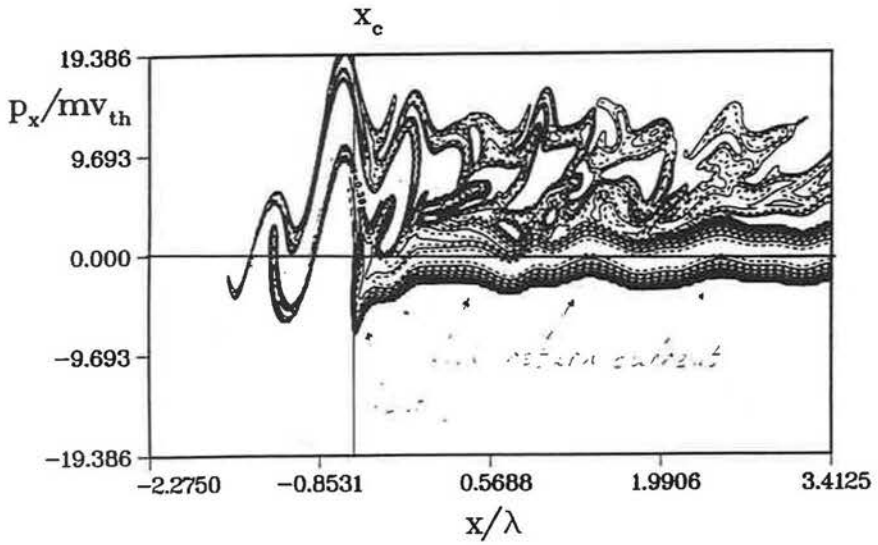

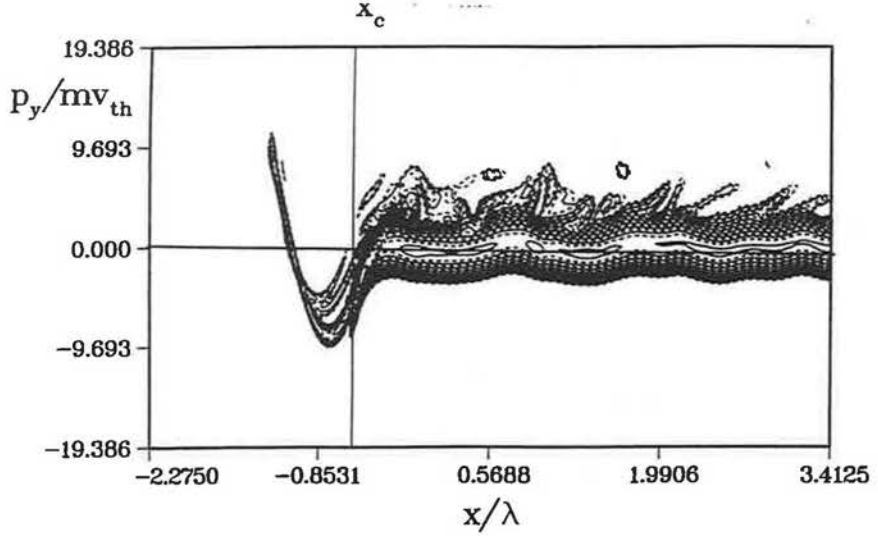

Electron distribution function: $I\lambda^2 = 10^{18}$

H. Ruhl (1995)
TQE, Darmstadt

$\vartheta = 0°$

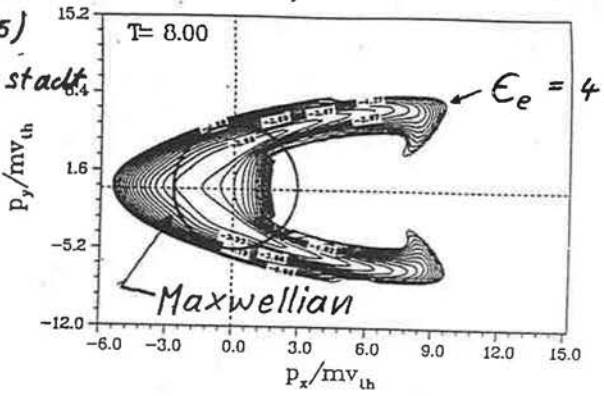

$\epsilon_e = 4\,\bar{\epsilon}_{os}$

Maxwellian

$\vartheta = 30°$

$\vec{j}_{dd} \neq 0$

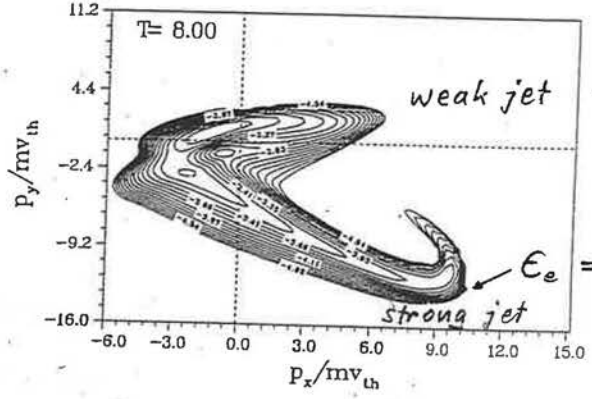

weak jet

energetic + weak jet

$\epsilon_e = 6\,\bar{\epsilon}_{os}$

strong jet

$\vartheta = 60°$

$\vec{j}_{dc} \neq 0$

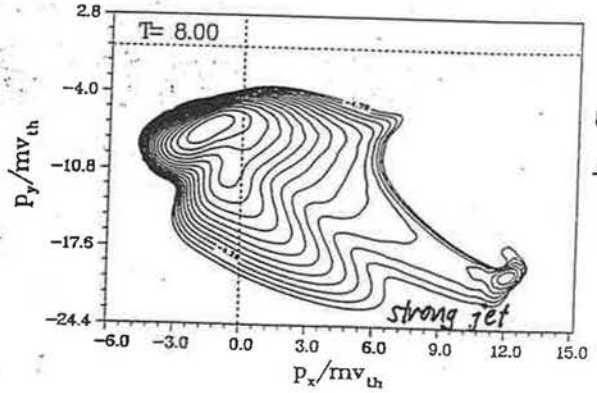

weak jets suppressed

strong jet

$\frac{n_e}{n_c} = 25$

$L/\lambda = 0{,}023$

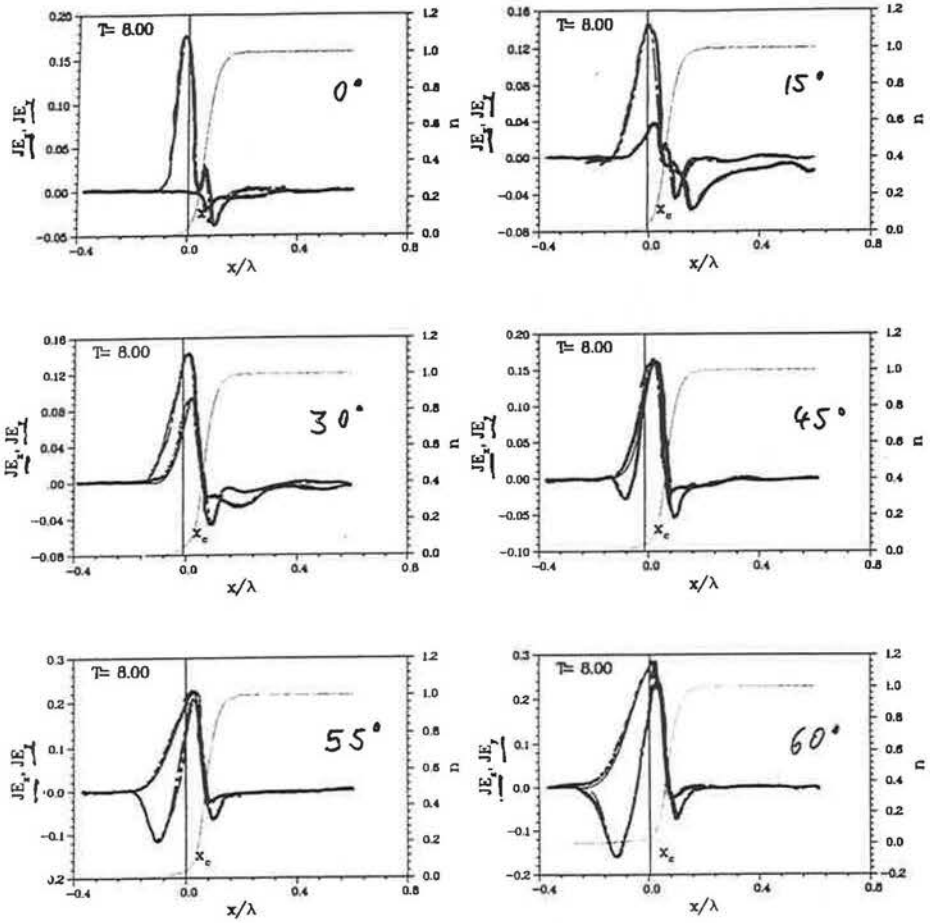

Lab frame

Abbildung 5.11: Zeitgemittelte Depositionsfunktionen $J_x E_x$ (durchgezogen) und $J_y E_y$ (punktgestrichelt) im Laborsystem in Einheiten $J_0 E_0$ für $\theta = 0°$, 15°, 30°, 45°, 55° und 60°. Die Parameter sind $\alpha = 5.0$, $\beta = 0.13989$ und $\eta = 6.085$ und $L/\lambda = 0.023$.

Skin layer absorption

Fraction of absorption

Density step $n_e/n_c = 25$

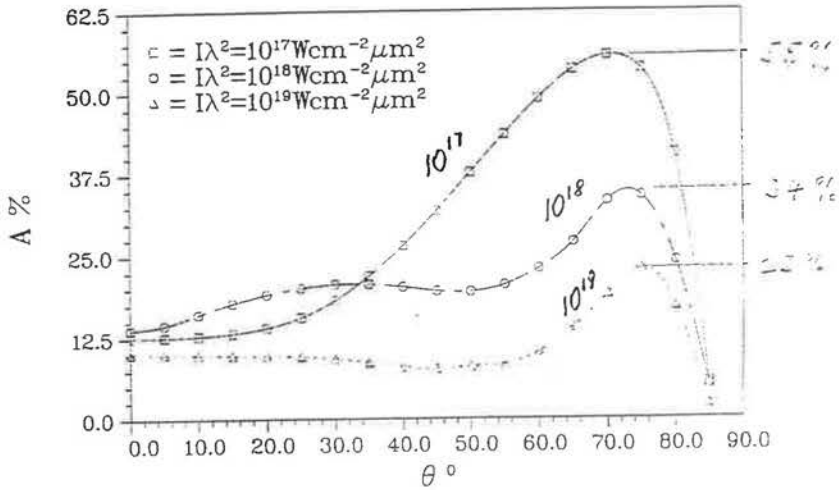

Superintense laser – solid interaction

(current understanding)

Signature: Generation of fast electrons (MeV!)

We claim:

- fast electrons are generated in the low density (relativistic) region
- bulk plasma moves fluid-like

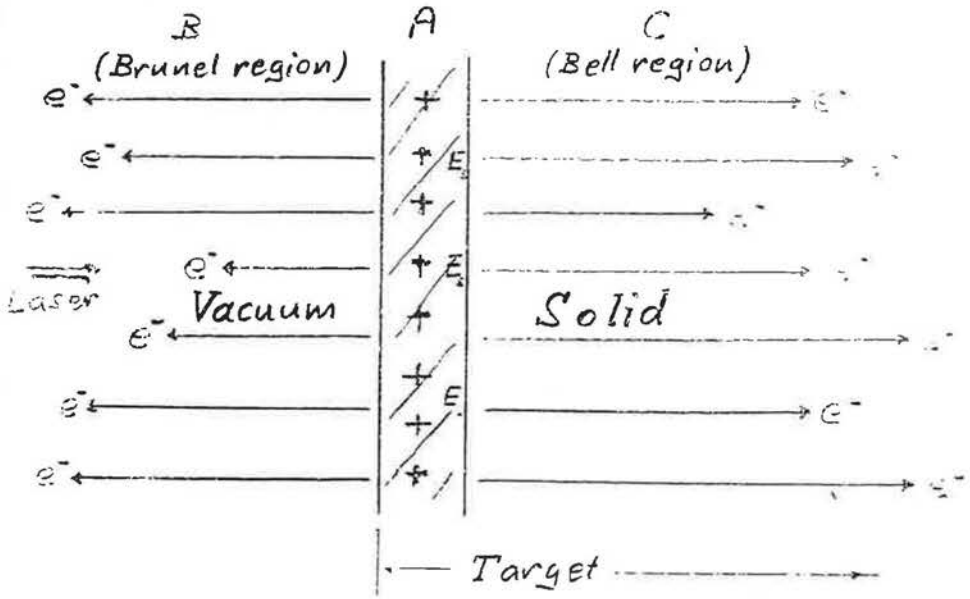

A: ponderomotively charged evanescent region

B: vacuum; generation of fast electrons by E_{Laser}: $\vec{v}_{os} \times \vec{B}_{Laser}$, $\vec{v}_{os} \times \vec{B}_{o}$, $\vec{v}_{o} \times \vec{B}_{Laser}$

C: preheated solid: low percentage of fast e^- escaping from backholding field E_s in A.

Absorption at 10^{18} W/cm^2

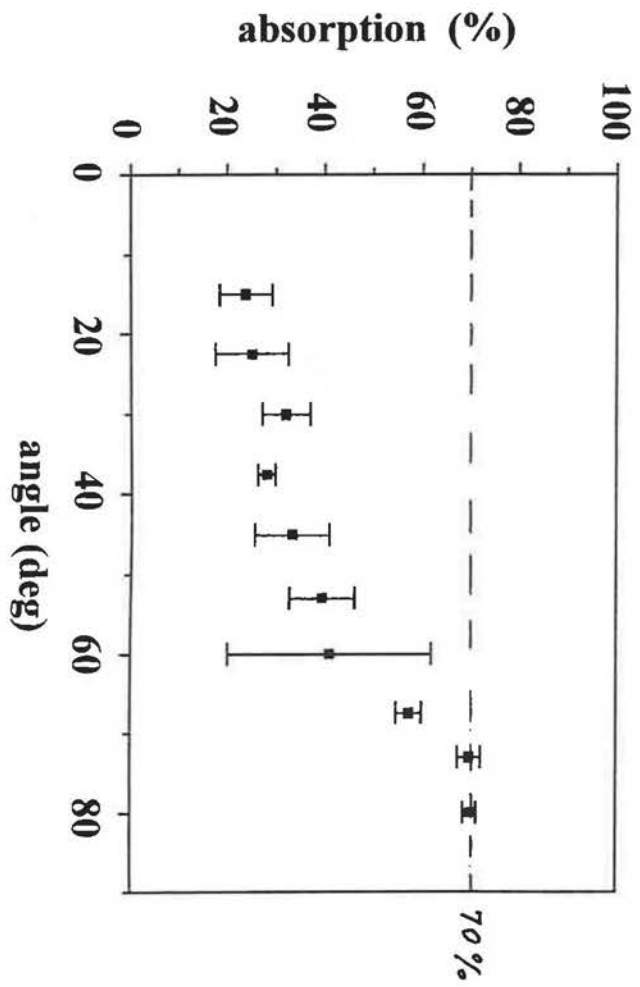

particles in a standing wave :
with backholding electric field :

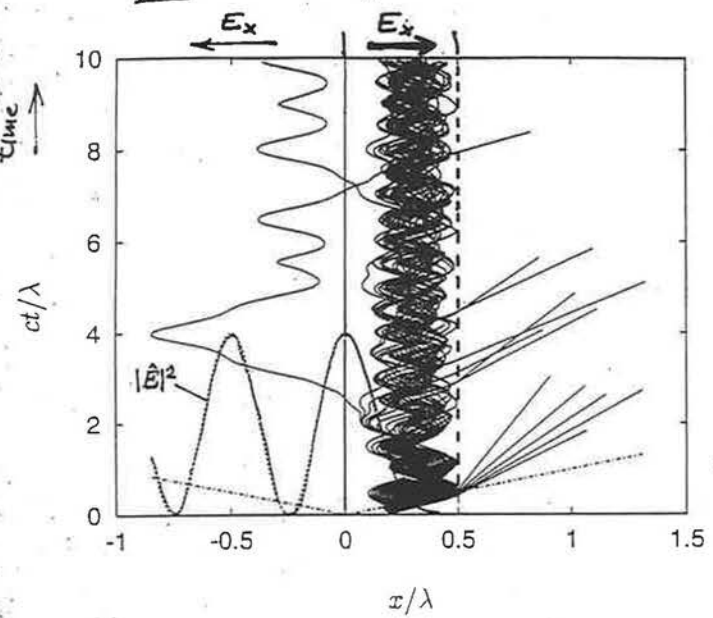

$I = 10^{19}\ \frac{W}{cm^2}$

$\lambda = 0.8\ \mu m$

most of the particles can be confined near the critical surface

⇒ bulk electron

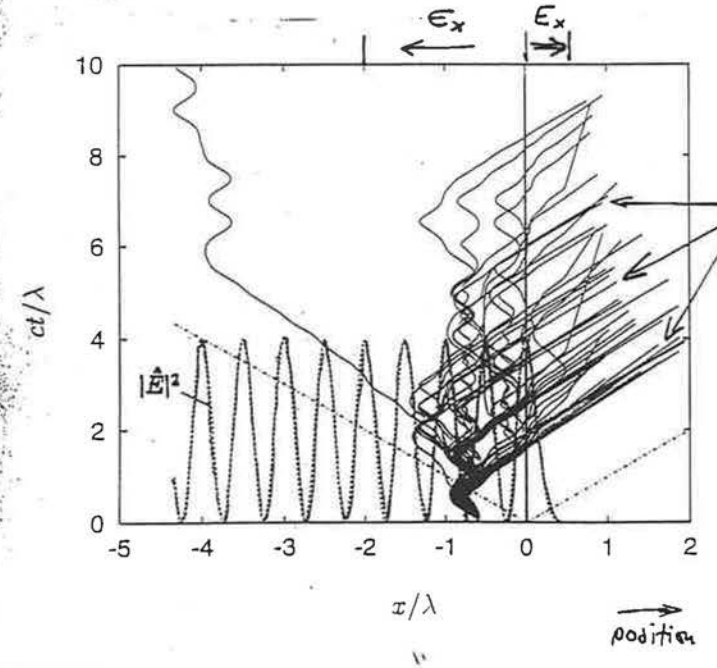

fast electrons (1.5 MeV)

longitudinal electric field E_x/E_0

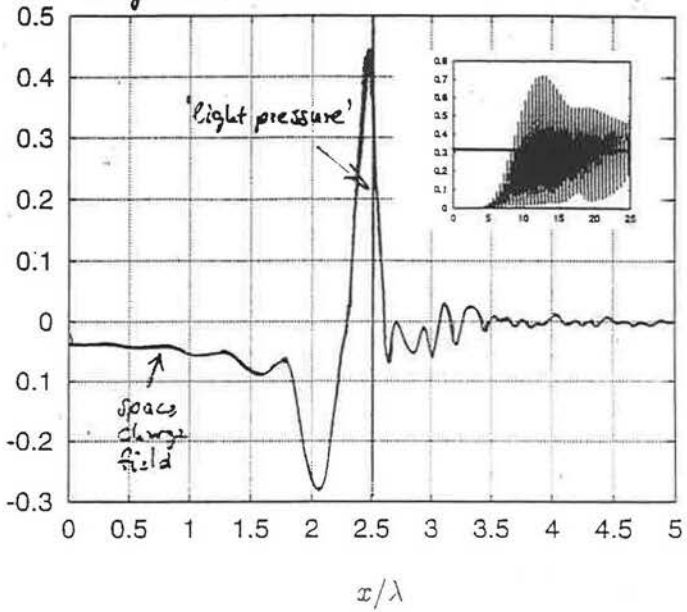

electric current density (longitudinal / transverse)

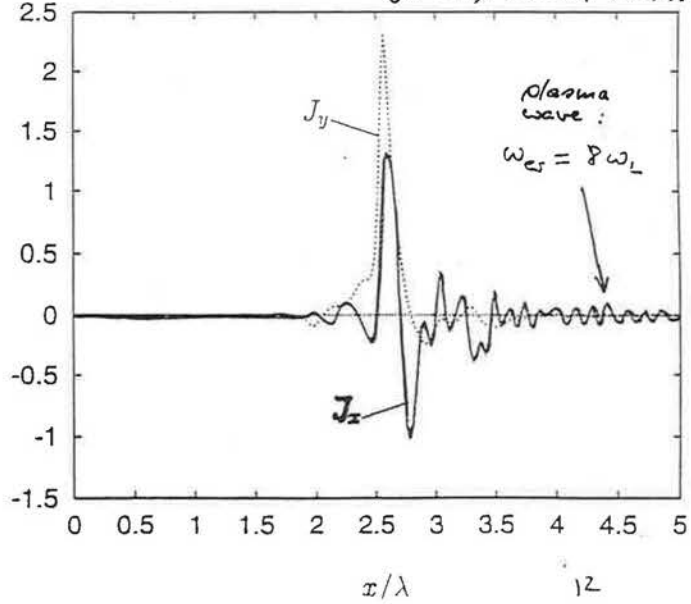

$\left(\frac{n_e}{n_c}\right)^{1/2} = 7.6$

no evidence for fast electrons in the particle current

$\hat{E}_y / E_0 = 1.7 \doteq 1 + \sqrt{R} \Rightarrow$ 50% absorption

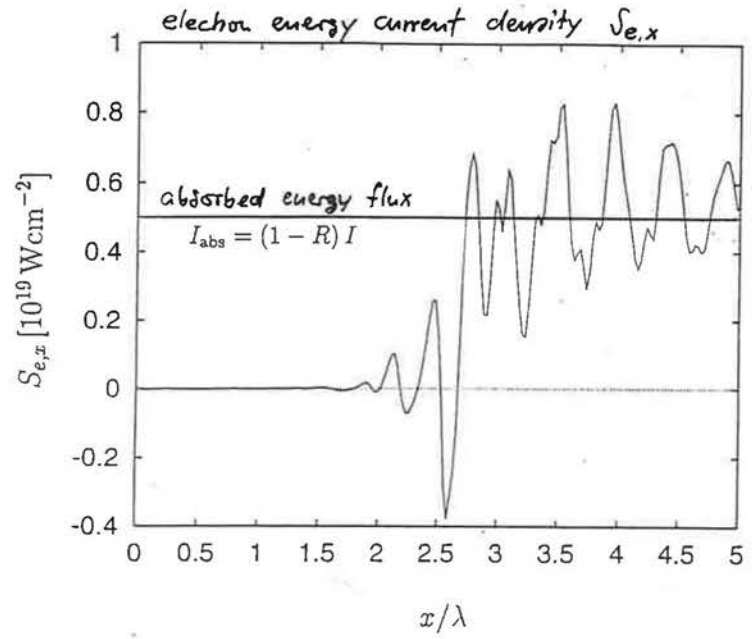

ballistic energy transport by fast electrons

nearly 100% of absorbed energy converted into fast electrons

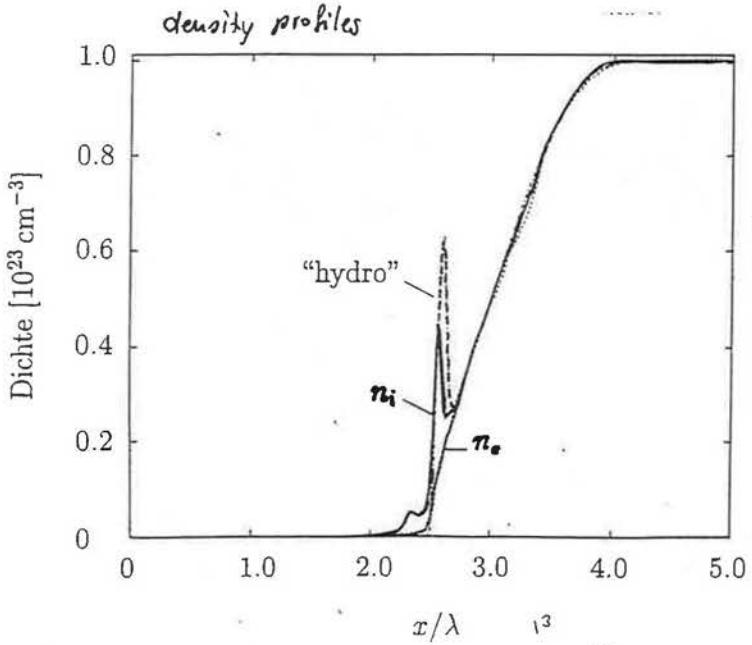

hydrodynamic phenomenon: shock formation

Fig.1

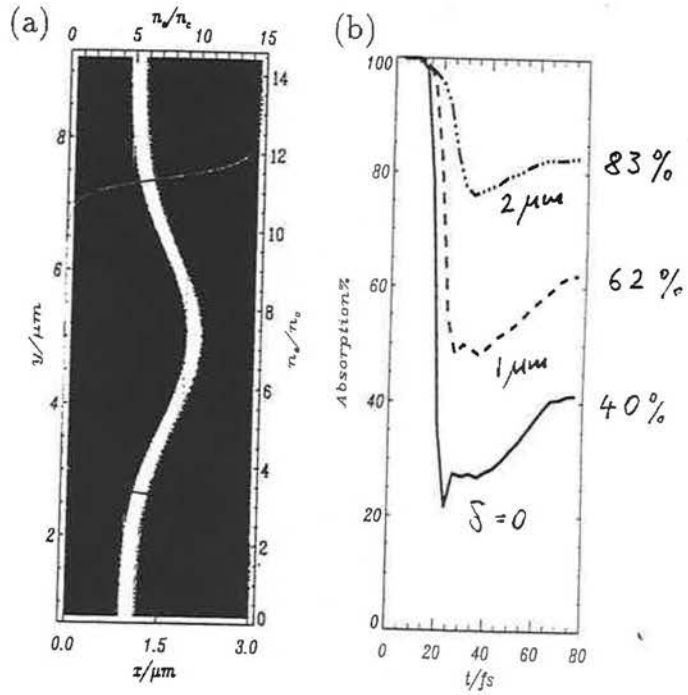

$I = 4 \times 10^{18}$

$n_e/n_c = 15$

Fig.2

$n_e/n_c = 15$

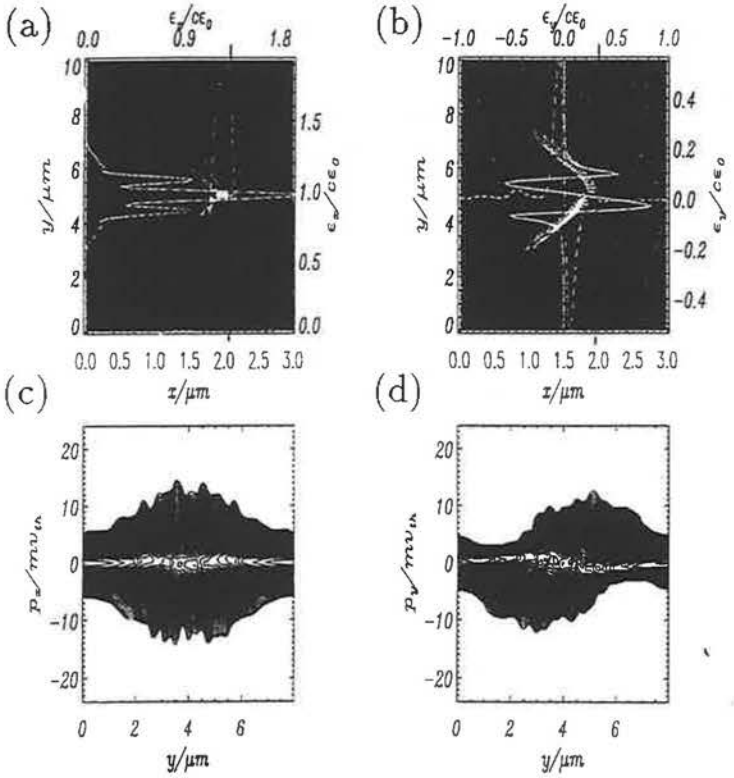

$I = 4 \times 10^{18}$ $n_e/n_c = 20$ $t = 66$ fs

$T = 8\%$

Fig.3

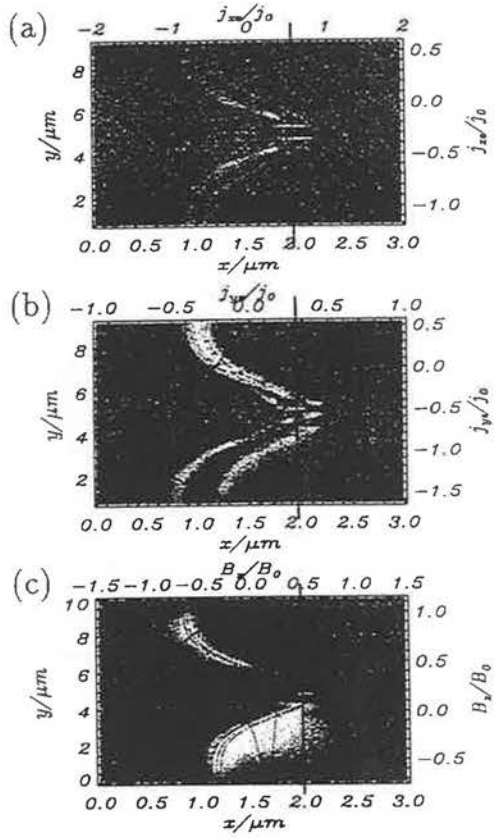

$I = 4 \times 10^{18}$, $\delta = 1\ \mu m$, $n_e/n_c = 15$, $t = 66$ fs

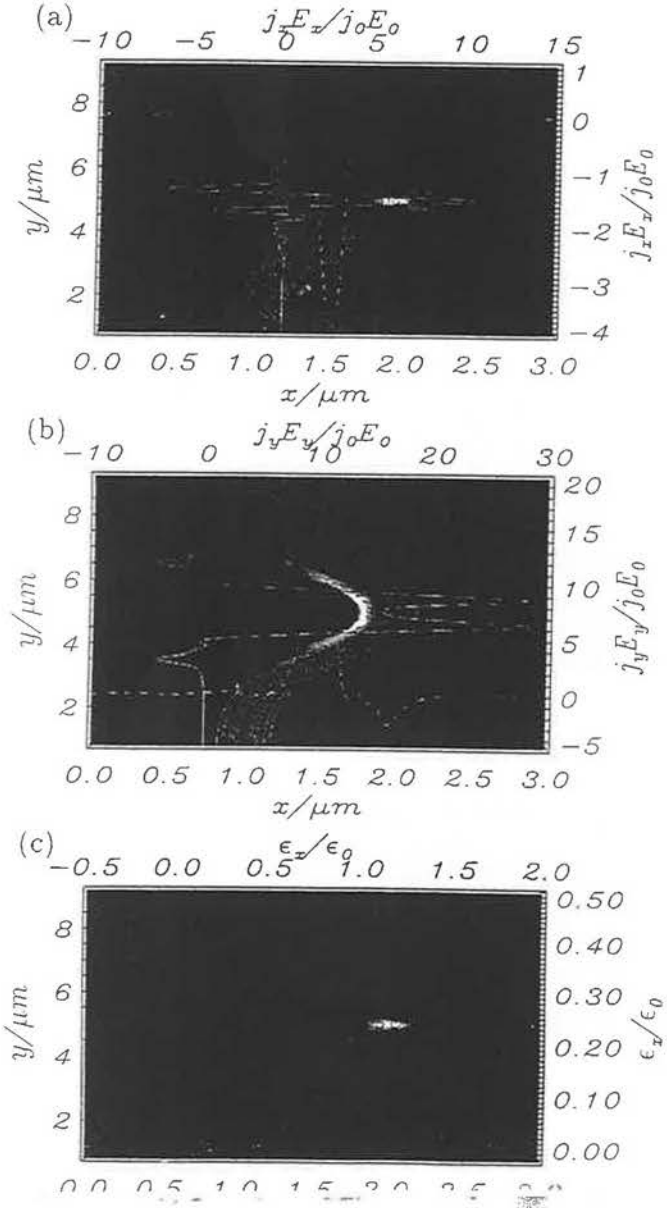

Collimated electron beam in thick targets

Fig.4

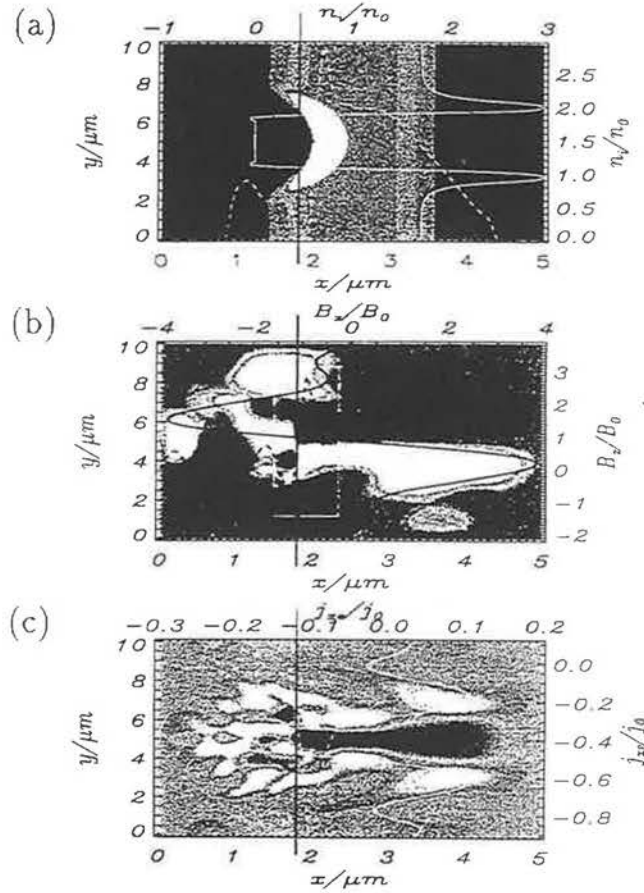

$B_0 = 3 \times 10^2$ Vs/m²

$j_0 = 4,6 \times 10$ A m⁻²

$I = 10^{18}$, $n_e/n_c = 2$, $t = 110$ fs

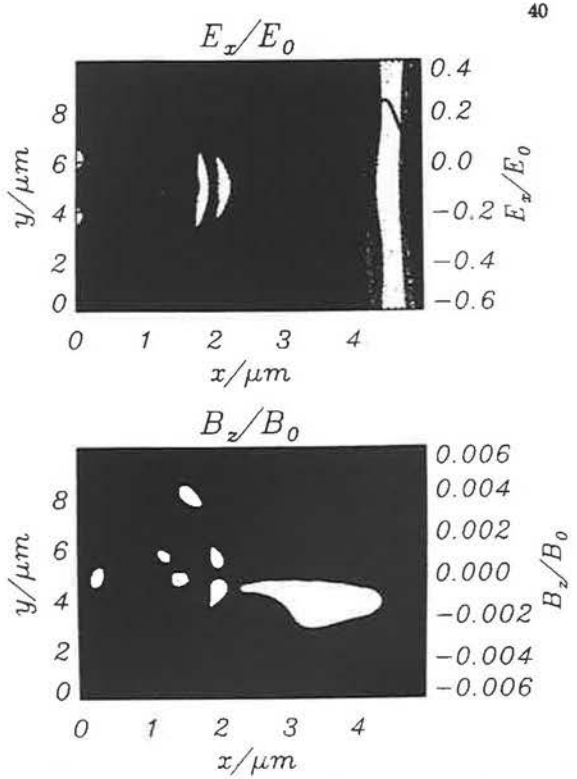

Figure 4.15: Cycle averaged fields E_x and B_z. The upper plot gives contour lines of E_x. The solid line is overplotted at $y = 5\mu$m. The lower plot gives B_z. Both plots are taken at $\tau = 110$fs. The solid is overplotted at $y = 4.17\mu$m and the dashed dotted line at $y = 5.74\mu$m. The parameters are $E_0 = 2.74 \cdot 10^{12}$V/m, $B_0 = 2.91 \cdot 10^5$Vs/m^2, $T_e = 10$keV, $T_i = 1$keV, $n_e = 2.22 \cdot 10^{27}$m^{-3} and $I\lambda^2 = 10^{18}$Wcm$^{-2}\mu$m^2.

$I = 10^{18}$, $n_e/n_c = 2.2$, $t = 110$ fs

Schematic picture of Fig. 4

Fig.5

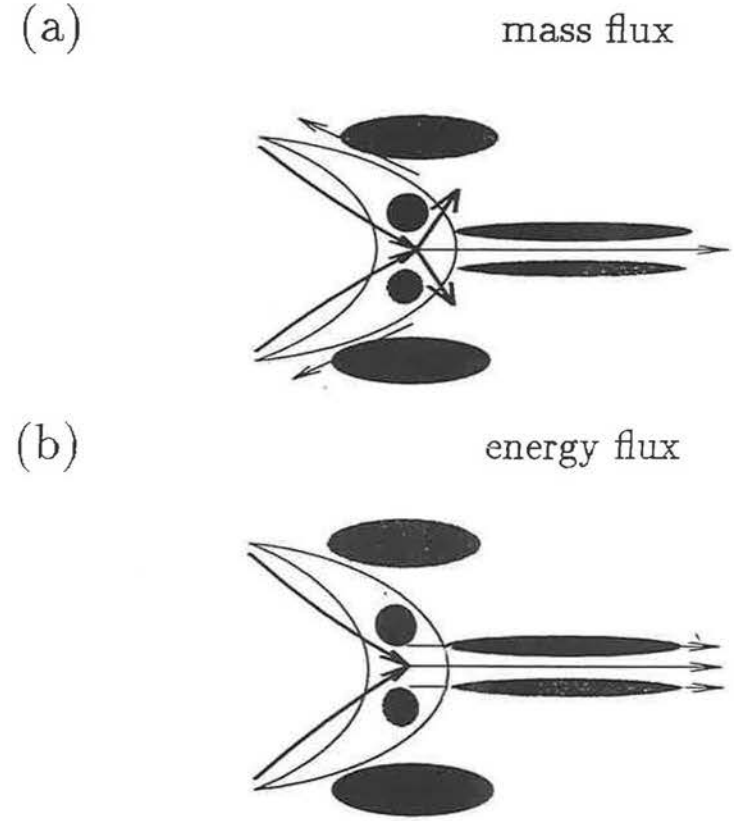

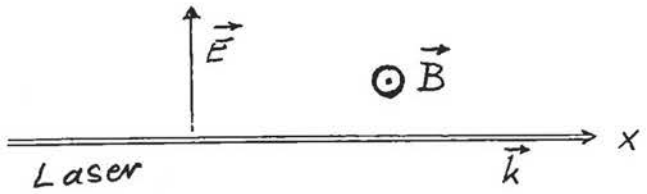

$B \simeq 20 - 100$ MG

$T_e \simeq 30 - 300$ keV

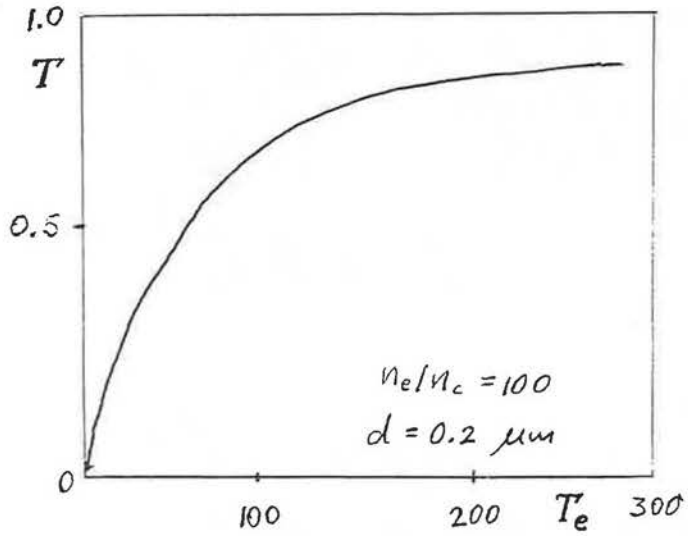

Cairns & Rae, St. Andrews

Fig. 3

Microparticle impact: Gold on S_{21}

$V_{Au} = 5 \times 10^8$ cms^{-1}, $m_{Au} = 1{,}25$ μg

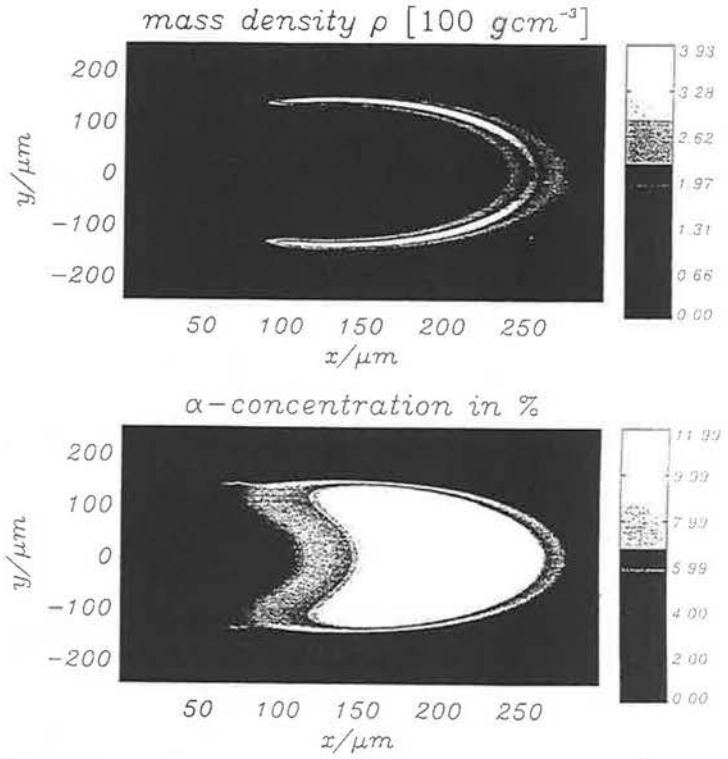

$t = 53$ ps

$T_e = 65$ keV, $T_i = 38$ keV

$v_{burn} = 4{,}9 \times 10^8$ cms^{-1}

$\mathcal{E} = 12$ kJ

Fig. 7b

Ignition by laser: $I = 10^{20}$ on $\rho_{DT} = 200\ g\,cm^{-3}$

(b)

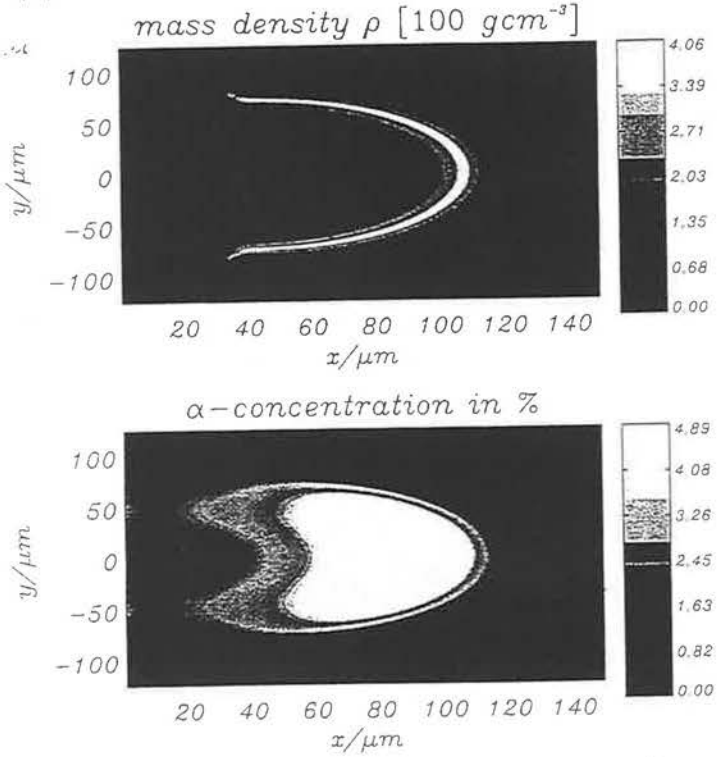

$t = 39$ ps

$T_e = 35$ keV , $T_i = 23$ keV

$V_{burn} = 2,7 \times 10^8$ cms^{-1}

Schockwelle → selbsterhaltende Brennfront

$t = 153$ ps (gesamt Pulsdauer: $2\tau = 200$ ps)

$\hat{I} = 4 \times 10^{15}$ W/cm² , $\hat{I}\tau \times (50\,\mu m)^2 = 100$ kJ

$\epsilon_b = 75$ MeV/u

$kT_e \simeq 20$ keV in Brennfront

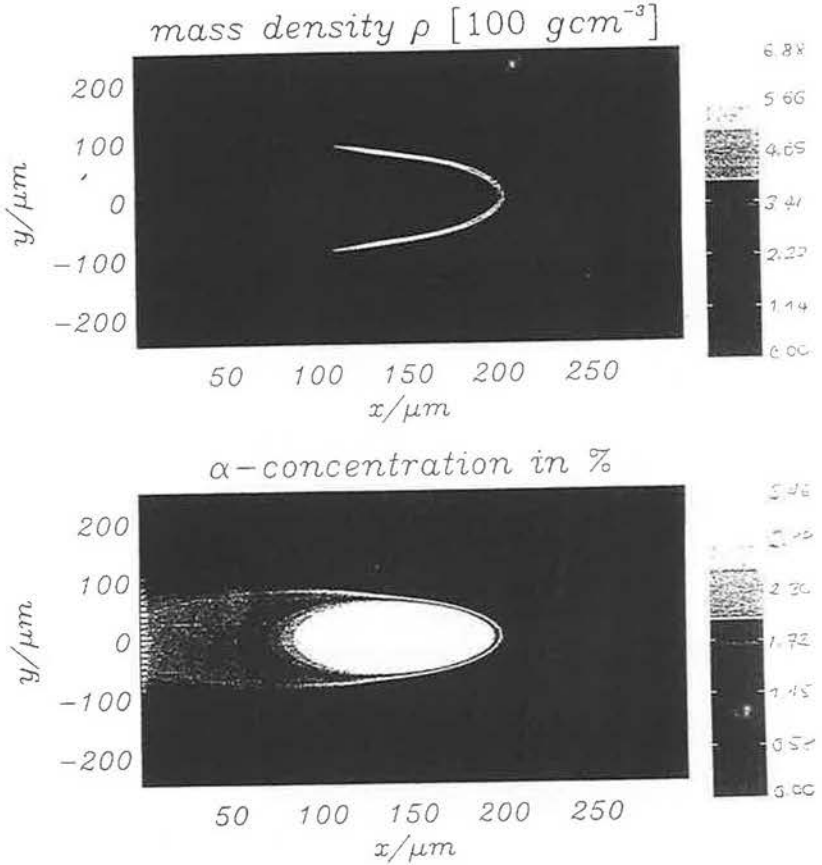

Ion beam , $t = 153$ ps , $I = 4 \times 10^{15}$

$T_e = 20$ keV

$\epsilon = 100$ kJ.

Conclusion

Geometry effects are important:

- increased absorption in deformed targe
- anomalous transparency ($\lesssim 8\%$ at 0.2 μ
- lateral energy flow in thin targets
- central jet in thick targets (5 μm beam

$\Rightarrow$ no central jet with 2×5 μm beam

- Supercritical beam propagation (Cairns)

- Ignition best with laser, 5–8 kJ
- worst with ion beam, 100 kJ.
- Hypervelocity impact comparable with laser

Contributions by

Cairns & Ram, St. Andrews
Cornolti & Macchi, Pisa
Feurer, Theobald, Sauerbrey, Jena
Hain & Ruhl, Darmstadt

MPQ

Virtual Laser Plasma Lab 3D

Short Pulse Laser Interaction with Near-Critical Plasma

A. Pukhov† and J. Meyer-ter-Vehn

I. Introduction. Massively parallel **PIC** code **VLPL.**

II. ***3D* PIC** simulations of laser-plasma interaction at powers ***from TW to PetaWatt:***

- **electron energy spectra**
- **ion energy spectra**
- **filamentation**

III. ***Mechanisms of electron acceleration in relativistic channels***

IV. Conclusions.

† Permanent address:

Moscow Institute for Physics and Technology, Russia

Fast Ignition of ICF Targets

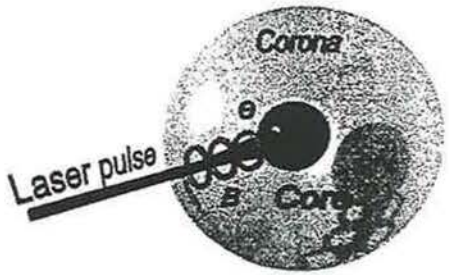

MPQ

Spectrometer

C. Gahn et al.

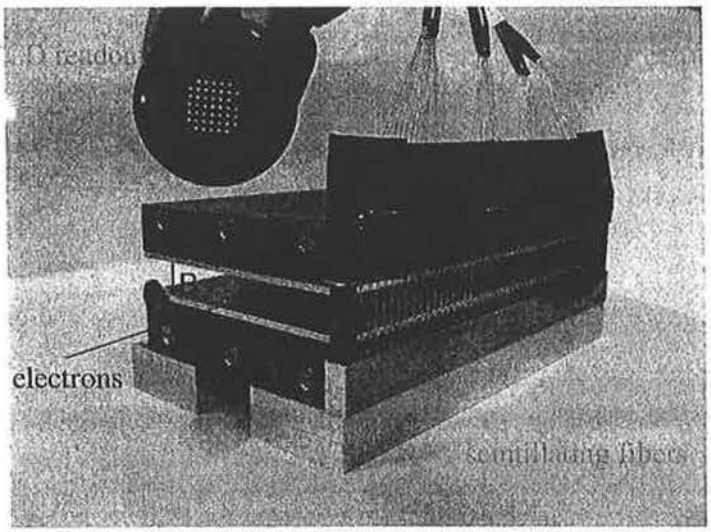

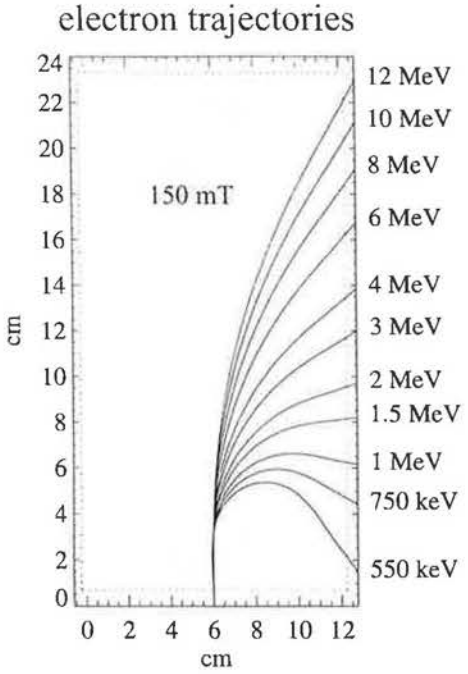

MPQ

Fast electron energy spectrum

C. Gahn et al.

electron density: $n_e = 10^{20}$ cm^{-3} (helium)

intensity: $I_{max} = 3 \times 10^{18}$ W/cm^2 and radius($1/e^2$) ~ 6μm

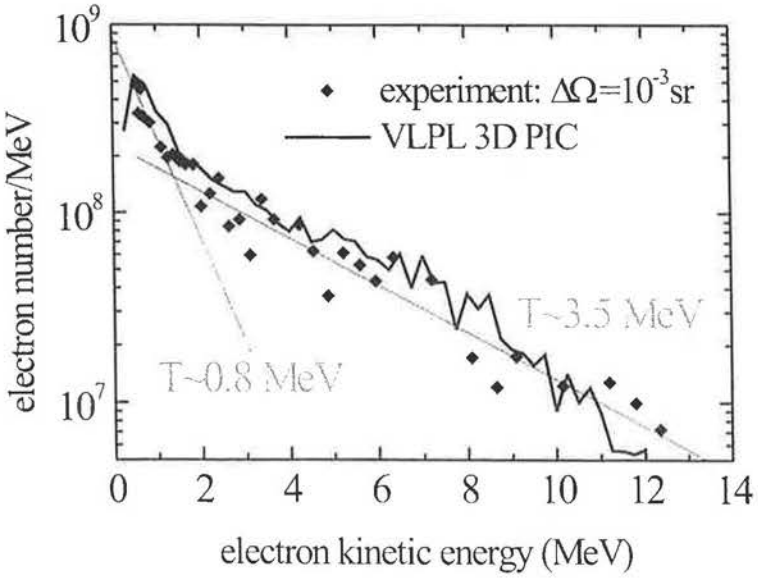

total fast electron number in 2π: **7x10^{10}** (assuming Lorentzian angular distribution)

MPQ

Summary

C. Gahn et al.

2 experiments concerning fast electrons

$I_{max}=10^{18}$W/cm^2, r(86%)=20μm
solid target, prepulse
=> $n_e=0.5n_c$

- 4×10^6 MeV-photons up to 2.5 MeV at 10 Hz
- 2.2×10^8 electrons with $T_e=0.9$ MeV
- $\eta_e=3\times10^{-4}$ (> 1 MeV)

$I_{max}=3\times10^{18}$W/cm^2, r(86%)=7μm
gas-jet target
=> $n_e=0.05n_c$

- divergence angle of Lorentzian beam profile: 15° FWHM
- 7×10^{10} electrons with $T_l=0.8$ MeV and $T_h=3.5$ MeV
- $\eta_e=5\times10^{-2}$ (>1 MeV)

MPQ

PARTICLE PHYSICS WITH PETAWATT LASERS

S. Karsch, D. Habs, T. Schätz, U. Schramm und P. Thirolf
Ludwig- Maximilians-Universität, München

J. Meyer-ter-Vehn, A. Pukhov, Ch. Gahn, G. Pretzler, G. Tsakiris und K. Witte
Max-Planck-Institut für Quantenoptik, Garching

1. Introduction

2. Production mechanisms

3. Experimental Approaches

PARTICLE PHYSICS WITH PETAWATT-LASERS MPQ

particle production mechanisms:

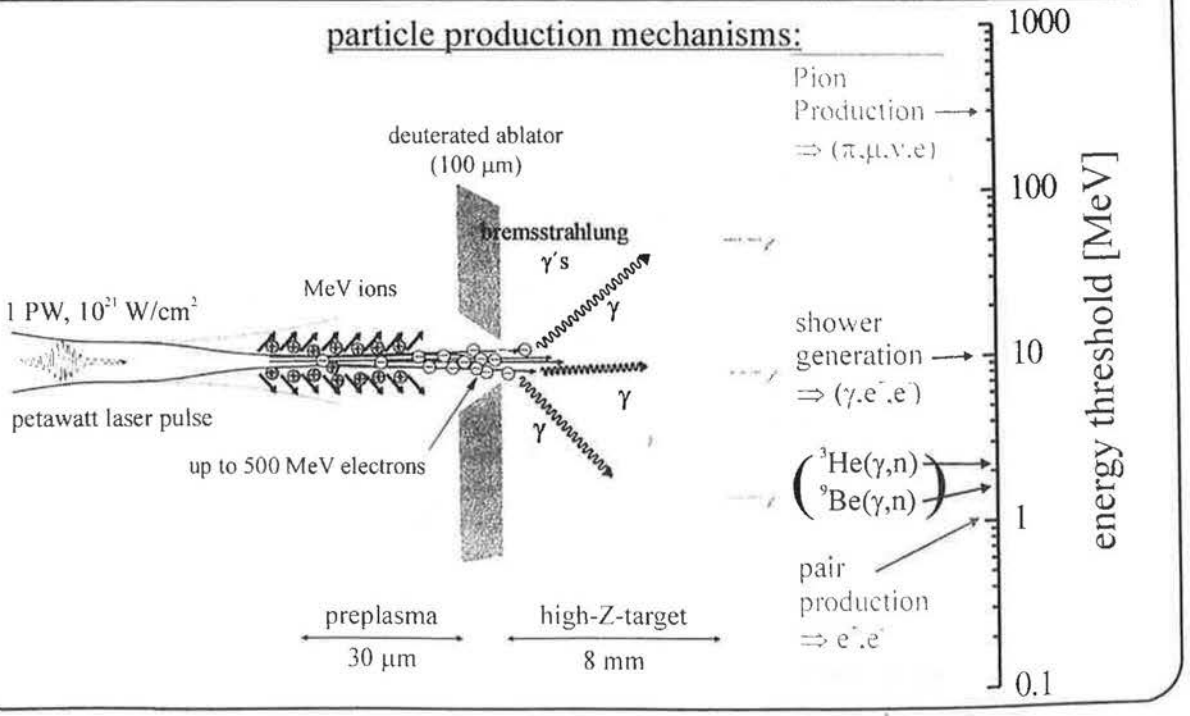

fusion neutrons

MPQ

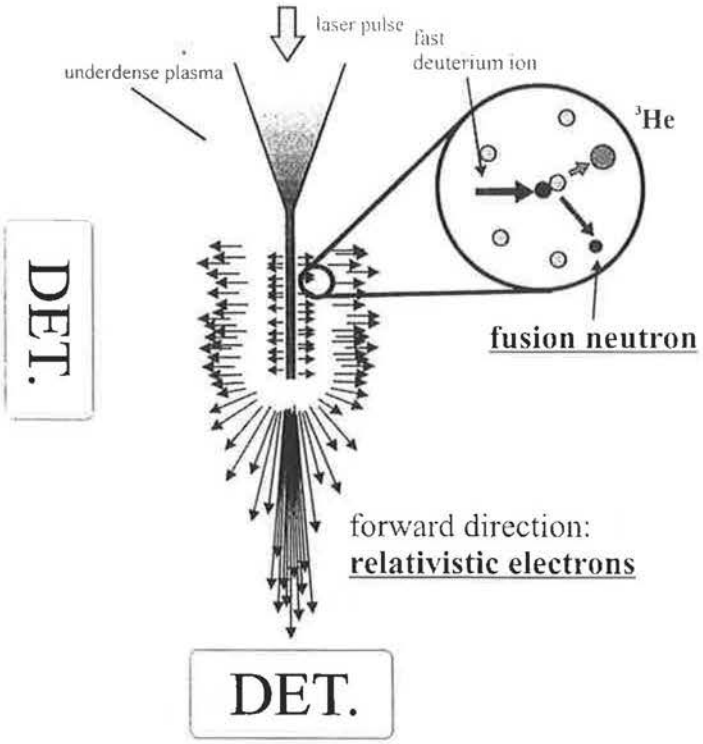

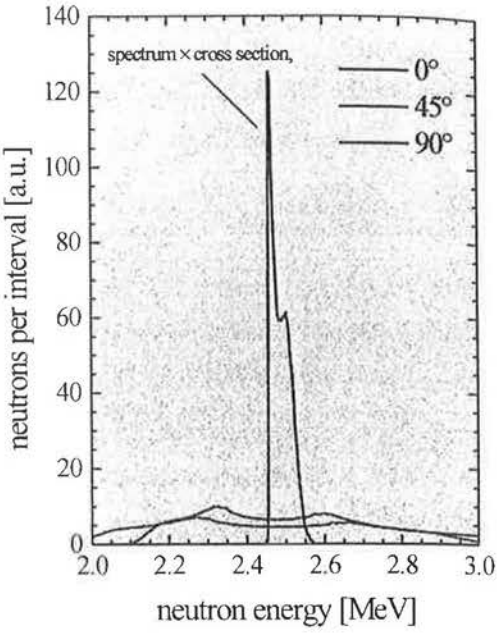

Neutrons

MPQ

γ-rays, fusion neutrons, and from a relativistic laser plasma

G. PRETZLER et al.
fs-laser produced neutrons

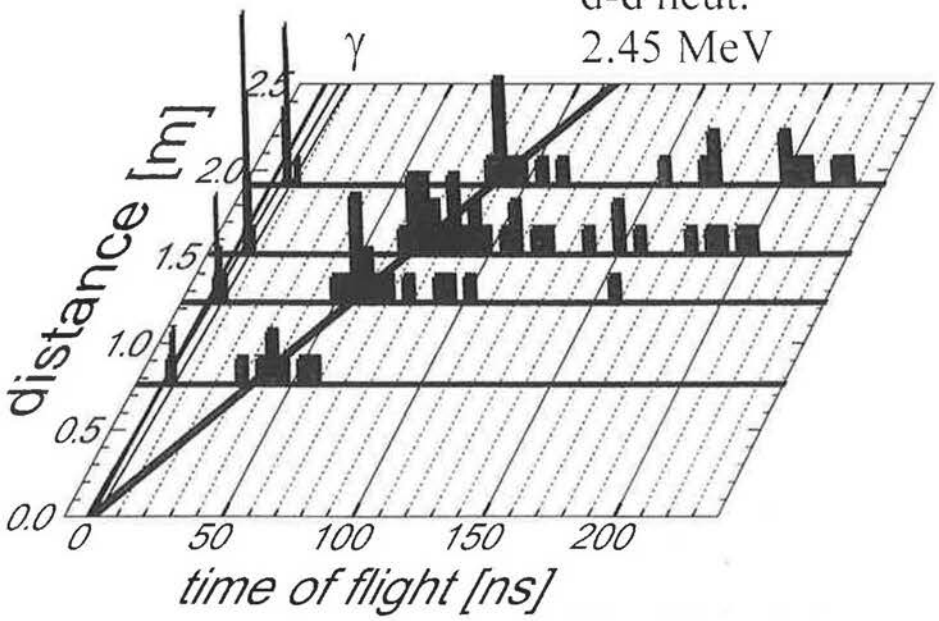

PARTICLE PHYSICS WITH PETAWATT-LASERS MPQ

Electron spectra from 1 TW to 1 PW (A. Pukhov, J. Meyer-ter-Vehn)

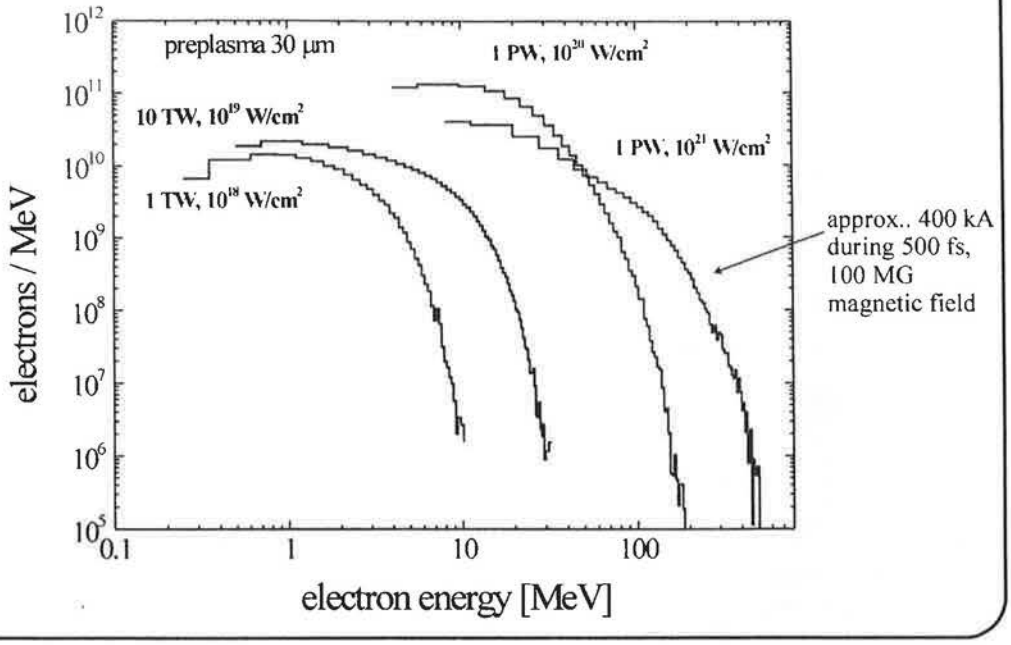

PARTICLE PHYSICS WITH PETAWATT-LASERS MPQ

γ-spektrum from GEANT- simulations using 8 mm tungsten absorber

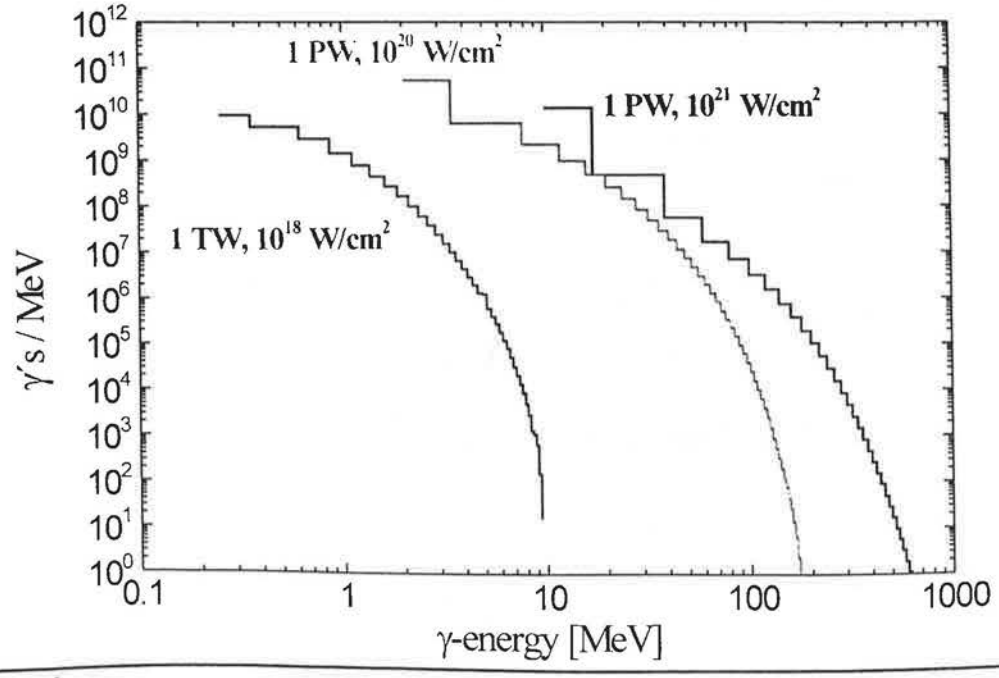

PARTICLE PHYSICS WITH PETAWATT-LASERS

MPQ

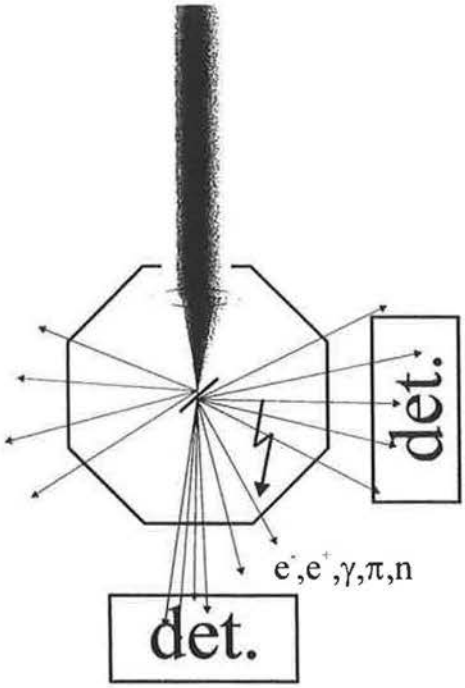

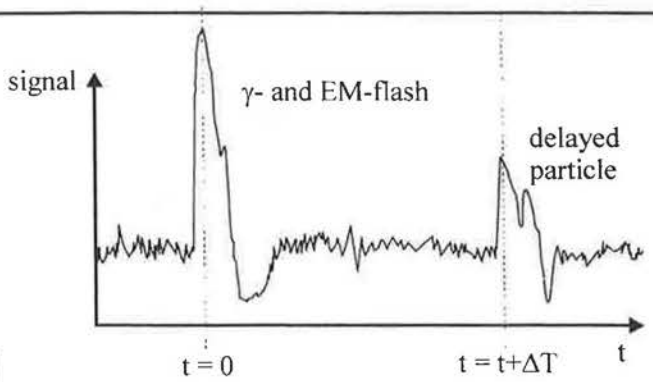

severe pile-up due to γ- and EM- flash

⇓

spectroscopy of primary particles can be facilitated by delayed reactions

⇓

time-of flight-measurement of delayed or slow particles

PARTICLE PHYSICS WITH PETAWATT-LASERS

MPQ

shower generation ($E_\gamma \geq 5$ MeV)

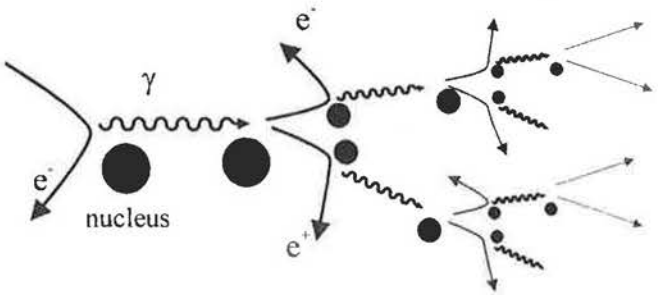

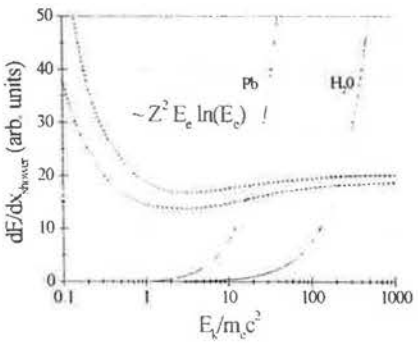

Dominant energy loss process of electrons in matter at energies > 10 $m_e c^2$

⇓

considerable fraction of electron energy contributes to shower

"neutral rays"

Neutron production from (γ,n)-process via giant dipole resonance

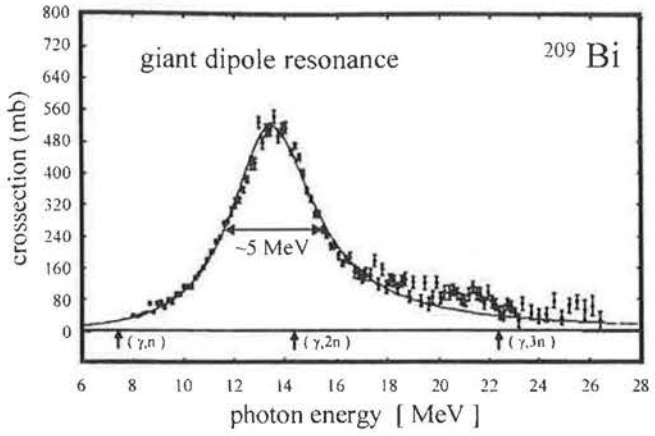

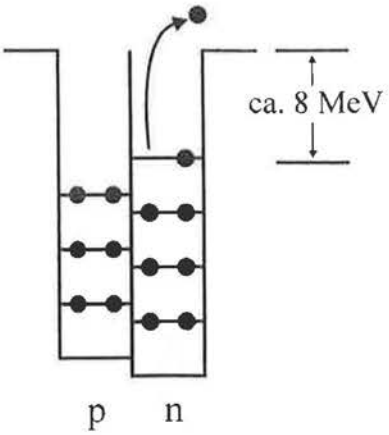

from S Cierjacks

Neutron yield for (γ-n) reactions:

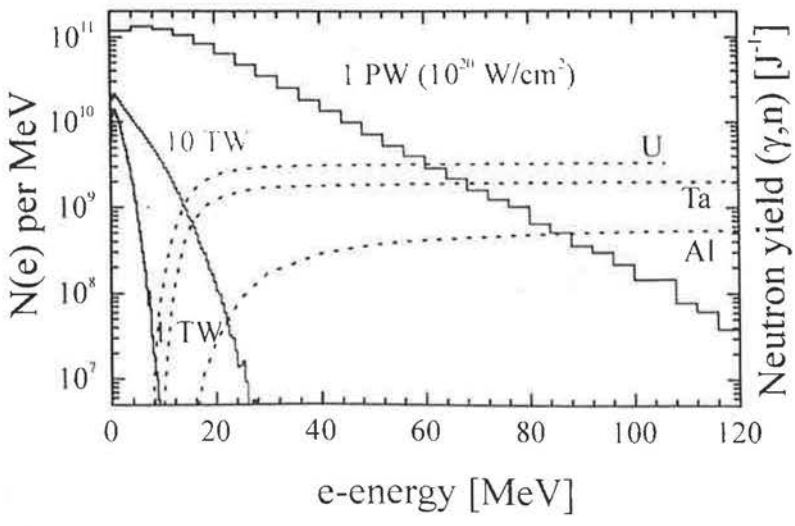

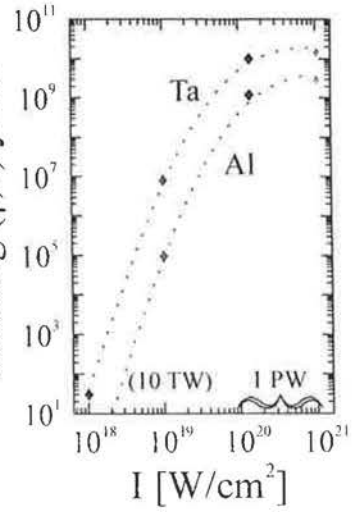

Photoproduction of pions ($E_\gamma \geq 310$ MeV)

Generation via Δ(1232)-resonance:

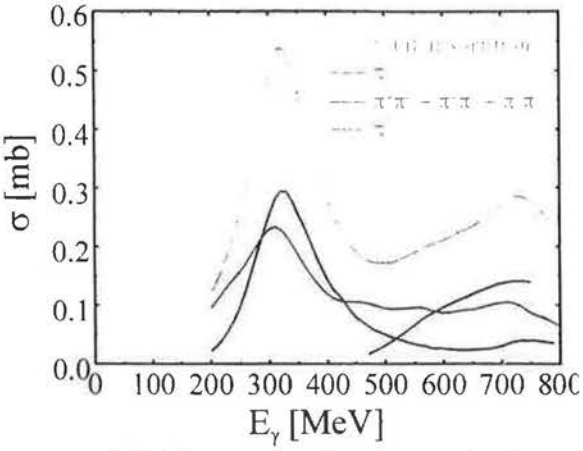

* V. Metag et al., private communication

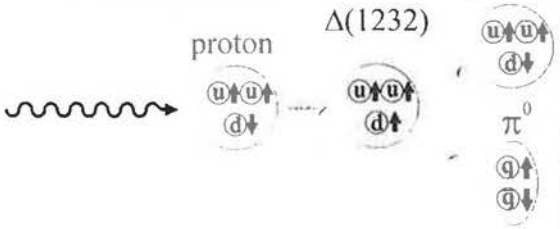

$\gamma + p \Rightarrow \Delta^+ \Rightarrow \pi^0 + p$

$\gamma + p \Rightarrow \Delta^+ \Rightarrow \pi^+ + n$

$\gamma + p \Rightarrow \Delta^+ \Rightarrow \pi^- + \pi^+ + p$

$\gamma + n \Rightarrow \Delta^0 \Rightarrow \pi^0 + n$

.....

PARTICLE PHYSICS WITH PETAWATT-LASERS MPQ

Detection of produced pions:

Geometry:

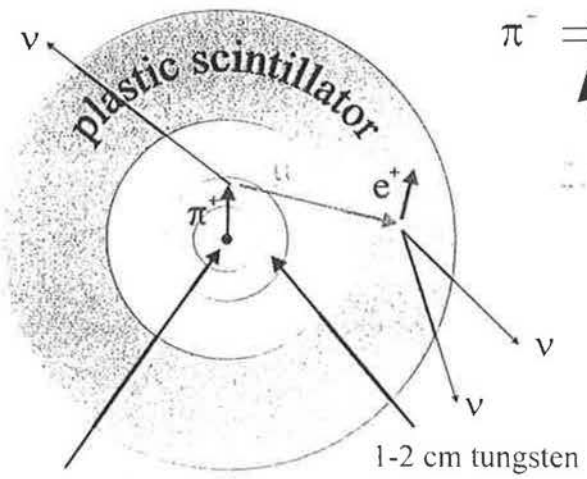

Vertex of pion production

$E_{\mu,kin}$=53 MeV

$\pi^- \Rightarrow \mu^- + \nu_\mu \Rightarrow e^- + \nu_\mu + \nu_e$

2.2×10^{-6} s

Signature:

Detection of delayed positrons in the scintillator, typical. time constant 2 μs

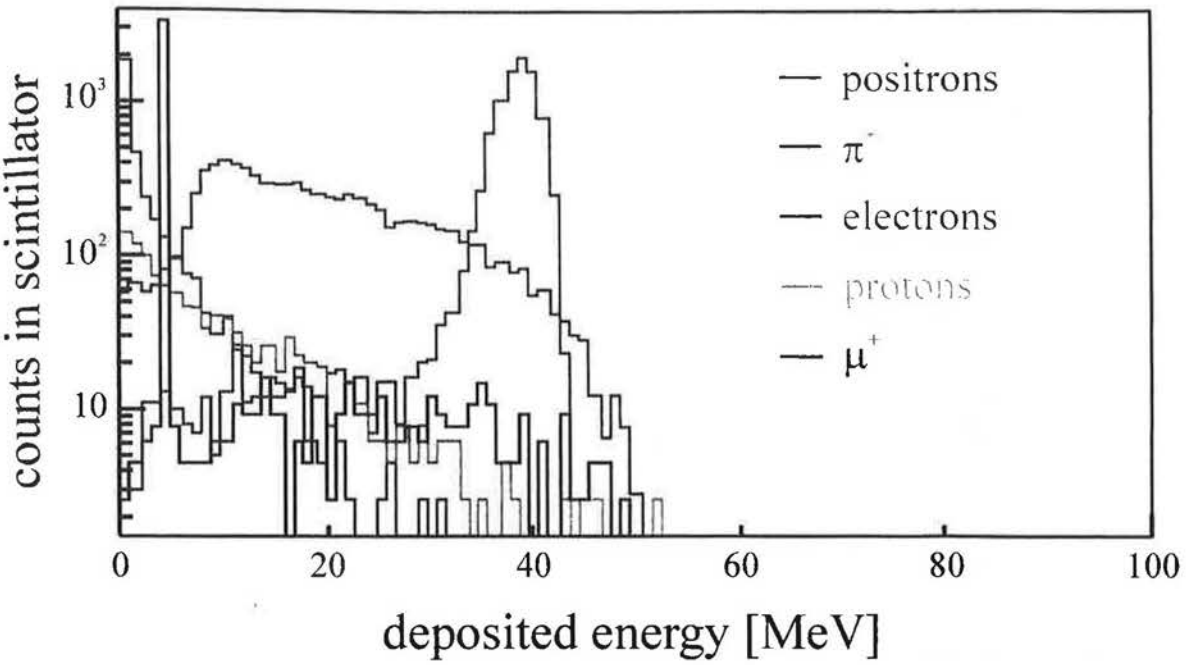

PARTICLE PHYSICS WITH PETAWATT-LASERS MPQ

calculated pion spectra (GEANT) (1 PW, 10^{21}W/cm^2):

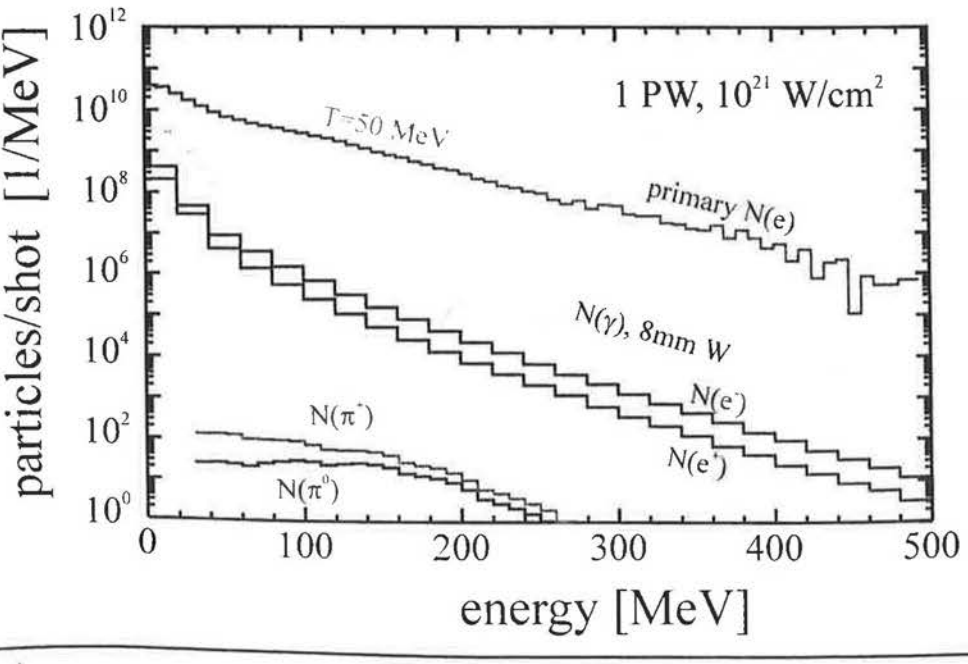

particle physics with high power lasers:

threshold reactions for electron spectra analysis.
1.7 MeV(Be(γ,n)), 2.2 MeV (D(γ,n)) , 5 MeV (shower),
15 MeV (high-Z (γ,n)) , 310 MeV (pions)

source for high energy particles with unique properties :
$T_{pulse} \approx$ 100 fs - 10 ns
small source size ≈ 10 μm - 1 cm ⇒ high brilliance

new insights on electron transport in relativistic laser plasmas

.....

EXPLOSIVE PUSHER NEUTRON SOURCE

George H. Miley
University of Illinois, UC Campus
Fast Ignition Workshop, RAL, UK
Sept 21-23, 1998

Overview

- Need for near-term test facili
  - –Optics damage issues
  - –Requirements
- ICF targets as a neutron source
- Petawatt laser approaches
  - –exploding pusher model
  - –in chamber sample concept
- Conclusions

Both KDP Crystals and Lenses face Damage I

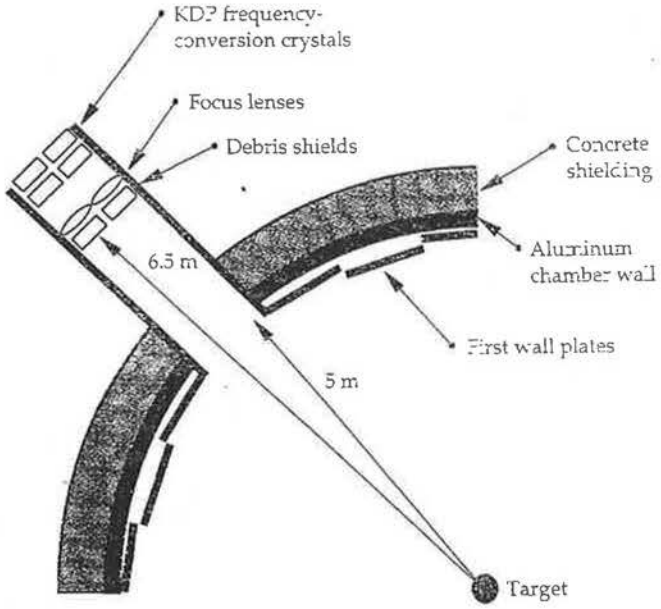

Transmission of silica rapidly decreases with successive radiation shots from a pulsed sion reactor.

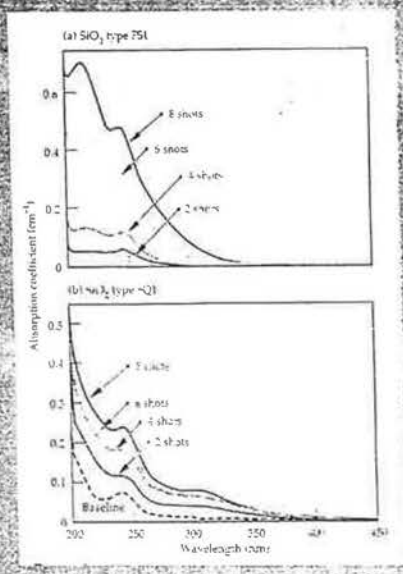

Gamma ray damage is expected to dominate effects in NIF KDP crystals.

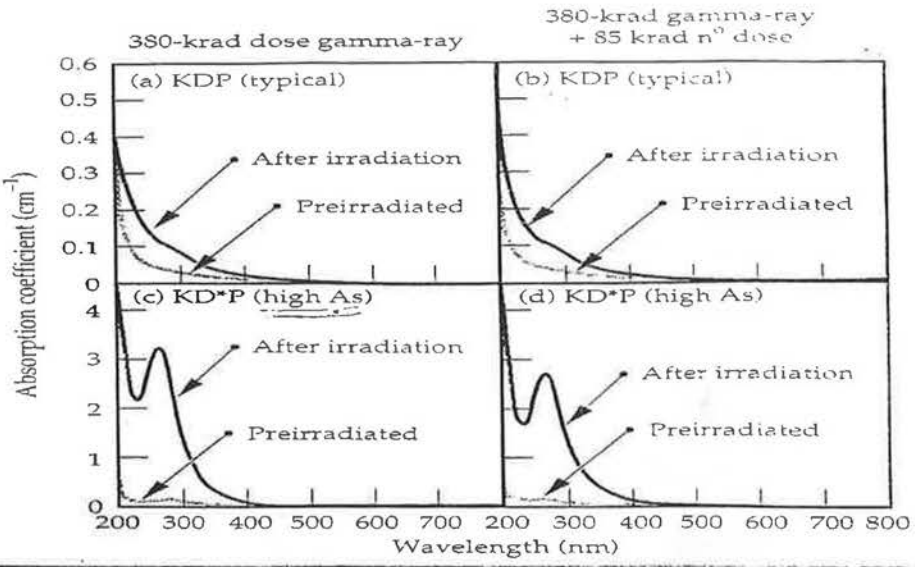

Expected Fluence on Optical Components

NIF (over lifetime

~ 1 M Rad neutrons

0.5 M Rad gammas

(10^{19} n/pulse at 6.5m ;

20 MJ yield shots // 20/yr)

Reactor

(~ 3×10^{8} pulses/yr)

(10^{12} n/pulse-cm² @ 40m)

~ 3×10^{11} Rad/yr

~ 1.6×10^{20} n/cm²-yr.

Possible near-term facility

- Employ port assembly for [illegible] insertion of samples
- High rep rate laser, e.g. 10 Hz
- Most input - 10 - 100 kJ
- Alternatives
  - petawatt laser and special liquid filled target
  - conventional laser with LHART type target

Port assembly for sample insertion

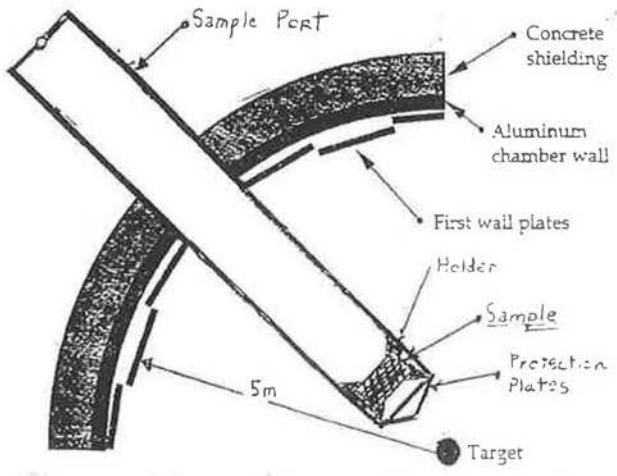

Distance to Test Sample can Compensate for Lower Yields

Example:

Assume: 10 Hz test: $RR/RR_o \sim 1$

1 year test: $t/t_o \sim 1$

test yield $\sim 10^{14}$ n/pulse

$$\frac{Y}{Y_o} \sim \frac{10^{14}}{10^{19}} \sim 10^{-5}$$

then - $\left(\frac{40}{d}\right)^2 \sim 10^{-5}$, $d \sim 16$ cm

Unique Liquid D-T Target for Petawatt Testing

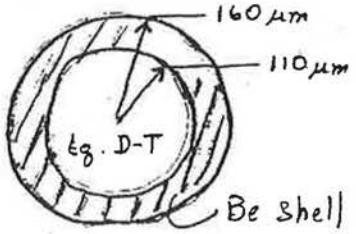

$\rho R_{DT} \sim 0.04$ g/cm^2

$\rho R_{Be} \sim 0.09$ g/cm^2

500 J, 2ps @ 60 μm focus

$\approx 10^{13}$ n/pulse

cf Mike Perry (LANL) Grant Logan (LLNL)

Physics Issues for D-T/Be Target

- Hot Electron Transport & Recirculation
- Magnetic Field Effects
- Space Charge Effects
- Uniformity and Robustness

Multiple decade long development cycles are required to carry new ICF laser architectures to maturity

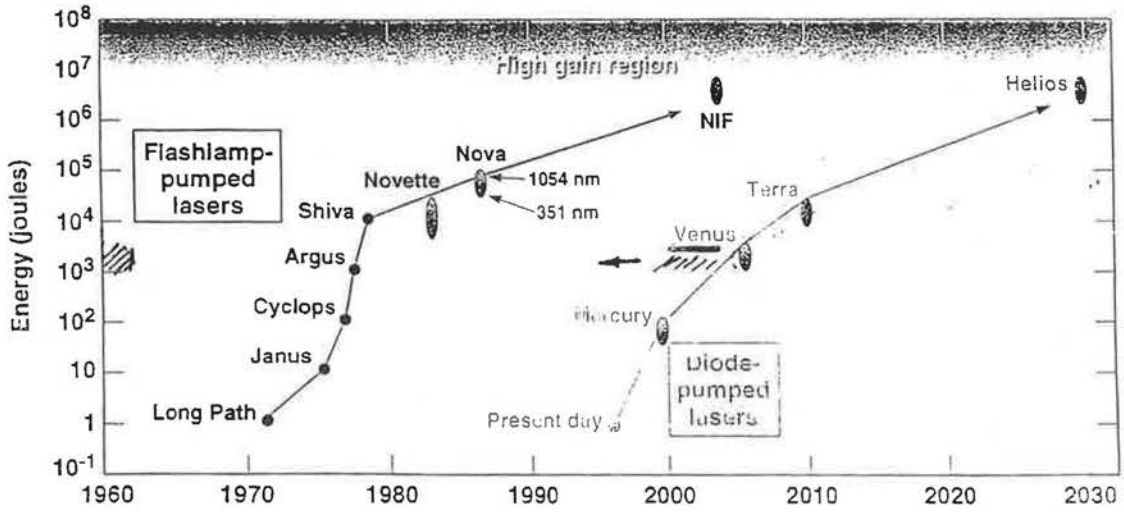

- Terra laser can serve concurrently with NIF as a Nova-class rep-rated system

Diode-pumped solid-state lasers (DPSSL) offer the option of higher rep-rate, better beam quality, and more compactness for advanced ICF drivers and other applications

02-15-0388-0678J

Approximate Model for Scoping Studies
~ modification of
explosive pusher model
Miley + Walch, Fusion Tech, 7, 334 (1985).
(measured α & p from glass microballon implosion)

II.A. ρR Model

During the compression burn phase, the fuel can be considered to be homogeneous in ρR. This greatly simplifies the fuel $\rho R(\rho R_f)$ calculation. Taking $\eta(t)$ as the fuel compression at time t, ρR_f is given by

$$\rho R_f = \eta(t)^{2/3} \rho_{f0} R_o \ , \qquad (1)$$

where ρ_{f0} and R_o are the initial fuel density and outer radius, respectively.

To determine the total pusher ρR, the pusher is split into two regions. The innermost region contains the imploding unablated material of the pusher. This region is steadily eroded away until it vanishes at maximum compression. The second region contains the outward-moving ablated material. The regions are only related through mass conservations and are considered separately.

II.A.1. Imploding Region

This region is relatively homogeneous. We therefore assume that the density does not change rapidly with time at a given radius. The continuity equation in spherical coordinates is given by

$$\frac{\partial \rho}{\partial t}(r,t) + r^{-2} \frac{\partial}{\partial r} \rho(r,t) v(r,t) r^2 = 0 \qquad (2)$$

and can then be reduced to

$$\rho = \frac{const}{v(r) r^2} \ . \qquad (3)$$

The velocity profile can be approximated by making use of two constraints:

1. The velocity is identically zero at some point inside the unablated region.
2. The velocity must fall off as r^{-1} near the ablation surface.[4]

The point at which the velocity vanishes is determined by the position of the initial shock front and remains at $r = 0$ upon coalescence. These conditions are satisfied by

$$v(r) = v_0 (R_v - r) R_i r^{-2} \ , \quad r \geq R_v \ , \qquad (4)$$

where

R_v = position of vanishing velocity

R_i = position of the fuel/pusher interface

v_0 = constant.

The density profile of the imploding region can then be determined from Eqs. (3) and (4) as

$$\Rightarrow \quad \rho(r) = \rho_a \frac{R_a - R_v}{r - R_v} \ , \quad R_i \leq r \leq R_a \ , \qquad (5)$$

where ρ_a and R_a are the density and radius of the ablated/unablated pusher interface, respectively.

II.A.2. Ablated Region

The laser energy is deposited entirely in this low-density ablating region. The heat flow is expected to be flux limited, particularly near the critical density. As described in detail by Max et al. in Ref. 5, for the steady-state assumption the density scales as

$$\rho(r) \propto r^{-n} , \tag{6}$$

where, for a flux limit less than unity, $n \sim 4$.

The solution in the ablated region must be fit to the cold region. Thus, the density profile for the entire pusher is given by

$$\rho(r) = \begin{cases} \rho_a \left(\dfrac{R_a - R_s}{r - R_s} \right) , & R_s \le r \le R_a \\ \rho_a \left(\dfrac{R_a}{r} \right)^4 , & R_a \le r \le R_o \end{cases} , \tag{7}$$

where ρ_a and R_a are yet to be determined. The conditions at the ablation surface are found using the conservation of mass and by assuming an ablation rate. In this way, the total mass in each region at a given time is known.

By integrating the mass density over r in the pusher and considering the conservation of mass, we obtain an equation relating ρ_a and R_a:

$$\Rightarrow \quad \int_{R_s}^{R_a} \rho(r) r^2 \, dr = \rho_{p0} R_a^2 W , \tag{8}$$

where ρ_{p0} and W are the initial pusher density and thickness, respectively.

The mass ablation rate is determined by considering that the rate declines until zero is reached at η_{max}. We therefore assume a constant decline in ablation rate starting at $t = 0$ and ending at $t = t_c$, where t_c is the collapse time. The entire pusher mass at $t = 0$ is in the unablated region. This region loses mass until the total mass is given up to the ablated region at t_c. This ablation rate assumption is discussed further in Sec. II.B. Thus, the second equation is given by

$$\Rightarrow \int_{R_s}^{R_a} \rho(r) r^2 \, dr = \rho_{p0} R_a^2 W \left[1 - \left(\frac{t}{t_c} \right)^2 \right] . \tag{9}$$

Equations (8) and (9) are solved simultaneously to determine ρ_a and R_a for a given $R_s(t/t_c)$. The value R_s is parameterized by considering the pusher velocity to be constant until the fuel compression ratio reaches 32, which is the maximum compression from a spherically converging strong shock. At this point, the pusher slows down uniformly from velocity v_p until stopping at t_c, which is defined as

$$t_c = R_o / v_p . \tag{10}$$

The interface position in terms of the dimensionless time $\tau = t/t_c$ is given by

$$R_s(\tau) = \begin{cases} R_o(1 - \tau) , & 0 \le \tau \le \tau_s \\ R_o \left[\left(\dfrac{\eta_s^{-1/3} - \eta_{max}^{-1/3}}{2\eta_s^{-1/3} - \eta_s^{-2/3}} \right) \right] (1 - \tau^2) + \eta_{max}^{-1/3} , & \\ & \tau_s \le \tau \le 1 , \end{cases} \tag{11}$$

where τ_s is $32^{-1/3}$.

To complete the ρR model, we now relate the shock position and pusher velocity to the shocked fuel-ion temperature $\theta_{fi}(\tau_s)$. From shock relations, the shock velocity relates to the temperature behind the front as[4]

$$v(\tau_s) = \left[\frac{3}{2} \frac{(\gamma + 1)}{2} \frac{32 n_{f0}}{15 \rho_{f0}} \theta_{fi}(\tau_s) \right]^{1/2} , \tag{12}$$

where

n_{f0} = initial ion number density in the fuel

γ = ratio of specific heats.

The factor 32/15 results from the fuel being compressed from 15 to 32 as the shock coalesces. According to Guderley,[6] the shock position is described by

$$R_s = R_o(1 - \tau_s)^{0.717} . \tag{13}$$

Furthermore, the shock velocity from differentiation of Eq. (13) becomes

$$v_s(\tau) = v_s(\tau_s)(\Delta x / R_s)^{0.4} , \tag{14}$$

where Δx is the shock thickness given by

$$\Delta x = \frac{R_o}{3} \left(\frac{\gamma - 1}{\gamma + 1} \right) . \tag{15}$$

Finally, the pusher velocity is obtained from the strong shock relation

$$\Rightarrow \quad v_p = \left(\frac{\gamma - 1}{\gamma + 1} \right) v_s(0) . \tag{16}$$

The target ρR is now completely scaled in terms of the implosion parameters η_{max} and $\theta_{fi}(\tau_s)$. The accuracy of this model is discussed in Sec. III and is shown to be quite good in the time span from shock coalescence to maximum compression. For compactness, the pusher ρR relations [i.e., Eqs. (7) through (16)] are represented symbolically later as

$$\rho R_p = \rho R_p(\tau) . \tag{17}$$

II.B. Temperature Scaling

Slowing down of the proton in the target is a weak function of the fuel and pusher electron temperatures. The proton's temperature sensitivity becomes significant when the electron thermal velocity nears the proton velocity (i.e., for $T_e \sim 1.6$ keV). We can therefore approximate the electron temperature in the cold pusher region. The pusher temperature remains nearly constant during the implosion, declining only slightly due to conduction and radiation effects. More care must be taken in determining the fuel temperature near peak ρR conditions. At that time, the fuel ρR approaches the pusher ρR and its contribution to slowing down becomes significant.

The pusher electron temperature θ_{pe} scales well with the specific absorbed energy ϵ_A for ablative, thin-walled targets based on simulations from the LILAC laser fusion code.[7] A reasonably good relation for θ_{pe} is given by

$$\Rightarrow \quad \theta_{pe} = 0.6\epsilon_A \ , \tag{18}$$

where ϵ_A is given in units of joules per nanogram and θ_{pe} is in kilo-electron-volts. This scaling appears to be accurate to within 10% for target walls up to 3 μm. The pusher temperature could be found independently using an x-ray diagnostic such as suggested by Yaakobi et al.[8]; however, such measurements are not assumed here.

During the compression burn phase, the fuel ions and electrons undergo an isentropic heating due to the compression. In addition, the shock-heated ions transfer energy to the colder electrons until thermal equilibrium is reached. Assuming these two processes are dominant, we can approximate the fuel-ion and electron temperatures θ_{fi} and θ_{fe} by

$$\Rightarrow \quad \dot{\theta}_{fi}(t) = \theta_{fi}\left(\frac{\dot{\eta}}{\eta}\right)^{2/3} + (\theta_{fe} - \theta_{fi})/\tau_{ie} \tag{19}$$

and

$$\Rightarrow \quad \theta_{fe}(t) = \theta_{fe}\left(\frac{\eta}{\eta}\right)^{2/3} + (\theta_{fi} - \theta_{fe})/\tau_{ie} \ . \tag{20}$$

Here, τ_{ie} is the electron-ion thermalization time. The validity of this result is considered in Sec. III.

Equations (19) and (20) can be solved simultaneously for θ_{fi}:

$$\Rightarrow \quad \theta_{fi}(t) = \eta^{2/3}[C_1 + C_2 \exp(-2t/\tau_{ie})] \ , \tag{21}$$

where C_1 and C_2 are arbitrary constants. For a large τ_{ie} compared to the burn time, the ion temperature during the compression burn phase is given by

$$\Rightarrow \quad \theta_{fi}(t) = \eta^{2/3}\theta_0\left[1 + \frac{(t_c - t)}{\tau^*}\right] \ , \tag{22}$$

where θ_0 and τ^* are the preheat and effective electron-ion equilibrium time implosion parameters, respectively.

At the time of shock burn τ_s, the fuel electron and ion temperatures are not uniform or near equilibrium. The shock causes the core region of the fuel to become relatively hot, so that this small region produces the vast majority of fusions. We select the core temperature $\theta_{fi}(\tau_s)$ as the implosion parameter for the shock ion temperature.

The electron temperature in the fuel is relatively cold over the time from τ_s to maximum fuel compression. For the purpose of determining the proton energy downshift, sufficient accuracy is obtained by expressing the electron temperature as

$$\Rightarrow \quad \theta_{fe}(\tau) = \eta^{2/3}\theta_0 \ . \tag{23}$$

The target implosion is now fully modeled in terms of four parameters: η_{max}, θ_0, τ^*, and $\theta_{fi}(\tau_s)$.

Prior Application to D-D proton emission

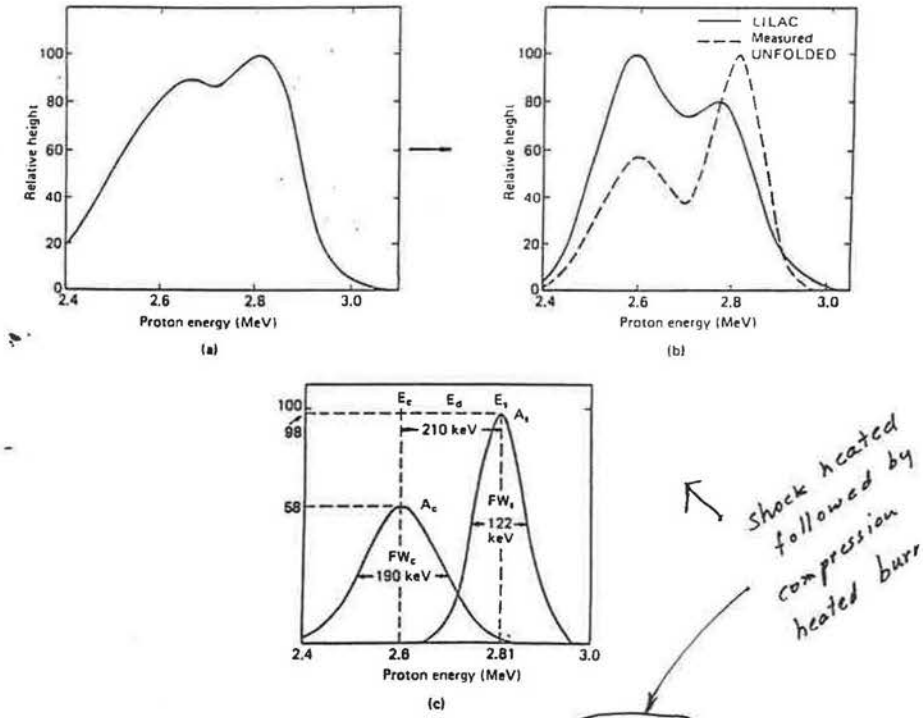

Fig. 6. (a) The measured proton energy spectrum of shot 8533 is given showing a doublet structure; (b) the measured spectrum is unfolded giving actual spectrum and is compared with LILAC; and (c) the unfolded spectrum is fit to two Gaussian peaks.

V.D. Neutron Yield

The neutron yield of a 50-50 D-T fuel target is a strong function of both θ_0 and τ^* and is weakly dependent on η_{max}. The fourth equation relating these parameters to the proton yield will close the set of equations.

The proton yield in the compressive peak can be related to the total neutron yield Y_n. The proportion of D-D reactions to D-T is given by[11]

$$\frac{R_{D\text{-}D}}{R_{D\text{-}T}} = 6.33 \times 10^{-3} \exp(1.18\theta_{fi}^{-1/3}) , \qquad (50)$$

for $\theta_{fi} < 25$ keV. The fraction of protons produced during the compression phase can also be calculated from the unfolded spectrum. The proton yield Y_p is then given by

$$\Rightarrow \quad Y_p = \frac{1}{2} Y_n \frac{R_{D\text{-}D}}{R_{D\text{-}T}} \left(1 + \frac{A_s F W_s}{A_e F W_e}\right)^{-1} \qquad (51)$$

The total proton yield is approximately equal to twice the yield obtained by integrating the reaction rate given in Eq. (35) over the entire compression phase:

$$\Rightarrow \quad Y_p = 2\int_0^1 d\tau t_c A \times \exp\left(-B\left(\theta_0\left[1 + \frac{t_s}{\tau^*}(1-\tau)\right]\right)^{-1/3} \eta^{-2\Lambda}\right) \eta^{5/9} \times \left(\theta_0\left[1 + \frac{t_s}{\tau^*}(1-\tau)\right]\right)^{2\Lambda} . \qquad (52)$$

where A is a function of the target initial conditions.

Using above:

50/50 DT Be target

2 kJ $\theta_e \sim 10$ keV

$\sim 10^{14}$ n/pulse

Summary

- Radiation effects on optics
- Near-term testability
- RR lasers under development
- Requires:
  - Efficient target at ~ 10 Hz
  - Close-in sample reality
  - Target injection system
  - Debris pumping system
- Conceptual design studies recommended

Self-generated magnetic fields can account for the collimated filament in the limit $I < I_{Alfven}$

For $I=I_{Alfven}$ the magnetic field reverses the orbits of the peripheral beam electrons :

$I_{Alfven}(A) = (17\times10^3)\beta_0\gamma_0 \approx 50\times10^3$ A for $E_c = 1$ MeV

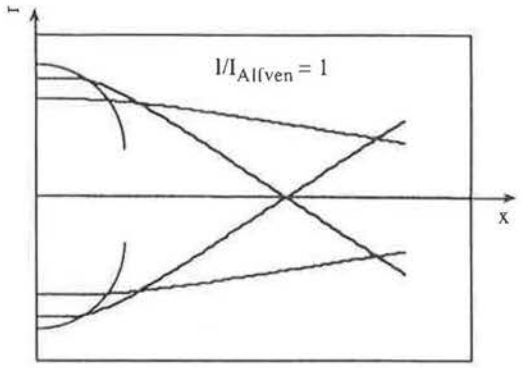

Now, a simple calculation yields $I_{hot} \approx (e\eta_{abs}E_{las})/(E_{cmoy}\,\tau_{las}) \approx 10^7$ A !

PROPEL : a 3D Monte Carlo code to simulate Kα and bremsstrahlung emission in solid targets

- Elastic collisions described using the screened Rutherford cross section for single scattering
  (Moliere, Z. Naturforsch 2a, 133 (1947))
- Slowing down calculated with the relativistic Bethe-Bloch formula
  (Rohrlich and Carlson, Phys. Rev. 93, 38 (1954))
- Kα cross section calculated with the relativistic Kolbenstvedt formula
  (Kolbenstvedt, J. App. Phys. 38, 4785 (1967))
- Bremsstrahlung emission sampled from tables given by Pratt *et al.* (At. Data and Nuc. Data Tables 20 (77)) for the energy spectrum and from the Koch-Motz cross section (Rev. Mod. Phys. 31, 920 (59)) for the angular spectrum

New 3D PIC code developped* to study fast electron transport in solid density targets

- Elastic collisions described by the Moliere distribution which is more accurate than the usual gaussian approximation (Bethe, Phys. Rev. 89, 1256 (1953))
- Slowing down calculated with the relativistic Bethe-Bloch formula (Rohrlich and Carlson, Phys. Rev. 93, 38 (1954))
- Self-generated magnetic field calculated from $\nabla \times \mathbf{B} = \mu_0 \mathbf{j}_{hot}$ where the return and displacement current have been neglected
- Planned upgrading : inclusion of the return current and the electric field, space and time-resolved energy deposition and ionization

*with G. Bonnaud, C. Lebourg, C. Toupin *CEA/Bruyères-le-Châtel*

In the absence of B field, the angular divergence of the 1 MeV beam grows faster

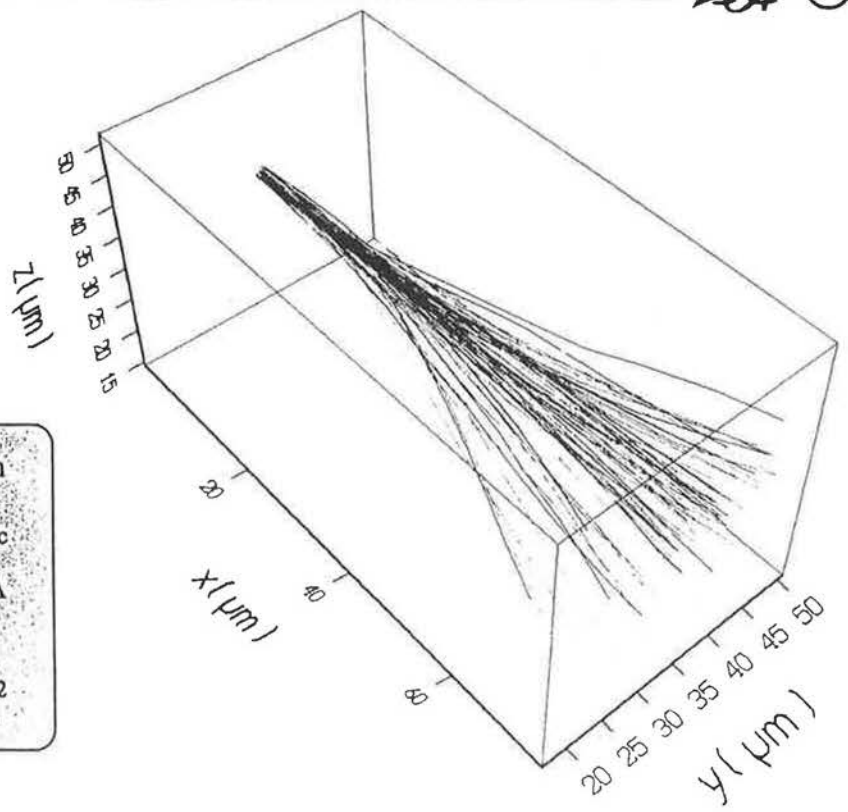

$R_{beam} = 1\ \mu m$
$n_{beam} = 0.1\ n_c$
$I_{beam} = 15\ kA$
$Z = 10$
$\rho = 2.2\ g/cm^2$

Self-generated B field pinches bulk of a 1 MeV beam at least up to ≈ 100μm in SiO_2

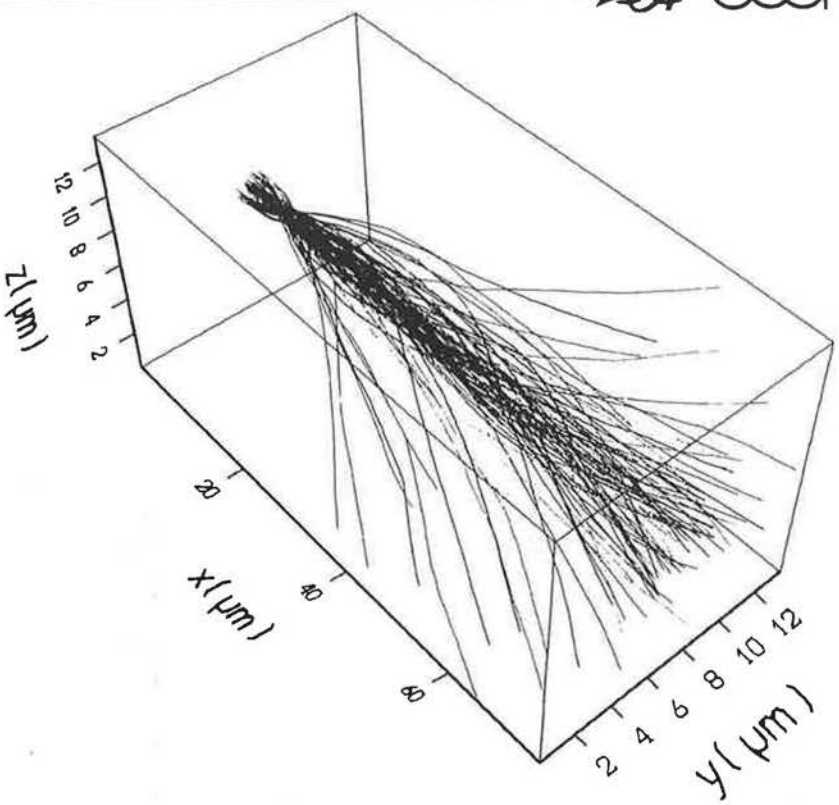

Time-resolved simulations of purely collisional electron propagation consistent with the cloud velocity

Maxwellian relativistic distribution with T_h=200 keV and no self-generated fields

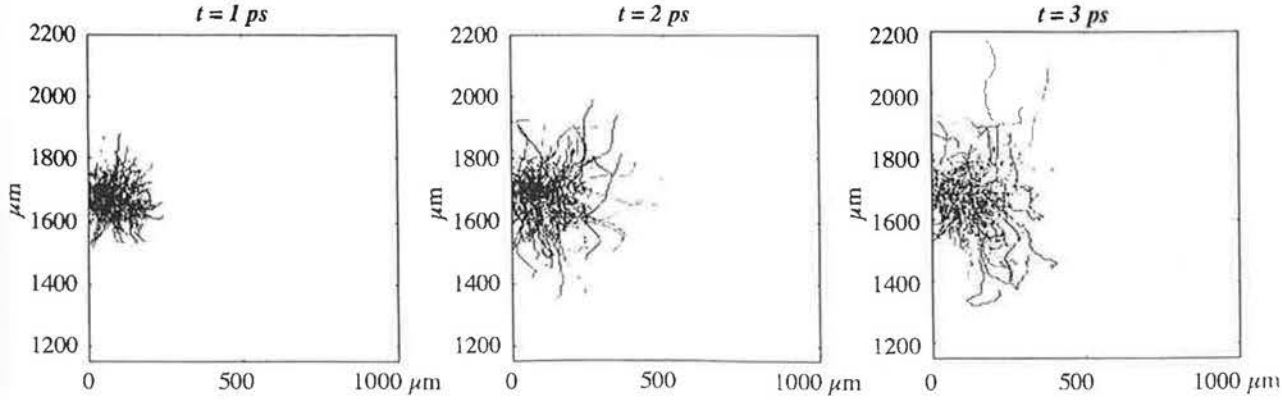

Discussion

- Collimated jet : possibly a relativistic electron beam originating from the center of the focal spot so as to satisfy $I_{net} < I_{Alfven}$

- Cloud : possibly a combination of :
  - peripheral fast electrons expulsed fro the laser axis by the radially increasing B field and propagating collisionally later on
  - hard X-rays (> 1 keV $\Rightarrow \lambda_{mfp} > 2\ \mu$m) emitted by the suprathermal electron distribution

  But certainly not due to soft X-ray thermal transport whose velocity cannot exceed 10^9 cm/s (Ditmire *et al.* Phys. Rev. Lett. 77, 498 (1996))

Rapid expansion of plasma observed : ions or electrons alone ?

$\Delta\tau$ = 2.5 ps $\Rightarrow V_{exp} \approx 3.2\times10^9$ cm/s

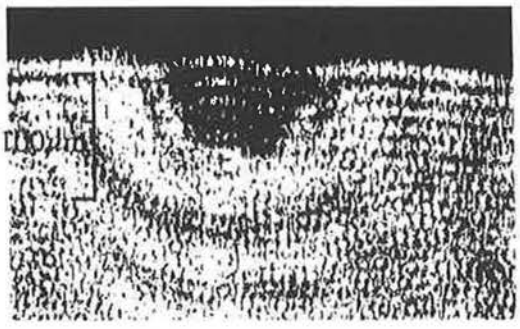

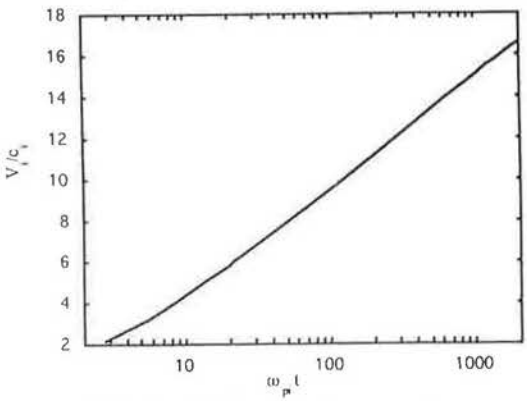

Velocity of the ion front as a function of time in the case of a non-neutral electrostatic sheath
(extrapolated from Crow et *al.*, J. Plasma Physics 14, 65 (1975))

Hypothesis 1 : ions dragged by the electrons

If we assume that locally T_h = 100 keV

$V_i \approx 16\ c_i \approx 3\times10^9$ cm/s but validity of Crow's model uncertain for $\omega_{pi}t >> 1$

Hypothesis 2 : only the electrons are moving

But they are *a priori* reflected on a scalelength $\approx \lambda_{Debye} << 1\mu$m !

time scales required

Self-consistent magnetic field competes with collisional scattering to favor straight-line electron propagation

- Work initiated on electron beam propagation, in presence of self-consistent **B**-field and collisions
  - ➢ Relativistic Fokker-Planck equation modeled by Langevin equations

    elastic collisions on infinite mass ions and inelastic collisions on plasma electrons/ions
  - ➢ B-field calculation assumes: charge and current neutralized

    $\Rightarrow$ no **E**-field and Ampere's law $\nabla \times \mathbf{B} = \mu_0 \mathbf{j}$

Analytical calculation with no B-field
w/wo pitch angle

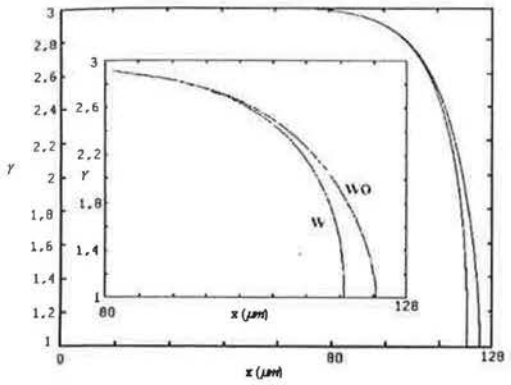

30 kA current of 1 MeV electrons
in a 3 keV Z = 1 plasma

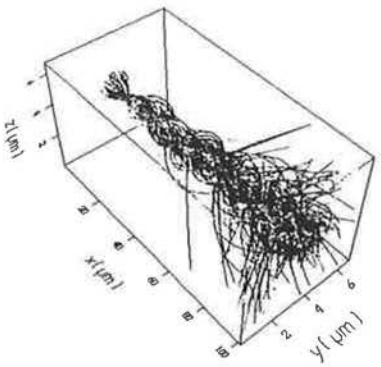

Explanations for the Increased Range of Fast Electrons in Shock Compressed Plasmas

D. BATANI, A. BERNARDINELLO (UNIV. OF MILAN, ITALY)

M. KOENIG, F. PISANI (LULI, CNRS, FRANCE)

J. DAVIES (IMPERIAL COLLEGE, LONDON, UK)

T. HALL (UNIV. OF ESSEX, UK)

P. NORREYS, A. DJAOUI, D. NEELY, S. ROSE (DRAL, UK)

This work was financed
by the EC (TMR):Large Facility Access (contrat ERBFMGEC950053)
by the LEA "HIGH POWER LASER SCIENCE"

Purpose

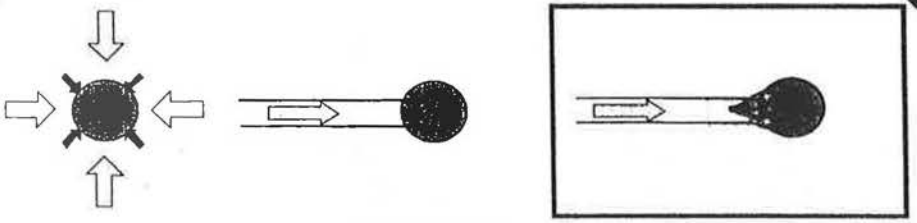

COMPRESSION HOLE-BORING IGNITION

This experiment is a preliminary step in the framework of the **fast ignitor** scheme. It is related to the final phase of this scheme where hot electrons, created by an ultra-intense laser pulse, contribute to the fuel heating.

Through K-α emission spectroscopy:

- characterisation of the fast electrons temperature
- study of the energy deposition of the fast electrons in cold and compressed matter

Experimental set-up

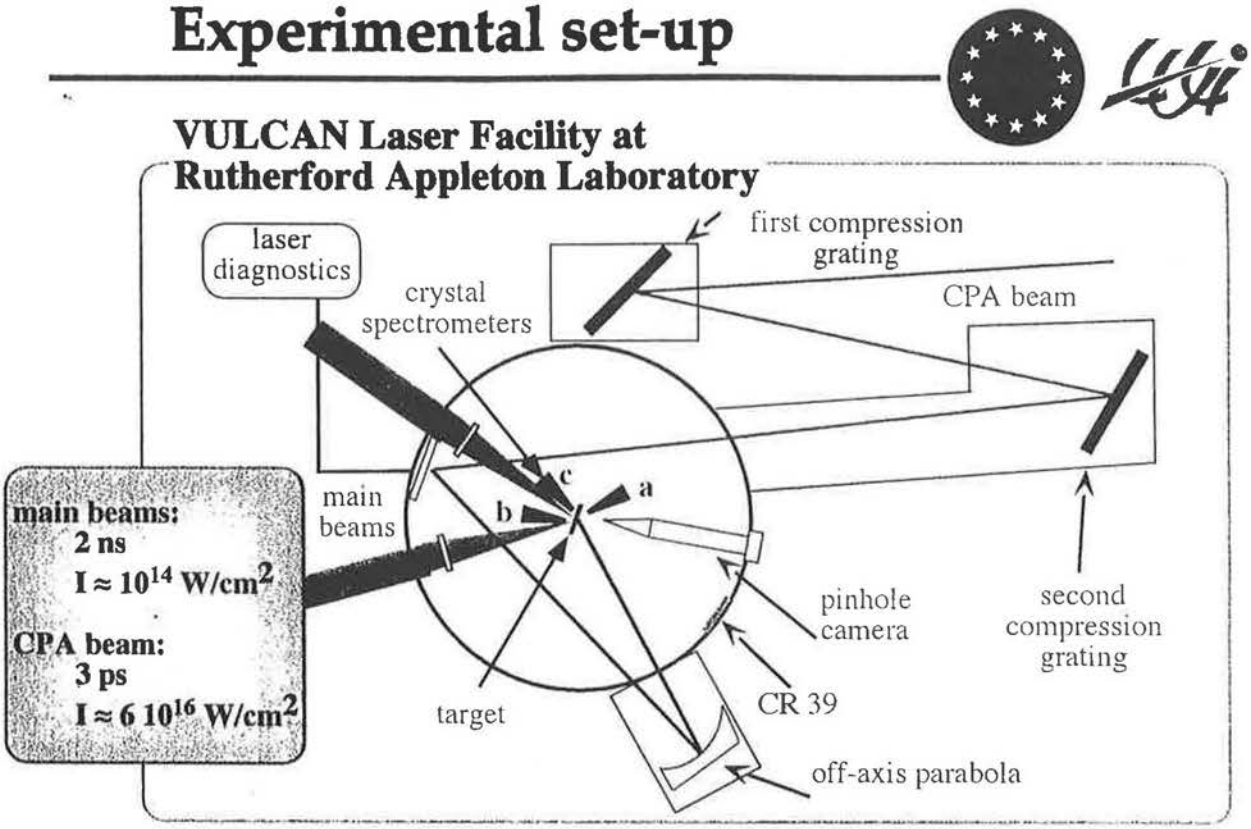

Target configuration

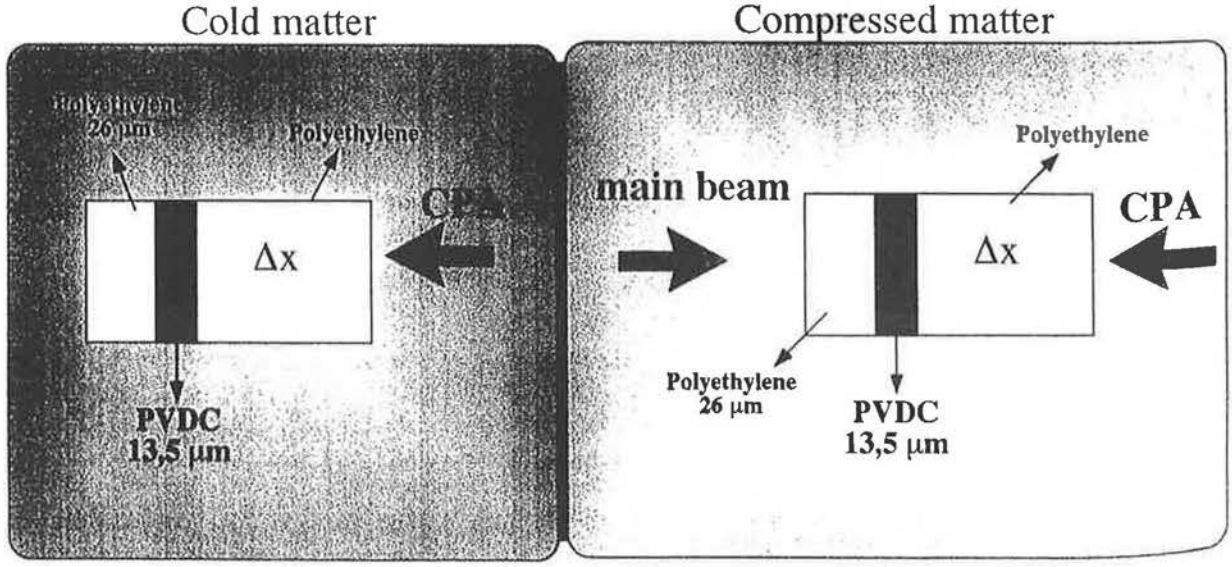

$\Delta x = 10, 26, 44, 70\ \mu m$

COMPARISON COLD-COMPRESSED MATTER

- **Type A targets**
  Data normalised to CPA energy

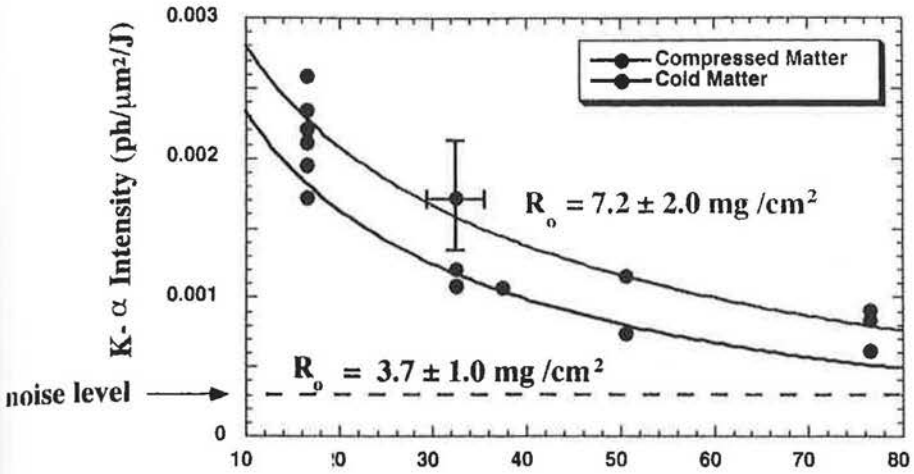

Phys. Rev. Lett., **81**, 1003 (1998)

- **Increased K- α emission for Compressed Matter**
- **ρΔx doesn't change when target is compressed**

DISCUSSION

- **Different fast electron production mechanism in the two cases**
- **Return current effects**
- **Dense plasma effects**

PREHEATING

- Influence of plasma density gradient on hot electron production
- CPA is fired before shock breakout
- No evidence of preheating

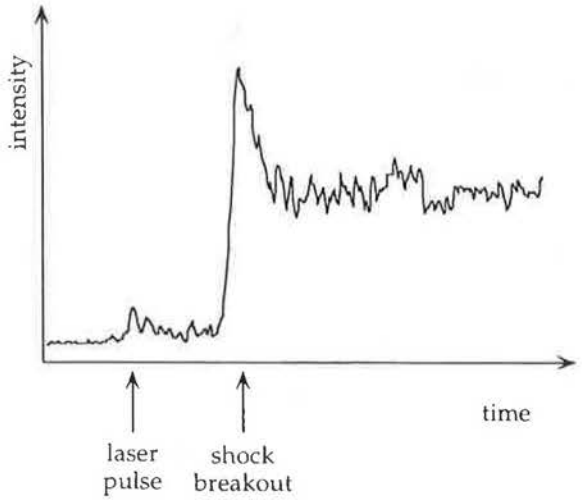

- Presence of low pedestal (contrast ratio $\approx 10^{-6}$)

DATA ANALYSIS

(following F.Beg et al., Phys.Plasma, 4, 447, 1997)

- **Gaussian distribution of hot electrons with temperature scaling $T_{hot} \approx (I\lambda^2)^{1/3} \approx 50$ keV (CR-39)**
- **Conversion of 10% of laser energy into hot electrons**
- **Stopping power approximation to calculate energy loss** $\frac{dE}{dx} = -\frac{4\pi n_i Ze^4}{mv^2} \ln \frac{4E}{I}$
- **K-shell ionisation cross section of Cl atoms** $\sigma\,(cm^2) = 7.9\ 10^{-14} \ln(U_k)/(E_k^2 U_k)$
- **Angular distribution**
- **X-rays absorption**

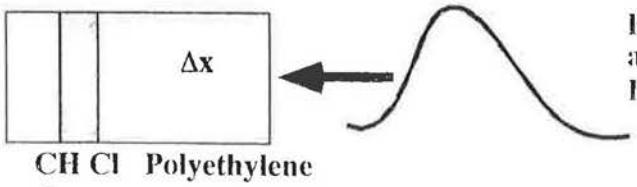

Electrons simulated between 0 and $5T_{hot}$ with 0.05 keV intervals. Plastic divided in 0.05 μm layers.

STOPPING POWER

Cold vs hot matter

Cold:

$$\frac{dE}{dx} = -\frac{4\pi n_i Ze^4}{mv^2} \ln\frac{4E}{I}$$

$$I = 9.75\,Z + 58.8\,Z^{-0.19} \quad (2)$$

Hot:

$$\frac{dE}{dx} = -\frac{4\pi n_i (Z - Z^*)e^4}{mv^2} \ln\frac{4E}{I^*} + \left(\frac{dE}{dx}\right)_{\text{free el.}} + \left(\frac{dE}{dx}\right)_{\text{pl. waves}} \quad (1)$$

$$I^* = a\,Z\,\frac{\exp\left[1.29\,(Z^*/Z)^{(0.72 - 0.18\,Z^*/Z)}\right]}{(1 - Z^*/Z)^{0.5}};$$

$$a = 10\ \text{eV} \quad (3)$$

(1) Val'chuk et al., Pl. Phys. Rep., 21, 159 (1995).
(2) Berger M.J., Seltzer S.M., 1964, in Studies of Penetration of Charged Particles in Matter: 1133 (Washington: National Academy of Sciences), 205.
(3) More R. M., 1985 Laser-Plasma Interaction 3, Proc. 29th Scottish Universities Summer School in Physics, St Andrews, 197.

STOPPING POWER

Cold vs. hot matter

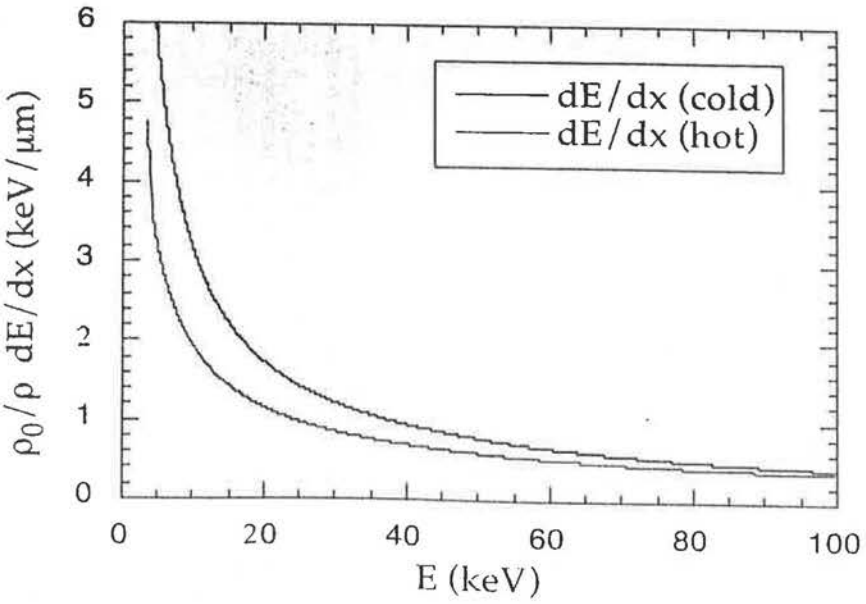

- Decrease of 30% in stopping power at 43 keV

COMPARISON COLD-COMPRESSED MATTER

Monodirectional electron beam with maxwellian distribution at T = 40 keV

All target uniformly compressed

$R_{0\,cold} = 5.7\ g/cm^2$

$R_{0\,comp} = 7.8\ g/cm^2$

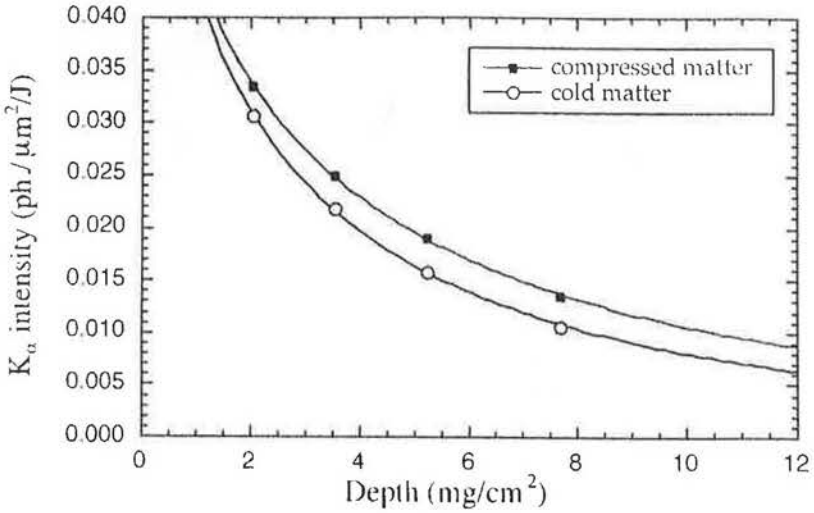

- 36% increase in penetration ⇒ lower than in the experiment
- Penetration higher than experiments ⇒ Need to introduce angular distribution

Modelisation results (cold matter)

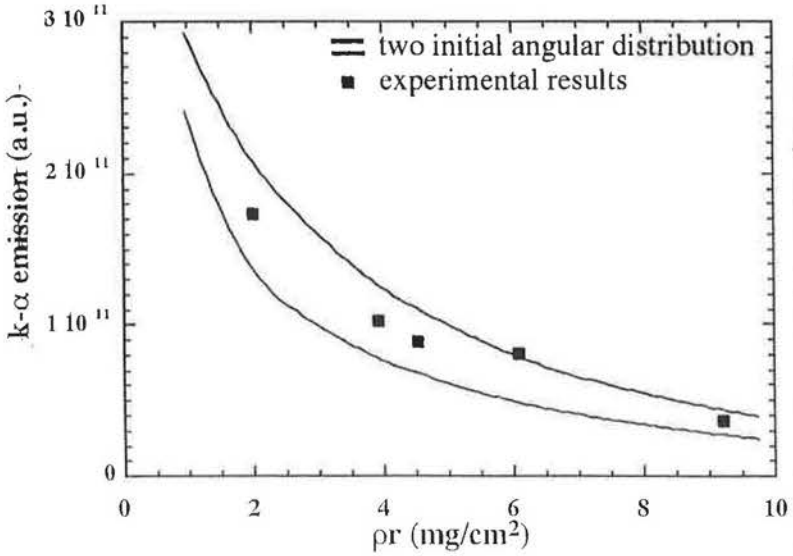

By interpolation with the Harrach and Kidder model, the range is found to be:

$r_0 = 4.3519 \pm 0.32502\ mg/cm^2$

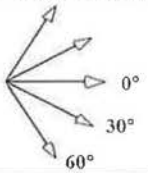

$r_0 = 2.5956 \pm 0.21562\ mg/cm^2$

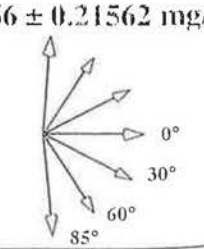

INHIBITION OF ELECTRON BEAM

Following Bell ($z_0 = 3\ 10^{-3}\ \sigma_6\ (kT_{hot})^2\ I_{17}^{-1}\ \mu m$):
penetration depth $z_0 \leq 1\ \mu m$

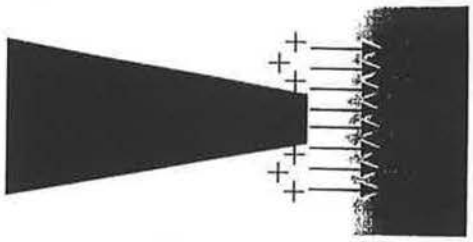

About 10^{14} electrons produced at $E \approx 40$ keV.
Displacement of charge creates $E = \frac{\sigma}{\varepsilon_0} \approx 10^8$ MV/m

INSTEAD NO EVIDENCE OF INHIBITION

- experimental penetration range
- number of photons produced

BEAM INHIBITION

Is matter really an insulator?

- $E_{breakdown} \approx 20$ MV/ m
- Induced heating ⟶ $T \approx 4 \div 8$ eV
- $E \approx 40$ keV $I \approx 40$ eV ⟶ 10^3 secondary electrons generated by incoming electron generate a plasma with typical density $n_e \approx 10^{22}\ cm^{-3}$

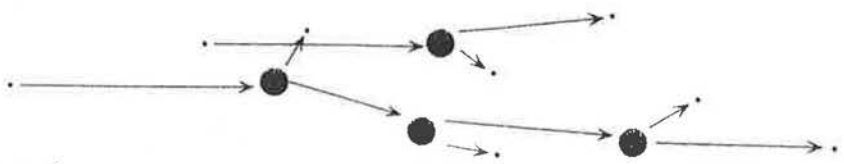

$$t \approx \frac{1}{\omega_p} \approx 0.2 \text{ fs}$$

FOKKER-PLANCK MONTE CARLO SIMULATIONS

(J. Davies et al., PRE, **56**, 7193 (1997))

- Angular distribution ≈ 15°
- 30% laser energy converted into hot electrons
- Electric field effects included
- Resistivity: $1/\eta = 1/\eta_0 + 1/\eta_{Spitzer}$ $\eta_0 = 2.3 \times 10^{-6}\ \Omega$ m
- Heating by hot electrons (thermal capacity)

FOKKER-PLANCK MONTE CARLO SIMULATIONS

Interpolation of data gives the penetration range:

cold $R_0 = 3.4$ mg/cm^2

compressed $R_0 = 5.7$ mg/cm^2

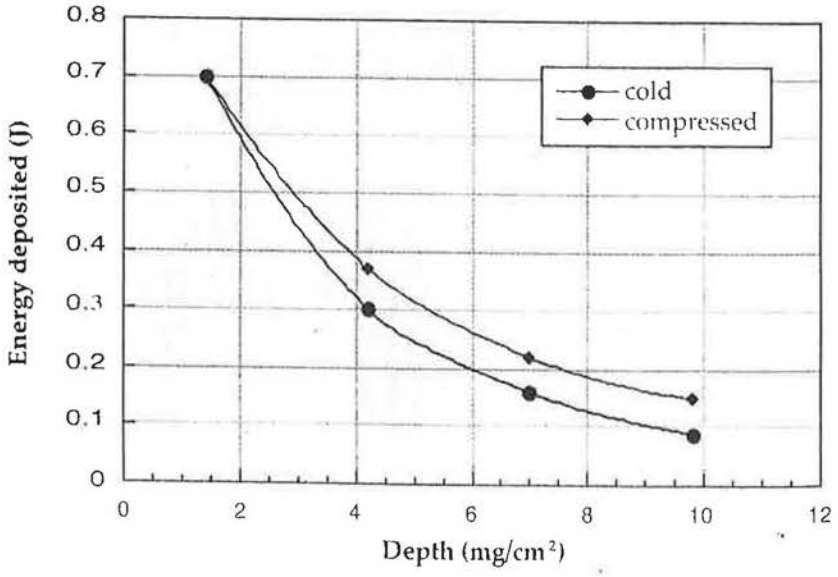

OPEN ISSUES

- Angular distribution opening
- Fraction of laser energy converted into hot electrons
- Possible effects due to degeneration ($E_F / T \approx 6$)
- Possible effects due to strong correlation ($\Gamma = E_P/T \approx 4$)
  For hot electrons: $\lambda_{DB} << R_i$

MULTI SIMULATIONS

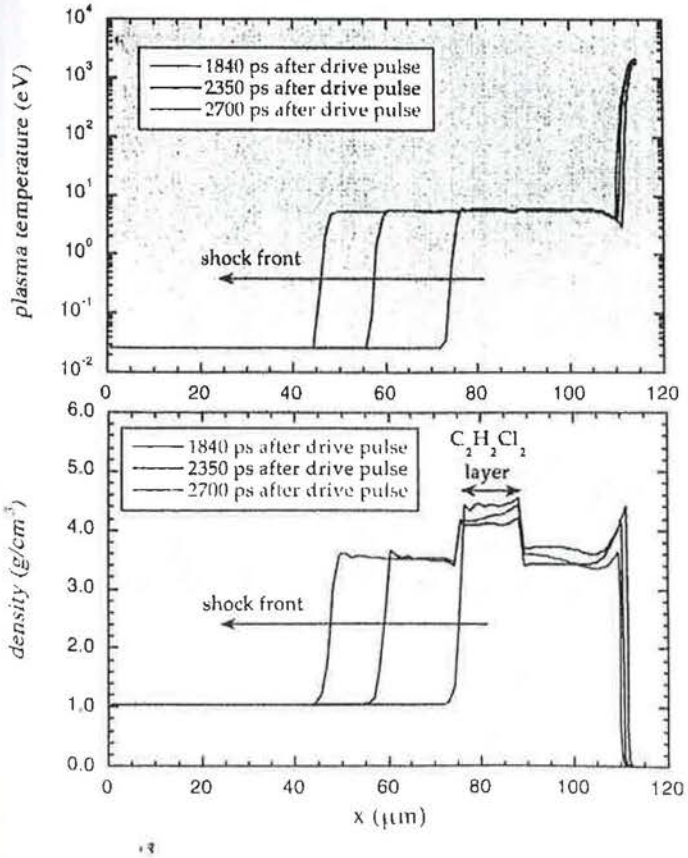

Uncompressed layer thickness (μm)

TOTAL	UNCOMPRESSED
49.5	8.2
65.5	8.9
83.5	9.6
109.5	22.9

$T \approx 6$ eV

$Z^* \approx 1.7$

$\rho/\rho_0 \approx 3.3$

CONCLUSIONS

Is our experiment relevant to the FAST IGNITOR?

- $I_L \approx 10^{16} W/cm^2$ FAST IGNITOR $I_L \approx 10^{19} W/cm^2$
  $T_e \sim I^{1/3}$ here $T_e \sim 40$ keV
  FAST IGNITOR $T_e \sim 400$ keV

- T_e higher ⟶ increased range ⟶ thicker targets ⟶ no uniform compression

  CLEAN EXPERIMENTS need uniform copression

- Density in FAST IGNITOR is higher, but matter correlated and degenerate

  NEED TO INCREASE DENSITY

PERSPECTIVES

- Comparison of penetration in metals vs. insulators
- Study of hot electron production vs. density gradient
- Increase compression

We acknowledge useful discussions with M. Basko, C. Deutsch, J.C. Gauthier, M. Lontano, R. Sigel, J. Meyer-ter-Vehn

Femtosecond laser driven transport experiments

by

T A Hall
University of Essex, Colchester, UK

Acknowledgments

Antonetti[3], A. Mysyrowicz[3], A. Djaoui[4]

(1) University of Essex,
(2) LULI, Ecole Polytechnique,
(3) Laboratoire d'Optique Appliquée,
(4) Rutherford Appleton Laboratory

The work is supported by the European Community under the Large Facilities programme, contract number: CHGE-CT93-0021 and under the Human Capital and Mobility programme, contract number CHRX-CT93-0338

Outline

- Previous results.
  - Frequency domain interferometry.
  - Its use measuring shock and particle velocities.
  - Summary of previous results.
- Measurements at higher irradiances.
  - Shock and particle velocities.
  - Shock precursor?
  - XUV preheat
  - Fast particle preheat

laser

- Ti:sapphire
- Output: 50 mJ, 120 fs, 10 Hz, λ = 800 nm
- Main beam fundamental or frequency doubled (5mJ, 150 fs)
- Focusing optics: f/4 Bowen telescope or f/8 lens unappertured.
- Focal spot diameter 7μm to 12μmfor unappertured beam.
- Maximum irradiance on target: $< 10^{17}$ W cm^{-2}
- Contrast ratio ~ 10^{-7} (fundamental) ~ 10^{-10} (frequency doubled).
- Best focus determined by hard X-ray emission and retro-reflection imaging.

Experiment

- Target: [illegible] aluminium layer (600 Å, 1000 Å, 2000 Å, 4000 Å) on a 2 mm thick fused quartz substrate. Target thicknesses measured/ checked with Tallystep.
- Main beam near normal incidence.
- Frequency domain reflectometry of rear surface with both s and p-polarisation. Incident at 10 degrees or 45 degrees in vacuum.
- Two near transform limited pulses in the time domain produce a cosine distribution in the frequency domain

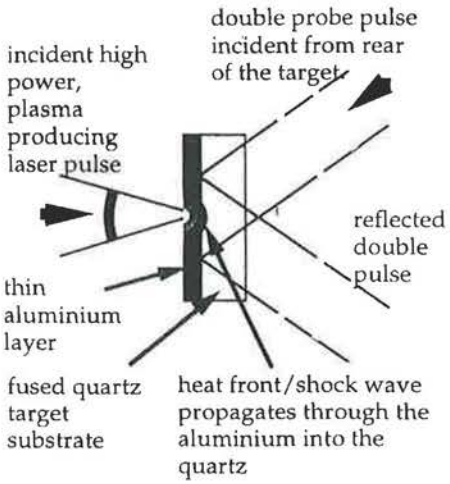

Changes in phase and reflectivity

- Operating [illegible] ph[illegible]
  - (i) Change in phase due to change in the optical properties of the reflecting surface.
  - (ii) Motion of the reflecting surface
  - (iii) Change of optical path through the material between the reflecting surface and the observer.
- There are also three possible contributions to the change reflectivity:
  - (i) For a steep density gradient, the change in the optical properties of metallic surface due to changes in the conductivity of the material.
  - (ii) For a steep density gradient, the change in the nature of the reflecting surface i.e. change from metal/ dielectric interface to an all dielectric interface.
  - (iii) If shock is sufficiently strong to produce ionisation, a density gradient is established in front of the reflecting critical density surface which is strongly absorbing.

Phase and reflectivity

- where u is the velocity of the front and θ is the angle of incidence. For a front velocity of ~ 10^4 m s^{-1} then for λ = 600 nm, this results in

$$\frac{\Delta\phi}{\Delta t} \sim 0.2 \text{ rad. ps}^{-1}$$

- The phase change associated with changes in the complex refractive index of the reflecting material can be large.
- For a steep gradient, the boundary between metal/plasma and dielectric is given by the Fresnel equations.
- The amplitude reflectivity for s - polarisation is :

$$r = \frac{\mu_1 \cos\theta_1 - \mu_2 \cos\theta_2}{\mu_1 \cos\theta_1 + \mu_2 \cos\theta_2}$$

where μ is the refractive index and θ is angle at the interface between the material 1 and 2. If material 2 is the metal/plasma then both μ_2 and θ_2 will be complex.

University of Essex
LOA

Phase and reflectivity

$$\varepsilon_1 = 1 - \frac{\omega_{pf}^2}{\omega^2 + \nu^2} - \omega_{pb}^2 \sum_{j=1} \frac{1}{\omega_j^2 - \omega^2}$$

$$\varepsilon_1 = -\frac{\omega_{pf}^2 \nu}{\omega(\omega^2 + \nu^2)}$$

- Collision frequency determined from an approximate fit to the conductivity model of Lee and More.
- This is modified at low temperatures to give correct values of the optical constants of aluminium:

$\mu = 1.1 + i\,6.4$ for 600 nm light

- The change of refractive index of the material between the reflecting surface and the observer can be significant under certain circumstances.

Phase and reflectivity

Reflectivity and Phase vs. temperature of solid density aluminium

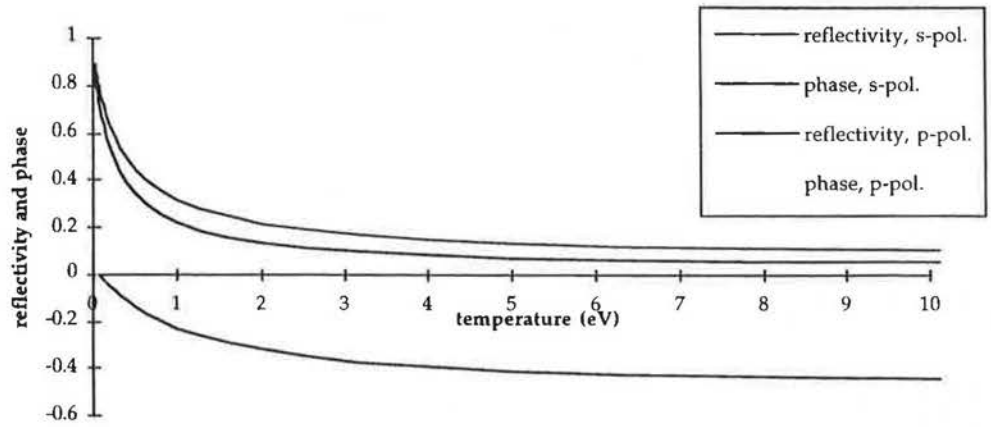

Previous results

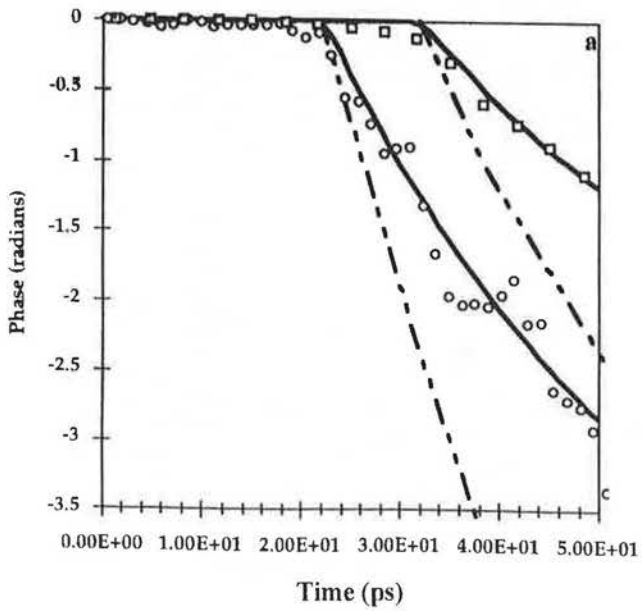

- Experiment: I = 2.6E14 Wcm-2
- Experiment: I = 7.7E13 Wcm-2
- I = 2.6E14 Wcm-2
- I = 2.6E14 Wcm-2 Shock Front
- I = 7.7E13 Wcm-2
- I = 7.7E13 Wcm-2 Shock Front

University of Essex

LOA

Results for various thickness aluminium layers

- Shock and particle velocities can be measured for various thicknesses of aluminium layers.
- Shock is not steady and slows down as it passes into the target.
- However, the comparison with SESAME EOS is good.

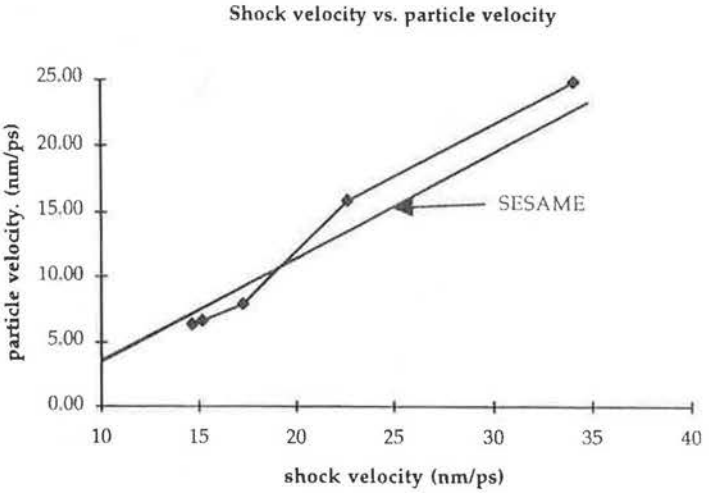

University of Essex

LOA

Conclusions from first results

- No change of phase before shock.
  - This implies that there is little or no preheat.
- Phase change after the shock is due to Doppler shift from the movement of the interface, i.e. not the shock front.
  - Implies that for first few picoseconds there is no significant ionisation in the quartz.
- Reflectivity measurements were not reliable from first experiments and no firm conclusions could be drawn from them.

University of Essex

LOA

Results for higher irradiances

- cooled 16 bit CCD camera
- range.
- Reflectance measurements taken on separate shots with single probe pulse
  - this eliminates the need to know the precise beam splitter and mirror reflectivities in the Michelson interferometer in order to obtain absolute reflectivity measurements.
- Irradiance range 3×10^{14} W cm^{-2} to 4×10^{16} Wcm^{-2} for 200 fs pulse
- and 5×10^{14} W cm^{-2} to 6.3×10^{14} W cm^{-2} for 0.5 ps pulse

University of Essex

LOA

Reflectivity and phase: irradiance 3×10^{14} W cm^{-2}

laser pulse length 200 fs

aluminium thickness 80 nm

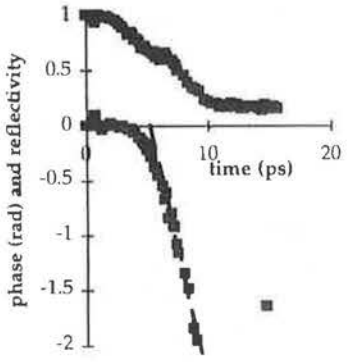

aluminium thickness 200 nm

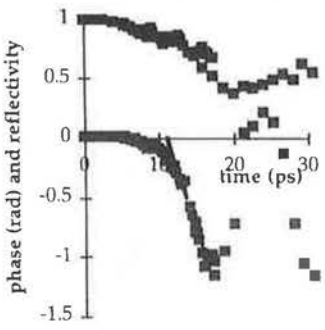

aluminium thickness 320 nm

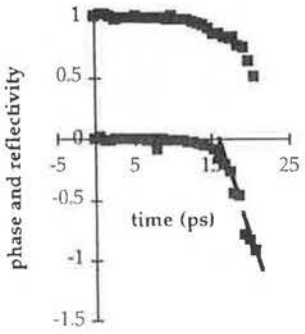

University of Essex

LOA

Reflectivity and phase: irradiance 3×10^{14} W cm^{-2}

- All result[illegible] reflectivity [illegible] the laser pulse [illegible] slowly [illegible] time. This change in reflectivity is attributed to radiative preheat (see later).
- 80 nm aluminium layer shows significant preheat increasing steadily from the time of the laser pulse. Reflectivity strongly affected, the phase less so.
  - Change in the slope of the reflectivity and the rapid change of phase indicate shock breakout into quartz.
- The results for the 200nm aluminium layer are qualitatively similar but with reduced preheat.
- The results for 320nm layer show significantly reduced preheat which does not appear to start at the time of the laser pulse.
- These preheat reflectivity results are very similar to those obtained with [illegible] drive pulses.

University of Essex

LOA

Reflectivity and phase: irradiance 2×10^{15} W cm^{-2}

laser pulse length 200 fs

aluminium thickness 80 nm

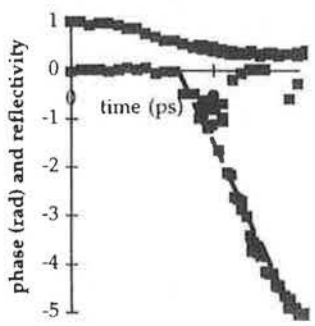

aluminium thickness 200nm

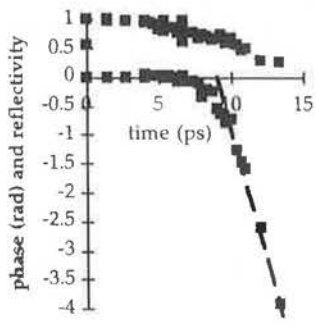

aluminium thickness 320 nm

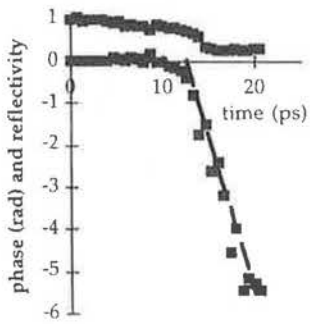

University of Essex

LOA

Reflectivity and phase: irradiance 1×10^{16} W cm^{-2}

laser pulse length 200 fs

aluminium thickness 70 nm

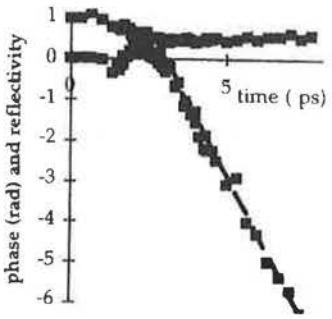

aluminium thickness 200 nm

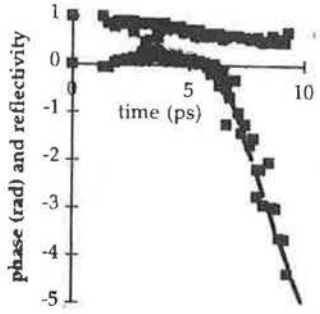

aluminium thickness 320 nm

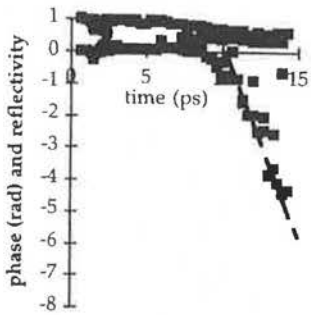

University of Essex

LOA

Reflectivity and phase

- The form of the phase change after shock breakout is similar to that at lower irradiances.
- Reflectivity measurements similar in form to low irradiance with slow continuous fall.
- However there a smaller perturbation to the reflectivity at shock breakout particularly high irradiances and thinner targets.
- Small positive phase change due to preheat consistent with an increased temperature.
- There is a small and non-reproducible perturbation to the phase and reflectivity at the start of the laser pulse.

University of Essex

LOA

Reflectivity and phase: irradiance 4×10^{16} W cm^{-2}

- [illegible] (to the p[illegible] and reflectivity) very large but rapidly returns to more normal levels.
- Pre-shock breakout phase change is significant.
- Rise time of the change ~250 fs (~laser pulse length) and the fall time ~500 fs.
- Both the phase and reflectivity results have more scatter than at lower irradiances.
- At higher irradiances still (>5x10^{16} W cm^{-2}) the reflectivity falls to low value at the time of the laser pulse and does not recover. No phase measurements are possible because of the low reflectivity of the target.

laser pulse length 200 fs

aluminium thickness 320 nm

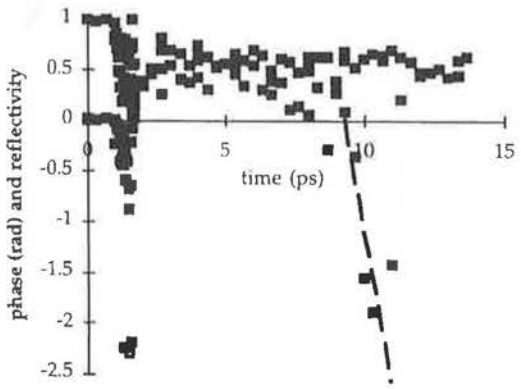

University of Essex

LOA

Discussion : shock and particle velocities

- [illegible] particle velocity [illegible] summarised by plotting particle velocity against shock velocity.

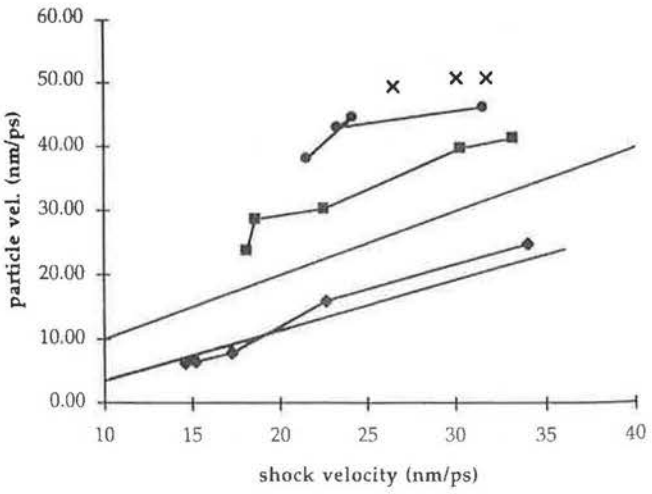

——— 3×10^{14} W cm^{-2}

——— 2×10^{15} W cm^{-2}

——— 1×10^{16} W cm^{-2}

4×10^{16} W cm^{-2}

——— $v_s = v_p$

——— SESAME

Discussion : shock and particle velocities

- [illegible] the shock velocity.
- Clearly, this is physically unacceptable.
- What could be the reasons for this?
  1) We have assumed that no ionisation takes place whilst the particle velocity measurements are being made. If at the higher irradiances, ionisation of the quartz takes place very quickly (<1 ps), then the particle velocity would be the same as the shock velocity.

     This, by itself, could not explain how the particle velocity can be greater than the shock velocity.
  2) The change of temperature of the reflecting surface could change the phase of the reflected wave.

     This could certainly have a small effect, but the change in temperature would have to be very large and continuous to explain the results.
  3) The quartz in front of the aluminium remains transparent and is compressed ahead of the shock front, leading to a change in the optical path between the source and the observer.

Radiative preheat

- MULTI simulation of reflectivity of 400 nm aluminium layer on quartz.
- Irradiance 5×10^{15} W cm^{-2}

- XUV and soft x-ray preheat result in a similar fall in reflectivity to those shown in the experiment whereas without preheat there is no change in reflectivity until shock breakout.
- Rapid change in reflectivity at shock breakout is more pronounced in simulations than in experiments.

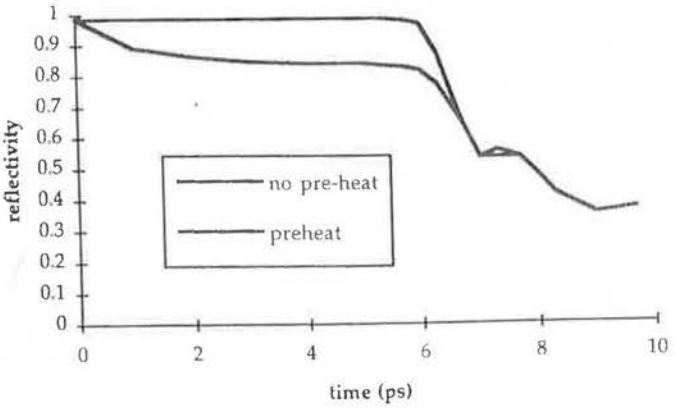

Fast electron preheat

- Results of probe absorption and reflectivity:
  - (i) At high irradiances, the rapid change in phase and reflectivity during the time of the laser pulse.
  - (ii) Rise time of the change ~250 fs (~laser pulse length), and the fall time ~500 fs.
  - (ii) Both the phase and reflectivity results have more scatter than at lower irradiances.
  - (iv) At higher irradiances still (>5×10^{16} W cm^{-2}, the reflectivity falls to low value at the time of the laser pulse and does not recover: no phase measurements are possible because of the low reflectivity of the target.
- This rapid changes could result from:
  - (i) light leakage through aluminium layer
  - (ii) fast electrons which penetrate the aluminium layer and cause absorption in the quartz.

University of Essex
LOA

Fast electron preheat

- New experiment set up to produce 2 dimensional images of rear side of the aluminium.
- Experimental setup is similar to frequency domain interferometry arrangement but without the Michelson (a single pulse used) and the spectrometer (2-D images recorded directly on the CCD camera).
- Drive pulse wavelength 800nm, pulse length 120 fs
- Irradiance on target 6×10^{16} W cm^{-2}
- Probe pulse 800nm, 120 fs

Fast electron preheat

- Sequence of images (but not on the same shot)
- Images not reproducible but tend to show the general behaviour shown.
- In early phases there are several absorption regions which may coalesce to form a single spot which then expands.
- At slightly lower irradiances the gets less at later times.
- Results appear to suggest that fast electrons penetrate into the quartz and cause ionisation.
- At intermediate irradiances this ionisation rapidly combines but at the higher irradiances, permanent damage results.

0 fs 70 fs 140 fs

210 fs 280 fs 350 fs

University of Essex
LOA

Conclusions

- At low irradiances the measurement of the probe beam change immediately [illegible] breakout appears to be related to the particle velocity.
- At higher irradiances this relationship breaks down and the "particle" velocity measured in this way exceeds the shock velocity.
- There is no clear understanding of why this is so but it may be because the quartz is not immediately ionised by the shock wave and the probe beam "looks through" the quartz to the aluminium interface layer.
- Radiative preheat appears to be responsible for a pre-shock breakout reduction in the reflectivity despite the fact that the laser energy incident on the target is only ~10 mJ.
- At high irradiances (> 10^16 W cm-2) a rapid reduction in reflectivity and change in phase is observed at the time of the laser pulse. This is considered to be consistent with fast electron ionisation in the quartz.

Photonuclear Activation Measurements with the LLNL Petawatt Laser

T. C. Sangster, M. A. Stoyer, T. E. Cowan, S. P. Hatchett,
E. A. Henry, M. H. Key, M. J. Moran, D. M. Pennington,
M. D. Perry, T. W. Phillips, M. S. Singh and R. A. Snavely
Lawrence Livermore National Laboratory

Third International Workshop on Fast Ignition
of Fusion Targets
Oxfordshire, England
September 21-25, 1998

Work performed under the auspices of the U. S. Department of Energy by the Lawrence Livermore National Laboratory under Contract No. W-7405-ENG-48.

TCS:TiSeFIWorkshop
9/16/98

A large number of diagnostics are routinely fielded on every Petawatt target shot.

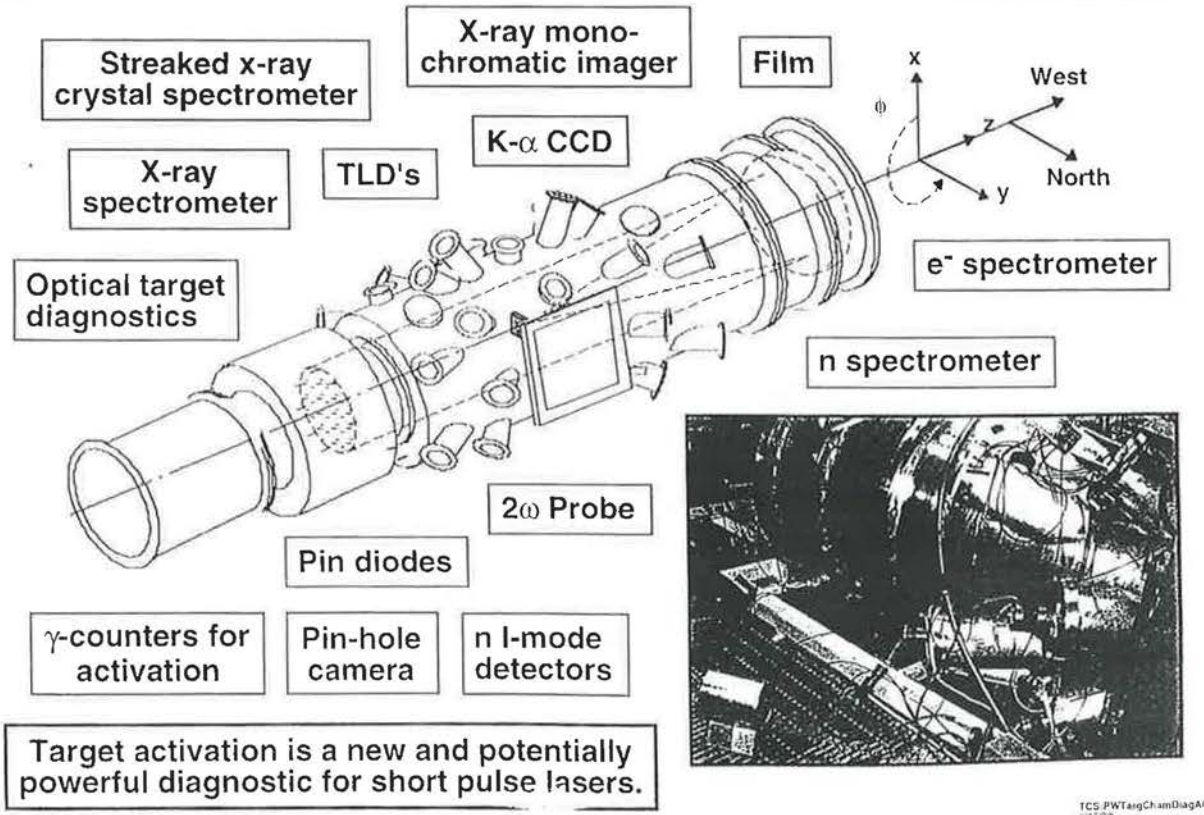

TCS:PWTargChamDiagACT

Activation is used to measure the absolute photon/e⁻ flux, angular distribution and effective temperature (slope).

What do we know?

1) A significant fraction of the laser energy is converted into electrons.

2) In a high Z target, many of these electrons are converted to photons via Bremsstrahlung.

3) For relativistic electrons, the final photon distribution is nearly identical to the electron distribution.

There are three relevant nuclear processes.

A(γ,n)A-1 $E\gamma > 8$ MeV
$E_n < 6$ MeV
$\langle E_n \rangle = 1\text{-}2$ MeV

A(γ,p)A-1 $E\gamma > 8$ MeV

(Giant Dipole Resonance)

A(n,γ)A+1 Any E_n
$E\gamma < 8$ MeV

(Neutron Capture)

D(γ,n)p 2.2 MeV <
$E\gamma <$ ~ 10 MeV

(Deuterium Photodissociation)

Suitable activation elements combine high cross sections with reasonable half lives.

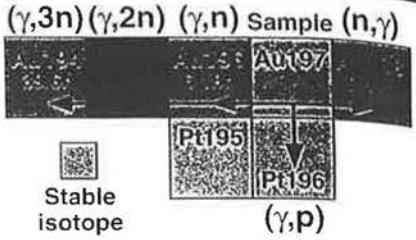

Multiple element samples with different thresholds can be used to determine the spectral Eγ slope.

(γ,xn) reactions at higher thresholds can also be used to determine the slope from a single elemental sample.

It is also essential to select activation elements with well known cross sections!

TCS:ActivationExplanation 9/15/98

The number of activated atoms at t_0 (laser shot time) can be determined using standard nuclear counting techniques.

High resolution germanium detectors are used to count the number of decays.

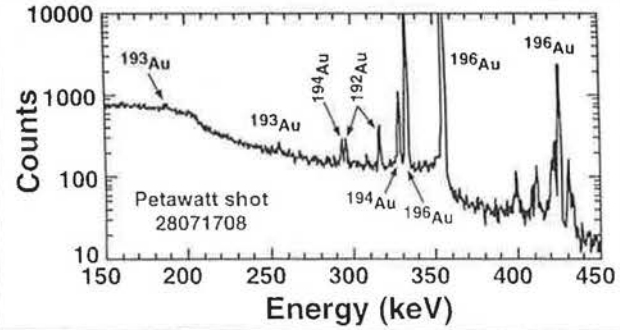

The number of activated atoms per target atom can be calculated from the number of decays using the known half-lives, the delay from t_0 and the duration of the count:

$$\frac{\#\text{activated}}{\#\text{target}} = \sigma(\gamma,n)\,\Phi_\gamma$$

(γ,n) cross sections for Ni, Au, In and Al

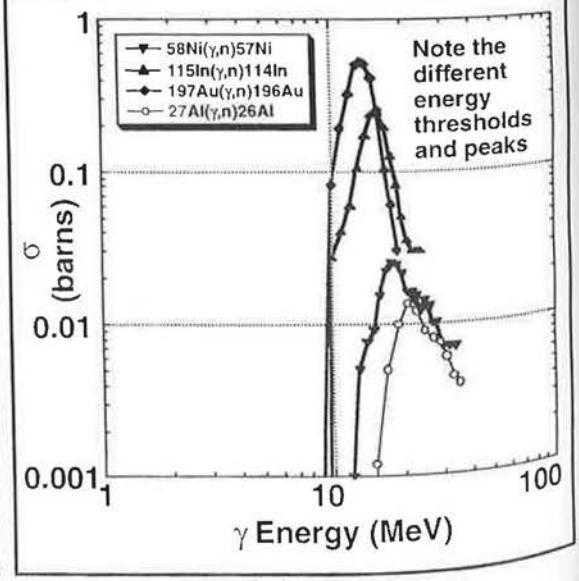

If $\sigma_{\gamma,n}(E\gamma)$ is known then the photon flux can be determined by using two or more elemental samples with different activation thresholds.

TCS:CountingExplanation 9/15/98

Target designs have been optimized to measure the photon flux, spectrum and angular distribution using activation.

Some early target designs included CD_2

Au-CD_2-In-Au-In-Au-Ti

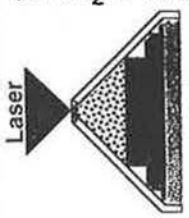

(γ,n) activation plus photodissociation of D

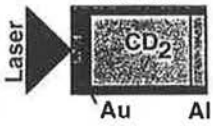

Photodissociation of deuterium to measure Eγ spectrum

Au-Ni-In-Al sandwich

First purely activation target; In for (n,γ) reaction

Next generation targets included segmentation for angular distributions

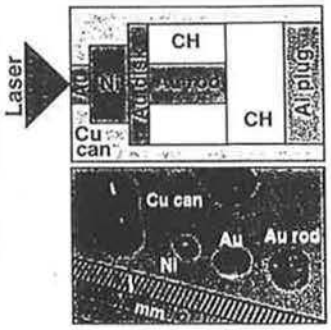

Ni and Au disks were cut in halves and oriented to give a 4 quadrant measurement

Au and Ni are optimal due to well separated thresholds and well known cross sections

Latest targets contain high and low resolution pixelated Au samples

Samples replace the Au disk in Cu can; 45° field-of-view half cone angle

HiRes target: x26 1mm dia x 1mm deep Au slugs

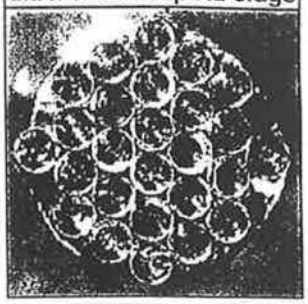

LoRes version has x7 2mm dia Au slugs.

TCS:ActTargetHistory 9/16/98

Both the Au activation and TLD arrays cover a 45 degree cone centered on the laser axis.

Petawatt Shot 28080116; $^{197}Au(\gamma,n)^{196}Au$ activation data on 1mm Au disks

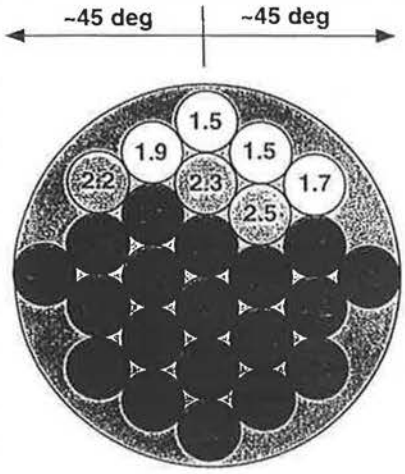

x10^{-14} atoms produced at t0 per target atom

- 6.0 - 6.9
- 5.0 - 5.9
- 4.0 - 4.9
- 3.0 - 3.9
- 2.0 - 2.9
- 1.0 - 1.9

Solid angle correction assumes an e^- point source at the target surface.

First evidence for multiple high energy electon (or photon) jets

Shot 0116 radiation dose from TLD array showing multiple electron jets

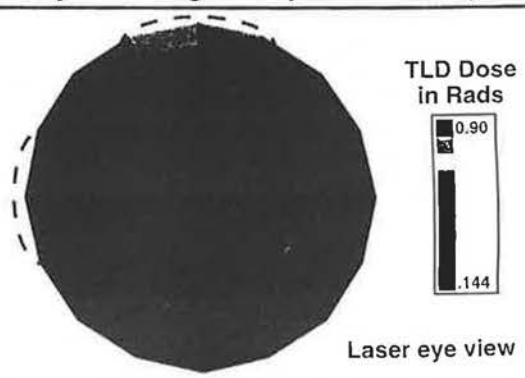

TLD's arrayed concentrically on laser axis at 0, 6, 13, 18, 22.5, 27, 36 and 45 degrees

In this shot, there appears to be no spatial correlation between the low energy (< few MeV) radiation dose and the high energy activation.

TCS:TLD-ACTComp0116 9/15/98

Typically only the larger 2 mm Au samples in the low resolution targets have enough $(\gamma,3n)$, ^{194}Au, to count.

Petawatt Shot 28081207; $^{197}Au(\gamma,n)^{196}Au$ activation data from 1mm Au disks.

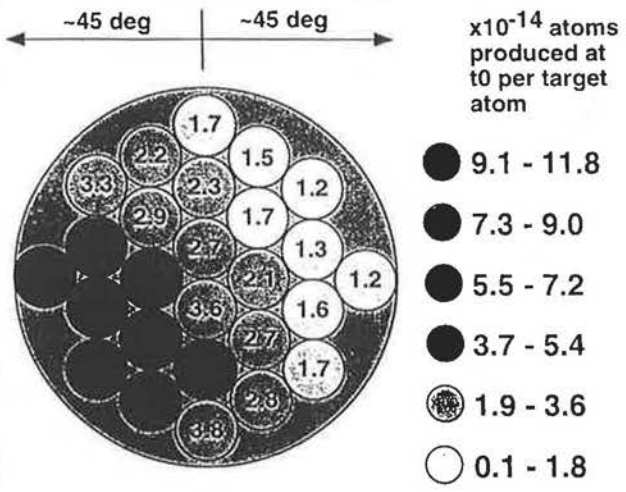

$x10^{-14}$ atoms produced at t0 per target atom

- 9.1 - 11.8
- 7.3 - 9.0
- 5.5 - 7.2
- 3.7 - 5.4
- 1.9 - 3.6
- 0.1 - 1.8

Solid angle correction assumes an e^- point source at the target surface.

The larger 2mm disks seem to indicate that the distribution of $(\gamma,3n)$ is not the same as (γ,n).

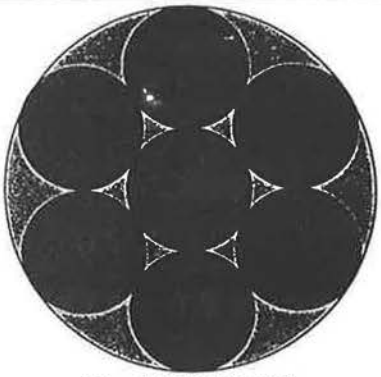

Shot 28082707

Upper: $x10^{-14}$ activated atoms (γ,n) at t_0 per target atom

Lower: $\#^{194}Au$ / $\#^{196}Au$ ratio

TCS:HiResLoResComp 9/17/98

A single maxwellian is used to model the photon spectrum above 8 MeV.

Measured

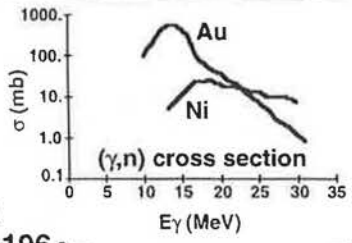

$$\frac{\#^{196}Au}{\#^{197}Au} = N \int \sigma_{Au}(E\gamma)\, e^{-E\gamma/T}\, dE\gamma$$

$$\frac{\#^{57}Ni}{\#^{58}Ni} = N \int \sigma_{Ni}(E\gamma)\, e^{-E\gamma/T}\, dE\gamma$$

Solving the equations gives the flux, N, and the slope, T

Note that the different T's indicate that the spectrum is not a single exponential!

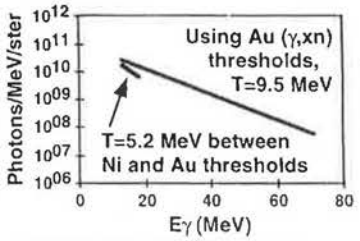

T may also depend on Θ and Φ

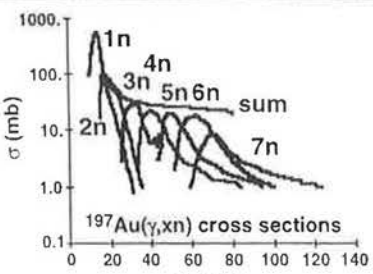

$$\frac{\#^{196}Au}{\#^{197}Au} = N \int \sigma_{\gamma,n}(E\gamma)\, e^{-E\gamma/T}\, dE\gamma$$

$$\frac{\#^{197-x}Au}{\#^{197}Au} = N \int \sigma_{\gamma,xn}(E\gamma)\, e^{-E\gamma/T}\, dE\gamma$$

Measured

TCS:PhotonSpectrum 9/17/98

The measured activation and photoneutron yield is consistent with e⁻, γ transport calculations (ITS).

Begin with a meas'd electron spectrum

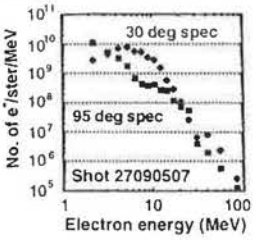

Input

e⁻,γ transport Monte Carlo (ITS)

Output

γ,e⁻ flux through target and chamber

Fold σ(γ,n)'s with flux to determine activation and n yield

ITS calculations reproduce the meas'd activation yields

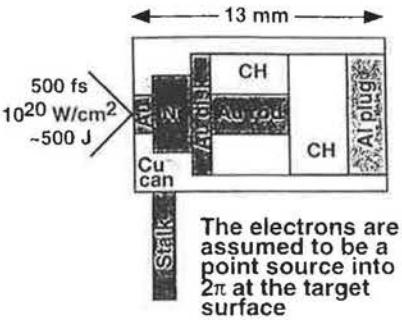

The electrons are assumed to be a point source into 2π at the target surface

(γ,n) Activation Yields Shot 28061708

Sample	Meas'd	Calc'd
Au disk	2.37E8	2.35E8
Au rod	5.96E7	6.61E7
Ni disk	1.27E7	1.16E7

And the photoneutron yield from all sources

Sample	(γ,xn) yield
Au target	2.63E8
Ni disk	1.71E7
Au disk	2.41E8
Au rod	7.55E7
Cu can	4.16E8
Al Target Chamber	1.50E8
Total Yield	1.01E9
Measured	9.10E8

Total neutron yield measured by a (n,γ) activation detector.

Note that multiple n emission contributes to the total photo-neutron yield.

TCS:ITSPhotoneutrons 9/16/98

Summary

Target activation is a powerful diagnostic tool for studying hot electrons from short pulse laser interactions.

Properly designed targets can yield the absolute photon flux and spectral shape above 8 MeV as well as the angular distribution of the flux intensity.

Target design criteria include:

- Activation thresholds (important for spectral measurements)
- Half lives (optimal values > several hours to days; not weeks)
- Total cross sections (can limit sample size if too small)
- Knowledge of cross section energy dependence (required for spectral measurements)
- Adequate decay photon energy for counting (typically > few 100 keV; lower energies impact counting efficiency due to self-attenuation)
- Multiple decay photons for consistency checks (not essential)
- Sample geometry (can significantly affect counting efficiency)

Optimal activation samples appear to be Ni and Au - largest threshold difference of any two elements with well known cross sections.

High energy (>8 MeV) electron jets with fluxes approaching 10E11 /MeV/ster have been observed via target activation with the Petawatt laser.

TCS:ITSummary 9/17/98

Neutron emission produced by high intensity subpicosecond laser pulse

L. Disdier, J-P. Garçonnet and J-L. Miquel

Workshop on Fast Ignition of Fusion Targets 98

- **Goals**

  - **Generation of fast ions**

    Laser plasma physics

  - **Short duration neutron source**

    ICF diagnostics tests

ILLUMINATION CONDITIONS

- **Laser P102**

  30 J chirped pulse at 1ω is compressed by means of grating pair. The pulse duration at 1ω is routinely 400 fs

  Laser pulse is frequency doubled at 2ω

  Focal spot size is 5 μm containing 30 % of the energy

  Maximum energy is 7J. Intensity is 3.5 10^{19} W/cm^2

  Contrast ratio is 10^{12} => laser interacts with target at solid density

LIGTH ON TARGET

- **An off axis parabola focuses the light on the target at normal incidence**

- **The target is made with a compressed powder of deuterated polyethylene**

- **Deuterium percentage (92%) is controlled by nuclear magnetic resonance**

- **Target density is 1 and thickness is 400 μm**

ELECTRON MEASUREMENTS

- **Electrons are measured in the laser axis direction 16.5 cm behind the target**

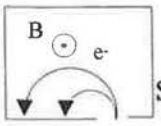

Electron spectrometer

- **Magnetic Spectrometer measures from 0.5 to 2.7 MeV**

CD_2 target

Laser 2ω

Parabola

ELECTRON SPECTRA

- **Electron spectra are non maxwellian at high intensity**

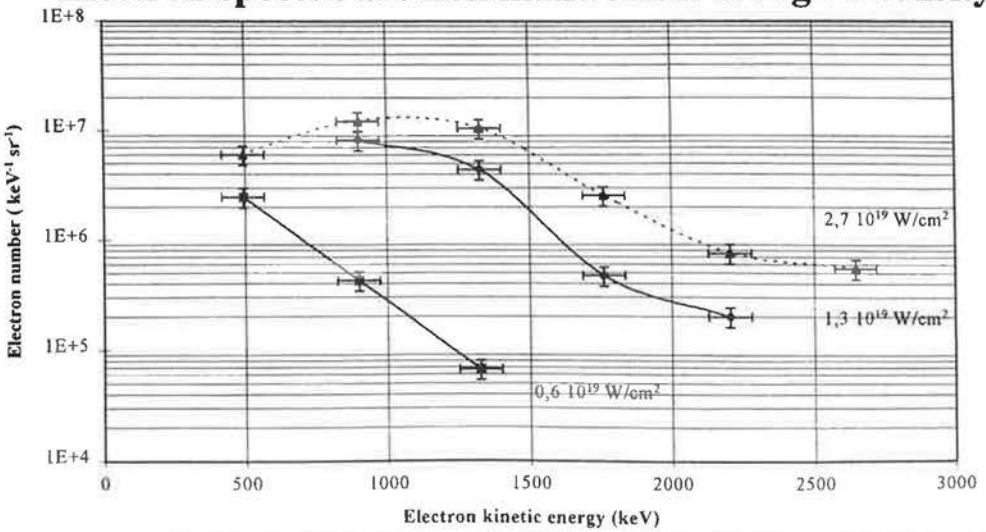

NEUTRON DETECTORS

- **Neutrons are detected via boron activation $^{10}B(n,\alpha)^{7}Li$**
- **Detector is made with a BF_3 tube surrounded by a moderator (CH_2)**
- **Discrimination against γ-rays or hard X-rays by amplitude level**

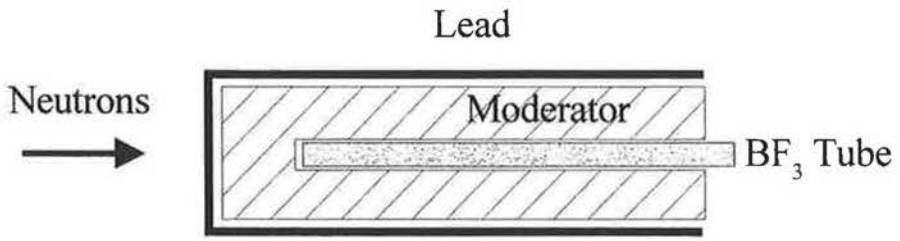

NEUTRON DETECTORS

- **AmBe and Cf neutron sources located at the center of experimental chamber calibrate the BF_3 detectors**

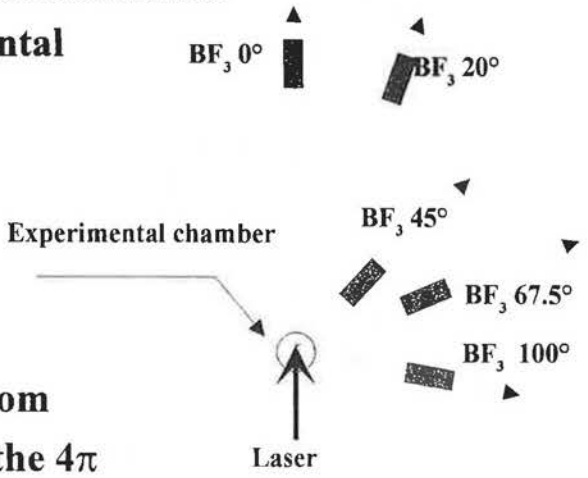

- **Measurement range is from 2×10^4 to 10^7 neutrons in the 4π**

NEUTRON PRODUCTION

- **Neutrons are detected only with CD_2 targets**
- **No neutron emission is observed with massive targets of Au and Al (Threshold of our measurements > $10^4/4\pi$)**
- **Typical signal:**
  n-events occur during 500 µs
  (due to the moderation of the neutron)

NEUTRONS VS LASER INTENSITY

- **Neutron emission depends strongly on optical intensity**

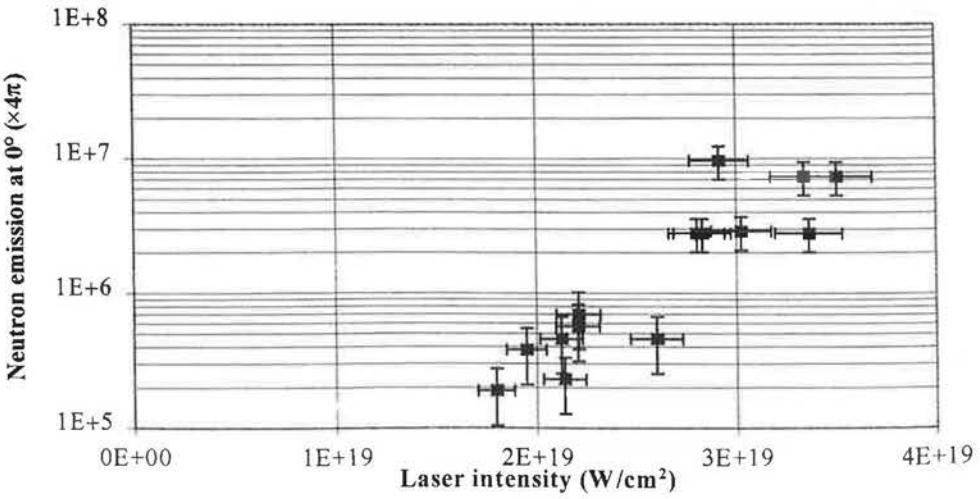

NEUTRONS VS FAST ELECTRONS

- **Neutrons at 90° exhibit an exponential law with energy in the electrons E_e**

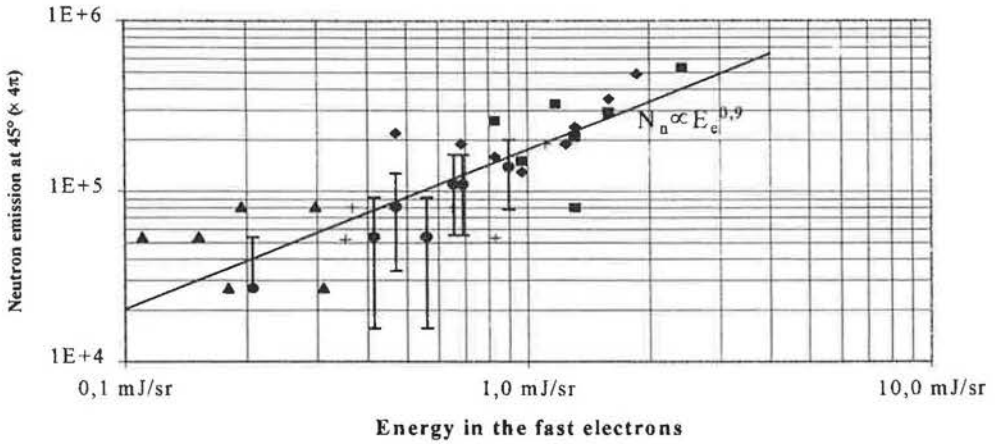

NEUTRONS VS FAST ELECTRONS

- **Neutrons at 0 ° show a sharp increase with energy in the electrons E_e**

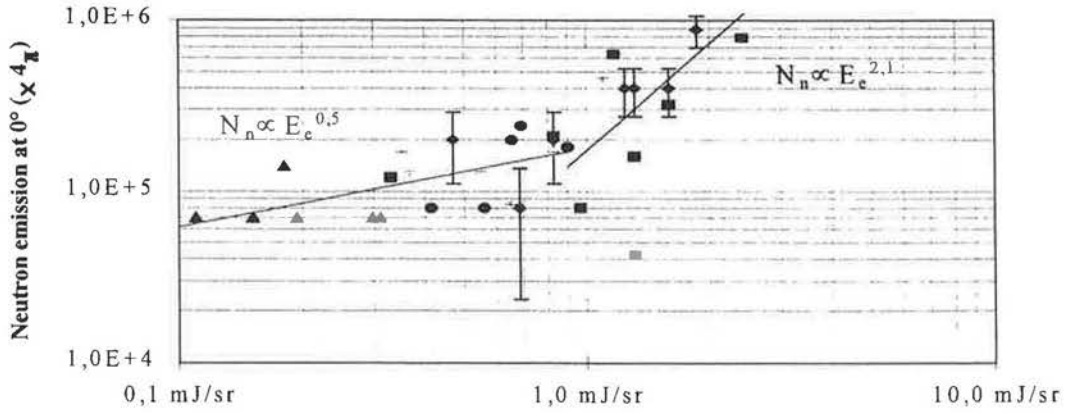

- **At high laser intensity ($I \sim 2.3 \times 10^{19}$ W/cm², $E_e = 2$ mJ/sr) Neutron yield is three times higher in the laser axis**

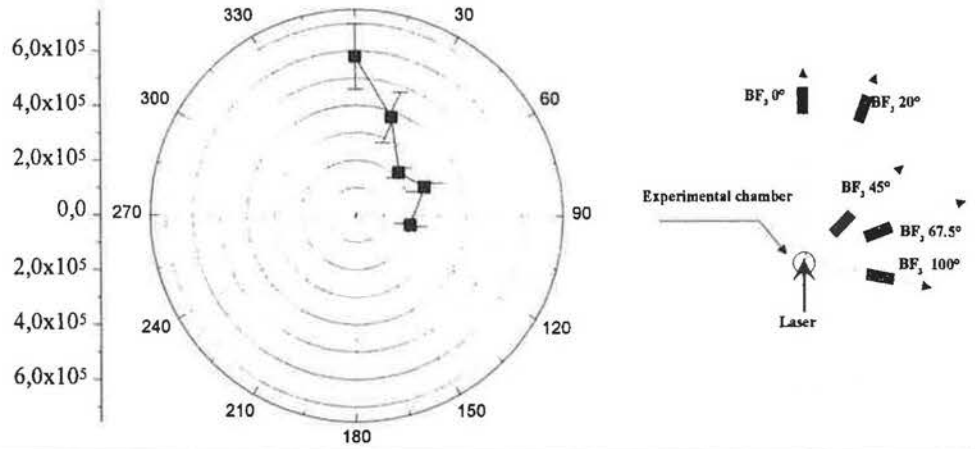

- **Neutron yield depends on direction of observation through the differential cross section σ of $D(d,n)^3He$ reaction**

- **In a beam-target model, the neutron yield Y(θ,Ed) is**

$$Y(\theta, E_d) = \int_0^{E_d} \frac{\sigma(\theta, E)}{\varepsilon(E)} dE \qquad (1)$$

- **Energy E_d of the fast ions D^+ is deduced from the angular diagram of the neutrons**

- **0.3 - 1 MeV ion range is deduced from the neutron anisotropy**

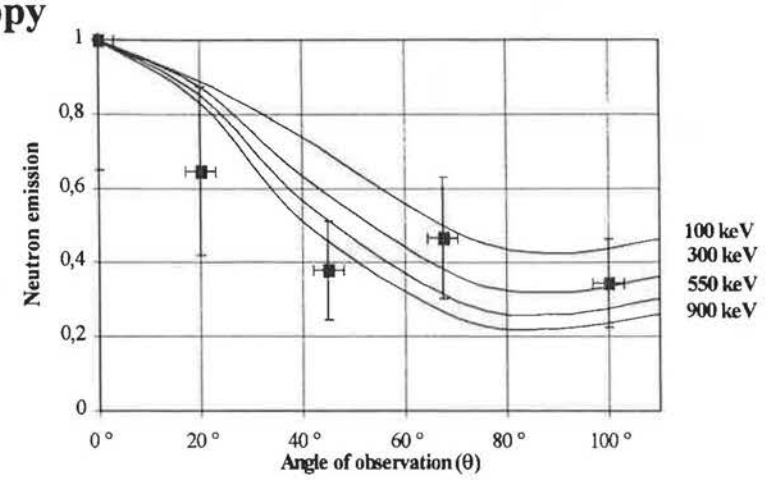

NEUTRON ANISOTROPY

- **Best fit is obtained with 550 keV ions**
- **$6\times10^5/4\pi$ neutrons at 0° => 10^{11} D^+ of 550 keV**
- **9 mJ in the fast ions.**

NEUTRON ENERGY

- **First hit neutron spectrometer made with an array of 96 detectors is set up at 2.5 m from target**
- **D-D neutrons are detected**

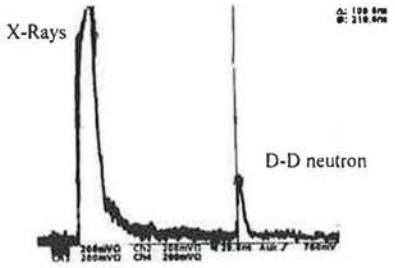

- **Only a few events for 5×10^5 neutron yield**
- **Energy is measured, spectrum not yet**

CONCLUSION

- **Neutron emission is anisotropic. It shows that fast ions are accelerated in the direction of the laser**
- **From angular diagram, energy of fast ions is measured**
- **Neutron emission is strongly correlated with energy in the electrons**
- **PIC calculations are in progress (C. Toupin et al)**
- **We plane to use DLi^7 targets. Energy of $D^+ > 400$ keV permits $^7Li(d,n)^8Be$ and creates neutrons of 10-13 MeV**

FAST ION GENERATION AND CORRELATED NEUTRON PRODUCTION IN THE INTERACTION OF A ULTRAINTENSE LASER PULSE WITH AN OVERDENSE PLASMA

C. Toupin, E. Lefebvre, G. Bonnaud

Commissariat à l'Energie Atomique, DPTA, Bruyères-le-Châtel (France)

Outline :

- Purpose
- Simulation tools & conditions
- Side-directed production of ions/neutrons in nearly critical plasmas
- Forward-directed production for intermediate and highly overdense plasmas
- Conclusion

Purpose

- When impinged upon a thick solid target, a ultra-intense laser pulse does not cause bulk electron expansion but kicks the surface electrons along forward and side directions with MeV energies.
- Acceleration of MeV ions is induced by the space-charge fields created by the escaping electrons.
- By colliding with immobile ions deeper in a deuterated target, fast neutrons are produced. This lays foundation for efficient high threshold diagnostic of laser plasma interaction.
- Present work aims at identifying and diagnosing the main processes of ion acceleration which underlie the present experimental neutron detection, by means of 2-D particle-in-cell (PIC) simulations.

Simulation tools

- MANET code:
  - 2D planar-geometry particle-in-cell, fully-relativistic particles
  - no collisions; particles escaping from simulation box are re-injected
  - full Maxwell equations
  - operated on parallel T3E/128 Cray computer
- Post-processor computing the 3D neutron distribution from axisymmetrized 2D ion distribution
  - neutron production, anisotropy calculation, energy spectra
  - ion slowing down modeled but ion pitch angle disregarded
  - neutrons via $D + D \rightarrow n + {}^3He + 3.266\ MeV$
  - ion stopping and reaction cross sections tabulated from experimental values
  - CD_2 target

Neutron production and energy modeling

- For a one-velocity collimated D ion beam impinging upon a CD_2 target:
  - neutron yield per beam ion/sr $= \boxed{\int_0^{E_i} dE \frac{\sigma(E,\theta_n)}{\varepsilon(E)}}$

    E_i = energy beam, θ_n = neutron/ion angle

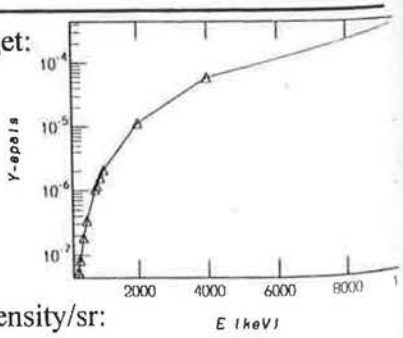

- For a general ion axisymmetric distribution $f(E_i,\theta_i,t)$, the neutron distribution is axisymmetric as well with neutron areal density/sr:
  - $\boxed{\frac{dN_n}{d\Omega_n} = dS \int_{E_i} dE_i E_i^2 \sqrt{\frac{2E_i}{M_D}} \int_{\theta_i} d\theta_i \sin\theta_i \int_{\varphi_i} d\varphi_i \int_t dt n_i(t) f(E_i,\theta_i,t) \int_0^{E_i} dE \frac{\sigma(E,\theta_n)}{\varepsilon(E)}}$

θ_i, φ_i azimuth and polar angles of the beam ions, M_D ion beam mass, $n_i(t)$ ion beam density.

- Energy of a neutron produced by D+D ➔ n+^{3}He is peaked in the forward direction:

$$E_n = \frac{M_D M_n}{(M_n + M_{He})^2} (\sqrt{\eta + \cos^2\theta_n} + \cos\theta_n)^2 \text{ with} \eta = \frac{M_n + M_{He}}{M_D M_n} (M_{He} - M_D + M_{He} \frac{3.266(MeV)}{E_i})$$

The laser beam penetrates in classically forbidden plasma by ponderomotive excavating of the plasma

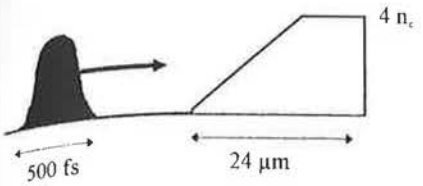

• Hole boring is more effective when relativistic transparency sets in: the effective channel density is below critical, and the average target density ~ 3 n_c

$I = 3\ 10^{18} W / cm^2$
$t = 580\ fs$

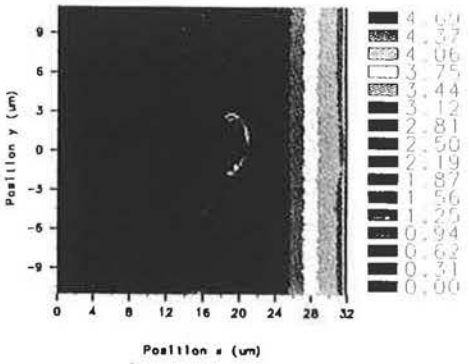

$I = 5\ 10^{19} W / cm^2$
$t = 450\ fs$

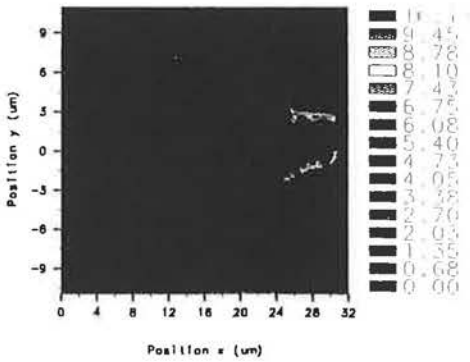

Ions dragged out of the laser drilled channel

• Large energy range up to a few MeV and large number of neutrons (> 3 10^8)

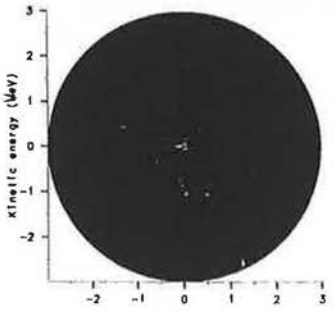

total yield: 1.8 e6
0 / 90 anisotropy: 1.44

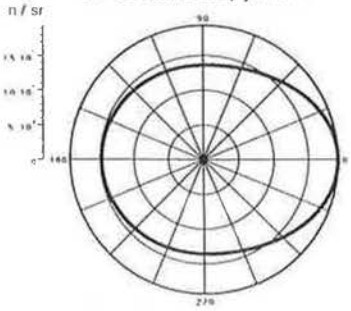

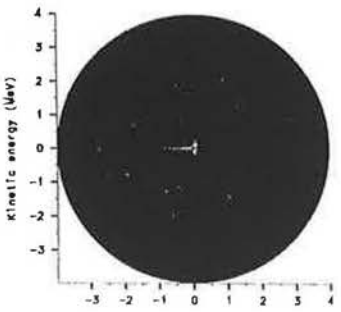

total yield: 9.9 e7
0 / 90 anisotropy: 0.80

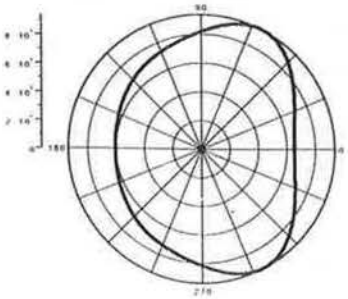

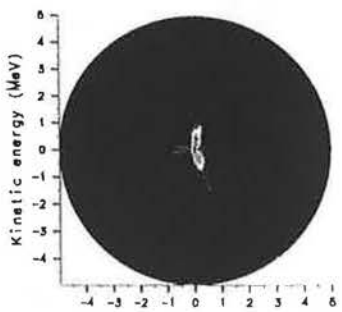

total yield: 3.5 e8
0 / 90 anisotropy: 0.45

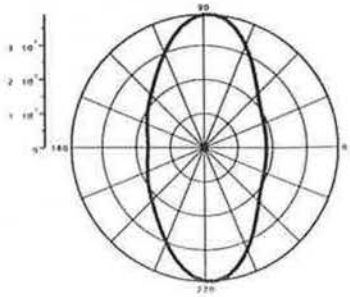

Spectra of neutron energies

- Neutron spectra extends from 2 MeV up to 8 MeV.

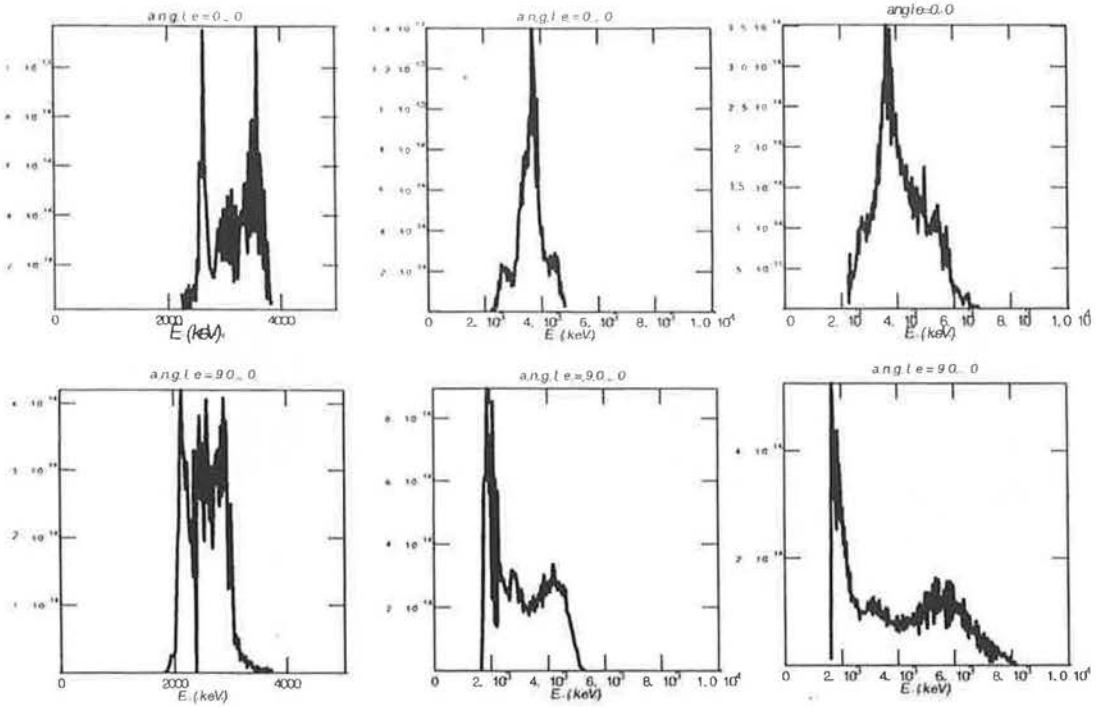

The laser beam drills a hole in intermediate density plasma

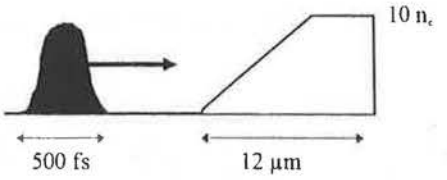

- Surface recesses at velocity 0.014 c/0.036 c for irradiances 10^{19} and 5 10^{19} W/cm^2
- No electrostatic shock is identified
- Surface corrugates via RT instability

$I = 1\ 10^{19} W / cm^2$

$t = 570\ fs$

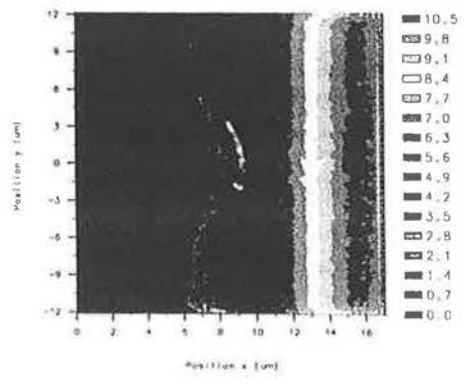

$I = 5\ 10^{19} W / cm^2$

$t = 570\ fs$

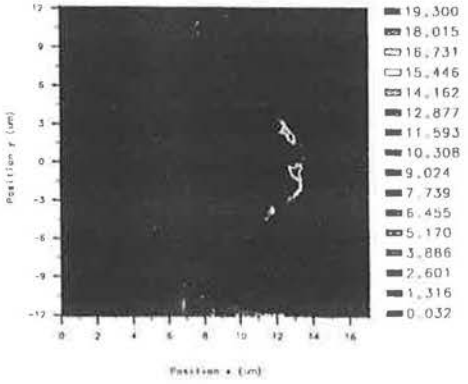

Ions pushed inward the target by laser pressure

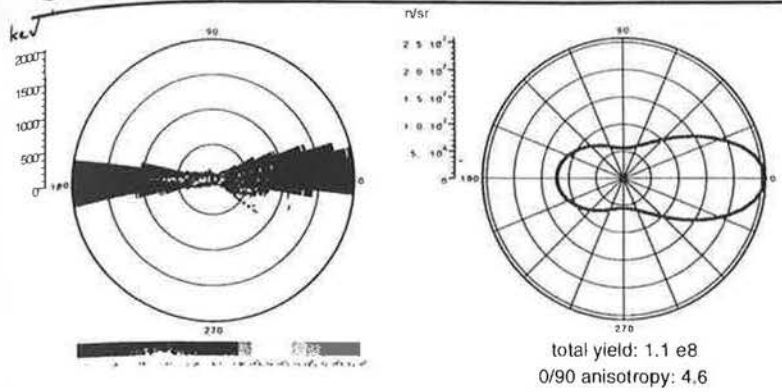

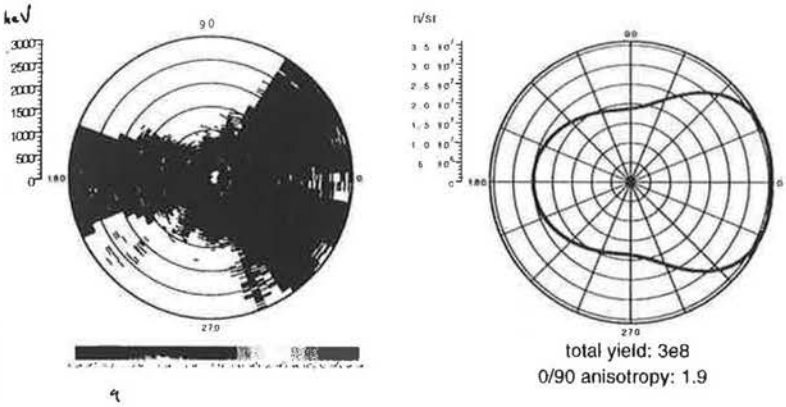

- Ions show flat energy distribution up to 2 MeV for $I=10^{19}$ W/cm^2
- Angle dispersion increases dramatically for irradiances > a few 10^{19} W/cm^2, due to RT instability

Spectra of neutron energies

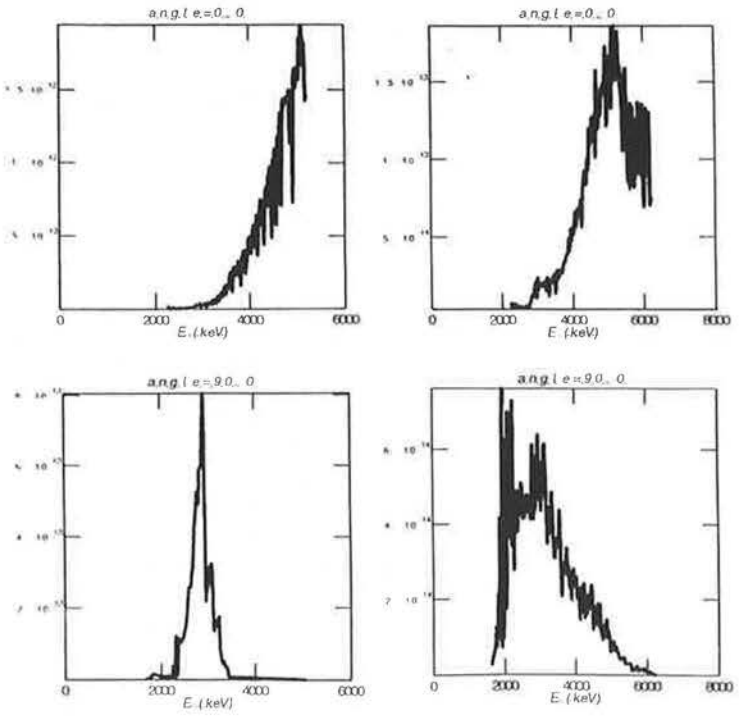

- At 0° angle, energy spectra extends beyond 5 MeV.
- At 90° angle, spectra peak around 2.5 MeV, with FWHM increasing with irradiance: energy peak is nearly intensity independent.

Ions accelerated by a collisionless shock

- Strong shock ➔ piston-like motion of the target surface inducing a monokinetic ion beam moving inward the target:
- Lower energy, compared to radially or axially pushed ions:

  0.5-1 MeV

➔ less neutrons produced

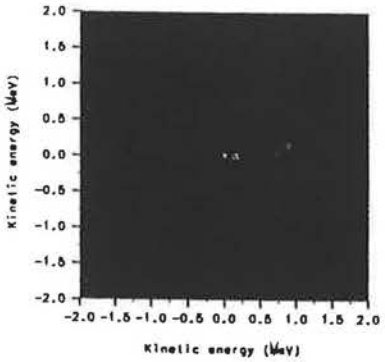

Interaction with a step-edged 50 n_c plasma,

I_0=3.5 10^{19} W /cm^2,

150 fs laser pulse

total yield: 9.5 e3
0 / 90 anisotropy: 4.6

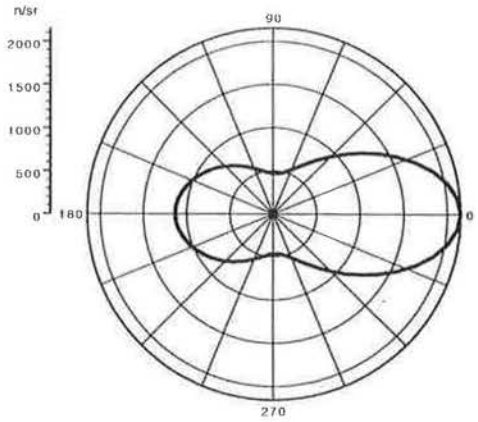

Conclusions

- Two kinds of accelerated ions identified via the neutron emission diagram for a CD_2 target:
  - ➢ transverse motion for slightly overdense targets:

    10^8 neutrons with anisotropy 1:2 at 0:90 degrees
  - ➢ axial motion for dense targets:

    10^3 neutrons with anisotropy 1:0.2 at 0:90 degrees for highly overdense target

    10^8 neutrons with anisotropy 1:0.5 at 0:90 degrees for intermediate density target
- Discussion of the RAL and CEA experiments :
  - ➢ RAL: on C_8D_8, assuming 100 keV fast ions, neutron yield predicted to be 4 10^{-5}. Our results should predict 2 10^{-8}. The experimentally measured number of neutrons (7 10^7) would thus evidence multi-MeV ions. D ion slowing down explains the discrepancy.
  - ➢ CEA (see Disdier's talk): on CD_2, angular dependence of neutron detection (anisotropy 1:0.33 at 0:90 degrees) should evidence axial acceleration via electrostatic shock or plasma pushing.

• Present some results for

First submission to the EU in 1990

Laser Induced Fission

Ledingham, Singhal & Magill (Karlsruhe)

Resubmitted to RAL at Easter 1998

Laser Induced Nuclear Reactions TEAM

McCanny, Graham, Fang, Singhal and Ledingham

A.Creswell, D. Sanderson R.Scott (SURRC)

Ric Allott, David Neely & Peter Norreys
Rutherford Appleton Laboratory

Marco Santala, Matthew Zepf, Ian Watts, Eugene Clark, Karl Krushelnick and Bucker Dangor
Blackett Laboratory, Imperial College,
Michael Tatarakis (I.C.)
Antonin Machecek and Justin Wark,
Clarendon Laboratory, University of Oxford,

- Present some results for photonuclear reactions with 10^{19} W cm^{-2} laser pulse.
- High intensity laser pulse can generate high energy collimated e^-.
- In a lead target these e^- generate high energy (> 10 MeV) gamma rays.
- γ-rays of 10 MeV energy can knock out a neutron from ^{63}Cu to produce ^{62}Cu.

$$^{63}Cu + \gamma \longrightarrow {}^{62}Cu + n$$

- ^{62}Cu has a half life of 9.7 minutes and decays to ^{62}Ni by positron emission

$$^{62}Cu \longrightarrow {}^{62}Ni + e^+ + \nu$$

- The positron comes to rest very quickly in Cu target and annihilates with an e^- to produce two γ-rays.

$$e^+ + e^- \longrightarrow \gamma + \gamma$$

- To conserve energy & momentum, the two γ-rays are emitted back to back, each having an energy of .511 MeV.

COINCIDENCE SETUP

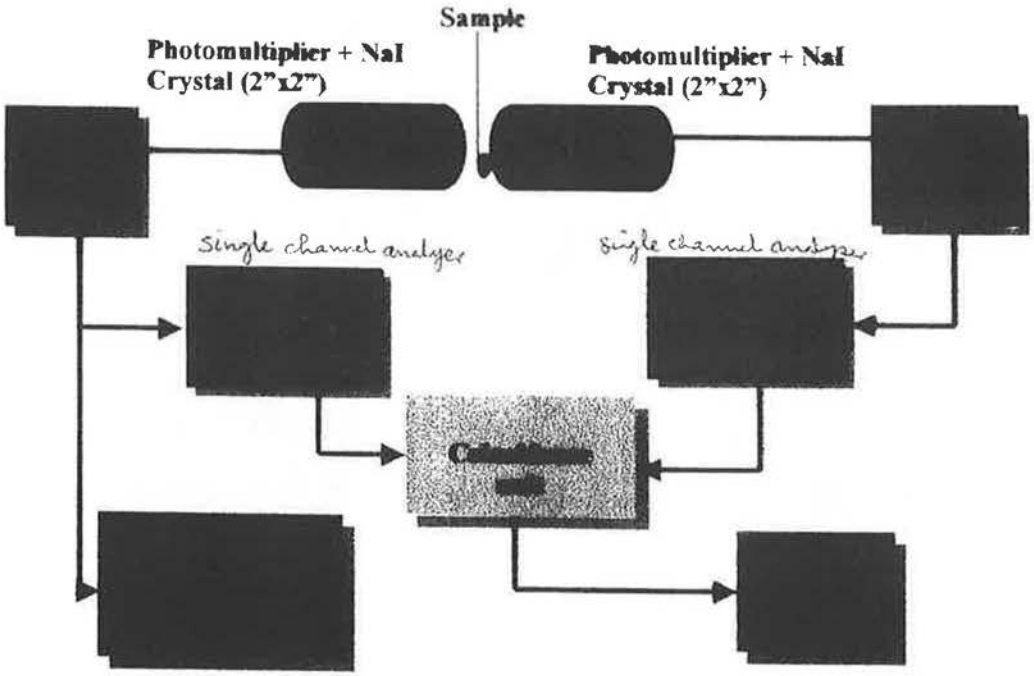

PETAWATT LASER BEAM

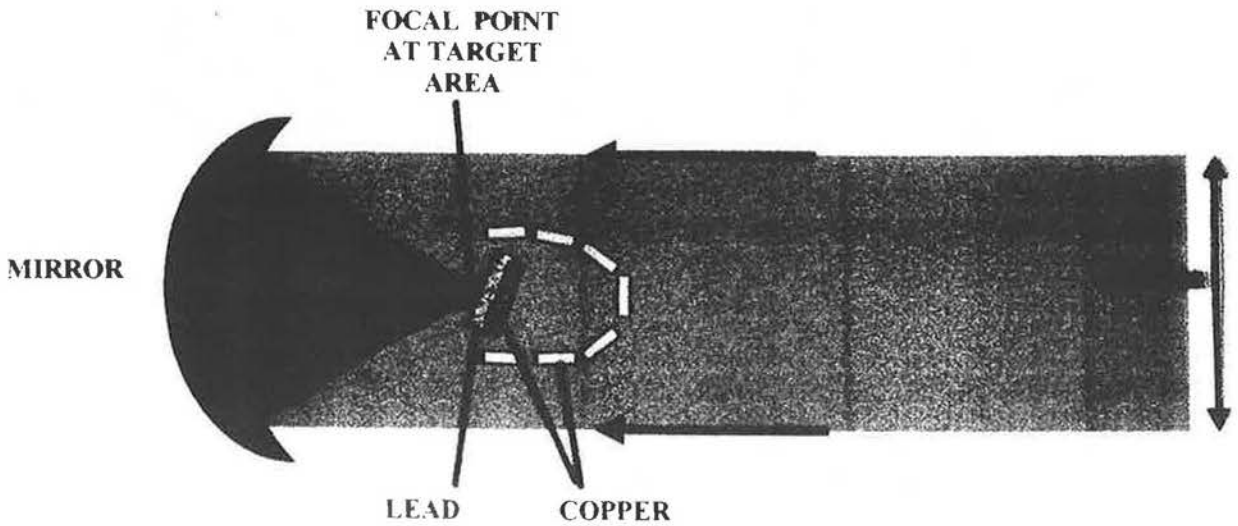

Target arrangement for activation studies

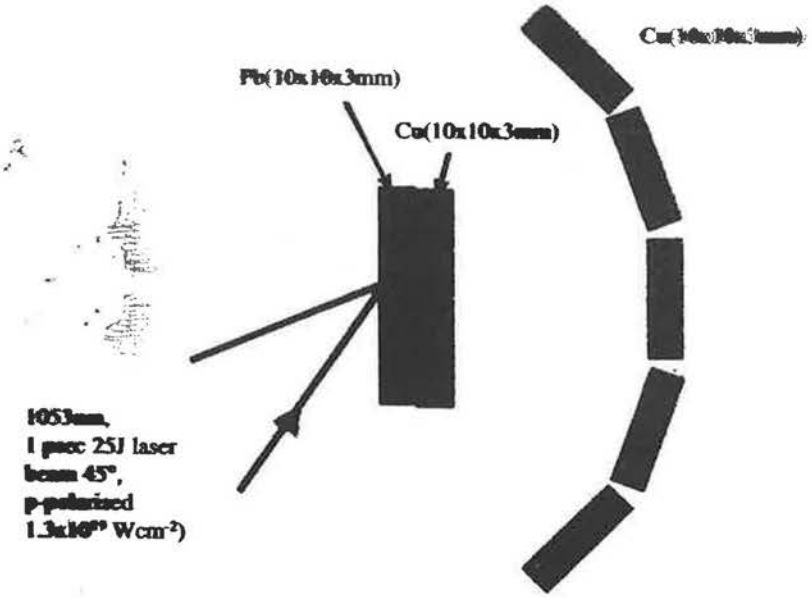

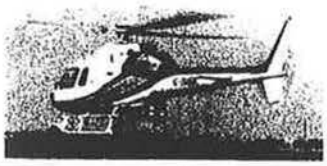

^{62}Cu half life measurements

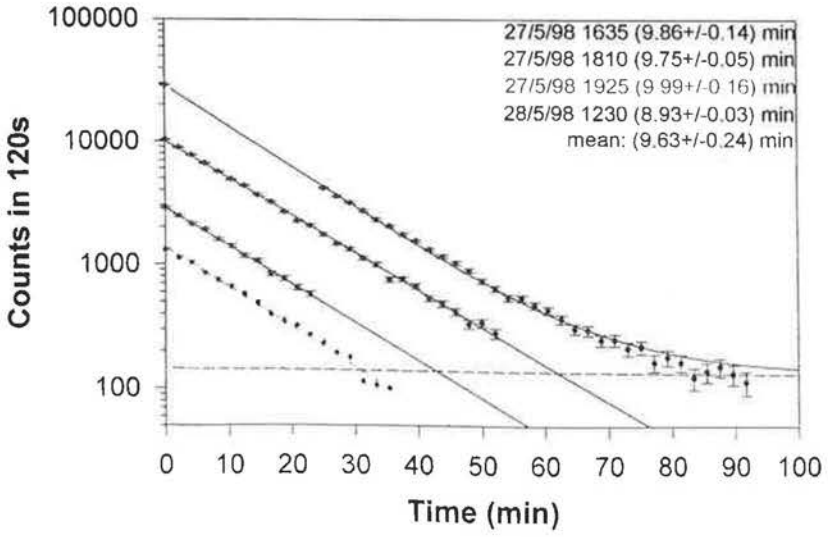

SURRC
Scottish Universities Research and Reactor Centre

Summed gated spectra

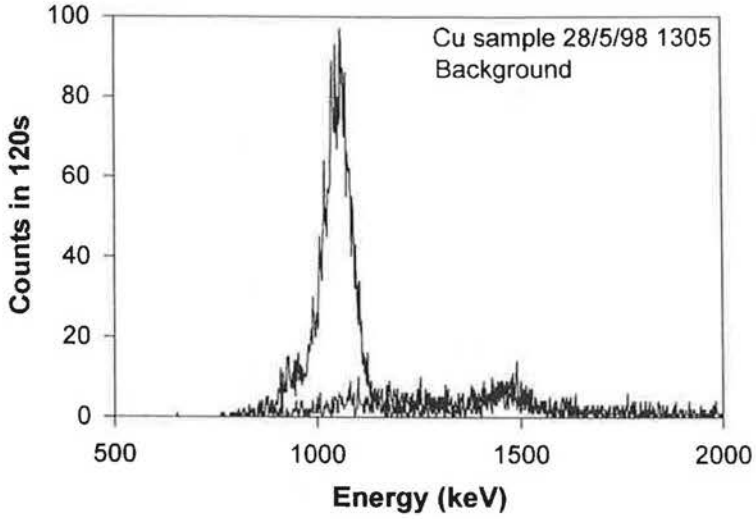

SURRC
Scottish Universities Research and Reactor Centre

Gama-ray angular distribution above 10 MeV by Cu activation

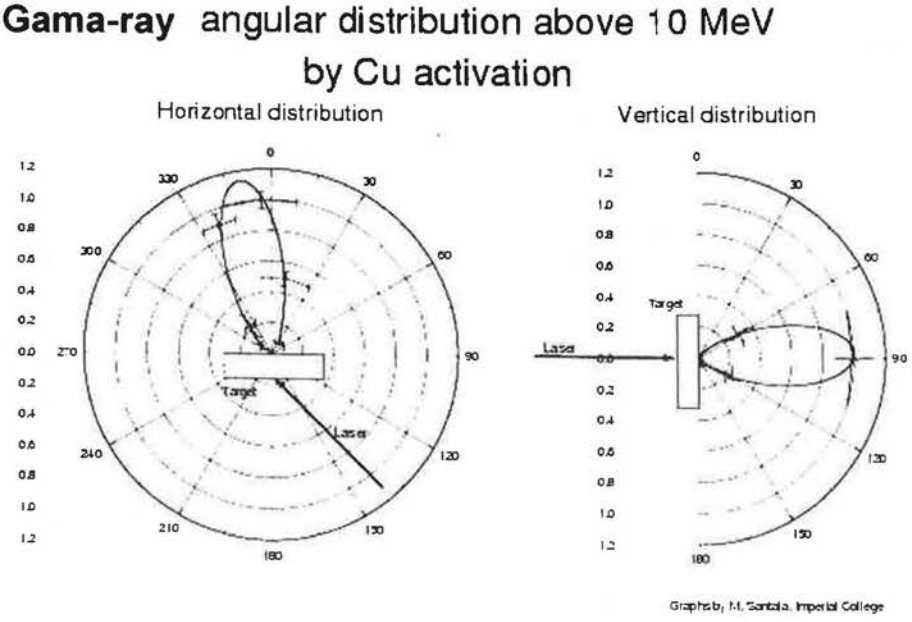

Graphs by M. Santala, Imperial College

GEANT SIMULATION

Magnetic Field is generated by a current flowing ⊥ to the surface of the target.

$B = 500$ T

$r = 20\ \mu m$

$l = 250\ \mu m$

Thermal e^- spectrum

$n(E) \propto e^{-E/kT}$

where $kT = 1$ MeV

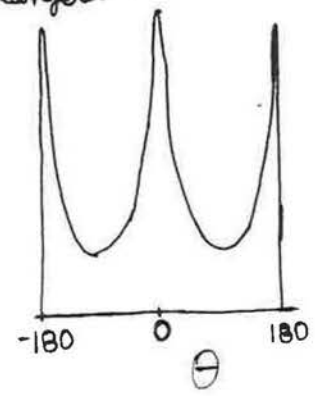

Horizontal Plane

Vertical Plane

$\phi = 0$ with $\pm 45°$ spread

2×10^6 electrons give 10000 photons above 10 MeV

(Conversion 5×10^{-3} or .05%)

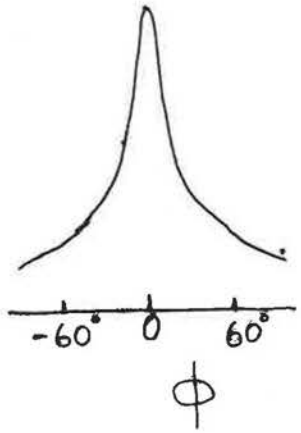

Applications for Laser Induced Nuclear Physics

- **Cheaper production of radio-isotopes especially short lived positron emitters necessary for positron emission tomography (PET)**
- **Point source of neutrons**
- **Conversion of long-lived radioactive waste to short lived components**

Looking Ahead

1. Study a number of targets with a range of Q-values.

   ⇒ Determine the energy spectrum of the high energy photons as a function of laser intensity:

Positron-emitting isotopes: 10^{19-20} W cm^{-2}

Element	Reaction	Half-life	Q-value (MeV)	Peak cross-section in mbarn
Carbon	$^{12}C(\gamma,n)^{11}C$	20.4 m	18.7	13.1
Oxygen	$^{16}O(\gamma,n)^{15}O$	226 s	16.4	8.7
Phosphorus	$^{31}P(\gamma,n)^{30}P$	2.5 m	12.31	16.6
Copper	$^{63}Cu(\gamma,n)^{62}Cu$	9.7 m	10.85	65
Silver	$^{107}Ag(\gamma,n)^{106}Ag$	24 m	9.54	160
Gold	$^{197}Au(\gamma,n)^{196}Au$	6.18 day	8.06	550

An exciting application of laser-induced nuclear reactions is that it can produce electron or photon induced fission.

The obvious candidates for a 1st study are ^{238}U & ^{232}Th

^{238}U half life = 4.5×10^{9} years
reaction ⇒ $^{238}U(\gamma,f)X\gamma n$
Q-value 7.8 MeV
σ_{peak} = 150 mb ($1\,b = 10^{-24}$ cm^2)

^{232}Th half-life = 1.4×10^{10} years
reaction ⇒ $^{232}Th(\gamma,f)X\gamma n$
Q-value 4 MeV
Peak cross section = 46 mb

Note Q-values for fission are much lower than for (γ,n) reactions
$\sigma_{fission}$ is normally greater than $\sigma_{(\gamma,n)}$

At 10^{19} W cm^{-2}: for $^{238}U(\gamma,f)$, the neutron flux is estimated to be $> 10^{12}$ per pulse

With proposed VULCAN upgrade, we hope to reach intensities of 10^{21} Wcm^{-2}.

If we scale the e^- energy by two orders of magnitude as well, then

e^- & photons of energy > 140 MeV will be produced

photons of energy > 140 MeV can induce pion reactions

for example,

$$^{27}Al + \gamma \longrightarrow {}^{27}Mg + \pi^+$$

^{27}Mg decays to ^{27}Al with a half life of 9.5 m and two characteristic γ-rays at 0.844 & 1.014 MeV are emitted.

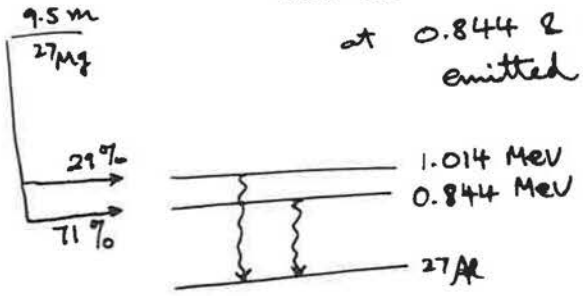

This reaction will be ideal for measuring γ-ray flux of energy > 140 MeV.

Observation and discussion of stimulated optical scattering in ultra-intense laser-solid interactions

Clarendon Laboratory,
University of Oxford.

A.C. Machacek, D.M. Chambers, J.S.Wark

Department of Physics, University of Oxford, UK

I. Watts, M. Zepf, A.E. Dangor, E. Clark, K. Krushelnick, M. Santala, M. Tatarakis

Imperial College of Science, Technology and Medicine, London, UK

P.A. Norreys, R. Allott, C.N. Danson, D. Neely

Rutherford Appleton Laboratory, Oxon, UK

R.S. Marjoribanks

Department of Physics, University of Toronto, Canada

Overview

Clarendon Laboratory,
University of Oxford.

- Presentation of Results from experiment on Vulcan CPA system
- Mechanisms for generating the features seen, and consequences for plasma diagnosis
  - Raman scattering from plasmons generated by two plasmon decay
  - A more generalised instability analysis
- Future experiments planned and work in progress.

Experimental Layout

Clarendon Laboratory,
University of Oxford.

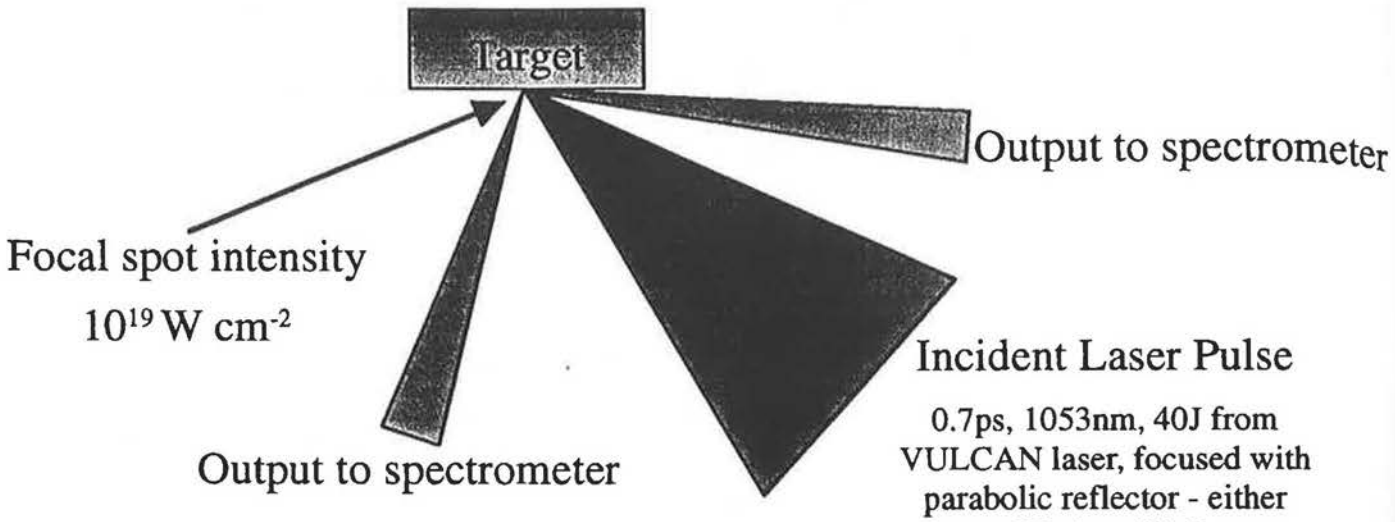

Form of Data

Clarendon Laboratory,
University of Oxford.

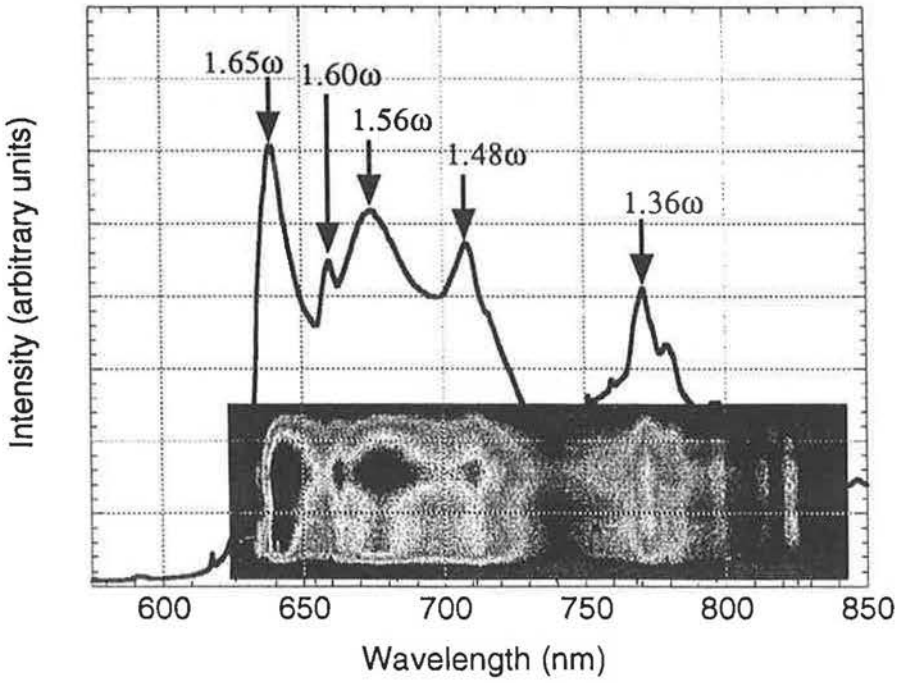

With typical arrangement, as shown below, the spectrum on the left was obtained

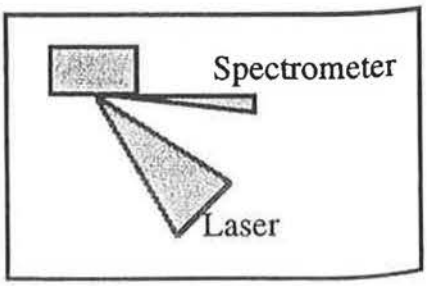

Intensity Dependence

Clarendon Laboratory,
University of Oxford.

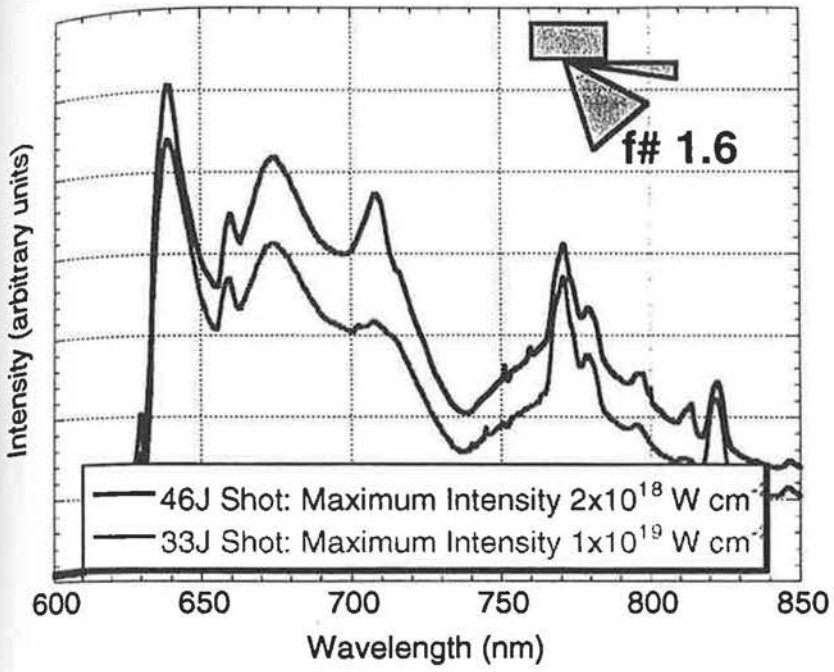

Intensities at central focal spot is determined from CR39 analysis, or from focal spot sizes inferred from soft X-ray penumbral imaging.

This enables deduction of intensity dependence.

We see that strength of signal is more affected by total pulse energy

Intensity vs. Energy Dependence

Clarendon Laboratory,
University of Oxford.

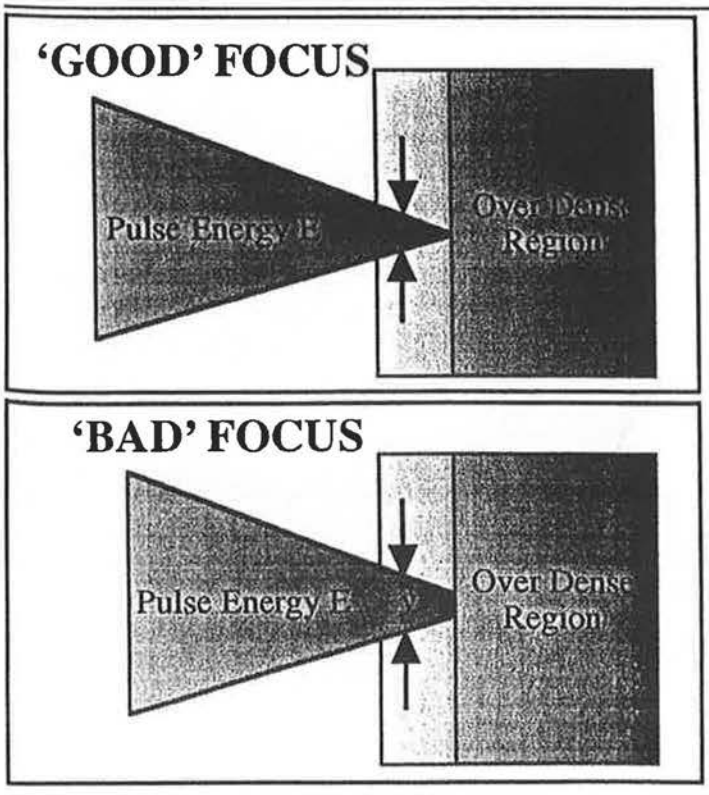

- Intensity at focus is a strong function both of focal quality and pulse power.
- Intensity in underdense region is only weakly affected by focal spot size, as shown in diagram as $x \approx y$.
- Strength of instabilities growing in underdense region will be dependent on pulse energy rather than focal spot intensity.

f# Dependence

Clarendon Laboratory,
University of Oxford.

The wavelengths of the peaks is significantly affected by wedge angle of incoming laser beam

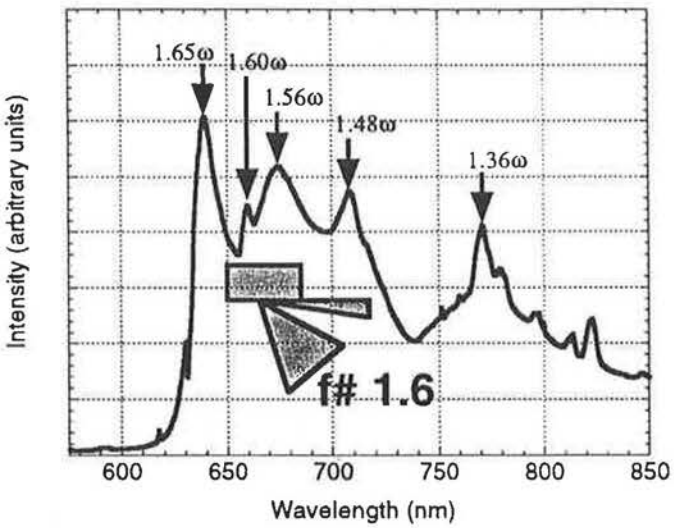

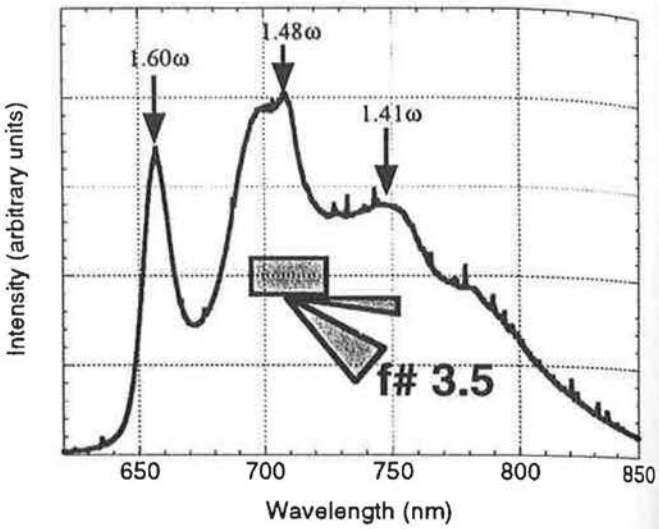

Effect of f# of Focal Optic

Clarendon Laboratory,
University of Oxford.

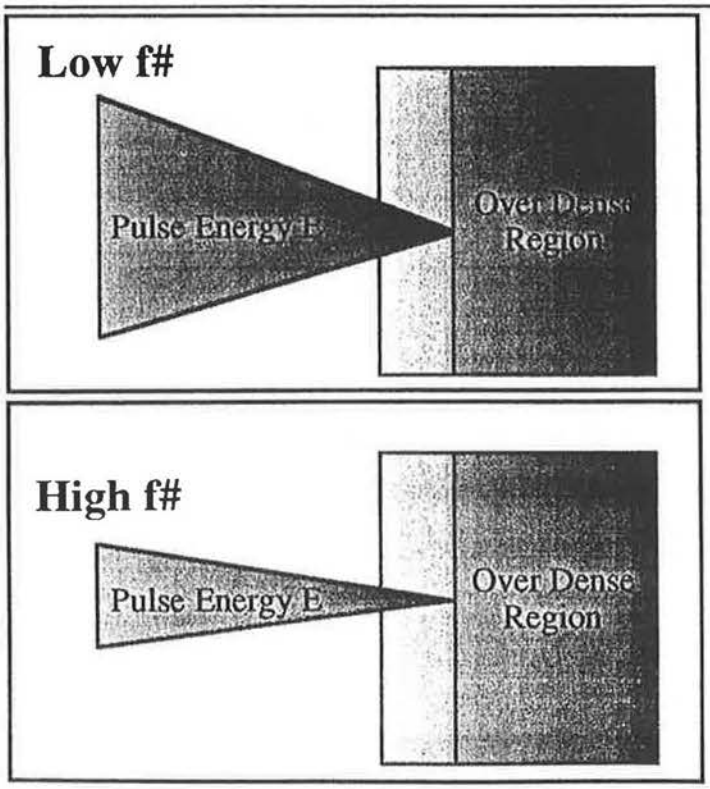

For a given intensity at the final focus, the intensity in the underdense region is higher when the f# of the optic is increased.

Thus a greater range of scattering processes exist above threshold, and overall spectrum looks smoother, as all these processes merge in frequency space.

Angular Dependence

Clarendon Laboratory,
University of Oxford.

Observation of the 3/2 harmonic impeded when viewing the interaction region along the target surface. Other features appear brighter when region viewed along surface.

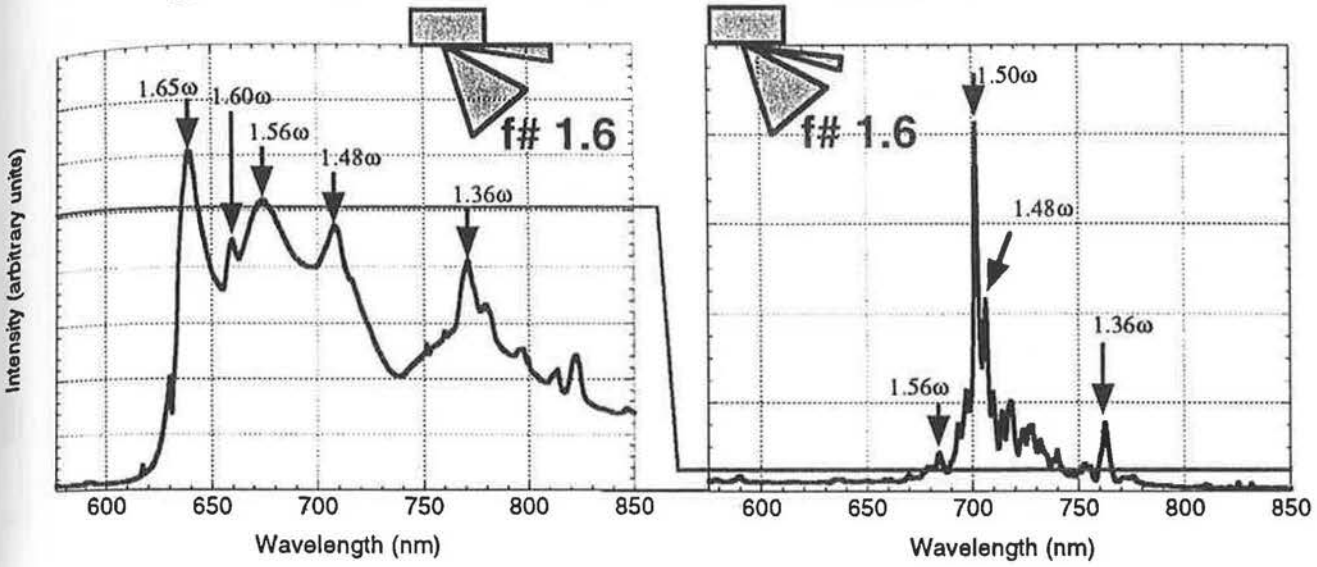

9

Spatial Extent of Emission

Clarendon Laboratory,
University of Oxford.

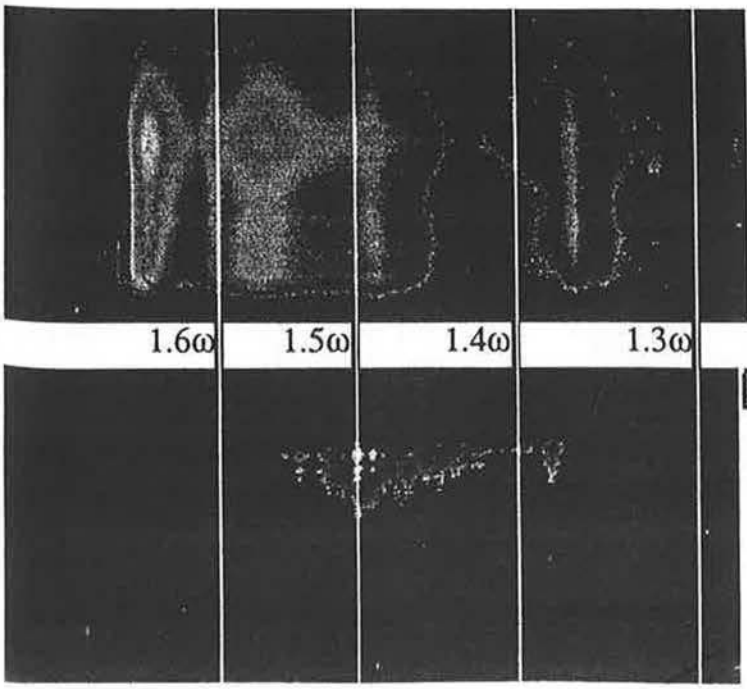

The 3ω/2 harmonic is emitted from a much smaller spatial region than the scatter features by a factor of about 10.

Please note that intensity scales are very different - 3ω/2 maximum is about 10 times brighter than brightest scatter features.

10

Effect of Prepulse

Clarendon Laboratory,
University of Oxford.

It can be seen that a significant prepulse has the effect of drastically increasing the emission at 3ω/2

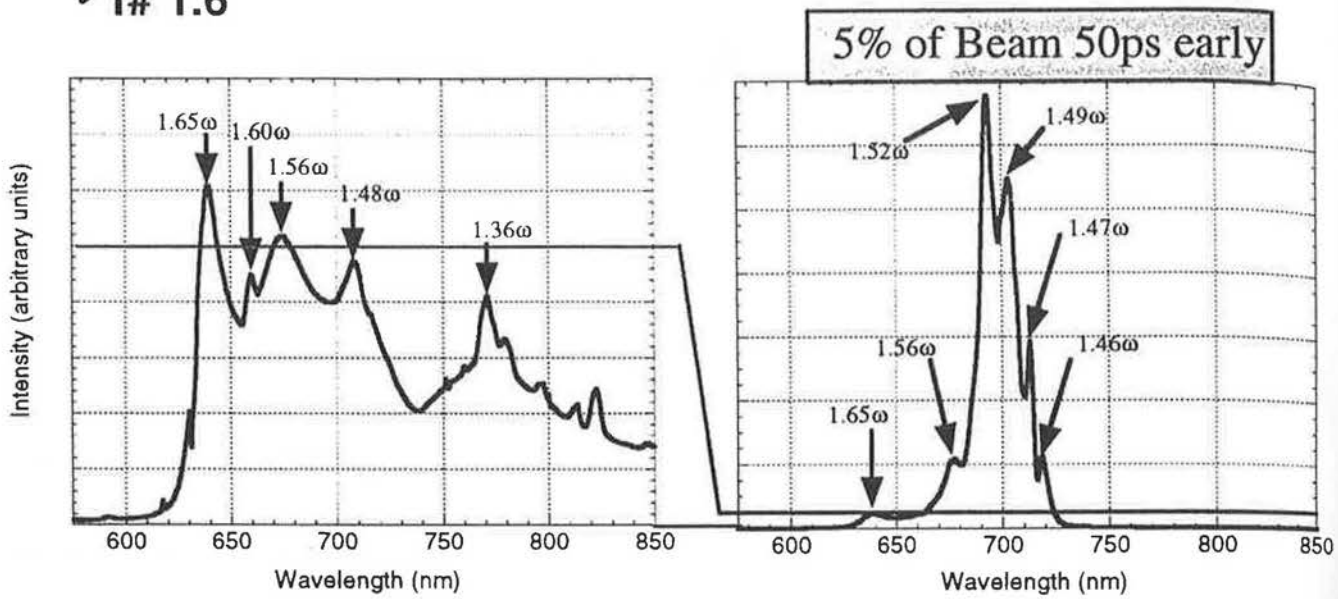

Traditional Explanation of 3/2 'Harmonic'

Clarendon Laboratory,
University of Oxford.

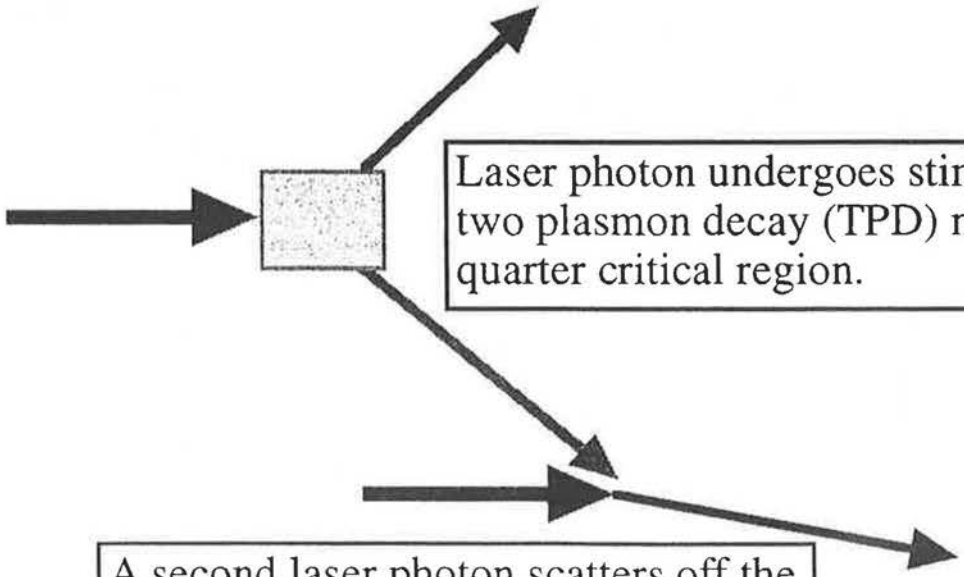

Laser photon undergoes stimulated two plasmon decay (TPD) near the quarter critical region.

A second laser photon scatters off the periodic density profile generated by the plasmons.

Raman Scatter off TPD Plasmons

Clarendon Laboratory,
University of Oxford.

Using a simple linear treatment of TPD, the scatter frequencies expected from this source can be estimated.

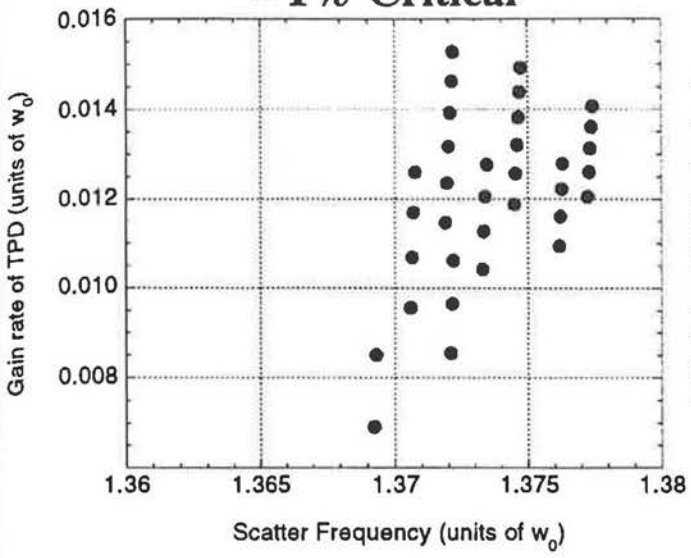

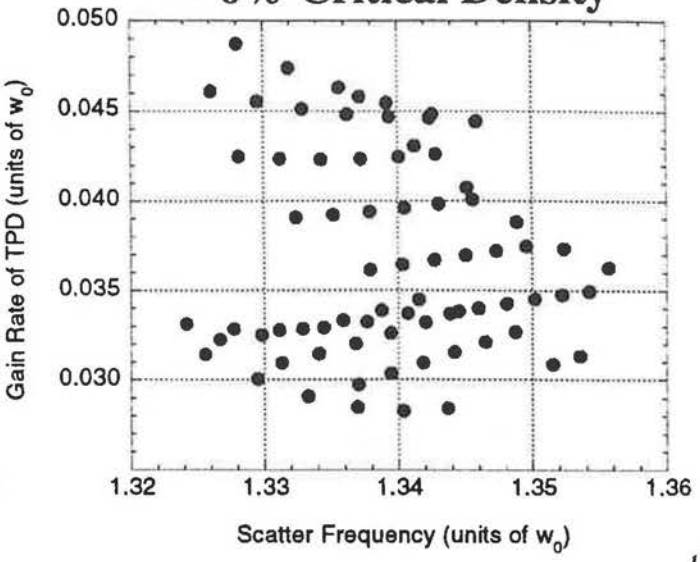

13

Alternative Possibility

Clarendon Laboratory,
University of Oxford.

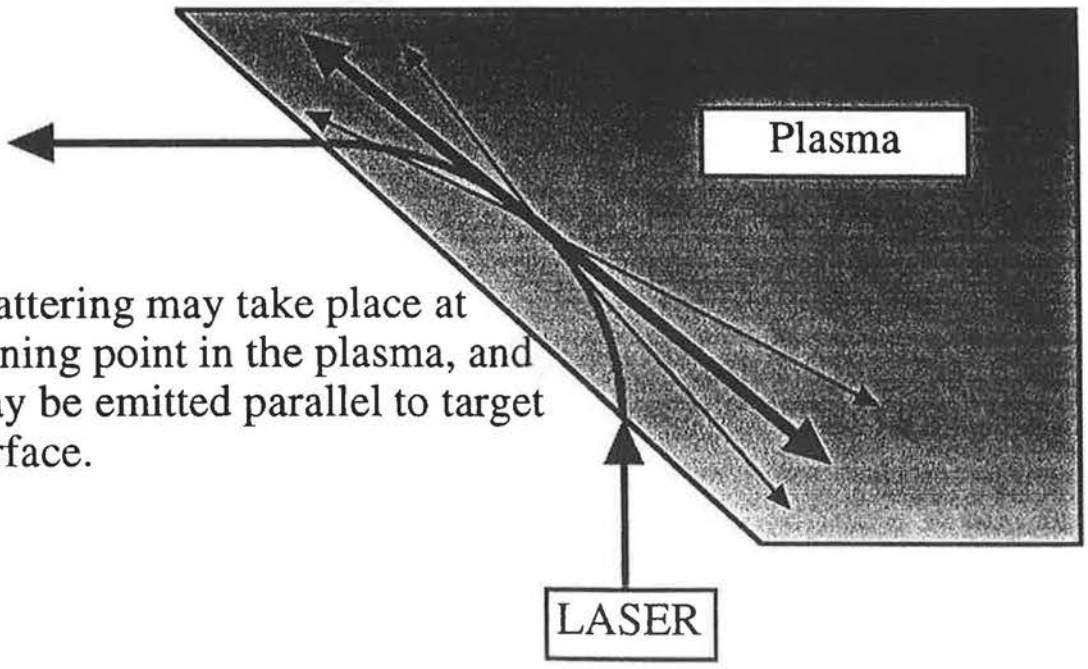

Scattering may take place at turning point in the plasma, and may be emitted parallel to target surface.

14

Analysis by Quesnel Matrix

Clarendon Laboratory,
University of Oxford.

Start with equations:

$$\frac{1}{c^2}\frac{\partial^2 \mathbf{A}}{\partial t^2} - \nabla^2 \mathbf{A} = -4\pi e n \frac{\mathbf{p}}{\gamma m c}$$

$$\nabla \bullet \mathbf{A} + \frac{1}{c}\frac{\partial \Phi}{\partial t} = 0$$

$$\frac{\partial n}{\partial t} + \nabla \bullet \left(\frac{n\mathbf{p}}{m\gamma}\right) = 0$$

$$\frac{\partial \mathbf{p}}{\partial t} = e\nabla\Phi + \frac{e}{c}\frac{\partial \mathbf{A}}{\partial t} - \nabla\left(\gamma m c^2\right)$$

Treat as first order perturbation $\mathbf{A}_1, \mathbf{p}_1, \mathrm{n}_1$ on top of the laser field

Expand n_1 and the components of $\mathbf{p}_1$ and $\mathbf{A}_1$ as a Floquet expansion:

$$f = \sum_{l=-L}^{L} f_l e^{i(\mathbf{k}+l\mathbf{k}_0)\bullet\mathbf{r} - i(\omega + l\omega_0)t} + c.c.$$

Writing the components in a vector: $X_l = \begin{pmatrix} A^+_{l+1} \\ p^+_{l+1} \\ A^z_l \\ n_l \\ p^z_l \\ A^-_{l-1} \\ p^-_{l-1} \end{pmatrix}$

The equations reduce to a matrix equation:

$$A_l \mathbf{X}_{l-2} + B_l \mathbf{X}_{l-1} + C_l \mathbf{X}_l + D_l \mathbf{X}_{l+1} + E_l \mathbf{X}_{l+2} = \mathbf{0}$$

B. Quesnel *et al* ~ Phys.Rev.Lett. **78** p2132, and Phys. Plasmas **4** p 3358

Predictions of the Matrix Method

Clarendon Laboratory,
University of Oxford.

Scattered radiation predicted to have frequencies given by:

$$\omega_{scatt} = \left|\Re(\omega) + l\omega_0\right|$$

with l integral, and with $\Re(\omega)$ being the real part of the eigenvalue of the large matrix just derived. The imaginary part gives the growth rate. Different l components will be scattered in different directions, and the relative magnitudes can be obtained from the matrix eigenvectors.

N.B. Example Only

Turning Point Scatter

Clarendon Laboratory,
University of Oxford.

For scatter emitted almost parallel to the laser beam, gain rates and scatter frequencies from an intensity of $\approx 10^{18}$ W cm^{-2} can be calculated.

Gain Rates

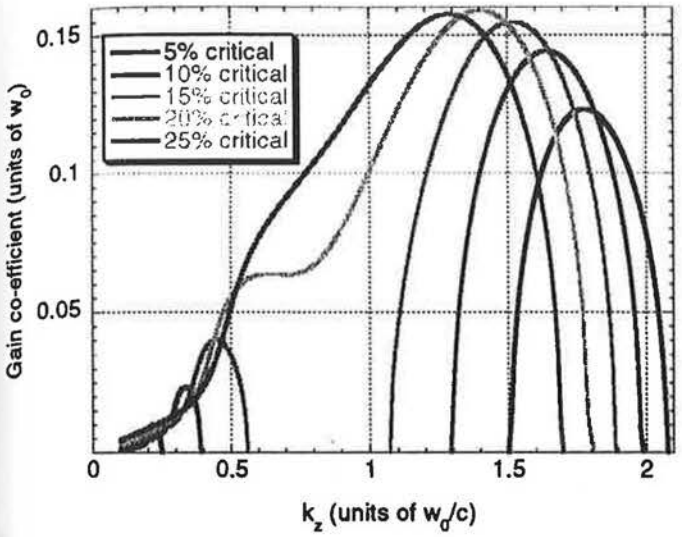

Scatter Frequencies

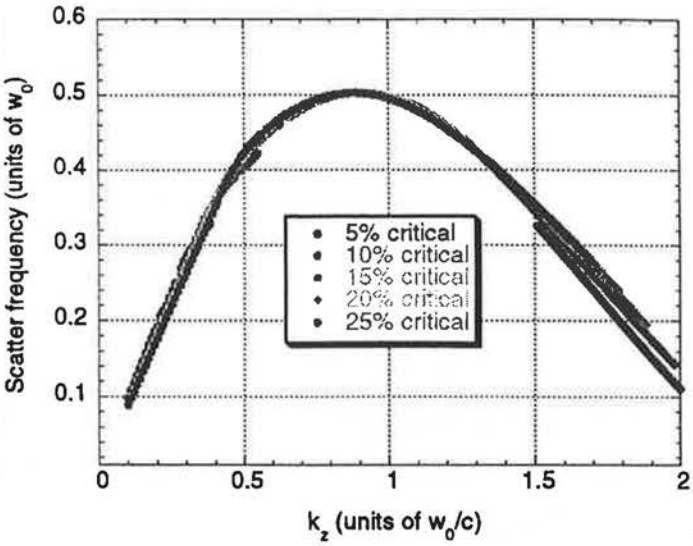

Scatter Frequencies

Clarendon Laboratory,
University of Oxford.

It is possible to choose plasma conditions such that the observed frequencies are predicted - as shown here

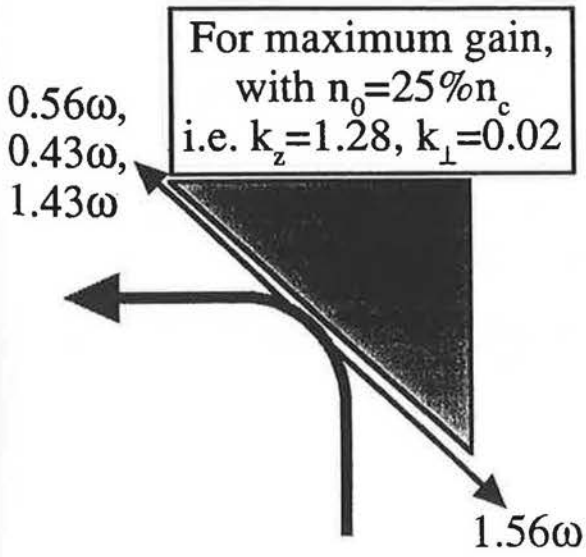

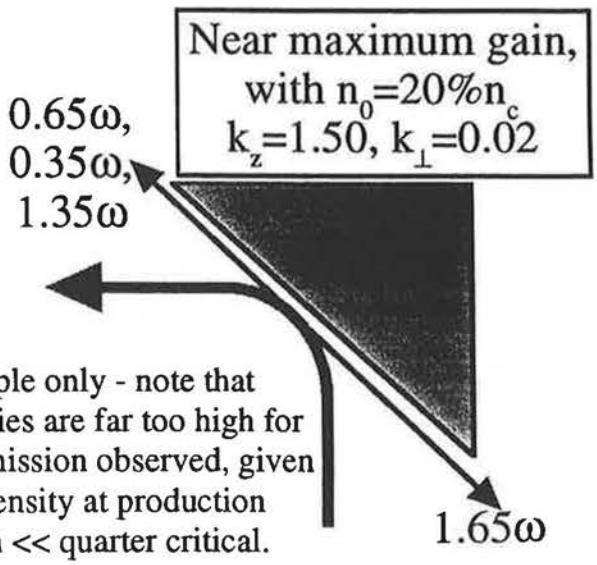

Example only - note that densities are far too high for the emission observed, given that density at production region << quarter critical.

The Reproducibility Question

Clarendon Laboratory,
University of Oxford.

- PIC code simulations of the plasma have shown that there is strong possibility of peaks in density profile, which could lead to peaks in the scatter.
- However, this must be considered in the light of the remarkable reproducibility of the peak frequencies with a variety of target materials (e.g. Cu, glass, plastic...)
  - While this shows that the target material (via e.g. its emission lines) is not the dependent factor, it also indicates that
  - Density maxima in the plasma are also unlikely to be the source, unless there exists some mechanism for ensuring that maxima occur at the same density on all shots with a given f# optic.

Conclusion

Clarendon Laboratory,
University of Oxford.

- Interesting spectral features have been observed in the vicinity of the $3\omega/2$ harmonic in ultra-intense laser-solid interaction.
- Theoretical frameworks for the production of these features have been discussed, although further work is needed to consider their applicability.
- Further experiment will measure spatial extent of region of generation, and also the spectra of the forward scatter along the target surface.
- During this experiment, the role of incident angle will be investigated more thoroughly.
- The data produced will inform further theoretical developments.

Propagation of ultra-intense laser pulses in underdense plasmas

P. Mora, J.C. Adam, A. Héron,
G. Laval, and B. Quesnel,

Centre de Physique Théorique,
Ecole Polytechnique, 91128 Palaiseau, France

RAL 1998 Fast Ignitor Workshop

Motivations

- Fast ignitor laser pulses will have to propagate a long way in an underdense plasma before reaching over-critical densities
- Strong parametric instabilities and resulting laser pulse depletion and electron heating might be important features in the fast ignitor context

1D cold plasma dispersion relation

- Generalization to the fully relativistic regime of
  - Forward Raman instability
  - Backward Raman instability
  - Relativistic modulational instability
- Growth rate can reach a significant fraction of ω_0: $\gamma_{max} = 0.52\omega_0$
- Convective or absolute nature of the instability

S. Guérin *et al.*, Phys. Plasmas **2**, 2807 (1995).

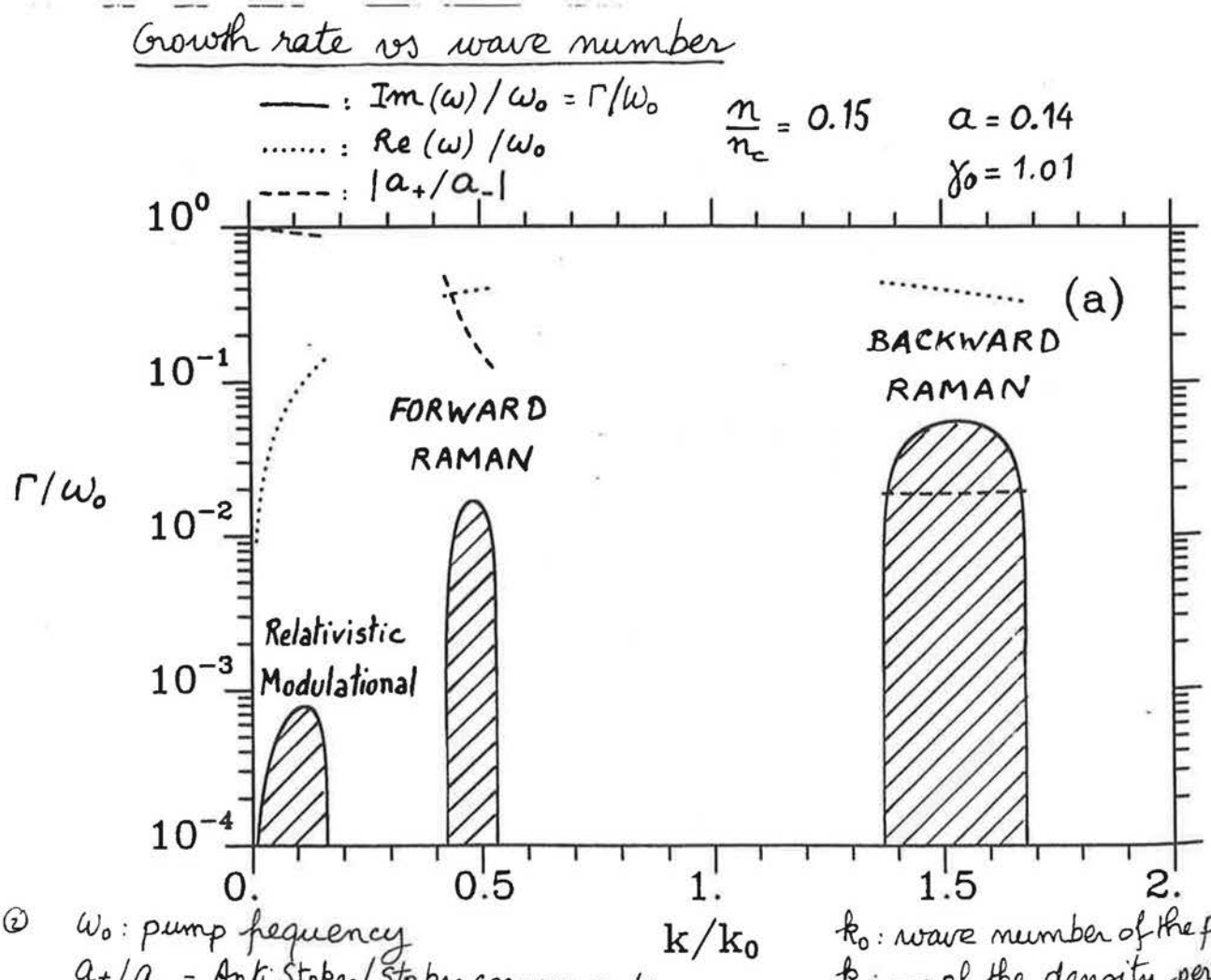

② ω_0 : pump frequency
a_+/a_- = Anti Stokes/Stokes component

k_0 : wave number of the pump
k : — of the density perturbation

③

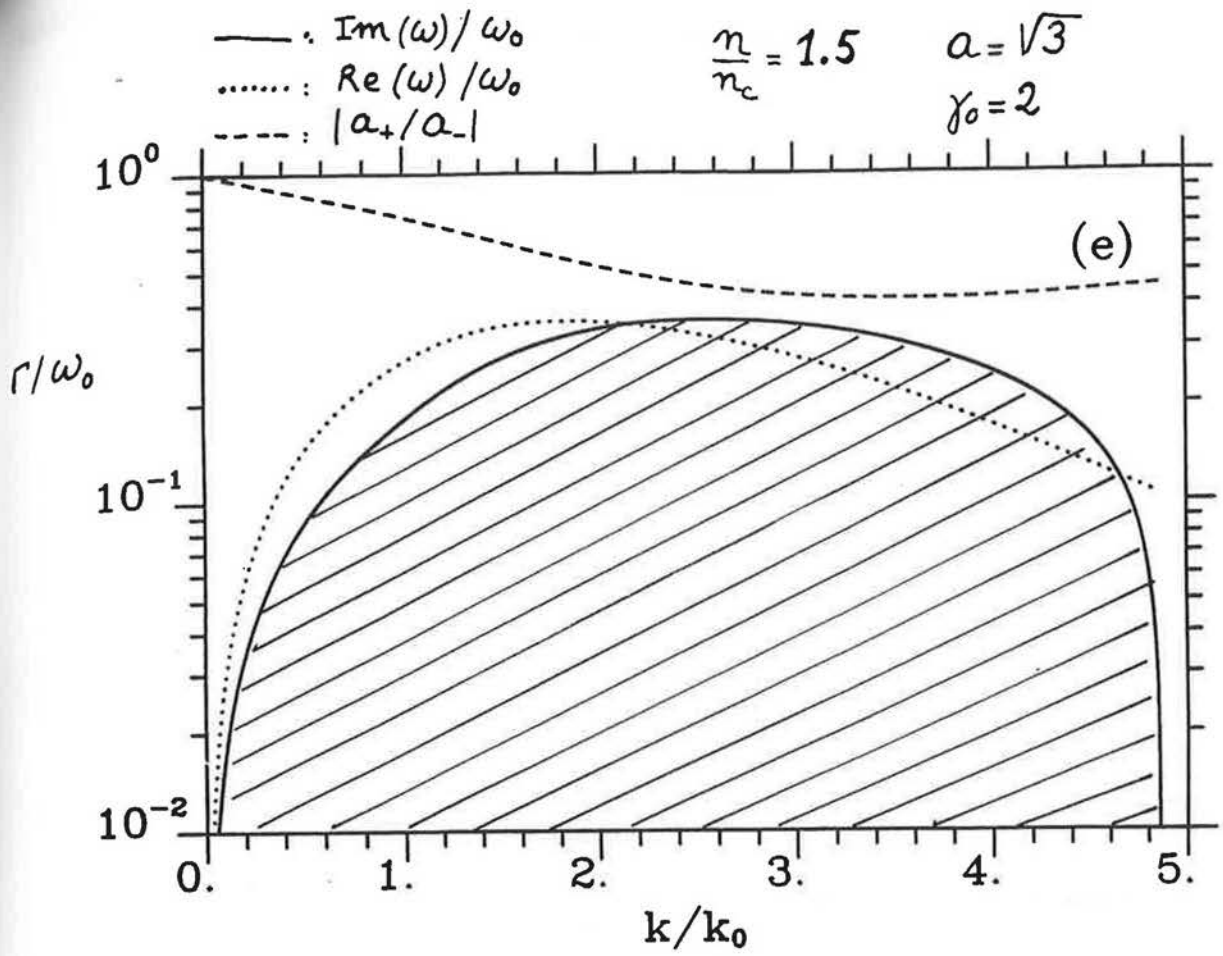

1, 2, 3 : number of unstable branches

A : absolute C : convective instability

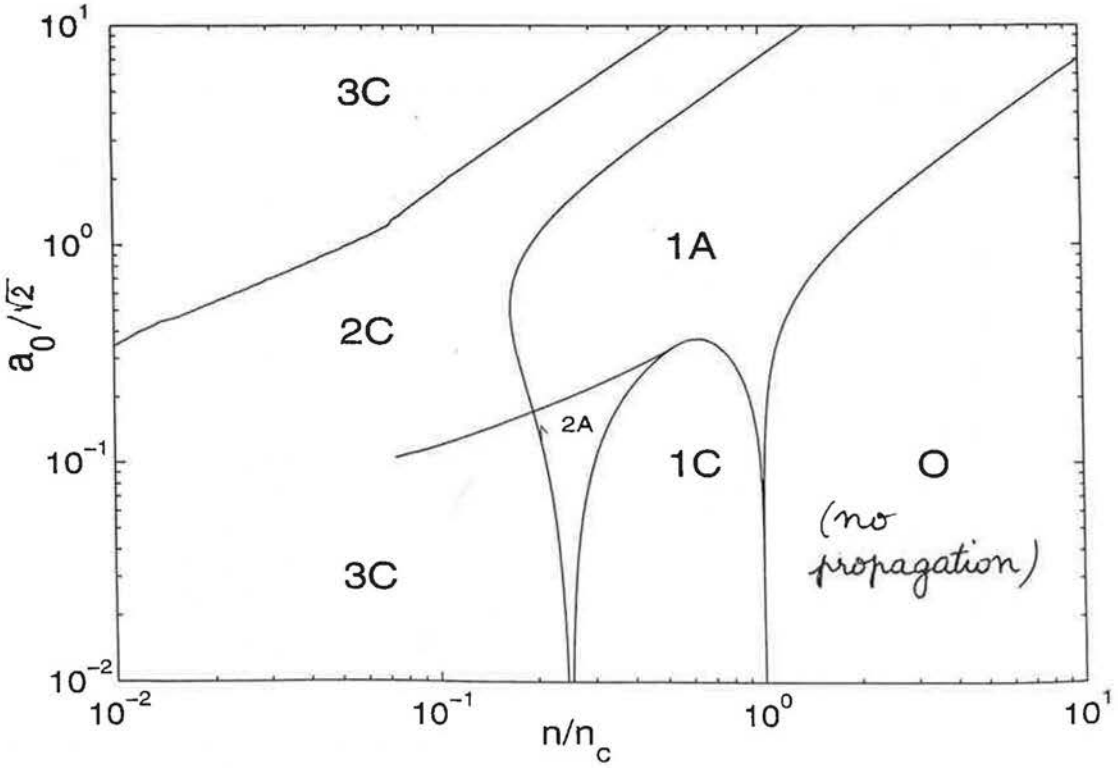

3D cold plasma dispersion relation

- Further generalization to the 3D case including
  - Sideward Raman instability
  - Two-plasmon instability
  - Relativistic filamentation instability
- First order perturbations expanded as

$$f = \sum_{l=-\infty}^{+\infty} f_l e^{i(\mathbf{k}+l\mathbf{k}_0)\cdot\mathbf{r}-i(\omega+l\omega_0)t} + \text{c.c.}$$

- $\Rightarrow$ infinite linear system truncated for $-L \leq l \leq L$, leading to an eigenvalue problem for a matrix of rank $14 \times (2L+1)$

B. Quesnel *et al.*, Phys. Rev. Lett. **78**, 2132 (1997) ; Phys. Plasmas **4**, 3358 (1997).

Growth rate

$a_0 = \sqrt{3}$ ($I \simeq 8 \times 10^{18}$ Wcm^{-2} for $\lambda = 1\mu$m, $\gamma_0 = 2$)

$n/n_c = 0.5$ $(n/\gamma_0 n_c = 0.25)$

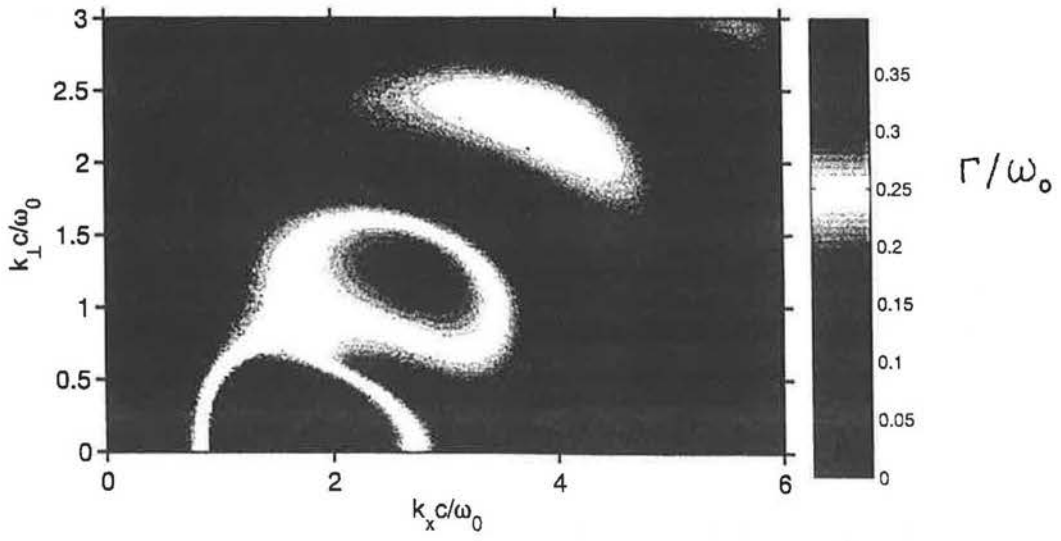

1D hot plasma dispersion relation

- Theory limited to anisotropic temperatures
- Relativistic electron temperature along $\mathbf{k}_0$ strongly reduces the growth rate

S. Guérin *et al.*, Phys. Plasmas **2**, 2807 (1995).

Longitudinal wave energy vs time (PIC simulation, 1D)

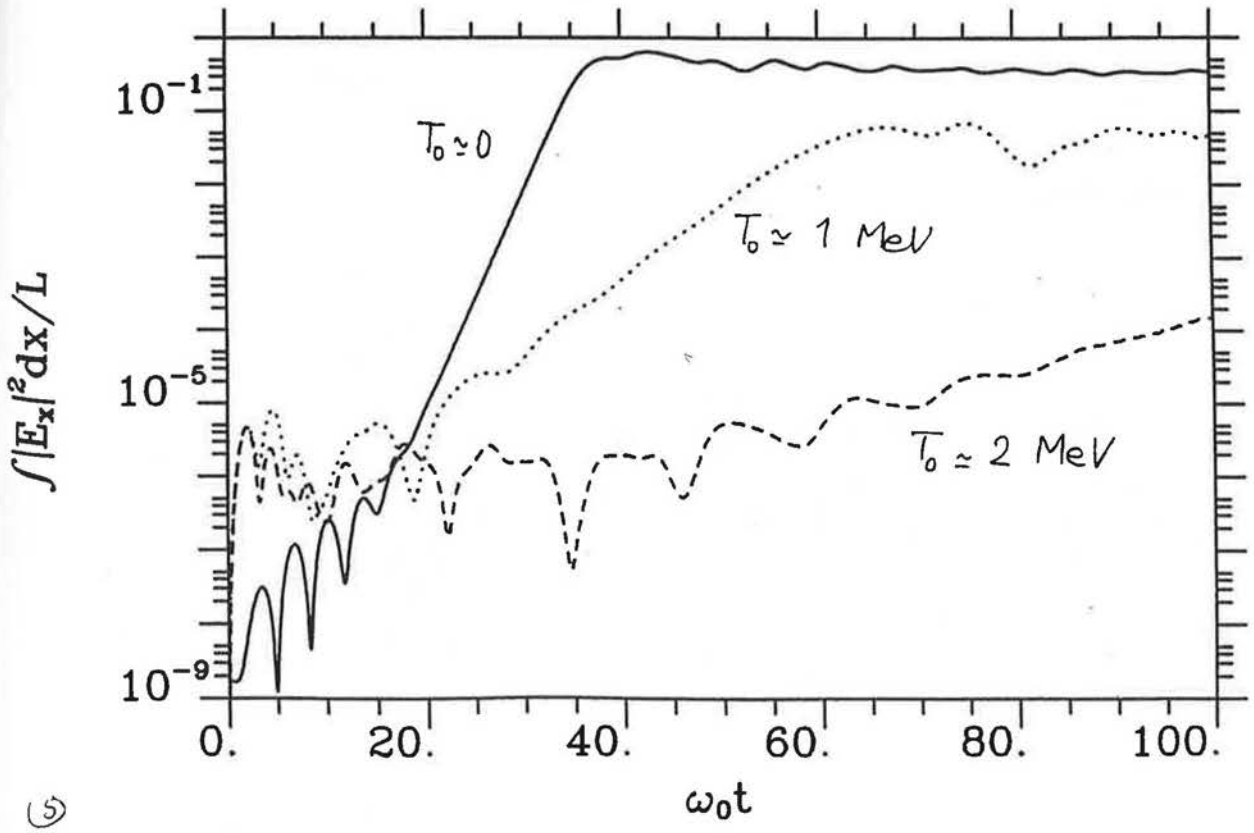

Comparison with 2D PIC simulation

- $2D\frac{1}{2}$ PIC code
- system size $51.2c/\omega_0 \times 51.2c/\omega_0$
- zero order circularly polarized wave at $t = 0$
- $a_0 = \sqrt{3}$ and $n/n_c = 0.5$
- $T_e = 100$ eV
- $dx = dy = 0.1c/\omega_0$, 16 particles per cell
- $dt \simeq 0.09\omega_0^{-1}$

Electrostatic spectrum at $\omega_0 t = 0, 9, 22$, and 50

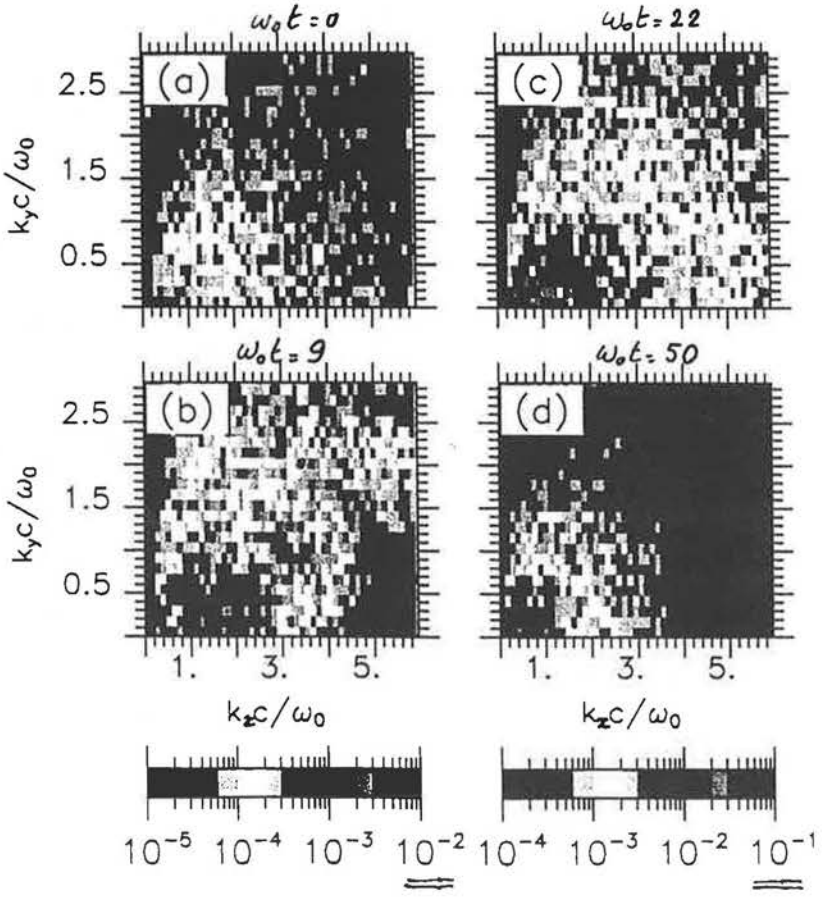

2D PIC simulations of short pulse propagation through plasma slab

- 2D$\frac{1}{2}$ PIC code
- pulse duration: 300fs (FWHM)
- waist: 10μm
- plasma width: 100 or 200μm
- plasma density: 0.025 to $0.5n_c$

Poynting vector S_x at $\omega_0 t = 600, 1200, 1800, 2400$ $I_{vacuum} = 10^{16}$ Wcm^{-2}

$n/n_c = 0.2$

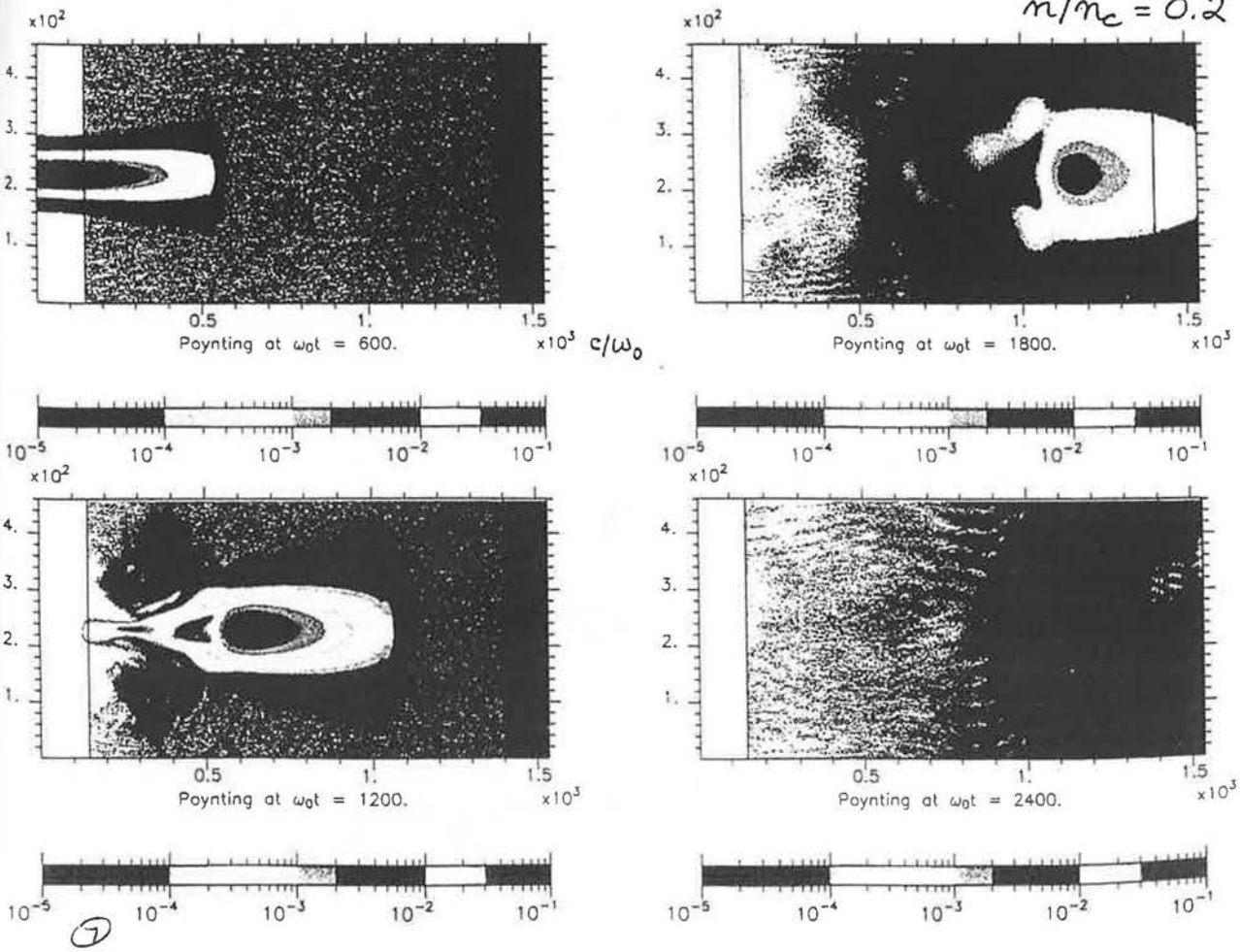

$n/n_c = 0.2$ $I = 10^{17}$ Wcm^{-2}

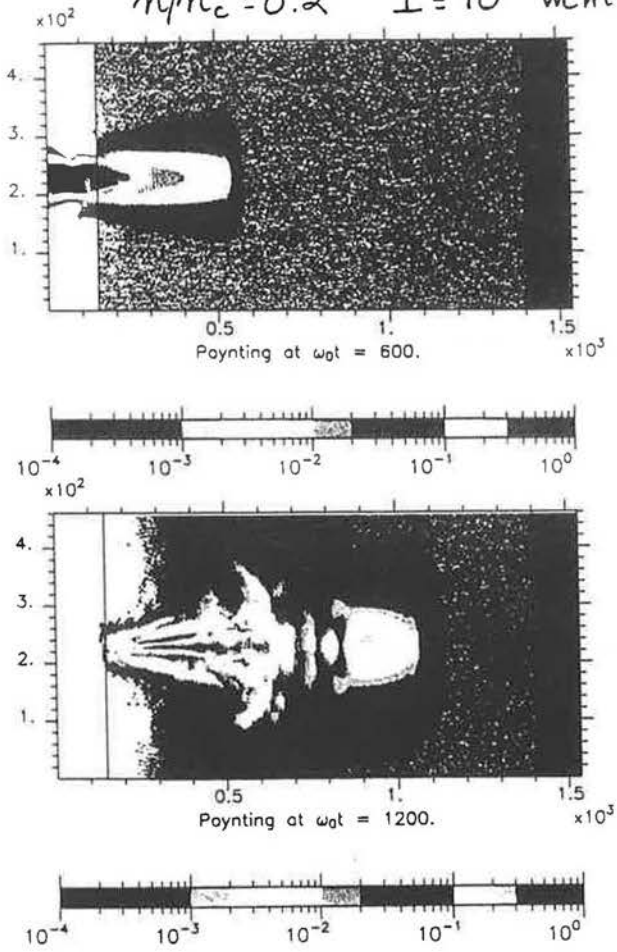

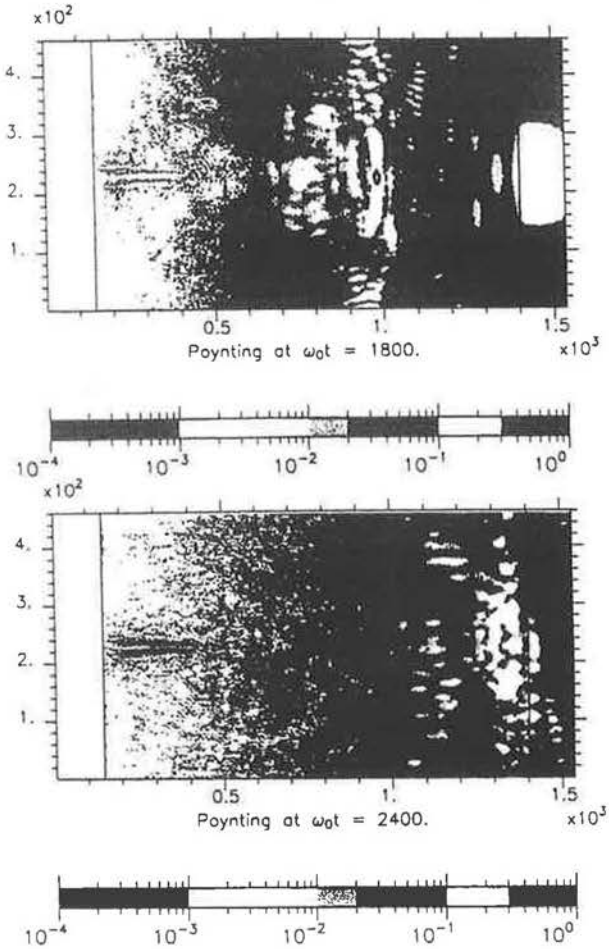

$n/n_c = 0.2$, $I = 10^{19}$ Wcm^{-2}

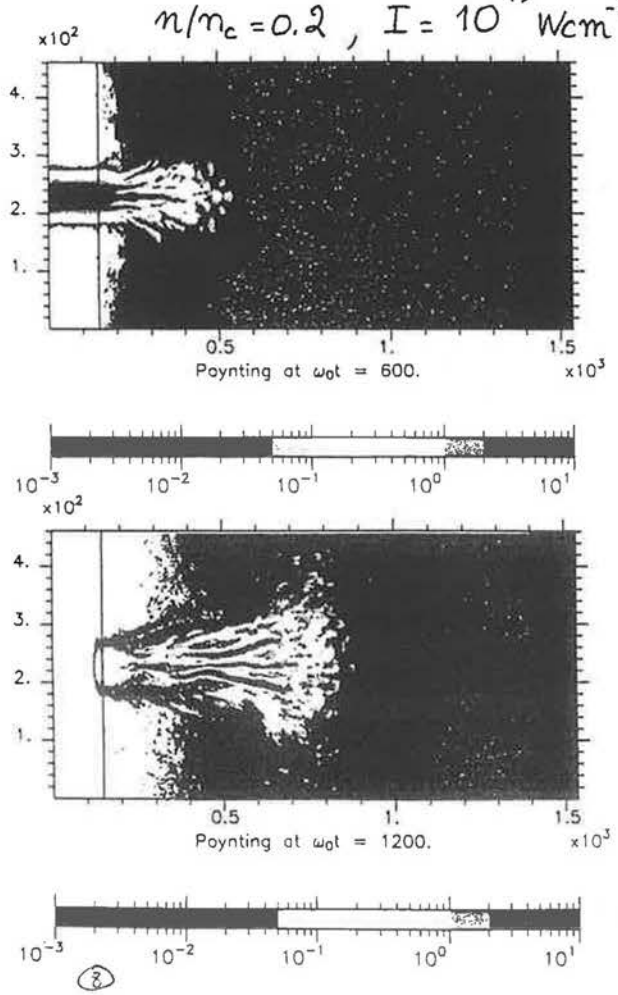

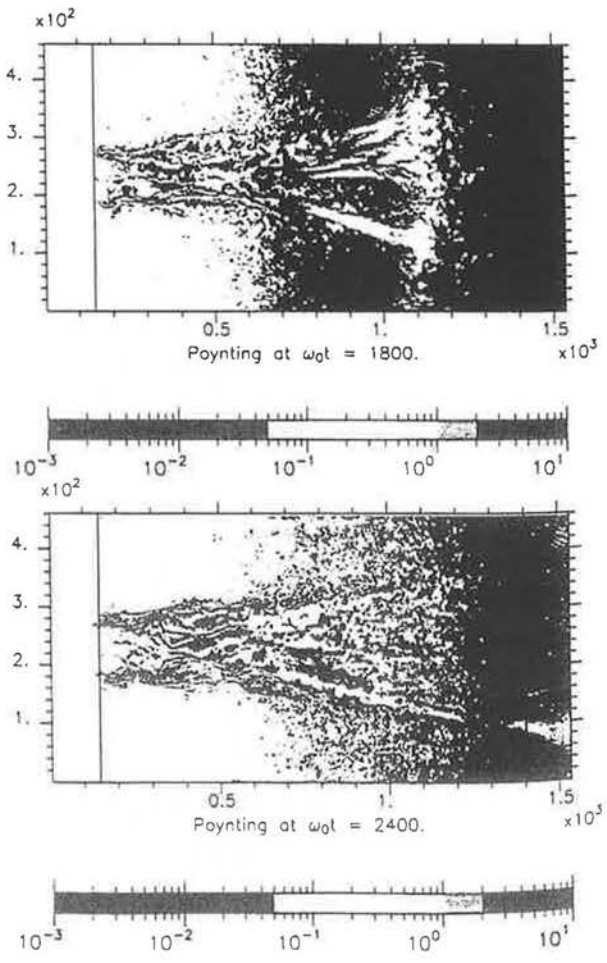

$n/n_c = 0.2$, $I = 10^{20}$ Wcm^{-2}

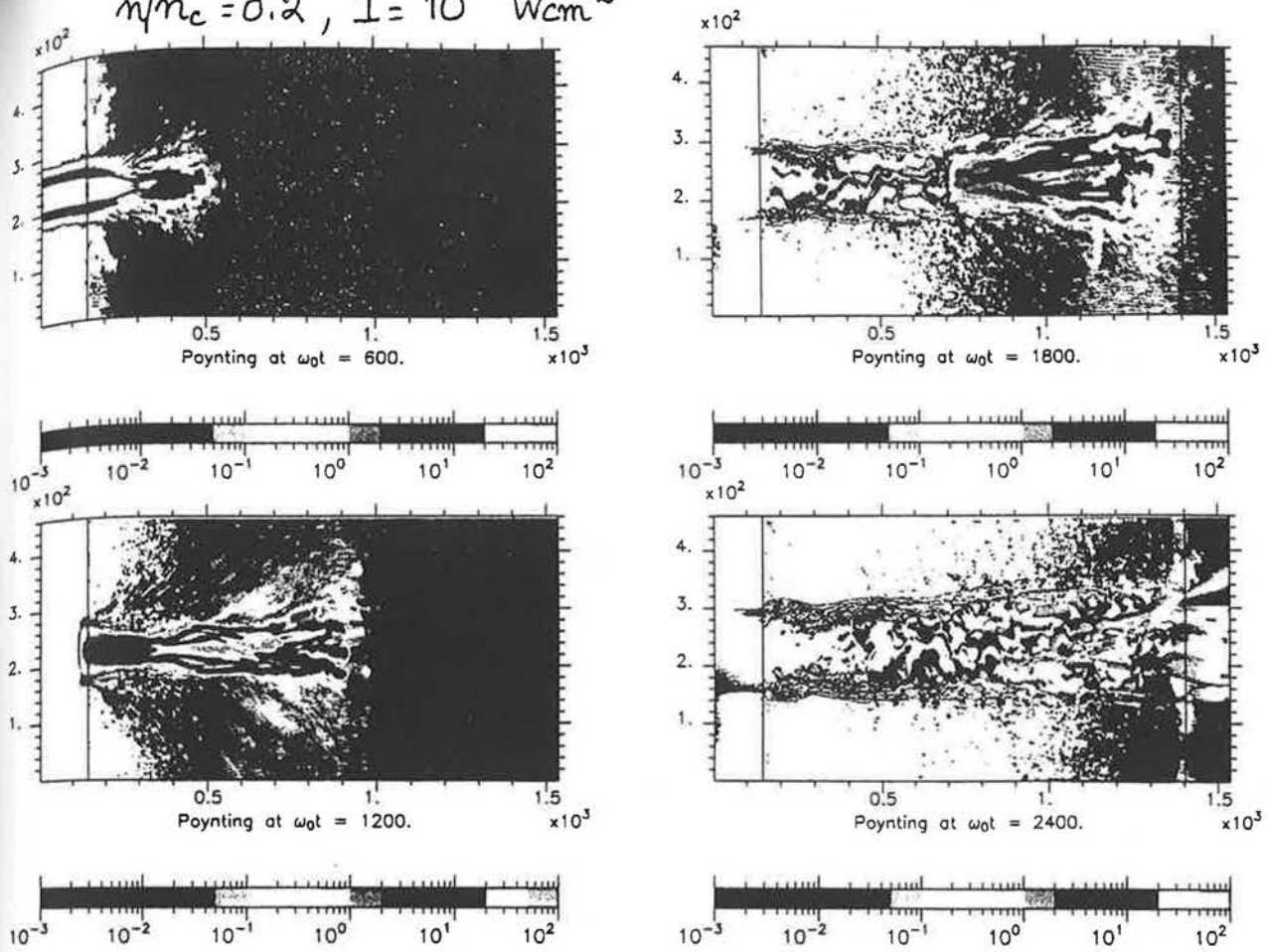

Transmission vs I for $l = 100$ and $200\ \mu m$

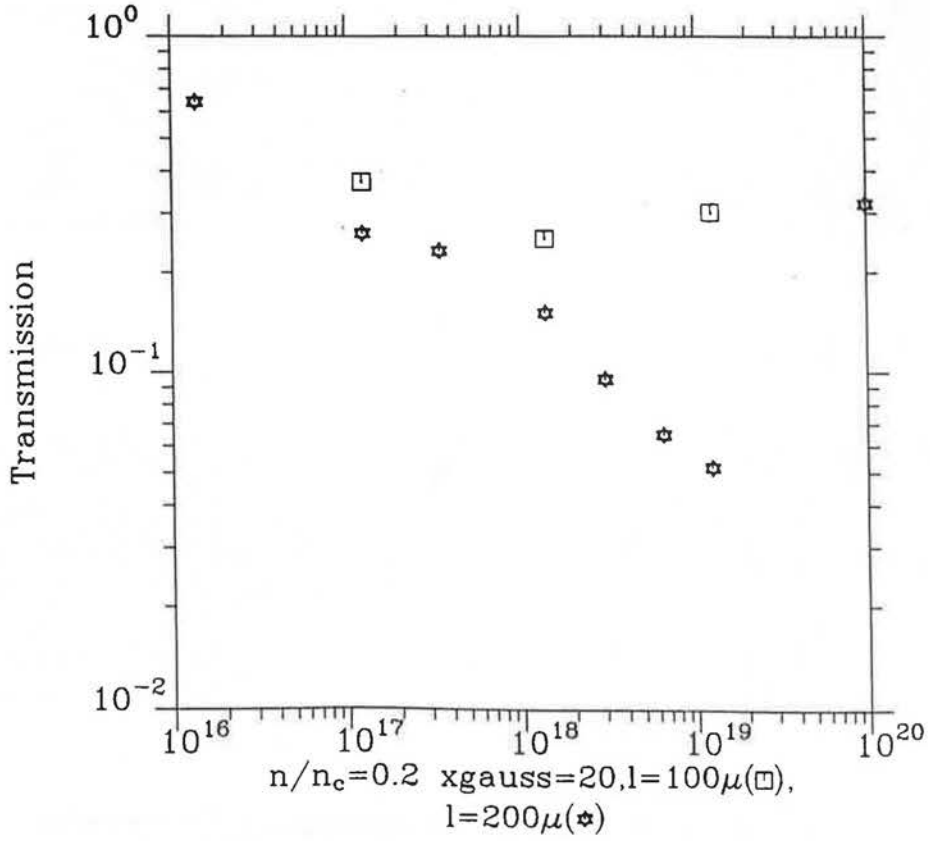

Electron density for $n_0/n_c = 0.2$, $I = 10^{19}\ W cm^{-2}$

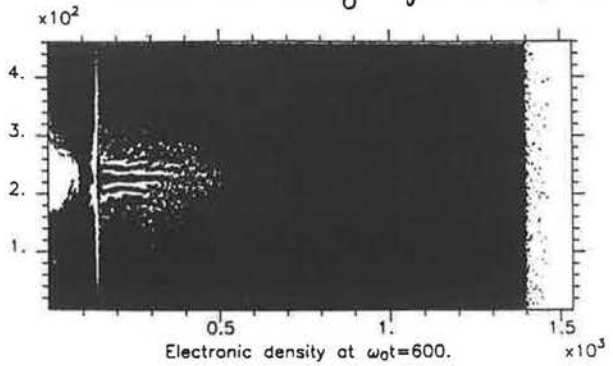

Electronic density at $\omega_0 t = 600$.

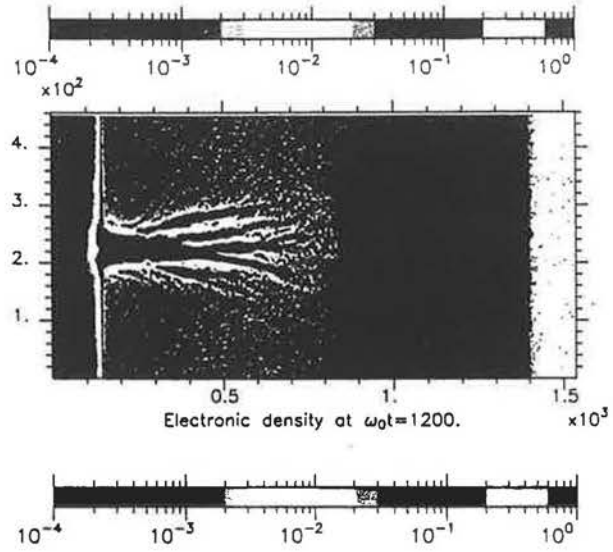

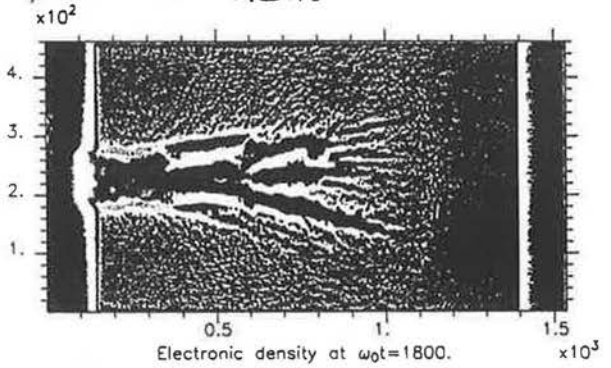

Electronic density at $\omega_0 t = 1800$.

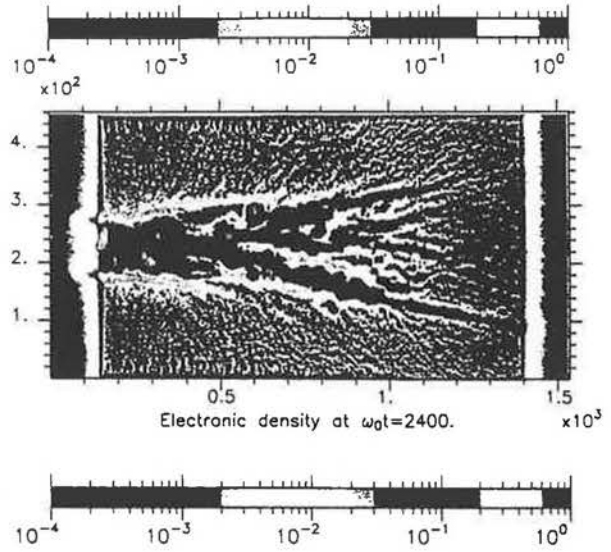

Electronic density at $\omega_0 t = 1200$.

Electronic density at $\omega_0 t = 2400$.

Electron density for $n_0/n_c = 0.2$, $I = 10^{20}\ W cm^{-2}$

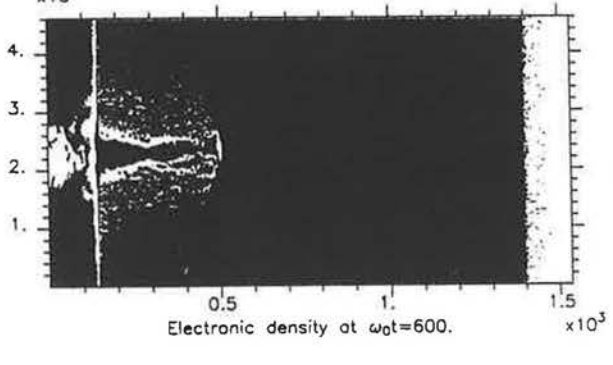

Electronic density at $\omega_0 t = 600$.

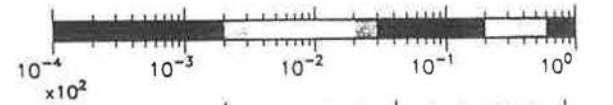

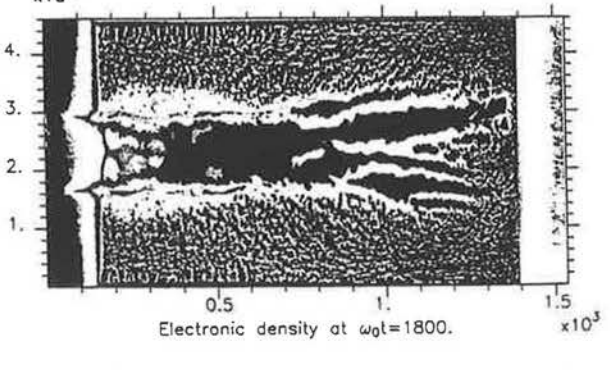

Electronic density at $\omega_0 t = 1800$.

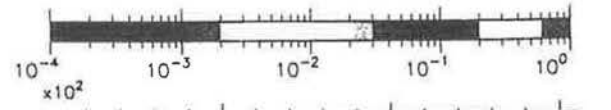

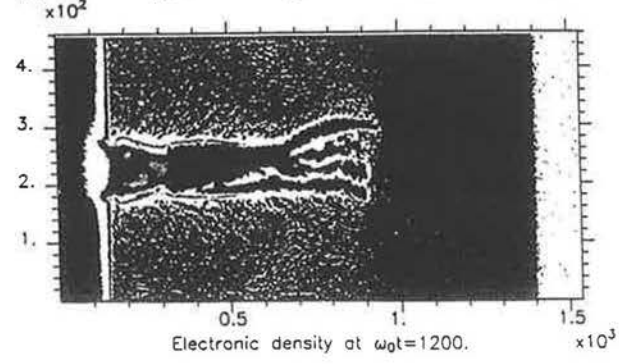

Electronic density at $\omega_0 t = 1200$.

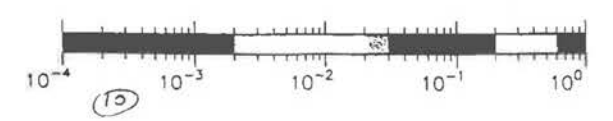

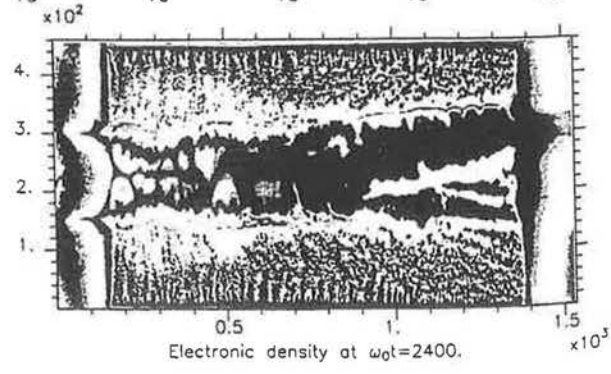

Electronic density at $\omega_0 t = 2400$.

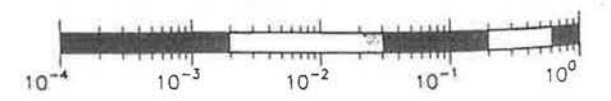

Transmission vs n_0/n_c for $I = 3 \times 10^{18}\ Wcm^{-2}$,

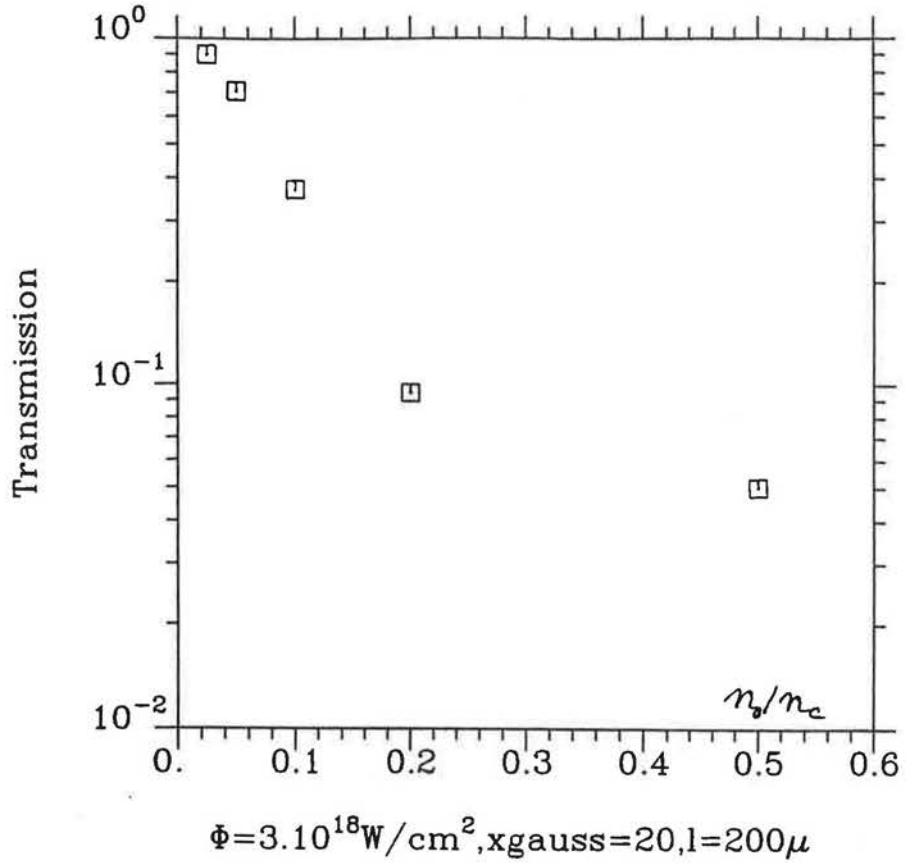

Conclusion

- Electron instabilities have strong growth rates in cold plasma. However the subsequent electron heating reduces the growth rate of the most unstable **modes** (of large k).
- 2D PIC simulations of short pulse propagation through plasma slab of moderate density show strong absorption in the relativistic regime.
- Propagation experiments in the relativistic regime and in slightly underdense long plasmas are needed to validate these conclusions.

About Amplification of *Ultra-Short (<10 fs)* Laser Pulses in Plasma

A. Pukhov — *MPQ, Garching, Germany*

G. Shvets

and — *PPPL, Princeton Univercity, U.S.A.*

N.J. Fisch

1. Amplification without CPA: colliding beams in the plasma
2. 1D VLPL PIC simulations
3. Theory

Plasma-based short pulse amplification

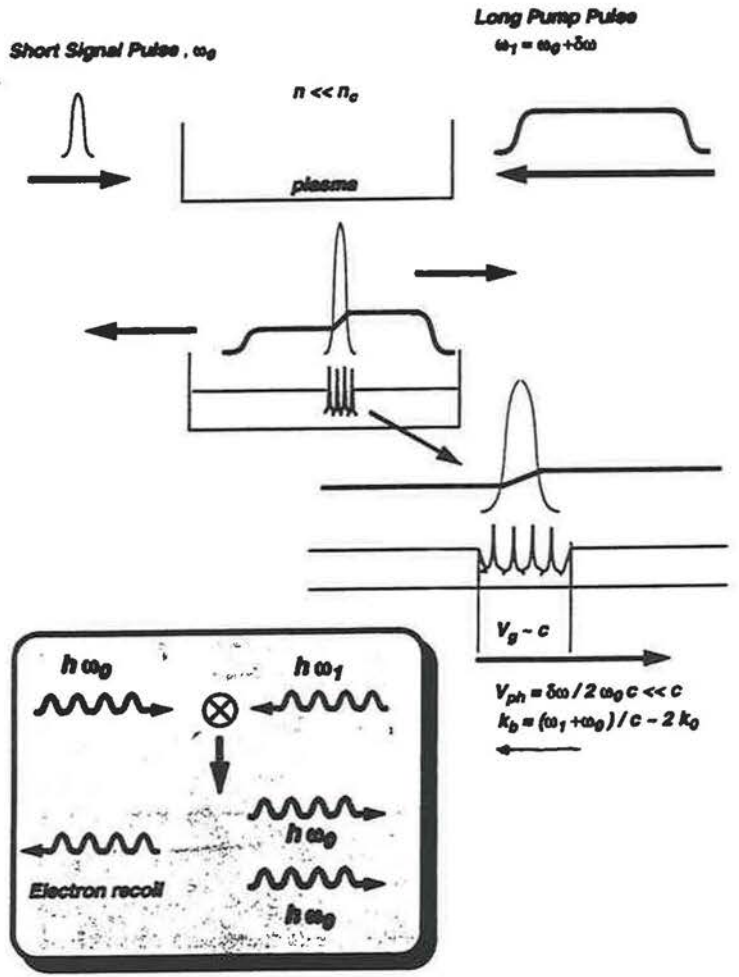

Parametric amplification of an ultra-short laser pulse in plasma

$n_p = 5 \times 10^{18} cc^{-1}$; $I_{pump} = 3 \times 10^{15}$ W/cm^2;

$I_{signal} = 3 \times 10^{15}$ W/cm^2;

$\omega_{pump} = 1.08\ \omega_{signal}$ Duration $\tau = 10$ fs

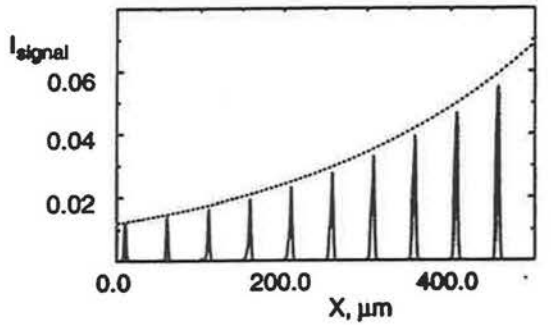

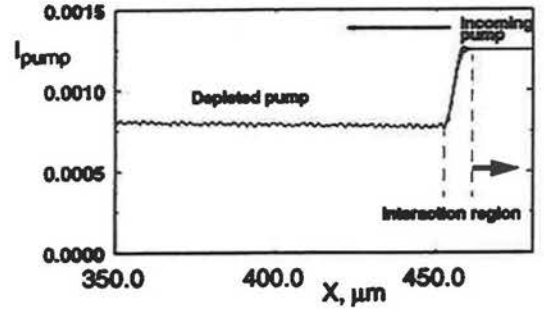

Parametric amplification of an ultra-short laser pulse in plasma

$n_p = 1.5 \times 10^{19} cc^{-1}$; $I_{pump} = 3.5 \times 10^{15}$ W/cm^2;

$I_{signal} = 3.5 \times 10^{15}$ W/cm^2;

$\omega_{pump} = 1.03\ \omega_{signal}$ Duration $\tau_0 = 10$ fs

After 60x amplification $\tau = 8$ fs

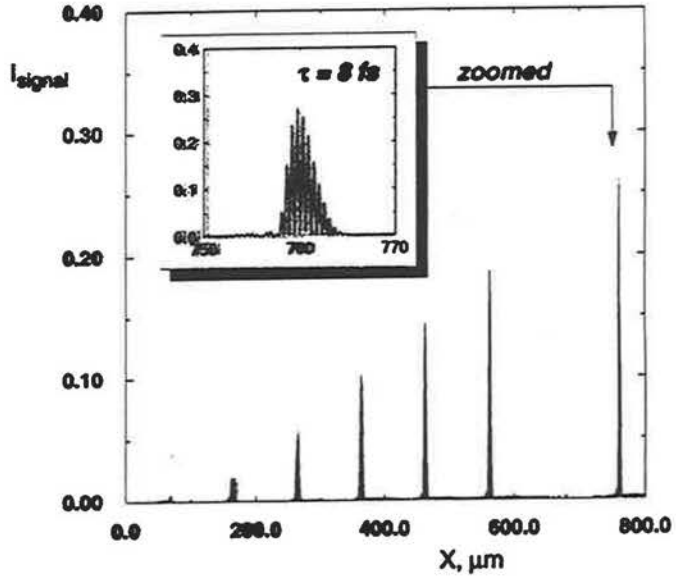

Plasma-based short pulse amplification

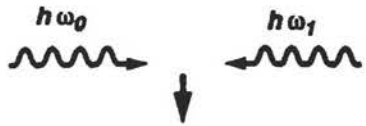

Ponderomotive beating at δω frequency

Introduce ponderomotive phase for electron j.

$$\varphi_j = (k_0 + k_1) z_j - \delta\omega\, t$$

Electron recoil

$$d_t^2\varphi_j + \omega_B^2 \sin\varphi_j = \underbrace{-\omega_p^2 \sum_{l=1}^{\infty} n_l \exp(i\, l\, \varphi_j)}_{\text{Plasma response}} - 2\,\omega_0\, e\, E_z / m\, c + c.c.$$

Here $\omega_B^2 = 4\,\omega_0^2 a_0 a_1$ is the electron bounce frequency in the ponderomotive lattice

When $\omega_B >> \omega_p$ the plasma response is negligible!

$$d_t^2\varphi_j + \omega_B^2 \sin\varphi_j = 0$$

For the efficient amplification must be

$$2\,\omega_B > \delta\omega$$

Plasma-based short pulse amplification

CONCLUSIONS

1. There is a novel mechanism of parametric laser pulse amplification in plasma
2. The mechanism does not require CPA, thus avoiding the expensive diffraction grids
3. Laser pulses shorter than 10 fs in duration can be amplified without stretching.
4. There is no principal limitation in the pulse duration and energy.

This work was supported by DoE contract DE-FG03-98DP00210 (Fast Ignitor contract): Fast Ignitor spin-off

OPTICAL PARAMETRIC CHIRPED PULSE AMPLIFICATION (OPCPA)

Ian Ross

Pavel Matousek, Mike Towrie, Andrew Langley

John Collier, Colin Danson, Dave Neely

Karoly Osvay

Requirements for High Intensity

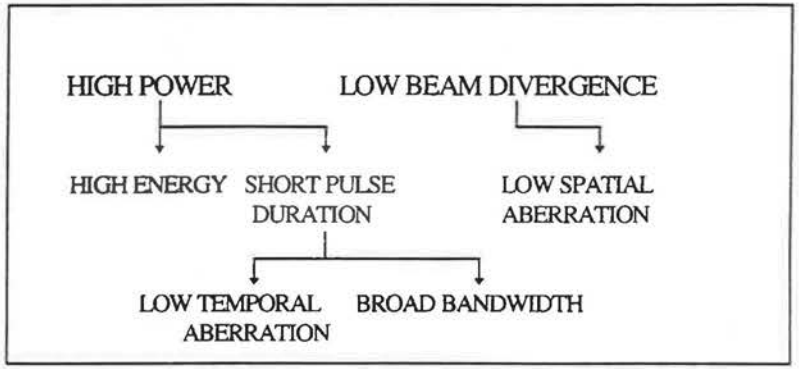

Amplifier Requirements

- High energy capacity at below damage fluence
- Large gain bandwidth
- Low phase distortion (Thermal, non-linear, GVD)
- Low prepulse energy and ASE

Optical Parametric Amplifier

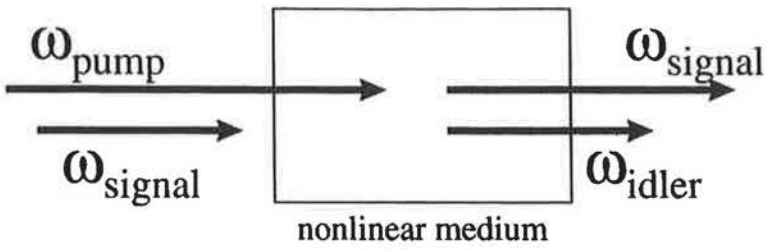

Conservation of Energy $\omega_p = \omega_s + \omega_i$

Phase-Matching Condition $n_p \omega_p = n_s \omega_s + n_i \omega_i$

CLRC

Chirped Pulse Amplification (CPA)

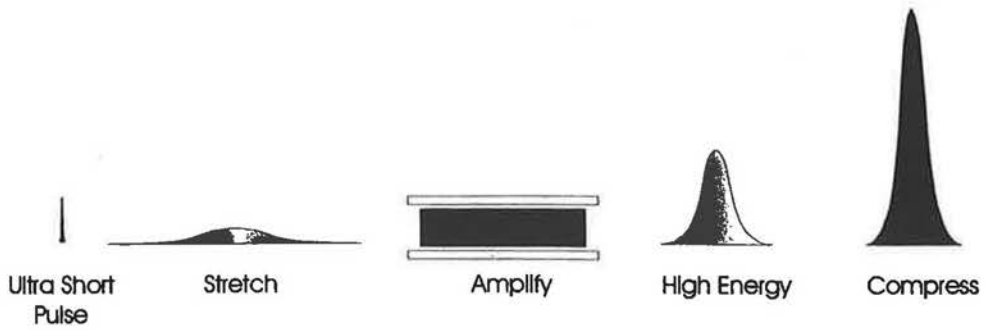

High Output Energy but Amplifier Gain Narrowing Limits Pulse Duration

CLRC

Optical Parametric Chirped Pulse Amplification (OPCPA)

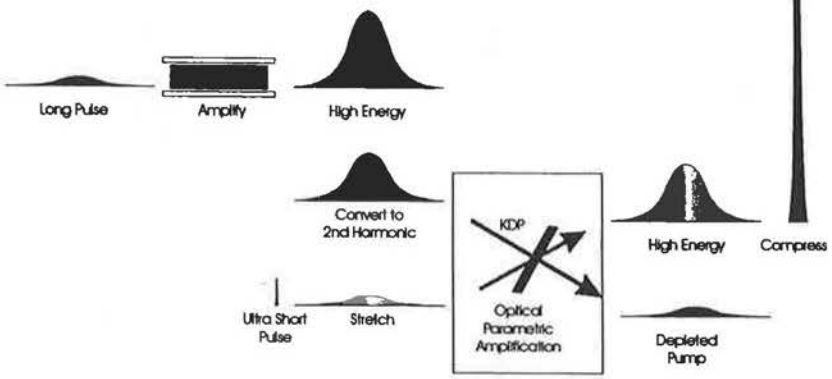

High Output Energy but No Gain Narrowing= Higher Output Power

CLRC

Rutherford Appleton Laboratory

Properties of the OPA Process

- Broad Bandwidth
- High Energy
- Good Beam Quality
- High Efficiency
- Contrast

Rutherford Appleton Laboratory

CLRC

OPA Bandwidths

Near-collinear geometry

(≤ 0.5°) KDP

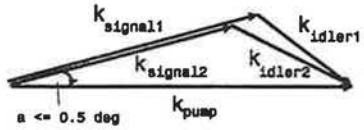

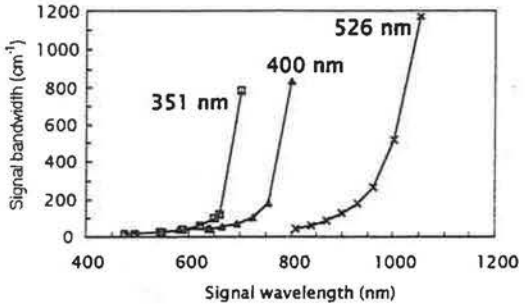

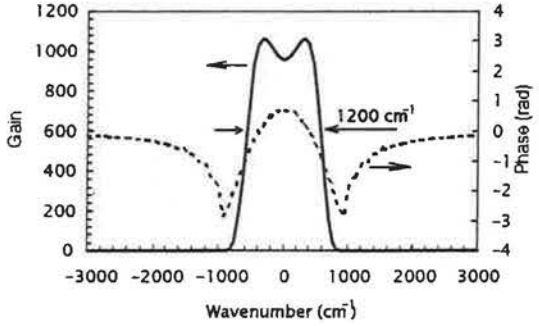

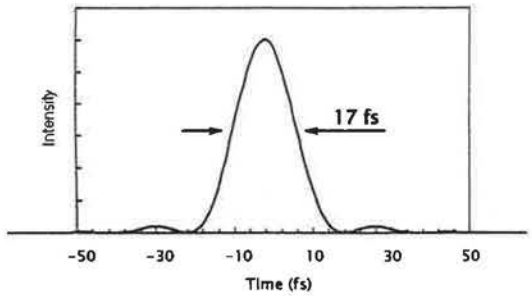

OPA Bandwidths

Non-collinear geometry

(typically > 1 °) LBO

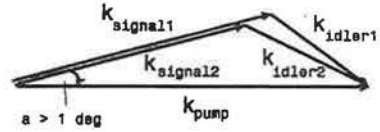

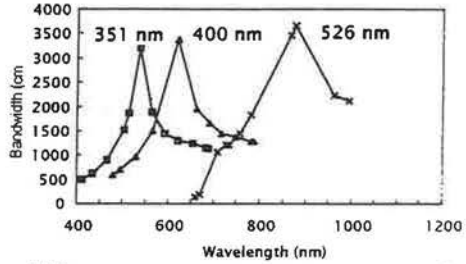

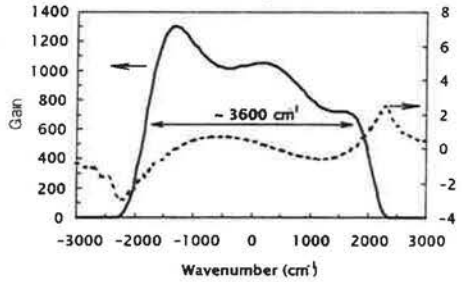

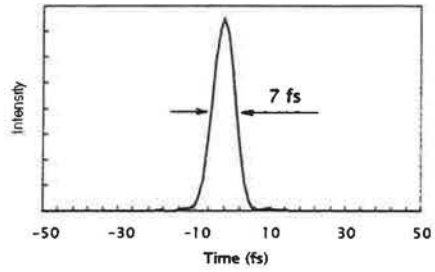

COMPARISON OF GAIN BANDWIDTHS FOR AN LBO OPA AND Ti:SAPPHIRE

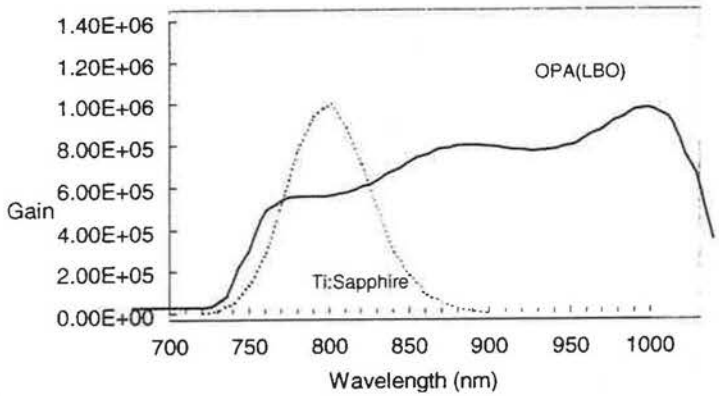

Energy Efficiency and Beam Quality

➲High Energy Efficiency
Pump to Seed ~ 30 % is typical

➲No transfer of pump aberration onto amplified signal

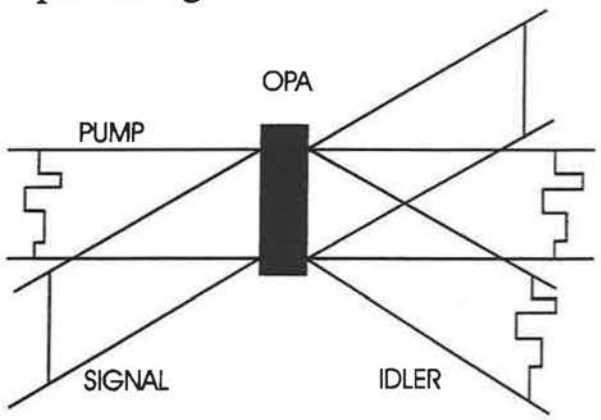

➲No energy deposition in crystal amplifier

➲Short crystal with high gain

- ➡ Low B- Integral
- ➡ Low GVD

PULSE CONTRAST

$$I_{ASE} = \frac{\pi}{4F^2} \frac{h\nu\Delta\nu}{\lambda^2} G_0$$

	ND:GLASS	TiS	OPA
ASE INTENSITY @ 10^{20} W/cm^2	10^{13}	10^{14}	10^{11}
ASE FLUENCE (J/cm^2)	10^5	10^6	100
AMPLIFIER GATE TIME (ns)	10	10	1

- DURATION OF PREPULSE/ASE DETERMINED BY GATE TIME

FOR OPA

→DURATION OF GAIN = DURATION OF THE SIGNAL

→PREPULSE/ASE EXPERIENCES SATURATED GAIN
NOT SMALL SIGNAL GAIN

Practical Schemes

Consider 2 Examples

- Table Top
  - ⇨ Power ~ 1 TW
  - ⇨ Standalone
  - ⇨ Preamplifier for Existing CPA Facilities
- Large Scale
  - ⇨ Power ~ 10 PW
  - ⇨ Replace Existing CPA Facilities

Nd:YAG OPCPA System

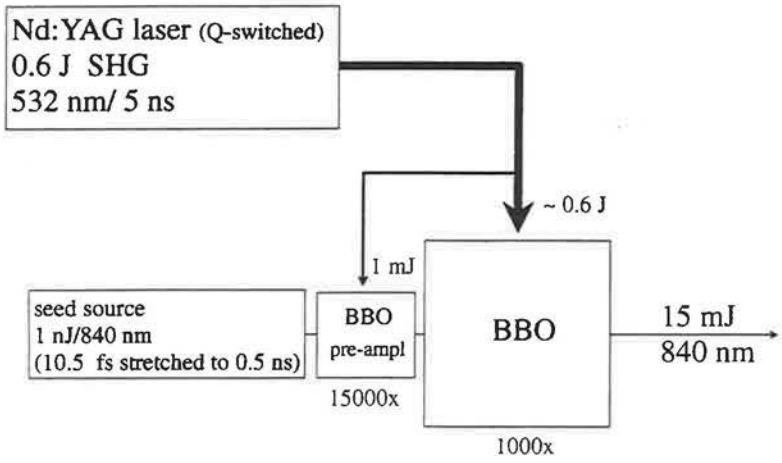

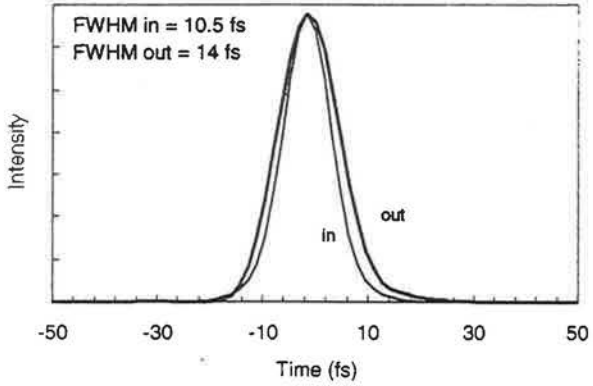

CLRC

Rutherford Appleton Laboratory

OPCPA - 1053 nm Ultrafast Pre-Amplifier

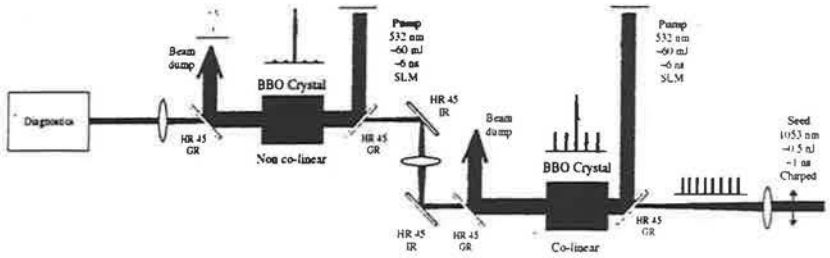

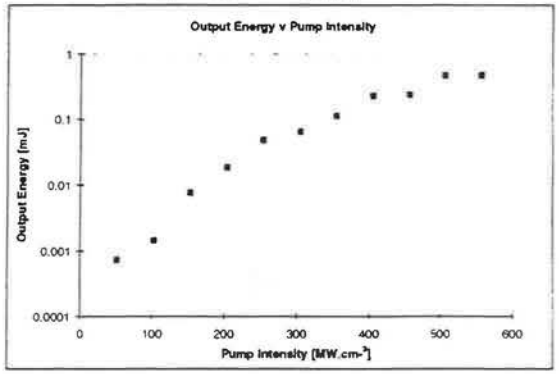

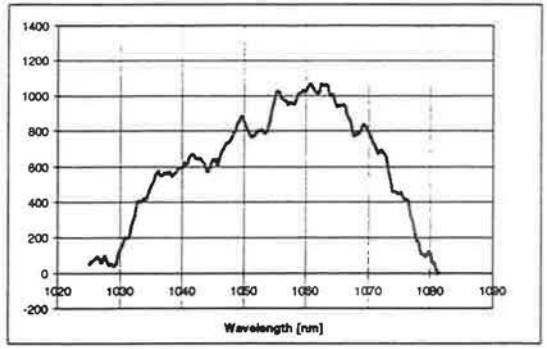

CLRC

Rutherford Appleton Laboratory

Nd:glass High-Power Laser System

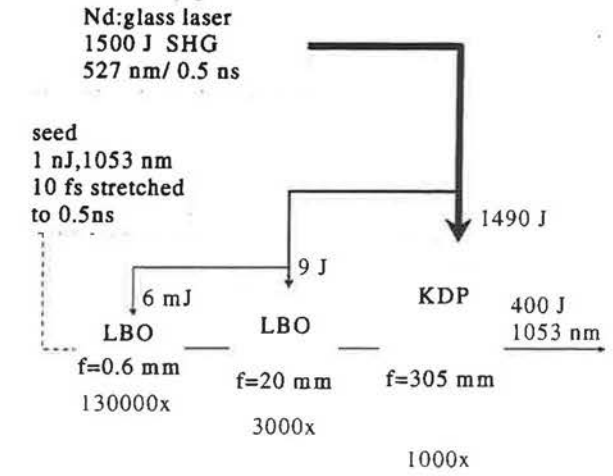

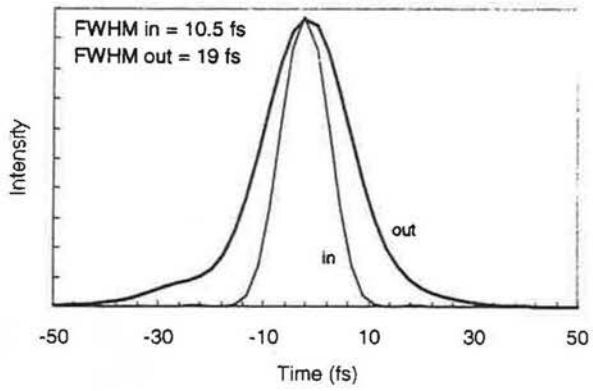

CLRC

Rutherford Appleton Laboratory

Overall Gain

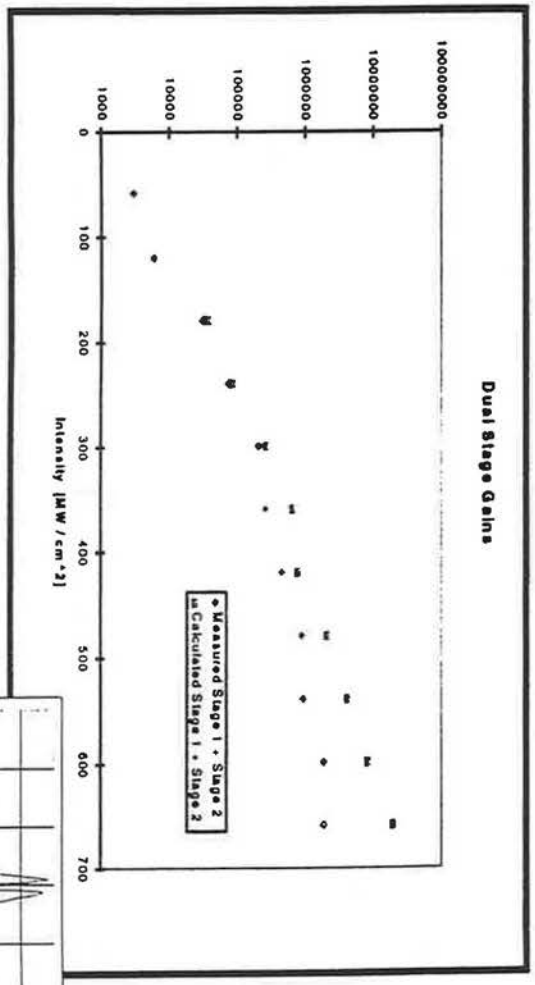

- System Saturates
- Potential Gain 10^7
- Saturated Gain 10^6
- Pulse energy ~ 1 mJ
- Efficiency limited by spatial / temporal overlap

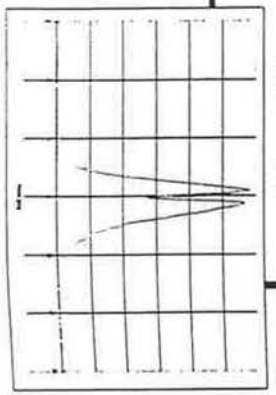

Pump Depletion

CLRC

Rutherford Appleton Laboratory

Summary

- Brings together well established technology - CPA and OPA
- Uses existing hardware of large and small lasers
- Experiments to date confirm predictions
- Broad range of applications
- Offers route to intensities unachievable using existing technologies

Single Beam Comparison

	Conventional Amplifier	OPA
	ND:GLASS	KDP
Fluence limit (J/cm^2)	3	1
Energy (J)	300	300
Minimum Pulse Duration (fs)	400	20
Maximum Power (PW)	1	15
Intensity with F/3 Optic (W/cm^2)	10^{21}	10^{23}
ASE Intensity @ 10^{20} W/ cm^2	10^{13}	10^{11}

'Long' pulse recompression for Fast Ignitor and interaction studies

D. Neely, C Danson, R Allott, R Clarke, M Notley, P Norreys, I Ross and M Stubbs

Rutherford Appleton Laboratory, Chilton, Didcot, Oxon, OX11 0QX, UK.
Telephone: (0)1235 821900 Fax: (0)1235 445888 e-mail: d.neely@rl.ac.uk

Introduction

- Why 'long' pulse recompression
- Technological developments
- System selection
- Ultimate limits of transmissive CPA
- Conclusion

CPA Technique

STRETCHING

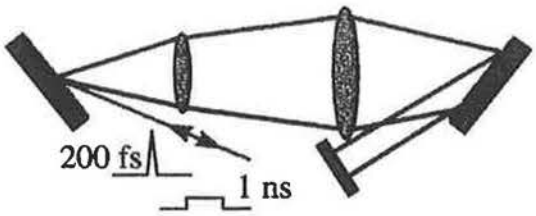

COMPRESSION

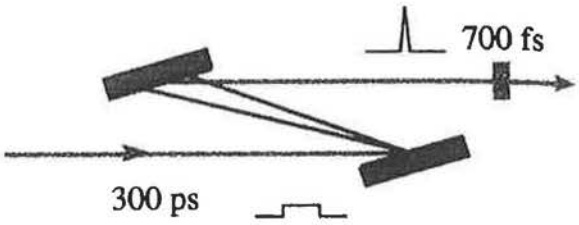

Stretching the pulse prior to amplification using diffraction gratings, then compressing close to target

Laser damage thresholds

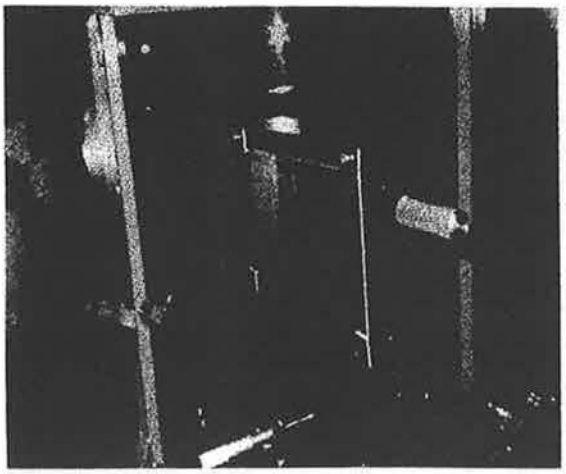

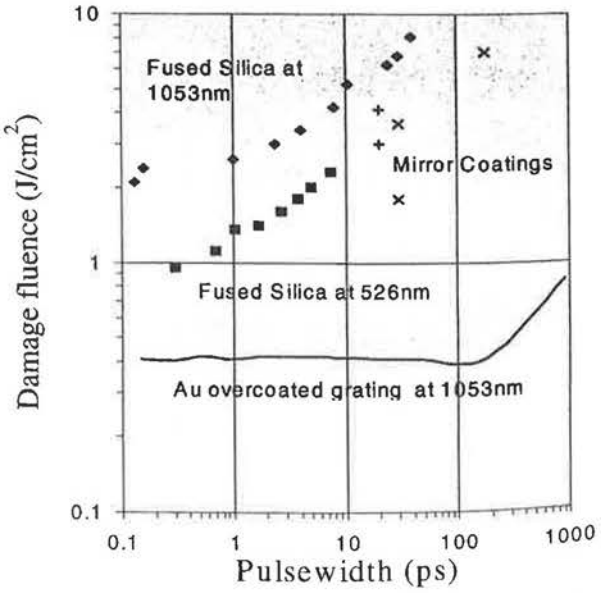

Groove profile

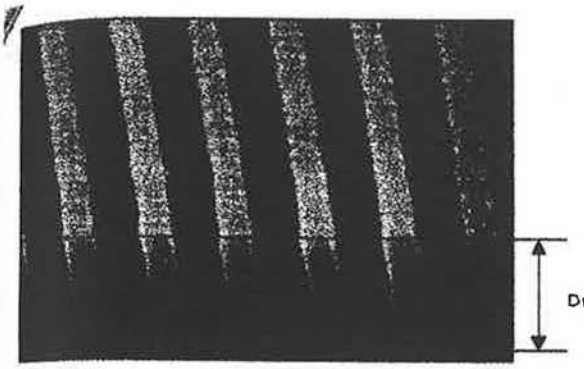

ION-ETCHED PROFILE (SCANNING ELECTRON MICROSCOPE IMAGE)

In reflection
depth ~ period / 2-3

In transmission
depth ~ 1.5-2 x period

Groove mark to space ratio and depth optimised for given wavelength, angle and polarisation

Design objectives

- Test bed facility on ϕ150 mm
- Power upgrade of 6 beam ϕ108 mm
- 10 KJ beamline requirements

Diffraction Geometry

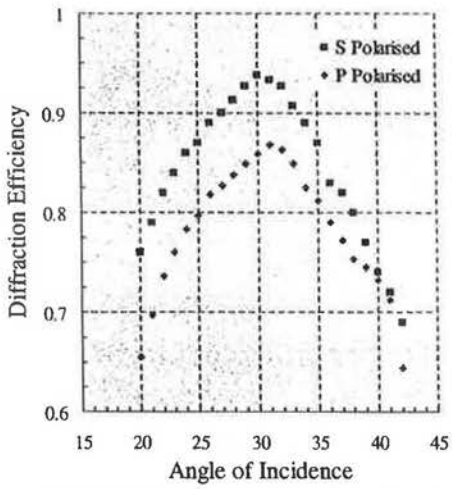

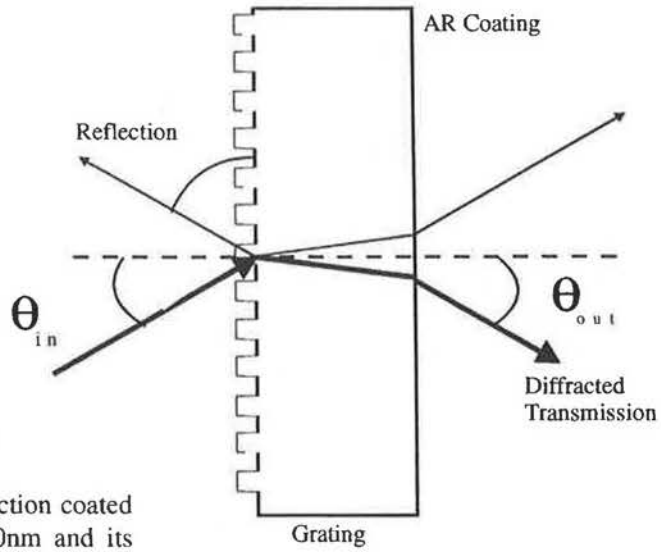

Diffraction efficiency of an anti-reflection coated grating with a groove period of 350nm and its dependence due to polarisation and incident angle of 351nm radiation. H.T. Nguyen et al 1997

7

Compression grating solution set

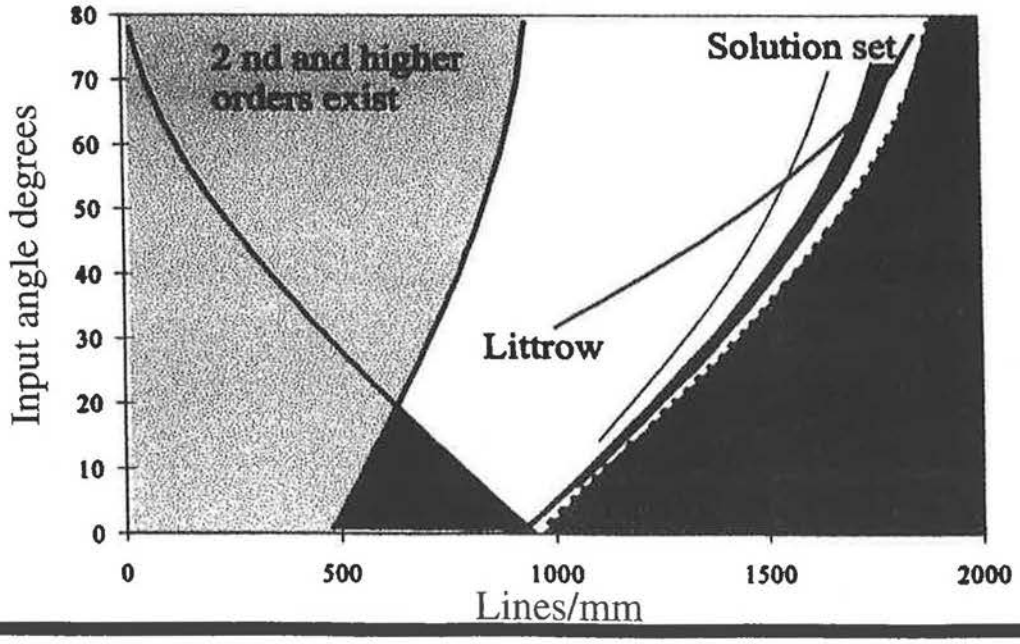

4

Transmission efficiency

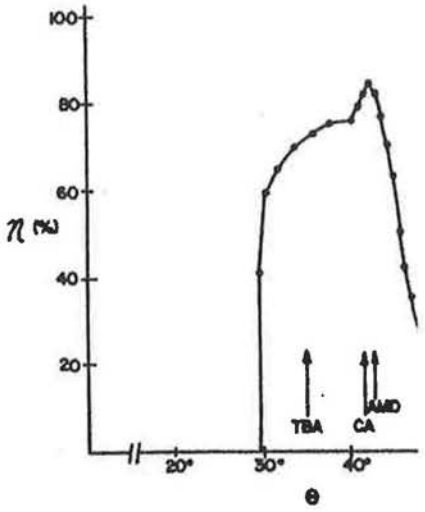

Enger and Case 1983, observed efficieny apex away from the Littrow condition. This was obtained on a photoresist deposited on a substrate with illumination incident through the substrate onto the grating.

$n\lambda p = \sin\theta_{in} + \sin\theta_{out}$

diffraction limit set when $\sin\theta_{out} = 1$

$\sin^{-1}\theta_c = \eta^{-1}$ when $\sin\theta = 1$

Both conditions are identical

Beam smoothing by spectral dispersion

- Typical operation of a Nd glass system will produce smoothing over ~ 15 - 30 % beam diameter

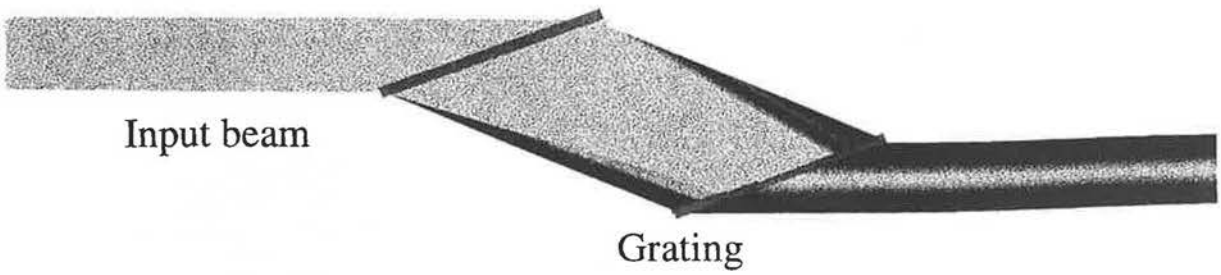

Optimum geometry ?

Grating lines/mm	Compression ps/m/nm	B 1st Grating L (cm) t (ps)	B 2nd Grating L (cm) t (ps)	Fractional Beam Divergence	1st Grating length cm	2nd Grating length cm
1200	100	40	28	0.23	14	24
1480	25	36	26	0.13	20	27
1480	50	38	27	0.15	18	25
1480	100	38	28	0.16	17	25
1740	100	29	21	0.07	30	36

Effect of B-intergral on focal quality

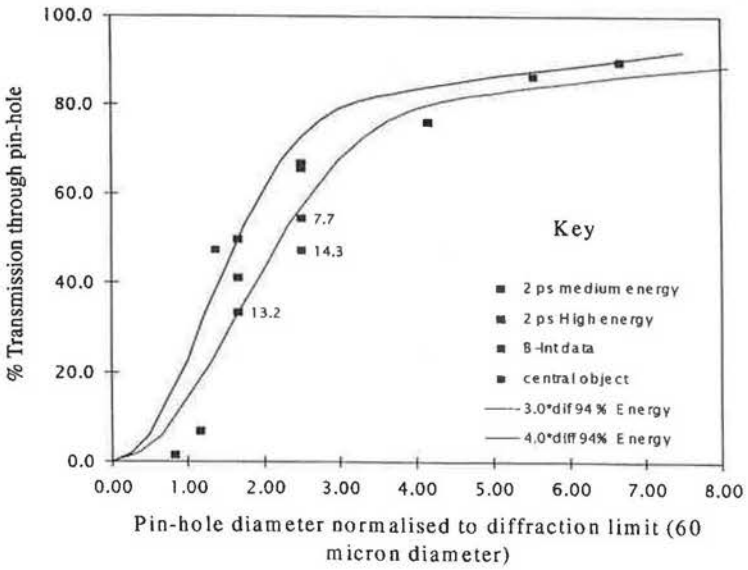

B=1

B=14

Grating period choice

- Fractional beam divergence is ~ constant for a given grating period and temporal compression
- Fractional beam divergence reduces as the grating period reduces
- Grating length increases as the period reduces
- Littrow operation at 0.57 μm period

Minimising B-Integral

Grating on exit surface

case 1

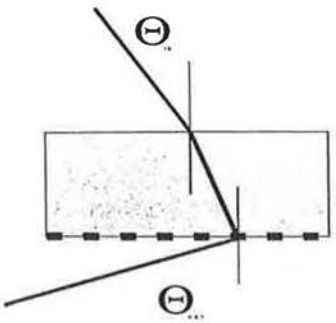

Grating on entrance surface

case 2

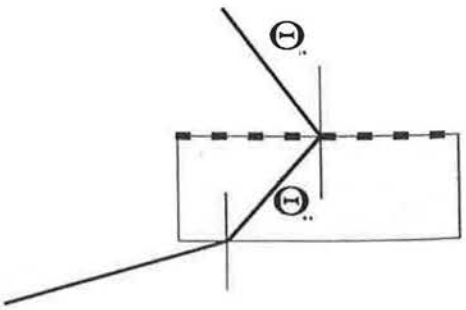

$$B_{g2} = \frac{2\pi}{\lambda} I \varepsilon t \gamma \frac{\cos\Theta_{in}}{\cos^2\Theta_{os}}$$

Distribution of B-integral

Component		B L (cm) t (ps)	Length (cm)	Pulse (ps)	B	Length (cm)	B
Input grating	1	38		600		6	0.38
	2	51	0.4	600	0.03		
Air path		0.12	100	600	0.004		
Vacuum window		104	1.5	400	0.39		
Final grating	1	45					
	2	28	0.4	20	0.56	0.4	0.56
Total					0.98		0.94

Lay-out schematic

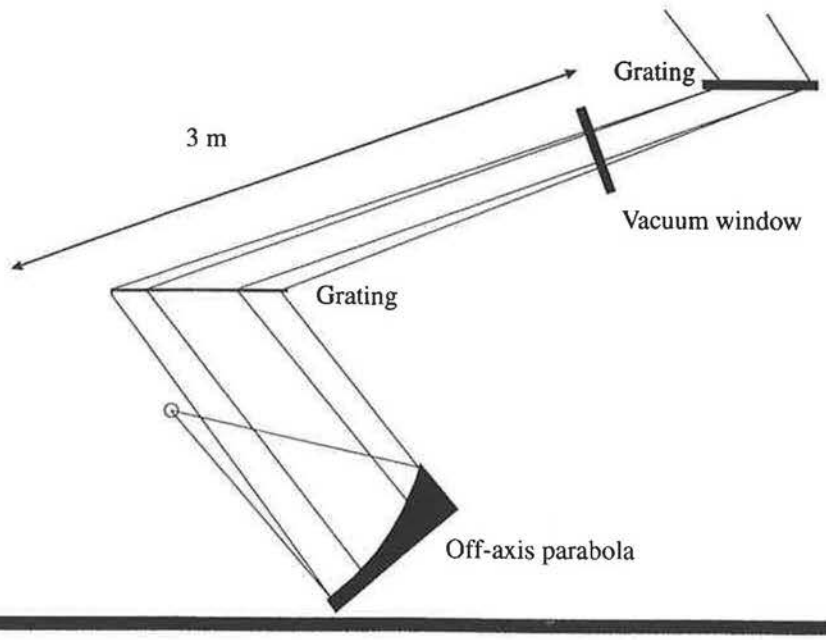

Conclusion

- 150 mm test line will deliver
  0.2 KJ in 20-100 ps 2-10 TW Early 99

- If the six 108 mm lines are upgraded they would deliver
  1KJ in 20-100 ps 10 - 50 TW

- Two 420-600 mm beams would be required to deliver
  10KJ in 20 ps 500 TW

- Ultra thin gratings 1 m diameter 10 mm (or less) thick ????

FOCUSING TRANSMISSION GRATINGS FOR HIGH ENERGY LASERS

BRUNO TOUZET, JEAN FLAMAND, ALAIN THEVENON, VIVIANE MILLET,
FRANCIS BONNEMASON, PHILIPPE GACOIN, BENOÎT DEVILLE

JOBIN-YVON DIVISION OF INSTRUMENTS SA
16-18 RUE DU CANAL – 91165 LONGJUMEAU CEDEX – FRANCE
TÉL : 33 1 64 54 13 00 – FAX : 33 1 69 09 93 19
E-MAIL : isajyoem@aol.com

ABSTRACT

To focus the third harmonic (351 nm wavelength) of high energy neodymium glass laser, the usage of focusing transmission diffractive gratings ion etched directly into fused silica blank brings major benefits in comparison with classical optical solutions using aspheric lenses. The damage threshold of such a diffractive component is same as the damage threshold of a high grade, thin, fused silica plane window. The transmission efficiency reaches 94% for polarization s or p. The image quality is nearly perfect : this diffractive component acts as a stigmatic lens. It separates the remaining first and second harmonic from the third one and in addition it creates a focused reflective order with 0.5% efficiency which offers the possibility to get a well focused sampling beam.

KEYWORDS : LASER - GRATING - ION ETCHING - FLUENCE - FOCUSING DIFFRACTIVE OPTICS

INTRODUCTION

To focus high energy laser beams, for example the third harmonic of Nd Yag laser at 351 nm, the level of required specifications is in general very high : The laser induced damage threshold (LIDT) has to be optimised, the light losses have to be minimum and the focusing properties need to be nearly diffraction limited. In addition it is necessary to separate the remaining first and second harmonic and also a well focused sampling beam is often required.

A highly efficient focusing transmission grating which can be ion etched directly into a fused silica blank will present many benefits in comparison with classical optical solutions using aspheric lenses :

Laser induced damage threshold (LIDT) is optimised by engraving the diffraction grating into a thin high grade fused silica plane parallel plate, with supersmooth polish.

The image quality is nearly perfect because this grating lens is stigmatic.

The groove profile can be optimised in order to obtain high transmission efficiency for s or for p polarization. The existence of a focused reflective order may be used to get a focused sampling beam.

Let see the manufacturing techniques used to produce the focusing transmission gratings and the performances of such gratings which have been recently manufactured.

MAJOR FUNCTIONS OF A FOCUSING TRANSMISSION GRATING

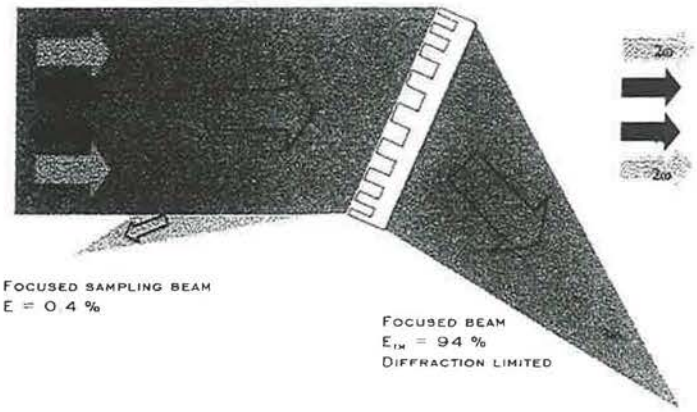

I . HOLOGRAPHIC RECORDING OF THE MASK

The manufacturing process consists to record a mask in photoresist deposited onto the fused silica plate and then to transfer by ion etching the mask modulation into the fused silica itself.

The first step of production is to polish a plane window made of best grade fused silica in order to achieve highest damage threshold. The most important parameter for polishing is the microroughness as it seems that better is the microroughness specification higher is the damage threshold. The flatness for transmissive diffractive optic is less stringent than for reflective diffractive optic as aberrant optical path due to optical figure is 2 times lower for a transmissive optical component than for a reflective one.

The thickness of the fused silica plate may be choosen in the range of 15 to 20 mm even for large components (500 mm size).

Second step is to deposit a thin layer of photoresist. Thickness uniformity of photoresist film has to be well monitored as it has an effect on the transmission efficiency uniformity (efficiency depends on groove depth). Two methods may be used depending on size and shape of components : dip coating or spin coating.

During the third step the photosensitive layer is exposed to interference fringes created at the intersection of two coherent laser beams.

Then, fourth step, chemical treatment of the photosensitive layer selectively dissolves the exposed areas forming grooves in relief.

The geometry of the laser wavefronts used to produce the interference fringes are calculated in order to produce a non linear groove distribution on the surface and so to perform the focusing properties at desired wavelength.

HOLOGRAPHIC RECORDING OF THE MASK

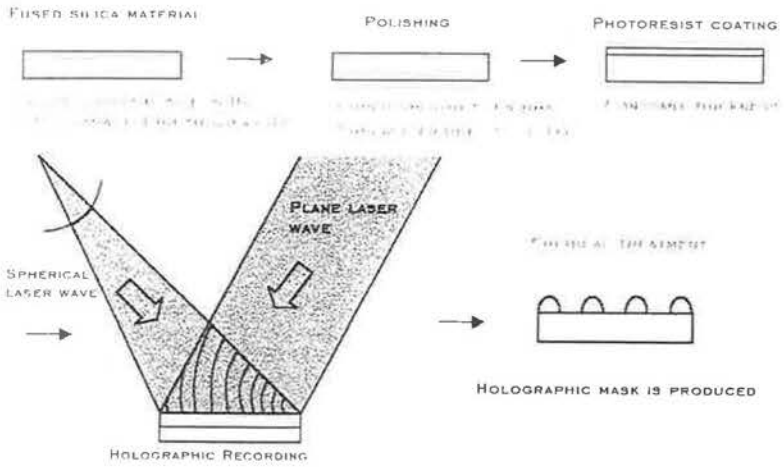

2. OPTICAL CALCULATION OF GROOVES PATTERN

To record the transmission focusing grating we use interference fringes created by 2 coherent laser beams issued from 2 point sources, one is at infinity. According to the holography principle, when we light the recorded hologram with one of the 2 waves we reconstruct the image of the other one across the blank (image - 1T).

This image is perfectly stigmatic when the wavelength used to record the hologram is same as the one to light it.

It exists a slight diffraction of light at the grating surface (about 0.5%) in the rear direction which is focused symetrically for same reasons. We call this image - 1R. This image is not perfectly stigmatic because the focused light beam - 1R is crossing the fused silica window. Nevertheless the image quality is good enough to get the desired well focused sampling beam representative of the entire wavefront.

If we want to focus a multiple wavelengths light beam we will record the transmission focusing grating by using two spherical waves at a well choosen wavelength. The grating lens obtained will exhibit good focusing properties while some residual aberrations will remain. Our optical calculation software permits to optimize the result and to give the spot diagram image at wavelength of interest. [1]

RECORDING THE FOCUSING GRATING PATTERN

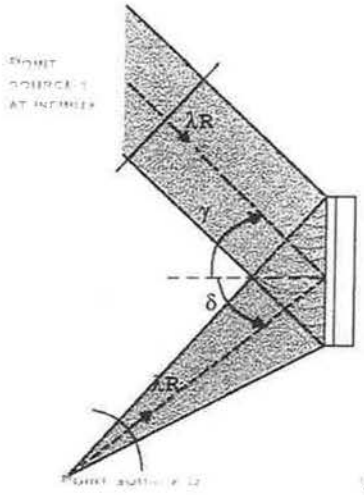

RECORDING CONFIGURATION

IMAGE RECONSTRUCTION

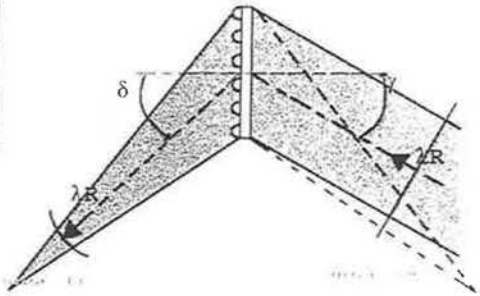

RECORDING OF A FOCUSING GRATING OPTIMISED FOR A GIVEN WAVELENGTH RANGE

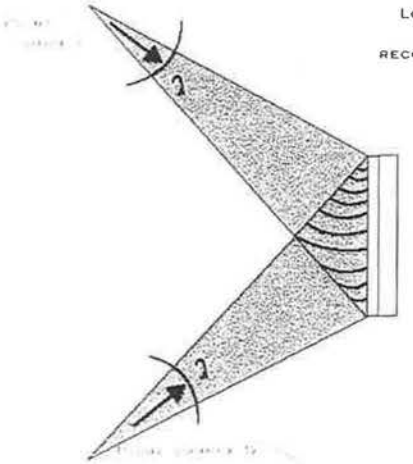

LOCATIONS OF POINT SOURCES C AND D ARE CALCULATED TO OPTIMIZE RECONSTRUCTED IMAGE QUALITY OVER THE DESIRED SPECTRAL RANGE

SPOT DIAGRAMS OF IMAGE - I T

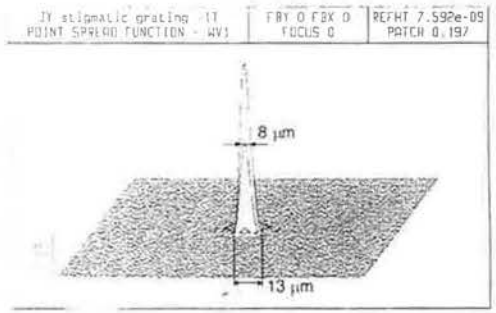

SPOT DIAGRAMS OF IMAGE - I R

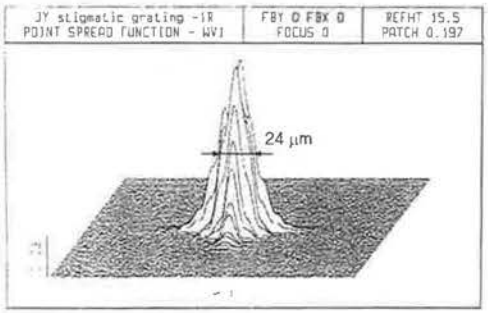

3. ION ETCHING PROCESS

INITIAL MASK

DURING ION ETCHING PROCESS

ION ETCHED GRATING

The profile of the holographically recorded mask is then transfered inside the fused silica blank using reactive ion etching process. There is no more photoresist at the end of the process.

The etch rate of photoresist mask and of fused silica substrate are different. This etch rate can be monitored accurately by introducing some gazes into the ion etcher chamber. It also depends on the angle of incidence of the ion beam with respect to the etched surface. So it is possible, using right parameters, to obtain a laminar profile with adequate depth of grooves and duty ratio to optimize efficiency. [2]

The focusing properties of the holographic mask are not affected by this ion etching process. The supersmooth polishing of the substrate remains the same or is even improved, which is an advantage for damage threshold value.

We calculate the required profile depth, duty cycle and aspect angle using electromagnetic theory equations.

THEORETICAL EFFICIENCY CALCULATION

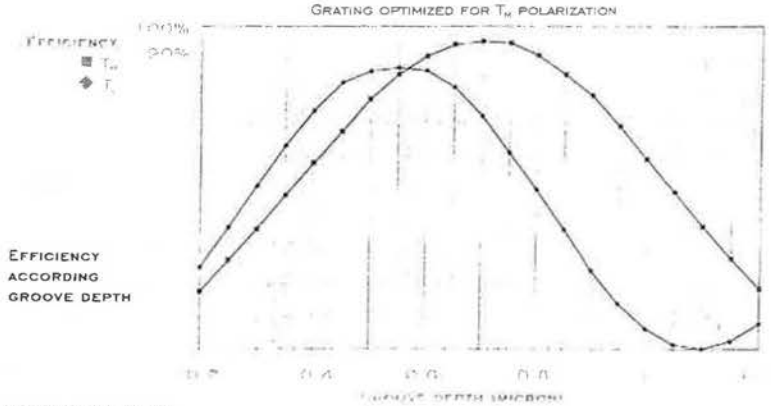

INCIDENCE 25 DEG WAVELENGTH 351 NM
PERIOD 400 NM DUTY CYCLE DC = 0,4

4. MANUFACTURED FOCUSING GRATING

4.1. SPECIFICATIONS OF GRATING PRODUCED

We have produced a focusing grating in dimension 150 mm diameter, ion etched into super polished fused silica blank

- Number of grooves = 2500 g/mm
- Wavelength of use = 351 nm
- Period of the grating : 400 nm
- Depth of groove : 700 nm
- Focal length : 2.4 meters
- Numerical aperture : f/16
- Blank dimensions = 150 mm dia - 10 mm thickness

The groove profile has been optimized to enhance the Tm polarization

MANUFACTURED GRATING CONFIGURATION

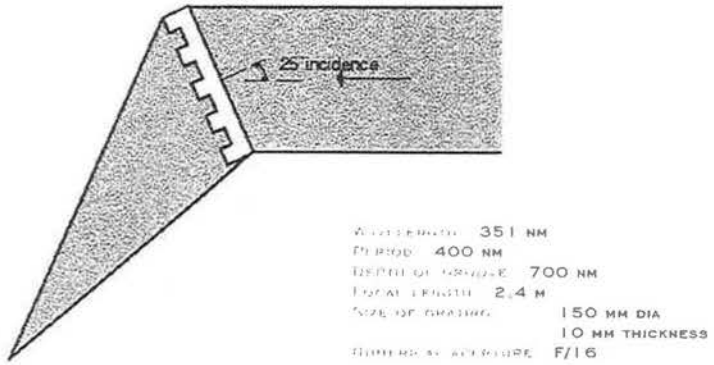

4.2. PERFORMANCES OF THE GRATING PRODUCED

4.2.1. IMAGE QUALITY

We have measured the diameter of the first black ring and found 13 microns. This is in good accordance with the theoretical image size. It demonstrates that this focusing diffractive element is well stigmatic at the wavelength of use.

SPOT IMAGE PHOTOGRAPHY

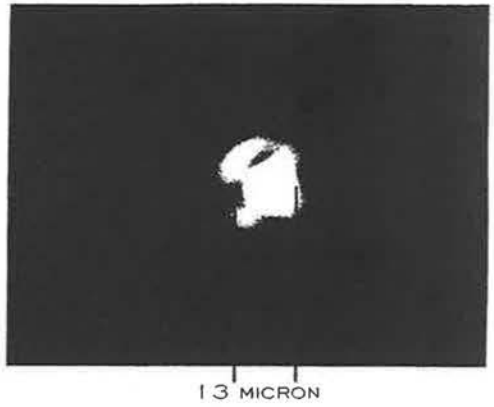

4.2.2. EFFICIENCY

We have checked the groove profile at each step of the production = holographic mask and laminar profile after ion-etching. We have used a scanning tunneling microscope for measuring the holographic mask and an AFM microscope for the ion etched profile. We have had also a measurement done on a sample grating similar to the large grating made with a scanning electron microscope.

MASK PROFILE

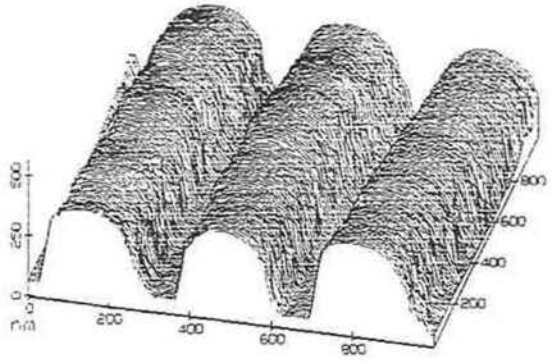

(SCANNING TUNNELING MICROSCOPE IMAGE)

DIMENSIONS ARE IN NM

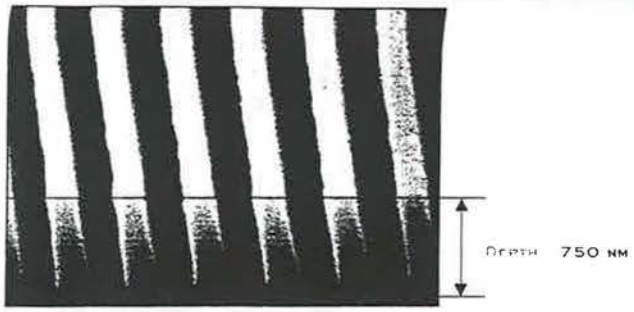

Ion-Etched Profile (scanning electron microscope image)

The measured modulation depth and duty cycle values are in accordance with the desired values.

Then we have measured efficiencies at 351 nm for the Tm polarization. Efficiency measurement is performed using a 351 nm laser beam at the nominal angle of incidence (25 degrees). These values are absolute efficiencies. The light reflection due to the reflection on the second interface are reduced to nearly 0 by using an antireflective coating.

- Order 0 3,5%
- Order - 1T 94%
- Order - 1R 1%
- Order OR 0,5%

Manufactured Lens Grating
Measured Efficiency

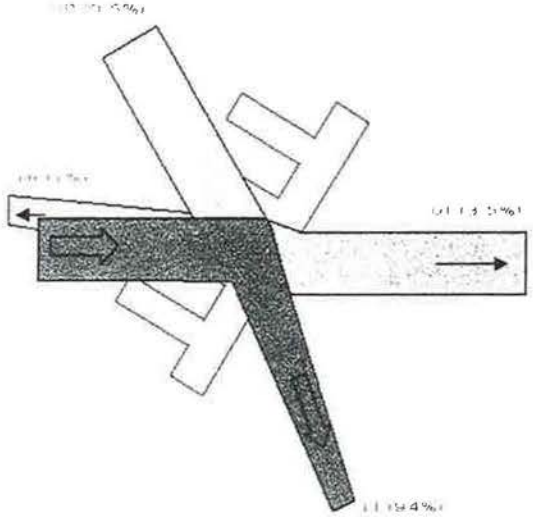

4.2.3. Damage threshold

The damaged threshold (LIDT) measurements made on sample gratings demonstrate that the diffractive structure threshold can reach similar level as the bare material threshold.

CONCLUSION

It is demonstrated that a single optical diffractive element : an ion etched focusing transmission grating, can be optimised to present similar damage threshold (LIDT) as a super polished fused silica window and performs 3 tasks :

- spectral dispersion (separation of the 3 harmonics)
- good focusing of laser beam (stigmatic image)
- sampling capabilities

We work right now to produce large dimension focusing diffraction gratings with cost effective methods.

Developments in the Fast Ignition of Conical Implosion Concept

P.A.Norreys, A.Djaoui and S.J.Rose

Plasma Physics Group.Central Laser Facility,

Rutherford Appleton Laboratory.

A.R.Bell

Blackett Laboratory, Imperial College, London.

prepared for the 3rd International Workshop on Fast Ignition of Fusion Targets, RAL Sept 21-23rd 1998

Conical Implosion Concept

- Compression energy requirements reduced by order of magnitude [100 kJ to 10kJ].
- Channel formation pulse / hole boring unnecessary

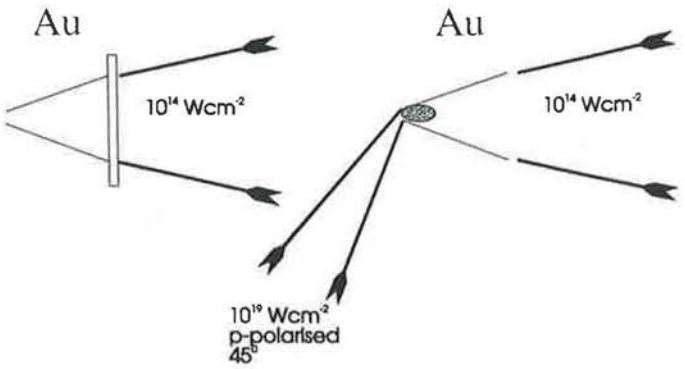

- Use 45^0 angle of incidence for heating beam [maximises conversion to hot electrons (~80%)]

Previous experiments with conical implosions - Los Alamos

R.J.Mason R.K.Fries and E.H.Farnum. Appl.Phys. Lett. 34(1) 14 (1979).

A DT filled cone of 190 μm radius capped with 13 μm thick PVA was irradiated with 160 J CO_2 laser, to compress the fuel in the exploding pusher mode. DT yields of 0, 7.4×10^4 and 2.8×10^5 DT neutrons were measured in three shots. $Y_{exp} / Y_{2d\ hydro} \sim 0.2$ were obtained.

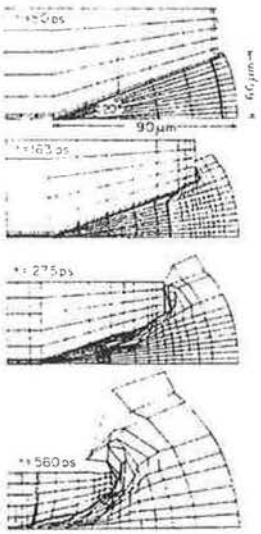

$\rho_{2d\ hydro} = 2\ gcm^{-3}$

Previous experiments with conical implosions - Lebedev

S.I.Anisimov et al. Sov. Tech. Phys. Lett. 4(4) 157 (1978).
0.2 -1 atm. DD filled cone irradiated at 1 μm, with a 54J / 22 nsec / $1.5 \times 10^{11}\ Wcm^{-2}$ laser pulse.

Their conclusions:

$Y_n = 4 \times 10^4$ were measured which were consistent with hydro estimates.
Thermal conduction losses in liner small.

Conical Guided Shock Compression

- Potentially, higher densities and ρR can be reached with convergent geometry and pulse shaping.

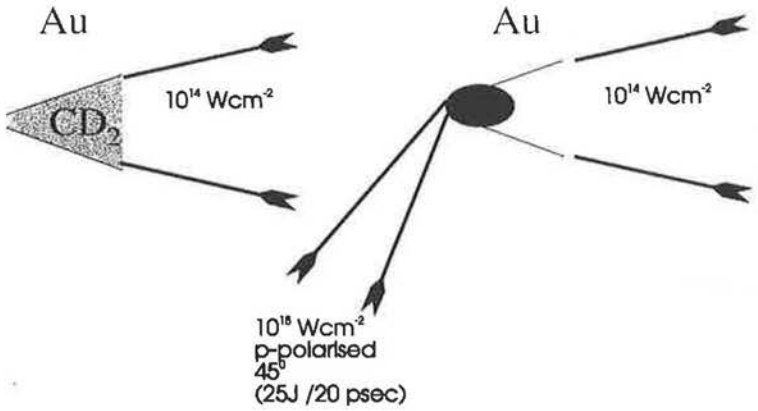

Simple estimate of neutron yield from compressed CDT plasma

If 25 J of CPA laser energy is transferred to electrons, then the temperature of the compressed material will raised to 2.5keV (neglecting thermal conduction into Au material). Energy out = f_b (burn up fraction) x E_{max} (maximum from shell).

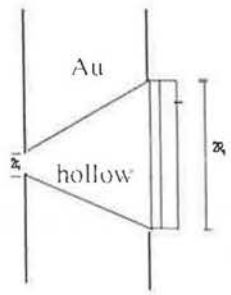

$$\rho_f = \frac{3\rho_{ini}.R_0^2.l}{4.r_f^3} \qquad (\rho R)_f = \frac{3.\rho_{ini}.R_0^2 l}{4r_f^2}$$

$$f_b \approx 5.6\times10^3(\rho R)\exp(-19.9/T_{keV}^{1/3})/T_{keV}^{7/6}$$

For a CDT shell with
l = 4 μm, R_0 = 200μm and r_f = 20 μm,
ρ = 30 gcm^{-3} E_{max} = 7758J, and
ρR = 3.0x10^{-2} gcm^{-2}

Assume that the reaction rate will be reduced in proportion to the density of carbon ions, deuterons and tritons compared with a pure DT plasma, then the total ρR for CDT will be 4/9 that of DT. *f_b ~ 2 x 10^{-6} and Y_n ~ 8.10^9 DT neutrons.*

1-D MEDUSA simulations of guided shock compression using VULCAN parameters

Spherical symmetry used.
Cone length = 150 μm
Large hole diameter = 250 μm

Simulations stopped as the shocks coalesce at the centre of the CD sphere (no reflections).

Pulse shaping give $\rho R \sim 30 mgcm^{-2}$.

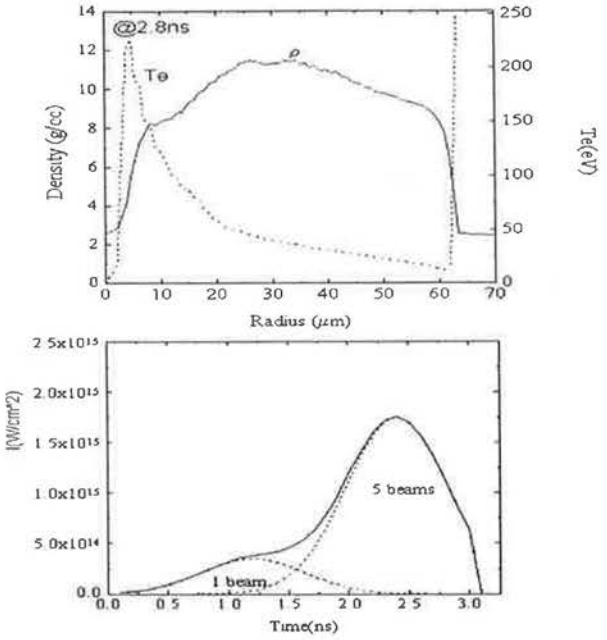

Further requirements needed for a successful experimental campaign

1. Highly uniform CDT foils to prevent hydrodynamic instability growth {highly uniform CH foils have already manufactured at RAL for R-T growth studies}

2. Suitable choice of high density guide material to prevent x-ray preheating of material during the compression.

3. Smooth cone for guiding either imploding material or shock convergence {excimer laser ablation followed by electroplating of Au; micromachining at RAL}

Excimer Laser Ablation / Au Electro-Plating Make Poor Quality Cones

Front entrance of cone

Apex of cone

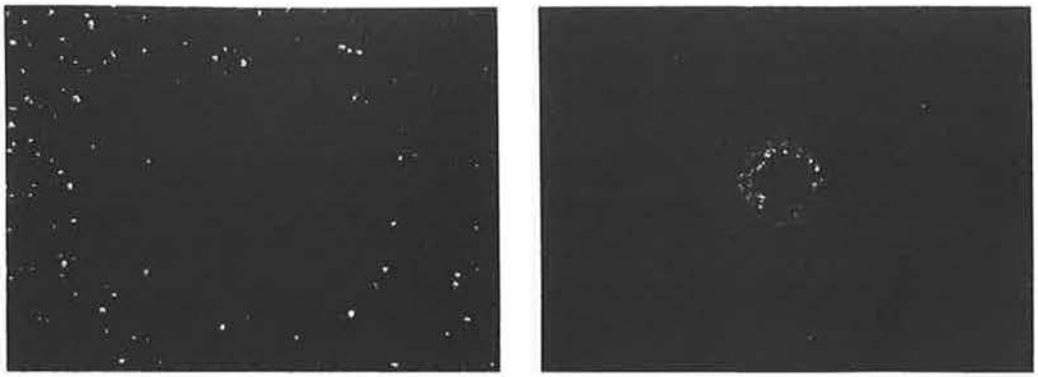

200µm

Micro-machining of conical targets in progress at RAL.

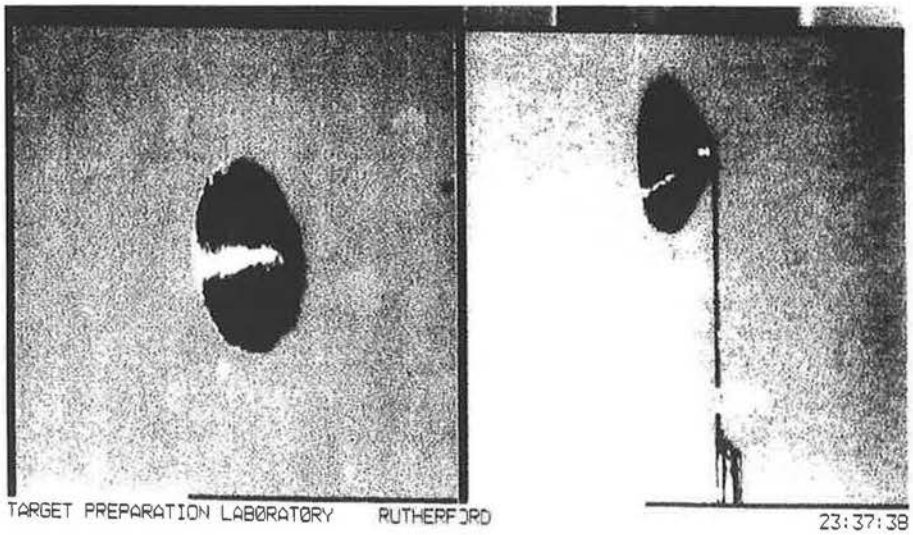

Summary

The study of guided conical compression promises a route to overcome some of the problems associated with the Fast Ignitor, but provides its own technological challenges.

The Rutherford Appleton Laboratory is vigourously pursuing this route and we hope to be able to present the first experimental results by the next Fast Ignitor Workshop.

γ-rays and fast electrons from high intensity laser-plasma interactions using ATLAS laser

C. Gahn[1], G. D. Tsakiris[1], G. Pretzler[1], P. Thirolf[2], D. Habs[2], and K. J. Witte[1]

further contributions by

PART I: A. Saemann[1], D. Gassmann[2], T. Schätz[2], U. Schramm[2]

PART II: A.Pukhov[1], J. Meyer-Ter-Vehn[1]

[1]*Max-Planck-Institut für Quantenoptik, Garching, Germany*

[2]*Sektion Physik, LMU München, Germany*

Outline

PART I

generation of MeV γ-rays from solid targets at 10 Hz

measurement of γ-rays and determination of the fast electron temperature

PART II

generation of fast electrons from gas-jet targets

measurement of the electron beam divergence and the energy spectrum

MPQ

Fast electrons and MeV γ-rays

C. Gahn et al.

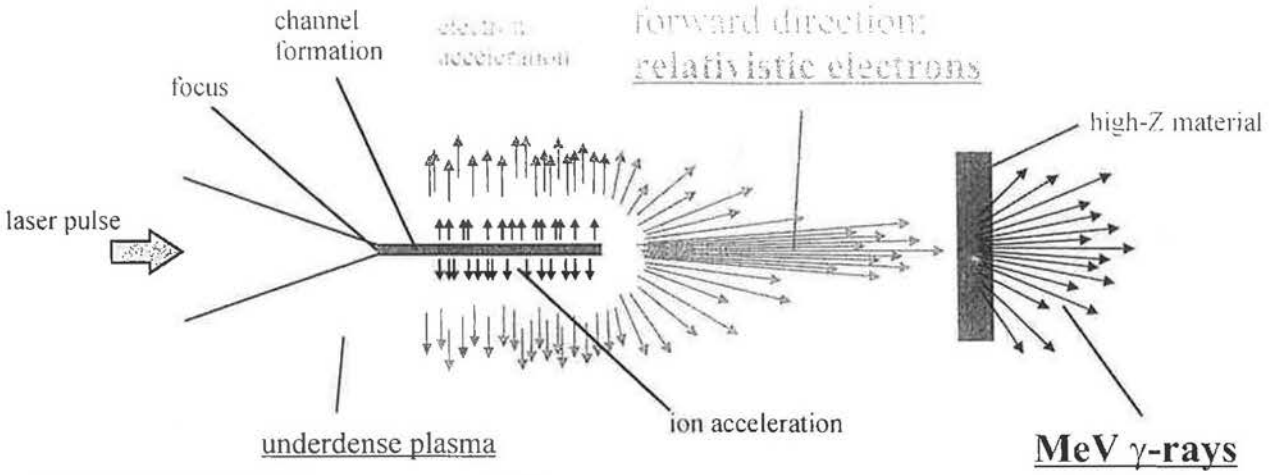

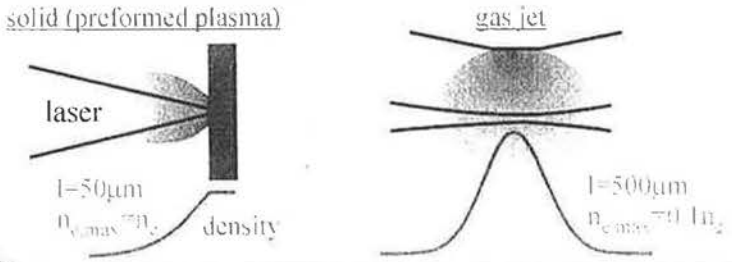

MPQ

Experimental setup (MeV γ-rays)

C. Gahn et al.

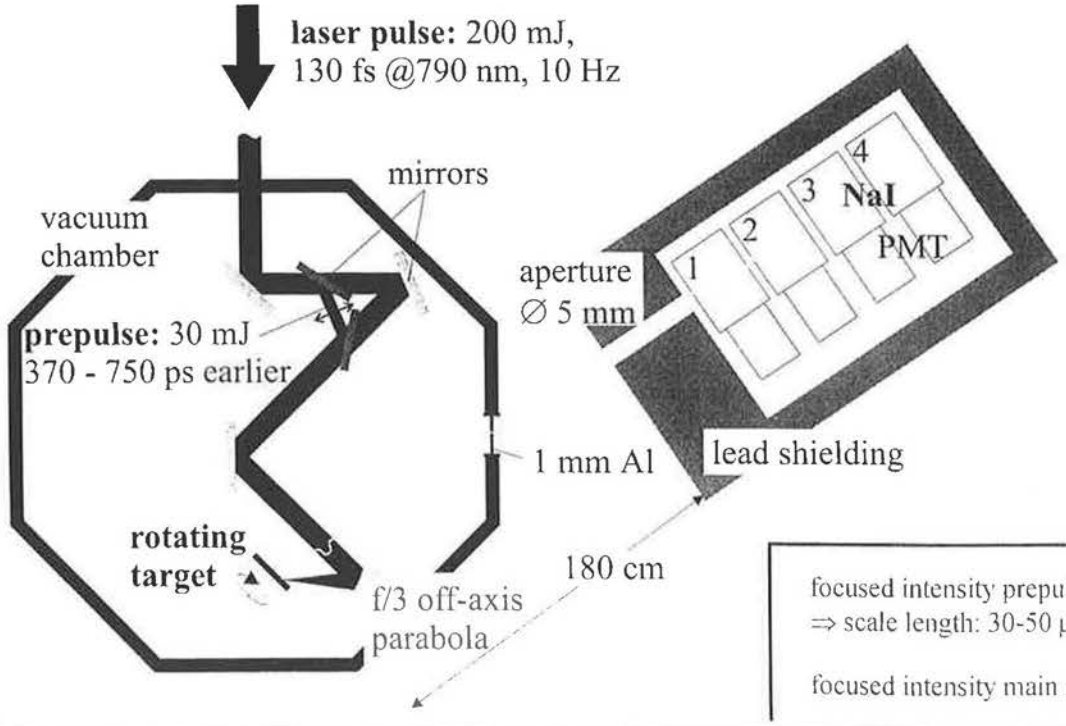

focused intensity prepulse: 10^{16} W/cm^2
⇒ scale length: 30-50 µm

focused intensity main pulse: 10^{18} W/cm^2

MeV γ-ray yield and electron temperature

C. Gahn et al.

pusle height spectrum (NaI 2)

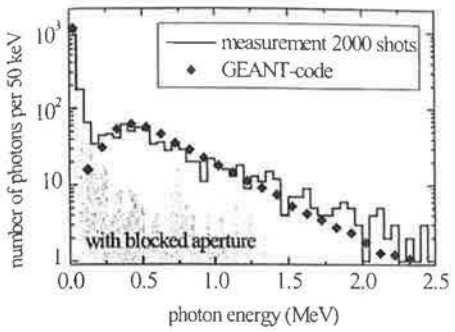

mean deposited energy

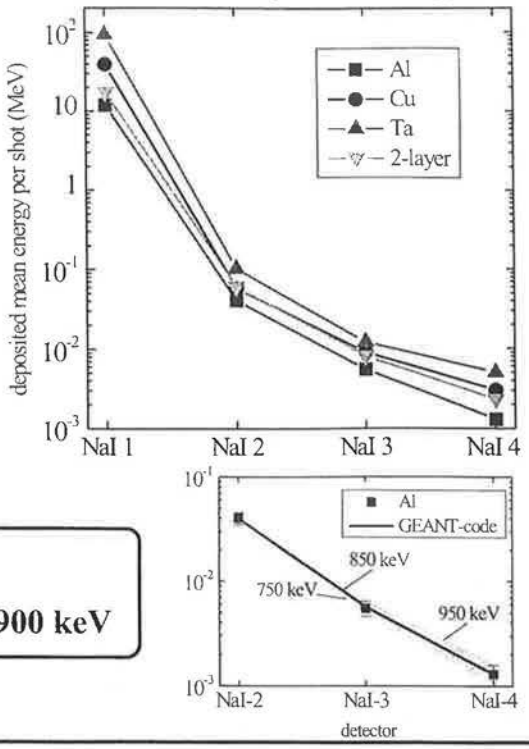

- γ-photons up to **2.5 MeV**
- GEANT-code ⇒ electron temperature $T_e \approx$ **900 keV**

Z-dependence of MeV-γ and fast electron yield

C. Gahn et al.

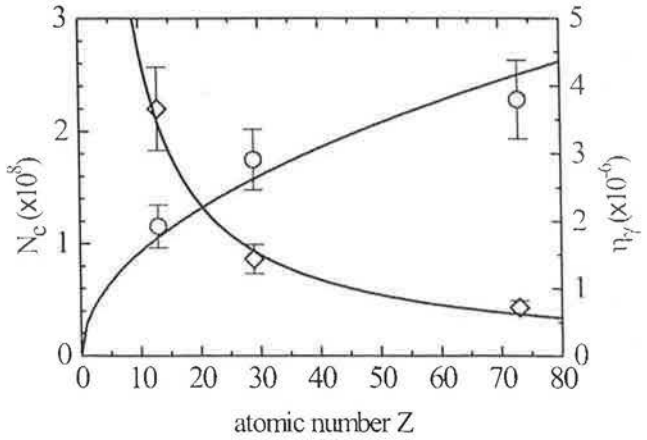

- 2.2x10^8 fast electrons (Al-target)
- $N_e \propto 1/Z$

- 4x10^7 MeV-photons (Ta-target)
  ⇒ laser energy into γ-ray conversion efficiency $\eta = 4\text{x}10^{-6}$
- $\eta \propto Z^{1.2}$

MPQ

Experimental setup (fast electron beam)

C. Gahn et al.

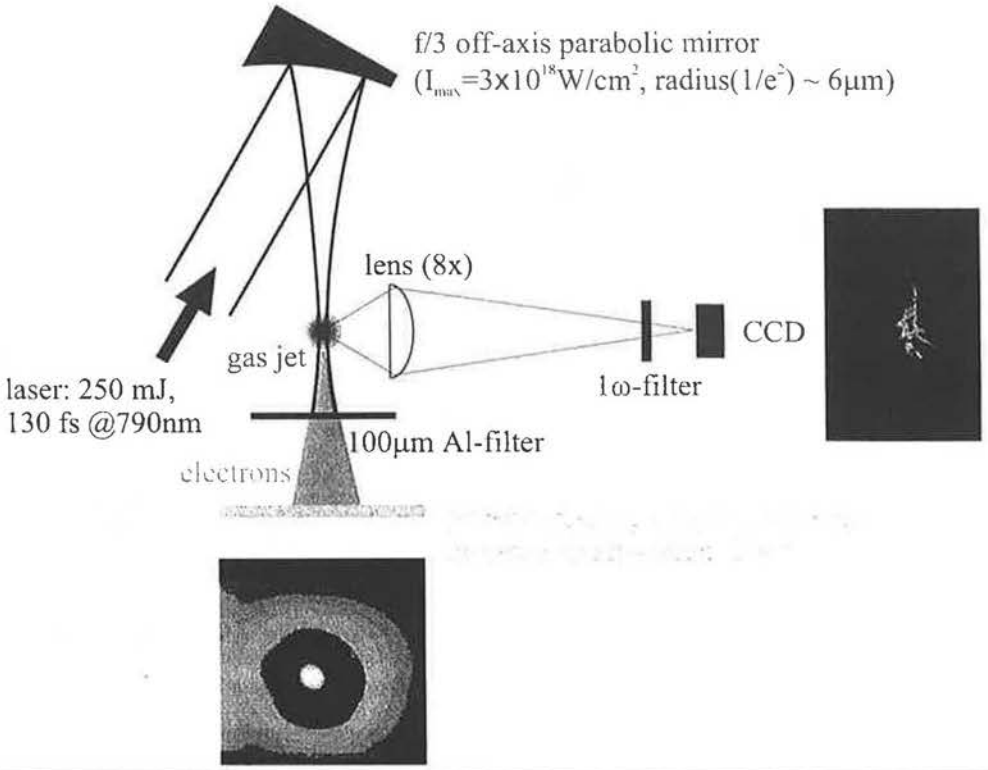

MPQ

Evidence of electrons

C. Gahn et al.

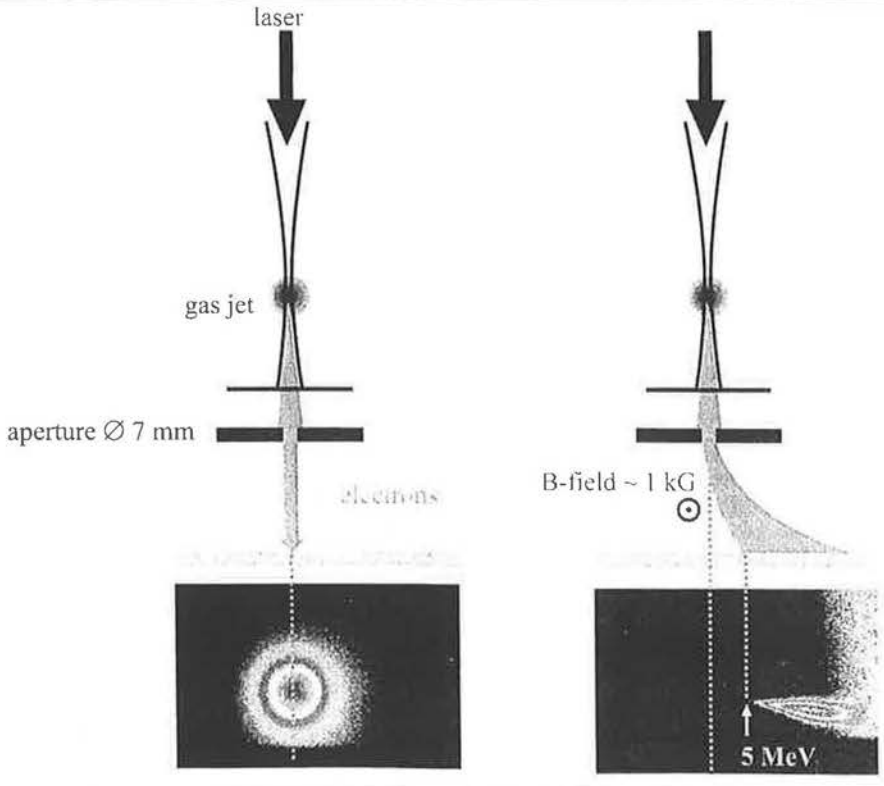

Channel and electron beam images

C. Gahn et al.

sidescattered image at 1ω | **electron beam image** | **electron beam divergence**

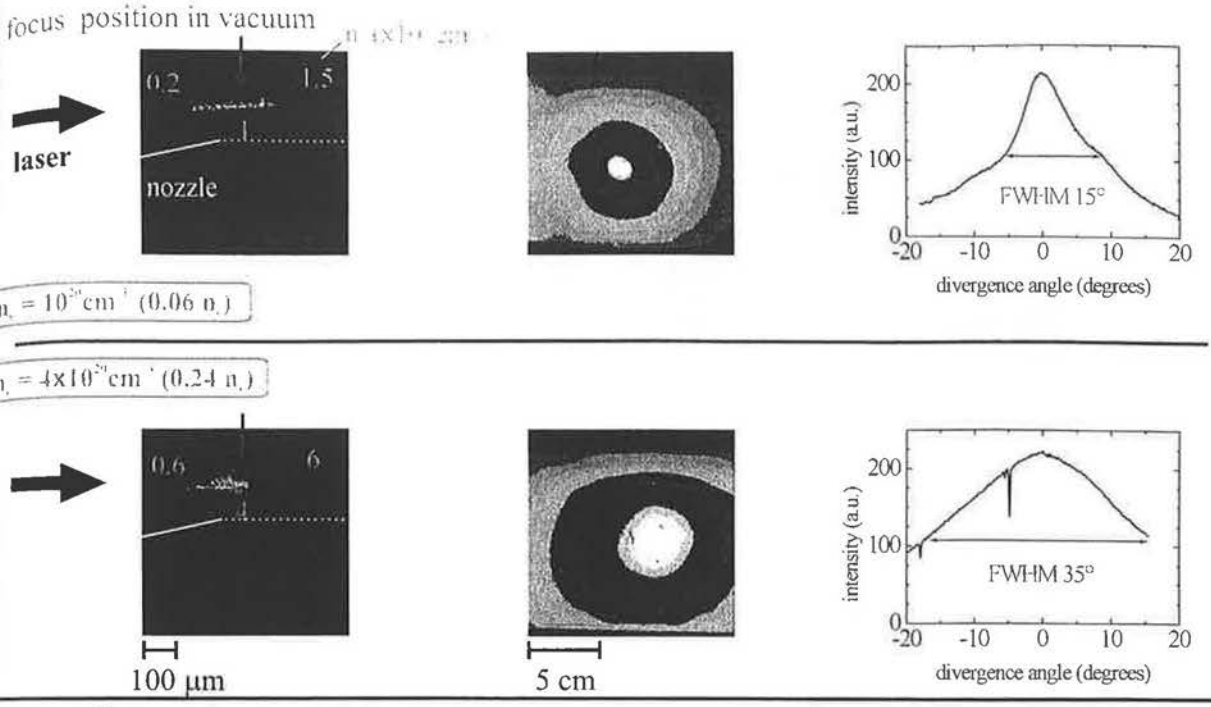

Experimental setup (fast electron energy spectrum)

C. Gahn et al.

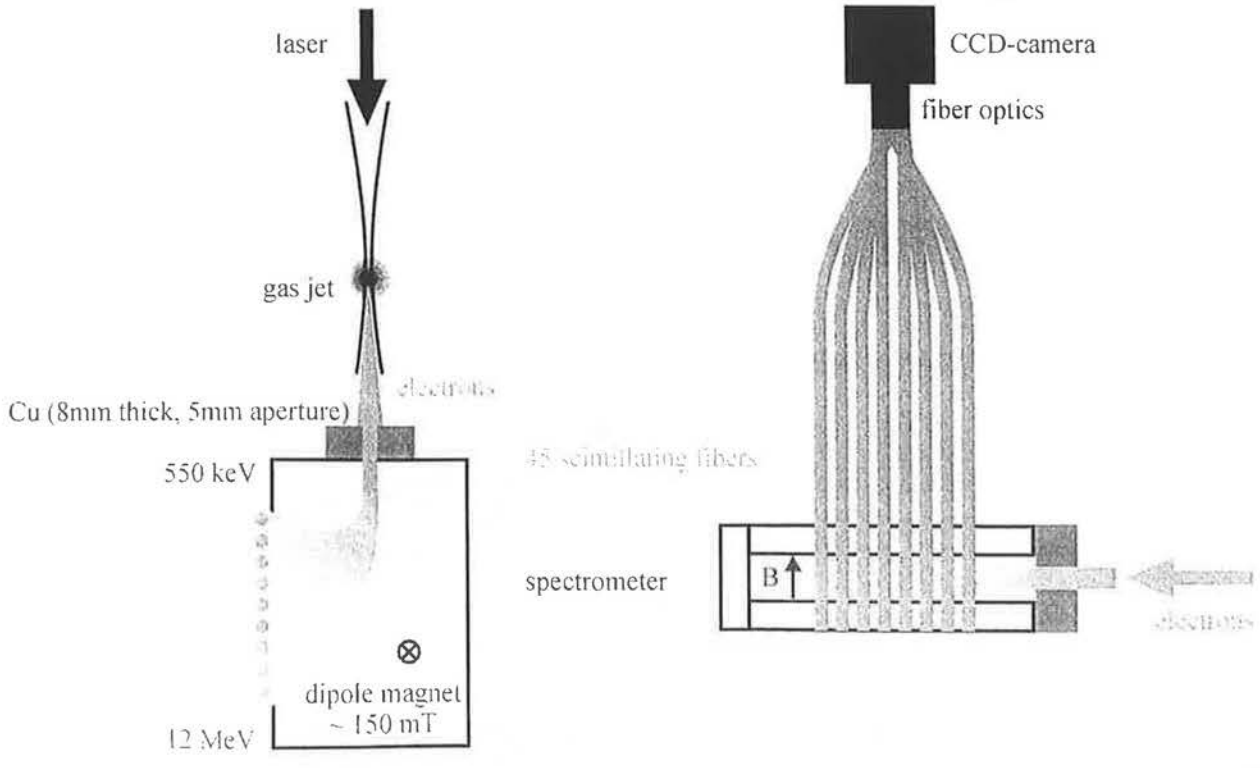

3rd Fast Ignition Workshop
RAL, Chilton 21-23 September 1998

Combined PIC and MC Simulations of Supra-thermal Electron Energy Deposition

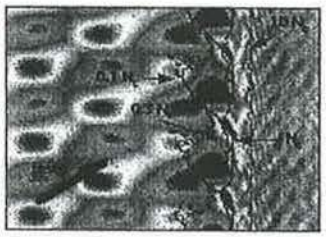

Jean-Claude Gauthier

Laboratoire pour l'Utilisation des Lasers Intenses

Centre National de la Recherche Scientifique

Ecole Polytechnique

Palaiseau (France)

Collaboration

- Th Schlegel LULI
- J.-P. Geindre LULI
- P. Audebert LULI
- S. Bastiani LULI
- L. Gremillet LULI
- G. Bonnaud CEA
- E. Lefebvre CEA
- J. Delettrez LLE
- G. Laval CPHT
- A. Héron CPHT
- J.-C. Adam CPHT
- P. Gibbon Jena

CENTRE NATIONAL DE LA RECHERCHE SCIENTIFIQUE

Outline

Purpose

- Otimization of hot electron production for Kα and bremsstrahlung X-ray source applications
- "Clean" conditions, control of the gradient scale length

Experiments

- Angularly-resolved electron emission
- Multi-layered targets

Numerical tools

- 1D 1/2 and 2D PIC simulations
- Monte Carlo simulations

Experimental layout

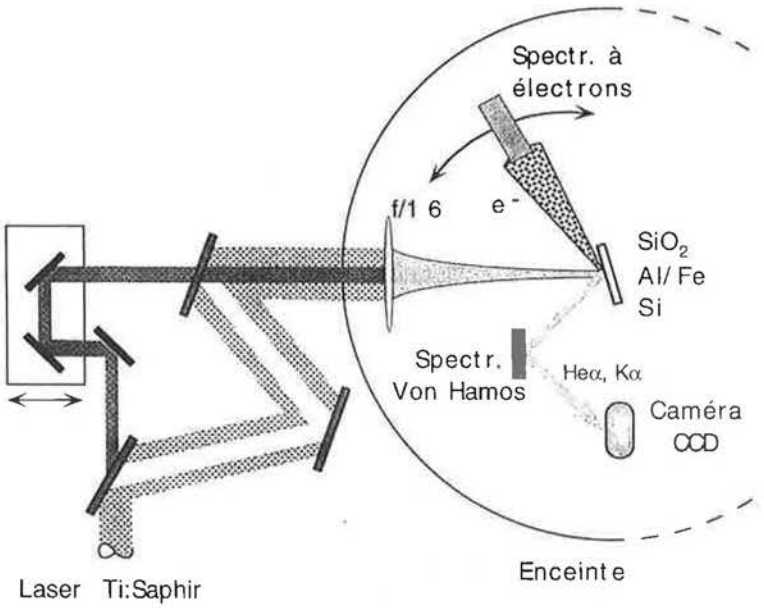

electron spectrometer:
6 diodes; 20 keV-200 keV
Filters: 1.6 µm Al

X-ray spectrometer:
PET (2d = 8.742 Å)
ADP (2d = 10.648 Å)
Quartz (2d = 2.451 Å)

0.8 µm, 50 mJ
120 fs, 10 Hz

$I_{pre} = 4 \cdot 10^{14}$ W/cm²
$I_{post} = 4 \cdot 10^{16}$ W/cm²

Total electron energy of front target electrons

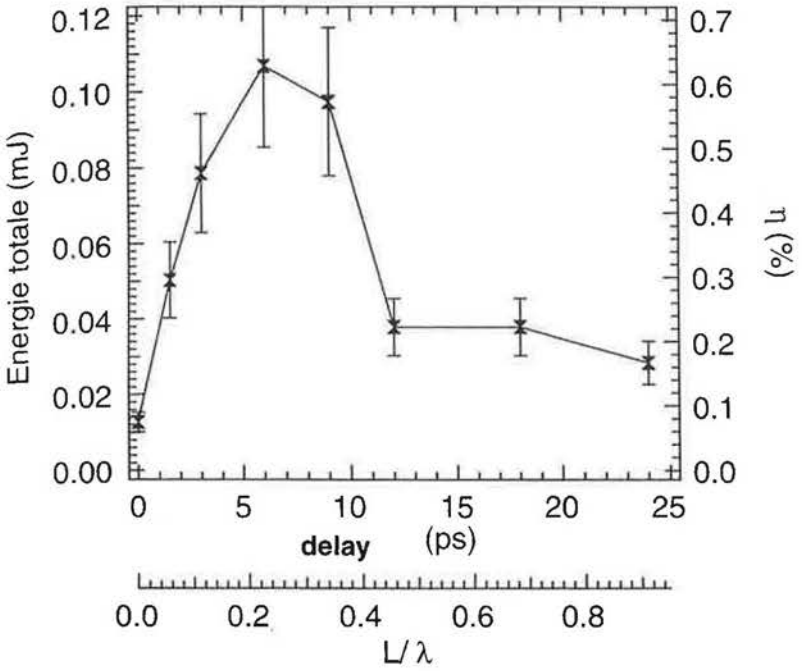

L/λ ≈ 0.25

optimized electron production of energies 20 < E < 200keV

Kα multi-layer target results

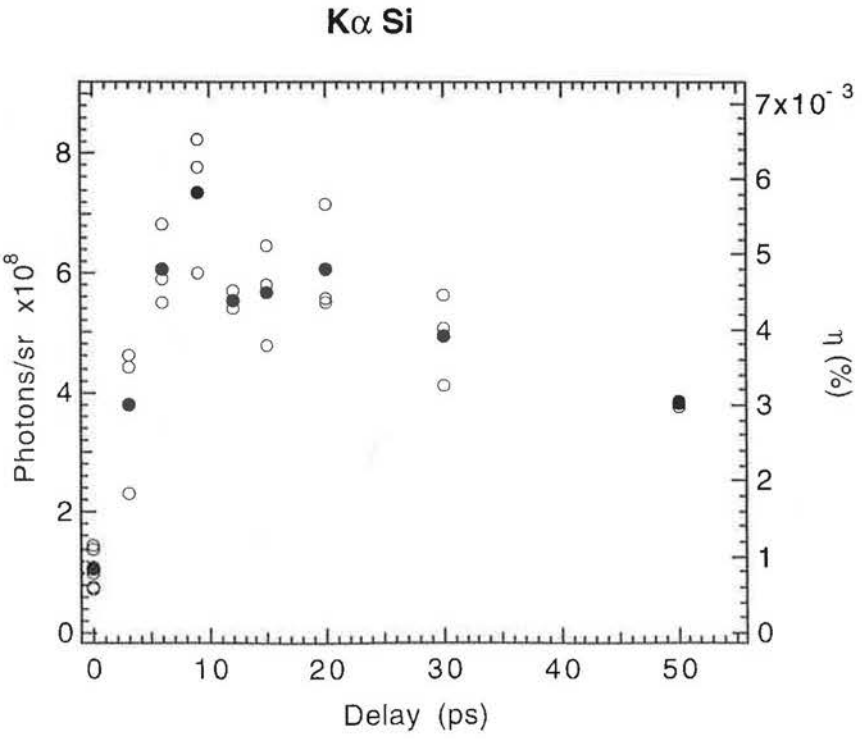

Measurement of electron distr. functions

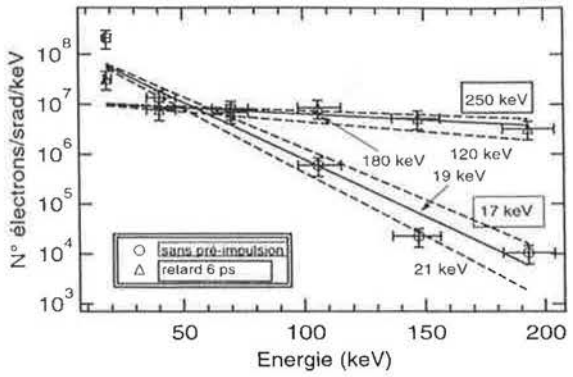

Principle of the simulations

PIC code: 1-Dim.

MonteCarlo code: 3-Dim.

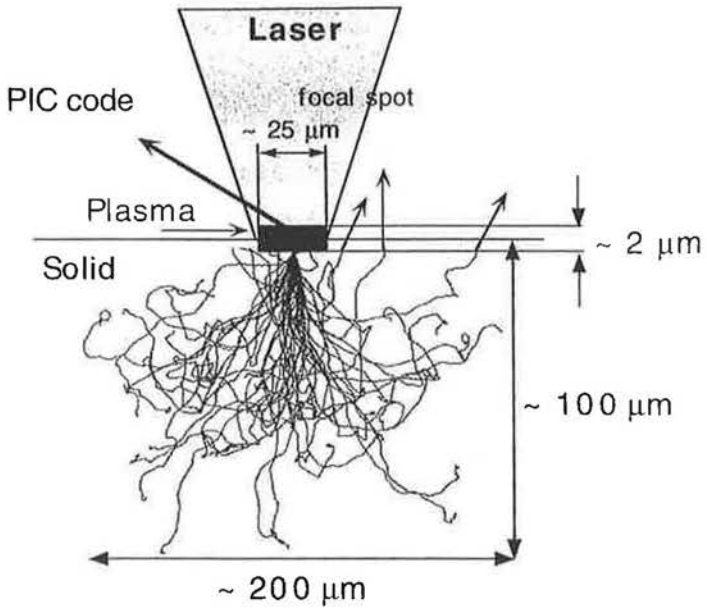

Backscattering coeff. ≈ 13% for E = 10 - 200 keV

2D simulation with EMI2D2V

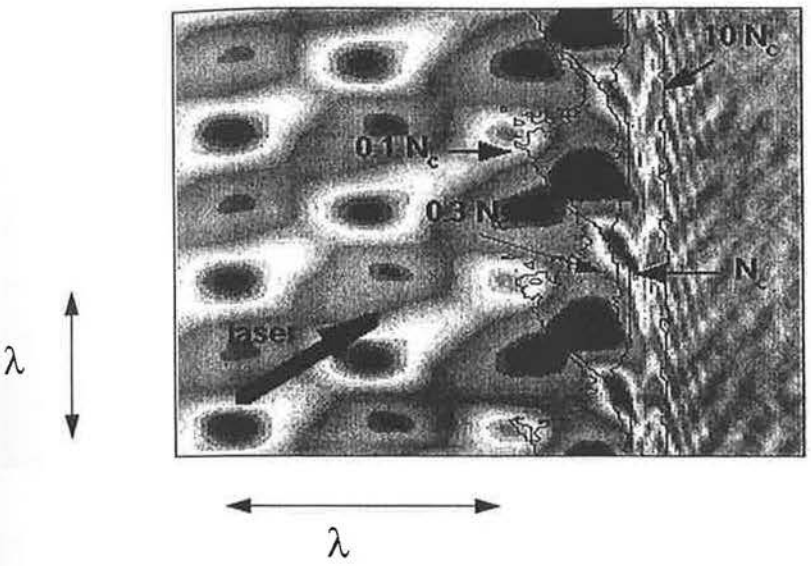

plane wave at laser peak, oblique incidence

Particle - in - cell methods

Simplification of the self-consistent field computation

boost - frame transformation

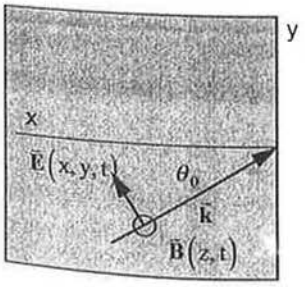

$$v_B = c \sin\theta_0 \quad \rightarrow \quad \gamma_B = \left[1 - \left(\frac{v_B}{c}\right)^2\right]^{-1/2} = c \sec\theta_0$$

$$k_y = k_0 \sin\theta_0 \quad \rightarrow \quad \omega' = \gamma_B \left(\omega_0 - v_B k_y\right) = \omega_0 \cos\theta_0$$

$$k_y' = \gamma_B \left(k_y - \frac{v_B}{c^2}\omega_0\right) = 0$$

units in the moving frame

$$u'_\omega = \omega'_0 = \omega_0 / \gamma_B = u_\omega / \gamma_B \qquad u'_t = 1/\omega'_0 = \gamma_B / \omega_0 = u_t \gamma_B$$

$$u'_x = c/\omega'_0 = u_x \gamma_B \qquad u'_E = c\, u'_B = c\, m_e \omega'_0 / e = u_E / \gamma_B$$

$$u'_p = m_e c = u_p \qquad u'_\mathcal{E} = m_e c^2 = u_\mathcal{E} \qquad u'_n = \frac{m_e \omega'^2_0}{4\pi e^2} = u_n / \gamma_B^2$$

Scalelength 0.2 - Longitudinal electric field

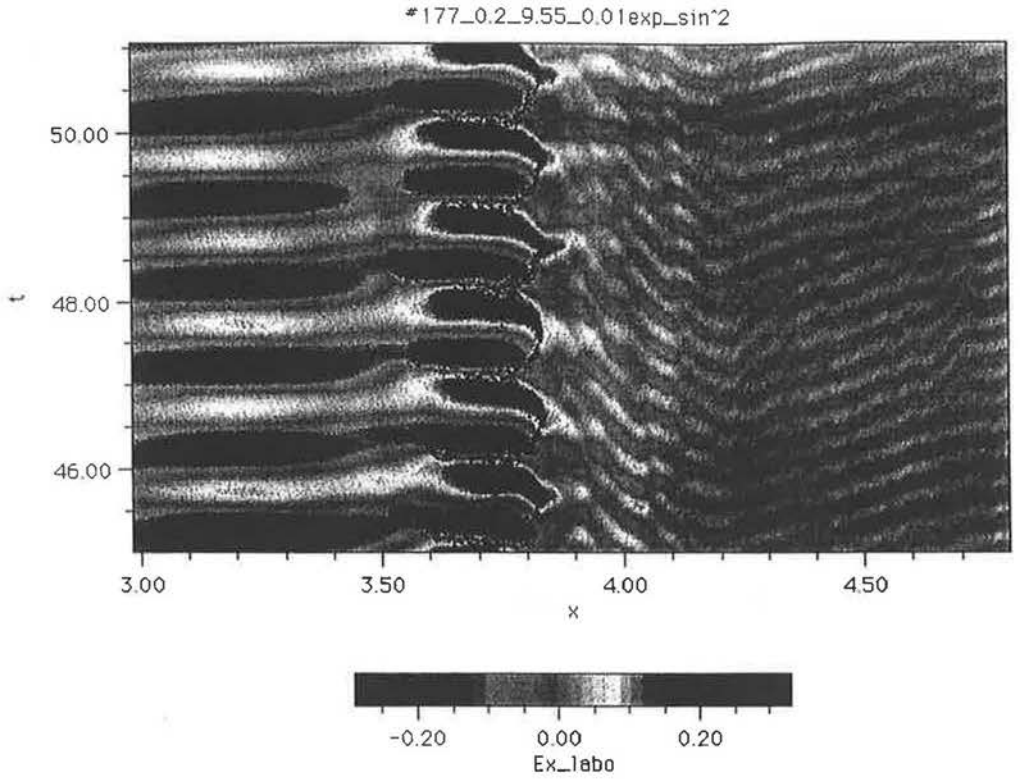

11

Absorption coefficient compared to experiment

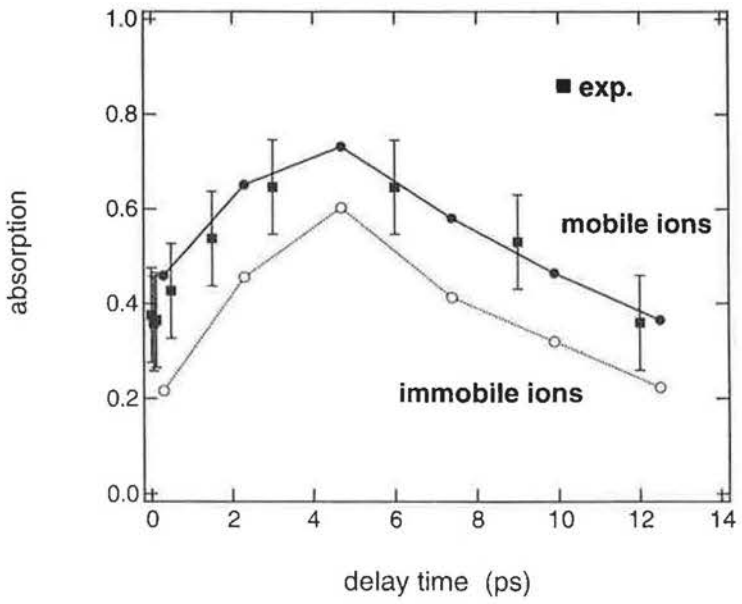

12

Electron energy distribution: mobile ions

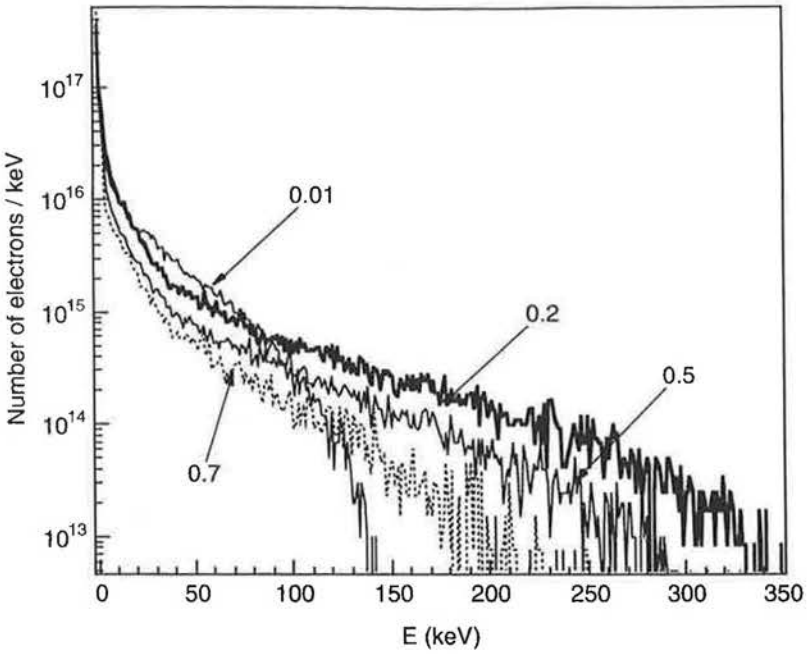

Electron energy distribution: immobile ions

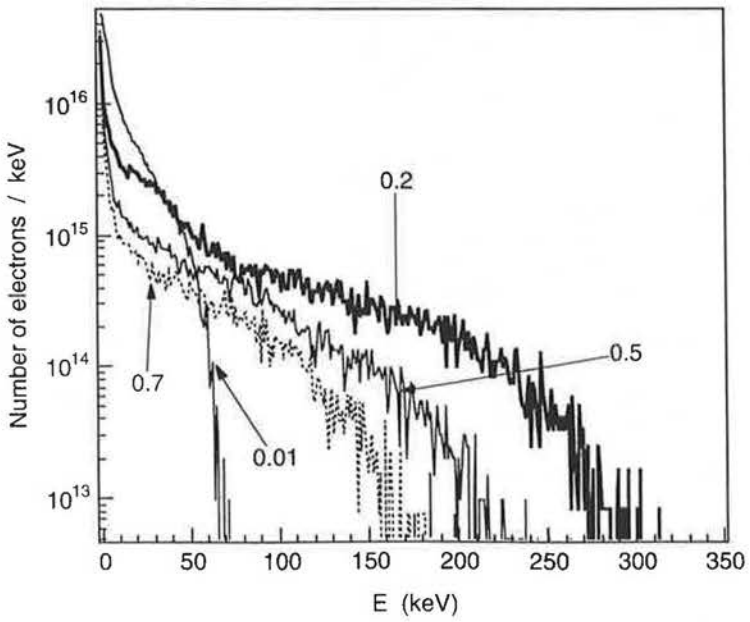

EDF from EUTERPE code

300fs pulse results at 510fs

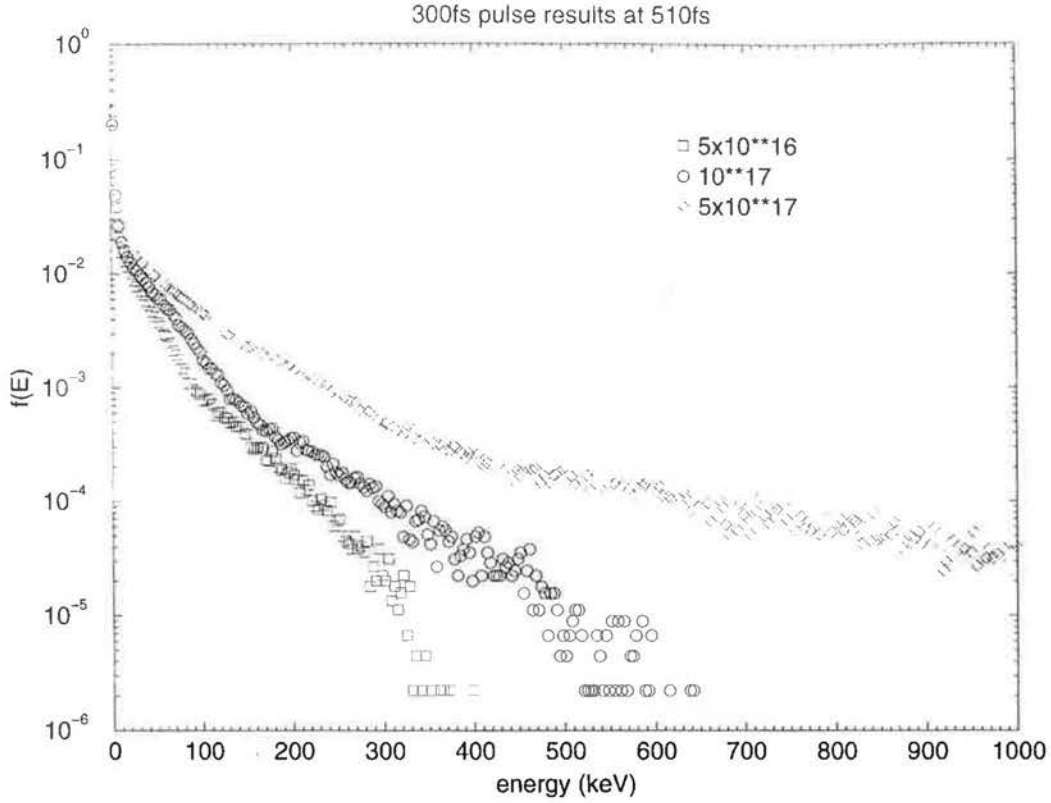

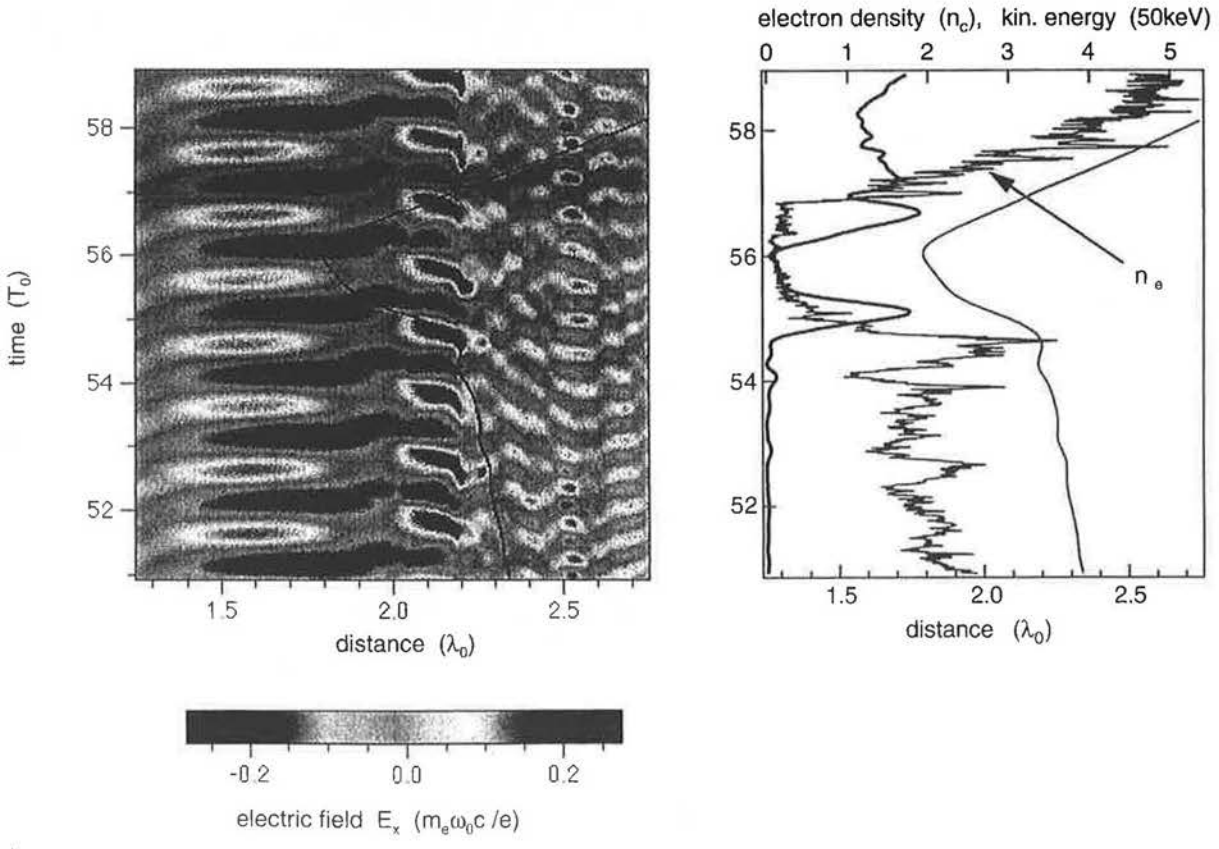

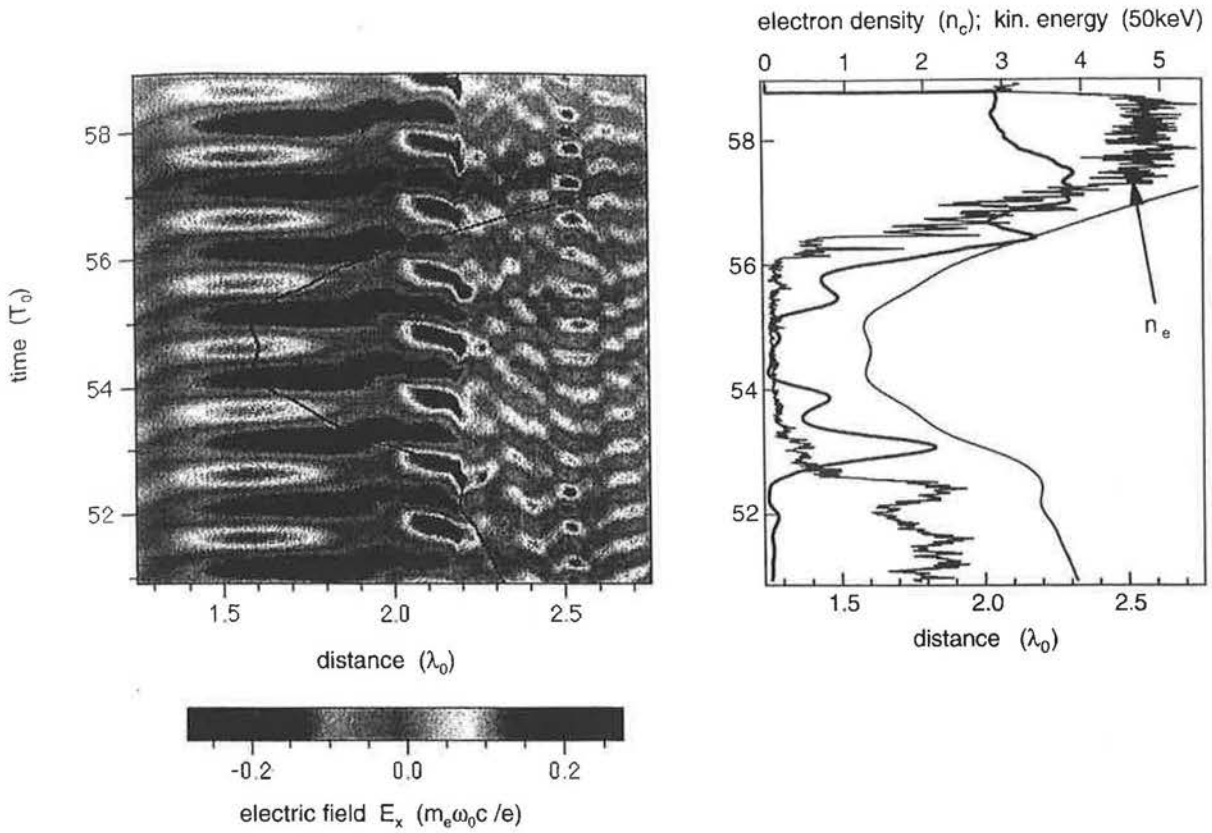

17

Hot electron temperature: comparison with expt.

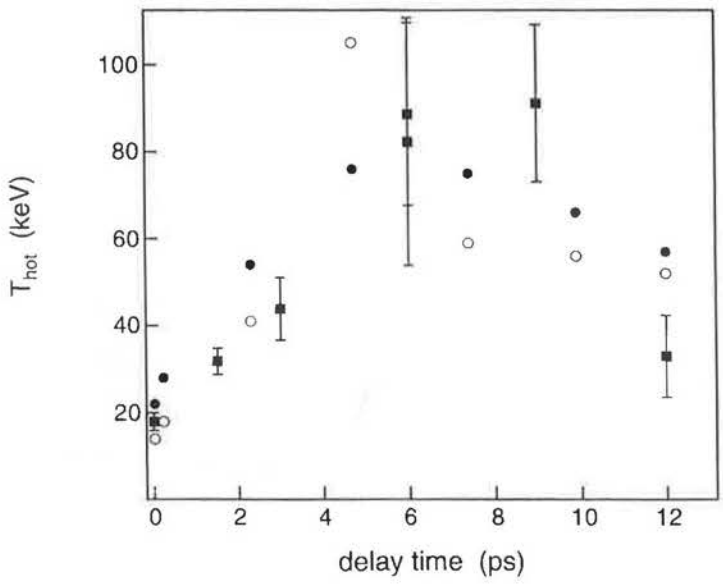

18

Monte Carlo electron transport code

- 3D geometry
- Energies from1 keV to 10 MeV
- Multilayer media, simple and compound elements
- Calculation of transmission and backscattering
- Energy and spatial distribution functions of transmitted and reflected electrons
- 1D profile of electron energy deposition and material heating
- Calculation of X K-α (isotropic) and bremsstrahlung (energy- and angularly-resolved) emission with opacity taken into account

Backscattering of fast electrons

Initial e.d.f.

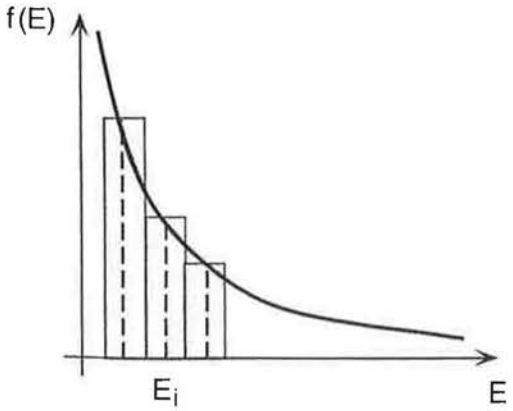

Monte Carlo code

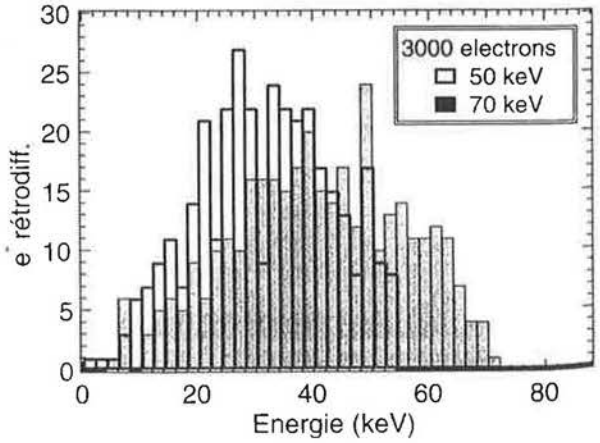

Distr. functions of backscattered electrons

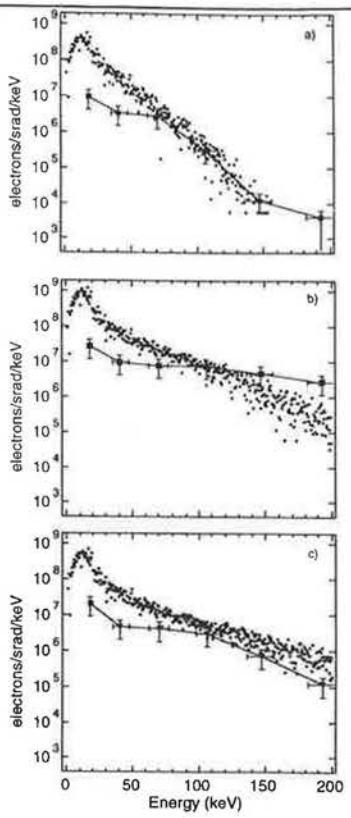

no prepulse

6ps delay

12ps delay

21

MC code results checked against ITS

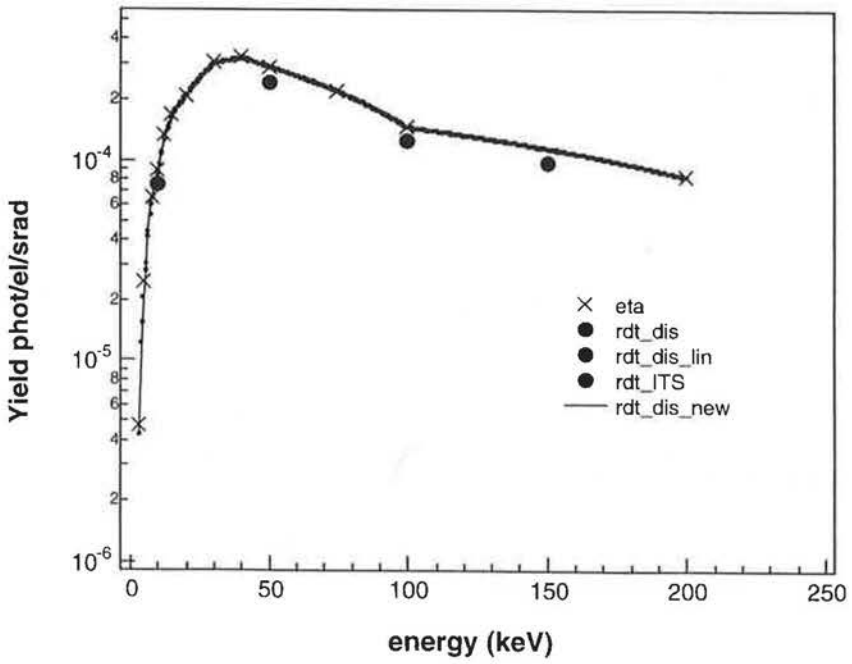

22

Measured Kα yield compared to PIC/MC simulation

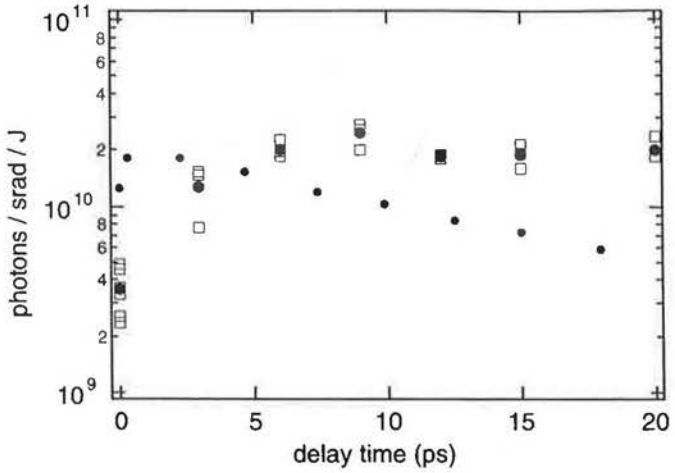

Summary and perspectives

- Optimization of scale length increases Kα yield by a factor of ~ 10,
- 1-D PIC simulations give good agreement on absorption,
- "Anomalously" high hot electron temperatures are obtained through resonance field electron acceleration,
- Studied the importance of backscattered electrons, explain the shape of the edf, and give the right hot electron temperature
- Combined PIC/MC simulations in good absolute agreement for the Kα yield

- Scale length tailoring will be modified by ponderomotive steepening at much higher intensities, studies under way,
- Need to incorporate collisions directly in the PIC simulation,
- Kα source duration measured to be < 500fs, 10^{12} photons/srad./J could be reached in the near future.

Theory and Simulation of Ultra-Intense Laser-Plasma Interactions Present in the PetaWatt Experiments at LLNL*

S. C. Wilks, B. Lasinski, A. B. Langdon, M. Key, S. Hatchett, T. Cowan, W. L. Kruer, J. Sefcik, and M. D. Perry

Lawrence Livermore National Laboratory, Livermore, CA 94550

For presentation to the Abingdon Fast Ignitor Workshop
Sept. 21, 1998

***Work performed under the auspices of the United States DoE by LLNL under contract No. W-7405-ENG-48.**

Outline

I. Introduction to Fast Ignitor

- **A. Laser-plasma emphasis.**
- **B. Main technical issues.**

II. Recent Underdense Modeling

- **A. Channel creation /rel. & pond. filamentation issues.**
- **B. Beam propagation issues (SRS/sidescatter, break-up.)**
- **C. High energy electrons near critical.**

III. Recent Overdense Modeling

- **A. Absorption at critical surface.**
- **B. Generation of hot electrons: T_{hot} and f_{hot}?**
- **C. Channeling: straight or bending?**

IV. Conclusions and Summary

The suprathermal electron range is comparable to an α particle range for laser intensities of interest

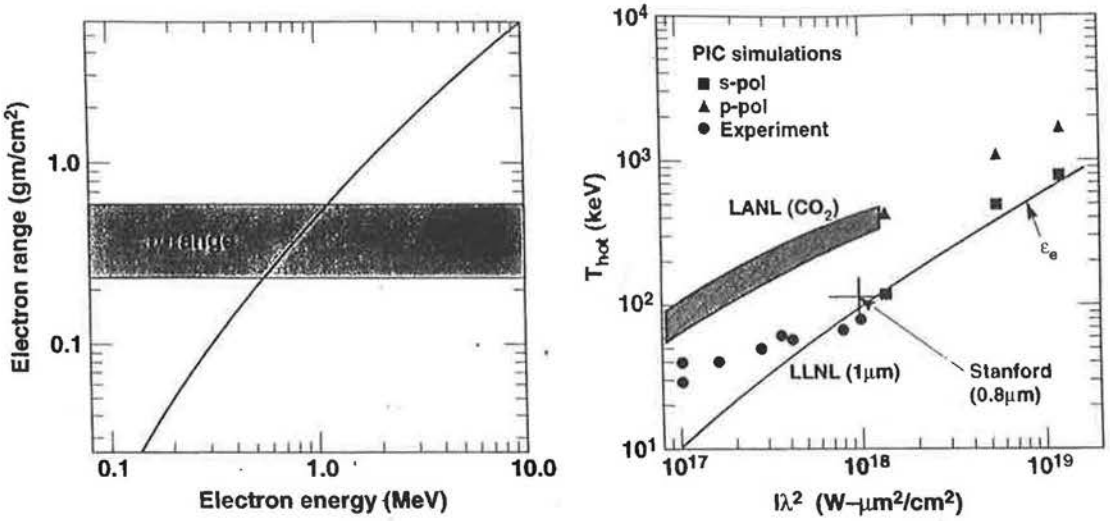

The electron range is also set by the self-generated electric and magnetic fields

50-02-1093-3689B

3

PIC simulations were critical in determining estimate for T_{hot}.

$I\lambda^2=10^{19}$ W/cm²

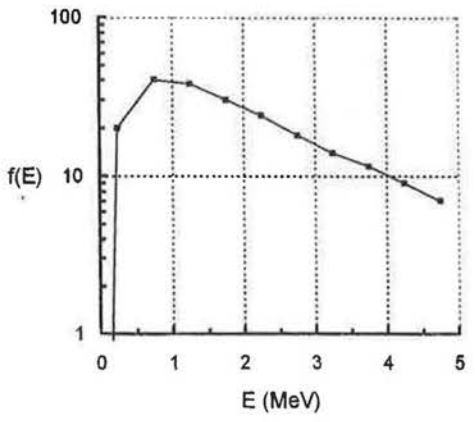

T_{hot} as function of laser intensity

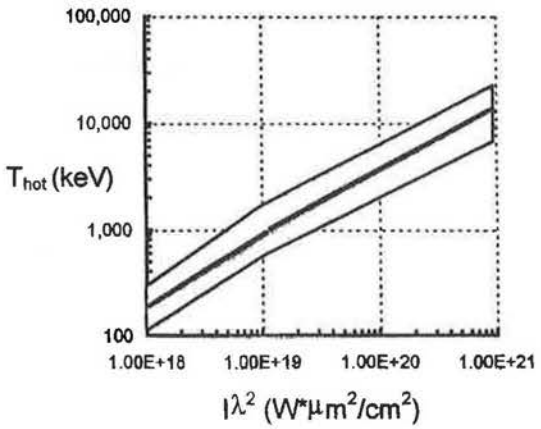

- We use this electron distribution as input for both ITS and Lasnex.

High energy (>10 MeV) electrons are readily achived from gold targets even at relatively low laser irradiance (~ 1.5 x 10^{18} W/cm^2)

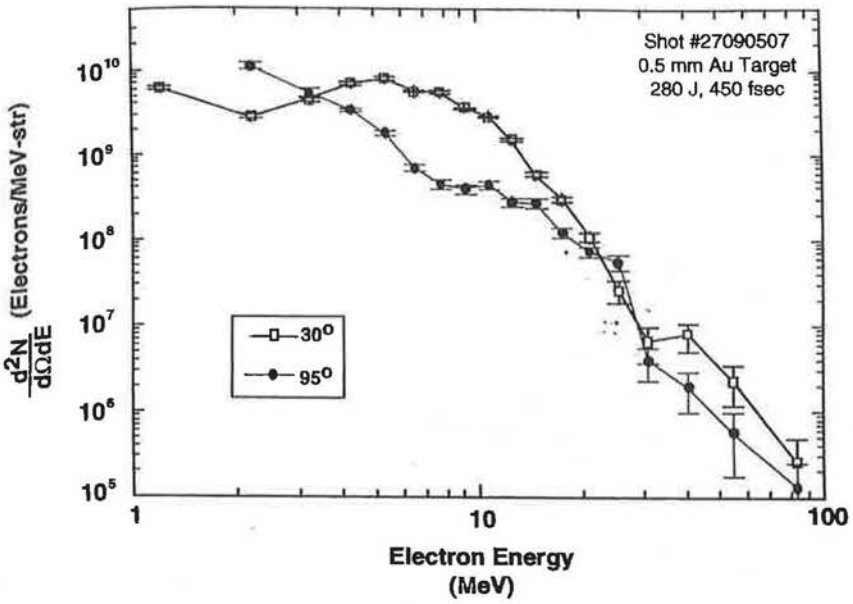

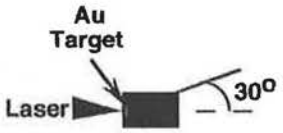

5

2-D PIC simulations of the underdense laser-plasma interaction show that eneries higher than U_{pond} can be produced.

[redacted]

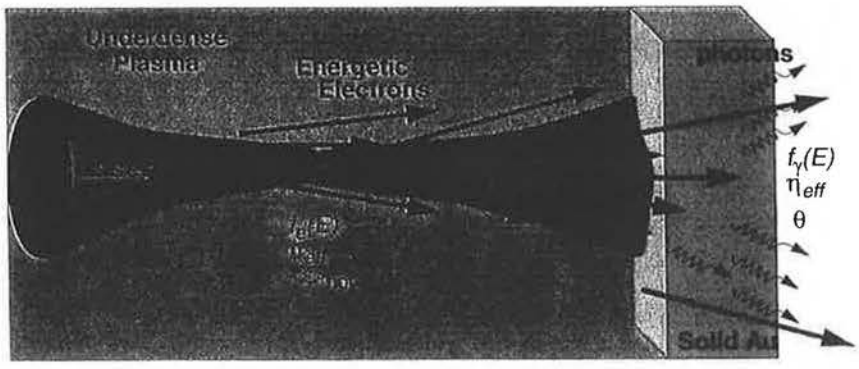

Typical ponderomotive scaling predicts T_{hot} ~ 2 MeV. However slope temperature measured from simulations gives T_{hot} ~ 7 MeV for an intensity 10^{20} W/cm^2, agreeing with experimental electron spectrometer data.

scw 06/07/98

6

What mechanisms could explain 10-100 MeV electron energies in these interactions?

Lawson-Woodward Theorem :

No net energy transfer from EM wave to electrons possible if:

1. the laser fields are in vacuum.
2. the electron is relativistic.
3. no static E or B fields are present.
4. the region of interaction is infinite
5. Nonlinear forces (pond.) are absent.

However, we are violating 1,2,3,4, and 5!

Laser focus: Intensity contours

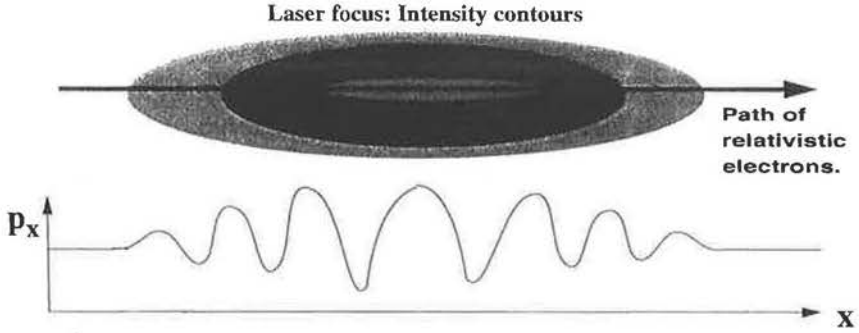

A focused TEM laser beam,has an E_x field, as well as vxB for acceleration.

Contours of B_z | Contours of E_x

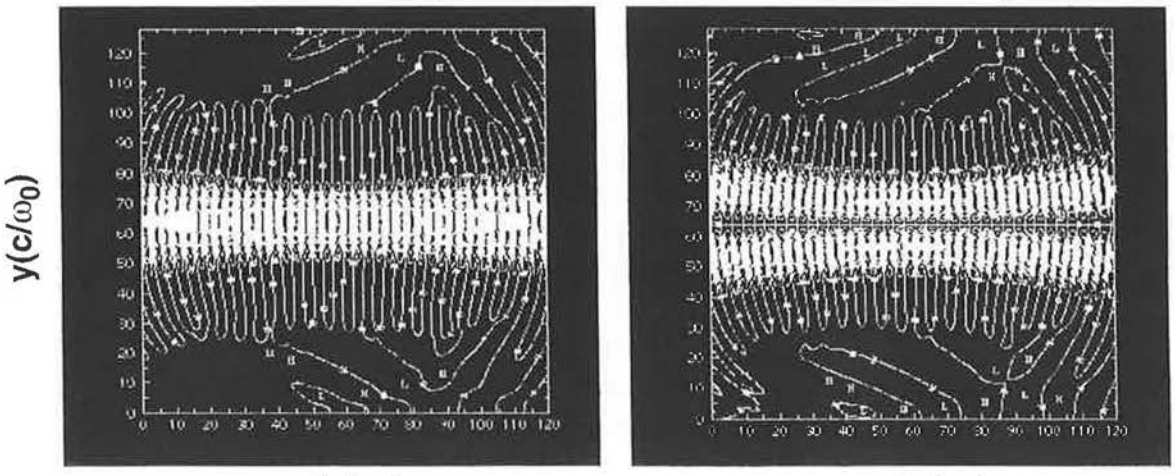

It is possible that this electrostatic field can also accelerate electrons near the critical density, leading to a "super-hot" distribution.

E_x still present in presence of plasma, similar to E_y still present: if electrons get trapped in this E_x, they can be accelerated to very high energies.

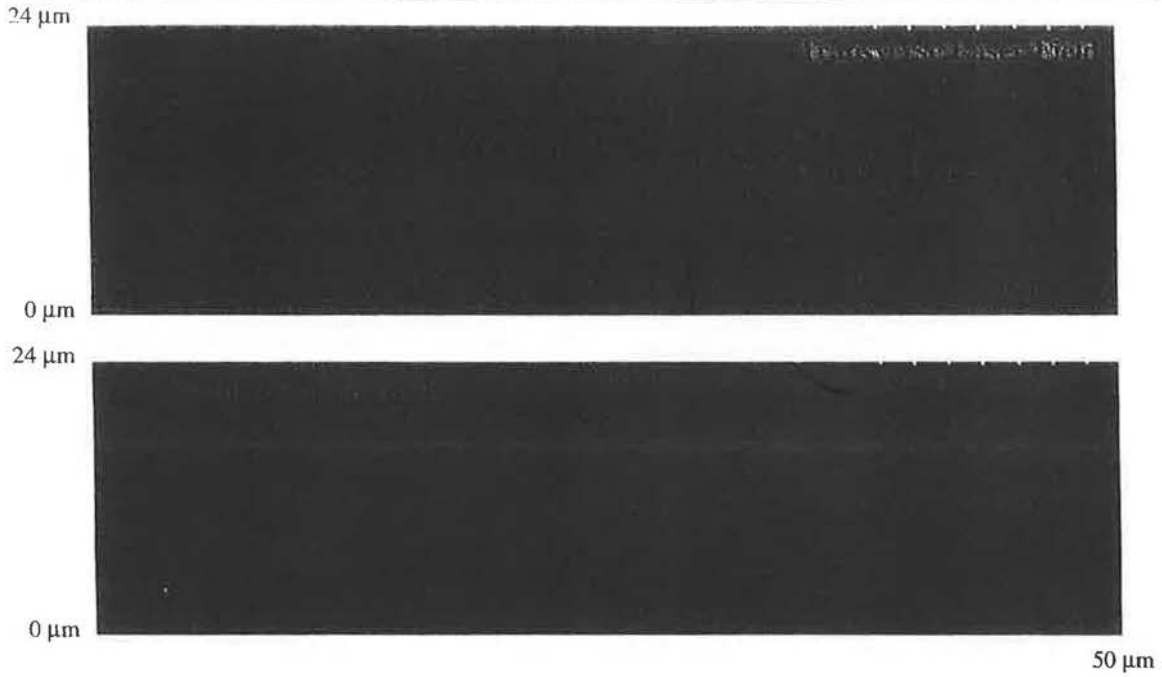

scw/09/14/96

Thus, we are essentially doing a modified, foil-terminated, free wave accelerator experiment on PetaWatt!

Transverse and longitudinal E-fields of focused laser pulse in vacuum.

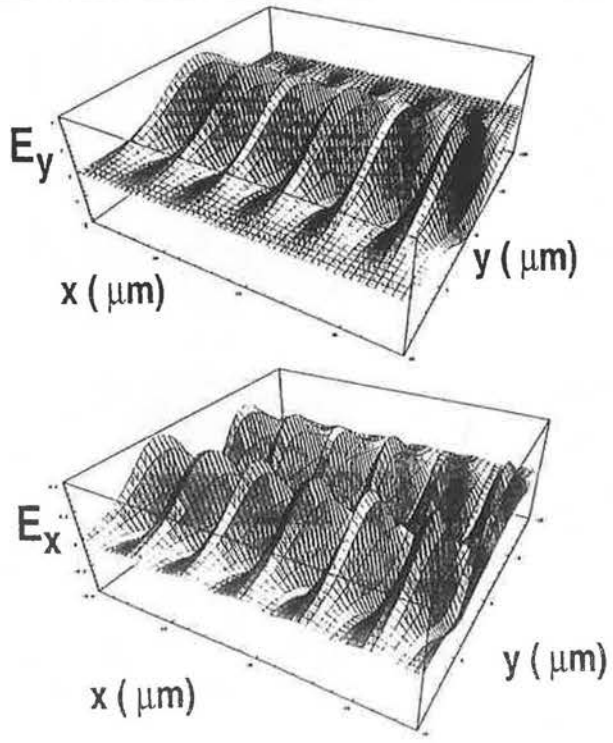

This is the electric field used to accelerate e 's to high energies in the free wave accelerator: They are still there when plasma is present.

Physical mechanism proposed: A combination of longitudinal laser electric field + plasma waves.

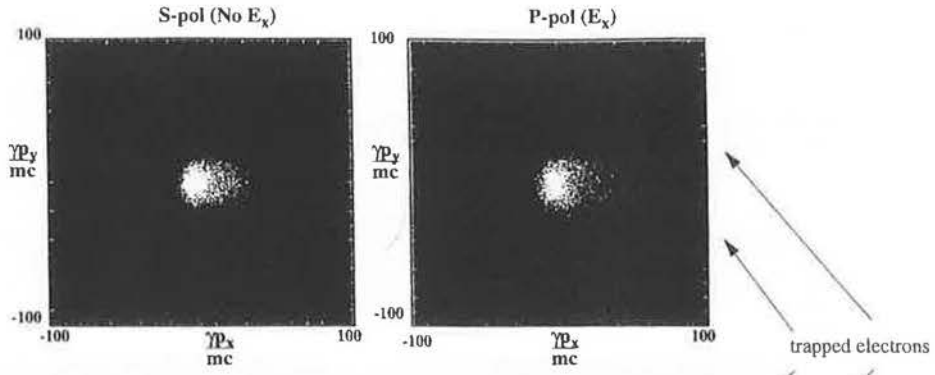

1. Electrons in presence of electromagnetic wave make a characteristic "C" motion in phase space.
2. Phase velocity of the EM wave is ordinarily too large for electrons to be trapped: they stay in "C".
3. If (somewhat dense) plasma is present, the phase velocity of the EM wave is slowed.
4. The electrons can then be trapped in the longitudinal wave and accelerated to well beyond a couple $\phi_{pond.}$

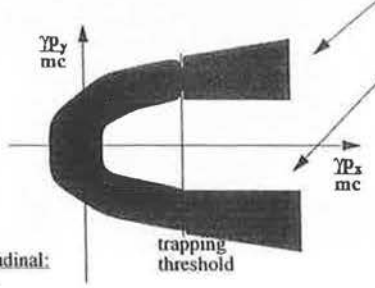

Eq. of Motion for Transverse:

$$m\frac{d}{dt}(\gamma v_y) = -eE_y + e\frac{v_x B_z}{c}$$

Eq. of Motion for Longitudinal:

$$m\frac{d}{dt}(\gamma v_x) = -e\frac{v_y B_z}{c}$$

Electron distributions for 2 different polarizations: clearly focusing field E_x increased maximum energy.

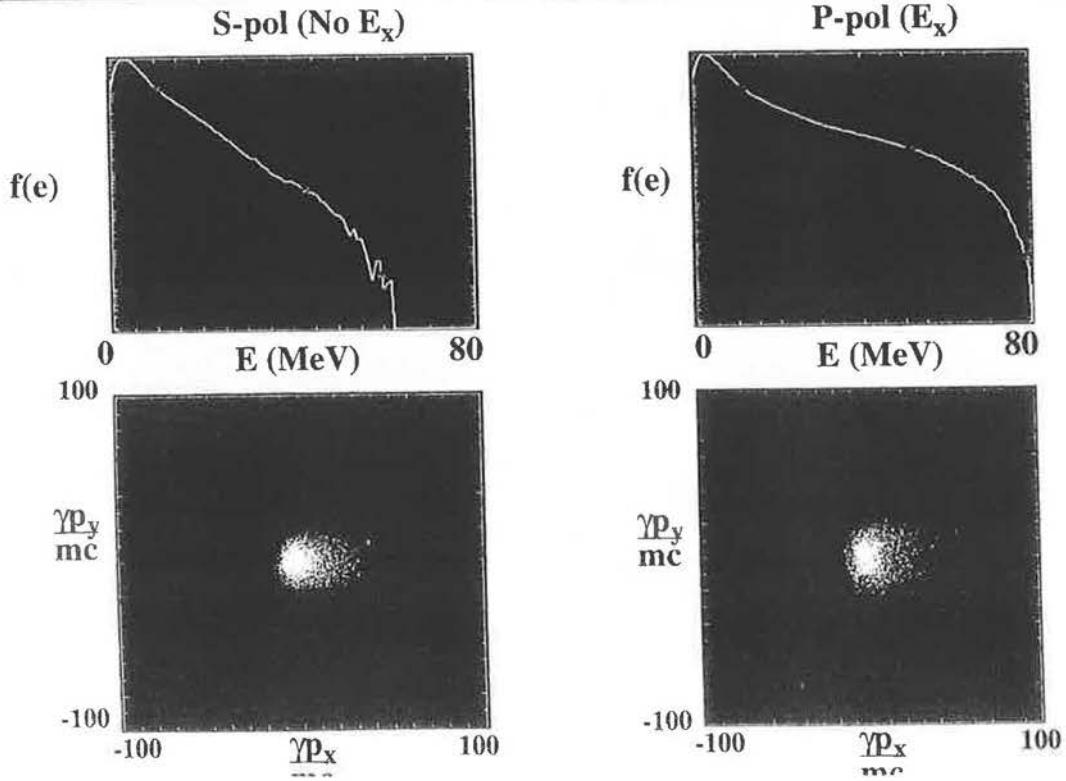

Pukov and Meyer-ter-Vehn hypothesize that B_z helps to increase electron energy.

Phase velocity of the wave: $v_{ph} = c\beta_{ph} = \frac{\omega}{k}$

Represent the longitudinal symmetry of the wave, by combining the particle kinetic energy and it's longitudinal momentum. This will give the first constant of the motion:

$$\varepsilon - c\beta_{ph}p_x = \varepsilon_o \qquad (2)$$

The 2nd follows from 1-D planar geometry and is an expression of conservation of the transverse generalized momentum.

$$\frac{p_\perp}{mc} - a = P_\perp^o \qquad (3)$$

Consider a plane EM wave in vacuum, with the speed c (β_{ph} =1 .) For an electron at rest, before the light wave hits it, one has ε_o=0 and p_{tr} = 0, and

$$p_\perp = mca; p_x = mc\frac{a^2}{2}; \varepsilon = mc^2\frac{a^2}{2} \qquad (4)$$

Thus, the KE of the electron within the light wave equals the ponderomotive potential ϕ=$mc^2a^2/2$.

However, if the electron already had a KE, or initial momentum of p_o, then it's momentum inside the pulse is

$$p_\perp = mca; p_x = p_o\left(1 + \frac{a^2}{2}\left(1 + \frac{\gamma_o}{p_o}\right)\right) \qquad (5)$$

where

$$\gamma_o = \sqrt{1 + p_o^2}$$

and in the ultra-relativistic limit γ_0>>1,

$$\boxed{\gamma = \gamma_o\sqrt{1 + a^2}} \qquad (6)$$

This holds only for an EM wave in vacuum. IF the laser pulse prpogates in a plasma, or is focused, it $\beta_{ph} > 1$. Starting from (3) and (2), you actually get a modified version of (5):

$$p_x = mc\gamma_{ph}\left(\sqrt{1 + a^2 + \left(1 + \frac{\varepsilon_o}{mc^2}\right)^2\gamma_{ph}^2} - \left(1 + \frac{\varepsilon_o}{mc^2}\right)\sqrt{\gamma_{ph}^2 + 1}\right)$$

where a new γ factor has been introduced, $\gamma_{ph} = 1/(\sqrt{\beta_{ph}^2 - 1})$

Equation (7) has two limiting cases:

Case 1: $1 << \gamma_o < \gamma_{ph}$ (slow electrons)

$\gamma = \gamma_o\sqrt{1 + a^2}$ compare with (6) above (is identical).

Case 2: $\gamma_o^2 > a^2\gamma_{ph}^2$ (fast electrons)

$\gamma \approx \gamma_o\left(1 + \left(\frac{a\gamma_{ph}}{\gamma_o}\right)^2\right)$ compare with (6) above (much less energy gain.)

The energy at which this "limiting" energy sets in, is:

$$\boxed{\varepsilon_c = \Lambda a\gamma_{ph}mc^2} \qquad (\Lambda \sim \text{unity})$$

Electron energy spectrum similar with/ without azimuthal B_z field.

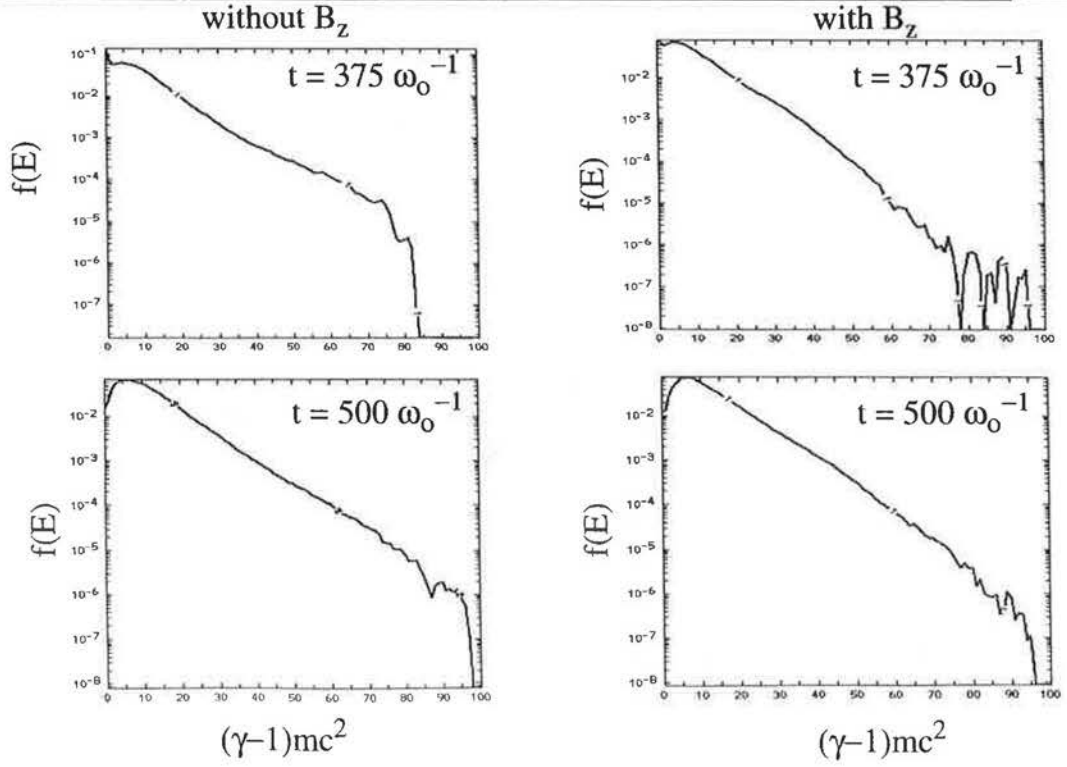

Conclusion: Electrons interacting with EM wave *in a plasma* can break Lawson-Woodward theorem, thus allowing very energetic electrons to be generated.

Relativistic laser-plasma interactions by multi-dimensional PIC simulations
A. Pukov and J. Meyer-ter-Vehn, Physics of Plasmas, **5**, 1880, May 1998

Magnetic field assisted particle acceleration ("B-loop" mechanism) relies essentially on electron gaining energy from EM wave similar to vacuum case, but due to the presence of the azimuthal B-field, electron is "dephased" in EM wave, and thus gains more energy than it otherwise would have.

Electron Beam Characteristics from Laser-Driven Wave Breaking
K-C Tzeng and W. B. Mori, Physical Review Letters, **79**, 5258, 29 December 1997

Observed that for extremely intense laser light shot into plasma, the electrons can gain considerably more energy then the 2-D de-phasing limit would predict. We have also observed this phenomenon in simulations for free wave accelerator design studies for Petawatt.

Trapping and Acceleration in Self-Modulated Laser Wakefields
E. Esarey, B. Hafizi, R. Hubbard, and A. Ting, Physical Review Letters, **80**, 5552, 22 June 1998

Trapping and acceleration of the background electrons can result from the coupling of Raman backscattering to the wakefield. (Threshold much lower than even the cold 1-D wave breaking limit.)

15

To test for self-focussing effects and hot-electron spectrum effects of pre-plasma, we use LASNEX to calculate the plasma conditions from measured ASE (amplified spontaneous emission) at main pulse time

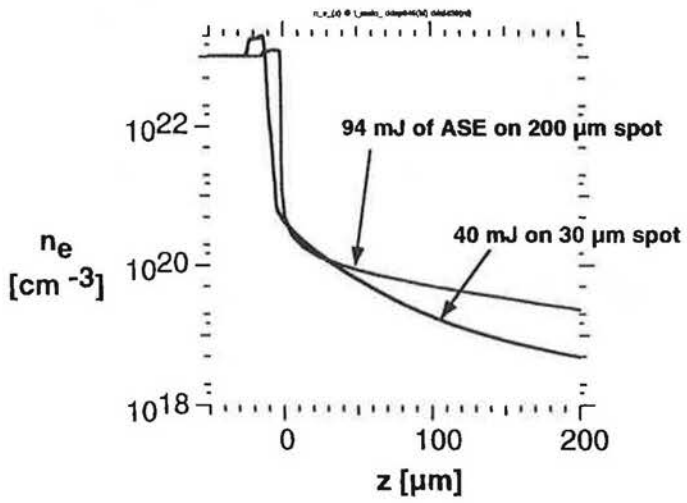

Results in regions of interest are input to PIC code.

Now use plasma blow-off obtained from LASNEX as plasma conditions for the 2-D PIC simulations.

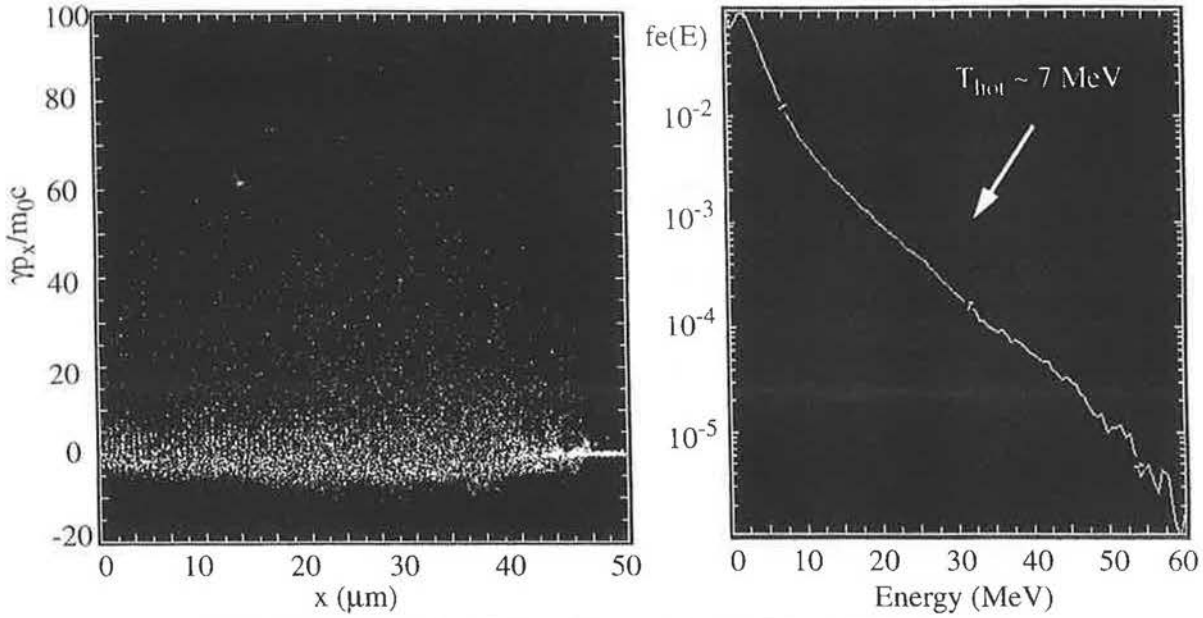

Note that even in the underdense, a significant number of high energy electrons are produced in the direction of the laser. We can now send these electrons into a solid w/ ITS.

scw/x-div

Comparison of LLNL-NASA/MSFC-UAH electron spectrometer data, with LASNEX/PIC/ITS results.*

PW 09/05/97 ~280 J, ~450 fs, 0.5 mm Au, ~1.1x10^{20} W/cm^2

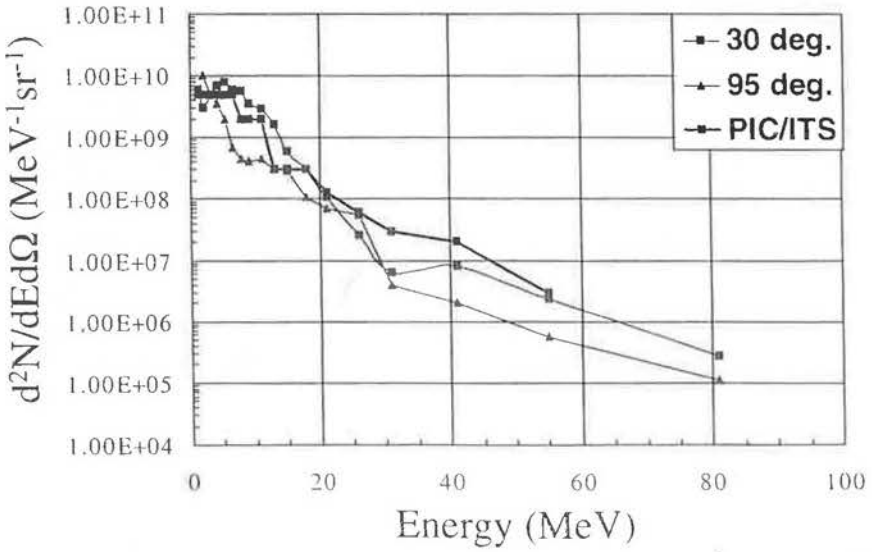

* Courtesy of Tom Cowan, et. al

scw xdiv

We can estimate the number of electrons as follows:

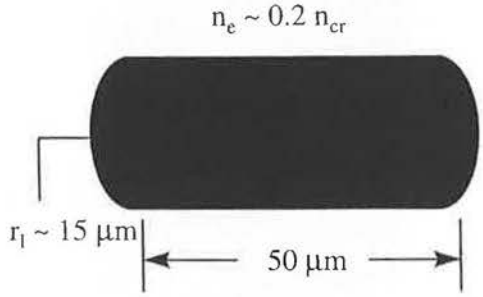

Volume = $\pi\ (15\times10^{-4})2\times50\times10^{-4}\ cm^3$
$\sim 4\times10^{-8}\ cm^3$

Number = $2\times10^{19}\times4\times10^{-8}$
$= 8\times10^{11}$ electrons
(Assumes 10% of the electrons heated to an average energy 7 MeV)

$N\langle E\rangle \sim 8\times10^{11}\times7\text{MeV}$

or the total energy is roughly 1 Joule, or 1/2% of the initial energy of 200 J.

Compare this to Spectrometer data:

$\frac{d^2N}{dEd\Omega} \sim 8\times10^{10}$ @ 7 MeV (Expt.)

$\frac{d^2N}{dEd\Omega} \sim 8\times10^{11}$ @ 7 MeV (Est.)

wilks.llnl.gov

At ~0.5 ps, a single channel is apparent behind the beam front.

Have we seen the evolution of the Weibel instability into longer wavelengths? Some dc B-field structure is still evident in front of the beam.

Plots of $(B_z)_{dc}$ and $(J_x)_{dc}$ from the simulation in p-polarization at 10^{21} W/cm^2, $n_e = 50\ n_c$, at 0.5 ps.

$(B_z)_{dc}$ at 0.5 ps

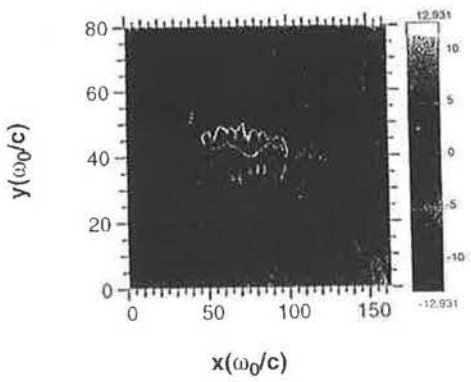

$(J_x)_{dc}$ at 0.5 ps

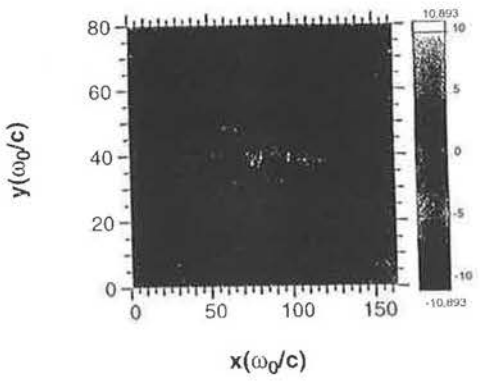

B-field bending over time is observed, effect is ill understood.

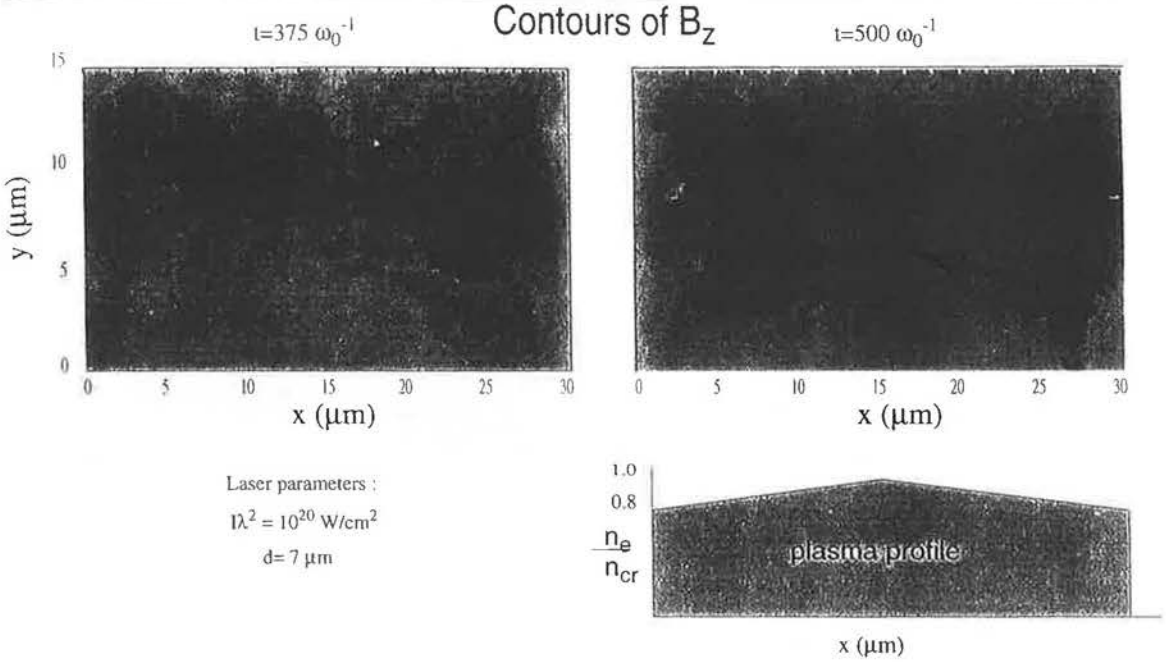

Beam deflection occurs in many ZOHAR simulations of laser penetration through plasma slabs.

- An example is a pair of simulations at 10^{19} W/cm^2
  The initial plasma density was 5 n_c which is overdense at this intensity.
- Here, the beam deflects in the same direction in both polarizations.

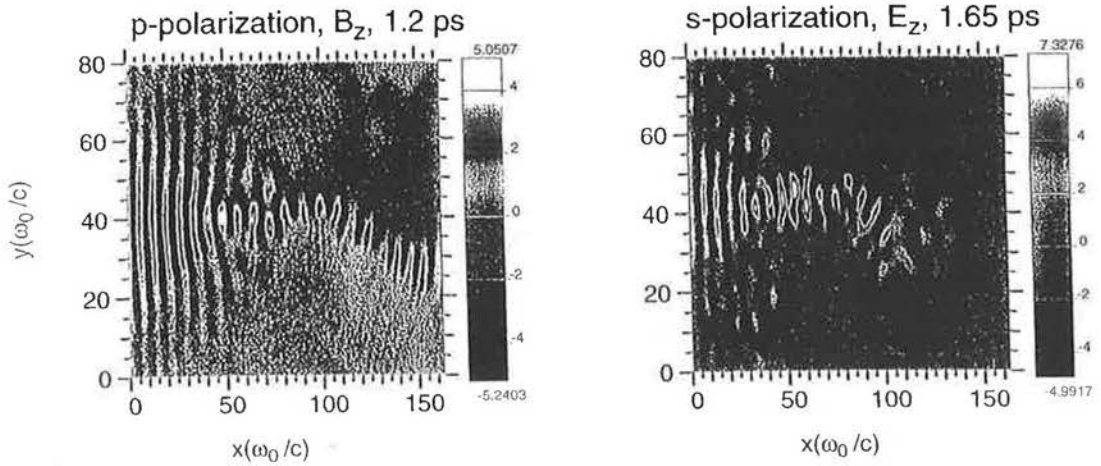

Relativistic filamentation occurs *and* the filaments coalesce at higher density in these Zohar simulations.

density 0 to .7n_c in 60 wavelengths

intensity 2x10^{19} W/cm^2 red light,

Gaussian beam,15 micron waist

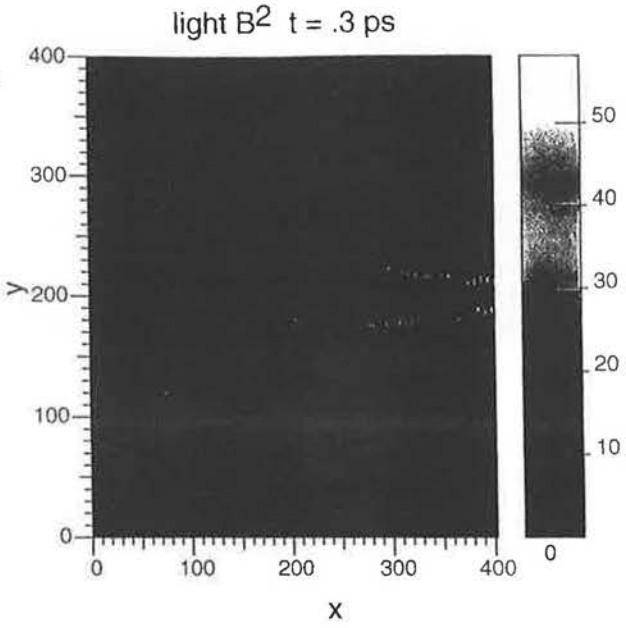

Langdon, 4/98

Summary and Conclusions

I. Reviewed plasma physics issues relevant to the recent PetaWatt experiments:

⇨ Underdense:

1. B-fields, channeling, electro-static fields, etc.
2. Quasi-TEM modes in underdense plasma.
3. "Beams" of electrons possible? T_{hot}? $f(\theta)$?

⇨ Overdense:

1. Absorption in overdense channel a worry.
2. Bending a potential problem?
3. Weibel seems to seed the B-field.

II. Fully relativistic PIC simulations confirm theoretical prediction of large energy gains: provide useful input to design and interpretation of experiments using ultra-short, intense lasers.

scw/09/14-96

Enhanced and correlated stopping of relativistic MeV electrons in supercompressed DT targets

C. DEUTSCH AND P. FROMY

LPGP, Bât. 210, Université Paris XI, 91405 Orsay, France

RANGE CALCULATION

Now, we consider the effective range

$$R = \int_{E_{max}=E_0=\ 1MeV}^{E_{min}=E_0/10=0.1MeV} \frac{dE}{dE/dx}\ , \qquad (1)$$

which is not an *a priori* rectilinear quantity ($\beta=v/c$).

The stopping power is then taken as the sum of

$$-\frac{dE}{dx}=\frac{2\pi n_p e^4}{me\beta^2c^2}\times\left[\ell n\frac{1}{2\tau_{min}}+\frac{1}{8}\left(\frac{\tau}{\tau+1}\right)-\left(\frac{2\tau+1}{\tau+1}\right)\ell n2+1-\ell n2\right]$$

where $\tau_{min}=\frac{\hbar(\text{projectile})}{mv}/\lambda_D$ (target electrons)

$\tau=\gamma-1$, and

$$-\frac{dE}{dx}=\frac{2\pi n_p e^4}{me\beta^2c^2}\,\ell n\left(\frac{V}{\omega_p\lambda_D\left(\frac{3}{2}\right)^{1/2}}\right)^2$$

Eq. (1) thus becomes ($V=\beta^2$) with $E=(\gamma-1)\,mec^2$,

$$R=\frac{(mec^2)^2}{4\pi n_p e^4}\times\int_{0.3025}^{0.8836}\frac{dvv}{(1-v)^{3/2}}\times\frac{1}{D(v)}=35\mu m$$

with

$$D(v)=\ell n(68.53v)+\ell n(68.026v^{1/2})+$$
$$+\frac{(1-\sqrt{1-v})^2}{8}-(2v+v-1)+1-\ell n2$$

- **Stopping 2-cluster calculation for the excitation of langmuir modes (collective contribution)**
- **Bohr impact parameter approach for single particle stopping adaptated by D.W. Rule/M.H. Cha *Phys. Rev.* A24, 55 (1981) to 2-cluster projectiles**
- **Supercompressed DT fuel mimiked by drude dielectric function**
- **2-cluster → N-cluster corrections to MeV R_{EB} stopping in dense DT**
- **Two electron projectiles in close vicinity $\left(R \equiv R_{12} \leq \frac{V}{\omega_p}\right)$ of each other may combine their separate stopping through target polarization**
- **Output: mostly positively enhanced energy loss**
- **Extension to relativistic velocities of the low velocity enhanced correlated stopping**
- **N-clusters taken as linear super-position of 2-clusters dynamically correlated**

TARGET DIELECTRIC FUNCTION

- $$\varepsilon(\omega) = 1 - \frac{\omega_p^2}{\omega(\omega + i\nu_{coll})} \quad ,$$

Drude suitable for high velocity REB

$$\nu_{coll} = \frac{3.8 \times 10^{-6} n_e(cm^{+3})}{T_e(eV)^{3/2}} \ell n \ \Lambda$$

$$\ell n \Lambda = \ell n[9 n_e \lambda_D] = 6.305 \qquad \text{for}$$

$T = 5$ keV and $n_e = 10^{26}$ e-cm^{-3}

- $$\int_0^\infty d\omega \, \omega \, \mathrm{Im} \frac{1}{\varepsilon(\omega)} = -\frac{\pi}{2} \omega_p^2$$

$$\vec{j} = \frac{1}{N} \frac{d\vec{P}}{dt} \delta(\vec{x}' - \vec{x}) + \frac{c}{N} \vec{\nabla} \times \vec{M} \delta(\vec{x}' - \vec{x})$$

Medium Current at $\vec{x}$

$\vec{P}$, polarization

$\vec{M}$, magnetic moment density

N, Target charge density

Following Jackson's discussion of the Bohr method, we write the total work done on an atom in the medium by a passing cluster of particles as

$$\Delta E = \int_{-\infty}^{\infty} dt \int \vec{E} \cdot \vec{j}\, d^3x .$$

In the usual way, this can be written in terms of Fourier transforms in frequency as

$$\Delta E = \frac{1}{2\pi N} \mathrm{Re} \int_0^{\infty} (-i\omega)[\epsilon(\omega)|\vec{E}|^2 + \mu(\omega)|\vec{H}|^2] d\omega ,$$

having introduced the linear relations

$$\vec{P}(\omega) = \frac{1}{4\pi}[\epsilon(\omega) - 1]\vec{E}(\omega)$$

and

$$\vec{M}(\omega) = \frac{1}{4\pi}[\mu(\omega) - 1]\vec{H}(\omega) .$$

The work done by a cluster in passing through a slab of medium with thickness dz is then given by

$$dE = N\, dz \int_{II} dx\, dy \frac{1}{2\pi N} \int_0^{\infty} d\omega\, \omega[\mathrm{Im}\epsilon(\omega)|\vec{E}|^2 + \mathrm{Im}\mu(\omega)|\vec{H}|^2] .$$

Therefore the energy loss per unit distance is

$$\frac{dE}{dz} = \frac{1}{2\pi} \int_{II} dx\, dy \int_0^{\infty} d\omega\, \omega[\mathrm{Im}\epsilon|\vec{E}|^2 + \mathrm{Im}\mu|\vec{H}|^2],$$

$$\frac{dE}{dz} = \frac{1}{2\pi} \int_a^{\infty} b\, db \int_0^{2\pi} d\phi \int_0^{\infty} \omega\, \mathrm{Im}\epsilon(\omega)|\vec{E}(\omega)|^2 d\omega$$

where

$$|\vec{E}|^2 = \Big|\sum_{i=1}^{n} \vec{E}_i\Big|^2 = \sum_{i=1}^{n} |\vec{E}_i|^2 + 2\,\mathrm{Re}\sum\sum_{i<j} \vec{E}_i^* \cdot \vec{E}_j .$$

This form suggests defining the following stopping-power components $dE_{ij}(\vec{R}_{ij})/dz$ which are functions of the separation vectors $\vec{R}_{ij}$, from the ith to the jth particle in the cluster:

$$\frac{dE_{ii}}{dz} = \frac{1}{2\pi} \int_a^{\infty} b\, db \int_0^{2\pi} d\phi \int_0^{\infty} \omega\, \mathrm{Im}\epsilon(\omega)|\vec{E}_i(\omega)|^2 d\omega$$

and

$$\frac{dE_{ij}(\vec{R}_{ij})}{dz} = \frac{1}{2\pi} \int_a^{\infty} b\, db \int_0^{2\pi} d\phi \int_0^{\infty} \omega\, \mathrm{Im}\epsilon(\omega) \times \mathrm{Re}\vec{E}_i^*(\omega) \cdot \vec{E}_j(\omega) d\omega ,$$

where a is the radius shown in Fig.

The energy loss for a cluster can then be expressed as

$$\boxed{\frac{dE}{dz} = \sum_{i=1}^{n} \frac{dE_{ii}}{dz} + \sum\sum_{i<j} \frac{dE_{ij}}{dz} + \sum\sum_{i<j} \frac{dE_{ji}}{dx} .}$$

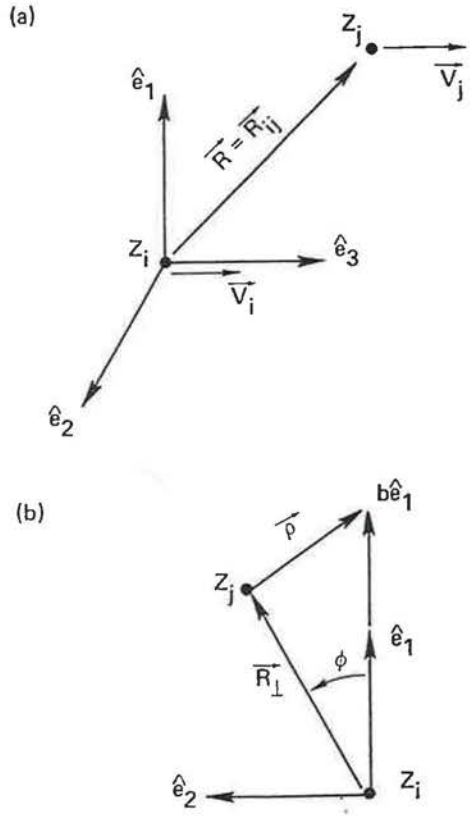

FIG. 2. (a) The coordinate system and the pair of particles at time $t=0$. (b) The $\hat{e}_1\hat{e}_2$ plane showing the vectors $\vec{b}$, $\vec{R}_\perp = R_1\hat{e}_1 + R_2\hat{e}_2$, and $\vec{\rho} = \vec{b} - \vec{R}_\perp$

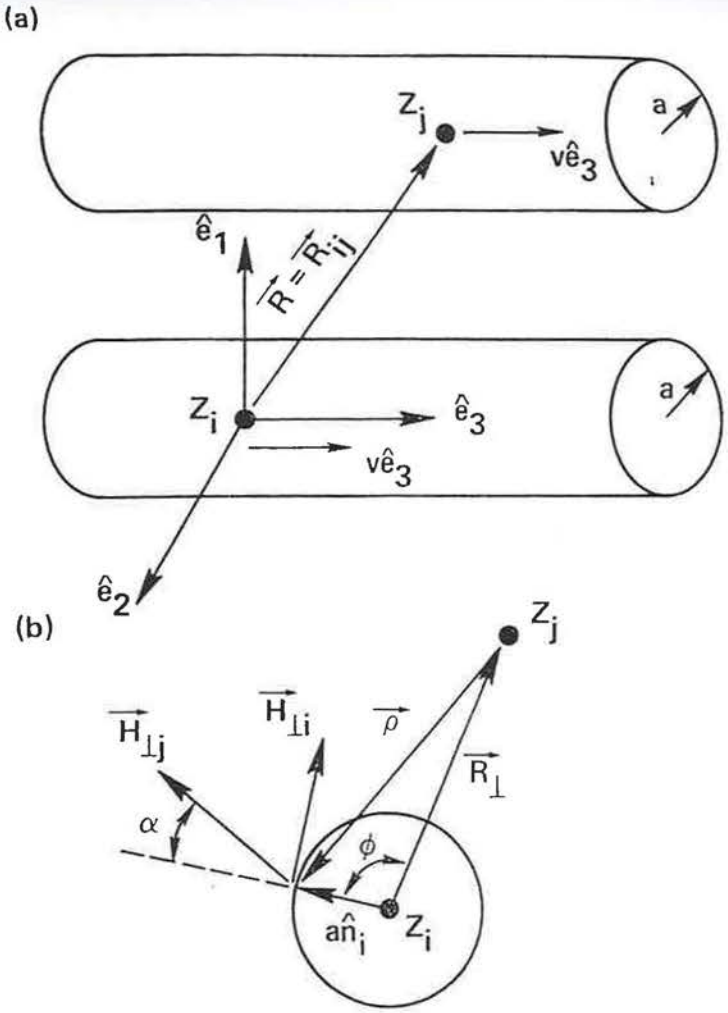

(a) The coordinate system used to calculate the energy loss by a dicluster using Fermi's method. (b) The view in the $\hat{e}_1\hat{e}_2$ plane shows the vectors and angles used in the analysis. Also shown are the fields $\vec{H}_{\perp i}$ and $\vec{H}_{\perp j}$ generated by particles i and j at the surface of the cylinder of radius a.

$$\vec{V}_1 = \vec{V}_2 = \vec{V}$$

If the velocities of the two particles are equal

$$\lambda \equiv \frac{|\omega|}{v}(1-\beta^2\epsilon)^{1/2} \quad \text{and} \quad \Lambda \equiv \lambda\left(\lambda^{*2}\frac{v^2}{\omega^2}-1\right).$$

$$\frac{dE_c}{dz} = \frac{4}{\pi} Z_i Z_j \frac{e^2}{v^2}\int_0^\infty d\omega\,\omega\,\frac{\mathrm{Im}\epsilon}{|\epsilon|^2}\cos\left(\frac{\omega R_3}{v}\right)\mathrm{Re}\,\frac{|\lambda|^2}{\lambda^2-\lambda^{*2}}\{K_0(\lambda R_\perp)[\Lambda b K_1(\lambda^* b)I_0(\lambda b)+\Lambda^* b K_0(\lambda^* b)I_1(\lambda b)]_a^{\bar a}$$
$$-2iI_0(\lambda R_\perp)\,\mathrm{Im}[\bar a \Lambda K_1(\lambda^*\bar a)K_0(\lambda\bar a)]\}.$$

$$\lambda_i \equiv \frac{|\omega|}{v_i}(1-\beta_i^2\epsilon)^{1/2} \quad (\mathrm{Re}\lambda_i>0,\ \ \mathrm{Im}\lambda_i<0)$$

with $\beta_i \equiv v_i/c$, and the K_n are modified Bessel functions.

$$\frac{dE_c}{dz} = \frac{2}{\pi}\frac{Z_i Z_j e^2}{v_i v_j}\int_0^\infty d\omega\,\omega\,\frac{\mathrm{Im}\epsilon}{|\epsilon|^2}\Big(\mathrm{Re}e^{-i\omega R_3/v_j}\frac{\lambda_i^*\lambda_j}{\lambda_j^2-\lambda_i^{*2}}\{K_0(\lambda_j R_\perp)[\Lambda_{ji} b K_1(\lambda_i^* b)I_0(\lambda_j b)+\Lambda_{ij}^* b K_0(\lambda_i^* b)I_1(\lambda_j b)]_a^{\bar a}$$
$$+I_0(\lambda_j R_\perp)[\Lambda_{ij}^*\bar a K_1(\lambda_j\bar a)K_0(\lambda_i^*\bar a)-\Lambda_{ji}\bar a K_0(\lambda_j\bar a)K_1(\lambda_i^*\bar a)]\}$$
$$+\mathrm{Re}\bar e^{i\omega R_3/v_i}\frac{\lambda_j^*\lambda_i}{\lambda_i^2-\lambda_j^{*2}}\{K_0(\lambda_i R_\perp)[\Lambda_{ij} b K_1(\lambda_j^* b)I_0(\lambda_i b)+\Lambda_{ji}^* b K_0(\lambda_j^* b)I_1(\lambda_i b)]_a^{\bar a}$$
$$+I_0(\lambda_i R_\perp)[\Lambda_{ji}^*\bar a K_1(\lambda_i\bar a)K_0(\lambda_j^*\bar a)-\Lambda_{ij}\bar a K_0(\lambda_i\bar a)K_1(\lambda_j^*\bar a)]\}\Big)$$

$$\bar a \equiv \begin{cases} R_\perp, & R_\perp > a \\ a, & R_\perp < a \end{cases}$$

$$\Lambda_{ij} \equiv \lambda_i\left(\lambda_j^{*2}\frac{v_i v_j}{\omega^2}-1\right)$$

Single particle Stopping

In the limit $R \to 0$

$$\frac{dE_s}{dz} = Z^2 S,$$

where

$$S \equiv -\frac{2}{\pi}\frac{e^2}{v^2}\int_0^\infty d\omega\, \omega\, \mathrm{Im}\left[K_0(\lambda a)\left(\frac{1}{\epsilon} - \beta^2\right)\right]$$

Cf. E. Fermi, Phys. Rev. 57, 485 (1940)

• C. Deutsch, H. Furukawa, K. Mima, M. Murakami and K. Nishihara, Phys. Rev. Lett. 77, 2483 (1996)

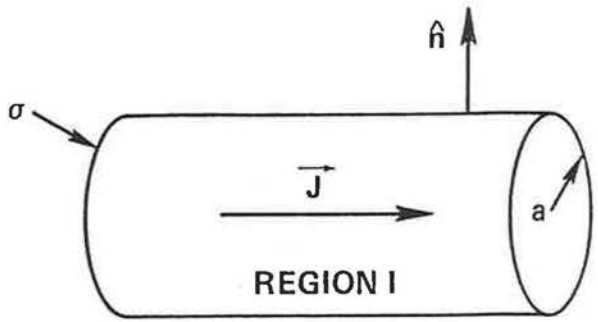

The separation of the medium into a close-collision part and a distant-collision part. The vectors $\hat{n}$ and $-\hat{n}$ are unit normals to the surface σ surrounding the current $\vec{j}$.

Stopping of MeV REB in Supercompressed DT

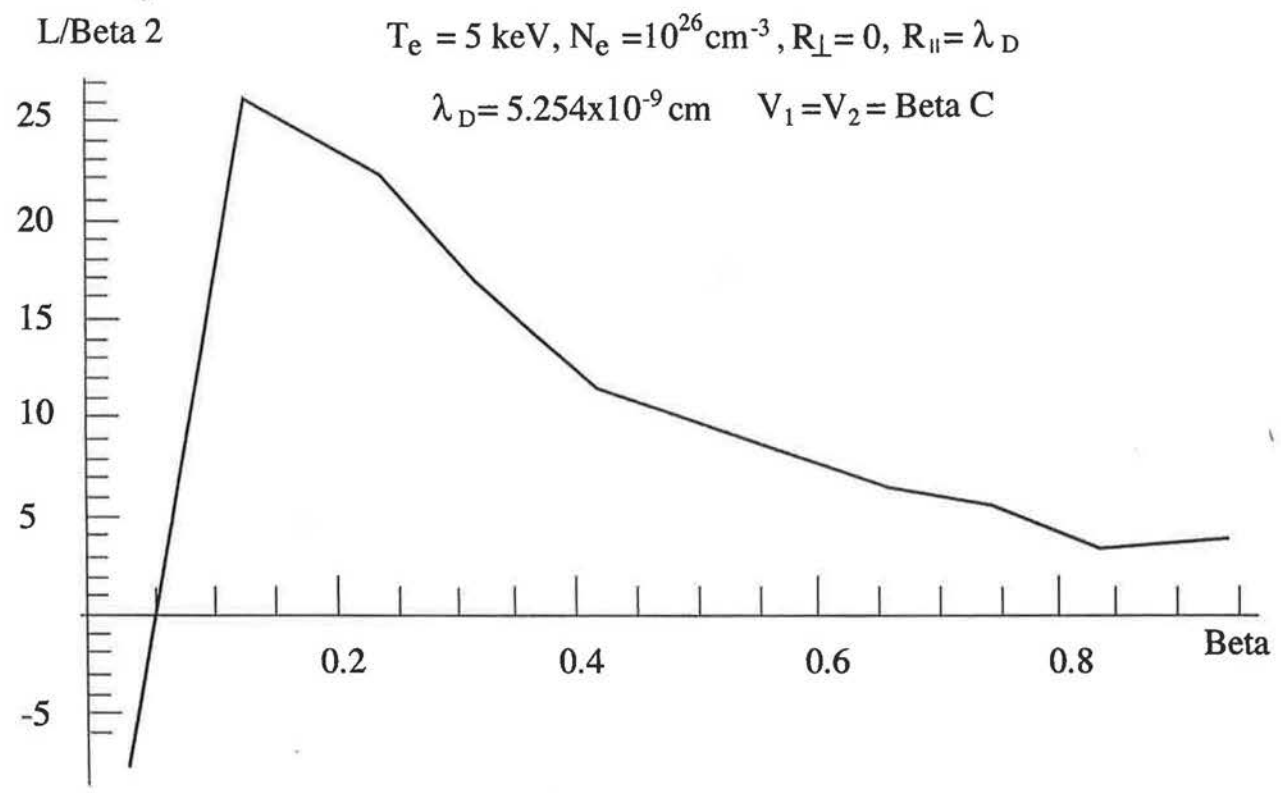

V-dependence of 2-correlations

1 MeV REB in 5 keV, 10^{26} e-cm^{-3} DT Target

$\beta_1 = 0.94$

$R_\perp = 0$

$R_\parallel = \lambda_D = 5.254 \times 10^{-9}$cm

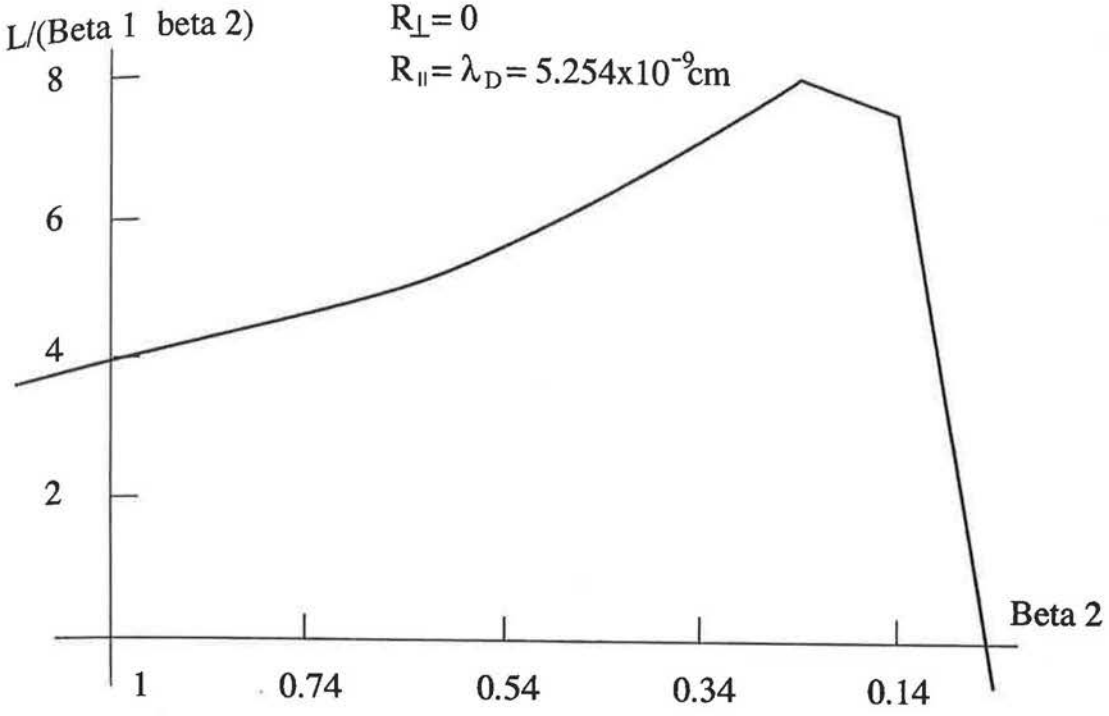

$V_1 \neq V_2$

dependence of 2-correlations

1 MeV REB in Supercompressed DT

$N_e = 10^{26}\,cm^{-3}$, $V_1 = V_2 = 0.94\,C$

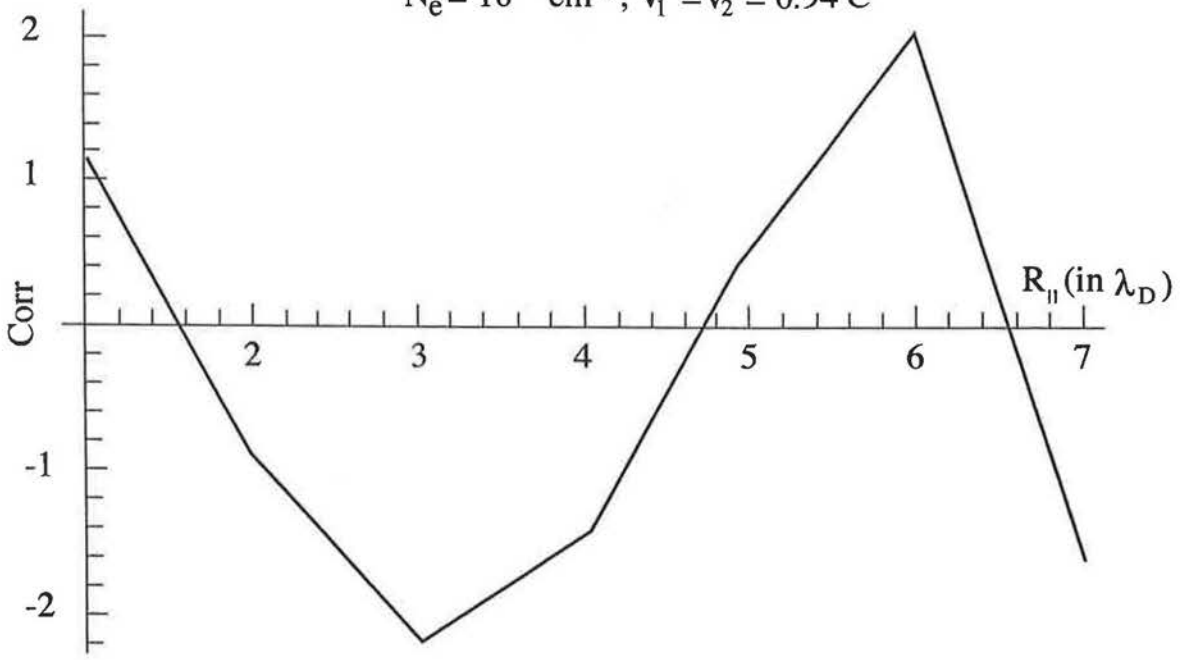

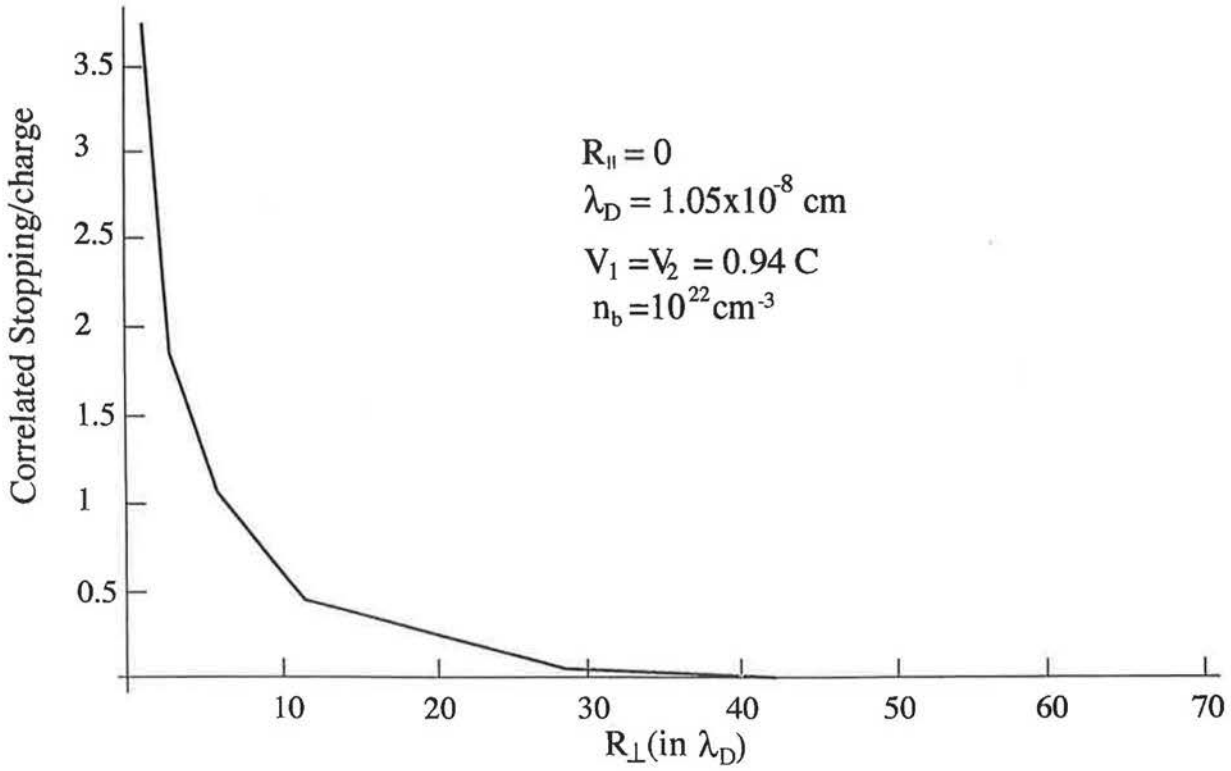

$R_{||} = 0$

$\lambda_D = 1.05 \times 10^{-8}$ cm

$V_1 = V_2 = 0.94\,C$

$n_b = 10^{22} cm^{-3}$

1 MeV REB in Supercompressed (DT 5 keV, 10^{26} e-cm^{-3})

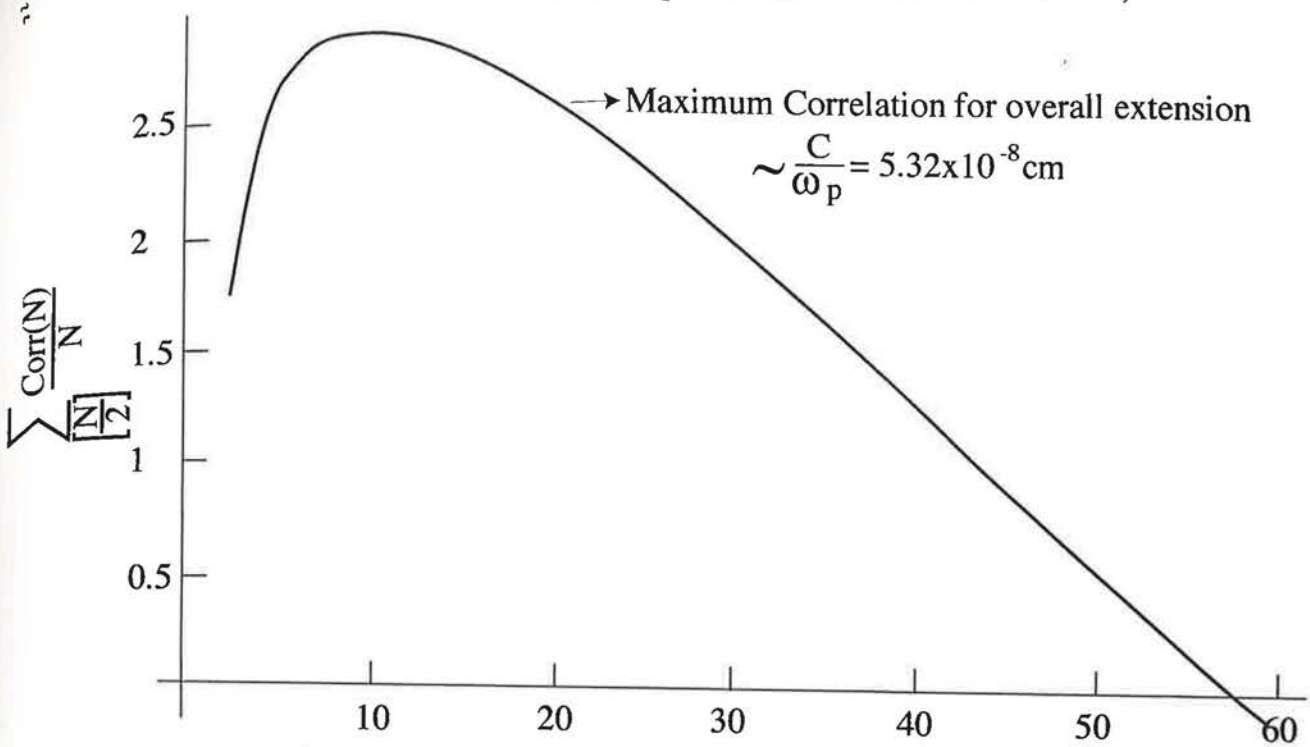

.5 Corr/Point

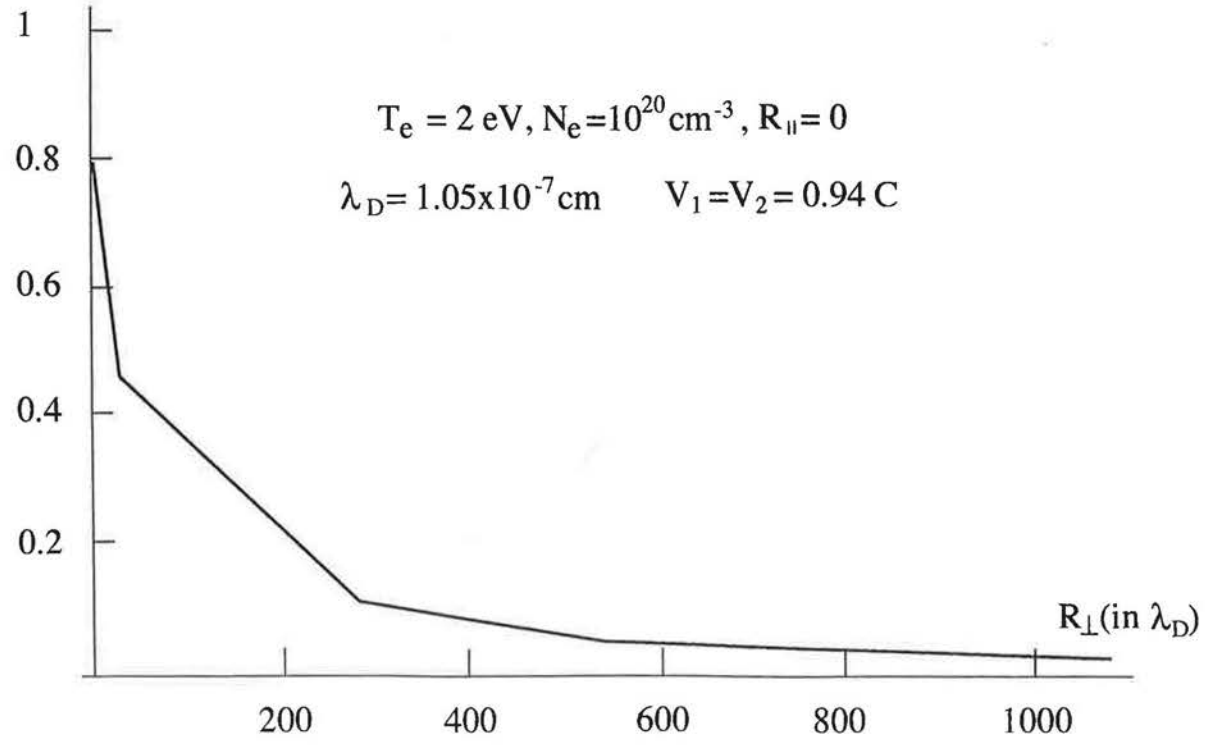

SUMMARY

- **Full relativistic calculation of 2-cluster stopping**
- **Correlation length much larger than target electron screening length, up to c/ω_p**
- **Transverse correlations W.R.T projectile velocity always produce significant stopping enhancement**
- **Longitudinal correlations are strongly modulated W.R.T number correlated beam electrons**
- **Globally, one expects range shortening by a factor 3 W.R.T uncorrelated stopping**

Interaction of ultra intense pulses with strongly overdense plasmas via 2D PIC simulations

JC ADAM - A. HÉRON

CENTRE DE PHYSIQUE THÉORIQUE
ÉCOLE POLYTECHNIQUE
(FRANCE)

Outline of the talk

- description of { physical parameters / numerical }
- First set of results : time evolution of plasma density, temperature, magnetic fields
- second set : a closer look to the structure of the magnetic field
- third set : represent the distribution of the thermal flux
- 4th set : spatial distribution of particles as a function of energy
- Conclusions (preliminary)

PHYSICAL PARAMETERS OF THE STUDY

pulse shape Gaussian in space $a = a_0 \exp - \frac{x^2}{2 x_c^2}$

flat plateau in intensity 1 - 2 ps ($2000\omega_0^{-1}$ - $4000\omega_0^{-1}$)

rise time : linear $\sim 12\omega_0^{-1} \sim 30$ fs

initial plasma density profile

density step function maximum value αn_c

range of parameters of the study

$x_c = 10 k_0^{-1}$, $(20 k_0^{-1})$, $40 k_0^{-1}$, $80 k_0^{-1}$ $= 3{,}77 \left(\frac{FWHM}{\lambda}\right) k_0^{-1}$

$\alpha = 10, 20, 40, (80)$

$\phi \sim 10^{20}$ W/cm^2, $5\,10^{20}$ W/cm^2, $(10^{21}$ W/cm$^2)$

E_{laser} (1 ps) $\begin{cases} 10^{20} \text{ W/cm}^2 \rightarrow \sim 20 \text{ J} \\ 10^{21} \text{ W/cm}^2 \rightarrow 200 \text{ J} \end{cases}$

The simulated system

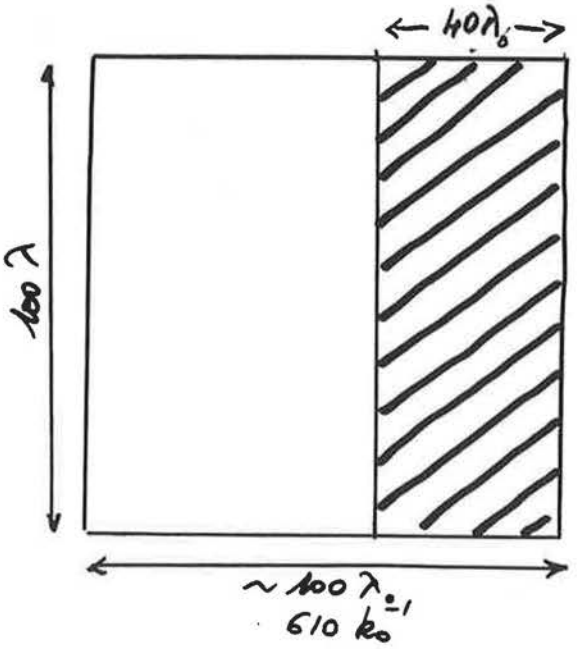

$dx \sim dy \sim 0.1\, k_0^{-1}$

$dt \sim 0.1\, \omega_0^{-1}$ (time splitting over Maxwell)

10 particles / cells

$2\,10^7$ total number of particles

$n_x = n_y = 6144$ (each species)

$\frac{n}{n_c} = 80$

periodic in y (depend on the simulation)

open ended in x

$x_c = 20 k_0^{-1} \sim$ FWHM in intensity $\sim 5\lambda$

$\phi = 10^{21}$ W/cm^2

$L_R = 0.22 (k_0 x_c)^2 \lambda$

$\sim 88\lambda$

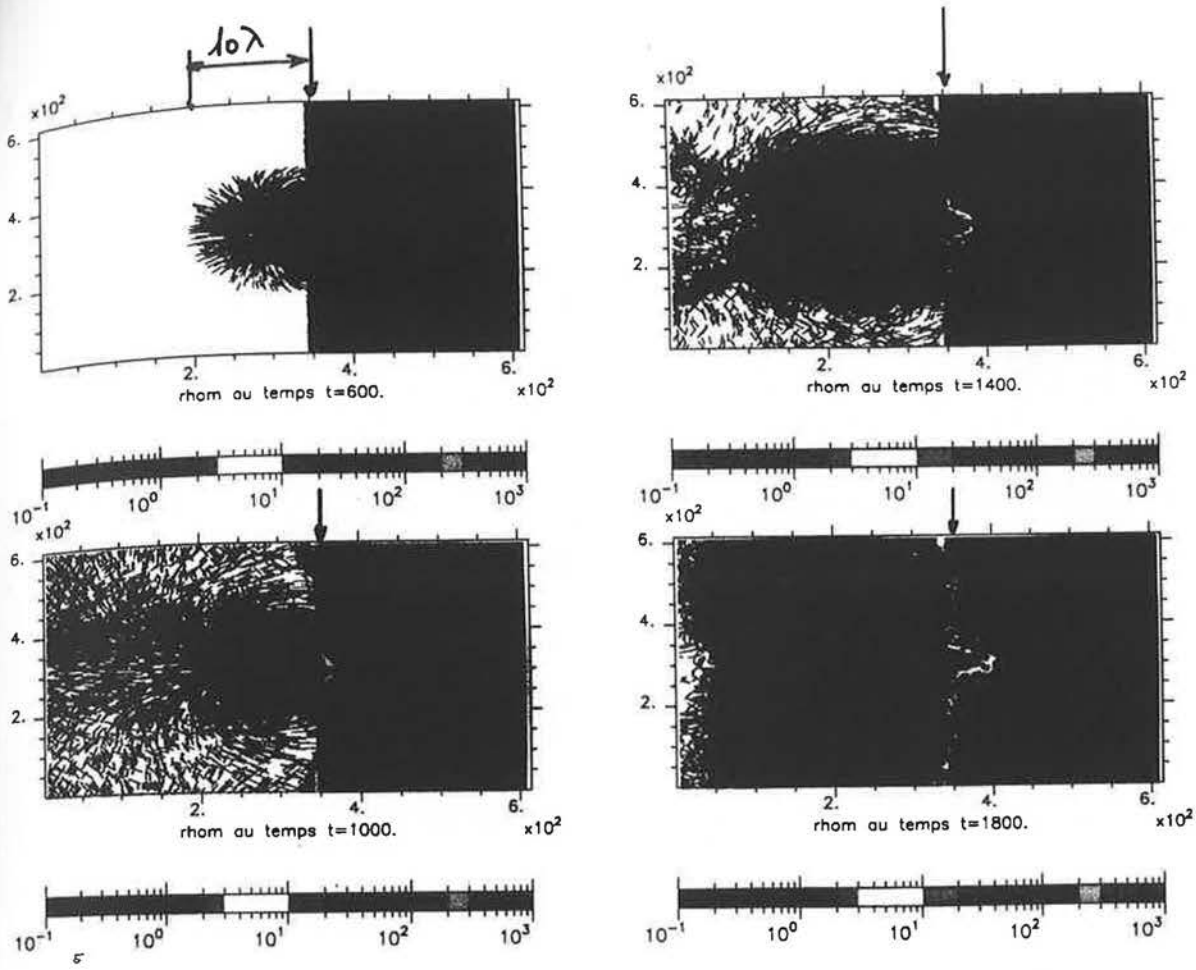
10λ
x10²
6.
4.
2.
rhom au temps t=600.
rhom au temps t=1400.
rhom au temps t=1000.
rhom au temps t=1800.
10⁻¹
10⁰
10¹
10²
10³

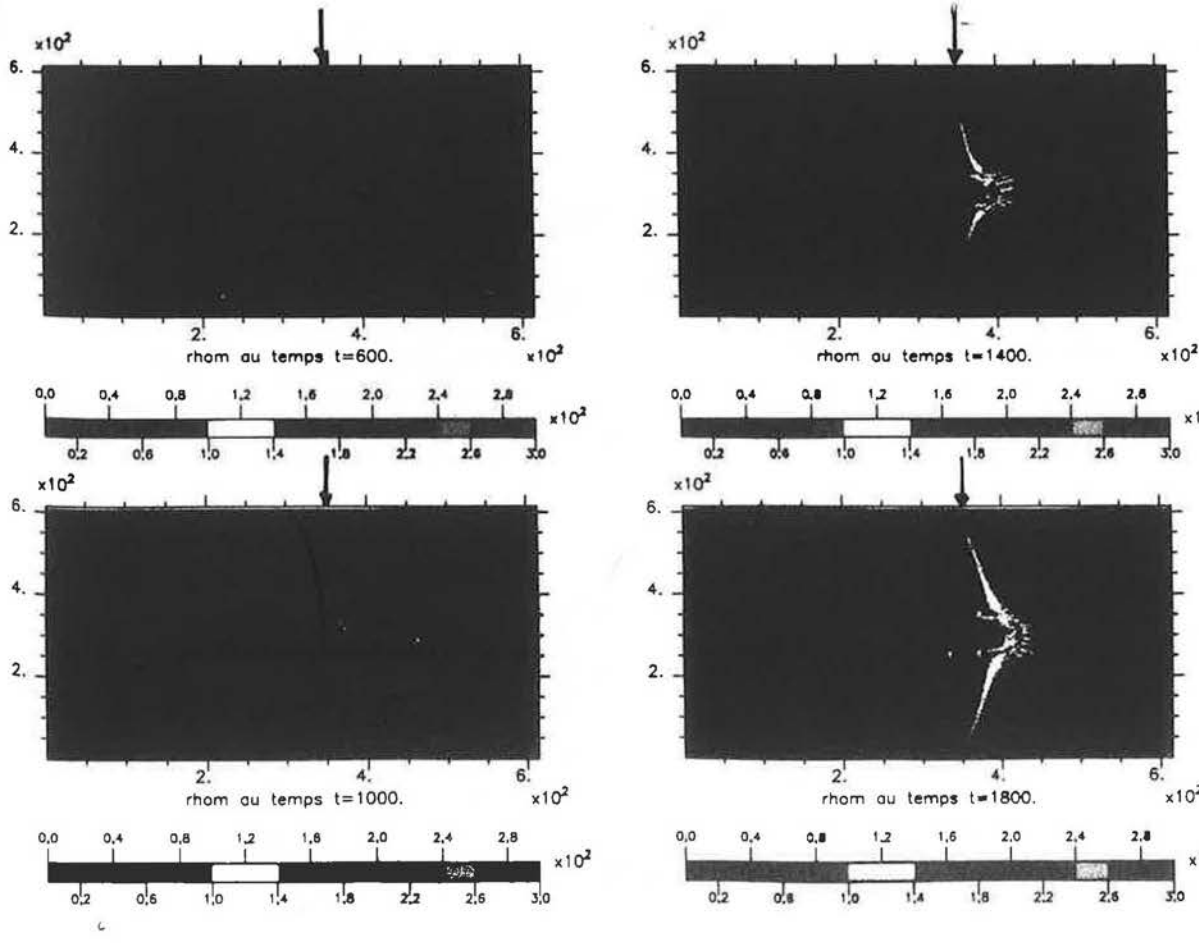
x10²
6.
4.
2.
rhom au temps t=600.
rhom au temps t=1400.
rhom au temps t=1000.
rhom au temps t=1800.
0,0
0,4
0,8
1,2
1,6
2,0
2,4
2,8
0,2
0,6
1,0
1,4
1,8
2,2
2,6
3,0

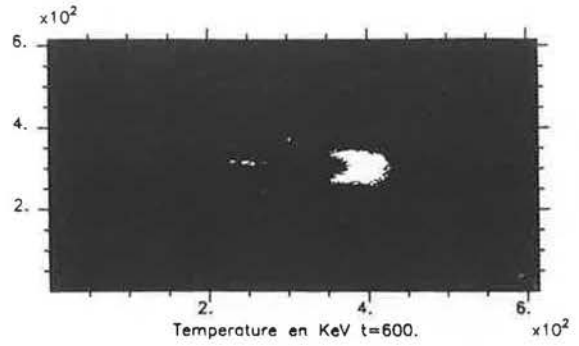

Temperature en KeV t=600.

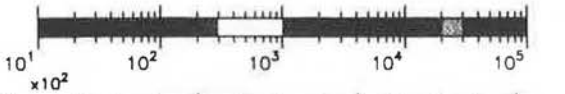

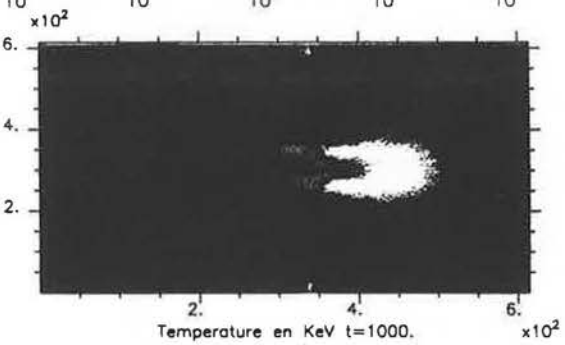

Temperature en KeV t=1000.

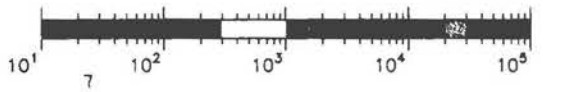

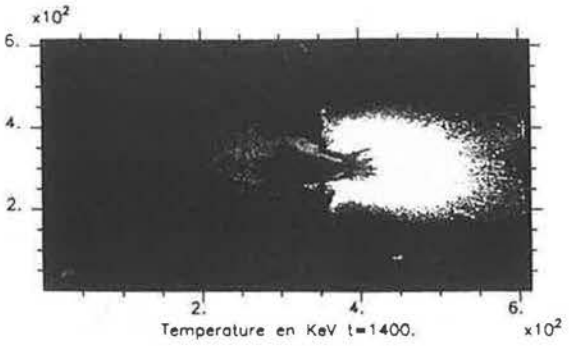

Temperature en KeV t=1400.

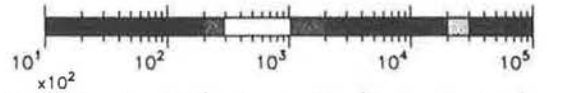

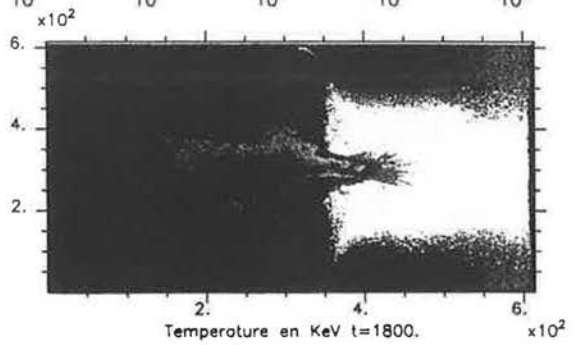

Temperature en KeV t=1800.

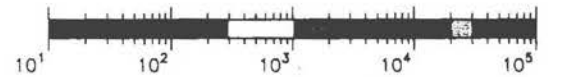

7

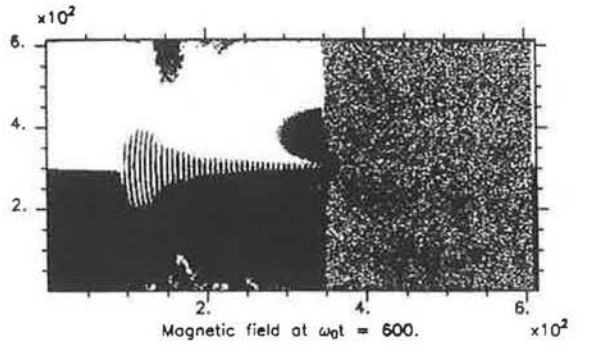

Magnetic field at $\omega_0 t$ = 600.

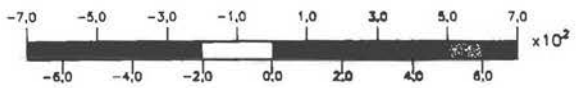

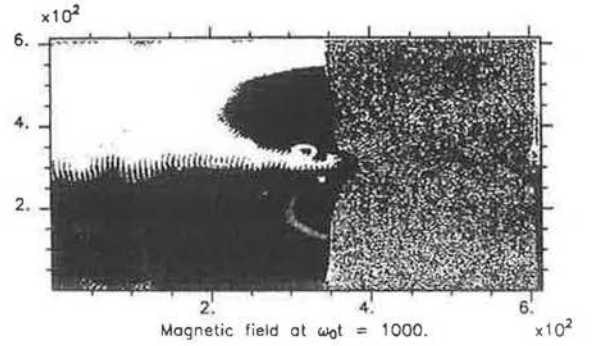

Magnetic field at $\omega_0 t$ = 1000.

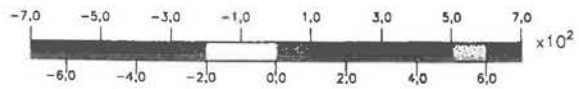

8

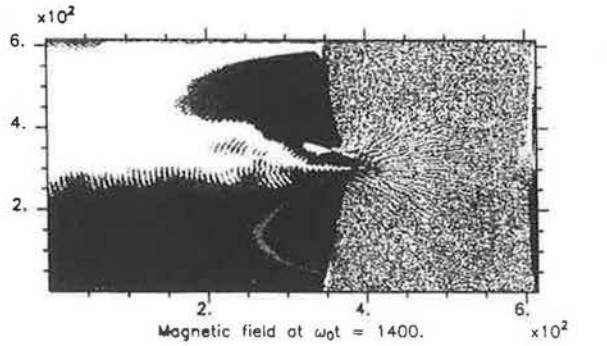

Magnetic field at $\omega_0 t$ = 1400.

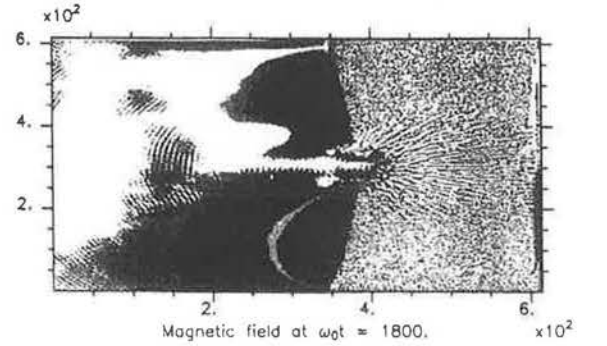

Magnetic field at $\omega_0 t$ = 1800.

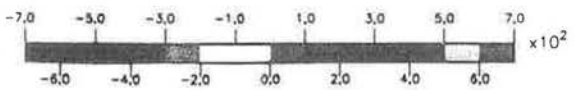

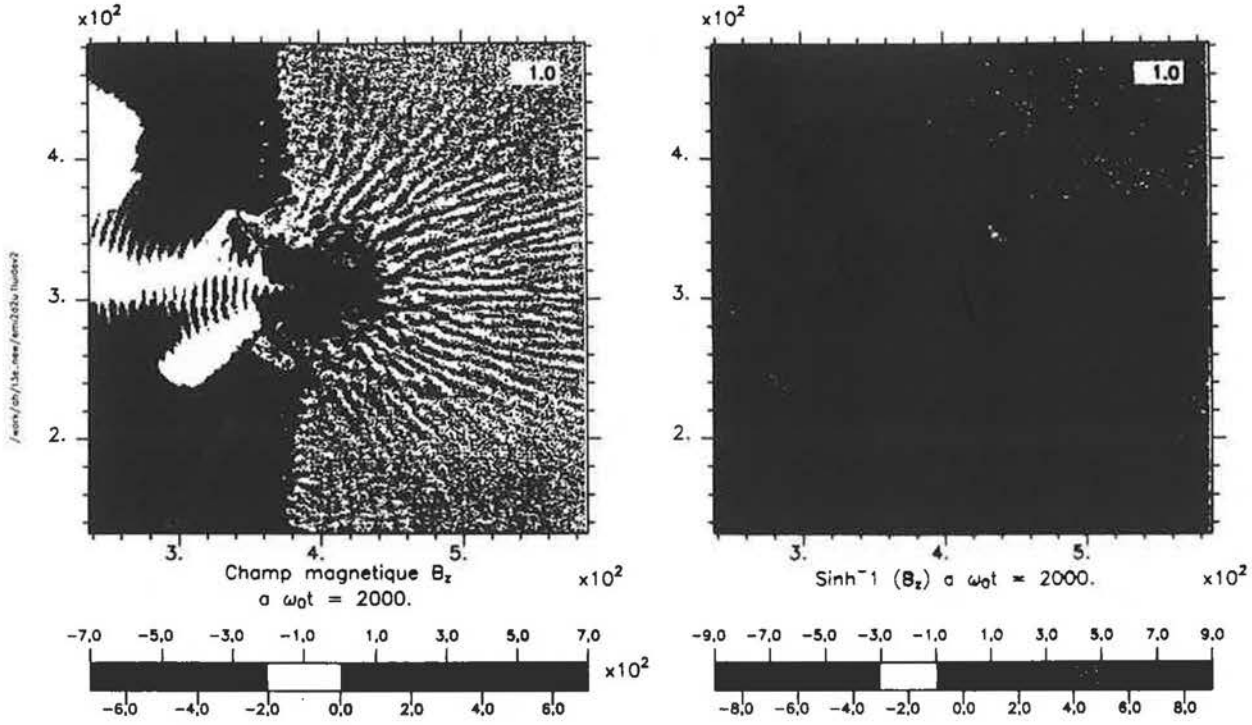

9

A recall : $y = \sinh^{-1}(x)$

$y = 5$	$\rightarrow x = 70$
6	$x = 200$
7	$x = 500$
8	$x = 1500$

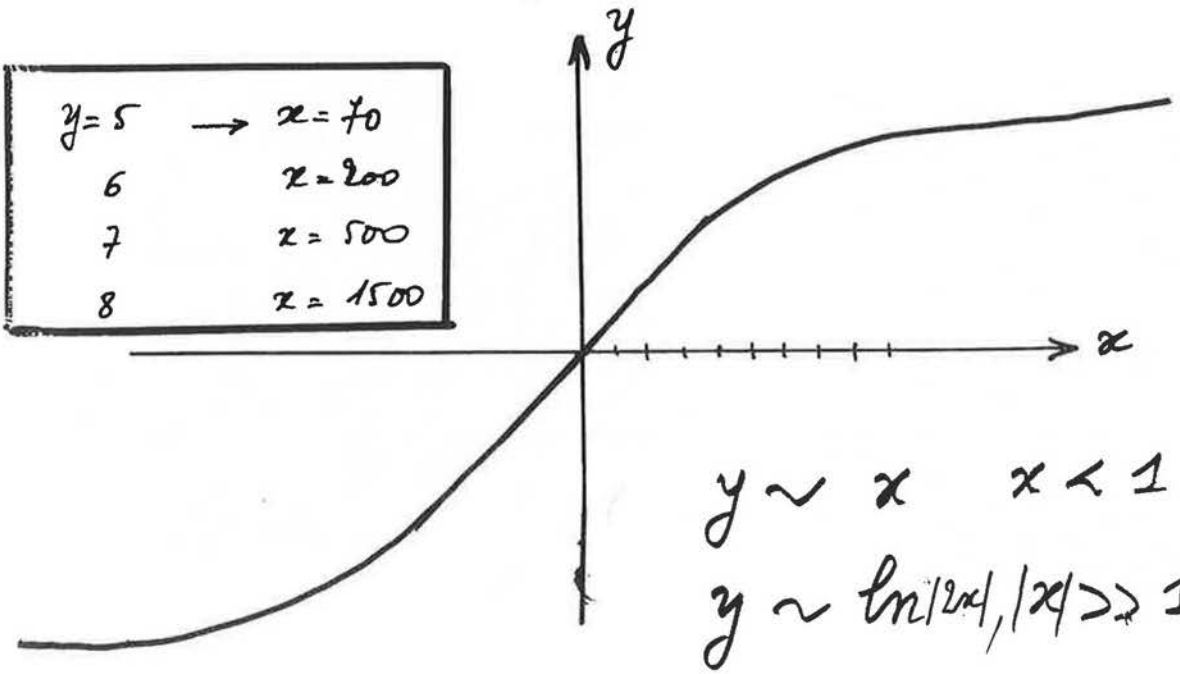

$y \sim x \quad x < 1$

$y \sim \ln|2x|, \; |x| >> 1$

use in some of the color plots

10

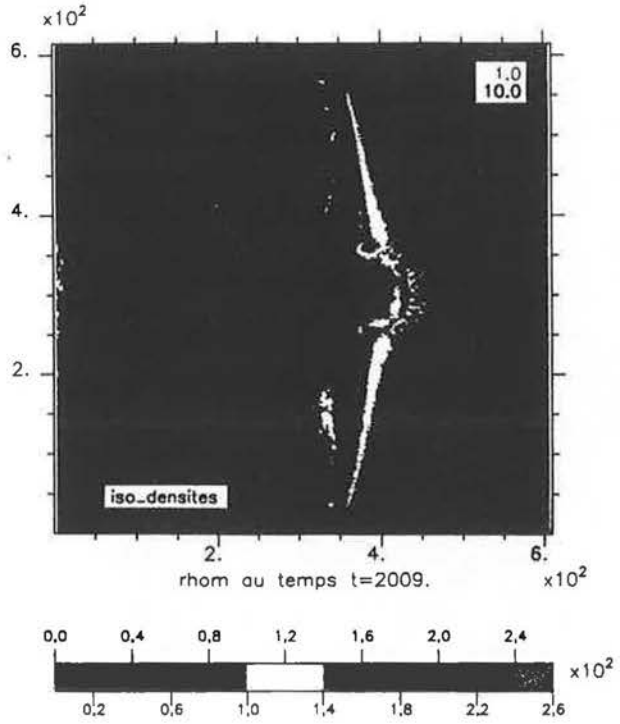
x10²
6.
4.
2.
1.0
10.0
iso_densites
2.
4.
6.
x10²
rhom au temps t=2009.
0,0 0,4 0,8 1,2 1,6 2,0 2,4
x10²
0,2 0,6 1,0 1,4 1,8 2,2 2,6

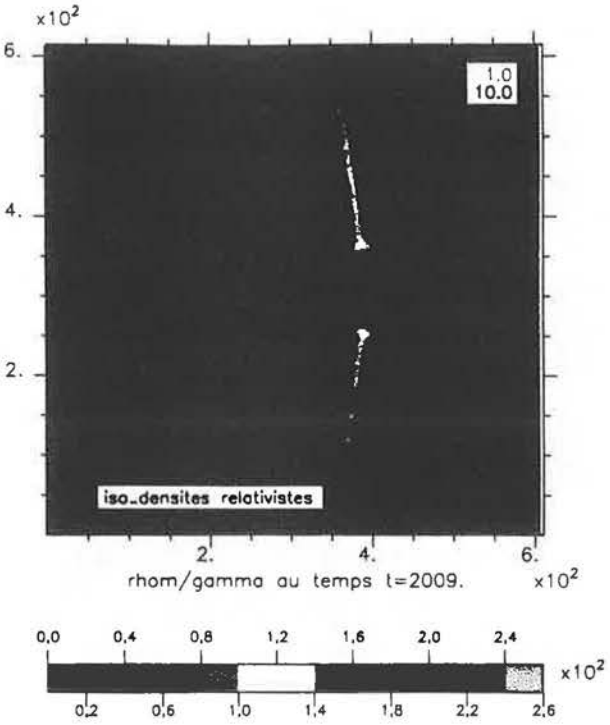
x10²
6.
4.
2.
1.0
10.0
iso_densites relativistes
2.
4.
6.
x10²
rhom/gamma au temps t=2009.
0,0 0,4 0,8 1,2 1,6 2,0 2,4
x10²
0,2 0,6 1,0 1,4 1,8 2,2 2,6

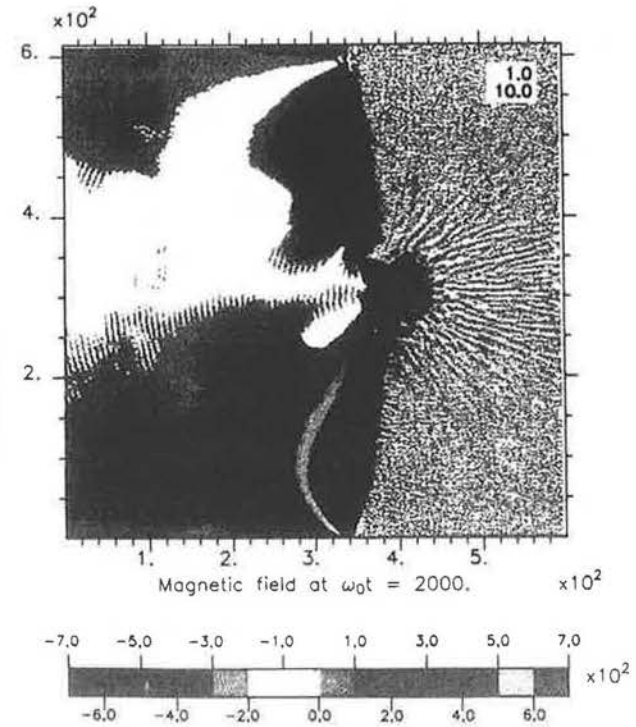
x10²
6.
4.
2.
1.0
10.0
1. 2. 3. 4. 5.
Magnetic field at ω₀t = 2000.
x10²
-7,0 -5,0 -3,0 -1,0 1,0 3,0 5,0 7,0
x10²
-6,0 -4,0 -2,0 0,0 2,0 4,0 6,0

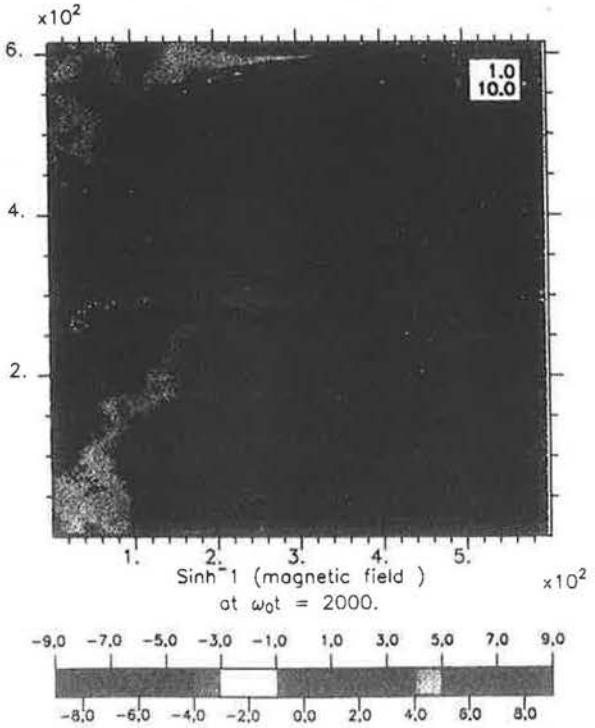
x10²
6.
4.
2.
1.0
10.0
1. 2. 3. 4. 5.
Sinh⁻1 (magnetic field)
at ω₀t = 2000.
x10²
-9,0 -7,0 -5,0 -3,0 -1,0 1,0 3,0 5,0 7,0 9,0
-8,0 -6,0 -4,0 -2,0 0,0 2,0 4,0 6,0 8,0

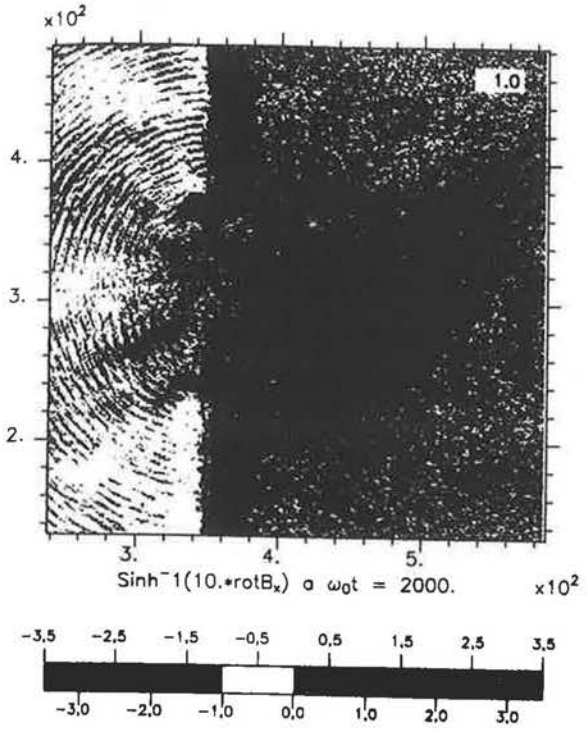
x10²
1.0
4.
3.
2.
3.
4.
5.
Sinh⁻1(10.*rotBx) a ω0t = 2000.
x10²
-3,5 -2,5 -1,5 -0,5 0,5 1,5 2,5 3,5
-3,0 -2,0 -1,0 0,0 1,0 2,0 3,0

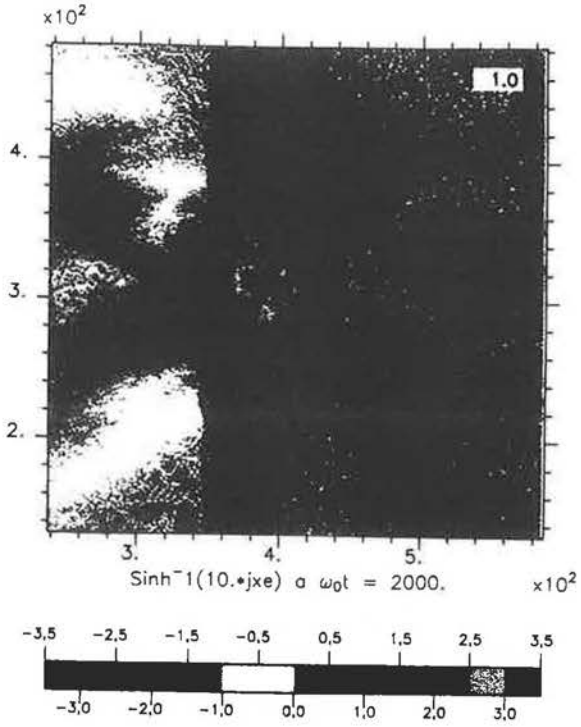
x10²
1.0
4.
3.
2.
3.
4.
5.
Sinh⁻1(10.*jxe) a ω0t = 2000.
x10²
-3,5 -2,5 -1,5 -0,5 0,5 1,5 2,5 3,5
-3,0 -2,0 -1,0 0,0 1,0 2,0 3,0

13

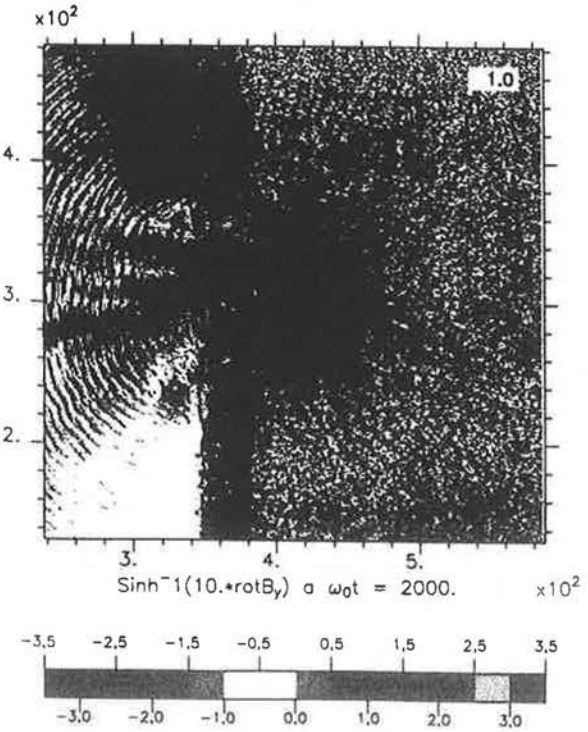
x10²
1.0
4.
3.
2.
3.
4.
5.
Sinh⁻1(10.*rotBy) a ω0t = 2000.
x10²
-3,5 -2,5 -1,5 -0,5 0,5 1,5 2,5 3,5
-3,0 -2,0 -1,0 0,0 1,0 2,0 3,0

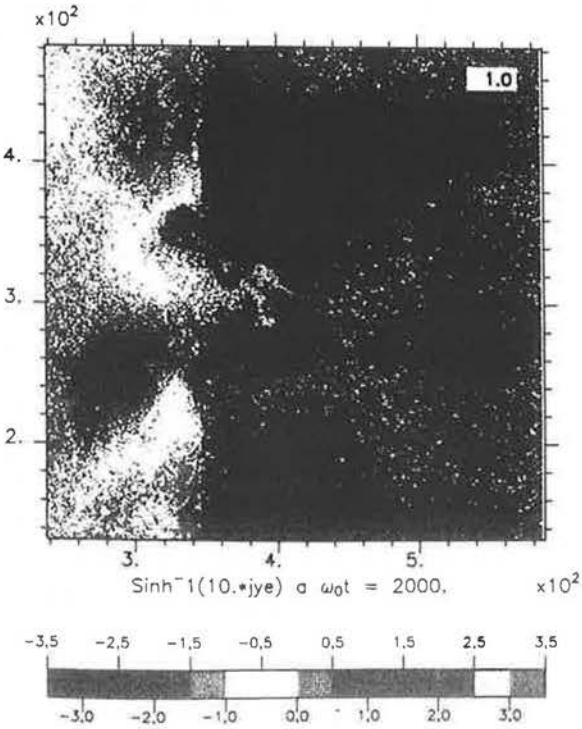
x10²
1.0
4.
3.
2.
3.
4.
5.
Sinh⁻1(10.*jye) a ω0t = 2000.
x10²
-3,5 -2,5 -1,5 -0,5 0,5 1,5 2,5 3,5
-3,0 -2,0 -1,0 0,0 1,0 2,0 3,0

14

Four Orders of Magnitude about magnetic fields

ω_0 $\lambda = 1\mu \sim 1.9\,10^{15}$ rd/s

$$\omega_{ce} = \frac{1.7}{\gamma}\,10^{15}\,B_{100\,MG}$$

$$r_L = \frac{\gamma\, m_0 v_T}{qB} = 0.17\,\gamma\left(\frac{v}{c}\right) B_{100\,MG}\,\mu$$

γ	1.2	1.6	3	7
T_e KeV	100	300	1000	3000
$\frac{v}{c}$	0.6	1.3	2.85	7
T_e	100	300	1000	3000

$\frac{v}{c}$	0.5	0.8	0.95	0.99
T_e	100	300	1000	3000

$r_L \sim 1\mu$ for $B = 100$ MG and $E_{cin} \sim 3000$ KeV

$r_L \sim 0.2\mu$ for $B = 100$ MG and $E_{cin} \sim 300$ KeV

15

Kinetic Pressure / Magnetic Pressure

$P_{cin} = nkT$

$T = 100$ KeV $= 10^9$ °K
$k = 1.38\,10^{-23}$ J/°K
$n_c = 10^{21}/cm^3 = 10^{27}/m^3$
$n = 100\,n_c = 10^{29}/m^3$

$P_{cin} = 1.38\,10^{15}$ N/m²

$P_{magnetic} = \frac{B^2}{2\mu_0}$ $\quad B = 100$ MG $= 10^{-4}$ T
$\mu_0 = 4\pi\,10^{-7}$

$P_{magnetic}\,/\,100\,MG = 4\,10^{14}$ N/m²

$P_{magnetic}\,/\,1000\,MG = 4\,10^{16}$ N/m² exceed P_{cin} even if $T_e = 1$ MeV !

16

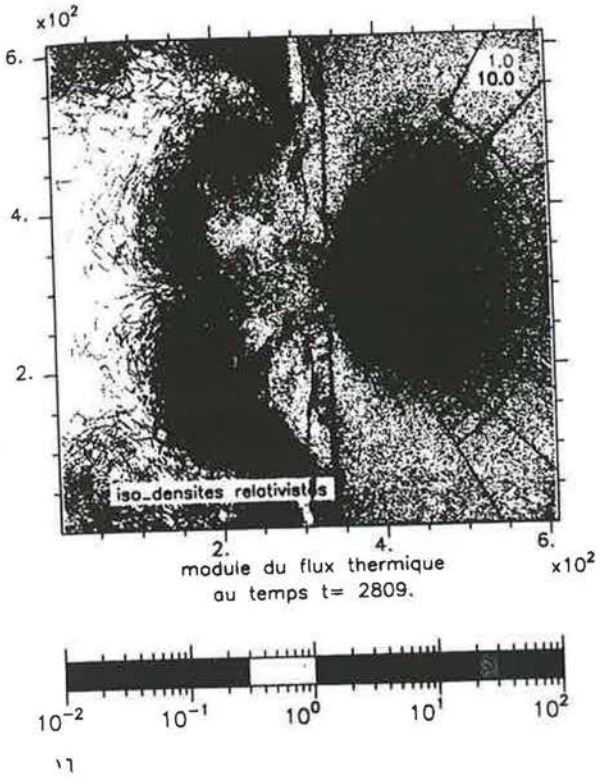

module du flux thermique
au temps t= 2809.

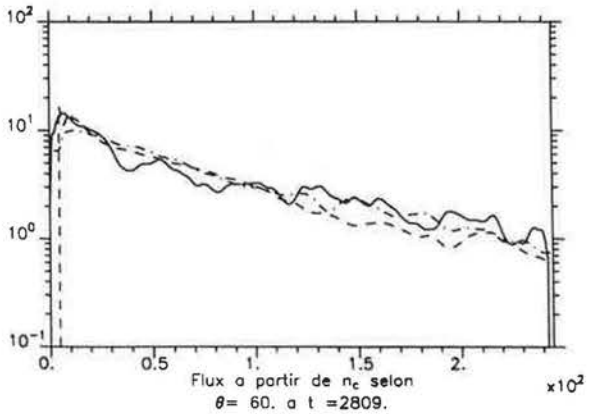

Flux a partir de n_c selon
θ= 60. a t =2809.

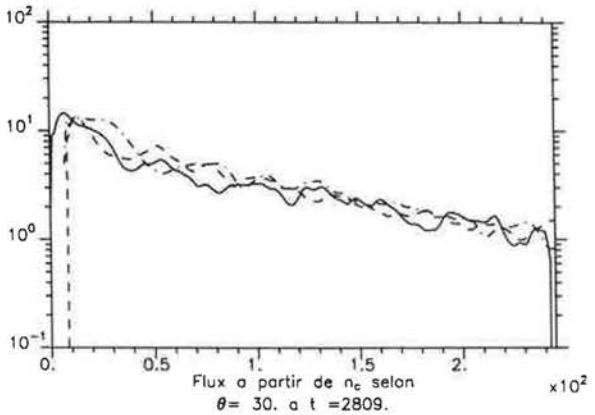

Flux a partir de n_c selon
θ= 30. a t =2809.

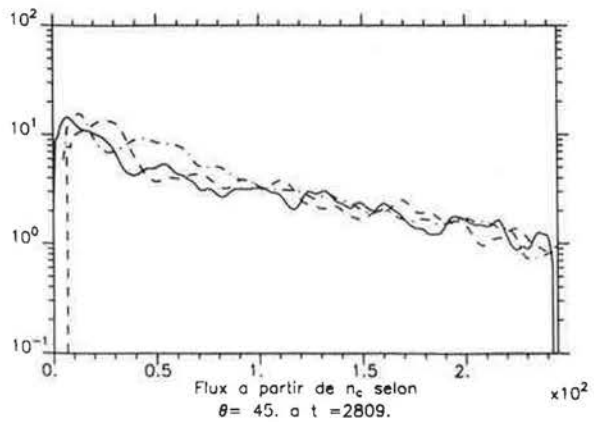

Flux a partir de n_c selon
θ= 45. a t =2809.

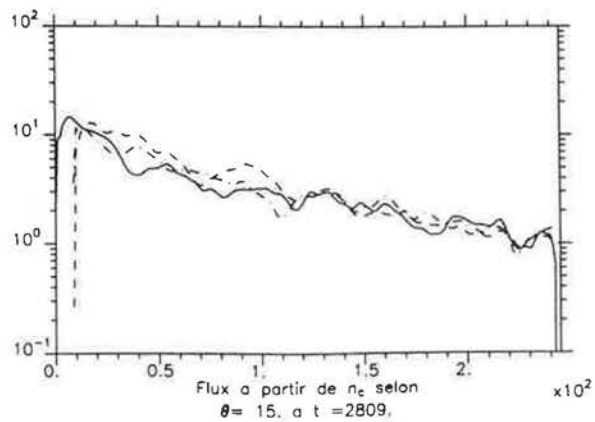

Flux a partir de n_c selon
θ= 15. a t =2809.

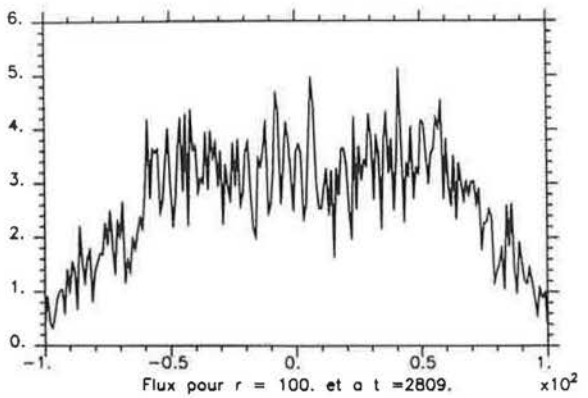
Flux pour r = 100. et a t =2809.
x10²

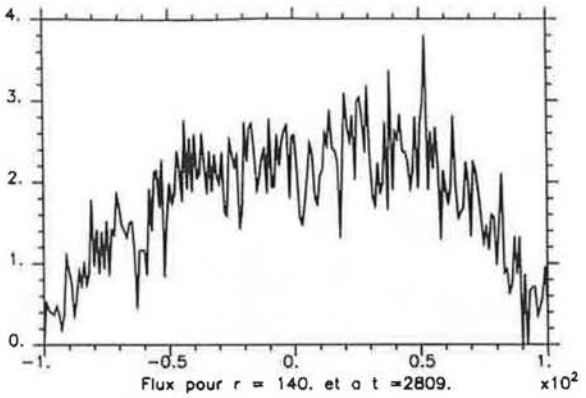
Flux pour r = 140. et a t =2809.
x10²

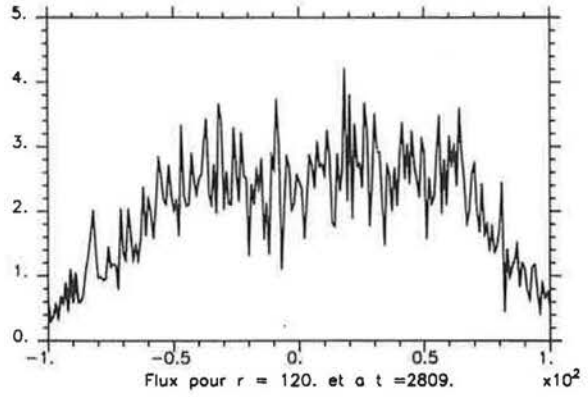
Flux pour r = 120. et a t =2809.
x10²

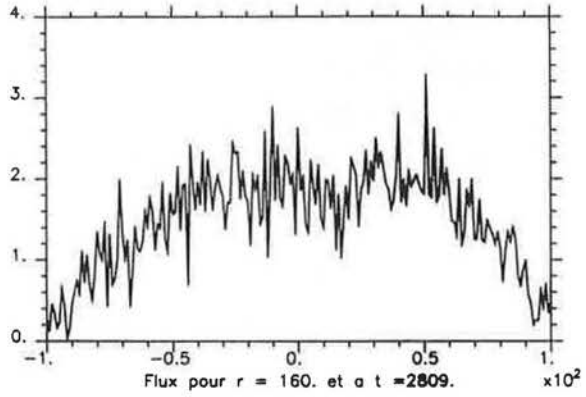
Flux pour r = 160. et a t =2809.
x10²

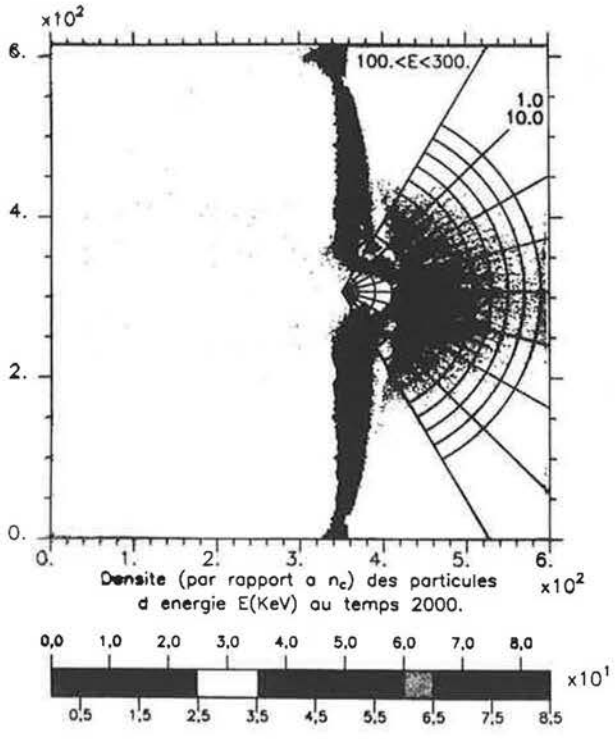
100.<E<300.
1.0
10.0
Densite (par rapport a nc) des particules
d energie E(KeV) au temps 2000.
x10²
x10¹

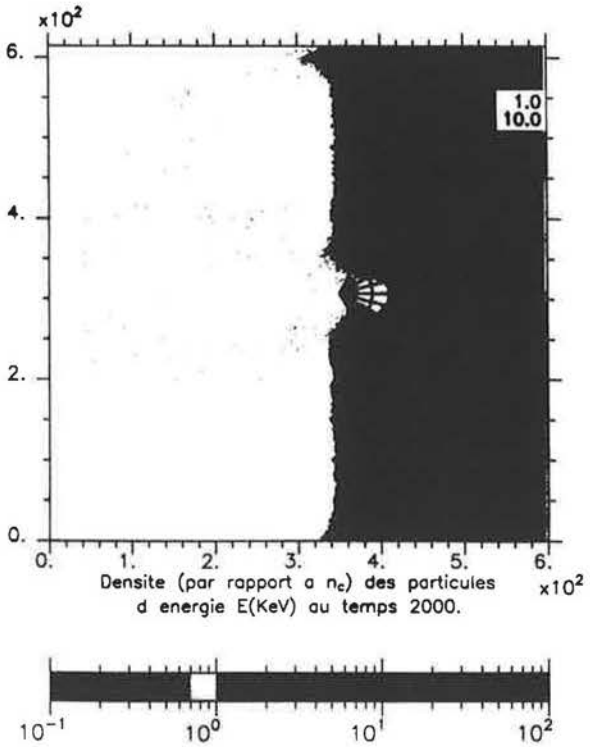
1.0
10.0
Densite (par rapport a nc) des particules
d energie E(KeV) au temps 2000.
x10²

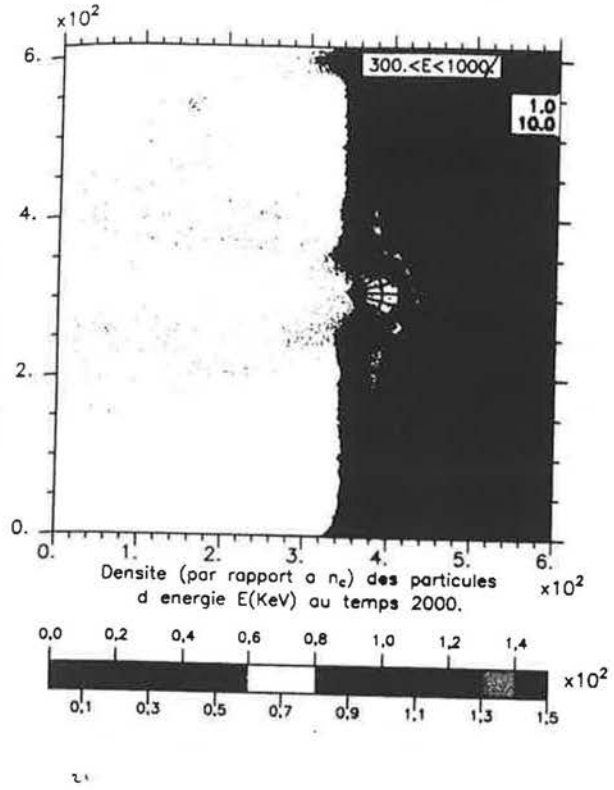
x10²
300.<E<1000.
1.0
10.0
Densite (par rapport a n_c) des particules
d energie E(KeV) au temps 2000.
x10²

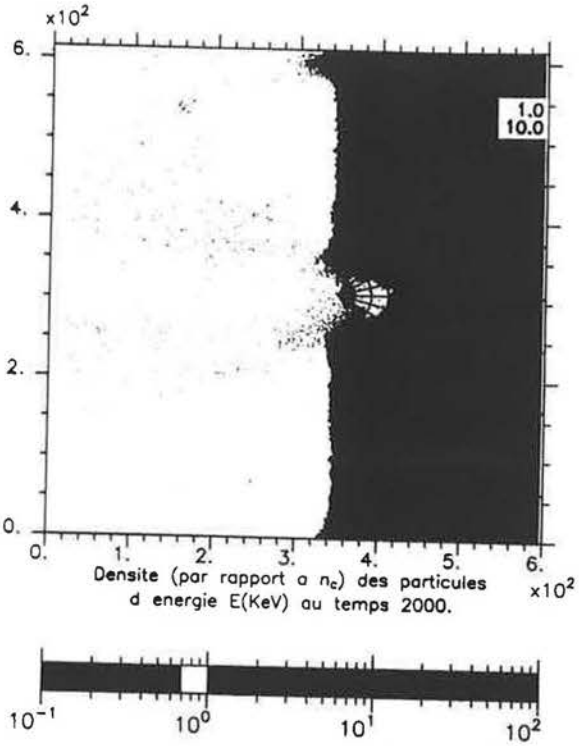
x10²
1.0
10.0
Densite (par rapport a n_c) des particules
d energie E(KeV) au temps 2000.
x10²

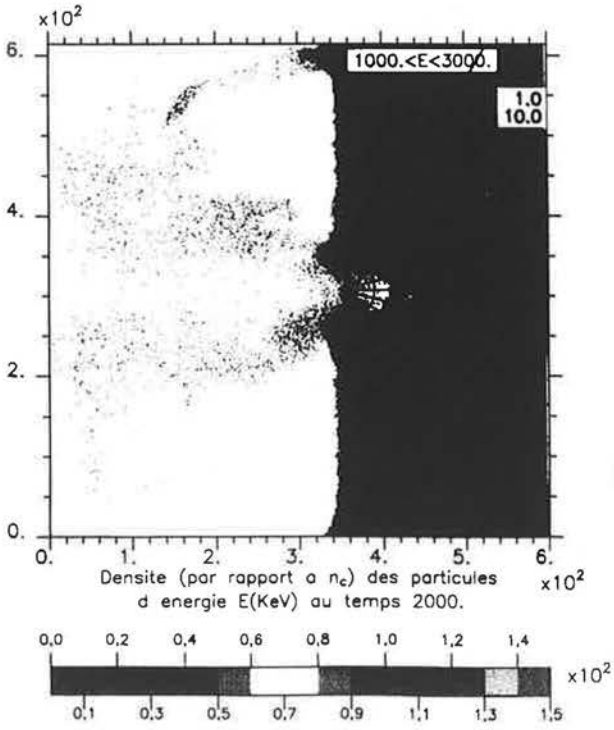
x10²
1000.<E<3000.
1.0
10.0
Densite (par rapport a n_c) des particules
d energie E(KeV) au temps 2000.
x10²

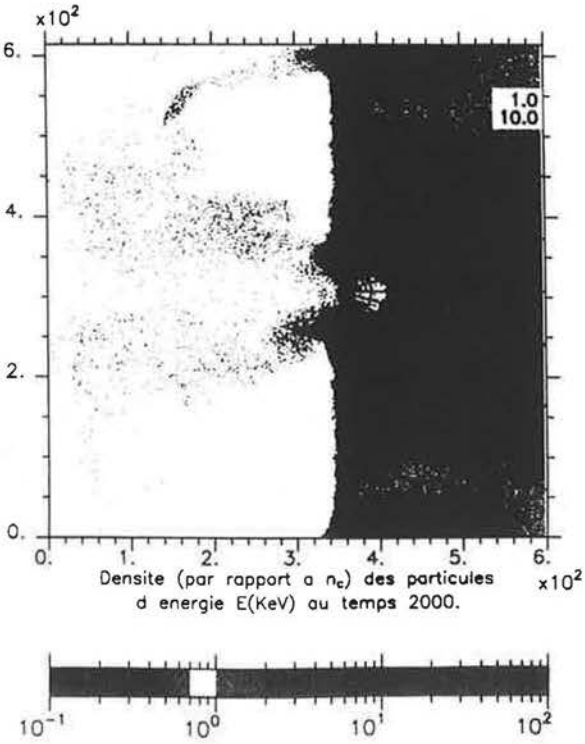
x10²
1.0
10.0
Densite (par rapport a n_c) des particules
d energie E(KeV) au temps 2000.
x10²

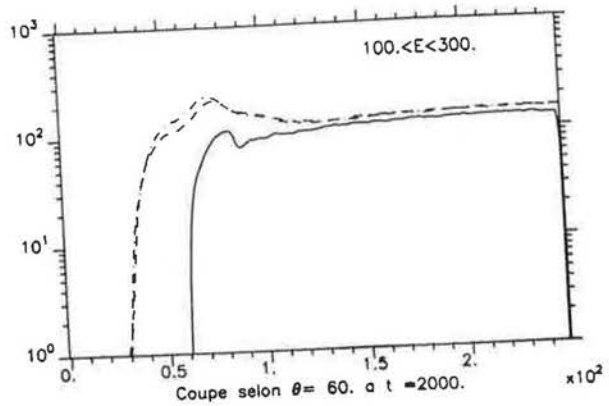
100.<E<300.
Coupe selon θ= 60. a t =2000.
x10²

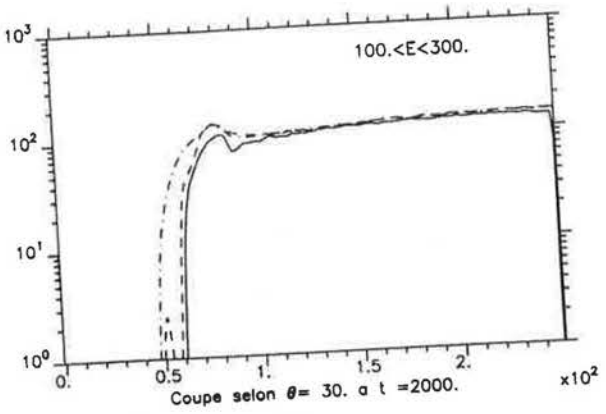
100.<E<300.
Coupe selon θ= 30. a t =2000.
x10²

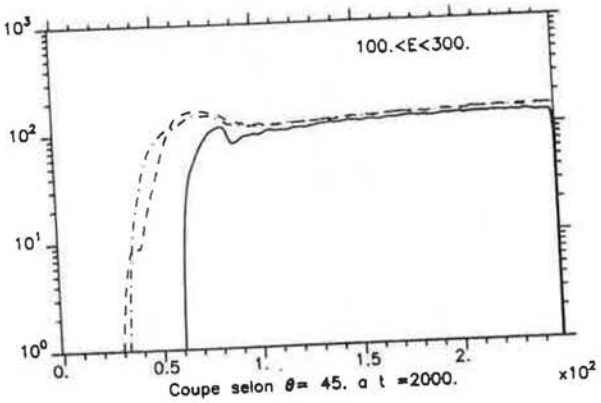
100.<E<300.
Coupe selon θ= 45. a t =2000.
x10²

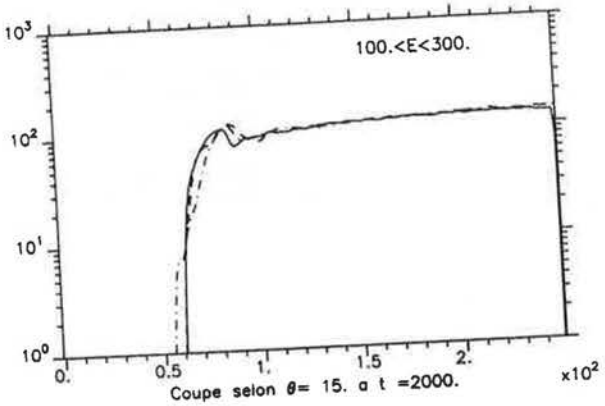
100.<E<300.
Coupe selon θ= 15. a t =2000.
x10²

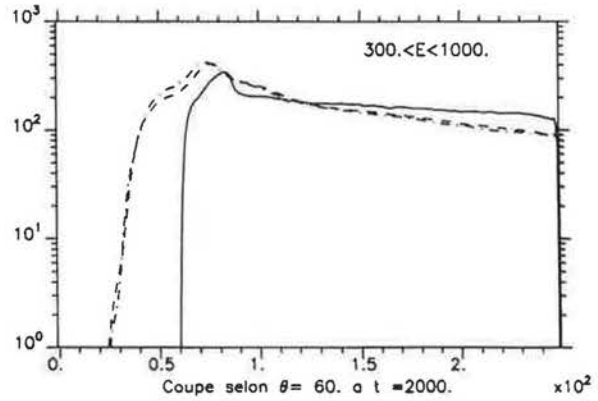
300.<E<1000.
Coupe selon θ= 60. a t =2000.
x10²

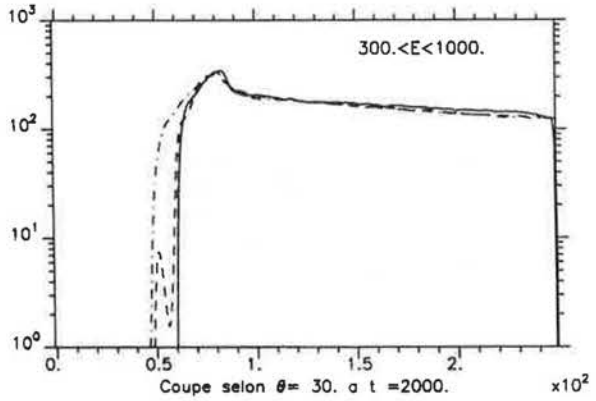
300.<E<1000.
Coupe selon θ= 30. a t =2000.
x10²

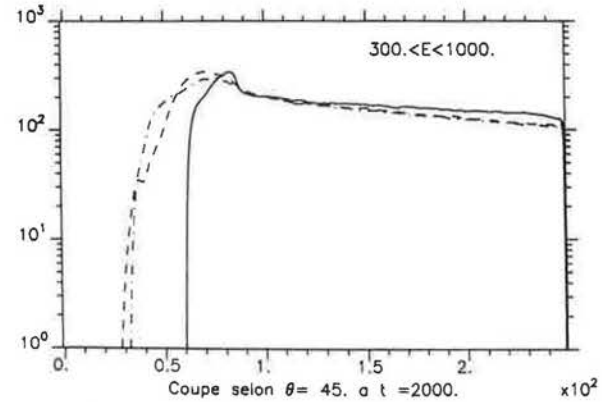
300.<E<1000.
Coupe selon θ= 45. a t =2000.
x10²

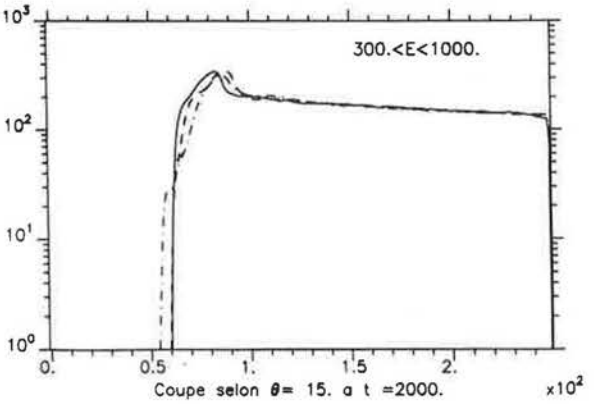
300.<E<1000.
Coupe selon θ= 15. a t =2000.
x10²

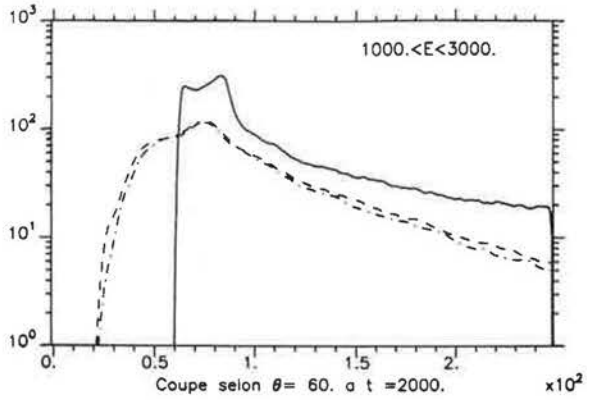
1000.<E<3000.
Coupe selon θ= 60. a t =2000.
x10²

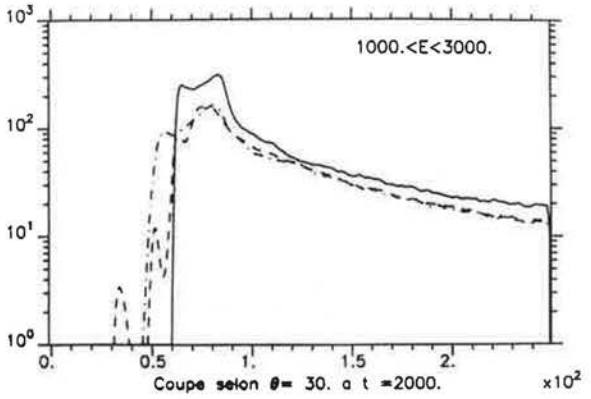
1000.<E<3000.
Coupe selon θ= 30. a t =2000.
x10²

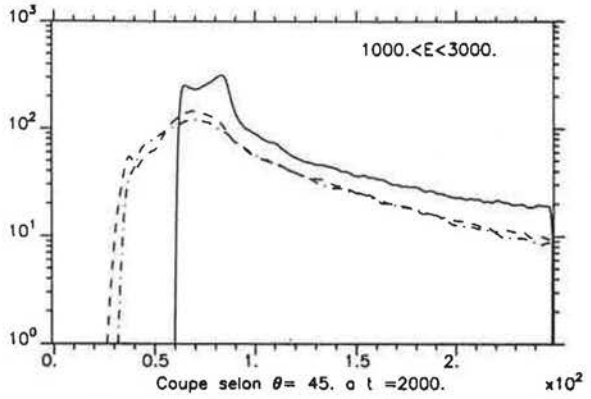
1000.<E<3000.
Coupe selon θ= 45. a t =2000.
x10²

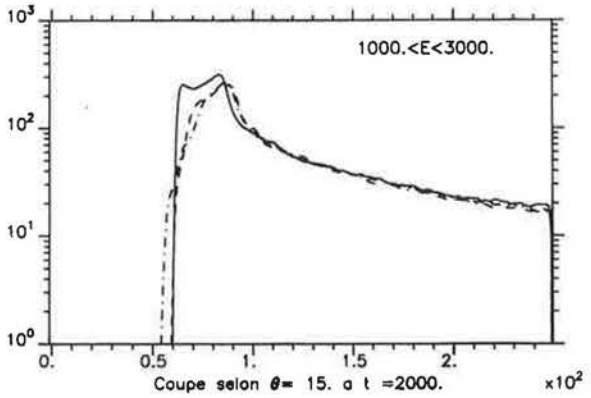
1000.<E<3000.
Coupe selon θ= 15. a t =2000.
x10²

Particle Simulation and Experiment on Plasma Jet Formation and Magnetic Field Generation

Y.Sentoku, H.Ruhl(1), K.Mima, R.Kodama and K.A.Tanaka(2)

Institute of Laser Engineering, Osaka University

(1) Theoretische Quantenelektronik, TH-Darmstadt

(2) Department of Electromagnetic Energy Engineering and Institute of Laser Engineering, Osaka University

Outline

ILE OSAKA

Experiment

Long-scale jet-like x-ray emission was observed in experiments on the interactions of 100 TW laser light with a long scale plasma.

Simulation

Two dimensional parallel PIC code has been used to analyze the experimetal results.

- Electron acceleration was investigated both for S- and P-polarization.
- Electrons are accelerated up to MeV outward in plasma corona.
- Strong quasi-static magnetic fields are generated and collimate out going high energy.

X-ray image with the large aperture pinhole camera showing a mm-scale jet-like emission.

ILE OSAKA

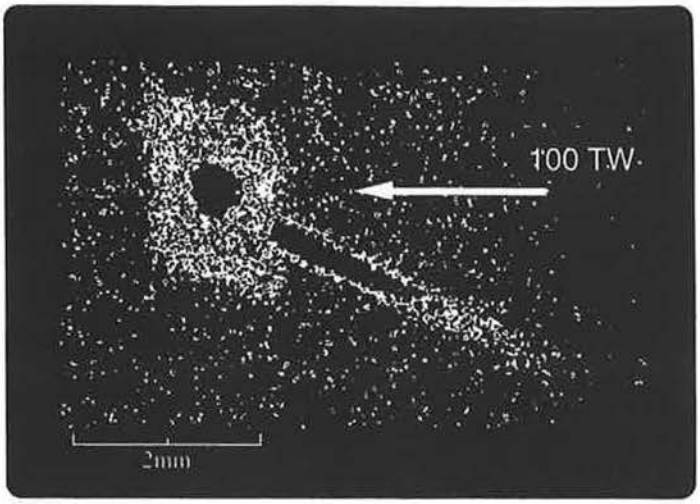

Experimental parameter

Power	100 TW
Pulse duration	0.5 psec

Preformed plasma created by 0.3 TW/100ps laser light.

X-ray image with the high-sensitive pinhole camera

ILE OSAKA

the target front veiw

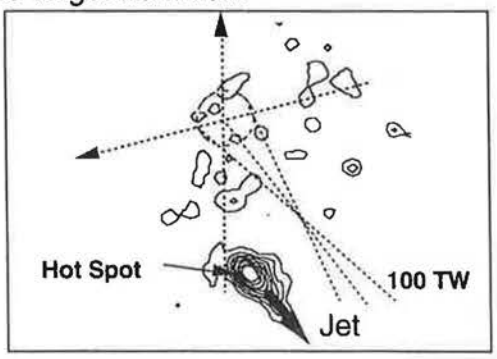

The position of the hot spot is far from the beam axis and out of the original focus con.

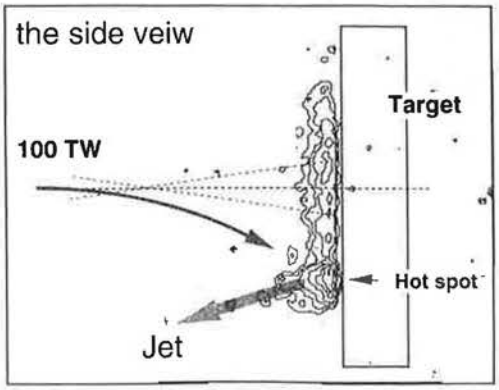

S-polarized 100 TW laser light was scattered in the preformed plasma and hit the target surface directly.

This jet-like emission was always appeared when the hot spot was observed on the target.

MeV-electron acceleration to the specular direction occurs in the case of S-polarized laser.

ILE OSAKA

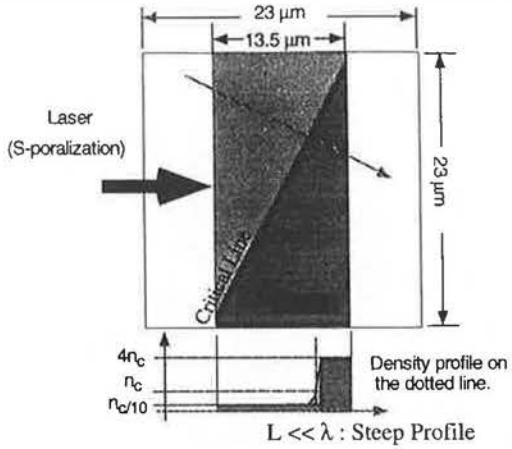

L << λ : Steep Profile

Initial Plasma

Temperature	10 keV
Peak density	4 n_c, $4.46 \cdot 10^{21}$ cm^{-3}
Ion spiecies	D^+

Laser parameter

Wave length	1 μm
Spot size	7 μm
Pulse shape	Gaussian
Intensity	$2 \cdot 10^{18}$
Angle of incidence	30 deg.

Simulation Time 200 fsec

These plots are time averaged in a laser cycle

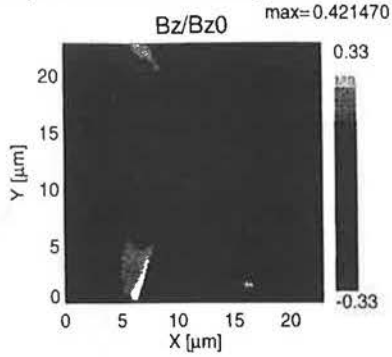

(a) quasistatic magnetic fields at 200 fsec

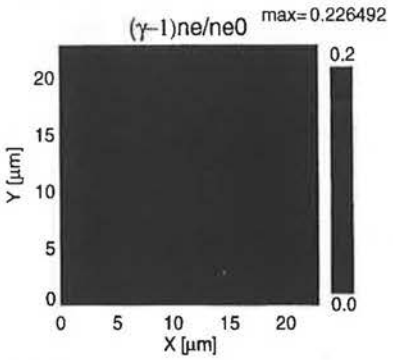

(b) Electron energy density at 200 fsec

The modulated reflected laser light accelarates electrons toward the specular direction

ILE OSAKA

S-polarized laser
Laser intensity $2 \cdot 10^{18}$ W/cm²
at 200 fsec

The laser is modulated in front of the critical surface, especially the reflected part.

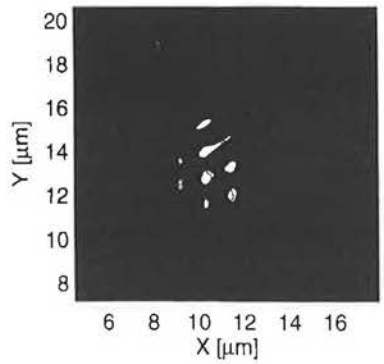

The instantenous plot of laser intensity with the electron energy density.

The high current density of electrons are genrated at the critical surface by the Brunel absorption mechanism

ILE OSAKA

P-polarized laser
Laser intensity $2 \cdot 10^{18}$ W/cm^2
at 120 fsec

(a)

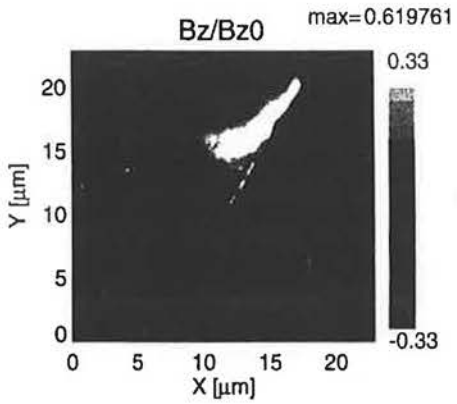

(b)

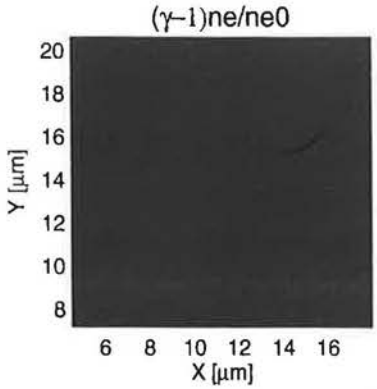

The quasi-static magnetic fields (a) and the electron energy density with the positve laser Bz fields (b). The average energy of jet electron is about 1.5 MeV and the quasi-static magnetic fields are up to 60 MG.

The outgoing electrons are extracted from the surface once in a laser oscillating period.

The angle of jet is 17 degree, smaller than the specular angle, 30 degree.

Scaling law for the angle of electron jets (P-polization Laser)

ILE OSAKA

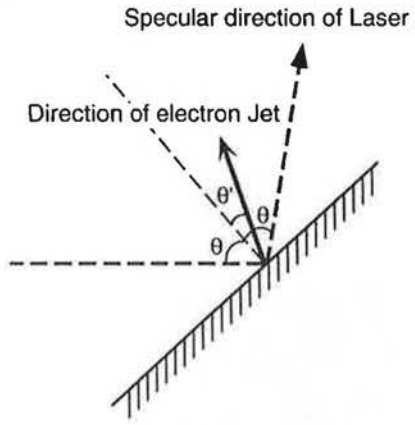

The kinetic energy of an electron : $(\gamma - 1)m_e c^2$

The momentum of an electron in the relativistic regime : $p \equiv \gamma m_e c$

The specular angle θ : $\sin\theta = \frac{k_{\parallel}}{k}$

The angle of jets θ' : $\sin\theta' = \frac{p_{\parallel}}{p}$

Since the parallel component of the canonical momentum along the plasma surface is always conserved, it is equal to the total momentum of the laser photons which interact with the electron.

The pararell component of momentum along the surface = The number of photons × The pararell component of photon momentum along the surface

$$p_{\parallel} = \frac{(\gamma-1)m_e c^2}{\hbar\omega} \cdot \hbar k_{\parallel}$$
$$= (\gamma-1)m_e c \cdot \frac{k_{\parallel}}{k} = (\gamma-1)m_e c \cdot \sin\theta$$

then, the angle of jets electron is given as following,

$$\sin\theta' = \frac{p_{\parallel}}{p} = \frac{\gamma-1}{\gamma}\sin\theta$$

For $2 \cdot 10^{18}$ W/cm^2, the averaged, not time averaged, enegy of bunched electrons is about 1.5MeV(γ=3), so θ'≈18 degree.This is the angle certainly observed electron jets at 120 fsec in PIC.

The electron jets are observed close to the specular direction in the case of higher intensity laser

ILE OSAKA

P-polarized laser
Laser intensity $2 \cdot 10^{19}$ W/cm^2
at 120 fsec

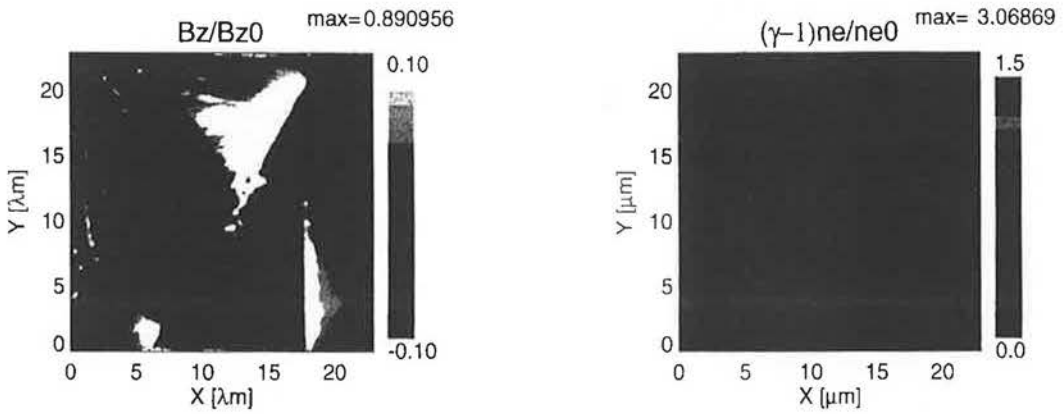

The time averaged electron energy density profile and the quasi-static magnetic fields.
The average energy of jet electron is up to $\gamma \approx 6$ and estimated angle is 28.2 degree, close to the specular direction.
The quasi-static magnetic fields are growing up to about 250 MG.

Without the corona plasma, no jets electron are observed.

ILE OSAKA

P-polarized laser
Laser intensity $2 \cdot 10^{18}$ W/cm^2
at 120 fsec

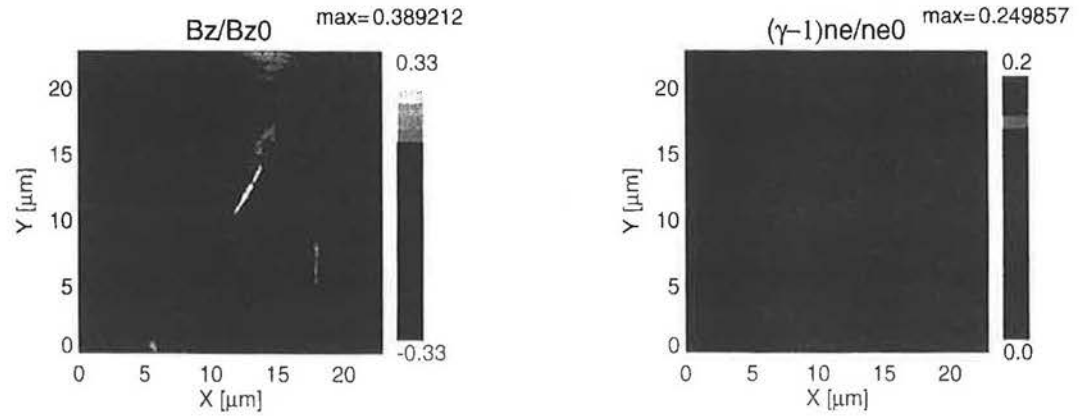

The time averaged electron energy density profile and the quasi-static magnetic fields.
The magnetic fields are localized on the critical surface and could'nt extend to outside.

Absorption efficiency and energy ratio of forward electrons to jets

ILE OSAKA

at the end of simulations.

	Absorption	Energy ratio (forward : jets)
P-pol	26.%	1.5 : 1
S-pol	7.8%	2.1 : 1

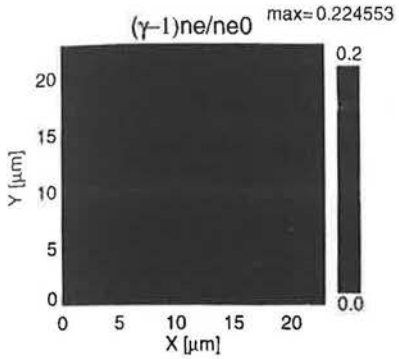

P-pol
at 120 fsec

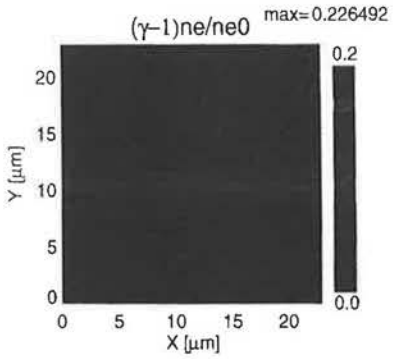

S-pol
at 200 fsec

In the overdense plasma, electrons run toward target normal direction for P-polarized laser and toward the laser incident direction for S-polarized laser.

The angular distribution of hard xray emission

ILE OSAKA

The hard xray emissions from hot electrons are evaluated in the PIC simulation. The photons, whose energy is from 1keV to 10MeV, are calculated.

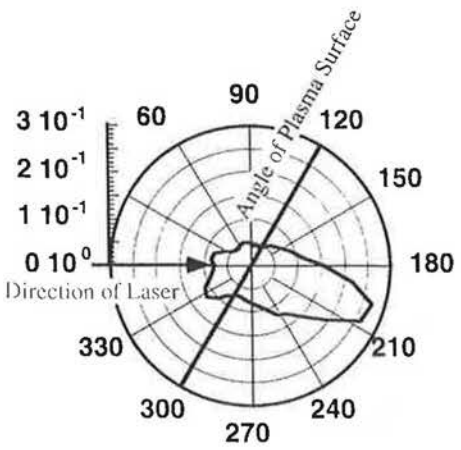

(a) for P-polarization

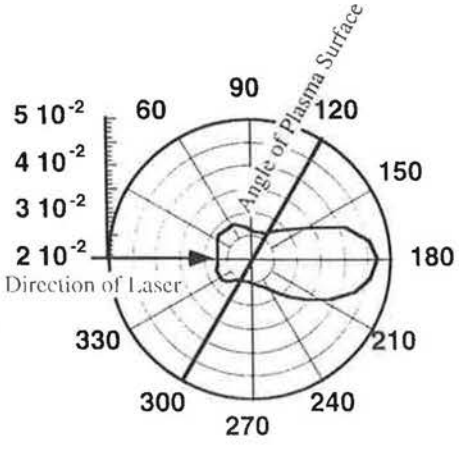

(b) for S-polarization

These plots are in the unit $10^{-29}/Z^2 n_i n_e$ W·cm^3.

The total emission power of S-polarized is 3 times smaller than the case of P-polarized.

Conclusions

ILE OSAKA

We have observed mm-scale jet-like x-ray emission in the direction of the specular reflected light at 100 TW laser plasma interactions.

Two dimensional PIC code have been performed to demonstrate the electron jets formation and quasistatic magnetic fields.

- Collimated electrons could be emitted from an overdense target with a low density plasma corona.

  P-pol. : Brunel absorption mechanism
  S-pol. : Ponderomotive force of the modulated reflected laser light

- Electron jets are propagating throgh the plasma with the guide of the quasi-static magnetic fields.

- P-polarized laser accelarate electrons into the overdense plasma toward the target normal direction.
  This is the good news for the fast ignitor!!

Optimum particle range for triggering fast ignition

A. R. Piriz and M. M. Sánchez *
E.T.S.I. Industriales, Universidad de Castilla-La Mancha
13071 Ciudad Real, Spain

PACS numbers: 52.58.Ns; 52.50 Jm; 28.52.Cx

Abstract

An analytic model for the dynamics of fast ignition is developed for the case in which the particle beam heats the fuel by generating a supersonic heat wave. It shows that the beam energy and intensity required for ignition increase with the particle range R. These results, together with previous ones for the subsonic regime of heating, allow for the determination of an optimun particle range value ($R \approx 0.25\ g/cm^2$). By decreasing the range below this value the ignition energy no longer decreases.

*Fellow of Junta de Comunidades de Castilla-La Mancha (U.C.L.M.)

To be published in Phys. Plasmas

I. INTRODUCTION

Fast ignition has been recently proposed as an alternative to the traditional central ignition concept currently considered in target design.[1] Although it is still in a rather speculative phase, fast ignition has attracted considerable attention essentially due to its potential capability to yield a higher energy gain than the central ignition. In such a scheme, the fuel is first ablatively imploded and, at a time close to maximum compression, a hot spot is created by heating a small part of the fuel directly with a particle beam. Because of the small size of a typical hot spot, which is of the order of 100 μm, a beam of relativistic electrons appears as the most suitable candidate for triggering fast ignition. Nevertheless, a couple of simulation studies have considered a 15 GeV Bi ion beam of range $R = 0.6\ g/cm^2$.[2,3] Regardless of the feasibility of using heavy ion beams for the generation of a hot spot, those investigations are relevant for understanding the fast ignition physics. Indeed, it only depends on the fuel density ϱ_0 and on the parameters which characterize the beam, namely, the beam focal spot r_0, intensity S_0 and energy E_0, and the particle range R.

Apart from the previous studies in which the beam energy and intensity required for ignition were addressed for a particle range $R = 0.6\ g/cm^2$, no further attempt has been done for understanding the scaling laws that rule the fast ignition dynamics. In fact, most of the work following the proposal by

Tabak et al.[1] have dealt with the problem of the beam propagation through the ablative corona surrounding the compressed fuel.[4-6] In spite of the fact that this is clearly a very important issue for fast ignition, it is also of interest to assess the dependence of the ignition energy and the beam intensity on the particle range. We have recently shown that, for a given range $R \geq 0.2 - 0.3\ g/cm^2$, the ignition energy is a minimum when the fuel heating proceeds subsonically.[7] Besides, we have found that this minimum energy E_{0m} decreases with the range as $E_{0m} \propto R^2$. However, for a range $R \leq 0.25\ g/cm^2$, the heating process becomes supersonic and the model developed in Ref. [7] breaks. Thus, it remains the concern regarding the behaviour of fast ignition for relatively small values of the range. In particular, it is of interest to analize the posible existence of a lower limit for the particle range below which the ignition energy cannot be further reduced.

In order to set the existence of such an optimum range, the supersonic regime of heating has to be studied. In this work we present an analytic model for the ignition of a precompressed fuel which is supersonically heated by a particle beam. We see that, for a range $R > 0.25\ g/cm^2$, the energy and intensity for ignition are higher than those required in the case of subsonic fuel heating, in agreement with the conclusions of Ref. [7]. Besides, the minimum ignition energy E_{0m} and intensity S_{0m} increase with the range as $E_{0m} \propto R^4$ and $S_{0m} \propto R^2$, respectively. The minimum values are achieved when the fuel is heated in a regime marginally sonic, for which the particle range is

$R \approx 0.25\ g/cm^2$. For a range shorter than such a value, the ignition energy becomes independent of R and, then, it no longer decreases. Instead, by reducing the range below $R = 0.25\ g/cm^2$, the beam intensity S_{0m} increases again approximately as $S_{0m} \propto R^{-2}$. Therefore, optimum conditions for fast ignition are found to occur for $R \approx 0.25\ g/cm^2$ when the fuel is heated in a sonic regime.

II. IGNITION MODEL FOR A SUPERSONICALLY HEATED FUEL

We consider a precompressed DT fuel of density ϱ_0 which is driven to ignition by directly heating it with a particle beam of focal spot r_0, particle range R and beam intensity S_0, so that the fuel heating proceeds in a supersonic regime. That is, a supersonic thermal wave is launched from the region directly irradiated by the particle beam and it heats the surrounding matter. In these circumstances, no change in the fuel density ϱ takes place during the heating ($\varrho = \varrho_0$). As in previous models,[8] we assume that ignition will be achieved if, at the end of the beam power pulse, the number of fusion reactions is so high that the power deposited into the fuel by the alpha particles is able to sustain the fuel temperature. Therefore, the volumetric rate of heating by alpha particles w_α must compensate for the energy loss from the hot spot:[7,8]

$$w_\alpha \geq w_B + p\vec{\nabla}.\vec{v} + \vec{\nabla}.\vec{q_T}\ , \qquad (1)$$

where

$$w_\alpha \left(\frac{erg}{s.cm^3}\right) = A_\alpha < \sigma v > \varrho_0^2 \,, \quad A_\alpha = 8 \times 10^{40} \,. \tag{2}$$

Here ϱ_0 is in g/cm^3, and the Maxwellian average reactivity $< \sigma v >$ for DT[9] is in cm^3/s. Besides, $p = (2/3)\varrho_0 \epsilon$ is the hot fuel pressure, $\epsilon = 3kT/A_{DT}m_p$ is the specific internal energy, T is the temperature, k is the Boltzmann constant, $A_{DT} = 2.5$ is the fuel mass number and m_p is the proton mass. The term $p\vec{\nabla}.\vec{v}$ represents the mechanical work performed as the thermal wave propagates outwards from the region directly heated by the beam. On the other hand, $\vec{q_T}$ is the thermal conduction flux:

$$\vec{q_T} = -\chi \epsilon^{5/2} \vec{\nabla} \epsilon \,, \quad \chi = 3.82 \times 10^{-34} \; g.s^4.cm^{-6} \,, \tag{3}$$

(if the Coulomb logarithm is $ln\Lambda = 5$); and w_B is the volumetric rate of energy loss by emission:

$$w_B \left(\frac{erg}{s.cm^3}\right) = A_B \varrho_0^2 \epsilon^{1/2} \,, \quad A_B = 9 \times 10^{15} \,, \tag{4}$$

where ϱ_0 is in g/cm^3 and ϵ is in erg/g.

If the alpha particles are completely deposited within the hot spot, we can perform an approximate integration of Eq.(1) over the hot spot volume. Such a volume is demarcated by the position of the heat wave at the ignition time and, therefore, thermal conduction can be neglected in the energy balance. Nevertheless, thermal conduction drives the heat wave and it has to be taken into account for the description of its motion. With these considerations, the

integration of Eq.(1) yields:

$$\left(A_\alpha < \sigma v > - A_B \epsilon^{1/2}\right) \varrho_0^2 \pi r_{hs}^3 \geq p v 3 \pi r_{hs}^2 \,, \tag{5}$$

where we have assumed that the hot spot is a cylinder of radius and length equals to r_{hs}, and v is the velocity of the heat wave at the ignition time. Since it is driven by thermal conduction, we can find a relationship between the heat wave velocity and the fuel temperature by considering that the heat wave motion is governed by a self-regulating mechanism for the characteristic length of the temperature gradient $l_T = \epsilon / |\vec{\nabla} \epsilon|$.[7,10] According to this mechanism, the length l_T must be of the order of the heated region size r. We will take $l_T \approx r/2$ and then, we can write:[7,10]

$$l_T = \frac{\chi \epsilon(t)^{7/2}}{p v(t)} \approx \frac{r}{2} \,, \tag{6}$$

where $\epsilon(t)$ is the instantaneous value of the specific internal energy, and $v(t) = dr/dt$ and $r = r(t)$ are, respectively, the instantaneous velocity and position of the heat wave at a time t before ignition. Using Eq.(6) when $r = r_{hs}$ and introducing it into Eq.(5) we obtain the following ignition condition:

$$H = Rx \geq \left(\frac{6\chi \epsilon^{7/2}}{A_\alpha < \sigma v > - A_B \epsilon^{1/2}}\right)^{1/2} \,, \tag{7}$$

where $H = \varrho_0 r_{hs}$ represents the inertial confinement fusion (ICF) parameter of the hot spot and $x = r_{hs}/r_0$. Actually, the ignition region is limited by the condition that, at igniton, the heat wave velocity v must be larger than the sound velocity $c \approx \epsilon^{1/2}$. We can calculate the velocity of the heat wave

by considering the self-regulating process expressed by Eq.(6). Then, in the supersonic regime, we have:

$$v > \epsilon^{1/2} \quad , \quad H < 3\chi\epsilon^2 \, . \tag{8}$$

In Fig.1 we have represented the ignition region delimited by Eqs.(6) and (8). As it can be seen, the minimum requirements correspond to the sonic limit for which $H \approx 0.27\ g/cm^2 = H_m$ and $T \approx 13\ keV = T_m$. This ignition region also determines the energy necessary to reach the ignition:[1-3,7]

$$E_0 = m\epsilon = \frac{\pi H^3 \epsilon}{\varrho_0^2} \, , \tag{9}$$

where $m = \varrho_0 \pi r_{hs}^3$ is the hot spot mass and, since ignition takes place for $T \geq 13\ keV$, we have neglected the energy loss by bremsstrahlung emission. This energy is a minimum just in the sonic limit. Similarly, we can consider that during the heating process, the beam energy is converted into fuel internal energy:

$$W_0 t = m(t)\epsilon(t) \, , \tag{10}$$

where $W_0 = \pi r_0^2 S_0$ is the beam power and $m(t) = \pi r^3 \varrho_0$ is the instantaneous mass of the heated region. In this way, the fuel temperature can be found from Eqs.(6) and (10):

$$\epsilon(t) = \epsilon_0 \frac{\left[(r/r_0)^{19/2} - 1\right]^{2/7}}{(r/r_0)^3} \quad ; \quad \epsilon_0 = \left(\frac{7}{57}\frac{S_0 R}{\chi \varrho_0}\right)^{2/7} \, . \tag{11}$$

At the ignition time, $r = r_{hs}$, $\varrho_0 r = \varrho_0 r_{hs} = H$ and $\epsilon(t) = \epsilon$, and these magnitudes are related through Eq.(7) [with the restriction imposed by Eq.(8)].

Therefore, the beam intensity S_0 results from Eq.(11):

$$\frac{S_0}{\varrho_0} = \frac{57}{7}\frac{\chi\epsilon^{7/2}}{R}\frac{x^{21/2}}{x^{19/2}-1} \, . \tag{12}$$

Notice that in Eq.(12) the specific internal energy ϵ of the fuel at ignition is given by Eq.(7) as an implicit function of x. In Fig.2 we have represented the intensity needed for ignition as a function of $x = H/R$, for different ranges R. It shows that $H > R$ for any finite value of the beam intensity. This express the quite intuitive fact that we cannot ignite a region of size exactly equal to the particle range unless we heat it instantaneously, that is, with an infinite intensity. Besides, we can see that for practically any interesting value of the range R, the minimum intensity S_{0m} corresponds to an ICF parameter H for which $x = 1.10 - 1.15$. For this optimun value of x, the ignition temperature, and thus the ignition energy, is determined by the particle range. In Fig.3, we have represented the minimum ignition energy E_{0m} as a function of the range, when the fuel is heated in a supersonic regime. For $R \approx 0.25\ g/cm^2$ the sonic limit is achieved and $H_m = 0.27\ g/cm^2$ and $T_m = 13\ keV$. For higher values of the range, the minimum energy increases with the range as $E_{0m} \propto R^4$ and the minimum intensity increases as $S_{0m} \propto R^2$. For $R < 0.25\ g/cm^2$ the beam energy E_{0m} remains constant and equal to the value corresponding to the sonic limit [$R \approx 0.25\ g/cm^2$, $E_{0m}(kJ) \approx 10/\varrho_*^2, \varrho_* = \varrho_0/(100\ g/cm^3)$]. Instead, the beam intensity S_{0m} increases again approximately as $S_{0m} \propto R^{-2}$. For comparison, we also show in Fig.3 the results of Ref. [7] for the subsonic

regime of heating. We can appreciate some differences for $R \sim 0.25\ g/cm^2$ between the energy given by the supersonic and the subsonic models. In fact, for such a range the heating proceeds in a regime marginally sonic and both models are expected to yield a rough approximation.

III. CONCLUDING REMARKS

On the basis of a relatively simple model for the ignition of a DT fuel mass which is supersonically heated by a particle beam, and from previous results which consider subsonic heating, we can set the existence of an optimun particle range R for triggering fast ignition. We find that such a value is around $0.25\ g/cm^2$ and it corresponds to a marginally sonic regime of heating. For larger values of R the ignition requires a higher energy, if the heating proceeds subsonically, and a higher energy and intensity if it proceeds supersonically. For ranges shorther than this optimum value, the ignition can only be achieved in a supersonic regime. In such a case, a higher intensity is necessary but the beam energy cannot be further reduced.

A more precise value of this optimum range should be assessed by numerical simulations but the present model show that a range between 0.2 and $0.3\ g/cm^2$ may be reasonable. In any case, more important than its exact value is the result that this optimum has to exists and it corresponds to a marginally sonic regime of heating. The existence of this optimum range arises essentially from the requirement that a minimum value of the ICF parameter H_m is needed in order to reach ignition. Thus, if the particle beam heats directly a region of smaller size ($R < H_m$) the ignition will not occur until the thermal conduction propagates the heating to a region of size H_m. Furthermore, ignition will not take place if the minimum energy determined by H_m and T_m is not transferred to the fuel. Conversely, if $R > H_m$, a larger hot spot must be created and more energy is needed.

Finally, it may be worth to point out that the range $R = 0.6\ g/cm^2$ has been suggested in Ref. [3] as the optimum value for fast ignition. But it cannot be confirmed by the present study.

ACKNOWLEDGMENTS

This work was partially supported by the Comisión Interministerial de Ciencia y Tecnología of Spain (PB96-0127).

References

[1]M. Tabak, J. Hammer, M. E. Glinsky, W. L. Kruer, S. C. Wilks, J. Woodworth, E. M. Campbell, M. D. Perry and R. J. Mason, Phys. Plasmas **1** 1626 (1994).

[2]A. Caruso and V. A. Pais, Nucl. Fusion, **36**, 745 (1996).

[3]S. Atzeni and M. L. Ciampi, Nucl. Fusion,**37**, 1665 (1997).

[4]R. Kodama, K. Takahashi, K. A. Tanaka, M. Tsukamoto, H. Hashimoto, Y. Kato, K. Mima, Phys. Rev. Lett. **77**, 4906 (1996).

[5]P. E. Young and P. R. Bolton, Phys. Rev. Lett. **77**, 4556 (1996).

[6]G. Bonnaud and E. Lefebvre, Phys. Rev. Lett. **74**, 2002 (1995).

[7]A. R. Piriz and M. M. Sanchez, Phys. Plasmas **5**, 2721 (1998).

[8]A. R. Piriz, Nucl. Fusion **36**, 1395 (1996).

[9]S. Hively, Nucl. Technol. /Fusion **3**, 199 (1983).

[10]A. R. Piriz and F. G. Tomasel, Phys. Rev. A **45**, 8787 (1992).

FIGURE CAPTIONS

- **Fig.1** Ignition region for a supersonically heated DT fuel mass.
- **Fig.2** Beam intensity S_0 as a function the dimensionless hot spot size $x = H/R$ for different ranges R.
- **Fig.3** Minimum beam energy E_{0m} times ϱ_*^2, and intensity S_{0m} divided by ϱ_* as functions of the particle range R for supersonic heating (label a) and for subsonic heating (label b).

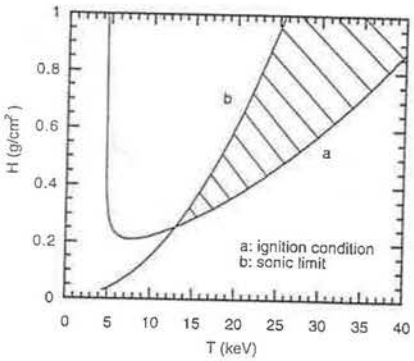

PIRIZ / SANCHEZ
Fig. 1

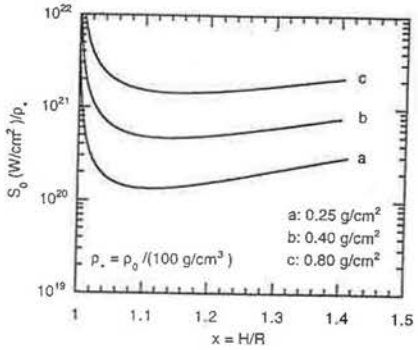

PIRIZ / SANCHEZ
Fig. 2

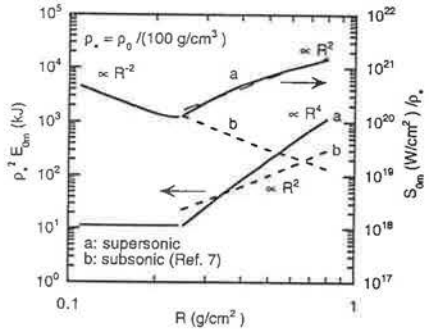

PIRIZ / SANCHEZ
Fig. 3

15

Analytic model for the dynamics of fast ignition

A. R. Piriz and M. M. Sánchez[a)]
E.T.S.I. Industriales, Universidad de Castilla—La Mancha, 13071 Ciudad Real, Spain

(Received 14 January 1998; accepted 6 April 1998)

A relatively simple model for the dynamics of fast ignitors is presented. The model describes the processes taking place when a precompressed fuel is heated by a particle beam (ions or electrons) characterized by its range R, and the focal spot and intensity of the beam. As a result, the ignition conditions are calculated in terms of such parameters and of the fuel density. The model provides scaling laws for the ignition energy and for the beam intensity in which the dependence on the particles range is included. Besides, it gives a simple interpretation of reported simulations and explains the apparent discrepancies between them and previous analytic estimations. The importance of using particles with $R \leqslant 0.3$ g/cm^2 turns out to be from the dependence of the ignition energy and the target gain on the range. © *1998 American Institute of Physics.*
[S1070-664X(98)01907-7]

I. INTRODUCTION

The economical feasibility of inertial confinement fusion (ICF) energy may depend on the possibility of finding new schemes requiring a relatively low driver energy for achieving ignition and high gain. Clearly, any alternative to the central ignition concept currently considered[1] has to appear today as highly speculative. However, the present confidence of the scientific community in the success of the National Ignition Facility[1] for demonstrating the scientific feasibility of the inertial fusion during the next decade may indicate that the time for proposing unconventional approaches is coming. Probably for such a reason, the fast ignition concept recently advanced by Tabak *et al.*[2] has attracted the attention of many researchers. Generally speaking, fast ignition consists of the formation of a hot spot by means of an electron beam that directly heats the deuterium–tritium (DT) fuel previously compressed during an ablative implosion. This method has the potential capability to yield higher-energy gain with lesser driver energy than the central ignition.

Following the proposal by Tabak *et al.*,[2] several numerical investigations have been reported that deal mainly with the physics of the hole boring in the corona of the ablatively imploded fuel.[3,4] Besides, Deutsch *et al.*[5] have addressed the important issue of the interaction physics of a relativistic electron beam (REB) with the precompressed fuel. As a result, they find that, for a REB with particle energy below 1.5 MeV impinging on a fuel target at 5 keV, the effective range is less than 0.3 g/cm^2.

On the other hand, a couple of two-dimensional (2-D) simulation studies have treated the ignition process when it is triggered by an ion beam of range $R = 0.6$ g/cm^2, which impinges on a DT fuel mass of density ρ_0.[6,7] Such studies have examined a 15 GeV Bi ion beam instead of a REB as in the Tabak *et al.*[2] proposal, but, since the only beam parameters relevant to the ignition physics are the particle range R, and the beam focal spot r_0 and intensity S_0, their results are of great interest for understanding the fast ignition dynamics. These results show that for $R = 0.6$ g/cm^2 the minimum beam energy required for ignition is much larger (a factor of 5) than that estimated in Ref. 2. Atzeni[7] has argued that this discrepancy is due to the ignition conditions assumed by Tabak *et al.*,[2] which would correspond to an isobaric fuel configuration (in Ref. 2 a hot spot temperature $T = 10$ keV and an ICF parameter $H = 0.4$ g/cm^2 have been used for calculating the ignition energy). Atzeni proposes somewhat more severe conditions that would result from an isochoric configuration: $T = 12$ keV, $H = 0.5$ g/cm^2.[7,8] Nevertheless, the observed discrepancy cannot be completely explained with such ignition parameters. Thus, 2-D effects are invoked,[7] although a physical discussion about the nature of these effects is not attempted. Besides, as those simulations are restricted to $R = 0.6$ g/cm^2, no insight of the scaling of the beam energy and intensity with the range R can be extracted. This scaling can be of importance to the light of the recent results obtained by Deutsch *et al.*,[5] and in order to set the adequate energy of the particles used to trigger the ignition.

Scaling laws, as well as a physical picture of the fast ignition dynamics, can be assessed more suitably by means of analytic models. In this paper we present a simple model for the description of the processes occurring when a precompressed DT fuel is driven to ignition by direct heating with a beam of particles. We find that in the regime of interest in which the beam energy required for ignition is a minimum, the fuel heating proceeds subsonically. So, the density in the hot spot region decreases, new mass is incorporated by ablation and a shock wave is launched into the cold fuel. Therefore, at the ignition time, the mass within the hot spot turns out to be larger than the mass directly heated by the beam. Besides, the hot spot temperature and density are determined by the beam intensity S_0 and the particle range R, for a given density ϱ_0 of the precompressed fuel. For the lowest intensities, the hot spot temperature is low, but its mass becomes considerably larger than the mass m_0 directly heated by the beam. Thus, ignition requires a relatively high

[a)]Fellow of Junta de Comunidades de Castilla—La Mancha (U.C.L.M.).

16

amount of energy. For the highest intensities, the hot spot mass is not much larger than m_0, but its temperature at ignition time is high. Again, the hot spot contains a relatively large amount of energy. There exists an intermediate situation for which the hot spot is driven to ignition with a minimum requirement of energy. In such a case, it has a moderate ignition temperature and a mass somewhat larger than m_0, both determined by the heating dynamics. This description provides a simple explanation of the simulation results and seems to show that 2-D effects are not relevant.

Finally, the ignition model is used for calculating the limiting gain by means of a modified Kidder model,[9,10] which includes a density jump $\delta=\varrho/\varrho_0$ between the hot spot of density ϱ and the surrounding cold fuel of density ϱ_0. We see that the energy gain depends on the particle range R through the ignition parameters of the hot spot, namely, T, H, and ϱ. For $R=1$ g/cm^2 it becomes a factor 2 lower than the estimated in Ref. 2 but, for $R=0.2$–0.3 g/cm^2, there is a good agreement.

II. THE IGNITION MODEL

We consider a mass of DT fuel that has been previously compressed to a high-density ϱ_0 and it is driven to ignition conditions by using a beam of charged particles (REB or ions) characterized by its focal spot radius r_0 and intensity S_0, and by the particle range R. For simplicity, we assume $r_0=R/\varrho_0$, as in the simulations of Refs. 6, 7. We will also assume that the heating proceeds subsonically, and we will see that, in this regime, a minimum beam energy is required for reaching ignition. Then, the beam heats directly a cylindrical volume of radius r_0 and mass $m_0=\pi r_0^3\varrho_0$, and the mass surrounding this volume is heated by thermal conduction. The thermal conduction drives an ablative wave, which is preceded by a shock wave launched into the cold fuel. The volume enclosed by the ablative wave contains the mass m_0 directly heated by the beam and the new mass incorporated by the ablation process that occurs in a tamped regime.[11,12] This volume defines the hot spot and it has a mean density $\varrho\leq\varrho_0$ and a temperature T. The ablation surface expands with a velocity v equal to the fluid velocity behind the shock wave, which is assumed to be a strong shock:[11,12]

$$v=\left(\frac{3p_a}{4\varrho_0}\right)^{1/2}, \tag{1}$$

where p_a is the ablation pressure and it is, in general, somewhat larger than the mean pressure $p=\frac{2}{3}\varrho\epsilon$ ($\epsilon=3kT/A_{DT}m_p$ is the specific internal energy, k is the Boltzmann constant, $A_{DT}=2.5$ is the fuel mass number, and m_p is the proton mass).[11] We will take $p_a=ap$ with $a\simeq 1.2$, and thus Eq. (1) reads as

$$v\simeq 0.77\epsilon^{1/2}\left(\frac{\varrho}{\varrho_0}\right)^{1/2}. \tag{2}$$

On the other hand, during the heating process, the hot spot loses energy by bremsstrahlung emission at the volumetric rate:

$$W_b=A_B\varrho^2\epsilon^{1/2}, \quad A_B\simeq 9\times 10^{15} \text{ erg s}^{-1}\text{ cm}^{-3}, \tag{3}$$

and fusion reactions occur that generate alpha particles at the volumetric rate:

$$W_\alpha=A_\alpha\langle\sigma v\rangle\varrho^2, \quad A_\alpha\simeq 8\times 10^{40} \text{ erg s}^{-1}\text{ cm}^{-3}, \tag{4}$$

where $\langle\sigma v\rangle$ is the Maxwellian average reactivity for DT, and we will adopt here the expression given in Ref. 13. The alpha particle's energy is considered to be deposited within the hot spot, contributing in this way to the heating process.[14]

In order to reach ignition, the power W_α deposited into the fuel by the alpha particles at the end of the power pulse has to be able to sustain the fuel temperature. For simplicity, we assume as in Ref. 14 that the alpha particle energy deposition rises to a relatively high value just close to the end of the beam pulse in order to ensure the transition from heating supported externally to the self-sustained alpha heating. Then, at the ignition time we require[14]

$$W_0\simeq\int_{V_{hs}} W_\alpha dV, \tag{5}$$

where W_0 is the beam power pulse and the integration extends over the total hot spot volume V_{hs}. Besides, ignition will occur if the volumetric rate W_α of heating energy deposited by the alpha particles compensates, at least, for the energy loss from the hot spot:[14,15]

$$W_\alpha\geq W_B+p\nabla\cdot\mathbf{v}+\nabla\cdot\mathbf{q}_T, \tag{6}$$

where $p\nabla\cdot\mathbf{v}$ represents the energy lost by expansion and $\mathbf{q}_T$ is the thermal conduction flux:

$$\mathbf{q}_t=\chi\epsilon^{5/2}\nabla\epsilon, \quad \chi=3.82\times 10^{-34} \text{ g s}^4\text{ cm}^{-6} \tag{7}$$

(if the Coulomb logarithm is $\ln\Lambda=5$).

Since the hot spot is composed by the mass $m_0$directly heated by the beam and by the mass incorporated by ablation, we perform an approximate integration of Eq. (6) separately for the mass m_0 and for the rest of the mass of the hot spot, respectively. Then, for the mass m_0 we assume that energy loss by expansion take place mainly through the free surface πr_0^2 and that it can be neglected in the other directions, where it is tamped by the ablated mass.[11] Therefore, integration of Eq. (6) over the mass m_0 yields

$$(A_\alpha\langle\sigma v\rangle-A_B\epsilon^{1/2})R\geq\tfrac{3}{2}\epsilon^{3/2}, \tag{8}$$

where we have assumed that the free surface expansion occurs to the sound speed $\epsilon^{1/2}$. Besides, taking into account that at ignition the alpha particles must sustain a uniform hot spot temperature, we have neglected the losses by thermal conduction from the mass m_0 toward the rest of the hot spot mass. Equation (8) gives a necessary condition for ignition, and it is satisfied, for a given particle range R, for a sufficiently high temperature. For instance, for $R=0.6$ g/cm^2 it turns out to be $T\geq 5$ keV.

In the same way, we obtain another necessary condition by integrating over the rest of the mass of the hot spot,

$$(A_\alpha\langle\sigma v\rangle-A_B\epsilon^{1/2})\varrho(m-m_0)\geq pv4\pi r^2, \tag{9}$$

where $m=\pi r^3\varrho$ is the total hot spot mass, r is the radius of the cylindrical region containing the hot spot, and we have assumed that its length is $z=r$. This is a reasonable assumption for the case we are studying in which $z_0=R/\varrho_0=r_0$,

and taking into account that, in the present situation of tamped ablation, the expansion velocity of the mass originally heated by the beam is much less than the ablation front velocity v.[11] Therefore, since the volume increase of the hot spot is dominated by the ablation front expansion we have $z-z_0\simeq r-r_0$, and then it turns out that $z\simeq r(z_0=r_0)$.

In writing Eq. (9) we have assumed, for simplicity, that the whole surface surrounding the hot spot expands with the same velocity v. Actually, a part of this surface, which is of the order of $\pi(r^2-r_0^2)$, faces the vacuum region and should be expected to expand with a velocity of the order of $\epsilon^{1/2}$. However, it can be checked *a posteriori* that the simpler expression used on the right-hand side of Eq. (9) gives a good account for the total energy lost by expansion.

In order to close the problem we need another relationship connecting the expansion velocity v with the fluid density ϱ behind the ablation front. As is well known, the propagation of a heat wave is governed by a self-regulating mechanism for the characteristic length of the temperature gradient $l_T=\epsilon/|\nabla\epsilon|$.[12] Such a length must be of the order of the dimensions of the heated region:

$$l_T=\frac{\chi\epsilon^{7/2}}{pv}\simeq\left(\frac{1}{r}+\frac{1}{z}\right)^{-1}\simeq\frac{r}{2}. \tag{10}$$

III. MODEL RESULTS

A. The minimum ignition energy and hot spot parameters

The previous set of equations allows for the calculation of the beam energy, of the parameters of the hot spot and of the ablation front velocity at ignition, in terms of the beam power W_0, its focal spot radius r_0, the particle range R, and the fuel density ϱ_0. In particular, the total power required for ignition can be obtained by adding Eqs. (8) and (9) and introducing the result into Eq. (5):

$$W_0\geq A_B\epsilon^{1/2}\varrho m+pv4\pi r^2\left[1+\frac{\epsilon^{1/2}}{4v}\left(\frac{r_0}{r}\right)^2\right]. \tag{11}$$

For the following calculations it is convenient to introduce the parameter $x^3=m/m_0$. Thus, we can write the ICF parameter of the hot spot $H=\varrho r$ in terms of x:

$$H=\left(\frac{\varrho}{\varrho_0}\right)^{2/3}Rx\simeq 1.42\frac{v^{4/3}}{\epsilon^{2/3}}Rx, \tag{12}$$

where we have used Eq. (2). Inserting this expression into Eq. (10), we find the velocity v of expansion of the ablation front:

$$v\simeq 1.38\left(\frac{x}{Rx}\right)^{3/7}\epsilon^{19/14}. \tag{13}$$

On the other hand, by introducing Eqs. (10) and (13) into Eq. (9) we obtain an implicit expression for the hot spot temperature in terms of the parameter x (for a given range R):

$$\frac{x^3-1}{x^{15/7}}\simeq\frac{1.7}{x^{1/7}R^{6/7}}\frac{\epsilon^{17/14}}{(A_\alpha\langle\sigma v\rangle-A_B\epsilon^{1/2})}. \tag{14}$$

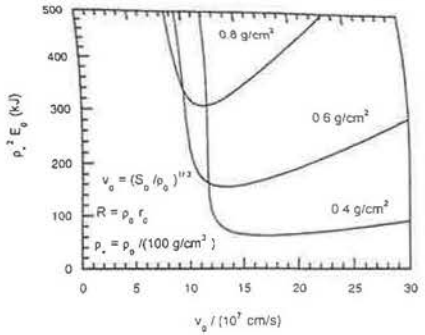

FIG. 1. Beam energy E_0 required for ignition times ϱ_*^2 as a function of the characteristic velocity $v_0=(S_0/\varrho_0)^{1/3}$, for different values of the ions range R. Here ϱ_* is a dimensionless fuel density and S_0 is the beam intensity.

In a similar way, we get the beam intensity $S_0=W_0/\pi r_0^2$ in terms of the parameter x from Eq. (11):

$$\frac{S_0}{\varrho_0}\simeq 3.2v^{5/3}x^2\epsilon^{2/3}\left(1+\frac{0.35}{x}\frac{v^{1/3}}{\epsilon^{1/6}}\right)+\frac{W_B}{\varrho_0\pi r_0^2}, \tag{15}$$

where

$$\frac{W_B}{\varrho_0\pi r_0^2}\simeq 0.53A_BRx\frac{v^{1/3}}{\epsilon^{7/6}}, \tag{16}$$

and v is given in terms of x and ϵ by means of Eq. (13). Note that Eqs. (15) and (16) determine the ratio S_0/ϱ_0 instead of the beam intensity S_0 and the density ϱ_0 separately. Then, we introduce the following characteristic velocity:[12]

$$v_0=\left(\frac{S_0}{\varrho_0}\right)^{1/3}, \tag{17}$$

and we will solve for the hot spot parameters in terms of v_0 through the parameter x such as it is given by Eq. (14). In particular, we find the hot spot energy as follows:

$$E_0=m\epsilon=\pi\frac{R^3}{\varrho_0^2}\epsilon x^3. \tag{18}$$

In Fig. 1 we have represented the product $E_0\varrho_0^2$ as a function of v_0 for different values of the range R. We can see that, for a given range, there exists a particular value of the ratio S_0/ϱ_0 for which the beam energy is a minimum. For the case $R=0.6$ g/cm^2 the following results:

$$E_0^{min}\simeq 155\left(\frac{100 \text{ g/cm}^3}{\varrho_0}\right)^2, \tag{19}$$

$$S_{0m}(\text{W/cm}^2)\simeq 2.5\times 10^{19}\left(\frac{\varrho_0}{100 \text{ g/cm}^3}\right). \tag{20}$$

These values are in good agreement with the simulation results of Refs. 6 and 7. As can be seen in Fig. 1, the energy required for ignition increases considerably for intensities lower than that given by Eq. (20). This is because the fuel

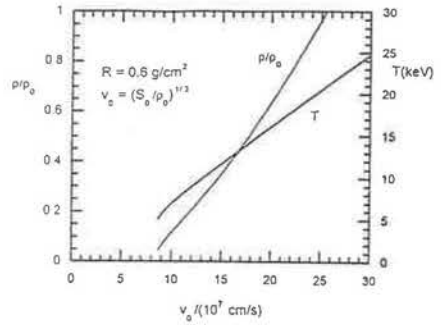

FIG. 2. Dimensionless hot spot density ϱ/ϱ_0 and temperature T as a function of the quantity $v_0=(S_0/\varrho_0)^{1/3}$, which represents the beam intensity, for $R=0.6$ g/cm^2.

heating proceeds relatively slowly, allowing for a long ablation time before ignition. Thus, although ignition occurs to the lowest temperature (Fig. 2), a relatively large amount of mass is incorporated by ablation (Fig. 3). Nevertheless, the hot spot temperature is always above the value imposed by Eq. (8), which is then satisfied automatically. This is shown in Fig. 2 for $R=0.6$ g/cm^2, where the hot spot temperature $T(T\geq 5$ keV) and the density ϱ have been represented.

For the highest intensities $S_0\geq S_{0m}$, the ignition energy increases again. In this case, the hot spot density is closer to ϱ_0 as the beam intensity rises (Fig. 2), and the heating may eventually become supersonic. The mass of the hot spot becomes slightly higher than m_0 (Fig. 3), but its temperature becomes rather high, and this fact leads again to a relatively high ignition energy. Then, in the regime in which a minimum beam energy is required for triggering the ignition, the fuel heating proceeds subsonically.

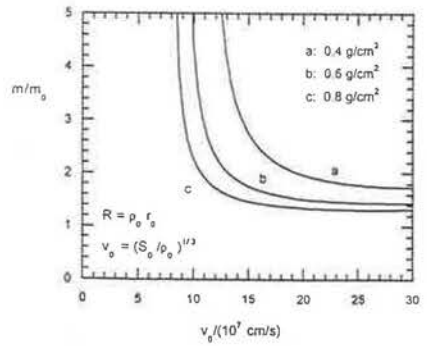

FIG. 3. Dimensionless hot spot mass m/m_0 as a function of $v_0=(S_0/\varrho_0)^{1/3}$ for different values of the particles range R.

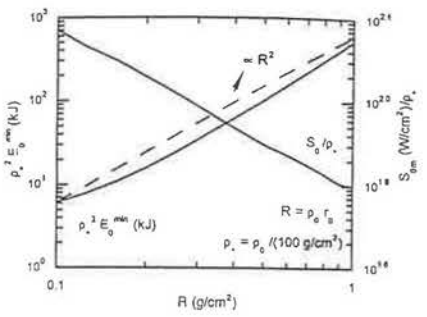

FIG. 4. Minimum beam energy E_0^{min} times ϱ_*^2, and intensity S_{0m} divided by ϱ_* as functions of the ions range R.

Figure 1 also shows that the minimum beam energy increases as the range does. However, because of the dependence on the range R of the hot spot mass [Eq. (14)], the scaling of the ignition energy is weaker than that expected by assuming a hot spot ICF parameter H proportional to R.[2] This is clearly seen in Fig. 4, where the minimum ignition energy and the beam intensity S_{0m} have been represented as a function of the particle range R. From this figure, we can infer the following approximate scaling laws:

$$E_0^{min}(\mathrm{MJ})\approx 4.3\times 10^3\left(\frac{R}{\varrho_0}\right)^2, \tag{21}$$

$$S_{0m}(\mathrm{W/cm^2})\approx 9\times 10^{16}\left(\frac{\varrho_0}{R^2}\right), \tag{22}$$

where R is in g/cm^2 and ϱ_0 in g/cm^3. In the same way, we find the scaling laws for the hot spot parameters:

$$T(\mathrm{keV})\approx 8.54R^{-0.35}, \tag{23}$$

$$H(\mathrm{g/cm^2})\approx 0.30R^{-0.075}, \tag{24}$$

$$\delta=\frac{\varrho}{\varrho_0}=0.14R^{-1.25}. \tag{25}$$

So far, we have obtained the minimum energy of the particle beam needed to drive to ignition a precompressed fuel. But, in order to calculate the total energy spent for ignition, we have to compute the energy E_D of the driver used to compress the fuel to a density ϱ_0. Since the hot spot is heated subsonically, the mass of fuel m_F compressed by implosion must be, in general, larger than the hot spot mass $m=m_0x^3$. In fact, ignition has to occur before the inward rarefaction wave generated in the external surface of the fuel (of radius r_e) arrives at the ablation surface. This rarefaction arises when the outward strong shock preceding the ablation front reaches $r=r_e$. Thus, the time t_i available for ignition is

$$t_i=\int_{r_0}^{r}\frac{dr}{v}=t_s+t_r, \tag{26}$$

where t_s is the transit time of the shock wave from r_0 to r_e:

$$t_s=\frac{3}{4}\int_{r_0}^{r_e}\frac{dr}{v}, \tag{27}$$

and t_r is the transit time of the rarefaction wave from r_e to r:

$$t_r=\int_{r}^{r_e}\frac{dr}{c}. \tag{28}$$

Here, $c=(5p/12\varrho_0)^{1/2}$ is the sound speed behind the shock and it is the velocity of propagation of the rarefaction in the shocked matter of density $\varrho_s=4\varrho_0$. From Eq. (2) we get $c\approx 0.91v$, and from Eqs. (26)–(28) we obtain, approximately, $r_e\approx r_s$. Thus, the ratios between the minimum fuel mass m_F and the hot spot mass become

$$\frac{m_F}{m}=\frac{\varrho_0 r_e^3}{\varrho r^3}\approx\frac{\varrho_0}{\varrho}=\frac{1}{\delta}, \tag{29}$$

and the minimum energy E_D^{min} is

$$E_D^{min}=\frac{m_F\epsilon_c}{\eta_D}\approx E_0^{min}\frac{3\alpha}{2a}\frac{\varrho_0^{2/3}}{\eta_D\epsilon}\left(\frac{\varrho_0}{\varrho}\right), \tag{30}$$

where $\epsilon_c=(3\alpha/2a)\varrho_0^{2/3}$ is the cold fuel temperature, α is the isentrope parameter that denotes the deviation of the cold fuel from complete degeneracy, $a=4.35\times 10^{-13}$ cm g$^{5/3}$/erg, and η_D is the total efficiency with which the driver couples to the fuel. In order to obtain the minimum total energy required for ignition, the driver energy E_D^{min} must be added to the trigger energy $E_i=E_0^{min}/\eta_i$, where η_i is the efficiency with which the trigger couples to the fuel. For an ion beam $\eta_i=1$, and for a REB generated by a femtosecond laser $\eta_i<1$, and it depends on the laser absorption and on the efficiency with which the hot electrons are transported from the subcritical corona to the fuel.[2] For the particular case of $R=0.6$ g/cm^2, $\alpha=2$, $\eta_D=0.1$, and $\varrho_0=300$ g/cm^3, we get $E_D^{min}/E_0^{min}\approx 1$. Of course, this fraction can be reduced by increasing the trigger intensity in such a way as to produce a supersonic heating of the hot spot. But, as we have previously mentioned, it would lead to an increase in the trigger energy, with the consequence of increasing the total energy required for ignition. For a shorter range, however, this fraction decreases as well as the value of E_0^{min} and then, relatively short ranges R of the order of 0.2–0.3 g/cm^2 should be preferred.[2] Nevertheless, it is worth noticing that if the range is reduced below 0.2 g/cm^2 the heating becomes supersonic and the present model is no longer valid. Thus, the problem of setting the possible existence of a minimum range requires the study of such a regime, and this is beyond the scope of this paper.

B. Target gain

As we have shown, the ignition conditions are determined by the hot spot heating dynamics and they depend on the range R of the particles used for triggering the ignition. Since the target energy gain depends on the particular values of the hot spot temperature and of the ICF parameter, it may be worth analyzing the effect of the range on the limiting gain. For this purpose, we use a modified version of the isochoric model, which allows for a density jump $\delta=\varrho/\varrho_0$ between a hot spot with density ϱ and the surrounding cold fuel with density ϱ_0.[10] After some straightforward calculations similar to those of Refs. 9 and 10, we get the following expression for the limiting gain:

$$G\approx 1.37\times 10^3\,\frac{\eta}{T}\,\frac{(\eta E_T/E_C)^{1/3}}{\left[1+(0.81H_B\delta^{2/3}/H)(E_C/\eta E_T)^{1/3}\right]^3}, \tag{31}$$

where $E_T=E_D+E_i$ is the total energy of the drivers used for compressing the fuel (E_D) and for triggering the ignition (E_i), $H_B=7$ g/cm^2 and

$$E_C=3\pi\left(\frac{\alpha}{a}\right)^3\frac{H^3}{\epsilon^2\delta^2}. \tag{32}$$

The hot spot parameters $\delta=\varrho/\varrho_0$, H and T (or ϵ) are functions of the range R given by Eqs. (23)–(25). Besides, η is the total efficiency with which both drivers couple to the fuel:

$$\eta E_T=\eta_D E_D+\eta_i E_i. \tag{33}$$

From the previous calculation of the limiting gain,[9,10] we also obtain that $\eta E_T\approx 4E_0^{min}$ and then, the following relationship among η, η_D, and η_i is found:

$$\eta=\frac{4\eta_D}{3+\eta_D/\eta_i}. \tag{34}$$

From this equation we can see that the real value of η_i has a weak effect on the total efficiency η for a given driver efficiency η_D. For instance, if we take $\eta_D=0.1$ and $0.1\leq\eta_i\leq 1$, the total efficiency η turns out to be $0.10\leq\eta\leq 0.13$. We have represented Eq. (31) in Fig. 5 for $R=0.2$ g/cm^2 and, for $R=1$ g/cm^2 (with $\eta=0.1$), together with that calculated in Ref. 2 (with $T=5$ keV and $H=0.3$ g/cm^2). As can be seen, the limiting gain decreases with the range and, for $R=1$ g/cm^2, it becomes about a factor 2 lower than the gain considered in Ref. 2. We can obtain the following approximate scaling law, which includes the dependence of the limiting gain on the range R:

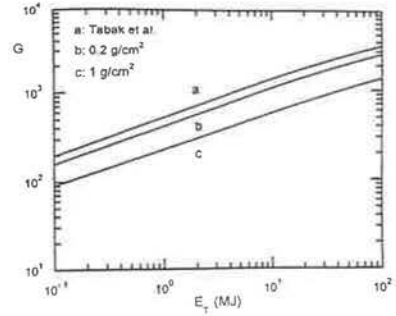

FIG. 5. Limiting gain G as a function of the total energy E_T required for ignition and compression of the target. (a) Calculated in Ref. 2; (b) for $R=0.2$ g/cm^2; and (c) for $R=1$ g/cm^2.

$$G \simeq 1.3\times 10^4 \eta \left(\frac{\eta E_T}{\alpha^3 R}\right)^{0.42}, \tag{35}$$

valid for $R \geq 0.2$ g/cm^2. In the previous equation E_T is in MJ and R is in g/cm^2. Once again, the advantage of using relatively short ranges can be perceived.

IV. CONCLUSIONS

We have developed a novel analytical model for the ignition of a precompressed DT fuel, which is heated by means of a beam of charged particles characterized by its range R and for the beam focal spot radius r_0. We have shown that the ignition conditions are determined by the dynamics of the heating process and that it depends on the particle range R. In the regime in which minimum beam energy is required for triggering the ignition, the hot spot heating proceeds subsonically and, in general, its mass becomes larger than the mass directly heated by the beam. This fact leads to scaling laws for the minimum ignition energy and beam intensity in terms of the range R and allows for a a simple interpretation of the simulation results of Refs. 6 and 7. Besides, the discrepancy observed between those simulations and the calculations by Tabak *et al.*[2] is seen to be caused by the larger range used in the simulations. In fact, by taking a more realistic particle range $R = 0.3$ g/cm^2,[5] and for $\varrho_0 = 300$ g/cm^2, Eq. (21) yields $E_0^{\min} \simeq 4.3$ kJ. This number compares very well with the 3 kJ estimated in Ref. 2 Similarly, for $R = 0.3$ g/cm^2 target gain turns out to be very close to the value obtained in that work (70% of such a value for $\eta_t = \eta_D = 0.1$ and practically equal to it for $\eta_t \geq 0.5$).

The situation is somewhat different for a relatively large $R (\simeq 1$ g/cm^2). In this case, the ignition energy increases considerably and the target gain is approximately a factor 2 lower than that considered in Ref. 2. These results show the convenience of keeping the particle range below 0.3 or 0.4 g/cm^2 in order to ensure a higher-energy gain than that achievable with the central ignition scheme with the same energy.

It may be worth noticing that since our model is based on integral conservation properties, we can expect that the present results obtained for the situations in which $r_0 = R/\varrho_0$, will not be very sensitive to the detailed shape of the hot spot at ignition. On the other hand, it should be clear that the scaling laws given by Eqs. (21)–(25) will change if different values of the range R are considered for a fixed focal spot r_0.

In conclusion, the present model seems to give an adequate physical picture of the processes involved in the hot spot heating that lead to the fuel ignition. As occurs with central ignition, static models are not suitable for the calculation of realistic ignition conditions.

ACKNOWLEDGMENTS

The authors appreciate useful discussions with Dr. A. Caruso, and they are also grateful to Dr. S. Atzeni for making available his work before publication.

This work was partially supported by the Comisión Interministerial de Ciencia y Tecnología of Spain (PB96-0127).

[1] J. Lindl, Phys. Plasmas 2, 3933 (1995).
[2] M. Tabak, J. Hammer, M. E. Glinsky, W. L. Kruer, S. C. Wilks, J. Woodworth, E. M. Campbell, M. D. Perry, and R. J. Mason, Phys. Plasmas 1, 1626 (1994).
[3] E. Lefebvre and G. Bonnaud, Phys. Rev. Lett. 74, 2002 (1995).
[4] A. Pukhov and J. Meyer-ter-Vehn, Phys. Rev. Lett. 76, 3995 (1996).
[5] C. Deutsch, H. Furukawa, K. Mima, M. Murakami, and K. Nishihara, Phys. Rev. Lett. 77, 2483 (1996).
[6] A. Caruso and V. A. Pais, Nucl. Fusion 36, 745 (1996).
[7] S. Atzeni, M. L. Ciampi, A. R. Piriz, M. Temporal, J. Meyer-ter-Vehn, M Basko, A. Pukhov, A. Rickert, J. Maruhn, K. H. Kang, K. J. Lutz, R Ramis, J. Ramirez, J. Sanz, and L. F. Ibañez, *Proceedings of the 16th International Conference on Plasma Physics and Controlled Nuclear Fusion Research*, Montreal, 7–11 October 1996, Paper No. IAEA-CN64/BP-2 (IAEA, Vienna, in press); S. Atzeni and M. L. Ciampi, Nucl. Fusion 37, 1665 (1997).
[8] S. Atzeni, Jpn. J. Appl. Phys. 34, 1980 (1995).
[9] R. E. Kidder, Nucl. Fusion 16, 405 (1976).
[10] See National Technical Information Service Document No. DE84017287/XAB (M. D. Rosen, J. D. Lindl, and A. R. Thiessen, Laser Program Annual Report 1983, Rep. UCRL-50021-83, Lawrence Livermore National Laboratory, CA, Sec. 3, p. 5). Copies may be ordered from the National Technical Information Service, Springfield, JA 22161.
[11] J. Sanz, A. R. Piriz, and F. G. Tomasel, Phys. Fluids B 4, 683 (1992).
[12] A. R. Piriz and F. G. Tomasel, Phys. Rev. A 45, 8787 (1992).
[13] S. Hively, Fusion 3, 199 (1983).
[14] A. R. Piriz, Nucl. Fusion 36, 1395 (1996).
[15] J. D. Lindl, in *Inertial Confinement Fusion*, Proceedings, Course and Workshop, Varenna, 1988 (Editrice Compositori, Bologna, 1989), p. 616.

Petawatt laser target physics studies

M H Key

Third International Workshop on fast ignition of fusion targets
21 - 23 Sept. 1998
Rutherford Appleton Laboratory . Chilton . UK

- **Petawatt laser and experimental system**
- **Studies of the electron source**
- **Fast ignition and NIF**
- **Studies of heating by electrons**

Work performed under the auspices of the U.S. Department of Energy by the Lawrence Livermore National Laboratory under Contract No. W-7405-ENG-48.

Co-authors

Michael Cable
David Chambers
Thomas Cowan
Bruce Hammel
Steve Hatchett
Joe Kilkenny
Jeff Koch
Bill Kruer
Bruce Langdon
Barbara Lasinski
Dick Lee
John Moody
Mike Moran
Jim Murray
Allen Offenberger
Mike Perry
Dee Pennington
Tom Phillips
Craig Sangster
Mike Singh
Richard Snavely
Mark Stoyer
Max Tabak
David Thompson
Greg Tietbohl
Masahiro Tsukamoto
Ken Wharton
Scott Wilks

PW laser generated 1-10 MeV electrons drive fast ignition or hard X-ray sources

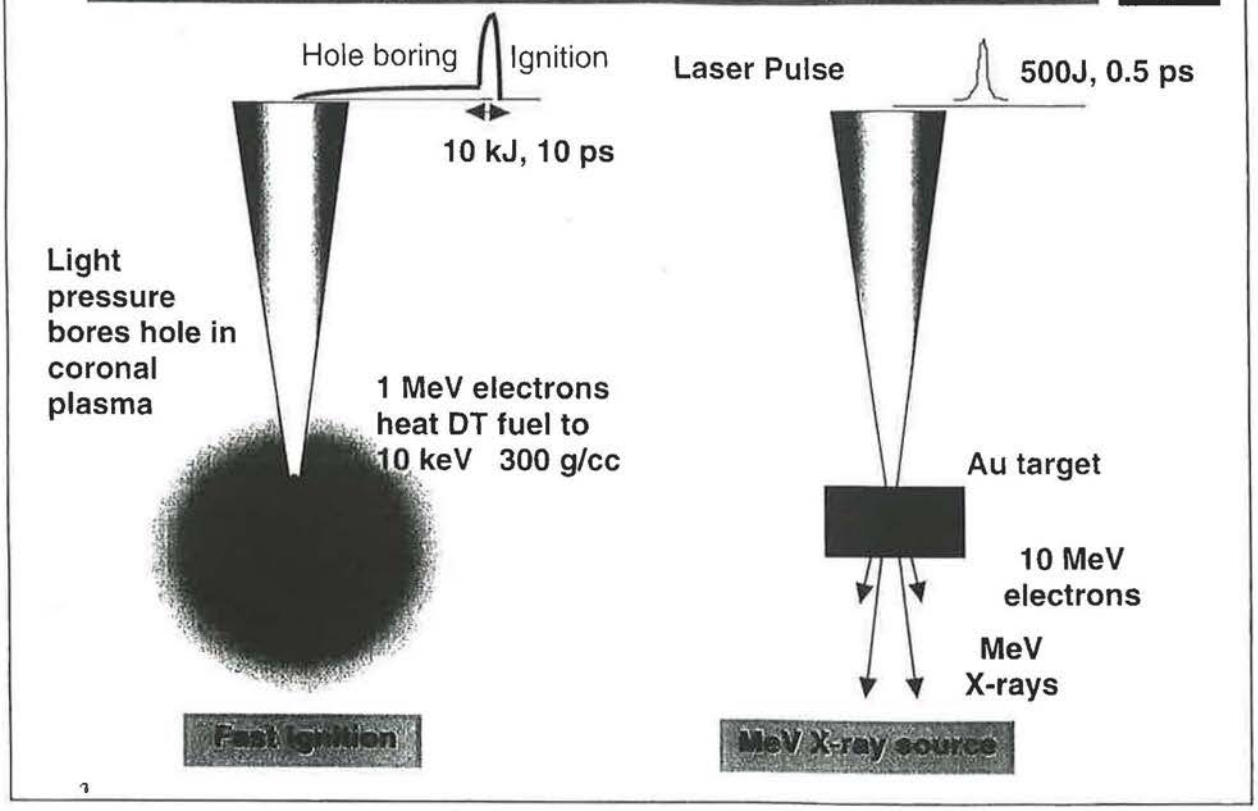

The PW target chambers has a wide range of diagnostics

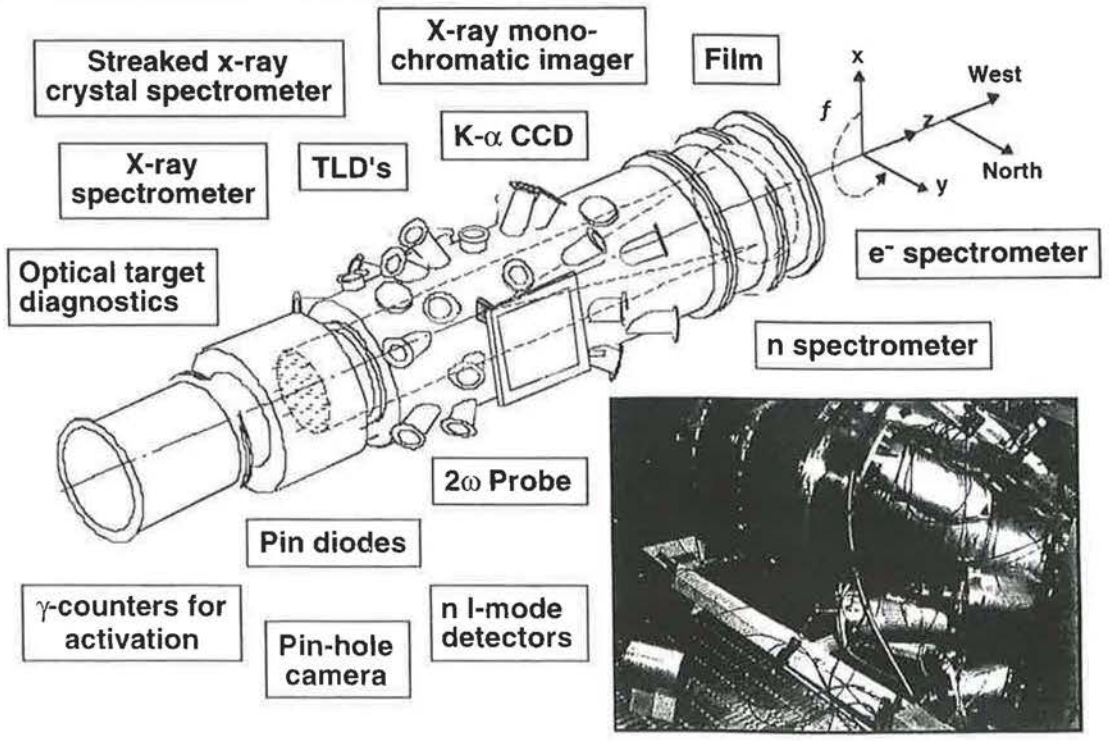

TCS:PWTargChamDiagnostics
HITemp98 5/98

For short pulses (< 5 ps), Petawatt is focused using an on-axis parabola in combination with a plasma mirror

- Debris shields cannot be used below ~ 5 ps pulse length
  - accumulated B-integral for double passing a 1-cm thick fused silica debris shield is 28 radians for a 500 fs pulse!

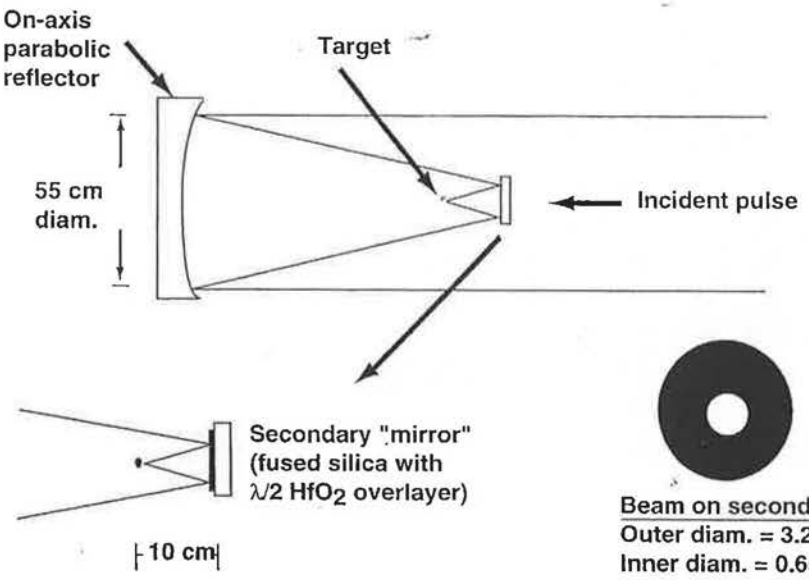

Beam on secondary mirror
Outer diam. = 3.25 cm
Inner diam. = 0.65 cm
Beam area = 8.0 cm^2
Fluence = 100 J/cm^2
Irradiance = 2 x 10^{14} W/cm^2

nwfocus5.ai

Wavefront correction system

Final control sensor is located at the output of the amplifier chain prior to compression

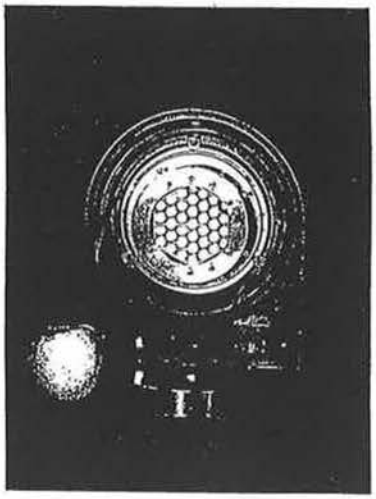

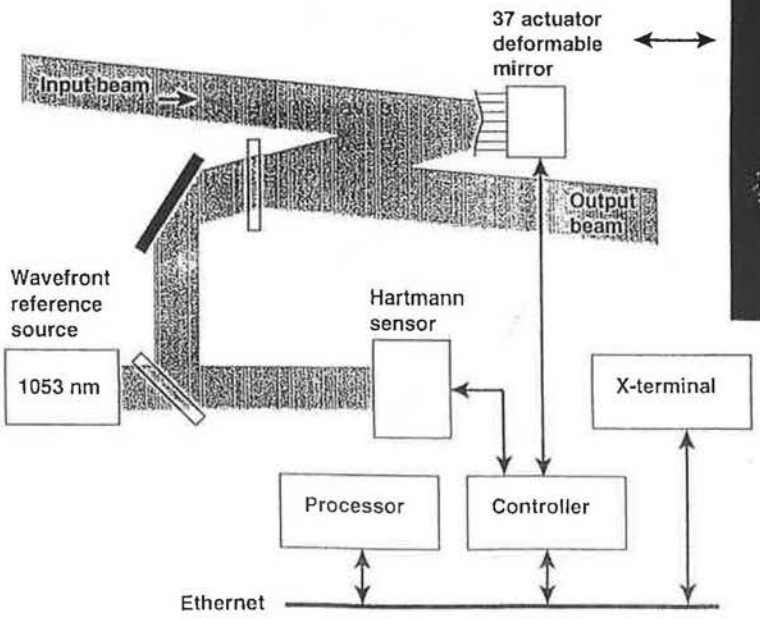

Deformable mirror (DM) gives reproducible smaller focal spot relative to a typical repeat shot with thermal effects

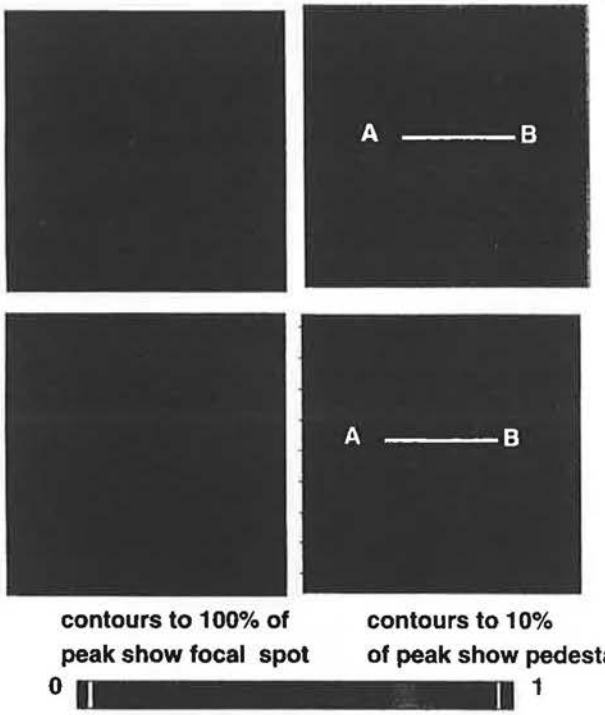

contours to 100% of peak show focal spot

contours to 10% of peak show pedestal

0 1

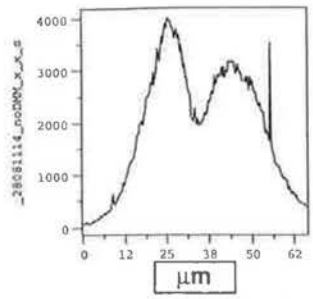

Deteriorated focus in second shot without DM (291J)

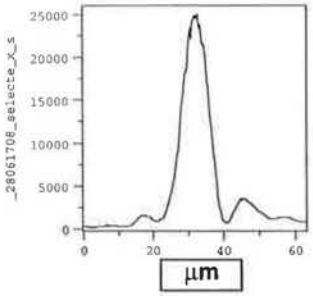

Stable result with DM (626J) (3x intensity/J)

Line outs A-B thro focal spot showing ccd image counts

For moderate pre-pulse levels, gold blowoff at main pulse time has developed a "ridge" of 0.1– 0.01 n_c plasma along f/3 angle.

10^{-5} Pre-pulse

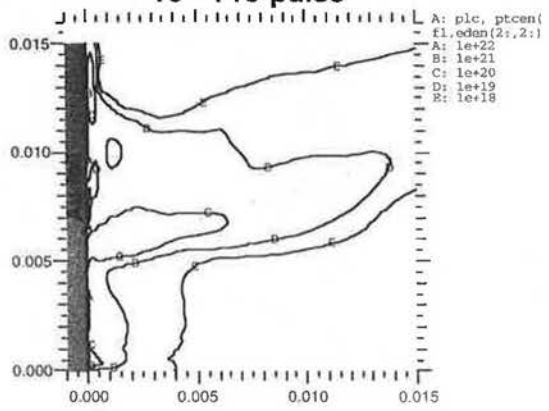

10^{-4} Pre-pulse

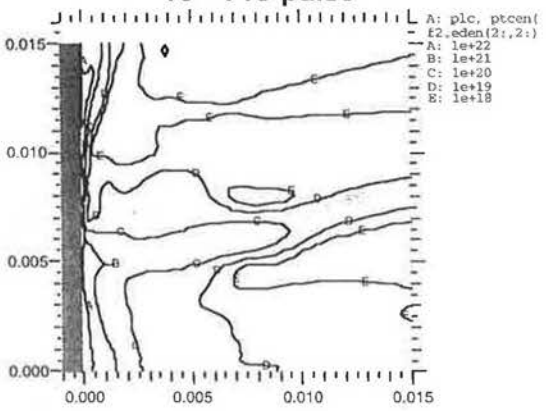

Plasma scale lengths in "channel" range from 1-10 µm at $n_e=n_c$ to 13-35 µm at $n_e=.001\ n_c$

Petawatt intensity exceeds $2x10^{20}$ Wcm^{-2} using deformable mirror wavefront control

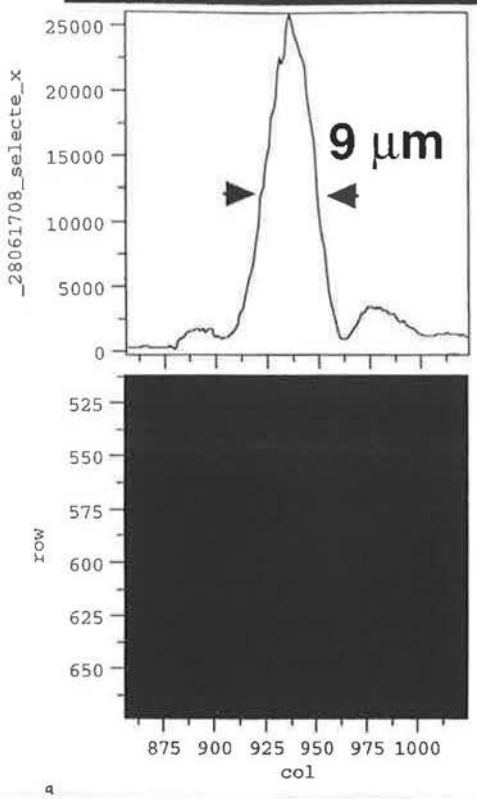

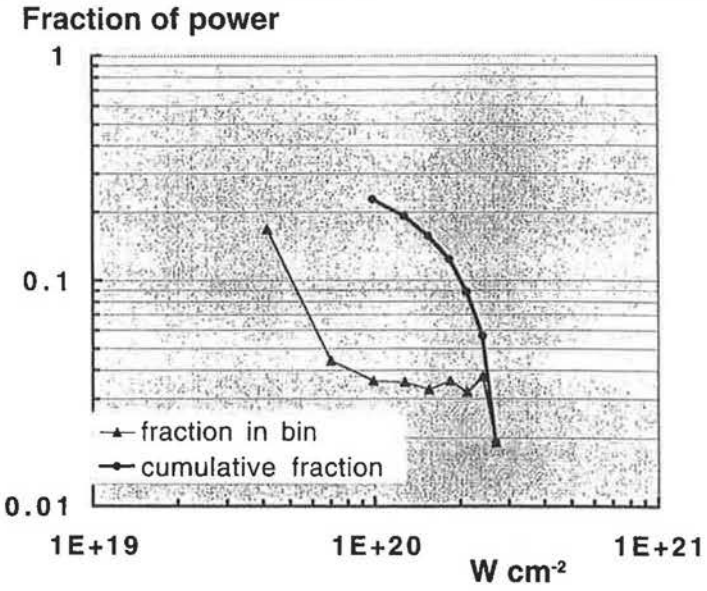

Analysis of 16 bit CCD far field image to give on target spectrum of intensity (shot 1708)

Petawatt focal spot has lower peak intensity than diffraction limit and about 28% power in the focal spot

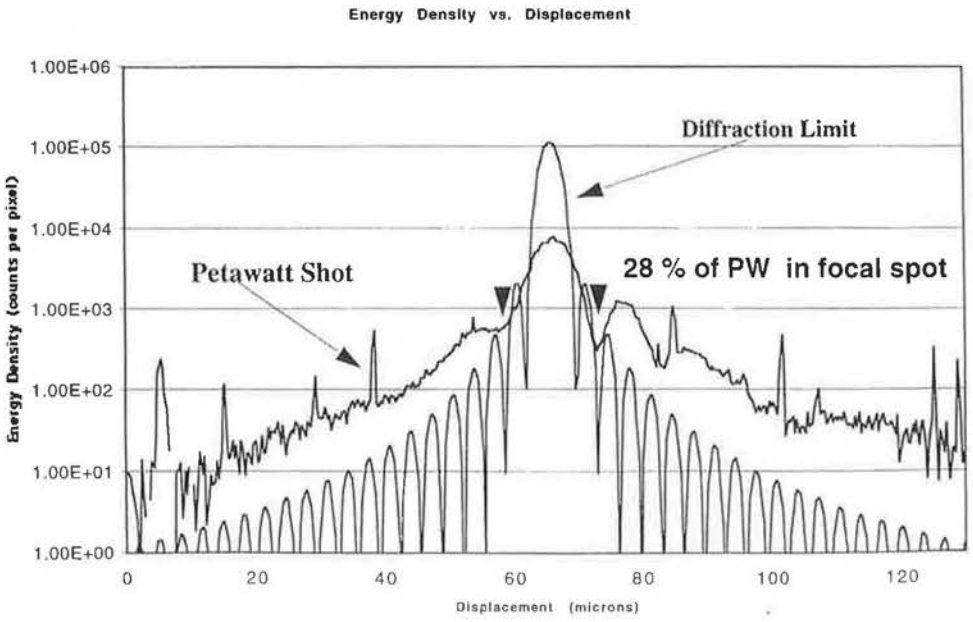

Analysis of CCD images gives the spectrum of intensity (using also pulse shape data)

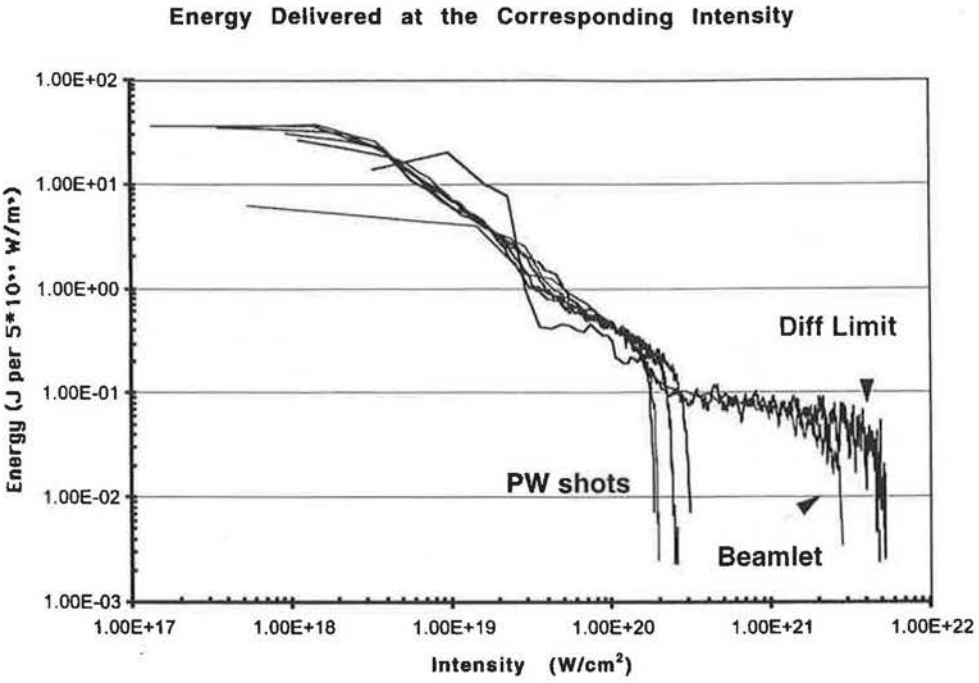

Prepulse has been varied from 4 x10^{-6} to 4 x10^{-2} .

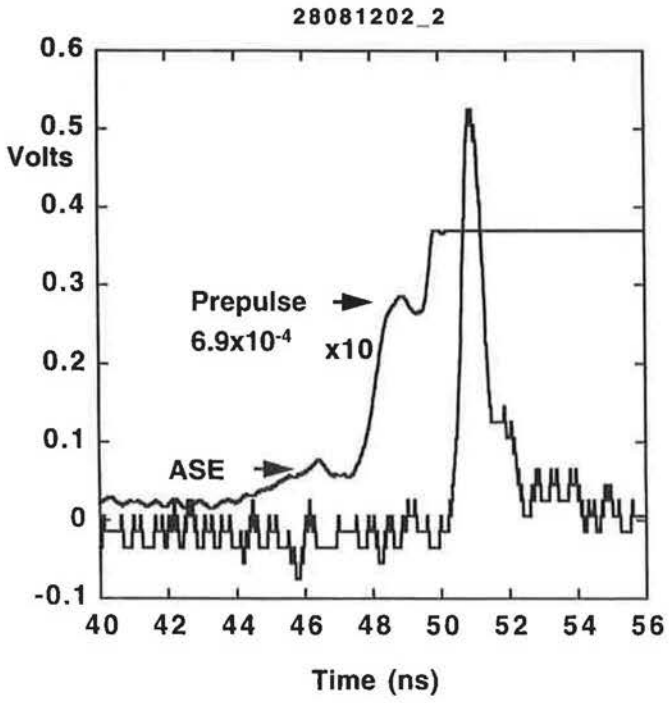

Laser system prepulse minimum is 10^{-4} and ASE is a few 10^{-4} . Use of 4% relecting SiO_2 plasma mirror gives minimum prepulse of 4 x10^{-6} and ASE of 10^{-5}

Interferograms (at 2 ω_0) taken a few ps before the main pulse are a sensitve indicator of the plasma blown off by ASE and any pre-pulse(s).

1.4 μm thick CH foil

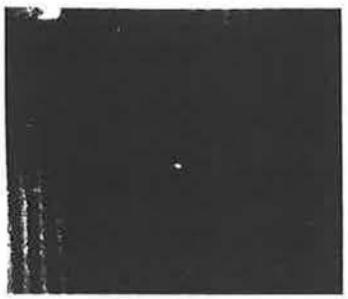

Experiment

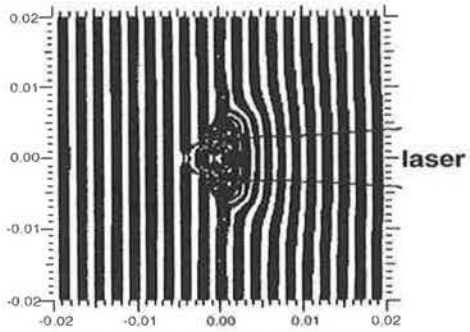

Calculation (LASNEX)

Model, assuming a 30 μm spot, reproduces the experimental results for thin foil very well.

simulation parameters: 1) ASE before main ramp for 1.5 ns, flat for 1.5ns, total energy of 1.1mj.

2) Prepulse: 2ns before main, 0.5 ps duration, 3.7 mJ, Gaussian spot of 30 μm FWHM.

sph_tppac01_05_12_98

13

Lasnex modelling of the preformed plasma on Au targets shows a ridge of higher density surrounding the focal spot

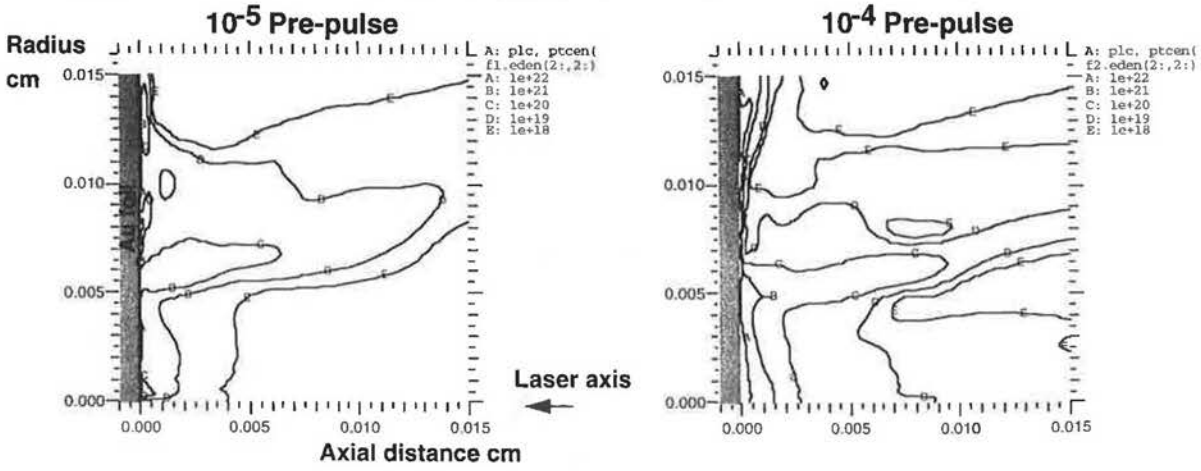

Plasma scale lengths in "channel" range from 1-10 μm at $n_e=n_c$ to 13-35 μm at $n_e=.001\ n_c$.

sph_mk01_9-17-98

14

A magnetic electron spectrometer confirms the generation of electrons with < E>=7MeV

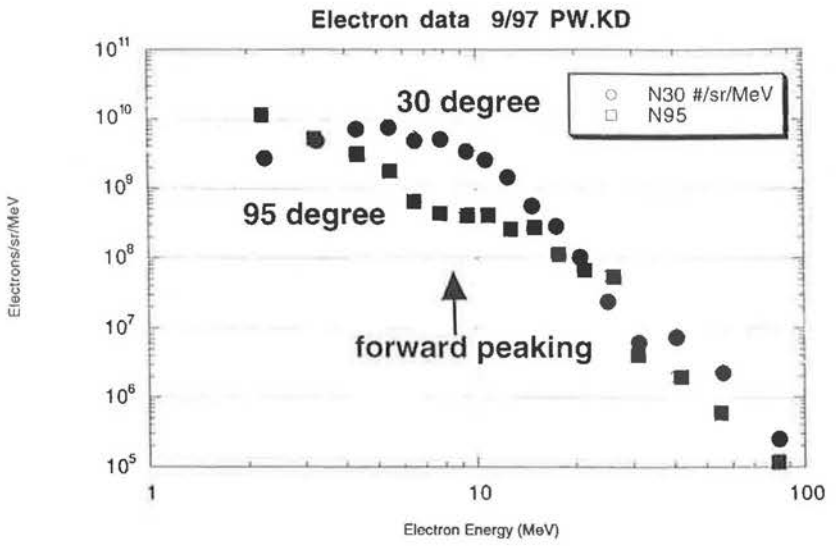

Hot tail electrons penetrate target and escape to vacuum

The forward peaking seen in the electrons is also seen in the Bremsstrahlung

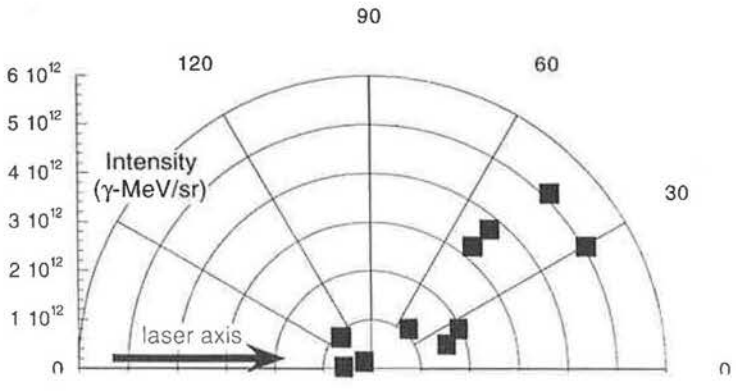

Diode filtered to 1MeV approx 300 J on 0.5 mm Au target

- **in 0.5 ps**
- **and 5 ps**

Bremsstrahlung of a relativisic electron is in cone angle of $1/\gamma$

Collimated source of electrons* in radiography targets produces bremsstrahlung with a distribution of angles.

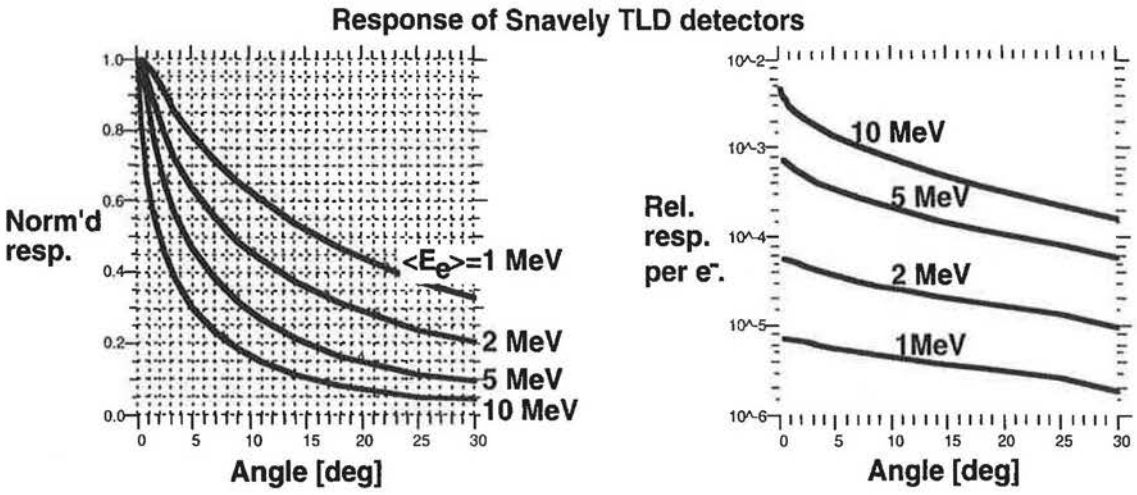

Width of angular distribution is primarily due to electron scattering within the target.

sph_mk02_9_17_98

*electrons assumed to have exponential energy distribution

(γ,n) activation of array of Au cylinders has pronounced off axis peak

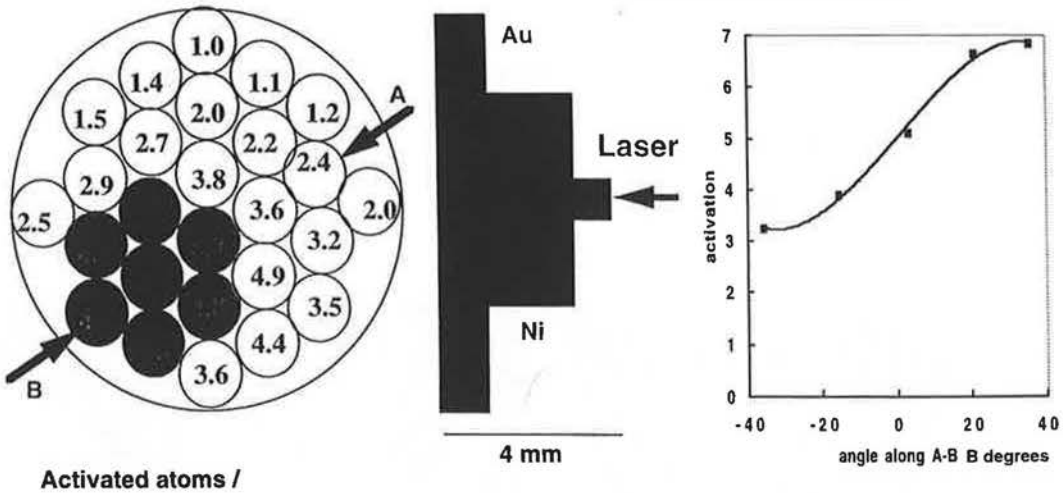

Activated atoms / target atoms x 10^{14}

Error range 1.9 to 5.1 %
(shot 28 09 0116)

Solid ange correction shows peak along A-B is at 40 degree edge of range of measurement

Array of 97 TLDs (filtered to respond at hν>0.2 MeV) shows multiple narrow peaks on a diffuse background

Possible correlation of jets with three spots in x-ray image for this shot

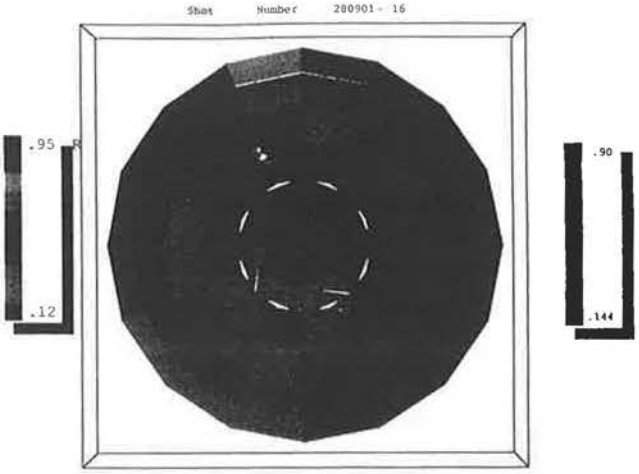

Different pattern from that seen on this shot in nuclear activation (order of magnitude difference in photon energy)

Variation of target position relative to focal plane shows evidence in x-ray images of self focussed channel formation

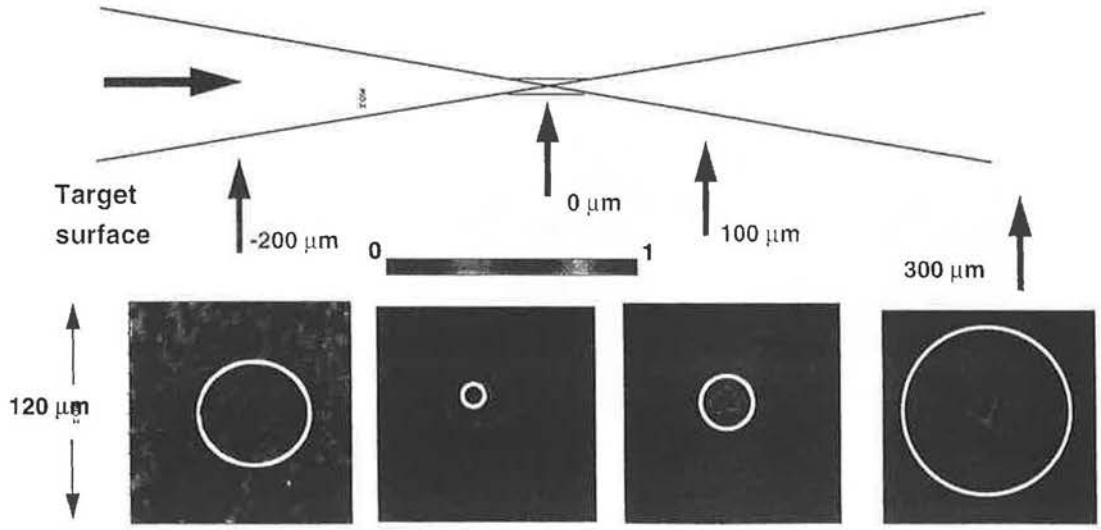

rel. x-ray phc peak intensity	3.9	20	14.9	17

Data strongly suggest self focussed channel formation when focus is in front of target

Total yield of photoneutrons drops sharply when laser is focused behind target surface

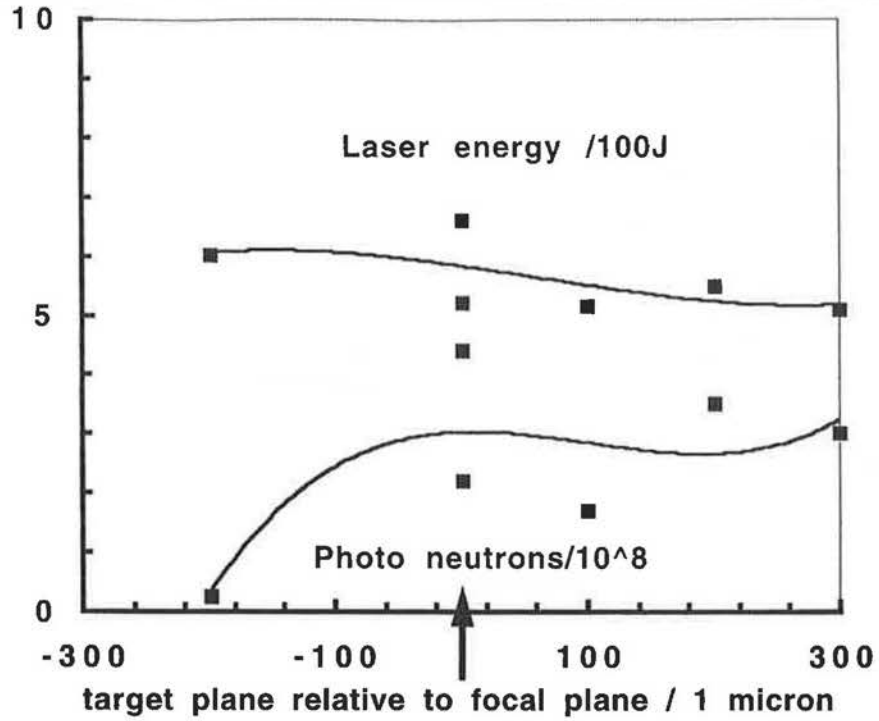

Absolute spectral intensity at high energy is deduced from Photonuclear Activation

(γ,n) cross-sections

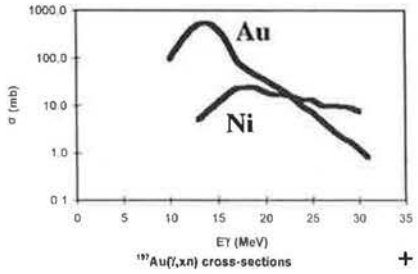

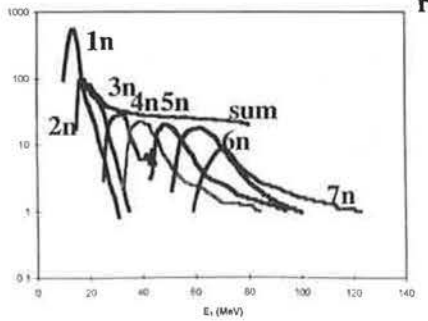

Black

+ measured activation ratios and model

Red

Absolute Intensity

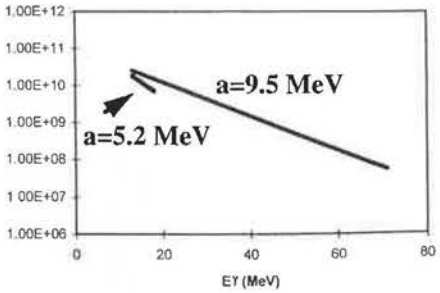

Range of spectral information is extended using higher order γn processes

Mechanisms influencing the electron source

- **Off axis jets- several possibilities**
  hosing type instability of a filament at near critical density (PIC modelling),
  Weibel type break up of relativistic electron flow (PIC modelling)
  refraction of filament due to structure of preformed plasma (Osaka effect)

- **Hot tail in the energy spectrum**
  - subcritical acceleration processes (PIC modelling)

23

The wide angular distribution of the hot electrons in overdense simulations are identified with the broad experimental x-ray spectra.

- T_{hot} determined by the ponderomotive potential and $\propto (I_{19}\,\lambda_{\mu}^{2})^{1/2}$ MeV
- Early results suggest that the hot particles are produced at large angles.

Energetic (E>10 MeV ~ T_{hot}) electron positions.

Very energetic (E>25 MeV) electron positions.

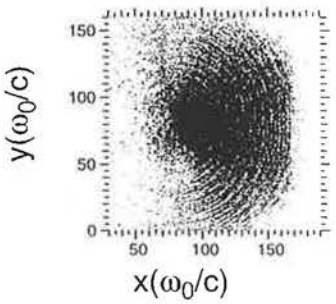

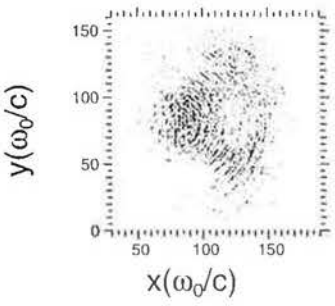

Simulation at 10^{21} W/cm^2 into 50 n_c.

Results at t=125 fs.

- Hot electrons occur in bursts and produce current filaments. We identify these bursts with emission at $2\omega_0$, associated with the J x B force.

Beam deflection occurs in many simulations of laser-plasma interaction in the overdense region.

Results from a simulation at 10^{21} W/cm^2, 50 n_c, 12 λ_0 long x 25 λ_0 wide plasma slab.

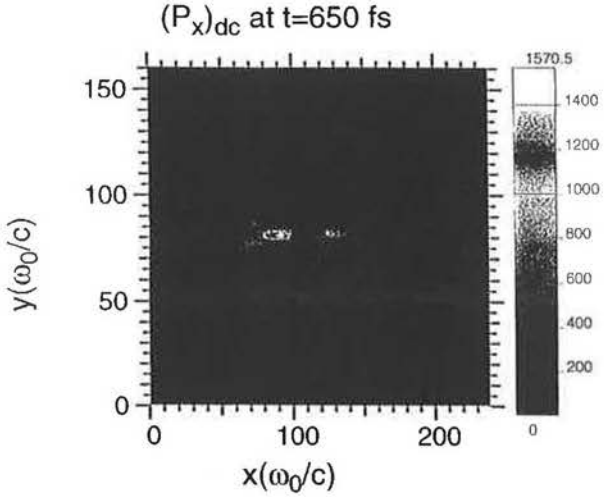

There is also evidence of a "kinking" instability in the propagation direction.

It is tempting to associate the off-axis x-ray features with the beam deflection.

2-D PIC simulations of the underdense laser-plasma interaction show that eneries much higher than U_{pond} can be produced: in fact, we see substantial 10-100 MeV electrons and photons.

PIC simulations predict higher T_e's

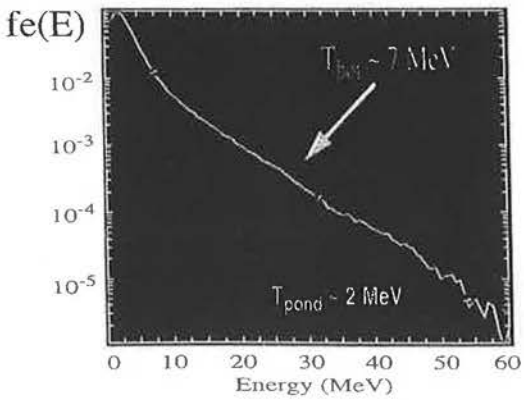

Comparison of LLNL-NASA/MSFC-UCAH electron spectrometer data, with LASNEX/PIC/ITS results.[3]

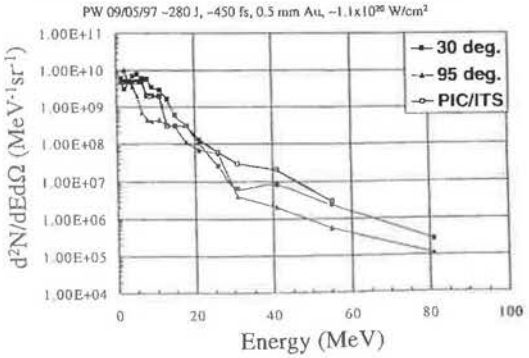

Longitudinal component of laser electric field accelerates electrons, which then collide with ions in the solid target, producing γ's

scw 06/07/98

We use Monte Carlo modelling to test our understanding of how the x-ray source is related to the spectrum of laser intensity

Intensity Spectrum —pond. scaling→ Electron Spectrum —ITS calc.→ Photon Spectrum

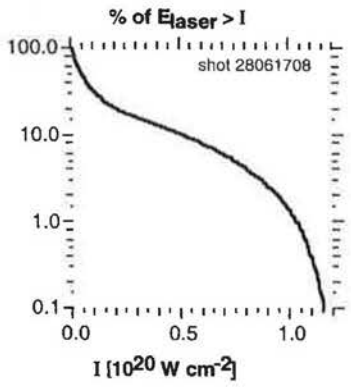

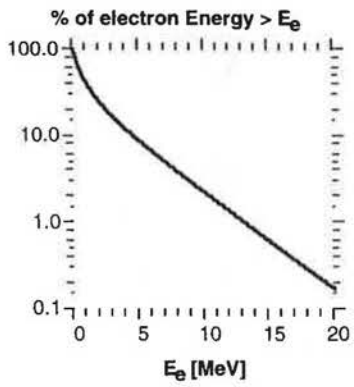

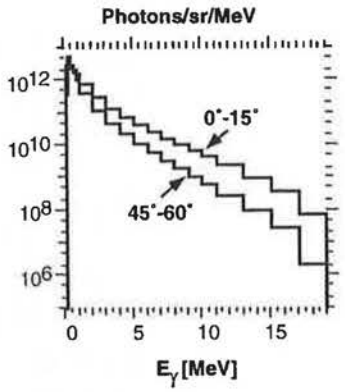

from equiv. plane image

PIN diodes, TLDs

(γ,xn) activation

We are developing a Monte Carlo based scaling model . The physics basis needs more investigation but initial results are interesting

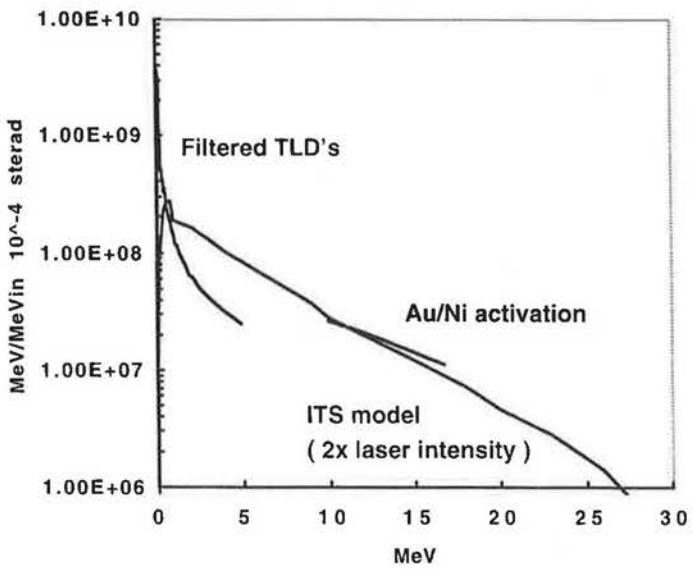

Model x-ray spectrum assuming Boltzman electron energy spectrum with kT= (ponderomotive potential) for each component of the intensity spectrum of the focal spot

2x laser intensity multiplier assumed presuming relativistic self focussing . Subcritical density processes also known to give kT>> ϕ_p

Scenario satisfying physics constraints for FI at NIF scale

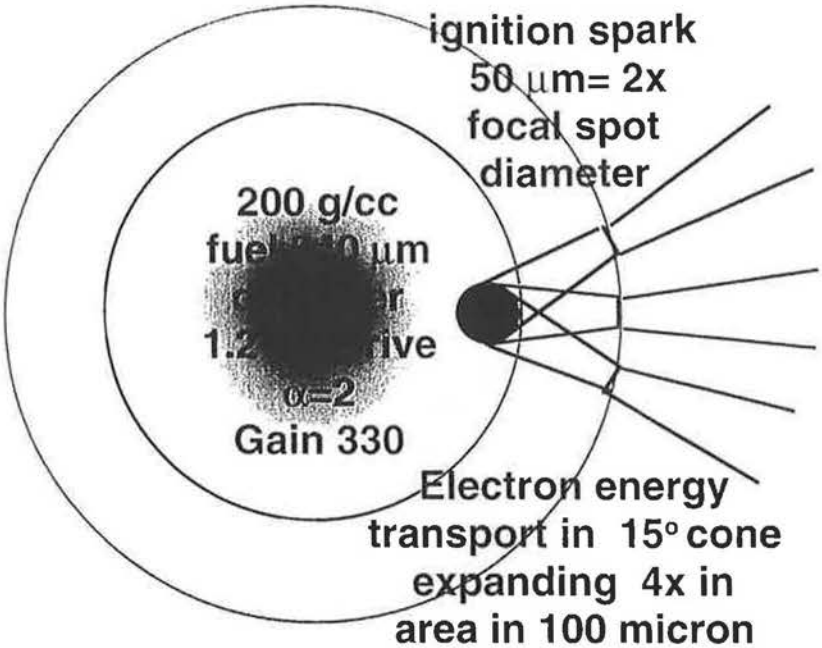

Ignitor pulse, 0.53 micron , 200kJ in 20 ps delivered in 19 off cluster of 25 μm focal spots 100 micron from dense core at 10^{20} Wcm^{-2}

Collimated transport is predicted by modelling penetration to within 100 μm may be a problem !

Reduced density eases constraint on $I\lambda^2$ but increases ignitor energy

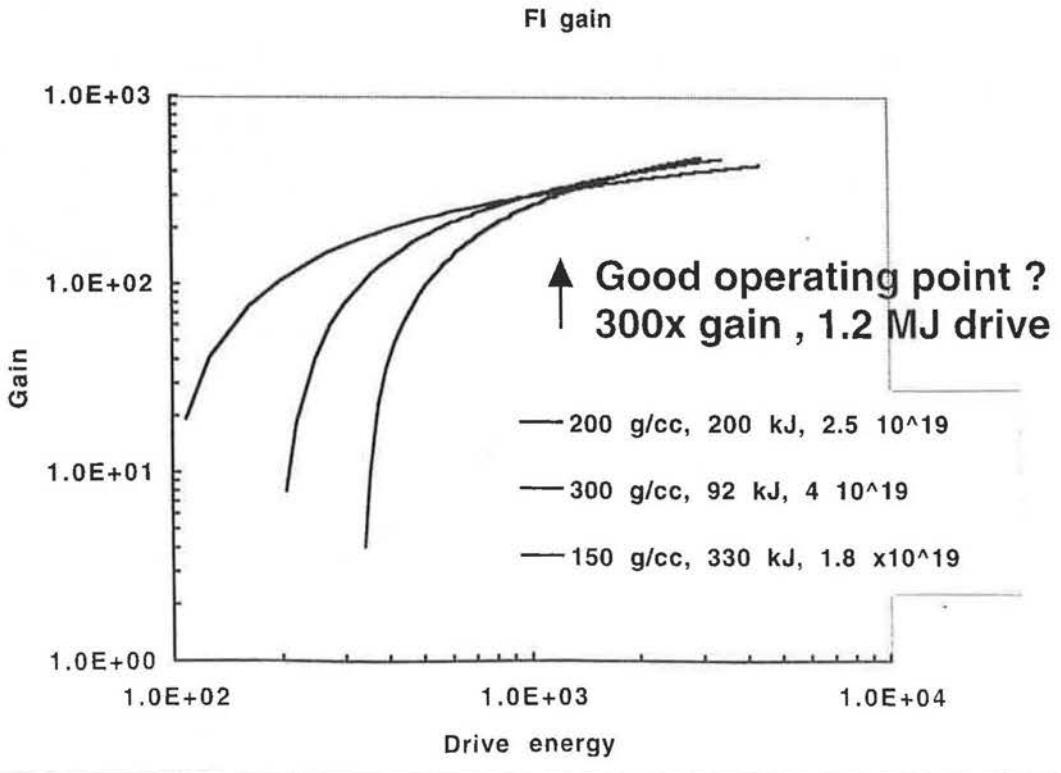

The gain advantage of FI over DD depends on difference in adiabat and density

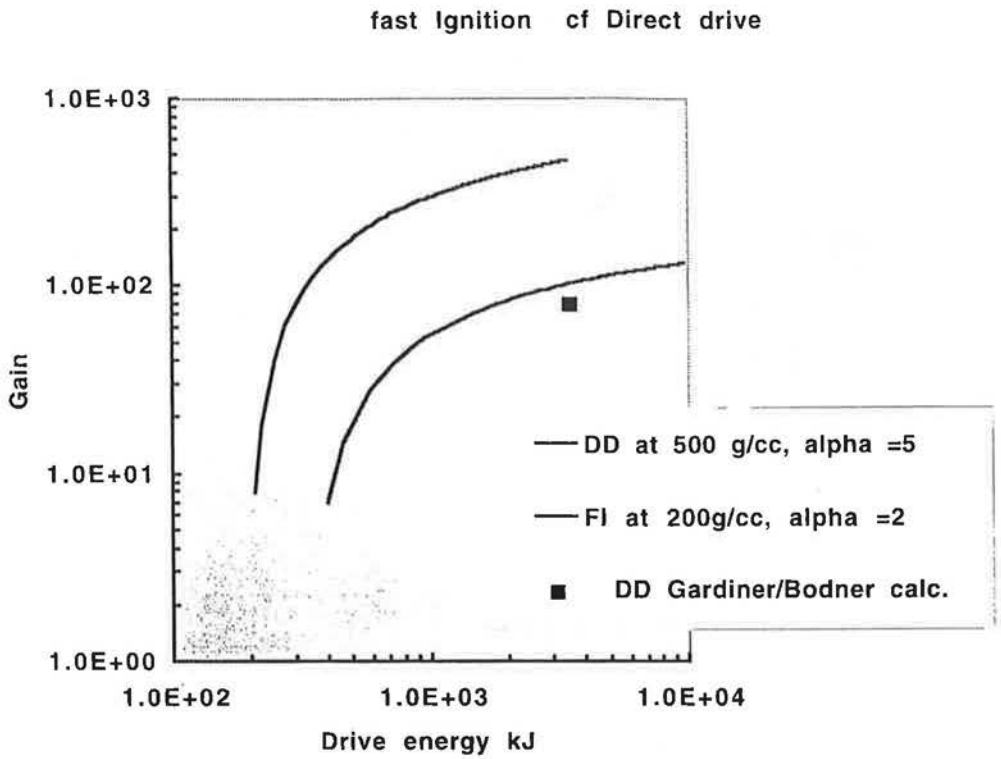

High resolution neutron TOF spectra show thermal D-D fusion by electron heating

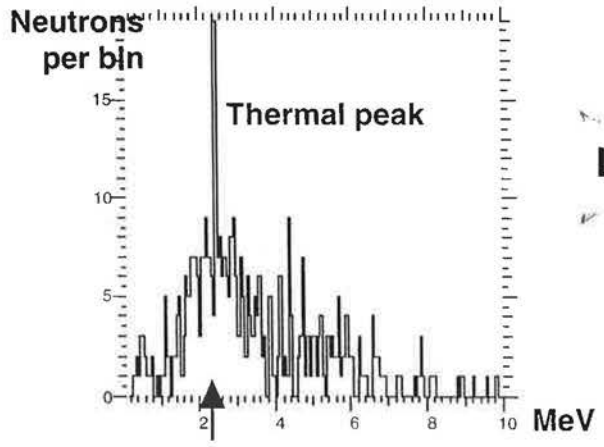

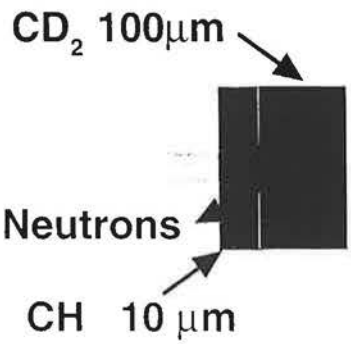

2.45 MeV DD fusion

Neutron time of flight energy spectrum. Emission of 6×10^4 THERMAL neutrons indicates heating to temperature approaching 1 keV

Data from 5 ps , 180 J irradiation of layered solid target

Scaling of DD neutron yield with temperature in 10 micron CD_2 layer from Lasnex 1D model

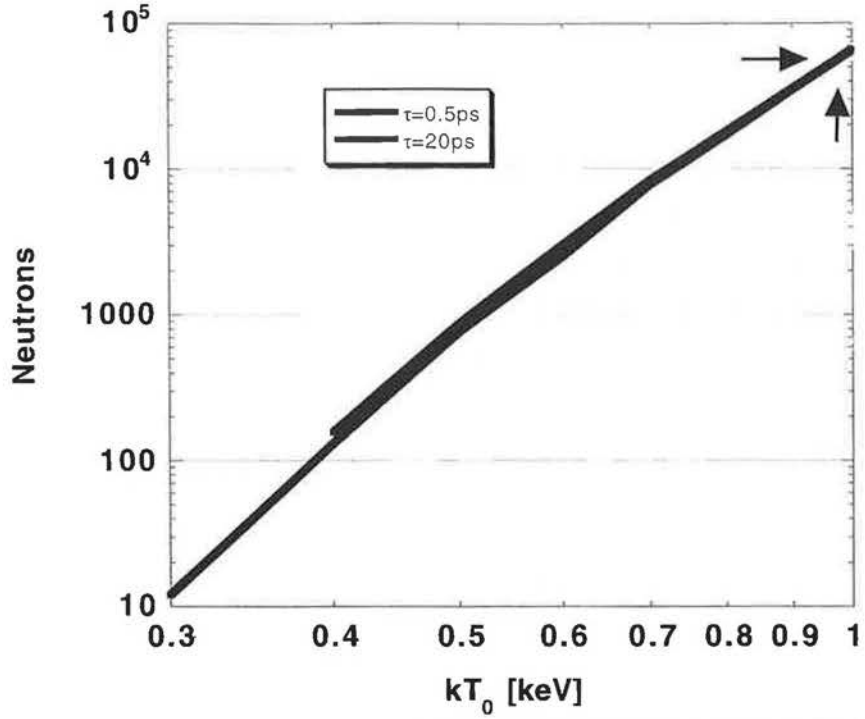

Experiment temperature approaches 1 keV

Background neutrons may be from electro-neutron effect in Deuterium

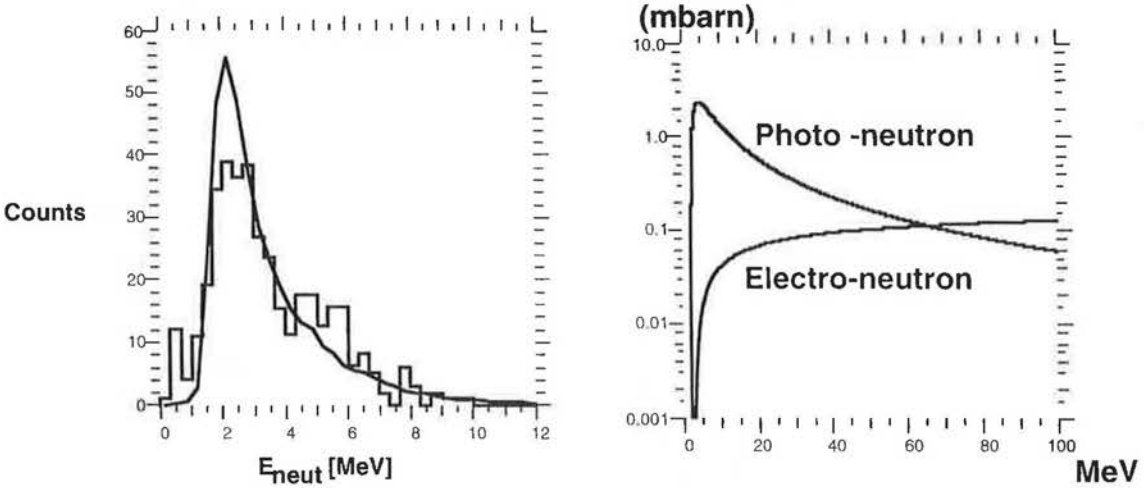

Experiment and modelled electro-neutron yield assuming 11 J of electrons in hot tail with <E>=8 MeV

Accelerated deuterium target ions generate a fusion peak in a deuterated catcher foil.

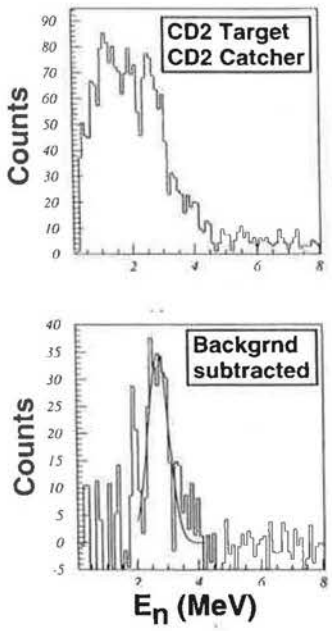

DD yield = 1.7 E06
DD peak = 2.7 MeV

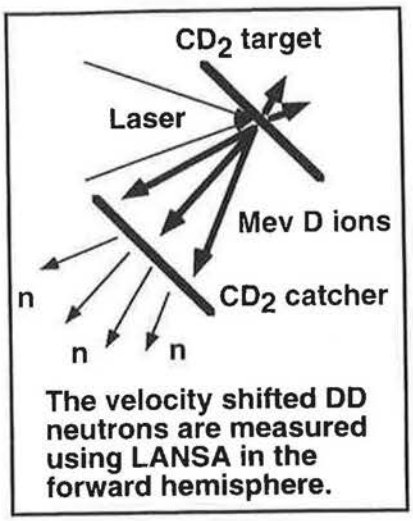

The velocity shifted DD neutrons are measured using LANSA in the forward hemisphere.

Background subtraction will be necessary for all nuclear-based signal interpretation.

TCS:ReboundTarget
HITemp98 5/98

35

Conclusions

- Petawatt laser with DM mirror gives much improved reproducible focal spot
- Electron source at 10^{20} Wcm^{-2} and PW power has hot tail and complex angular pattern - several mechanisms may contibute
- Assessment of fast ignition at NIF scale is encouraging
- Initial studies of heating by electrons will be continued with current better laser beam quality

7-

Studies of Intense Laser-Plasma Interactions for the Fast Ignitor Concept

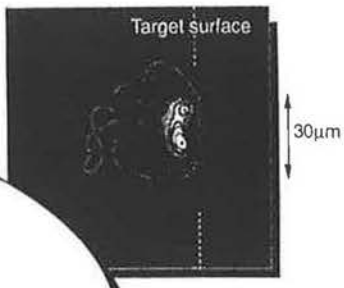

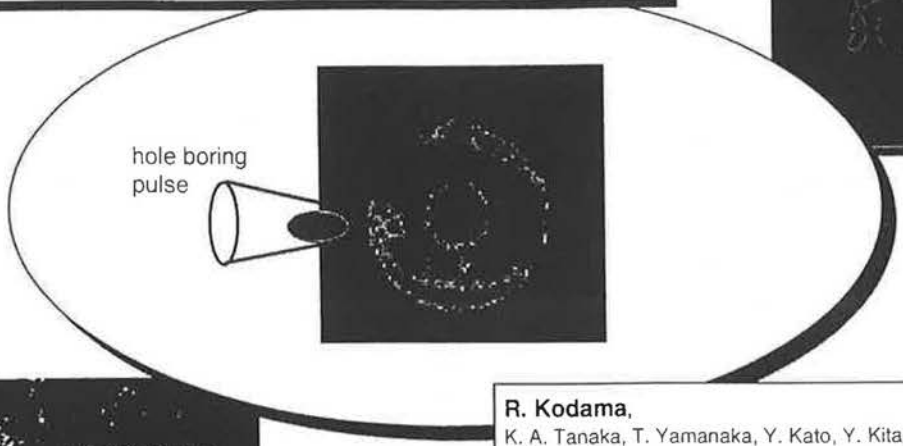

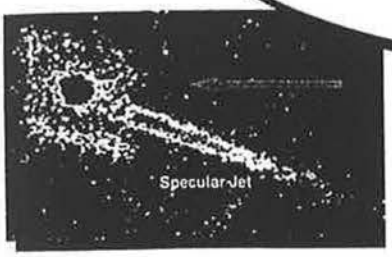

ILE Osaka Univ.

R. Kodama,
K. A. Tanaka, T. Yamanaka, Y. Kato, Y. Kitagawa, Y. Sentoku
H. Fujita, T. Kanabe, N. Izumi, K. Takahashi, H. Habara,
K. Okada, M. Iwata, T. Matsushita and K. Mima
ILE, Osaka University, Japan

for the 3rd International Workshop on the Fast Ignition of Fusion Targets at RAL in UK on Sept 21-Sept 23 1998.

Outline of Intense-Laser Plasma Interactions Related to the Fast Ignitor at ILE

ILE Osaka Univ.

- **Introduction to the Fast Ignitor**
  - What do we need to study the feasibility of the Fast Ignition
- Laser-hole Boring into Overdense Plasmas with 100 ps / 1 TW Laser Light
  - Propagation of laser light into overdense plasmas
  - **Generation of high energy particles in the channel**
  - **Demonstration of laser hole boring into implosion plasmas**
- Ultra-Intense Laser Plasma Interactions by using 100TW/0.5 ps Laser Light
  - Laser propagation in long scale-length plasmas
  - **Long scale specular jets** ⟶ by Y. Sentoku
  - Hot electron generation and transport
  - **Generation of high energy ions**
- Summary

Propagation of Intense Laser Light into Over-dense Region

- ○ Laser channel boring with photon pressures
- □ A few 10 to 100 psecs will be required to bore a few 100 μm hole into over-dense plasmas.

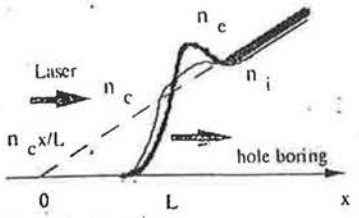

- ○ Snow plow model

$$\frac{d}{dt}\left[\int_0^{x(t)} \frac{x}{L}\rho_i dx\left(2\dot{x}(t)\right)\right] = P_r = \frac{I_L}{c}(1+R)$$

$$\dot{x}(t) = 1.2\times10^9\left(\frac{1\mu sec}{t}\right)^{1/3}\left(\frac{I_L}{10^{19}W/cm^2}\right)^{1/3} cm/s$$

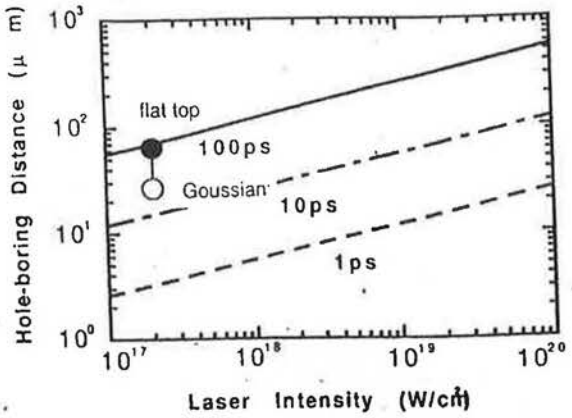

Experimental Simulation of Laser-Hole Boring

1μm laser light with a 100ps pulse duration interacted with a long scalength plasma preformed on a 150-μm thick plastic (CH) target.

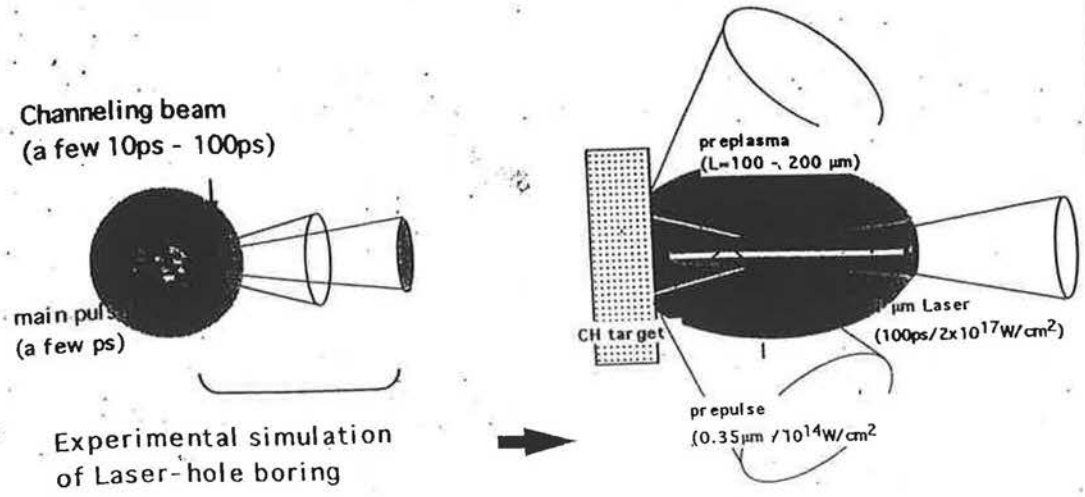

1-D Electron Density Profile Obtained with the XRL-GIR and UV Interferometer

ILE Osaka Univ.

The density profile from the XRL-GIR is consistent with that extrapolated from the profile obtained by the UV interferometer. Solid lines present one-dimensional hydrodynamic simulations (ILESTA) for different initial target diameters (target radius in 1 D simulation: R=∞ and R=2Rs(spot radius)) to take account of a 3-D effect on the plasma expansion.

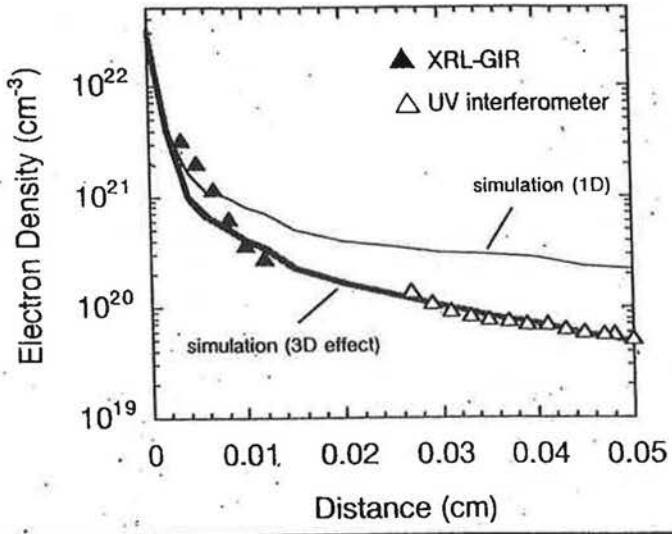

Experimental Studies of Hole Boring

ILE Osaka Univ.

from underdense into over dense region.

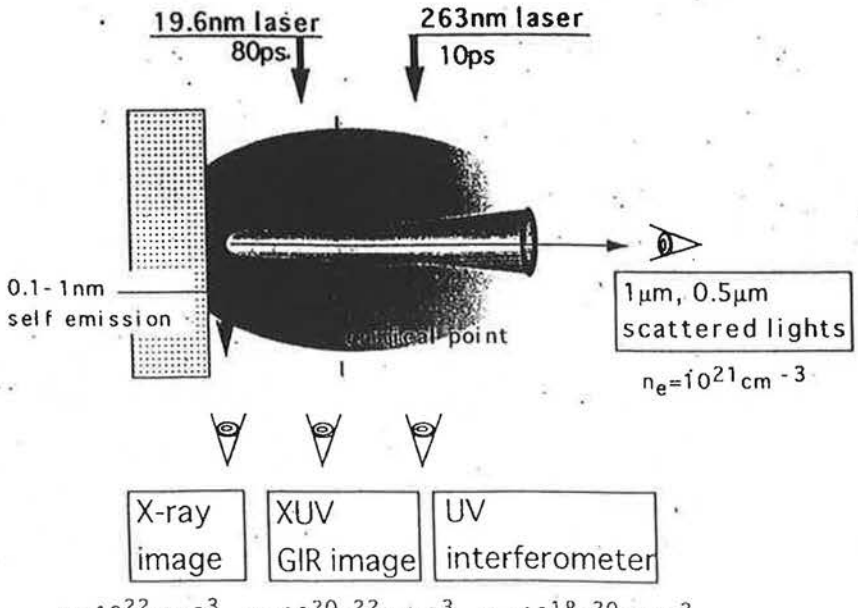

IR & UV drilling beams show totally different behaviors

ILE OSAKA

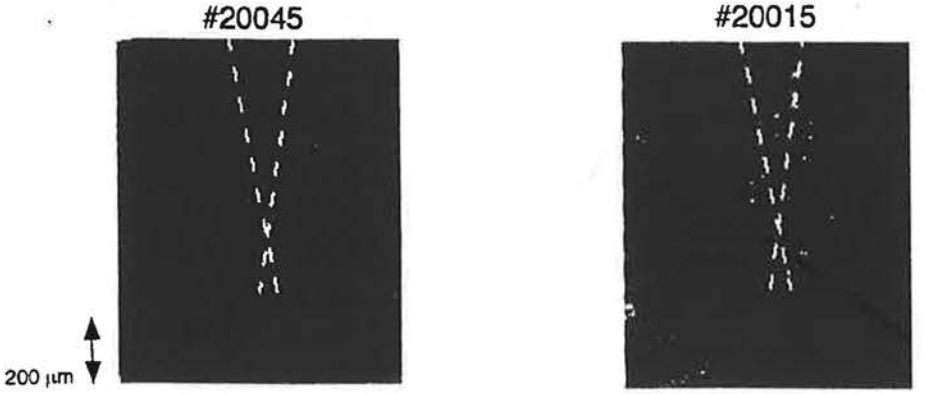

I_L=2 x 10^{17}W/cm^2
#02 3w,8.1J,d=-900
#07 3w,10.4J,d=-900
#08 w,130.5J, d=+210
single pulse
Target CH200um

I_L=1.2 x 10^{17}W/cm^2
#03 3w,5.2J,d=-900
#05 3w,6.6J,d=-900
#09 3w,84.8J, d=+250
single pulse
Target CH100um

$I\lambda^2$ 50 : 1

Backscattered light spectrum and x-ray pinhole picture

ILE OSAKA

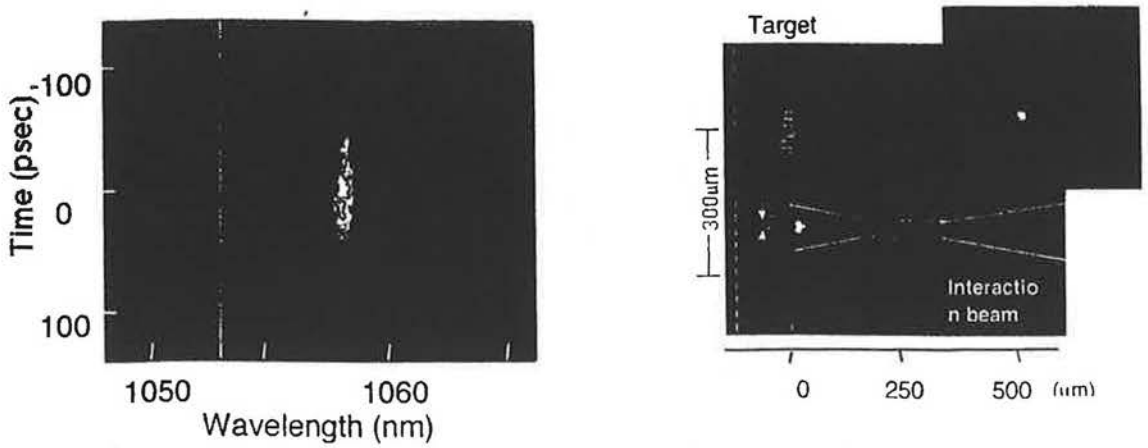

Backscattered light spectrum: large Doppler shift, indicative of the laser drill penetrating into a plasma with a very high speed.

X-ray pinhole pictures: the drilling laser reached the original target surface keeping a very tight spot size, indicative of whole beam self focusing.

Formation of Laser-Channeling in Overdense Plasmas

Cross section of the electron density profile at 55 μm far from the initial target surface estimated from the XRL-GIR image. The original center axis of the channeling beam is located at 0 μm on the horizontal axis.

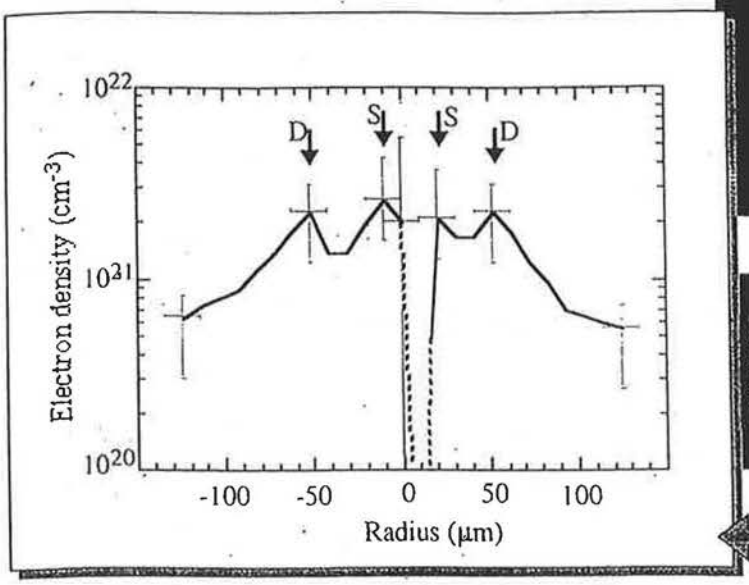

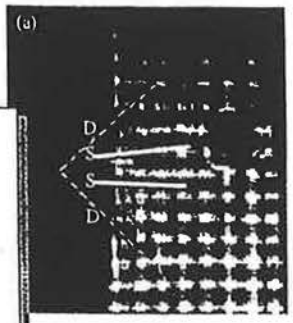

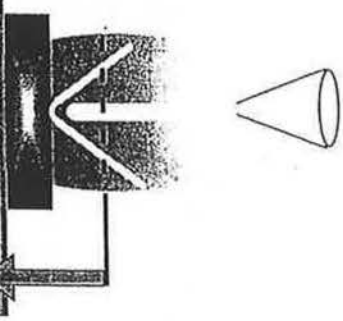

9

Supersonic Propagation of the Channel Front was Proved by Observation of a Mach Cone

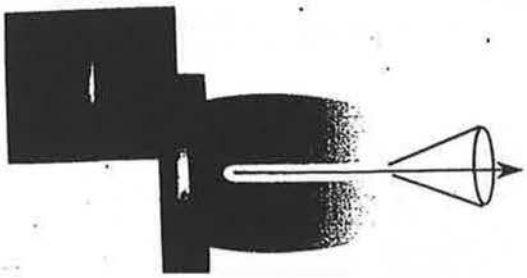

Propagation speed of the channel front from the Doppler shift of the backscatter spectra was 7×10^7 cm/s.

$\theta = \sin(1/M)$

Mach cone angle: 43 deg. for 3keV.

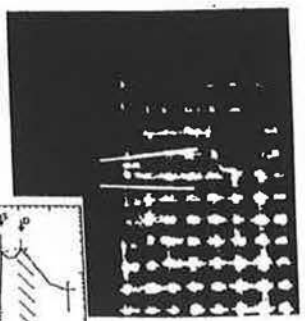

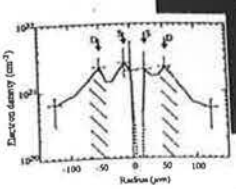

Mach cone angle: 45 deg.

10

Backscatter Spectra Indicates Three Types of the Propagation

ILE Osaka Univ.

Mode A

The spectra is consistent with a calculation.

Mode B

The strong red shift implies hole boring into over dense region.

Mode C

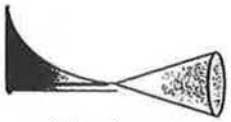

The modulated spectra may be ascribed to the filamentation.

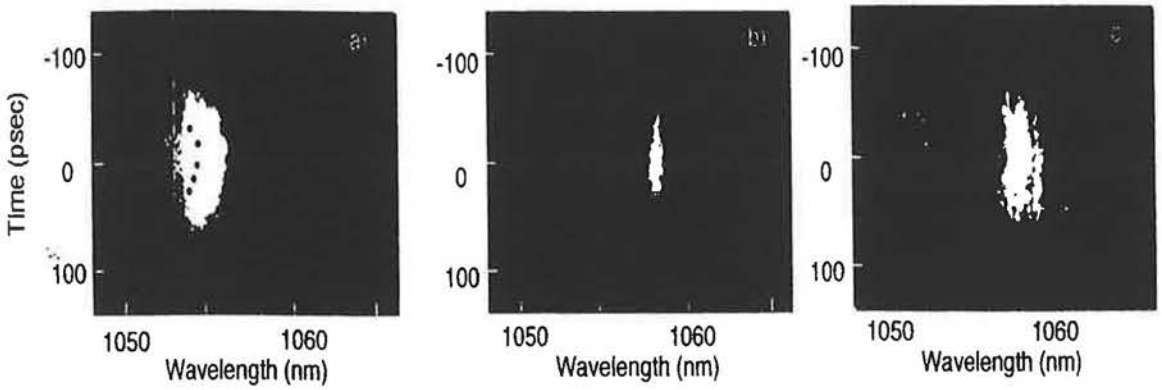

X-ray Imgaes Show Three Different Propagation Modes

ILE Osaka Univ.

front view

Mode A

No hot spot

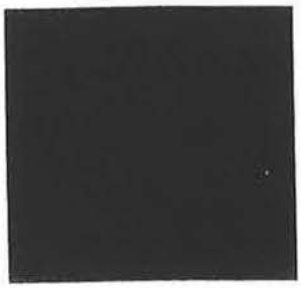

Mode B

Single hot spot on the target surface implies the whole beam self focusing.

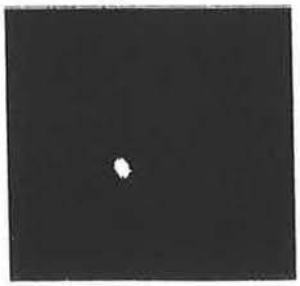

Mode C

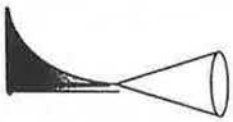

Many hot spot may be ascribed to the beam filamentation.

Hot Electron Energy vs Laser Intensity

ILE OSAKA

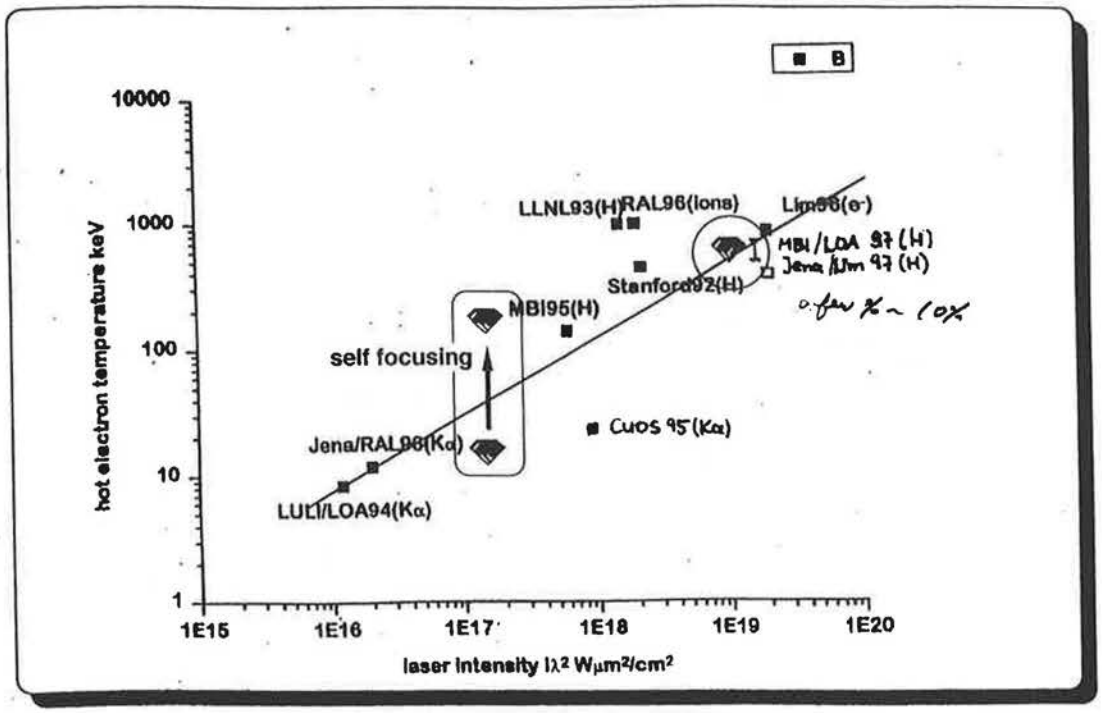

* P.V.Nickles
"Hot electron generation"
Summary of Fast Ignitor Physics Workshop 1997.3.23-25 in U.C. Berkeley

13

implosion | 100 ps | DP

X-Ray Images Indicate Additional Heating of the Shell

ILE Osaka Univ.

1 μm laser light self focused when a CD shell target was imploded by 10 beams of 0.53μm laser light.

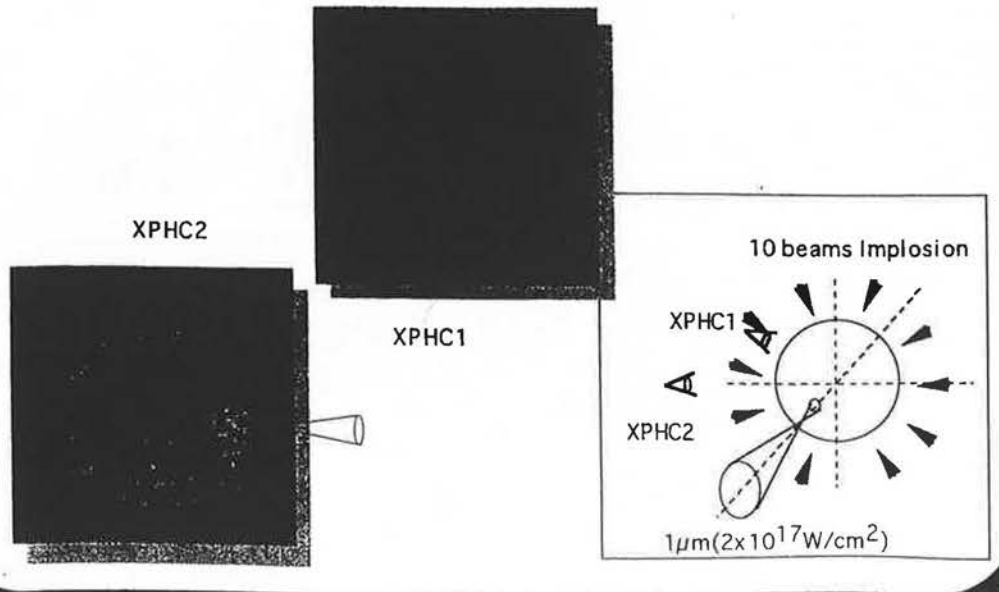

14

3rd Step: Ultra-intense Ignitor Laser Pulse Propagation, Absorption and Creation of High Energy Particles

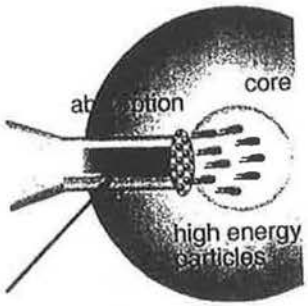

Ignitor pulse

- Propagation of the ignitor pulse in the channel
  - Will ignitor pulse filament in the channel?
  - Will parametric instabilities cause beam break-up?
- Absorption into high energy particles.
  - What is the absorption efficiency to the high energy particles?
  - Where is the laser light absorbed in the channel?
- Generation of hot electrons/high energy ion(T) at a correct temperature.
  - Dependence of T_{hot} and/or T_{ion} on I_L?
- Transport electrons to the core.
  - Magnetic fields?
  - Electron and ion transport?
  - angular distribution of the electrons and ions?

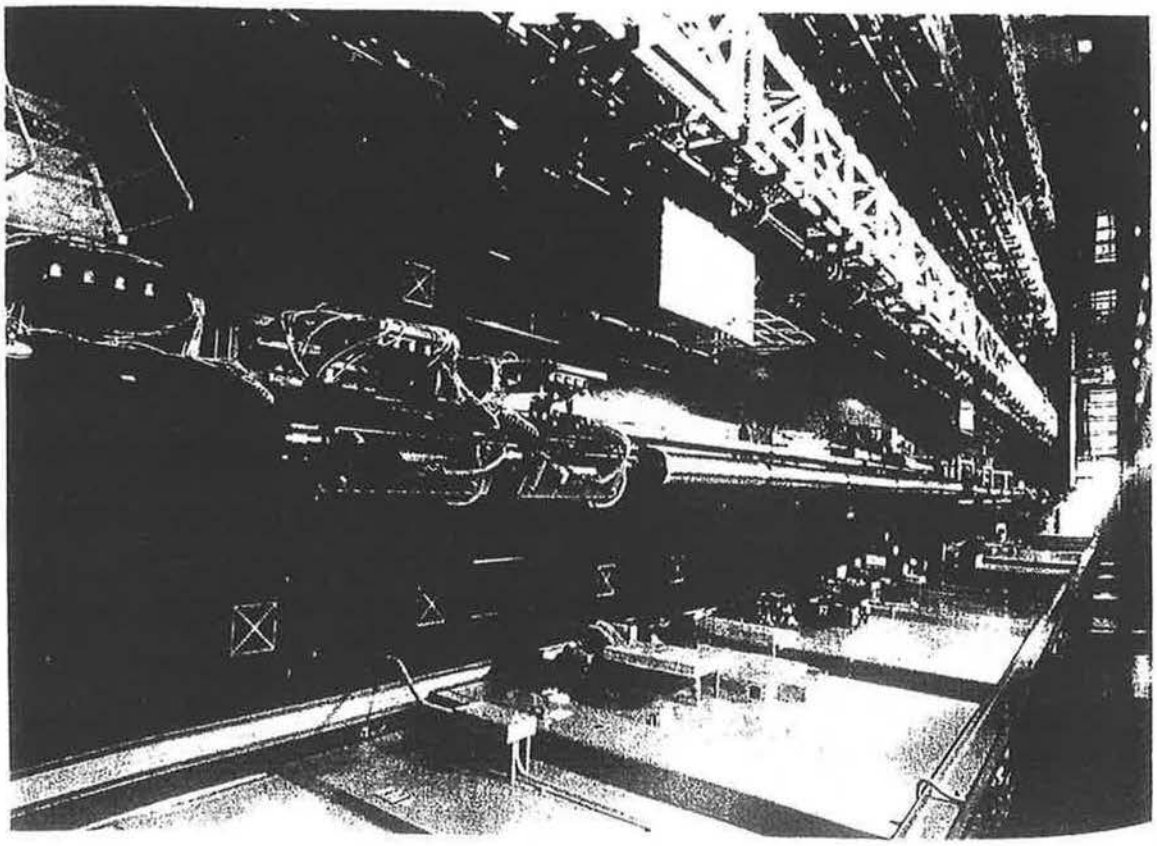

Peta Watt Module

ILE Osaka

- Pulse Duration: 0.5 - 1 ps
- Peak Power: 100TW
- Energy: 50J (limited by gratings)
- Focused Intensity: 1e19 W/cm^2
- Synchronization with GEKKO XII: 100 psec

- GEKKO XII: 12 beams green or blue
  - Pulse :100 ps - 2 ns
  - Energy: 8 kJ total (in green)

Principle **The spectrum of neutrons reflects the momentum of fast deuteron.**

ILE OSAKA

The velocity of neutrons are shifted by center of mass velocity of reacting deuterons.

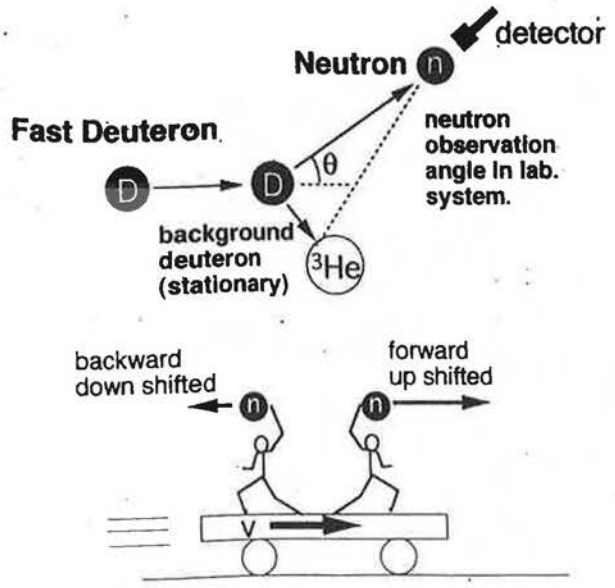

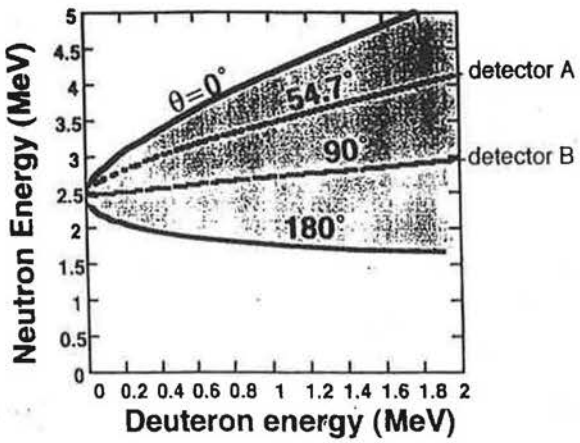

The kinetic energy of neutrons were decided by kinetic energy of deuterons and observation angle of neutrons.

Principle

The energy spectrum reflects the direction of fast deuterons.

ILE OSAKA

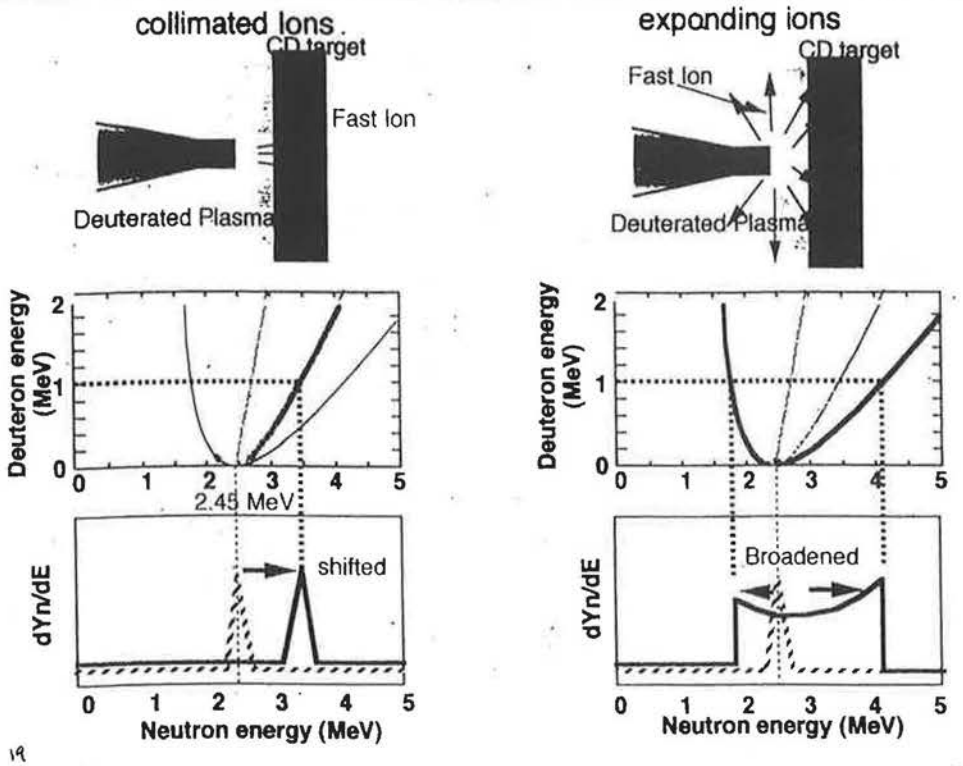

19

June 3,1998 N. Izumi

A large neutron time-of-flight detector array "MANDALA" was developed for ion temperature and fuel areal density measurement in ICF implosion experiments.

ILE OSAKA

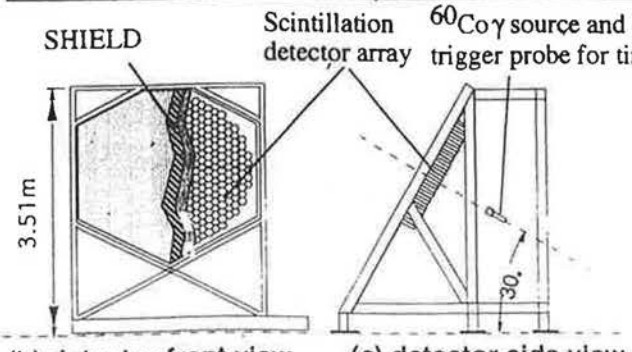

(b) detector front view (c) detector side view

Highly efficient neutron spectroscopy is crucial for the diagnosis of the ion temperature and the areal density measurement.

The "MANDALA" consists of 842 (421ch ×2 port) elements of the plastic scintillation detectors (Bicron BC408) and the data acquisition system.

The "MANDALA" enables us to obtain accurate neutron spectra for yields higher than 1.2×10^5.
(With more than 100 detectors hit by the neutron.)

The energy resolution is 29 keV for D-D neutrons and 270 keV for D-T neutrons which is enough for the Ion temperature and rho-R measurement.

20

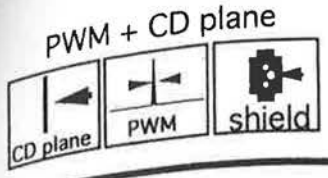

We observed fusion neutrons from CD target irradiated by ultra-high intense laser.

ILE OSAKA

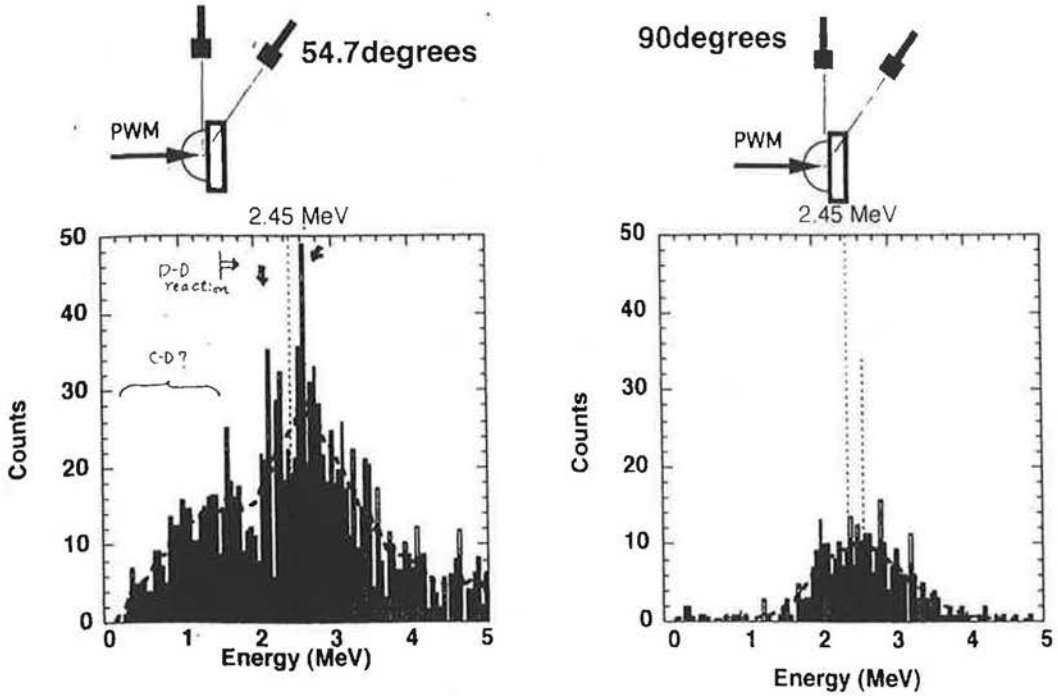

Angular distribution and energy spectra of D-D neutron

ILE OSAKA

2D PIC parameter

Density profile	linear
Peask density	20nc
Intensity	$6 \cdot 10^{19}$ W/cm^2
Spot size	7μm
Simulation time	500 fsec

Total counts 2.19·10⁸

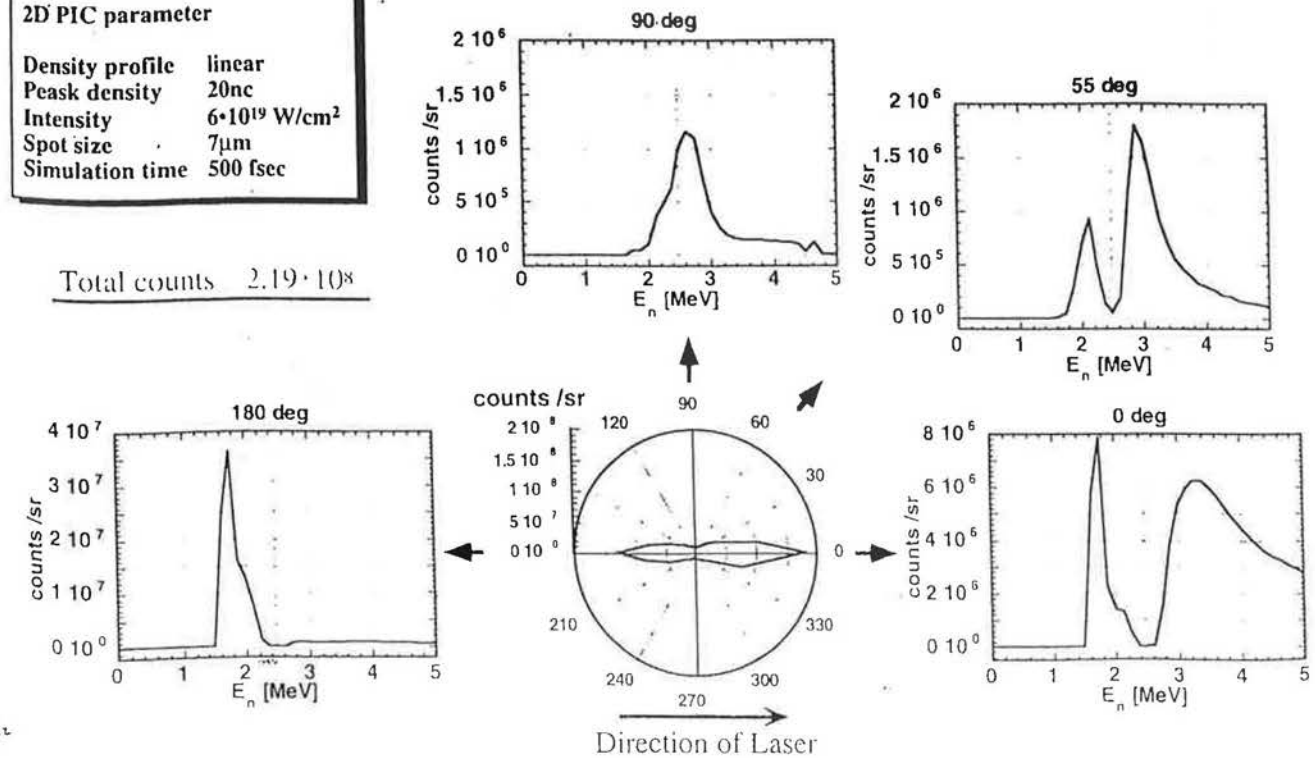

Summary

ILE Osaka Univ.

- Laser-hole boring details have been studied by 100ps laser light.

  Self focusing of 100 ps laser light into overdense plasmas was confirmed by UV and XUV laser probes.

  Channeling of laser light enhanced the hot electron temperature and generation efficiency as well as the high energy ions.

  Channeling was demonstrated in the implosion plasma .

- Ultra-intense short-pulse laser interactions have been experimentally studied at $10^{19}W/cm^2$.

  Laser propagation in a long scale-length plasma was investigated from x-ray images.

  Neutron spectra was obtained to study details of the high energy ion generation (energy and spatial distribution).

  Long scale jets to the direction of the specular reflected light was observed on x ray images.

Fast Electron Generation and Propagation into Thick Solid Targets in High Intensity Laser-Solid Interactions

21-23 September 1998, Rutherford Appleton Laboratory

3rd International Workshop on Fast Ignition of Fusion Targets

Michael Tatarakis

Imperial College

Collaborators

E.L.Clark
K. Krushelnick
J. R. Davies
A. R. Bell
M. Santala
M. Zepf
I. Watts
A.E. Dangor
M.G. Haines

Imperial College, Blackett Laboratory

P.A.Norreys
R.Allott

Central Laser facility, Rutherford Appleton Laboratory

A. Machacek
D.M. Chambers
J.S. Wark

University of Oxford

CHARACTERISTICS OF THE LASER USED IN THE EXPERIMENT

Laser parameters	LMA oscillator
Wavelength	1.054 μm
pulse duration	0.7-1.3ps
Energy on target	5-30 J
focal spot size using 44 cm f/4.2 off axis parabola	Ø=12 μm
Power	30(TW)
Maximum intensity	3.8×10^{19} (Wcm^{-2})

The experiments show :

- A plasma jet at the rear surface of the target exactly in line with the laser focus. The earliest time that such a plasma is observable is at 22 ps for a 140 μm thick CD2 target and the diameter of the plasma at this time is very small (~ 6μm).

- For lower intensities on the target (<10^{18} Wcm^{-2}) the plasma on the rear surface is observed to diverge from the focal line indicating that an instability has probably developed.

- The estimated temperatures of the plasma at the rear are consistent with calculations. They are in the range 1 - 3 keV 25 psec after the interaction pulse, depending on the areal density of the target material irradiated.

Experimental Layout

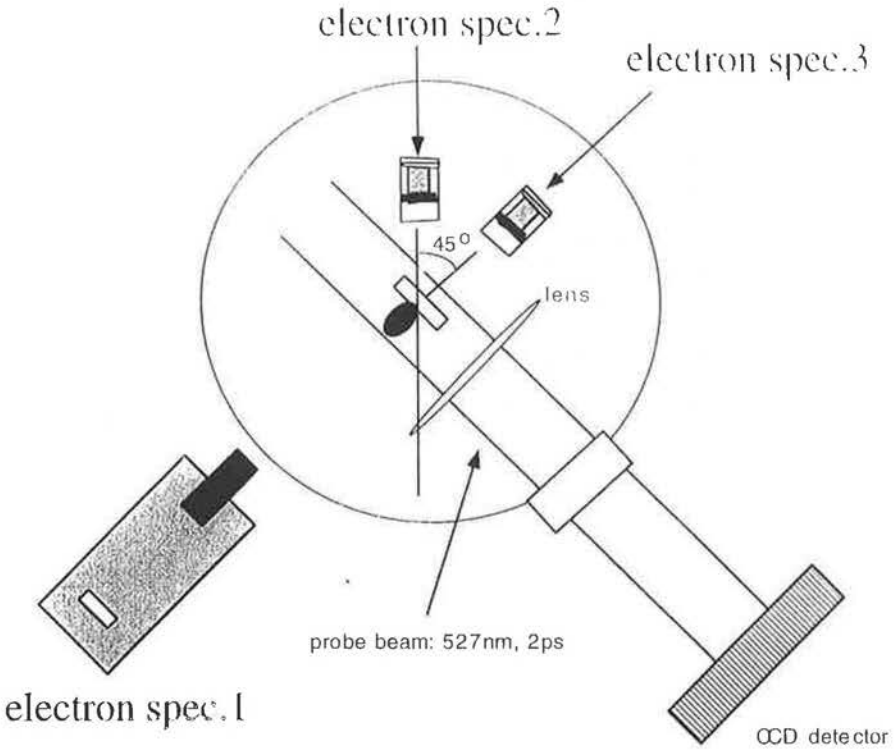

Shadowgrams of CD2 targets from experiments on Vulcan

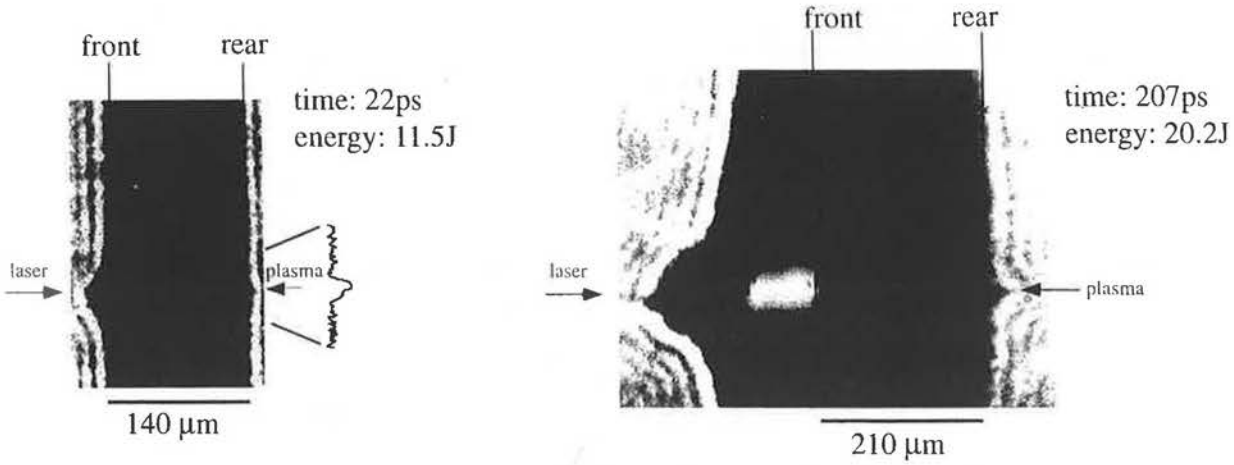

Wavelength: 1.054 μm, Pulse duration: 0.7-1.3 ps, Energy on target: 5-30 J
Spot diameter: 12 μm, Power: 30 TW, Maximum intensity: 3.8×10^{19} Wcm^{-2}
Probe: 0.527 μm, 2 ps
Targets: 5mm x 5mm slabs

M. Tatarakis et al. PRL, 81(5), 999 (1998)

Al Targets

For lower intensities the plasma on the rear surface is observed to move randomly

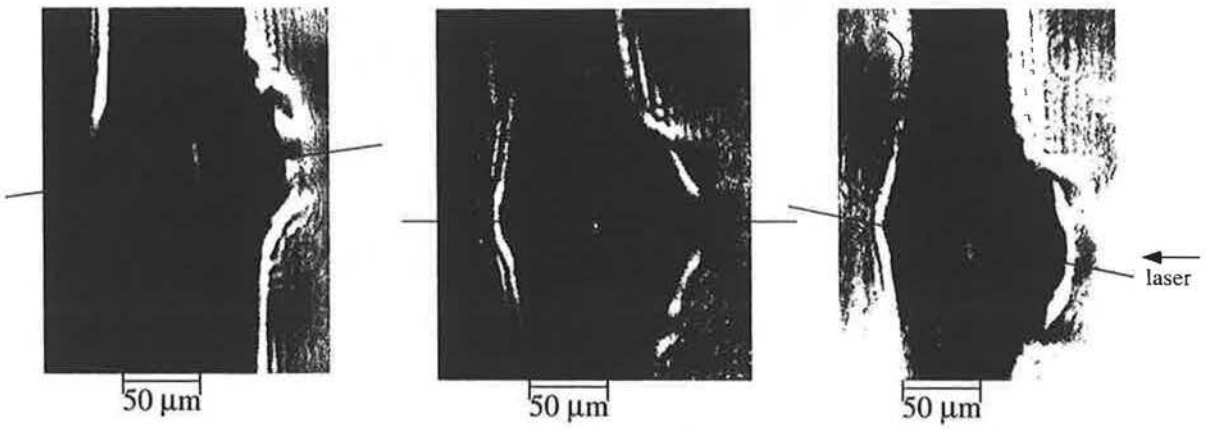

$I<10^{18}$ Wcm^{-2} $I>10^{18}$ Wcm^{-2} $I<10^{18}$ Wcm^{-2}

7

How can this plasma be generated?

- **The prepulse at ~10^{13}Wcm^{-2} is above the target damage threshold (~5 to 10μm scalelength preplasma has been observed). Formation on Al and Al coated CH targets rules out the possibility that the leading edge of the prepulse is transmitted and sharply focused at the rear.**
- **The quick formation (< 22ps) and the small plasma size rules out transport around the target and shock breakout.**
- **Transmission of fast ions is ruled out by the target thickness.**
- **The reproducible diameter and formation on Al rules out electrical breakout. Also see F. Amiranoff et al., PRA 32(6), 3535 (1985).**

Fast Electrons

- **The measured fast electron temperature is ~ 500keV at 10^{19}Wcm^{-2}. An electron with this kinetic energy has a speed of 0.88c, so can account for the rapid formation.**
- **A 250keV electron has a stopping distance of ~ 500μm in plastic. As a result of angular scattering the mean range of electrons in the target is at most a factor of $\sqrt{6}$ lower than the stopping distance.**
- **Therefore the bulk of fast electrons will pass through e.g. the 210μm thick plastic target or 50μm Al.**

However...

- **Resistive inhibition could prevent penetration. A mean penetration depth from 1D model (Bell et.al, Plasma Phys. Control. Fusion 39, 653 (1997)) including only the electric field and assuming Spitzer resistivity is:**

$$z_o \approx 0.0026\left(\frac{1}{f_{abs}}\right)\left(\frac{T_b}{eV}\right)^{3/2}\left(\frac{20}{Z\ln\Lambda}\right)\left(\frac{1.8\times10^{19}Wcm^{-2}}{I}\right)^{1/3}\mu m$$

- **But this will rapidly heat the background lowering the resistivity and allowing the fast electrons to penetrate further.**
- **If *fabs*20J heated every electron in a cylinder of CD2 with a diameter of the laser spot and a length of 210μm then *kTb=10fabs keV*. This gives $z_o = f_{abs}^{1/2}\,2600\mu m$. So for z_o>210μm requires *fabs* > 6.5x10^{-3}. Similar for 50μm thick Al, *kTb=19fabs keV* and *fabs* > 5.4x10^{-5}. Even for *fabs* ~ 0.1 fast electrons are transmitted and can heat the target all the way through sufficiently to form a plasma at the rear.**

Rear surface ionisation

- As the fast electrons leave the rear surface they set up a space charge electric field which reflects them, forming an electron sheath with a scalelength given by the Debye length. The electric field in this sheath is:

$$E \sim \frac{T_f}{d} \approx 1.3\times10^{-4}\left(n_f T_f\right)^{1/2} Vm^{-1}$$

- Field ionisation of hydrogen requires an electric field of $5\text{x}10^{11}\text{Vm}^{-1}$. For $E > 5\text{x}10^{11}\text{Vm}^{-1}$ the fraction of the generated fast electron flux leaving the rear surface has to be:

$$f_{rear} > 0.008\left(\frac{0.4}{f_{abs}}\right)\left(\frac{1.8\times10^{19}Wcm^{-2}}{I}\right)\left(\frac{u_f}{0.88c}\right)$$

- If the fast electrons propagated freely then for this not to satisfied they must be emitted into a full cone angle >51° e.g. in the 140 μm target.

12

Magnetic field

- However, the observed radius of the plasma at the rear is small, i.e 6μm for the 140μm thick plastic target. This can be explained by an azimuthal magnetic field in the target. It is generated by the finite radius of the axial electric field generated by the fast electrons in the target. An estimate of the magnetic field growth rate in this situation (Davies et.al, PRE 56, 7193 (1997), M.E. Glinsky, Phys. Plasmas 2, 2796 (1995)) is:

$$\frac{\partial B}{\partial t} \sim 1.3\left(\frac{f_{abs}}{0.4}\right)\left(\frac{keV}{T_b}\right)^{3/2}\left(\frac{Z\ln\Lambda}{20}\right)\left(\frac{I}{1.8\times10^{19}Wcm^{-2}}\right)^{2/3}\left(\frac{6\mu m}{r_s}\right)\text{kTps-1}$$

- Thus a large magnetic field will be rapidly formed ⇒ High degree of collimation is not surprising.

13

Modelling

- To investigate the fast electron propagation in the solid target a 2D PIC code is developed by Bell and Davies treating the electrons by a relativistic Fokker-Plank equation. Collisions, electric and magnetic fields and changes in resistivity due to heating of the background are included.

- The results show that the fast electron flow is strongly collimated all the way through the target by the azimuthal magnetic field generated by the radial variation in the axial electric field in the target. The collimation of the electron flow can explain the small radius of the plasma formed at the rear surface of the target and its alignment with respect to the laser spot. The radial extend of the heated region on the rear surface is in line with the experimental results (e.g. ~ 6μm radius for the case of the 140μm thick CD_2 target).

Conclusion

- Given that formation by fast electron transmission appears to be the only reasonable explanation, the experimental results show that:

- The fast electrons that generate the plasma at the rear surface of the target are strongly collimated.

- Give indirect evidence for the presence of a large magnetic field in the target.

MPQ

to be presented at the fast ignitor workshop, 21-23 Sept 98

Electron transport experiments with high contrast 150 fs pulses

K. Eidmann

contributors:

A. Saemann U. Andiel E. Fill G. Pretzler	MPQ, Garching, Germany
I. E. Golovkin R. Mancini	University of Nevada
E. Foerster E. Andersson	Friedrich-Schiller-University, Jena, Germany

MPQ

main motivation:

generation of a thermal plasma at very high density

topics:

- energy transport with layered targets (Al on NaCl)
- Al-K-shell emission
- fast electrons (K_{α} emission)

hydro simulation with multi-fs

$I_{abs} = 7 \times 10^{16} W/cm^2$ (p-pol, 45°, τ=150 fs)

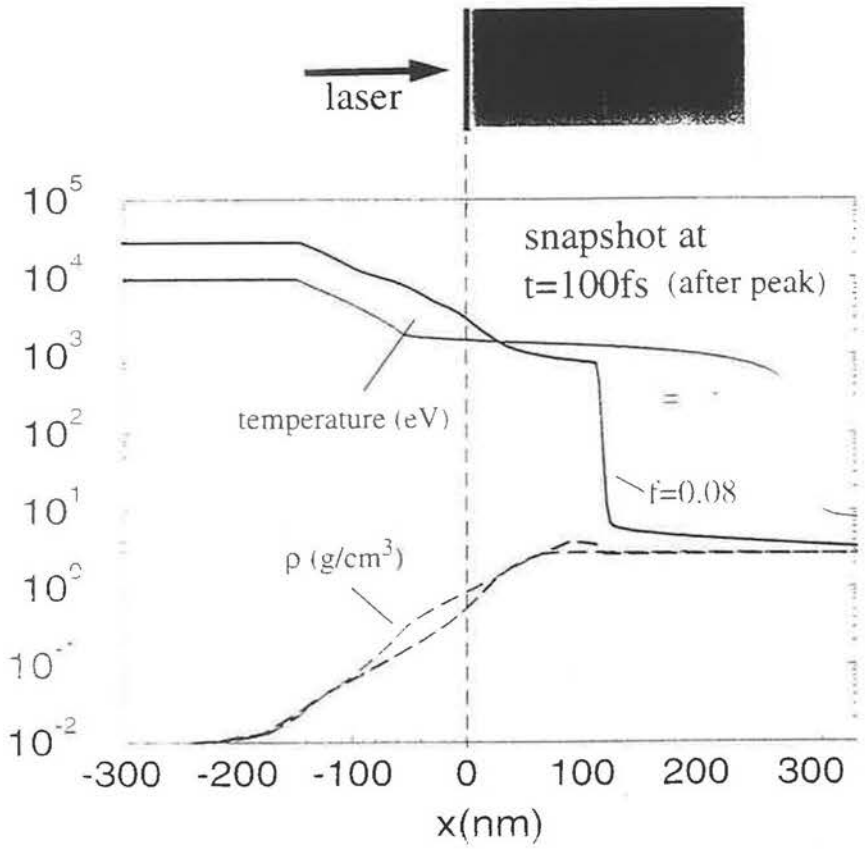

16 September 1998
hydro_f.xmgr.frm

ATLAS performance at 2ω

contrast at 1ps:	10^6-10^8 at 2ω
prepulse contrast:	10^{12} at 2ω
energy :	70mJ at 2ω
pulse duration:	150fs
peak intensity:	5×10^{17} W/cm² (Ø=4-5μm)
mean intensity:	1×10^{17} W/cm² (Ø=20μm)

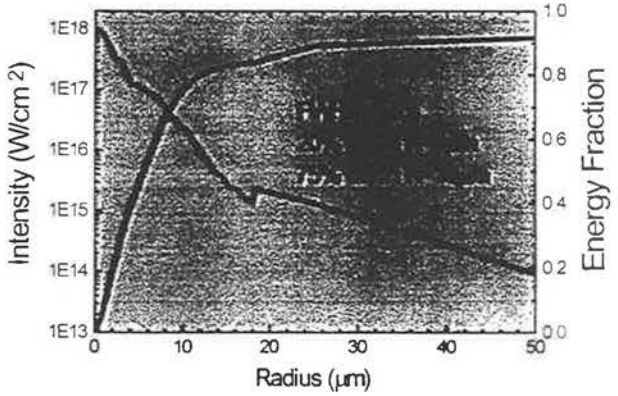

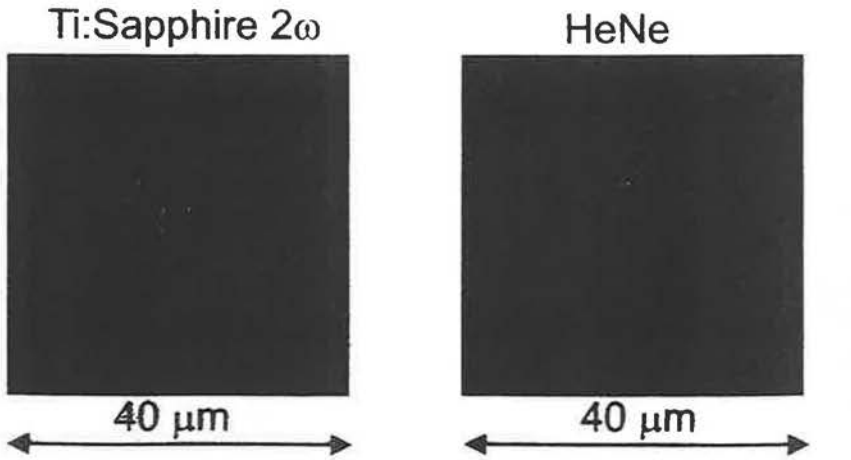

14.05.98 parabel5.cdr

Absorbed energy

peak intensity: 5×10^{17} W/cm^2 (∅=4-5μm)
mean intensity: 1×10^{17} W/cm^2 (∅=20μm)

normal incidence:

absorbed energy = 7%

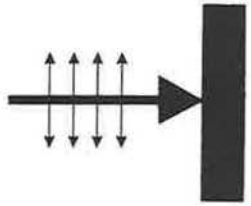

oblique incidence at 45°:

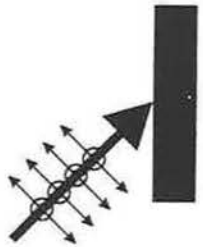

s-polarisation
absorbed energy = 4%

p-polarisation
absorbed energy = 49%

the amount of diffuse scattered light is negligible

Source size measurement

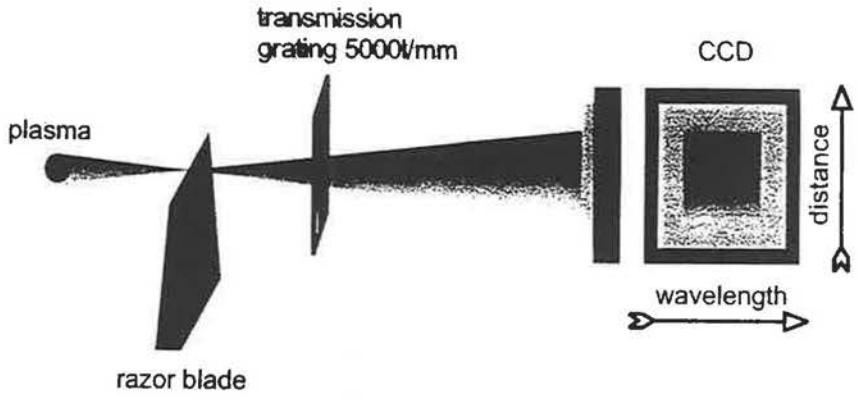

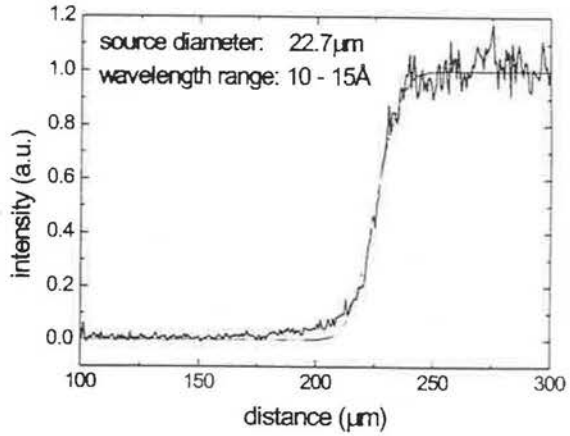

wavelength range (Å)	diameter (μm)	intensity (W/cm^2)
5*	6.7	$\geq 5 \times 10^{17}$
10-15	22.7	$\geq 5 \times 10^{16}$
15-20	29.2	$\geq 5 \times 10^{15}$
45-50	53.9	$\geq 2 \times 10^{15}$

*gold M-band

heating of sodium under Al-layers of different thickness confirms free-stream limit (f=0.6)
(compare G. Guethlein et al. PRL 77, 1055 (1996))

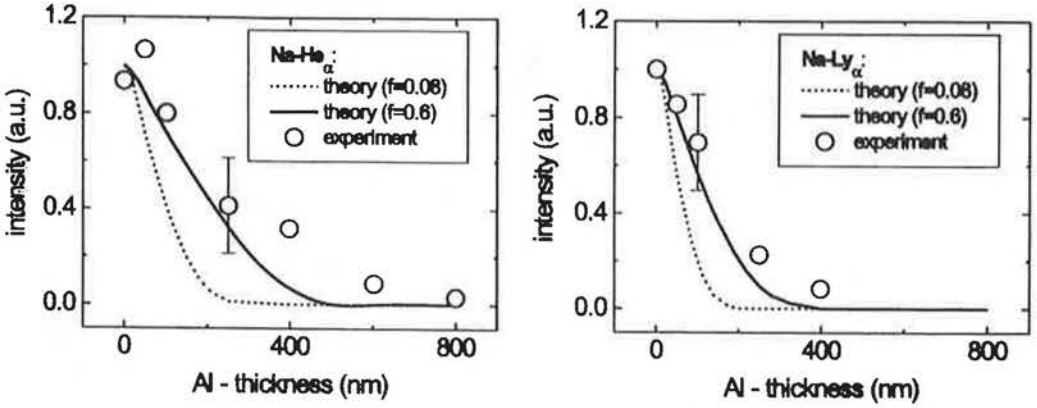

($S_L=10^{17}$ W/cm^2, 45° incidence, p-pol.)

18/9/98
Na-heating frm

emission from a layered target:

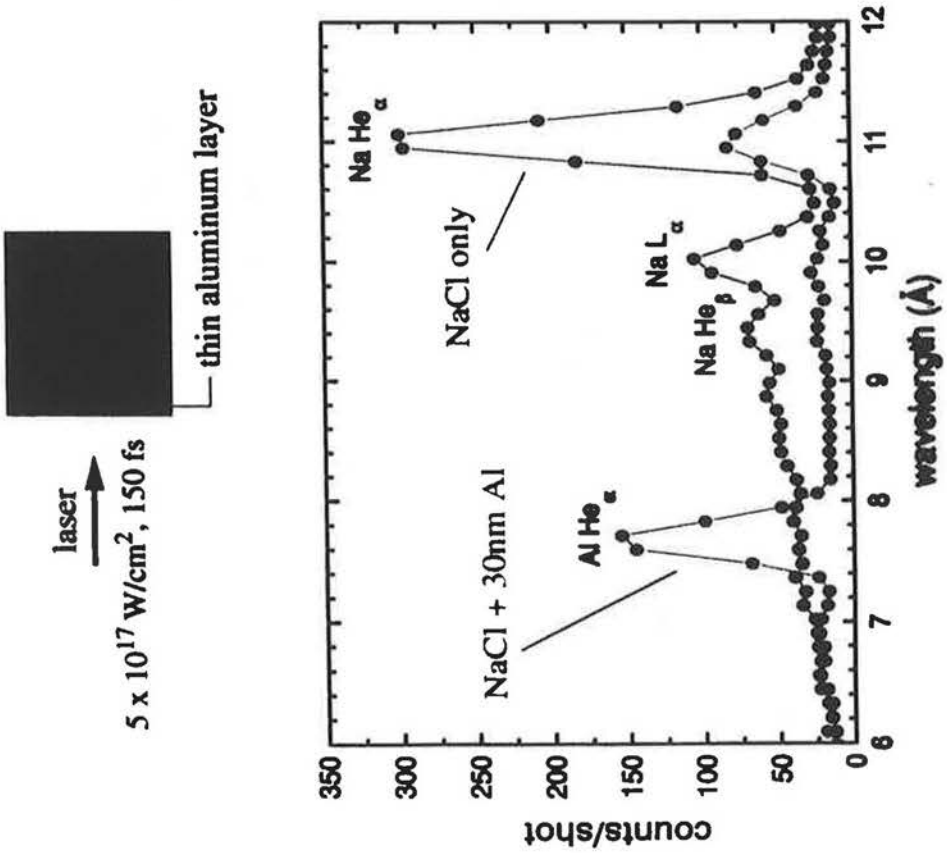

Time-integrated K-shell emission of aluminum

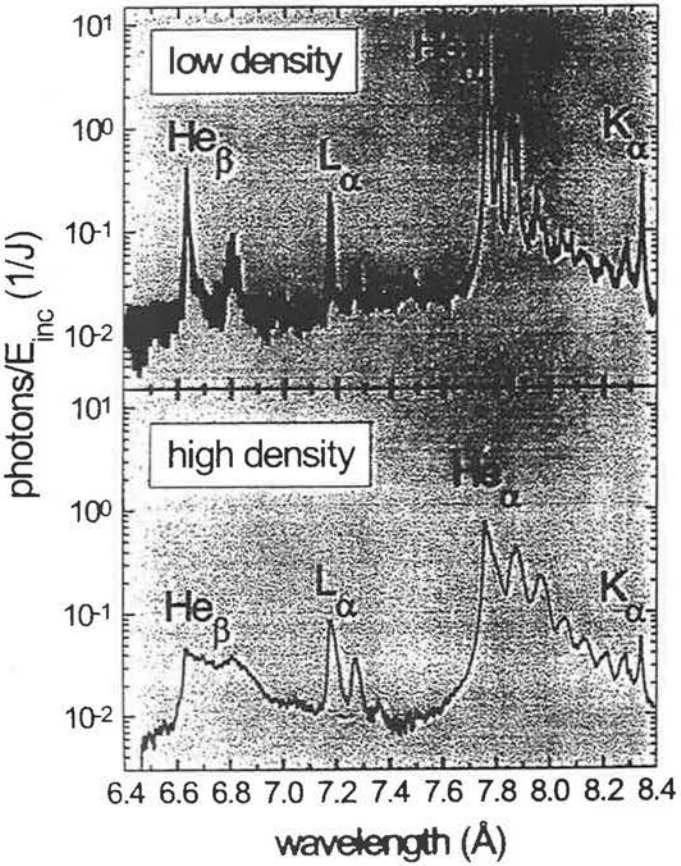

subsequently we will analyse the
Al-L_α and Al-He_β lines and satellites

04.06.98 uebersichts-spektrum2.cdr

The art of generating a high density plasma by using tamped targets

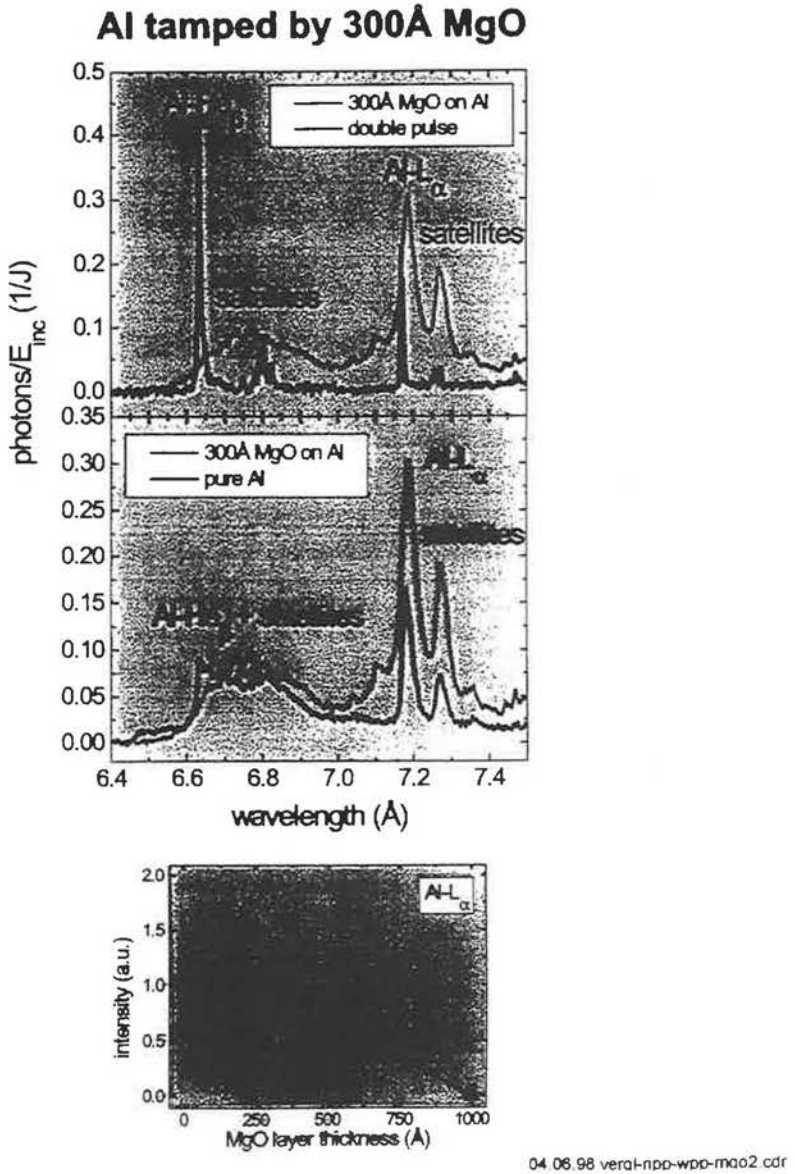

04.06.98 vergl-npp-wpp-mgo2.cdr

duration of Al K-shell (He_α) emission

filters along the slit:

10μm Be +0.7μm Al $\lambda < 15$Å

0.7μm Al $\lambda < 30$Å

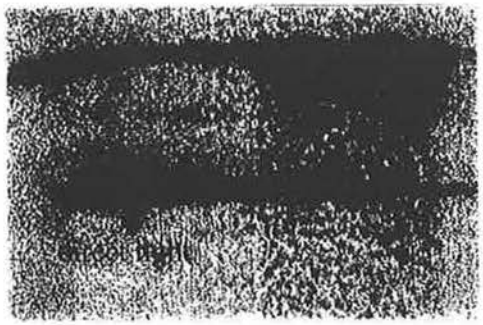

streak recorded with axis-px camera
in jitter-free triggering operation
(100 shots were accumulated)

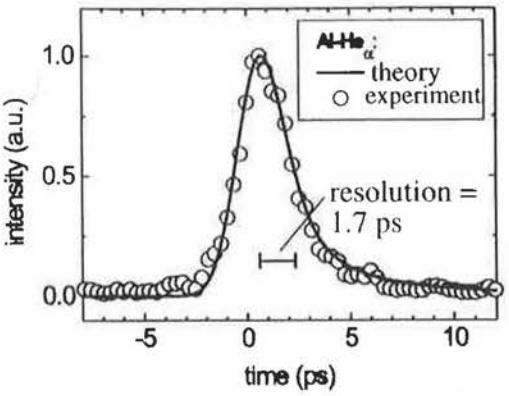

duration (FWHM) = 2.5 ps

comparison of measured spectra with theory

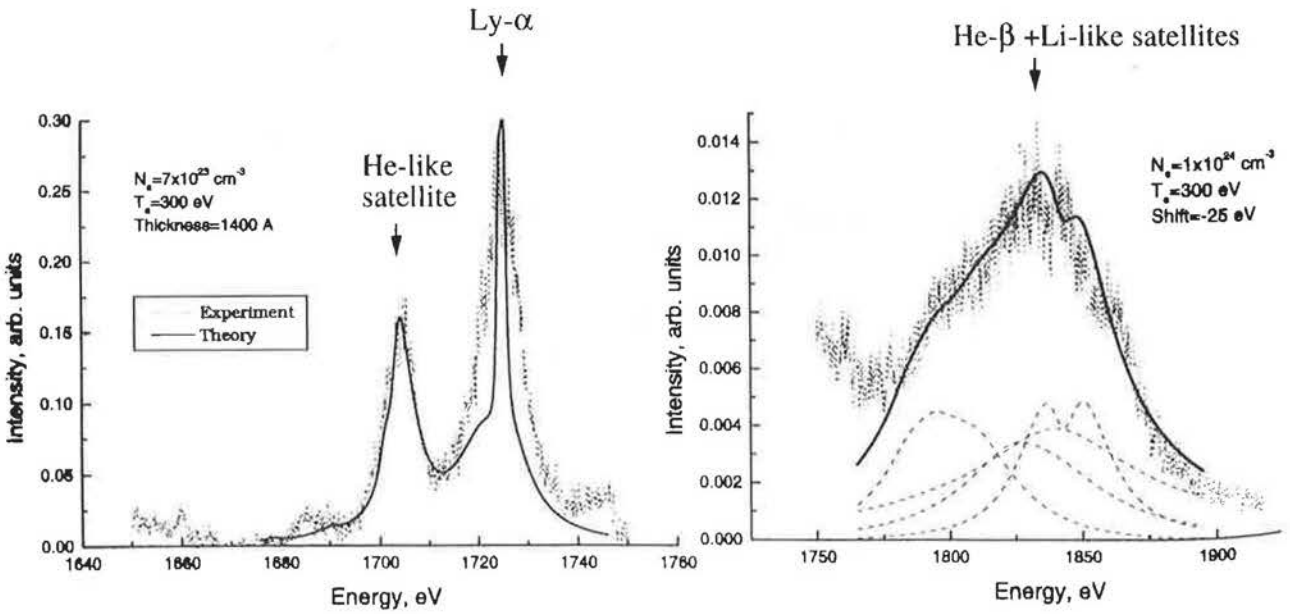

conclusion from spectra analysis:

$T_e = 300 - 400$ eV, $n_e = (0.7 - 1.0) \times 10^{24}$ cm^{-3}

Hot electron temperature

estimation of the total energy (normalized to E_{laser}) carried by fast electrons propagating into the solid target

1.5% **for normal incidence**
8.5% **for oblique incidence and p-polarisation**

(using x-ray tube formula: $\eta \approx 10^{-6}\, Z\, \varepsilon$[keV])

fast electron energy deduced from the number of K_α photons (frequency doubled laser)

E_{laser} = [illegible] J

polari-zation	absorp-tion	#photons He_α	#photons K_α	$\frac{E_{fast\ el}}{E_{inc}}$	$\frac{E_{fast\ el}}{E_{abs}}$
p-pol	50%	3×10^{10}/sr	8×10^{8}/sr	(4±1.7)%	(8±3.5)%
s-pol	4%	2.7×10^{9}/sr	2×10^{8}/sr	(1.4±0.2)%	35%

CONCLUSIONS

- λ=400 nm , 120fs fT-Stapp pulses with a high pre pulse main pulse contrast are efficiently coupled into dense solid Al
- a dense strongly coupled plasma with n_e (0.1–1.0)x10^{24} cm^{-3} and kT_e = 300 - 400 eV is generated (~ Ni-like Transient)
- segregement with hydro calculations with free-streaming limit (f=0.06)
- from K_α emission follows:

  with p-polarized light only <10^{16} of absorbed energy is coupled into fast ≈ 10keV electrons penetrating into the solid Al

Fast electrons deposition experiment with the new LULI 100 TW laser. Part I: K_α spectroscopy

Presented at
3th International Workshop on Fast Ignition of Fusion Targets
Rutherford Appleton Laboratory, Didcot, UK. 21st-23rd September 1998

F. Pisani, L. Gremillet, M. Koenig, F. Amiranoff, E. Martinolli (LULI, France)
P. Norreys, A. Djaoui (RAL, UK)
T. Hall (Univ. of Essex, UK)
D. Batani, A. Antonucci (Univ. of Milan, Italy)
C. Rousseaux (CEA, France)
H. Pepin, H. Bandulet (INRS, Canada)
P. Fews (Univ. of Bristol, UK)

Work supported by the European TMR Program under contract number ERBFMGECT950044 .

Purpose

Improve the understanding of the suprathermal electron transport, their propagation and their energy deposition.

In the interaction of a 2ω short pulse with a solid target, through K_α spectroscopy:

- different kind of materials - insulator (CH) and conductor (Al)
- with a preplasma

Experimental set-up

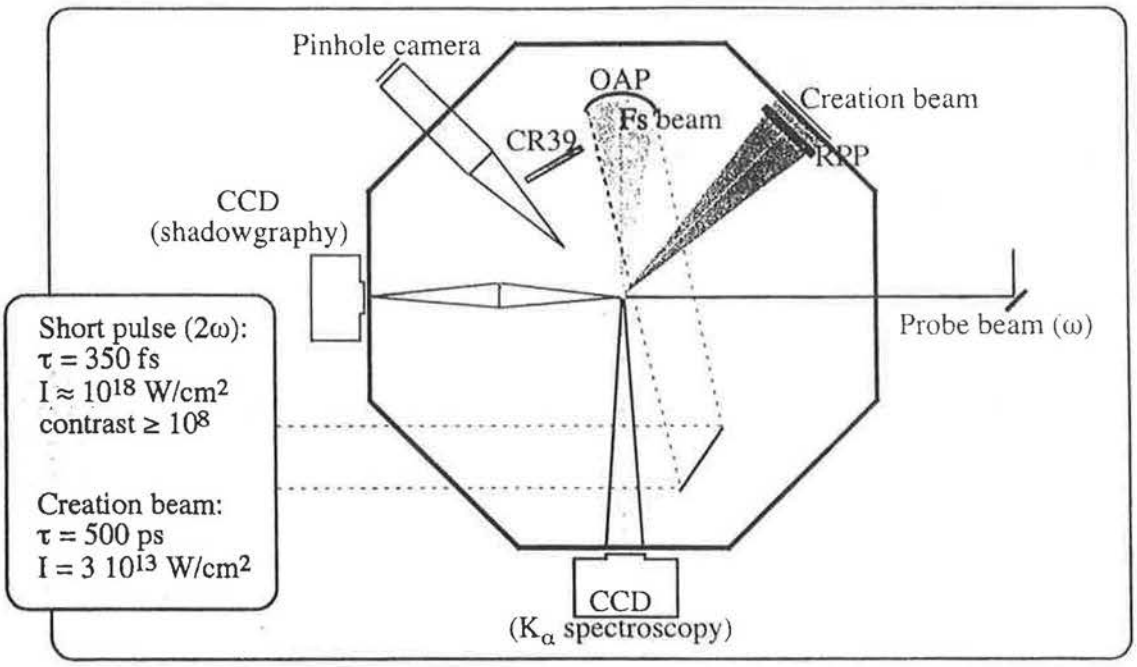

Target configuration for K_α spectroscopy

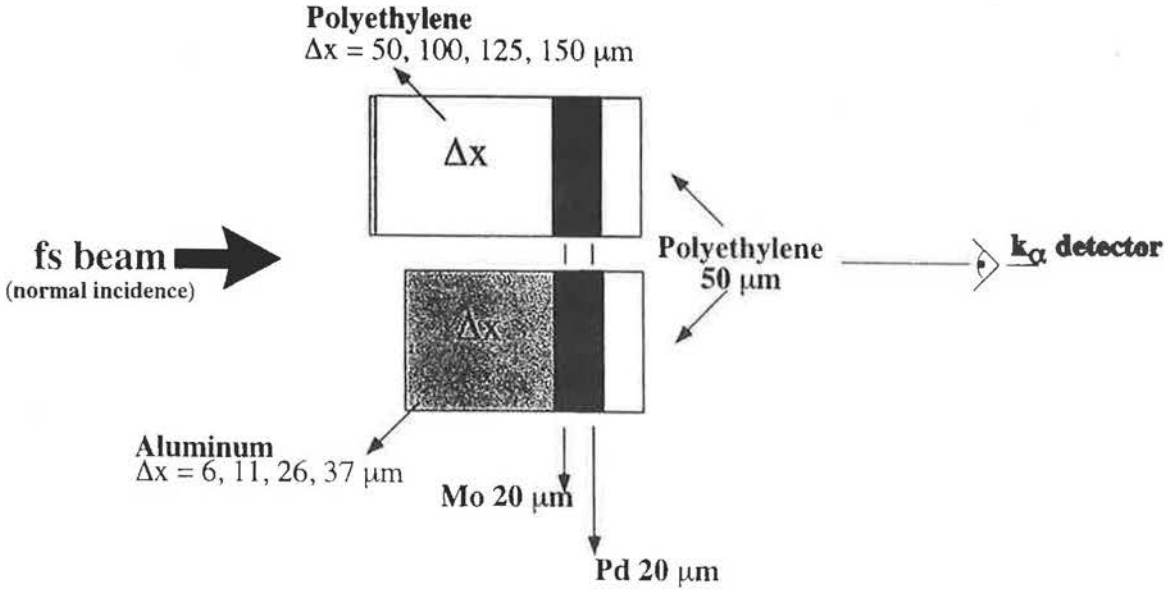

10^{18} W/cm² intensity on the target

Focal spot:
5 μm resolution pin-hole image

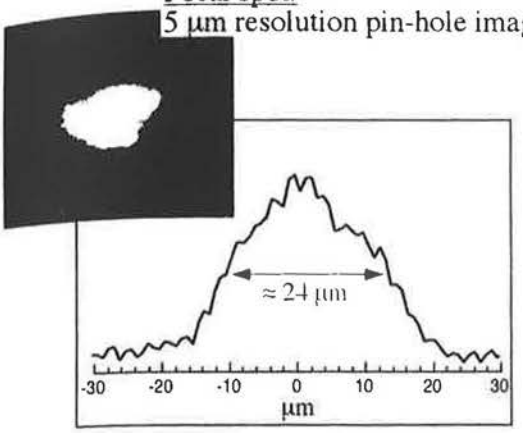

Autocorrelator image

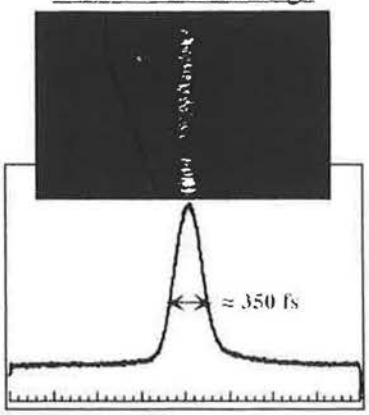

expected T_h for $I \approx 10^{18}$ W/cm²

*kT_{hot} (keV) = 100 $(I_{17})^{1/3}$ → **$kT_{hot} \approx 215$ keV**

kT_{hot} (MeV) = 0.511 $\{(1+I_{18}/1.37)^{1/2} - 1\}$ → **$kT_{hot} \approx 160$ keV

* Beg *et al.*, Phys. Plasmas **4**, (1997)
** Wilks *et al.*, Phys. Rev. Lett. **69**, (1992)

K_α spectroscopy: obtained spectrum

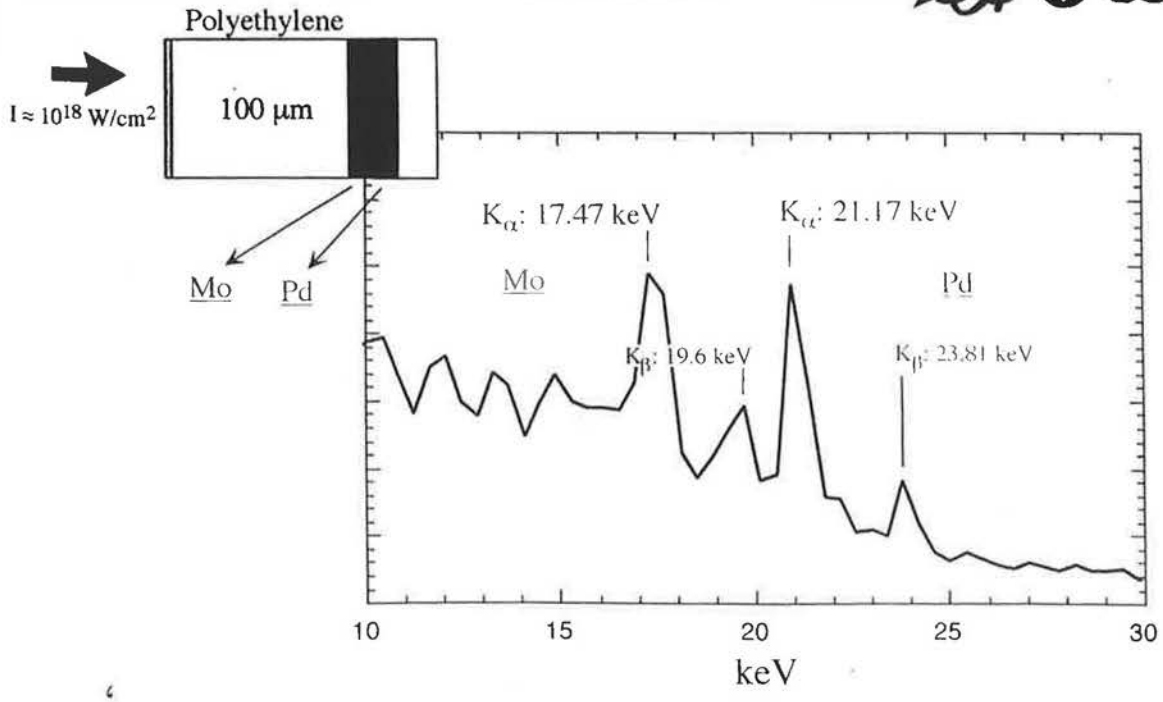

Results in Aluminium

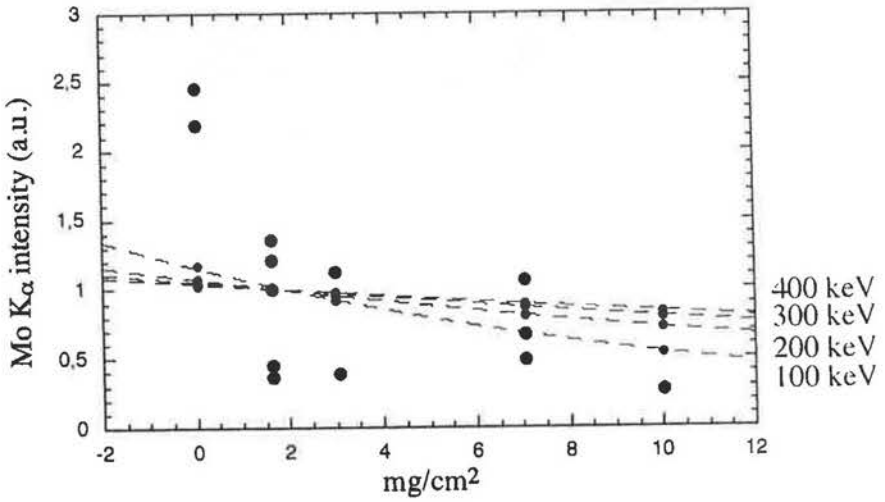

Results in polyethylene

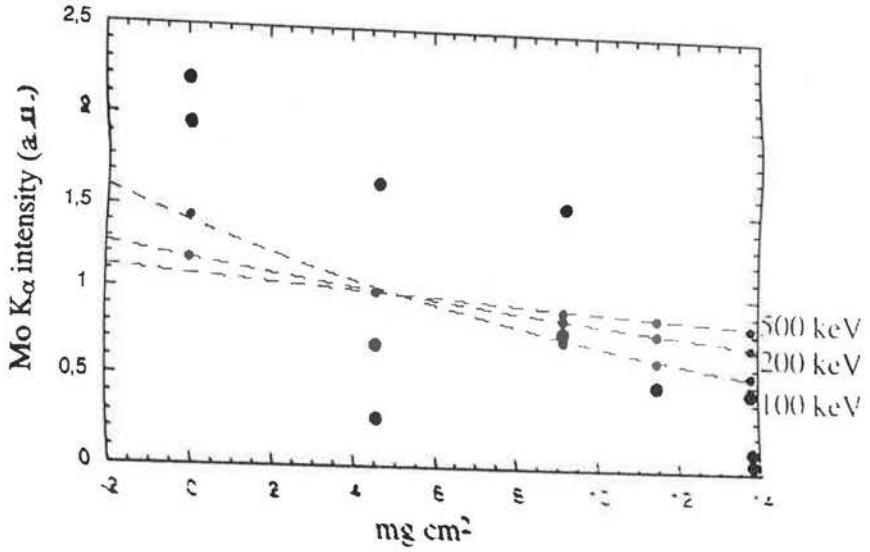

Aluminium: $T_h \approx 200$ keV

The ratio of K_α photons from the Pd on the Mo layer is weakly depending on the target depth (mg/cm^2).

By comparing this ratio with simulations we found an electron temperature in the Aluminium of ≈ 200 keV

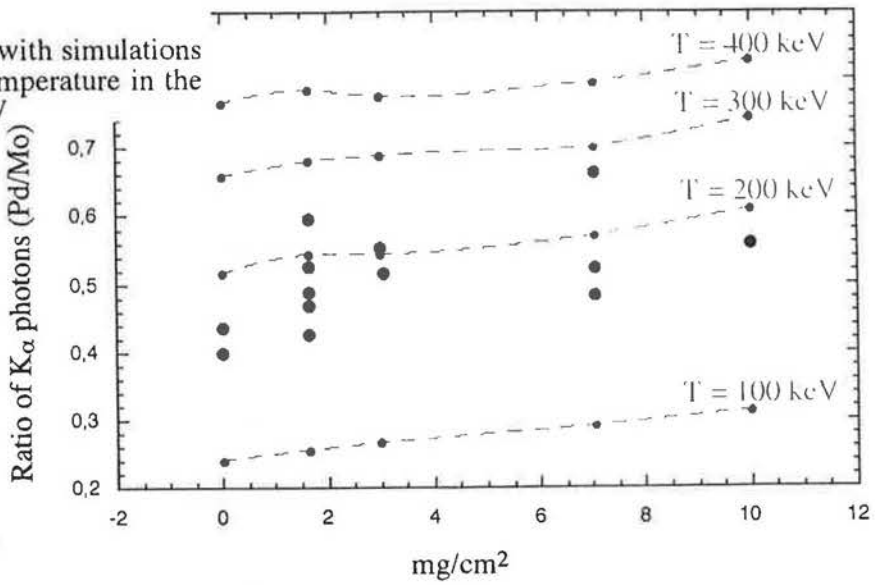

Polyethylene and Aluminium

Stopping power:

$$\frac{1}{\rho Z}\frac{dE}{dx} \propto -\frac{4\pi}{E}\ln\frac{4E}{I}$$

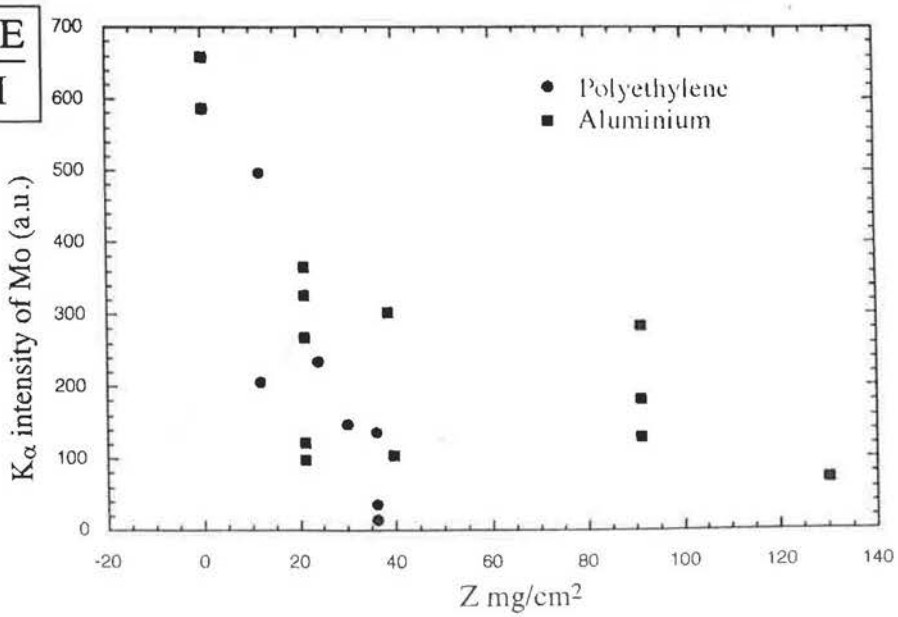

Hydrodynamic of the preplasma

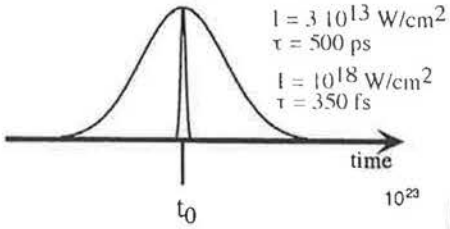

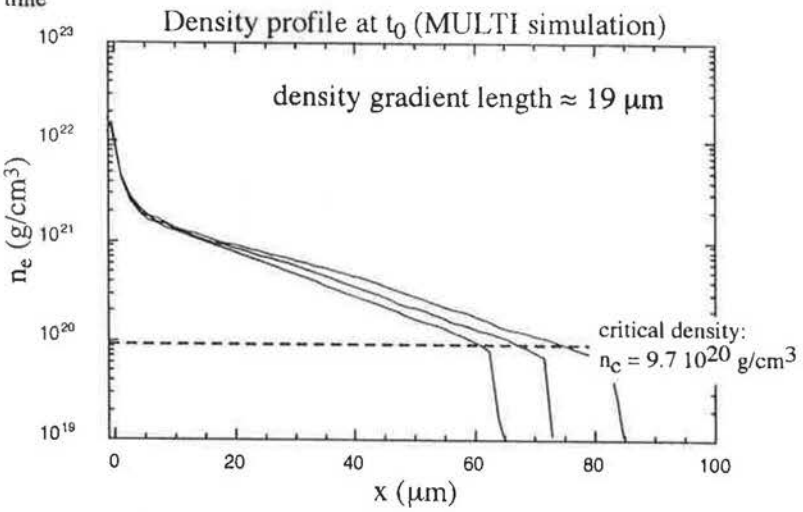

Very small difference in presence of a preplasma

- experimental points missing
- saturation of the CCD camera
- too short density scale length

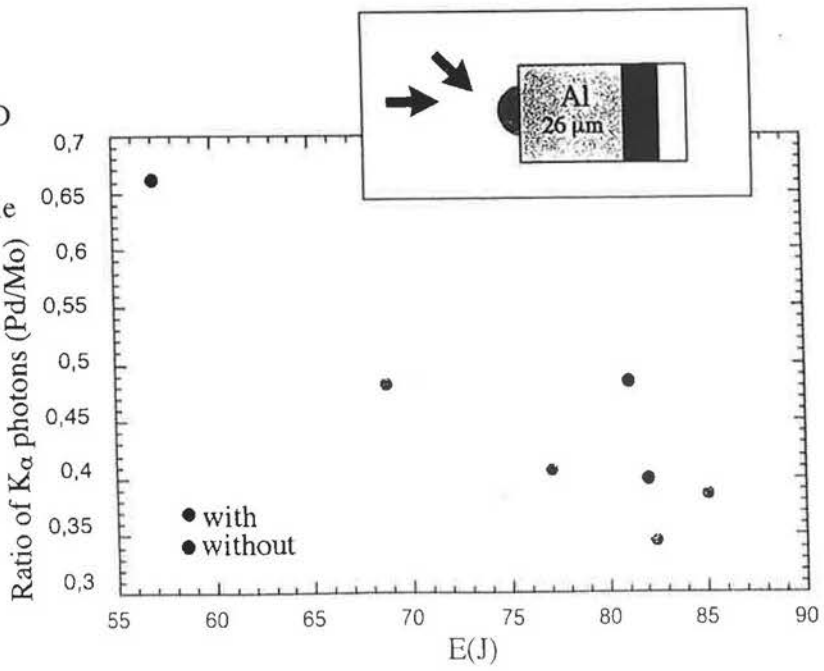

Conclusions

Very preliminary analysis of the obtained results.

- estimation of the electron temperature ≈ 200 keV
- dubious comparison with Monte Carlo simulations
- no evidence of strong change in presence of a preplasma

Fast electron deposition with the new LULI 100 TW laser

Part 2 : Shadowgraphy through transparent targets

Presented at
the 3rd International Workshop on Fast Ignition of Fusion Targets
21st -23rd September 1998
Rutherford Appleton Laboratory, Chilton, Didcot, UK

F. Amiranoff, L. Gremillet, M. Koenig, F. Pisani, E. Martinolli	*LULI, France*
P. Norreys, A. Djaoui	*RAL, UK*
T. Hall	*Univ. of Essex, UK*
D. Batani, A. Antonicci	*Univ. of Milan, Italy*
C. Rousseaux	*CEA/Bruyères, France*
H. Pépin, H. Bandulet	*INRS, Canada*
P. Fews	*Univ. of Bristol, UK*

This work was financed by the European TMR program
under contract number ERBFMGECT950044

Rear heating of a 30 μm thick solid CH target
if self-similar expansion $\Rightarrow$ *50 keV* + half-angle ~ 20/25°

CEA LULI INRS

- interaction beam @ 527 nm, I λ^2 # 3e18 W.cm^{-2}.μm^2
- transverse interferometry beam @ 350 nm, 1 ps duration
- interferogram taken 5 ps after the interaction beam

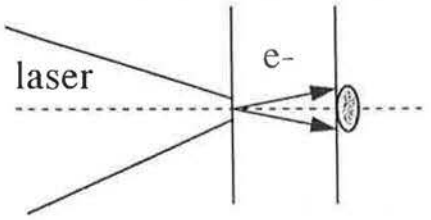

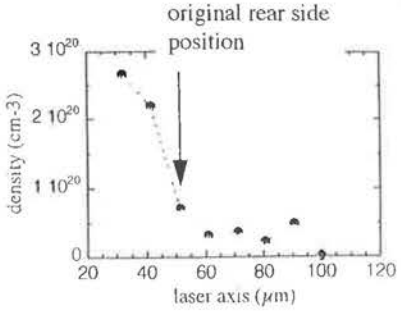

30 μm solid CH foil

interaction beam

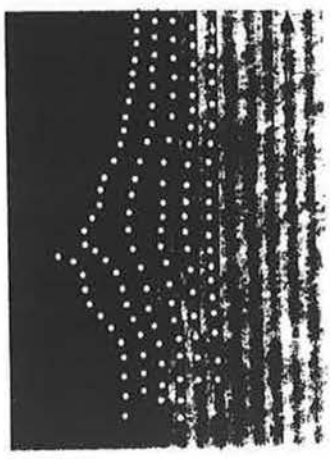

Purpose of the experiment

- Growing body of evidence as for the generation of collimated electron jets in laser-solid interaction at relativistic intensities
- If confirmed, this behaviour is critical for the success of Fast Ignitor
- Need of a new diagnostic visualizing directly what is going on into the target with a time-resolution

[redacted]

Experimental set-up (1)

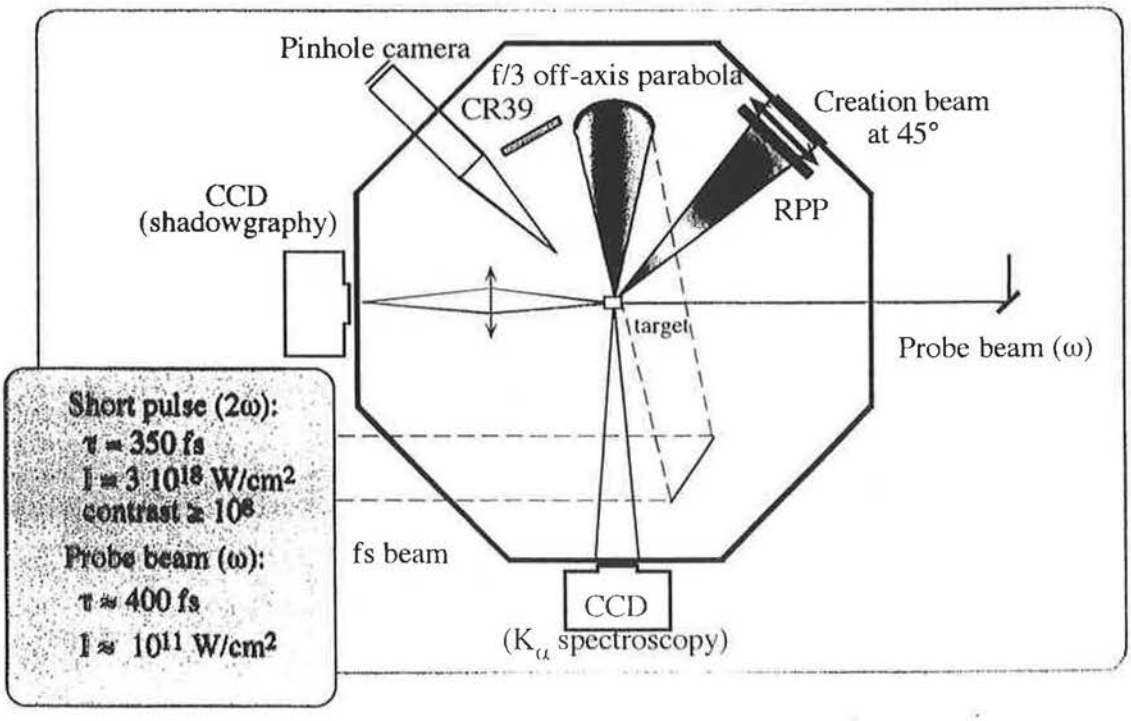

Experimental set-up (2)

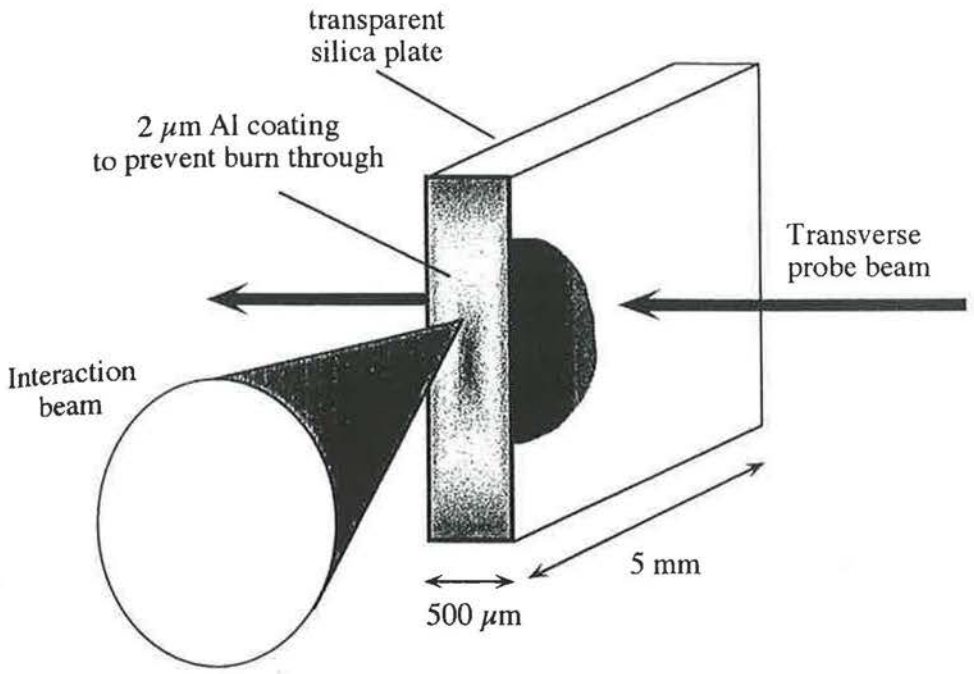

Formation of a relativistic collimated jet detected

Bright spot at $\Delta\tau = 0$
$\Rightarrow$ stimulated down-conversion of the interaction beam ?

$\Delta\tau = 1$ ps
$v_{jet} \approx c$

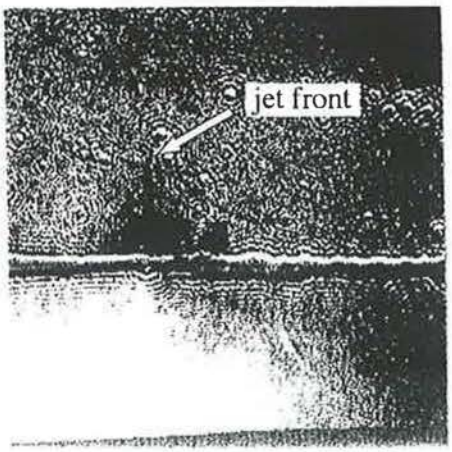

filament width < 30 μm (# focal spot)
$\Rightarrow$ not spatially resolved

Following the jet, a diffusive cloud is seen to expand on later times at v ≈ c/3-c/2

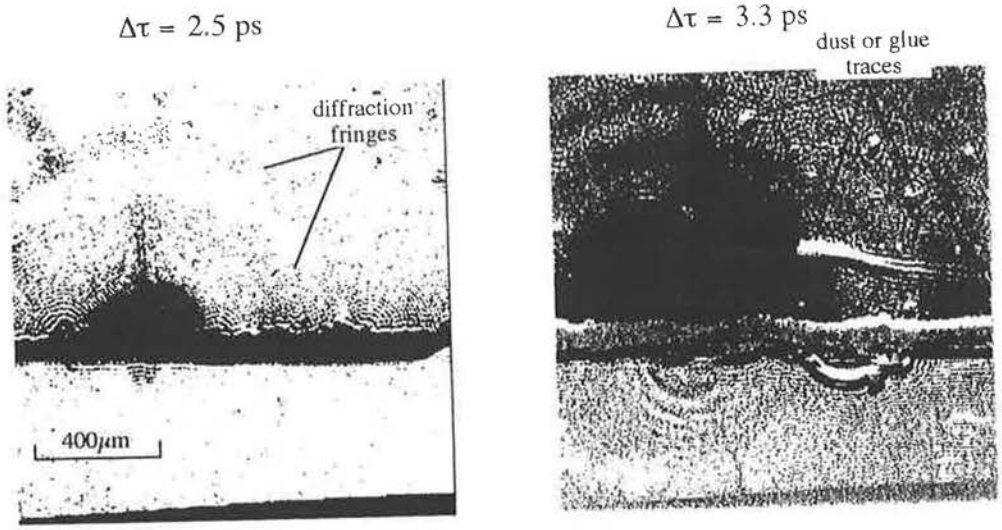

7

A laser filament seems very unlikely

- 2D PIC simulations show no laser transmission through 2μm Al at 10^{18}W/cm^2 and the bulk of the SiO target is highly overcritical as soon as the ionization takes place
- 2ω conversion allows a contrast ratio of the order of 10^8 : 1
- 2ω coating reflective optics located between the KDP crystal and the target reduce the residual 1ω energy by a factor < 10^8

thermal electrons or hard X-rays

7

Virtual Laser Plasma Lab

3D Particle-in-Cell, Electro-Magnetic, Relativistic

Massively Parallel Processing

CRAY-T3E

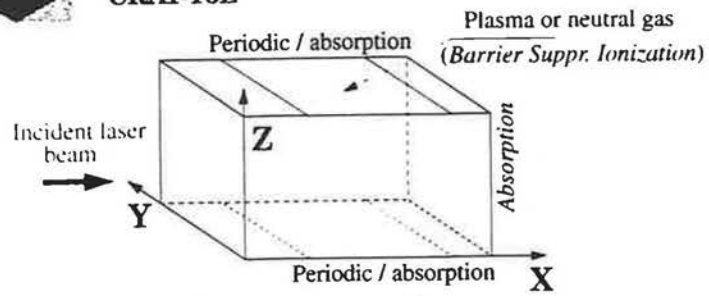

We use up to 10^9 particles and 10^8 grid cells, when run on 512 PEs of T3E.

Single PE performance: 3μs per particle per time step
Parallel efficiency: more than 90 %.

Numerical Dispersion Free (NDF) algorithm
A. Pukhov, ICNSP Proc., p.18 (1998)

Fields:

$$rot\bar{B} = \frac{1}{c}\frac{\partial \bar{E}}{\partial t} + \frac{4\pi}{c}\bar{j}$$

$$rot\bar{E} = -\frac{1}{c}\frac{\partial \bar{B}}{\partial t}$$

$$div\bar{E} = 4\pi\rho$$

$$div\bar{B} = 0$$

Particles:

$$\frac{d\bar{p}}{dt} = q\bar{E} + \frac{q}{m\gamma}[\bar{p}\times\bar{B}]$$

$$\gamma = \sqrt{1 + \frac{p^2}{m^2c^2}}$$

Fast electron generation by relativistic self-focusing and

Detailed studies show, that fast electrons are produced when $P > P_c$: *threshold behaviour.*

$$P_{cr} = 17\left(\omega^2/\omega_p^2\right)GW$$

R.Wagner et al., PRL 78, 3125 (1997)

R. Fedosejevs, X. F. Wang, G. D. Tsakiris, Phys. Rev. E, October (1997)

Fast electron energy spectrum

C. Gahn et al.

electron density: $n_e=10^{20}$ cm^{-3} (helium)

intensity: $I_{max}= 3\times10^{18}$ W/cm^2 and radius($1/e^2$) ~ 6μm

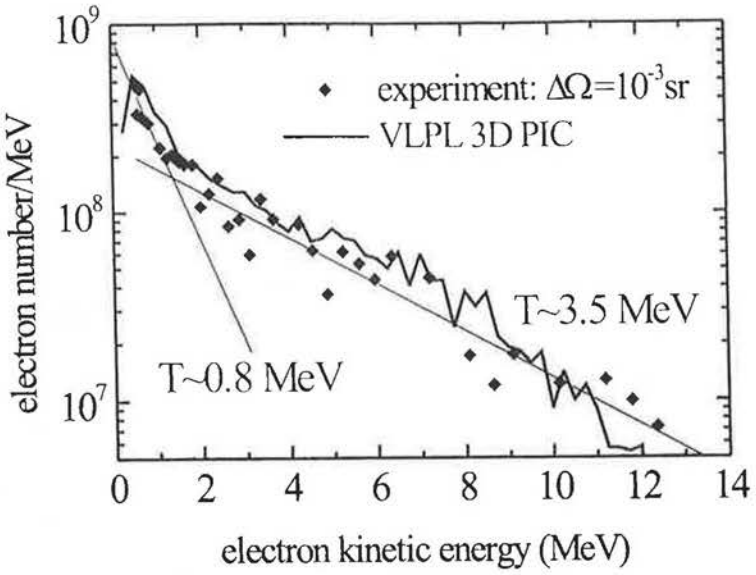

total fast electron number in 2π: **7x10^{10}** (assuming Lorentzian angular distribution)

MeV electrons generated with fs pulses from ATLAS laser

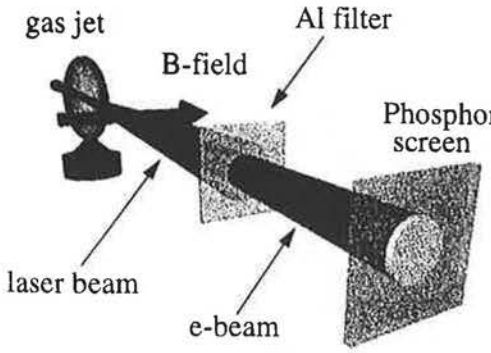

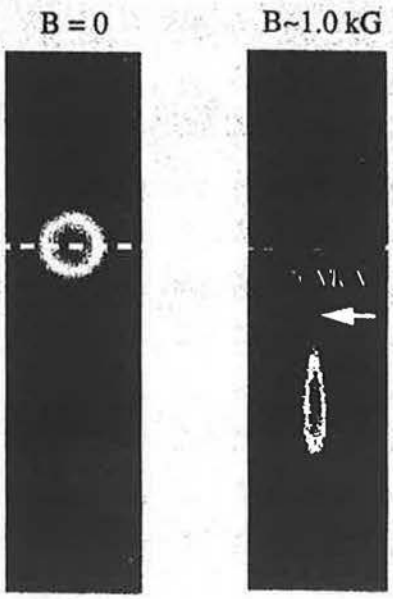

C. Gahn, G. D. Tsakiris *et al.*

Virtual Laser Plasma Lab

3D PIC simulations.

Fast electron generation in underdense plasma

Plasma density in the simulation $n_e = 3.9 \times 10^{19}$ cm^{-3}; length = 0.7 mm.
Critical power $P_c = 0.470$ TW
Laser parameters: $\lambda = 1$ μm; r =8.5λ (Gauss, intensity e^{-2});
Full pulse duration: 460 fs (Gauss, intensity e^{-2}).

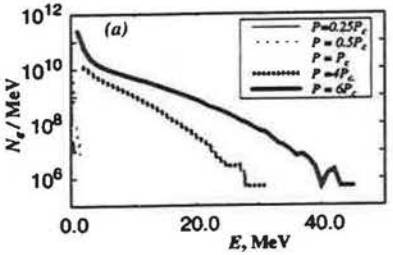

Energy spectra of accelerated lectrons

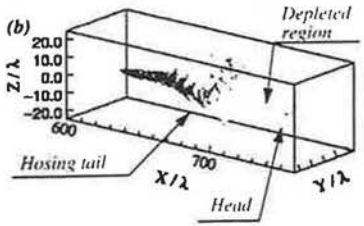

Depletion of laser pulse with $P = 4\ P_c$ after passing of 0.66 mm of plasma.

Virtual Laser Plasma Lab

3D PIC simulations.

Fast electron generation in underdense plasma

A.Pukhov and J.Meyer-ter-Vehn, *Phys.Plasmas*, 5, p.1880. (1998).

Plasma density in the simulation $n_e = 3.9 \times 10^{19}$ cm^{-3}: length = 0.7 mm.

Laser with $P = 6\ P_c$

when passed 0.4 mm of plasma.

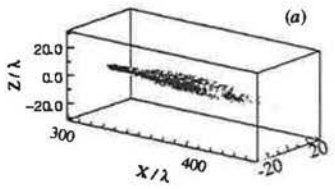

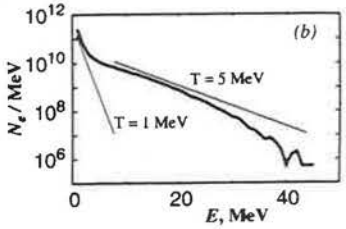

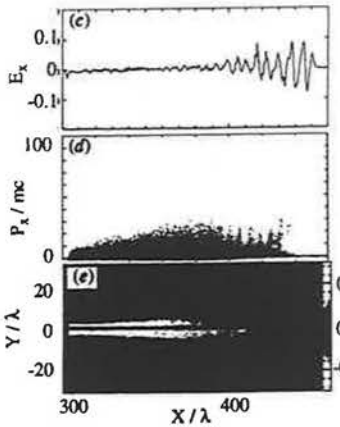

Plasma wake E_x - field, all modes shorter than laser wavelength are filtered out.

Electron phase space.
Longitudinal momentum P_x vs X
Two different regions are evident.

Quasistatic magnetic field B_z

Electron acceleration in a relativistic channel

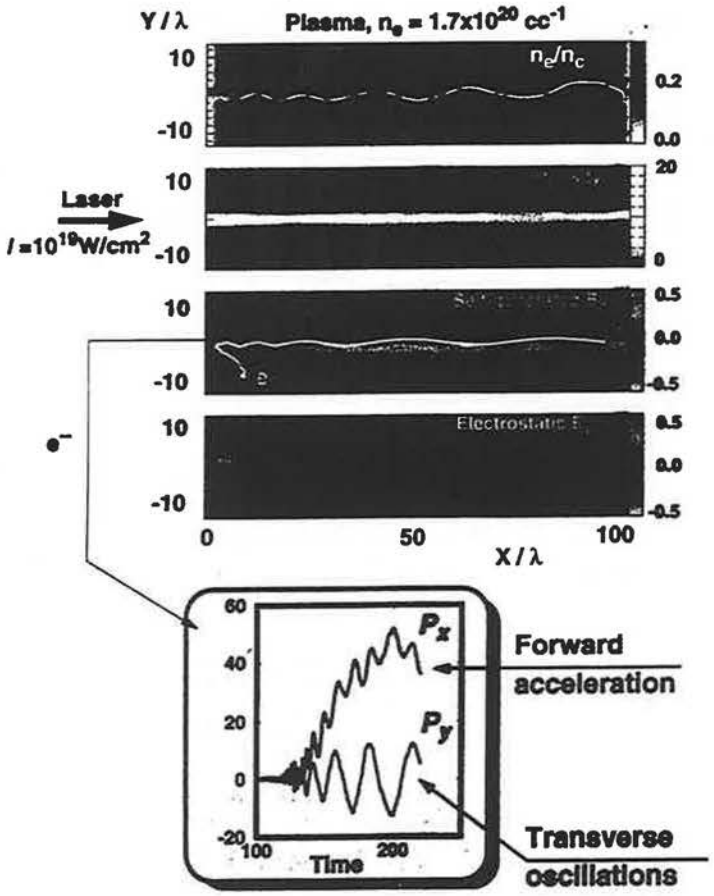

PetaWatt Laser Pulse Interaction with Preformed Plasmas

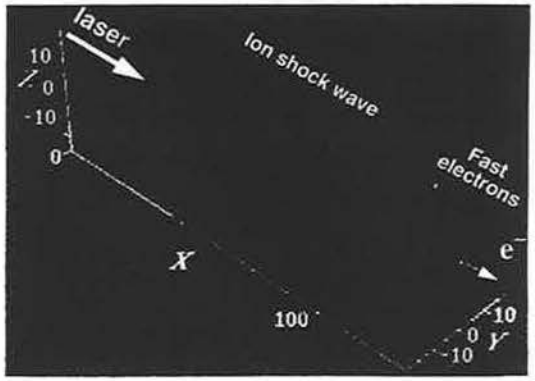

MPQ

Virtual Laser Plasma Lab 3D

Energy Spectra of Fast Electrons

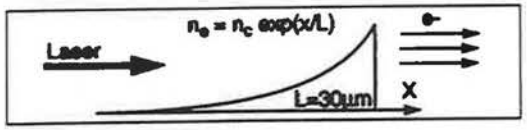

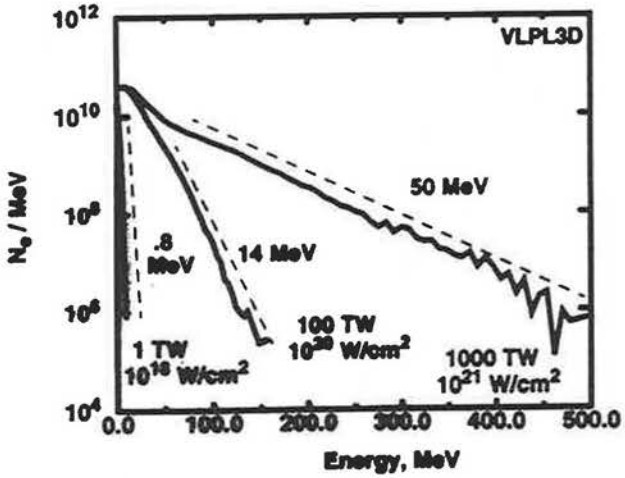

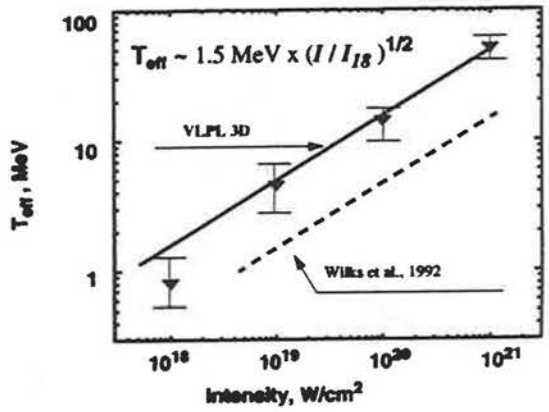

10 TW laser: Ø=9 μm, T =150 fs, $I=10^{19}$

Energy Spectra of Fast Electrons

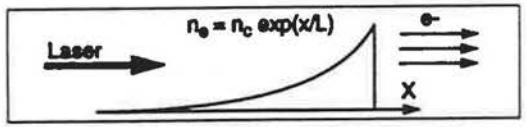

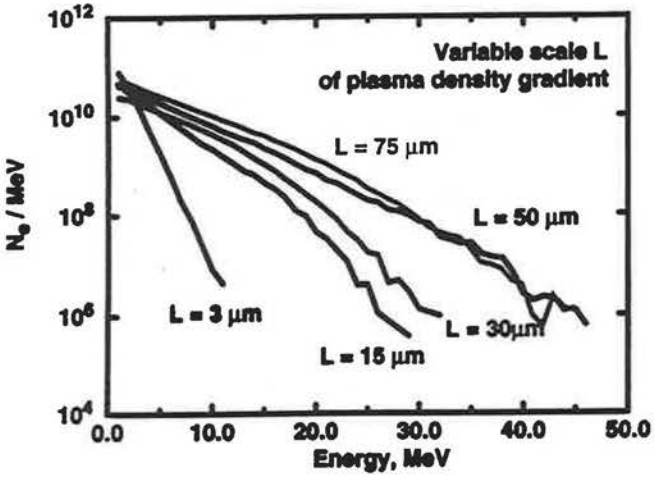

Energy Spectra of *Deuterons* Accelerated by Channel Expansion

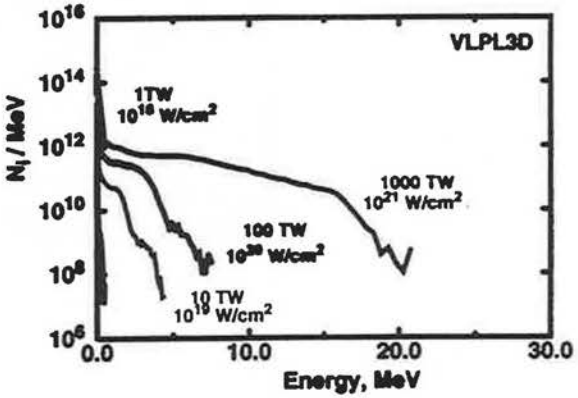

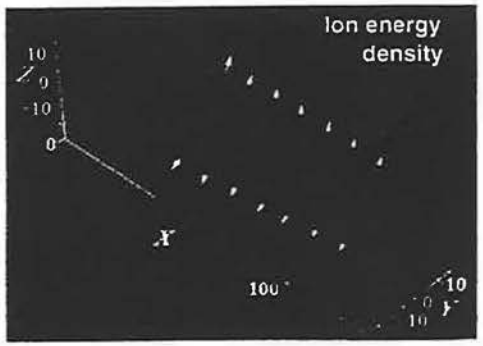

Relativistic Magnetic Self-Channeling

A. Pukhov, J. Meyer-ter-Vehn, Phys. Rev. Lett., 76, p.3975 (1996).

Relativistically strong, $a >> 1$, laser pulse propagating in slightly underdense plasma accelerates the electrons in forward direction to 1-10 MeV producing a net current

$$j = -enc$$

and a toroidal magnetic field

$$B \sim \omega_p mca/e \sim 10^8 Gauss$$

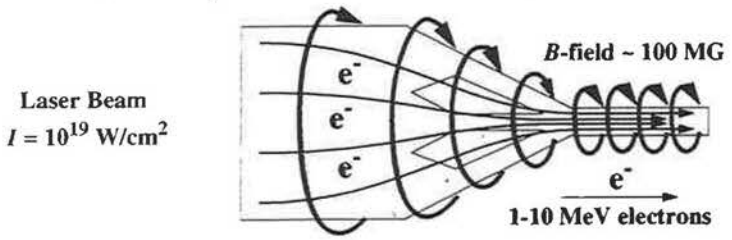

The magnetic field pinches the relativistic electrons and the light follows the modified refraction index.

This results in filaments coalescence and the Super-Channel formation.

Relativistic Magnetic Self-Channeling in Near-Critical Plasma.

A. Pukhov, J. Meyer-ter-Vehn, Phys. Rev. Lett., 76, p.3975 (1996).

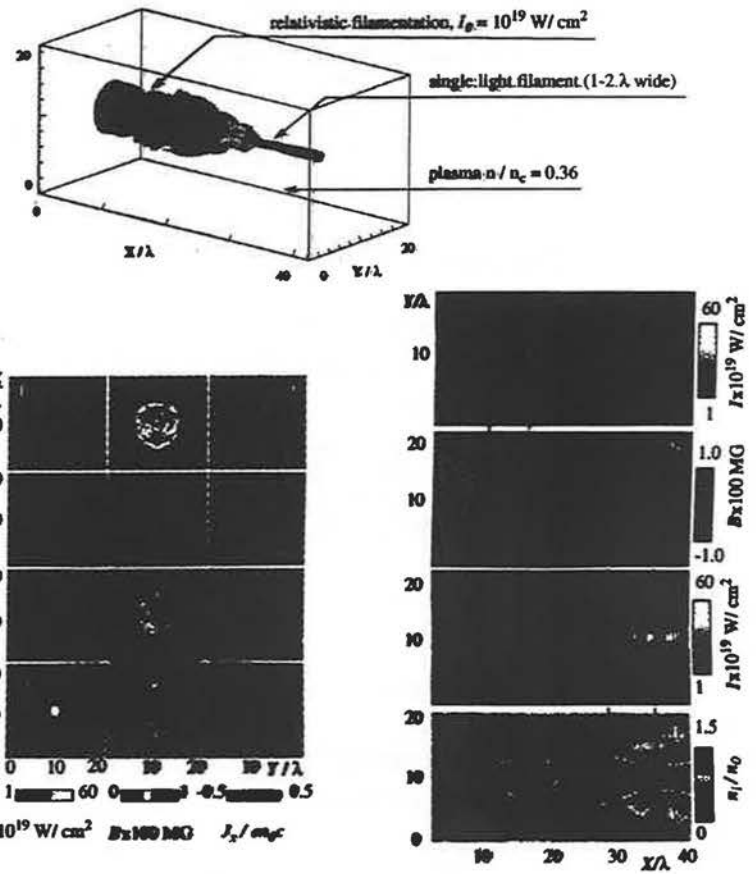

Transverse cuts *Longitudinal cuts*

Virtual Laser Plasma Lab

3D PIC simulation

PetaWatt Laser Pulse in a Preformed Plasma

"Real" laser: Ø =30 μm, T =330 fs, $I = 10^{20}$ W/cm^2

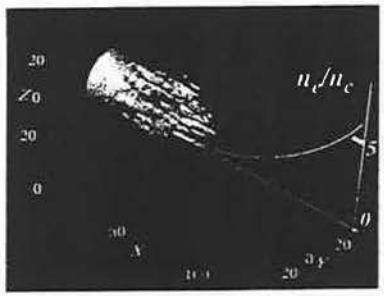

Time = 330 fs

Strong filamentation occurs at $n_e \sim 3 \times 10^{20}$ cc^{-1}

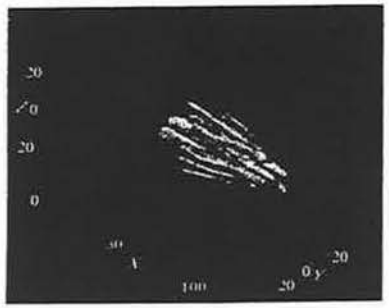

Time = 660 fs

Tree-like coalescence of the filaments into larger ones.

Preformed plasma on a surface of a solid state body, exponential density profile, scale length 30 μm.

Virtual Laser Plasma Lab

3D PIC simulation

PetaWatt Laser Pulse in a Preformed Plasma

"Ideal" laser: Ø =9 μm, T =150 fs, $I = 10^{21}$ W/cm^2

Single filament

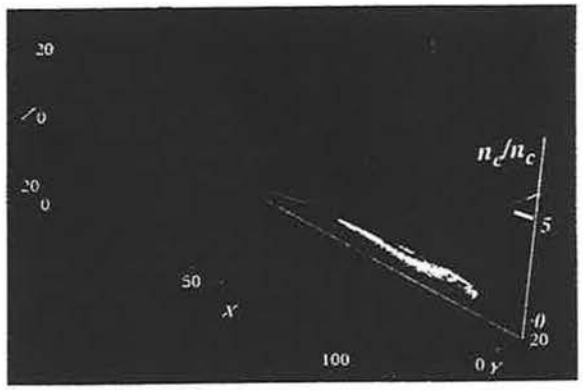

Preformed plasma on a surface of a solid state body, exponential density profile, scale length 30 μm.

MPQ

Virtual Laser Plasma Lab 2D

A. Pukhov and J. Meyer-ter-Vehn, PRL, 79, p.2686 (1997)

Hole boring in 10x overdense plasmas by
laser pulse with $I=10^{20}$ W/cm^2

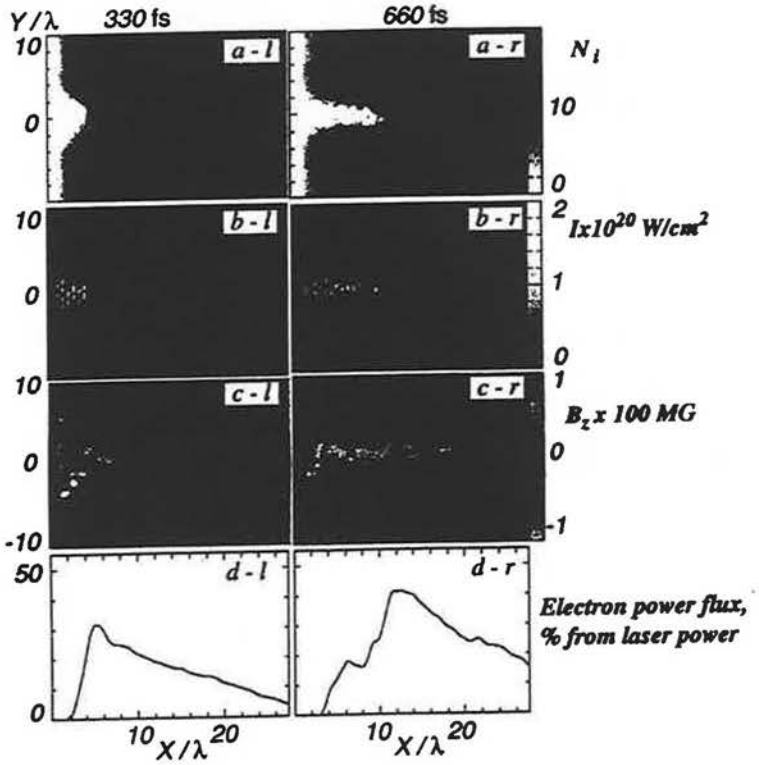

CONCLUSIONS

1. **The fast electrons appear as soon as laser power overcomes the critical one for self-focusing**

2. **In near-critical plasma electrons are accelerated at betatron resonance to multi-MeV energies**

3. **A *Peta Watt* laser can accelerate ~10^{10} electrons up to >100 MeV energies on a distance ~100 μm. Acceleration rate > 1 TeV / m**

4. **The fast electrons propagate through the overdense plasmas as magnetized jets. Strong collective stopping due to anomalous resistivity is observed.**

5. **Ions are accelerated to MeV energies by radial expansion of the channel produced by the laser.**

Formation of a hot filament at the channel axis in converging plasma flows

Askar'yan G.A.,
Bulanov S.V.,
Sokolov I.V.

General Physics Institute RAS,
Moscow, Russia

3d Int. Workshop on Fast Ignition
RAL, 21 September 199

1. Introduction

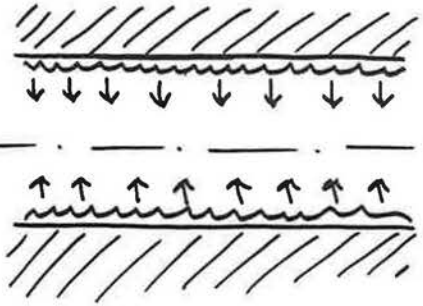

Implosion ?!

Guderley G., (1942)
Landau L.D. & Stanyukovich K.P. (1945)

Spherically converging shock wave

$R \sim t^{1/\varkappa}$, $\rho \sim u^2 \sim R^{-1.142} \to \infty$ $R \to 0$

$\varkappa = 1.571$

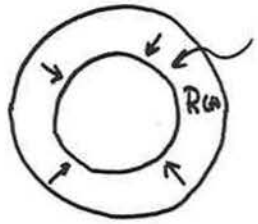

Gandelman (1951)
Reflection of the shock wave at the [redacted] centre

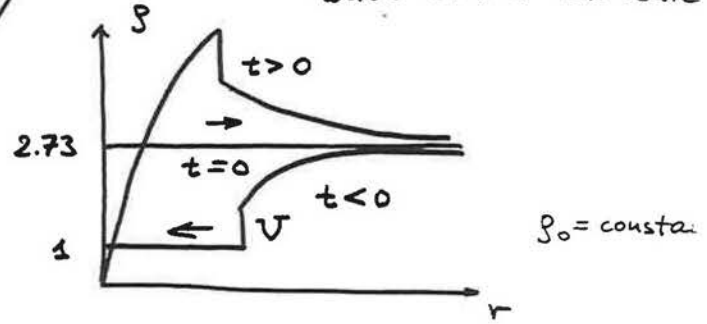

ρ_0 = constant

$\rho_0 \sim r^{\alpha}$ $\quad \alpha$ = constant

$U \sim \rho_0^{-k}$

$k \approx \left[2 + \left(\frac{2\alpha}{\alpha-1}\right)^{1/2}\right]^{-1} \approx 0.24$

$T \sim \rho_0^{-0.48}$

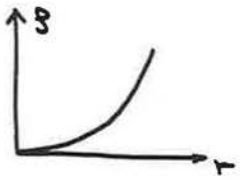

Experiments:

1. IFAM - CNR, Pisa

   a) Einaudi G., Giammanco F., Giuletti A., Vaselli M., Nuovo Cimento B, 51, 280 (1979)

   b) Giuletti A., Vaselli M., Giammanco F., Opt. Commun. 33, 251 (1980)

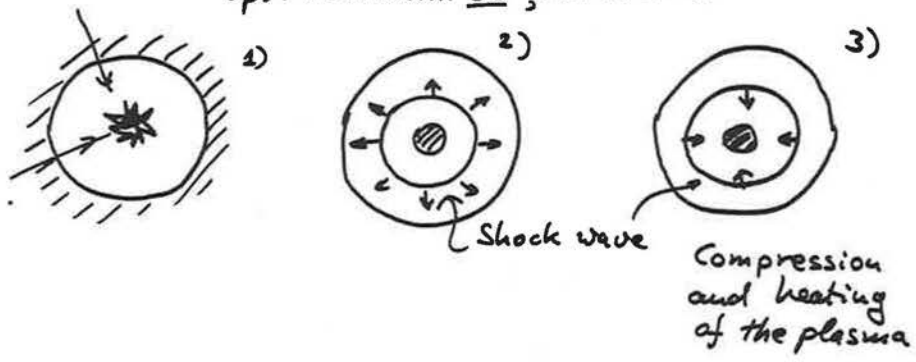

2. ISKRA-5

   Bessarab A.B., et al., JETP, 102, 1800 (199-

3. Bern group : X-ray Laser $\nu=1$

The theory is similar to the theory of the collapse of empty bubble done by Rayleigh

3D: $|U| \sim R^{-3/2}$, $\rho U^2 \to \infty$ incompressibe flow

ODE for $R(t)$ - position of the boundary.

In the theory presented below $\rho U^2 \not\to \infty$ however $T \to \infty$

This is due to specific behavior of the entropy at the shock wave front

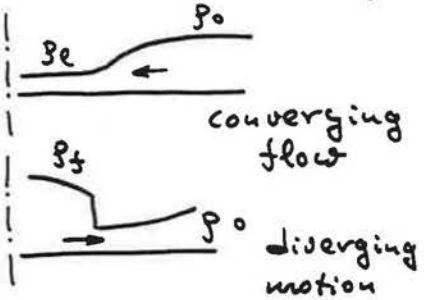

$\rho_e \ll \rho_0$

At the shock front

$\rho/\rho_0 \approx \frac{\gamma+1}{\gamma-1} \simeq 4$

$T \sim v^2 \sim T_0$

Change in the entropy is

$\Delta S = T/\rho^{\gamma-1}$

$\Delta S \simeq T_0/\rho_e^{\gamma-1} \to \infty$ as $\rho_e \to 0$

Adiabatic smoothing in the pressure distribution leads to $T_\delta \approx T_0 \left(\rho_0/\rho_e\right)^{\frac{\gamma-1}{\gamma}} \gg T_0$

$\rho_f \sim \rho_0^{1/\gamma} \rho_e^{(\gamma-)/\gamma}$ at the axis

1D case : Ya. B. Zel'dovich & K. P. Stanyukovich, J

Theory:

In the adiabatic approximation we have

$$\partial_t v + v\partial_r v + \frac{2}{\gamma-1} c\partial_r c = 0,$$

$$\partial_t c + v\partial_r c + \frac{\gamma-1}{2} c\left(\partial_t v + \nu \frac{v}{r}\right) = 0,$$

$$\rho = \rho_0 \left(\frac{c}{c_0}\right)^{2/(\gamma-1)}, \quad P = \frac{c_0^2}{\gamma}\rho_0\left(\frac{c}{c_0}\right)^{\frac{2\gamma}{\gamma-1}}$$

v is the gas velocity, c sound speed

$\nu = 0, 1, 2$ for the plane, cylinder, sphere

The index "0" refers the quantity at $t=0$, $r>R$

At the gas boundary we have

$$P, \rho, T = 0 \quad \text{and} \quad \underline{c\partial_r c = 0}$$

The rarefaction wave moves inward the channe ($\nu=1$

with constant velocity $v = -\frac{2c_0}{\gamma-1}$

The gradients are finite at $t < t_0$

t_0 is otime of the collap

For the gradients of c and v,

$$S = \partial_r c \quad \text{and} \quad W = \partial_r v$$

we have ODE:

$$\frac{dS}{d\tau} + \frac{\gamma+1}{2} SW + \frac{\gamma-1}{2}\frac{\nu S}{\tau} = 0,$$

$$\frac{dW}{d\tau} + W^2 + \frac{2}{\gamma-1} S^2 = 0,$$

$$\tau = t + R_0/V$$

This is dere to degeneration of the hyperbolic system of equations in partial derivatives at the boundary.

Changing the variables as

$$S = s/\tau, \quad W = \omega/\tau, \quad \tau = \frac{R_0}{V}\exp(-\xi)$$

we obtain

$$\frac{d\omega}{d\xi} = \omega(\omega-1) + \frac{2}{\gamma-1} s^2,$$

$$\frac{ds}{d\xi} = s\left(\frac{\gamma+1}{2}\omega + \alpha\right), \quad \alpha = \frac{\gamma-1}{2}\nu - 1$$

The system does not contain the independent variable τ.

Theory:

In the adiabatic approximation we have

$$\partial_t v + v\partial_r v + \frac{2}{\gamma-1} c\partial_r c = 0,$$

$$\partial_t c + v\partial_r c + \frac{\gamma-1}{2} c\left(\partial_t v + \nu \frac{v}{r}\right) = 0,$$

$$\rho = \rho_0 \left(\frac{c}{c_0}\right)^{2/(\gamma-1)}, \quad P = \frac{c_0^2}{\gamma}\rho_0 \left(\frac{c}{c_0}\right)^{\frac{2\gamma}{\gamma-1}}$$

v is the gas velocity, c sound speed

$\nu = 0, 1, 2$ for the plane, cylinder, sphere

The index "0" refers the quantity at $t=0$, $r>R$

At the gas boundary we have

$$P, \rho, T = 0 \quad \text{and} \quad \underline{c\partial_r c = 0}$$

The rarefaction wave moves inward the chamber ($\nu = 1$) with constant velocity $v = -\frac{2c_0}{\gamma-1}$

The gradients are finite at $t < t_0$

t_0 is ctime of the collap

For the gradients of c and v,

$$S = \partial_r c \quad \text{and} \quad W = \partial_r v$$

we have ODE:

$$\frac{dS}{d\tau} + \frac{\gamma+1}{2} SW + \frac{\gamma-1}{2}\frac{\nu S}{\tau} = 0,$$

$$\frac{dW}{d\tau} + W^2 + \frac{2}{\gamma-1} S^2 = 0,$$

$$\tau = t + R_0/V$$

This is due to degeneration of the hyperbolic system of equations in partial derivatives at the boundary.

Changing the variables as

$$S = \zeta/\tau, \quad W = \omega/\tau, \quad \tau = \frac{R_0}{V}\exp(-\xi)$$

we obtain

$$\frac{d\omega}{d\xi} = \omega(\omega-1) + \frac{2}{\gamma-1}\zeta^2,$$

$$\frac{d\zeta}{d\xi} = \zeta\left(\frac{\gamma+1}{2}\omega + \alpha\right), \quad \alpha = \frac{\gamma-1}{2}\nu - 1$$

The system does not contain the independent variable τ.

A. If $\alpha > 2$ that is for $\gamma > 3$ if $\nu = 2$ and for $\gamma > 2$ if $\nu = 1$ no regular solution.
We have the trajectory self-intersection → → shock waves etc.
Cyderley, Landau & Stanyukovich solutions must be used.

B. Converging motion without shock waves if $\alpha < 2$. It is so for $\gamma = 5/3$.

The conclusion has been obtained for the plasma behavior at the boundary, but the boundary is the characteristic of full system of equations, which belongs both to A and B family.

For $\nu = 1$, $\gamma = 5/3$ in the cylinder geometry we have

$$\left(\omega(\omega-1) - 9\beta^2\right)\beta^{-3/2} = \text{constant}$$

constant = 0

$$W = \frac{(t_0 - t)^{1/3}}{t_0^{4/3} - (t_0 - t)^{4/3}},$$

$$S = \frac{t_0^{2/3}}{3(t_0 - t)^{1/3}\left(t_0^{4/3} - (t_0 - t)^{4/3}\right)},$$

$$t_0 = -R_0/U$$

Near the channel walls at $t \approx t_0$ we have
$\partial_r v \sim 1/t$, $\partial_r c \sim 1/t$ as in the plane case

At $(t_0 - t) \to 0$ near the collapse

$$\partial_r v \sim (t_0 - t)^{1/3} \to 0$$

$$\partial_r c \sim (t_0 - t)^{-1/3} \to \infty$$

$\nu = 2$, $\gamma = 7/5$ Sphere

$$W = \frac{(t_0 - t)^{2/5}}{t_0^{6/5} - (t_0 - t)^{6/5}},$$

$$S = \frac{t_0^{3/5}}{(t_0 - t)^{2/5}\left(t_0^{6/5} - (t_0 - t)^{6/5}\right)}.$$

Plasma parameters after the flow focusing

Plasma parameters after the flow focusing

$\nu = 1$, $\gamma = 5/3$

At $0 < (t_0 - t) \ll t_0$ just before the singularity

$$\rho = \rho_0 \left(\frac{c}{c_0}\right)^3 = \frac{\rho_0}{t_0^2 (t_0 - t)} \left(\frac{\xi}{2 c_0}\right)^3$$

$\xi = r - U(t - t$

$\xi > 0$

$t \to t_0$

The Lagrange variable ξ:

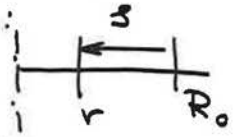

$$M(\xi) = \int_0^{\xi} \rho r \, dr = \frac{\rho_0 |U| \xi^4}{2 t_0^2 (3 c_0)^3}$$

$$\rho(r) = \frac{1}{r} \frac{dM}{dr} = \frac{\rho_0 r^2}{R_0^2} \left(\frac{U}{3 c_0}\right)^3$$

$\nu = 2$, $\gamma = 7/5$

$$|U| = + \frac{2 c_0}{\gamma - 1}$$

$$\rho = \frac{\rho_0 r^3}{R_0^3} \left(\frac{U}{5 c_0}\right)^5$$

Reflection of the shock wave from the axis can be described by the self-similar solutic

$\nu = 1$, $\gamma = 5/3$

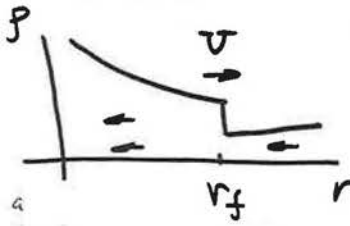

$$c^2 = 4 c_0^2 \left(\frac{U}{3 c_0}\right)^2 \left(\frac{r}{r_f}\right)^{-1/2}$$

$r < r_f$

$r_f \simeq 0.2\, U\, |t - t_0|$

$T \sim r^{-1/2} \to \infty$

The MHD simulations of capillary discharges in evacuated narrow channel.

1. Bobrova N.A., Bulanov S.V., Razinkova T.L., Sasorov P.V., Plasma Phys. Rep. 22, 387, (1996).

The simulations were to explain the plasma behavior in experiments:

Steden C., Kunze H.-J., Phys. Lett. A, 151, 534 (1990)

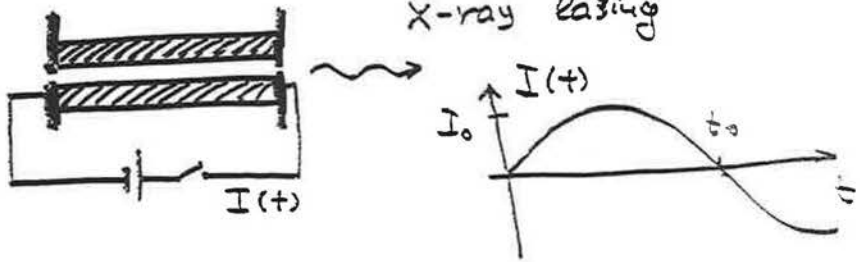

$R_0 = 0.5$ mm

$I_0 = 18$ kA

$t_0 = 120$ ns

$T_{max} \approx 300$ eV for $\langle T \rangle \sim 30 \div 40$ eV

It can't be explained by slowing down of the plasma flows.

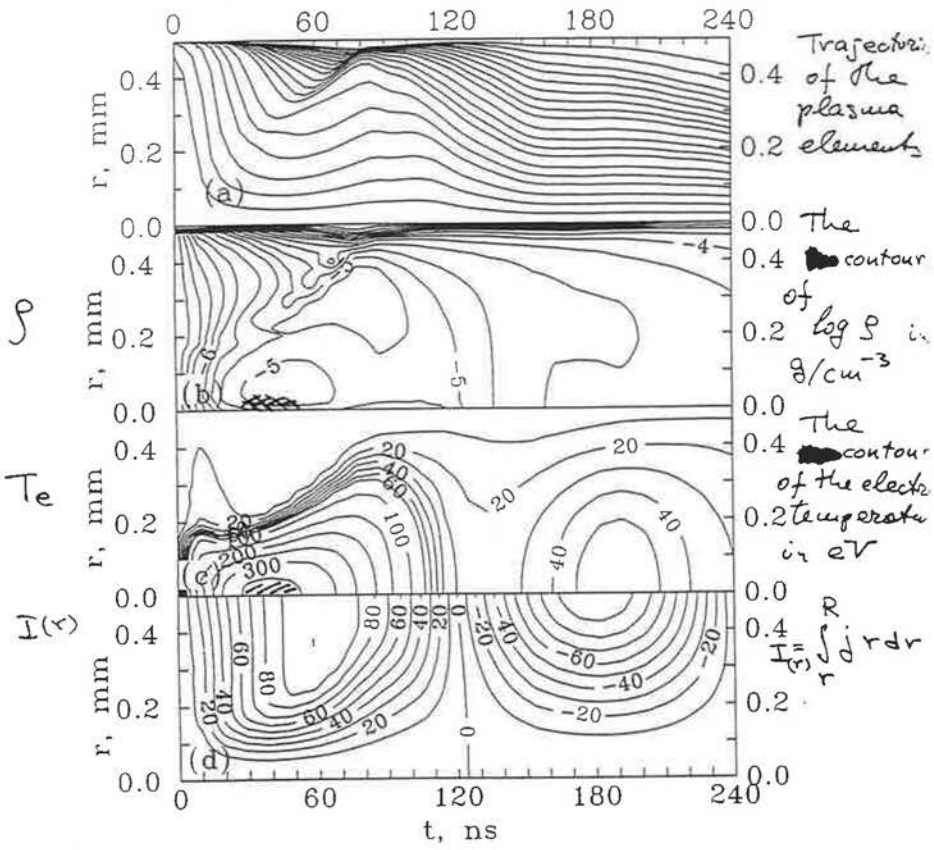

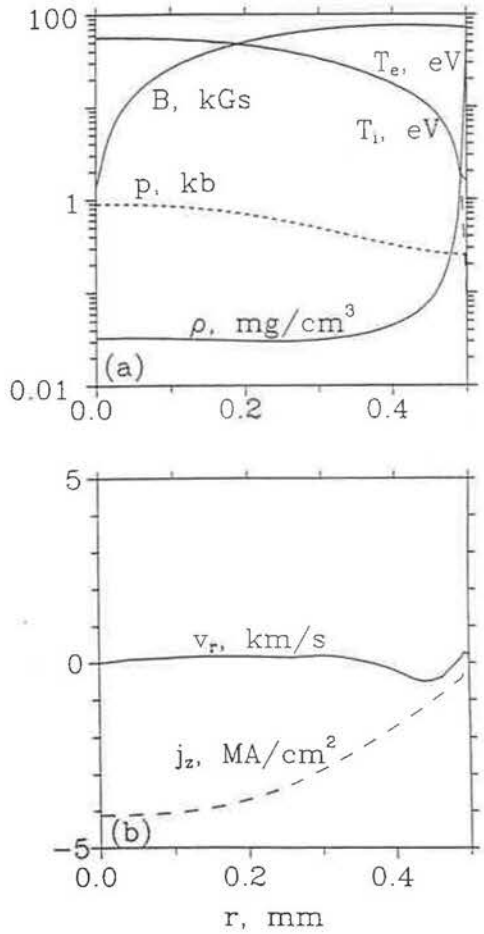

Dissipative MHD simulation of Capillary

Dissipative MHD simulation of Capillary Plasmas for Guiding of High Intense Ultra Short Laser Pulses

N.A. Bobrova, S.V. Bulanov, D. Farina, R. Pozzoli, T.L. Razinkova, J.-I. Sakai, P.V. Sasorov

Journ. Phys. Soc. Japan., 67, N10 (1998)

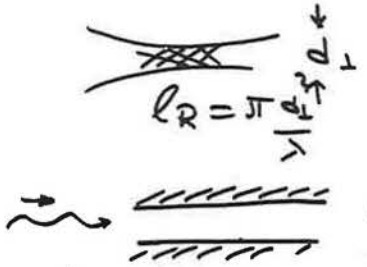

$l_R \overset{?}{>} l_{acc} = \frac{c}{\omega_p}\left(\frac{\omega_0}{\omega_p}\right)^2$

- laser pulse should be detached from the wall
- Smooth plasma profile
- Free of instabilities

$(\omega_0/\omega_p) \sim n_e^{-1/2} \approx 10 \div 100$

Y. Ehrich, C. Cohen, A. Zigler, J. Krall, P. Sprangle, E. Esarey, Phys. Rev. Lett. 77, 393 (1996).

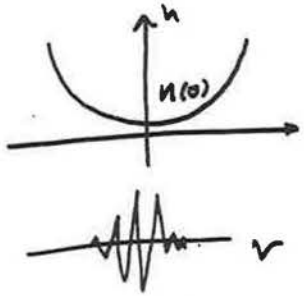

$n_e(r) = n_e(0) + n''(0) r^2/2$

$l_{acc} = \frac{\lambda}{2\pi}\left(\frac{n_{cr}}{n(0)}\right)^{3/2}$

$r_w = (\lambda R_0)^{1/2}\left(\frac{n_{cr}}{2\pi^2 n(0)}\right)^{1/4} \cdot \left(n_0(0)/n''(0) R^2\right)^{1/4}$

$r_w \approx \sqrt{d_e h}$ $\quad n = n_0\left(1 + \frac{r^2}{2L^2}\right)$

$R > \frac{c}{(\omega_{p2}^2 - \omega_{p1}^2)^{1/2}}$ LWFA

$\lambda \simeq 1\,\mu m$

$R_0 \simeq 10\,\mu m$ or $r_w \simeq 10\,\mu m$

$n(0) \simeq 10^{19}\,cm^{-3}$

$\lambda = 10\,\mu m$ $\quad CO_2$ - laser

$R_0 \simeq 100\,\mu m$, $\quad r_w \simeq 100\,\mu m$

$n(0) = 10^{17}\,cm^{-3}$

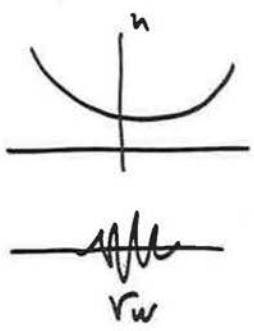

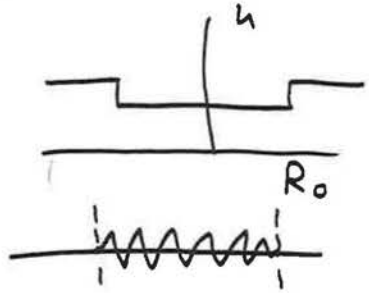

Physical Model

$$\rho \frac{dv}{dt} = -\frac{\partial P}{\partial r} - \frac{1}{c} j B - \frac{\partial}{\partial r} \Pi_{rr} - \frac{1}{r}(\Pi_{rr} - \Pi_{\varphi\varphi})$$

$$\frac{d\rho}{dt} = -\frac{\rho}{r}\frac{\partial}{\partial r}(rv),$$

$$\frac{d}{dt}\left(\frac{B}{\rho r}\right) = \frac{c}{\rho r}\frac{\partial E_z}{\partial r},$$

$$\rho \frac{d\varepsilon_e}{dt} = -\frac{P_e}{r}\frac{\partial}{\partial r}(rv) + j E_z - \frac{1}{r}\frac{\partial}{\partial r}(r q_e) - Q_r + C_{ei}(T_i - T_e),$$

$$\rho \frac{d\varepsilon_i}{dt} + \frac{P_i}{r}\frac{\partial}{\partial r}(rv) = -\frac{1}{r}\frac{\partial}{\partial r}(r q_i) + C_{ei}(T_e - T_i) - \Pi_{rr}\frac{1}{r}\frac{\partial}{\partial r}(rv) - \frac{v}{r}(\Pi_{\varphi\varphi} - \Pi_{rr}).$$

Here $\frac{d}{dt} = \frac{\partial}{\partial t} + v\frac{\partial}{\partial r}$

$p = P_e + P_i$, $j = \frac{c}{4\pi r}\frac{\partial}{\partial r}(Br)$

$$E_z = j/\sigma_\perp - N T B \frac{\partial T_e}{\partial r},$$

$$q_e = \varkappa_\perp \frac{\partial T_e}{\partial r} + N B T_e j.$$

$$\Pi_{rr} = \frac{2}{3}\eta_0\left(\frac{v}{r} - 2\frac{\partial v}{\partial r}\right)$$

$$\Pi_{\varphi\varphi} = \frac{2}{3}\eta_0 r^2 \frac{\partial}{\partial r}\frac{v}{r^2}.$$

Capillary Discharge Free of MHD Instabilities.

It is well known that the z-pinch is stable during the first compression. Then we need to switch off the electric current in the external circuit

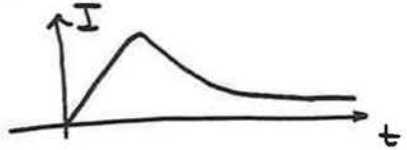

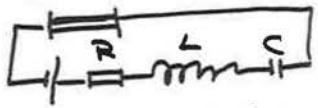

$R = 2(L/C)$

$$I(t) = I_0 \, t \, e^{-t/t_0}$$

$$t_0 = \sqrt{LC}$$

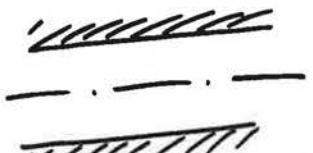

$(CH_2O)_n$ polyacetal

$Z = 7$
$A = 14$
$\rho_0 = 1\ g/cm^3$
$I_0 = 32\ kA$
$t_0 = 32\ ns$

Dimensionless parameter

$$\frac{t_c}{t_0} = (\pi \rho_0)^{1/2} \frac{c R_0^2}{I_0 t_0} \approx 1$$

- For CO_2 laser

  $R_0 \simeq 3.0$ mm

  $\rho_0 = 3 \cdot 10^{-7}$ g/cm^3

  $T_0 = 1.0$ eV

  $I_0 = 32$ kA

  $t_0 = 23$ ns

  filled with deiterium

  inside the chamber

  $n_e(0) = 1.6 \cdot 10^{17}$ cm^{-3}

  $r_w = 200 \mu$m

- For 1 μm laser

  $R_0 = 0.2$ mm

  $\rho_0 = 4.0 \times 10^{-5}$ g/cm^3

  $T_0 = 1.0$ eV

  $I_0 = 10$ kA, $t_0 = 8$ ns

  $r_w = 20 \mu$m at $t = 100$ ns

  $n_e(0) = 2 \cdot 10^{19}$ cm^{-3}

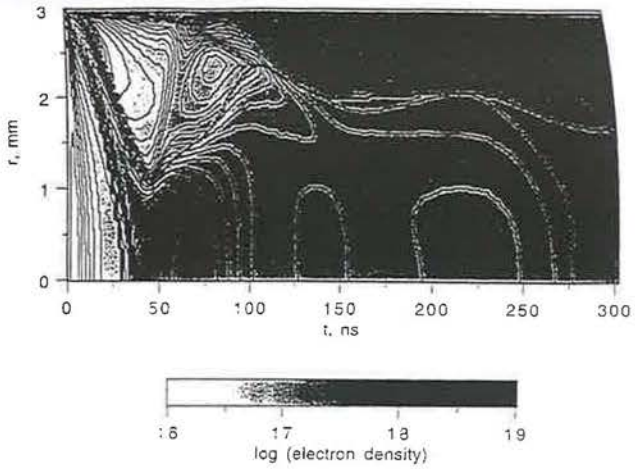

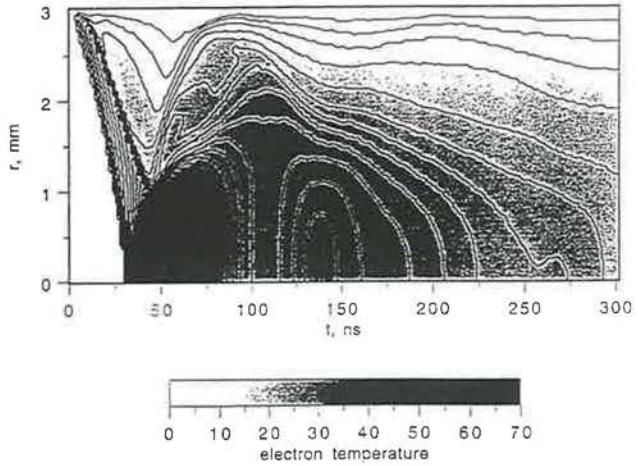

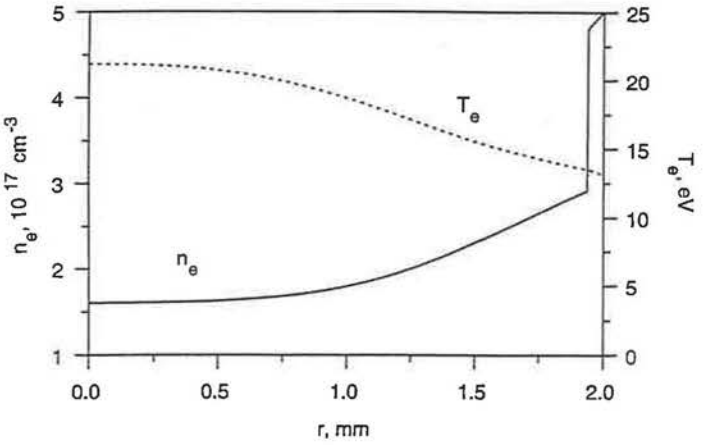

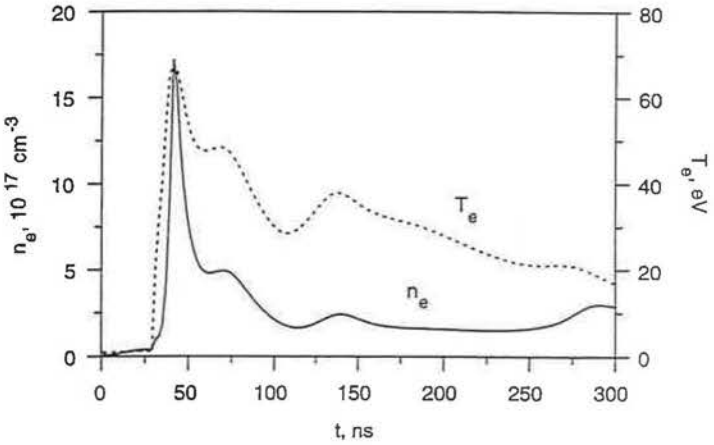

$t = 250\,ns$ CO_2

CO_2

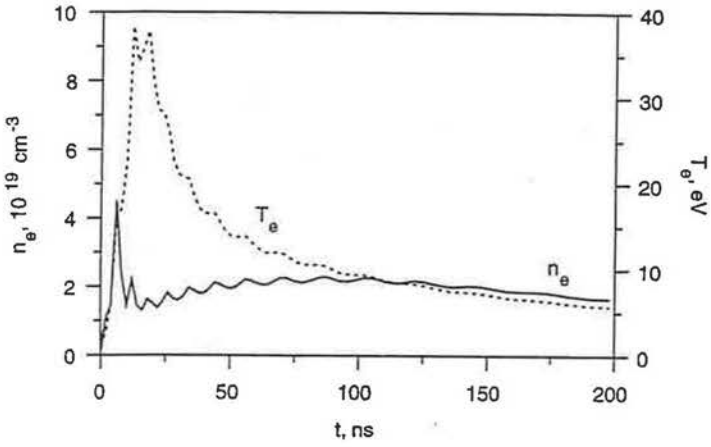

1/μm

Multispecies plasma

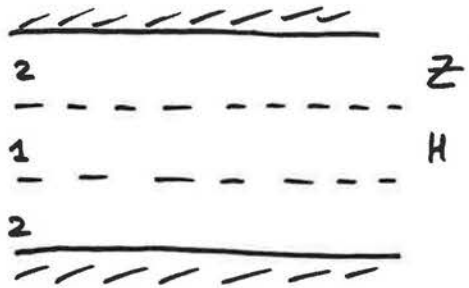

At the equilibrium

$$P_1 = P_2$$

$$n_{1i} T_{1i} + n_{1e} T_{1e} = n_{2i} T_{2i} + n_{2e} T_{2e}$$

$$n_{\alpha e} = Z_\alpha n_{\alpha i}$$

$$\frac{n_{1e}}{n_{2e}} = \frac{Z_1}{Z_2} \frac{T_{2i} + Z_2 T_{2e}}{T_{1i} + Z_1 T_{1e}}$$

$T_1 \approx T_2$

$Z_2 \gg 1$

$$\frac{n_{1e}}{n_{2e}} \cong \frac{Z_1}{1 + Z_1}$$

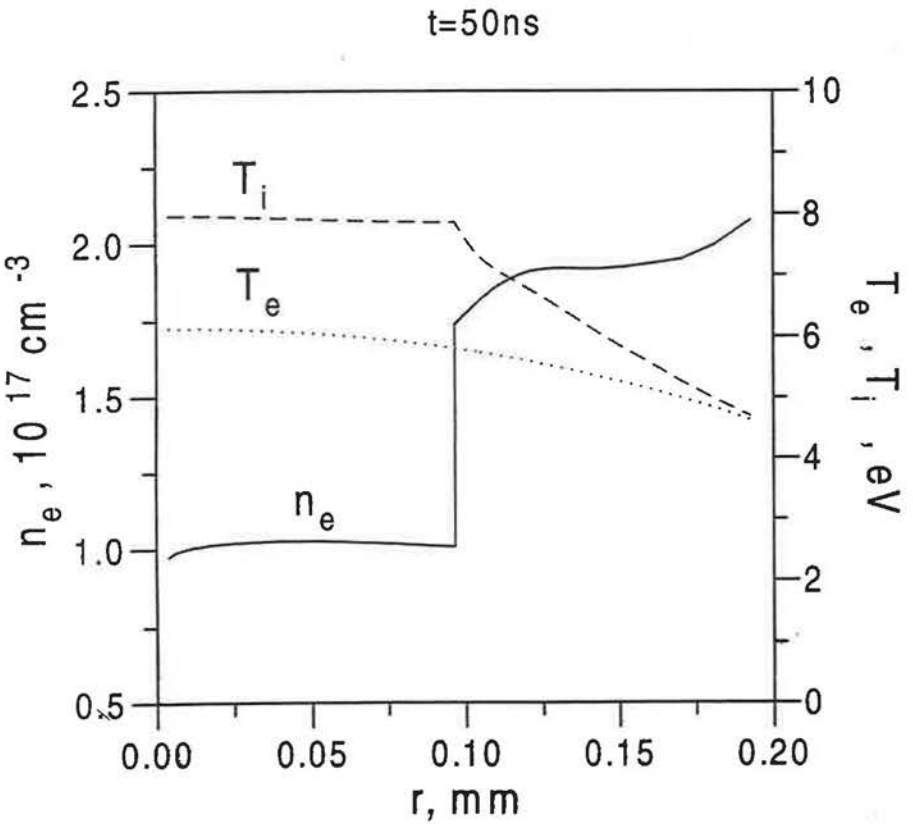
t=50ns
2.5
2.0
1.5
1.0
0.5
10
8
6
4
2
0
T_i
T_e
n_e
n_e , 10^{17} cm^{-3}
T_e , T_i , eV
0.00
0.05
0.10
0.15
0.20
r, mm

Experiments on propagation of intense ultra-short laser pulses through thin foil plasmas

Antonio Giulietti

Istituto di Fisica Atomica e Molecolare, Pisa

Third International Workshop on
FAST IGNITION OF FUSION TARGETS
Rutherford Appleton Laboratory, 21st - 23rd September 1998

consiglio nazionale delle ricerche

IFAM -----> · <----- Pisa

Experiments performed at
Laboratoire d'Optique Appliquée, Palaiseau
in collaboration with:
A. Mysyrowicz, J.P. Chambaret, P. Chessa, A. Rousse

A. Giulietti, L.A. Gizzi
IFAM-CNR, Pisa, Italy

D. Giulietti
Università di Pisa, Italy

D. Teychenné
Università di Pisa, SILASI postdoc fellow

A. Macchi
Scuola Normale Superiore, Pisa, Italy

Phys. Rev. Lett. **76**, 2278 (1996)

Phys. Rev. Lett. **79**, 3194 (1997)

Phys. Rev. E **58**, 1245 (1998)

consiglio nazionale delle ricerche **----IFAM ----> · <---- Pisa**

Experiments performed at
Laboratoire d'Optique Appliquée, Palaiseau
in collaboration with:
A. Mysyrowicz, J.P. Chambaret, P. Chessa, A. Rousse

A. Giulietti, L.A. Gizzi
IFAM-CNR, Pisa, Italy

D. Giulietti
Università di Pisa, Italy

D. Teychenné
Università di Pisa, SILASI postdoc fellow

A. Macchi
Scuola Normale Superiore, Pisa, Italy

Phys. Rev. Lett. **76**, 2278 (1996)

Phys. Rev. Lett. **79**, 3194 (1997)

Phys. Rev. E **58**, 1245 (1998)

Third International Workshop on
FAST IGNITION OF FUSION TARGETS
Rutherford Appleton Laboratory, 21st - 23rd September 1998

Antonio Giulietti
Istituto di Fisica Atomica e Molecolare, Pisa

Experiments on propagation of intense ultra-short laser pulses through thin foil plasmas

consiglio nazionale delle ricerche

IFAM -----> • <----- Pisa

Experiments performed @ LOA - Palaiseau

MEASUREMENTS	150 fs pol "p" to "s" no ASE-plasma	30 fs pol "p" 20° no ASE-plasma	30 fs pol "p" 20° with ASE-plasma	30 fs 0° with ASE-plasma
Transmittivity	≤ 5%	up to ≈70%	≤ 1%	≤ 1%
Tra. background	2 - 3%	≈ 1%	≈ 1%	≈ 1%
Tra. vs intensity		plot		
Tra. vs targ. pos.		plot		
Tra. spectra	broaden,modulat.	blue shifted		
Tra. near field		spatial filtering	diffused	diffused
Reflectivity	very high	very low ≈ 1%	very high	
Specular image		boundary refl.	full spot	
2ω specular	observed	absent	observed	
2ω vs polarisation	plot			
2ω spectra	laser band limited		spat.& spec.mod.	
3/2 ω specular		absent	observed	
3/2 ω spectra			very broad	
2ω at 40°				modulated
hard X-rays from the target	≈ 60 keV plot vs polarisat.		≈ 100 keV	≈ 100 keV
hard X-rays from outscatterers		> 1 MeV	≈ 400 keV	≈ 400 keV

consiglio nazionale delle ricerche
IFAM -----> · <----Pisa

Experiments performed @ LOA - Palaiseau
EXPERIMENTAL CONDITIONS

Ti-Sapphire $\lambda \approx 815$ nm

duration FWHM	150 fs	30 fs	30 fs
bandwidth	$\Delta\lambda \approx 8$ nm	$\Delta\lambda \approx 40$ nm	$\Delta\lambda \approx 40$ nm
focusing	f/4.0	f/7.5	f/7.5
spot diameter	$\approx 7\ \mu$m	$\approx 10\ \mu$m	$\approx 10\ \mu$m
contrast ratio	> 10^7	> 10^7	≈ 10^6
target	0.08 μm plast. foil	0.1 & 1.0 μm p.f.	0.1 & 1.0 μm p.f.
angle of inciden.	20° pol "p" to "s"	20° pol "p"	20° "p" & 0°
intensity	5 10^17	5 10^16 - 3 10^18	10^17 - 3 10^18
ASE pre-plasma	NO	NO	YES
plasma scalelen.	< 0.1 μm	<< 0.1 μm	>> 1 μm

TRANSMITTED PULSE SPECTRA
5×10^{16} W/cm^2

SPECTRUM: 1-D profiles

consiglio nazionale delle ricerche **IFAM** -----> • <----- Pisa

30-fs laser pulse propagation in absence of preformed plasma

IFAM - CNR - Laser-Plasma Interaction Group - http://xray.ifam.pi.cnr.it

7

TRANSMITTED PULSE SPECTRA
4×10^{17} W/cm^2

SPECTRUM: 1-D profiles

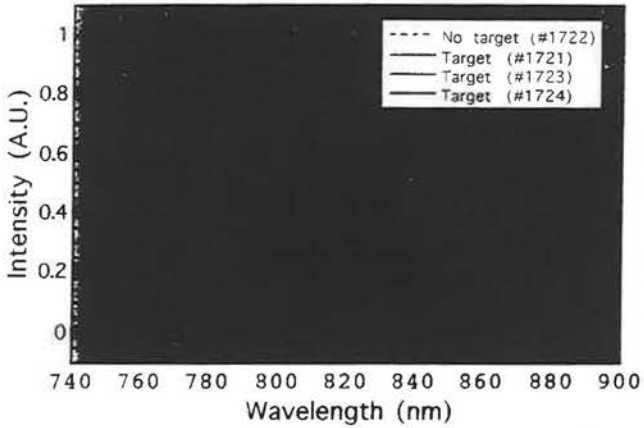

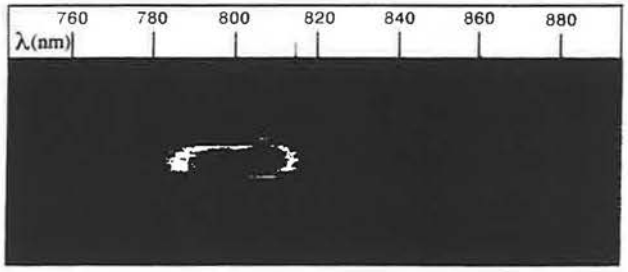

8

TRANSMITTED PULSE SPECTRA
3×10^{18} W/cm^2

SPECTRUM: 1-D profiles

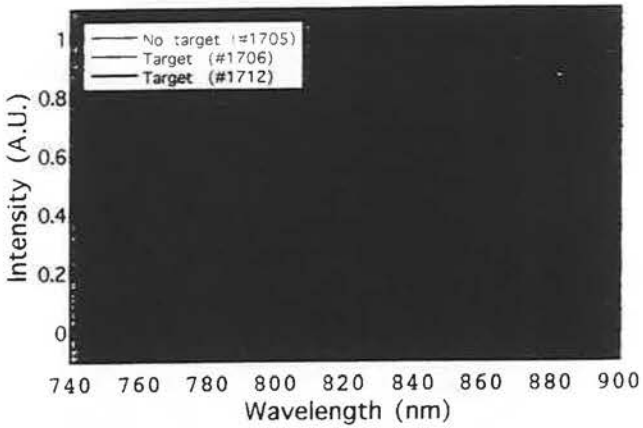

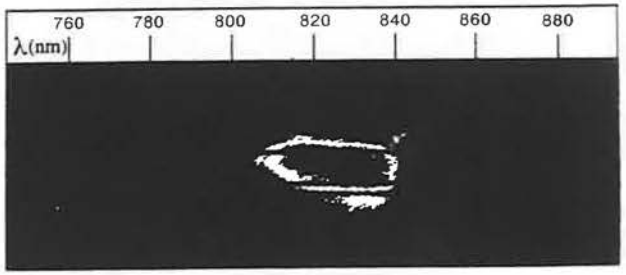

INTERACTION WITHOUT *PRECURSOR* PLASMA

IMAGE OF THE LASER FOCAL SPOT (specular direction)

Laser intensity: $\approx 3\times10^{18}$ W/cm^2

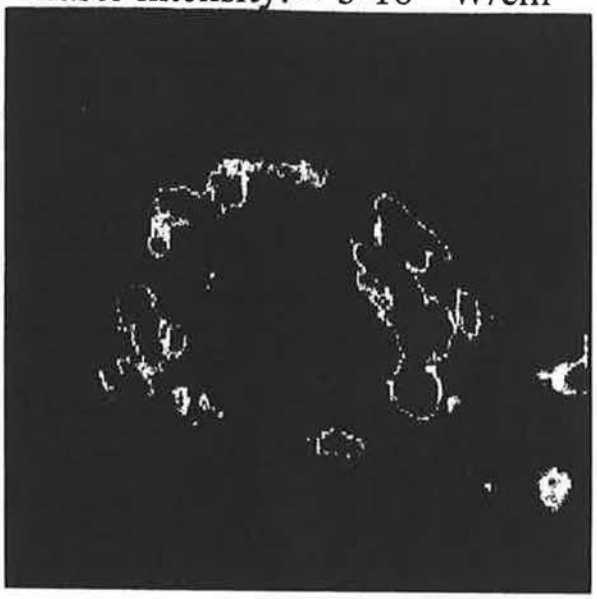

Evidence for ultra-fast ionisation

The blue shift of the transmitted pulse is a clear signature of ultra-fast ionisation.

Blue shift: $\approx$ 13 nm @ 5 10^{16} W/cm^2	20 nm @ 4 10^{17} W/cm^2

Let us attribute the shift to self-phase modulation of the laser pulse, namely to the ultra-fast decrease in the refractive index due to the laser induced ionisation.

$$\Delta\omega \approx (L/c)\,(\Delta\mu/\Delta t)\,\omega_0.$$

Taking the interaction path L equal to the foil thickness 0.1 μm, we found

$\Delta t \approx 20$ fs	$\Delta t \approx 13$ fs

The absence of shift in condition close to the full transparency, namely @ 3 10^{18} W/cm^2, suggests that in this case the ionisation involves a negligible portion of the pulse, while the spectral variability observed at intermediate intensity may be due to the proximity of a sort of threshold for the effect leading to the transparency.

SECOND HARMONIC EMISSION

SPACE RESOLVED SPECTRUM OF SPECULAR SH EMISSION FROM 30-fs INTERACTION WITH THIN FILMS IN PRESENCE OF PRECURSOR PLASMA

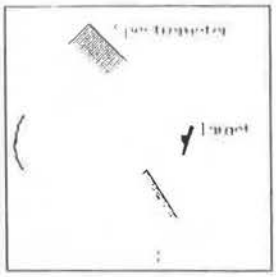

NO SH EMISSION WAS OBSERVED IN 30 FS INTERACTIONS IN ABSENCE OF PRECURSOR PLASMA

INTERACTION WITH*PRECURSOR* PLASMA

IMAGE OF THE LASER FOCAL SPOT (specular direction)
Laser intensity: ≈ 3×10^{18} W/cm^2

3/2 HARMONIC EMISSION

SPACE RESOLVED SPECTRUM OF SPECULAR 3/2 ω EMISSION FROM 30 FS INTERACTION WITH THIN FILMS IN PRESENCE OF PRECURSOR PLASMA

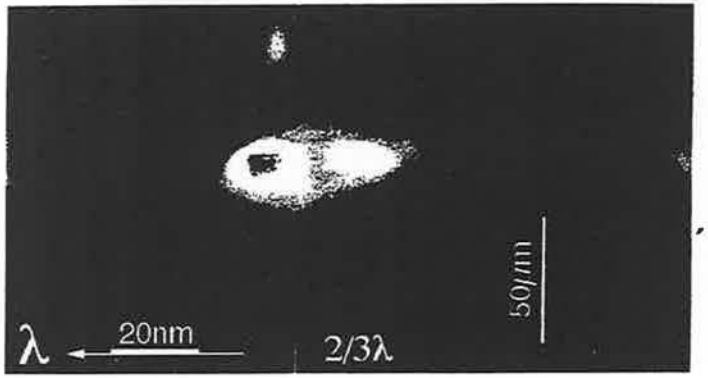

NO 3/2 ω EMISSION WAS OBSERVED IN 30 FS INTERACTIONS IN ABSENCE OF PRECURSOR PLASMA

Experimental set up:
NaI(Tl) detectors

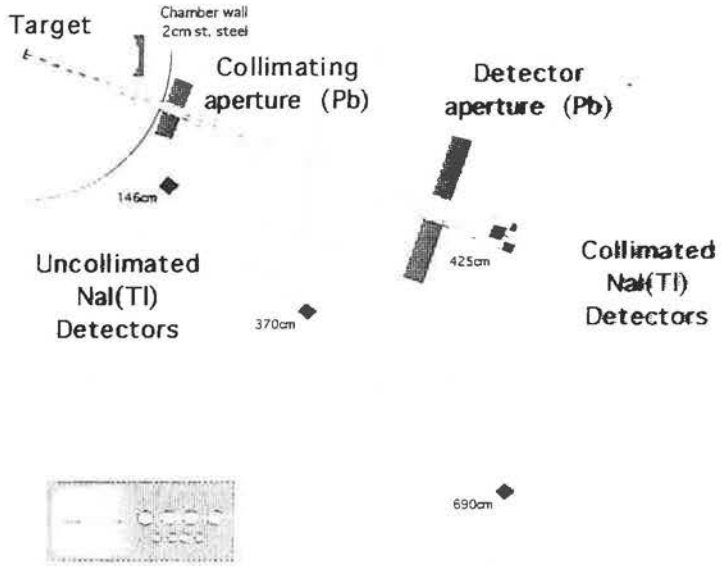

- Uncollimated detectors: diffused background
- Collimated detectors: target emission

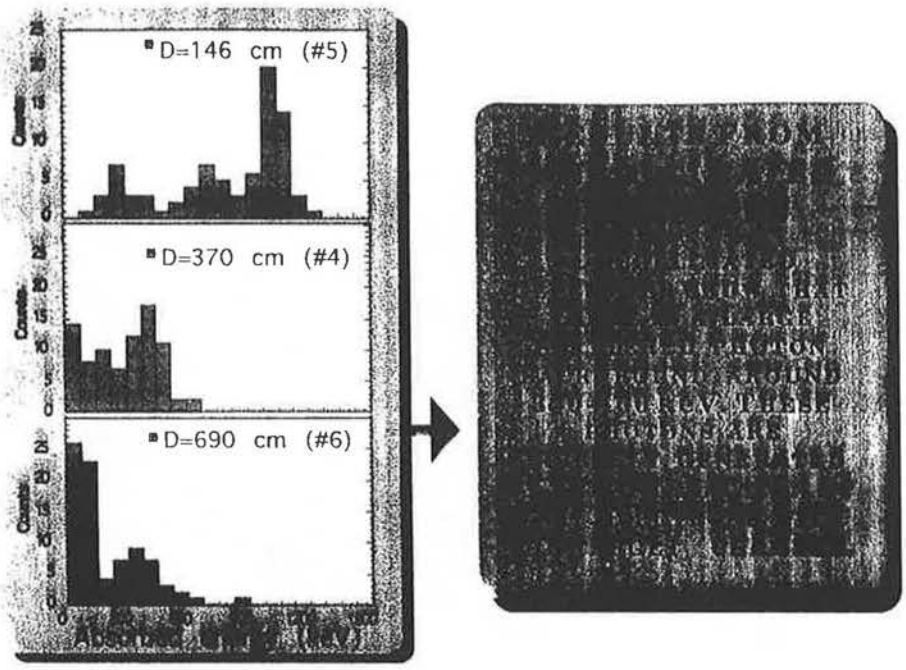
D=146 cm (#5)
D=370 cm (#4)
D=690 cm (#6)

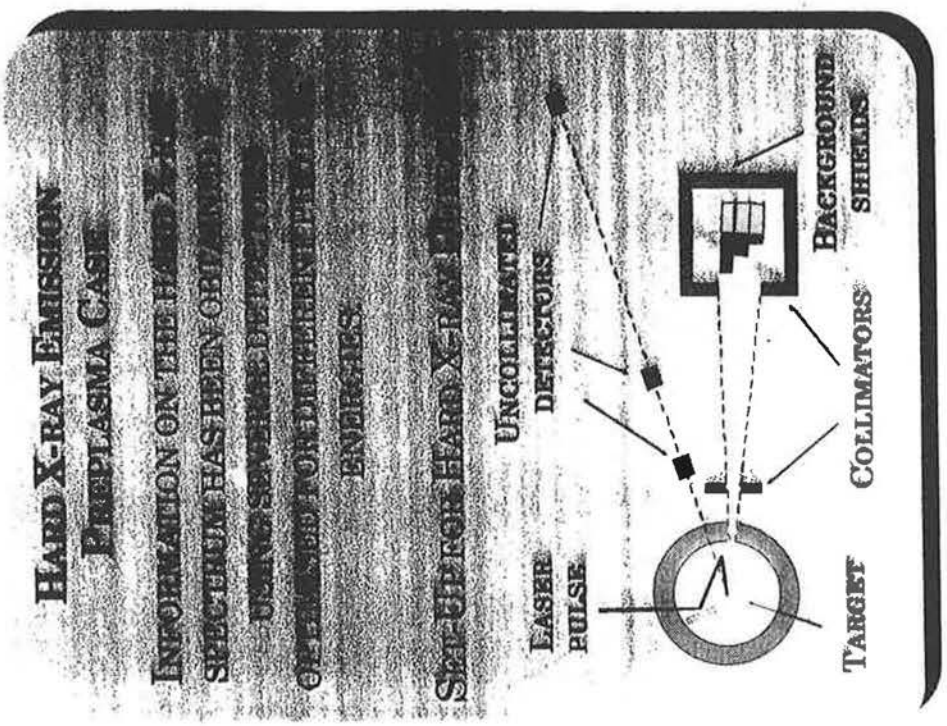
HARD X-RAY EMISSION
PLASMA CASE
INFORMATION ON
SPECTRUM HAS BEEN
ENERGETICS
UNCOLLIMATED
DETECTORS
LASER
PULSE
BACKGROUND
SHIELDS
COLLIMATORS
TARGET

- Discussion and theoretical issues at
  Pisa SILASI "TOP" Summit - **T**ransmittivity of **O**verdense **P**lasmas July 25th, 1998
- Teychenné *et al* . PR E (Rapid Comm.) **58**, 1245 (1998) based on
  S.C.Wilks*et al* . PRL **61**, 337 (1988)
- Problem of ultrafast (virtually *single-cicle*) ionisation of an initially transparent medium (magnetic field, etc.)
- Data from other experiments: Kodama *et al*, Fast Ignition W., Garching 1997: J.Fuchs *et al* . PRL **80** 2326 (1998), Jena group (in publication).....
- It is crucial to characterise each experiment in terms of the effect of the prepulse on the target, e.g. interferometrically
- How to measure magnetic fields into overdense plasmas?

consiglio nazionale delle ricerche ——— **IFAM -----> • <----- Pisa**

IFAM